Proceedings of the

FLUID AMPLIFICATION SYMPOSIUM

October 1965

VOLUME II

U.S. ARMY MATERIEL COMMAND
HARRY DIAMOND LABORATORIES
WASHINGTON, D.C. 20438

BLANK PAGES
IN THIS
DOCUMENT
WERE NOT
FILMED

DISCLAIMER NOTICE

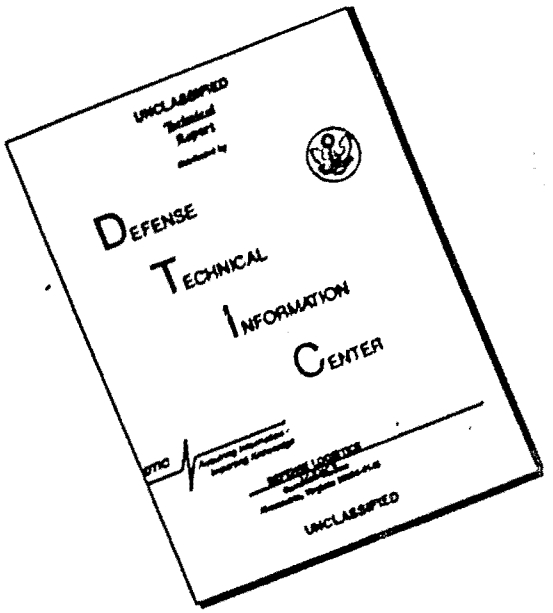

THIS DOCUMENT IS BEST QUALITY AVAILABLE. THE COPY FURNISHED TO DTIC CONTAINED A SIGNIFICANT NUMBER OF PAGES WHICH DO NOT REPRODUCE LEGIBLY.

Proceedings of the

FLUID AMPLIFICATION SYMPOSIUM

Sponsored by the

HARRY DIAMOND LABORATORIES

26, 27, and 28 October 1965

VOLUME II

U.S. ARMY MATERIEL COMMAND
HARRY DIAMOND LABORATORIES
WASHINGTON, D.C. 20438

CONTENTS

CONTENTS (Cont'd)

HARRY DIAMOND LABORATORIES
Washington, D.C. 20438

A TEMPERATURE-INSENSITIVE PNEUMATIC OSCILLATOR AND A PRESSURE-CONTROLLED PNEUMATIC OSCILLATOR

by

J. M. Kirshner
C. J. Campagnuolo

ABSTRACT

Theoretical developments and confirmatory experimental results are given for (1) an oscillator insensitive to temperature (over a limited range) and (2) an oscillator with frequency proportional to pressure.

1. A Temperature-Insensitive Oscillator

For certain purposes it is desirable to have a pneumatic oscillator whose frequency is relatively insensitive to temperature.

Although the speed of sound in free space is prcportional to the square root of the temperature, the complex speed of propagation of a wave in a duct is a function of the distributed inertance, capacitance, and resistance.

The magnitude of the complex speed of propagation in a duct of constant cross section is given approximately for small amplitude waves by

$$|c|^4 = \frac{a^4}{1 + \frac{R^2}{\omega^2 L^2}} \qquad (1)$$

where c = complex speed of wave propagation
a = free speed of sound, proportional to $T^{1/2}$
T = temperature
R = resistance per unit length of duct
ω = angular frequency
L = inertance per unit length

R and L in turn are given for a circular duct by

$$R \cong \frac{8\pi\mu}{A^2}$$

$$L = \frac{\rho}{A}$$

where μ = viscosity, approximately proportional to $T^{3/4}$
A = area of the duct
ρ = density of the fluid used

On the basis of the ideal gas law,

$$\rho = \frac{p}{R_g T}$$

where R_g is the gas constant for the particular gas used.

In terms of the temperature then,

$$|c|^4 = \frac{a_1}{\frac{1}{T^2} + \frac{a_2\ T^{3/2}}{\omega^2\ A^2\ p^2}} \qquad (2)$$

where a_1 and a_2 are constants.

Inspection of equation 2 shows that for $T = 0$ and for $T \to \infty$, $|c| = 0$; consequently $|c|$ has a maximum value at some temperature and should be least sensitive to temperature in the vicinity of the maximum.

It follows that if a uniform duct is used in the feedback path of the oscillator, the frequency will be temperature insensitive if the speed of propagation is temperature insensitive since

$$\omega = \frac{2\pi|c|}{\ell} \qquad (3)$$

where ℓ is the path length (which in many oscillators will be twice the length of the duct used).

In general the uniform duct will not make up the entire path length of interest. This, however, will affect the results only quantitatively; i.e., there will still exist a range of temperature insensitivity.

It should be noted, however, that temperature insensitivity is obtained at the expense of pressure sensitivity. This can be seen from equation 2 which shows that whereas for large A, the speed of propagation is pressure insensitive, for small A, the propagation speed, and consequently the frequency, becomes pressure sensitive.

Since $|c|$ obviously is maximum when the denominator of (2) is a minimum, for the sake of simplicity we seek this minimum.

$$D \equiv \frac{1}{T^2} + \frac{a_2 T^{3/2}}{\omega^2 A^2 p^2}$$

$$\frac{dD}{dT} = -\frac{2}{T^3} + \frac{3a_2 T^{1/2}}{2\omega^2 A^2 p^2}$$

Setting this equal to zero,

$$T_m = \left(\frac{4\omega^2 A^2 p^2}{3a_2}\right)^{2/7} \qquad (4)$$

This gives the temperature T_m at which the magnitude of the complex speed of sound will be a maximum for a given angular frequency ω, static pressure p, and cross-sectional area A.

The procedure for making the oscillator insensitive to temperature in the vicinity of a given temperature T_1 is to let $T_1 = T_m$ of equation 4. This determines the required value of ωAp. For a given A and p, this, therefore, specifies ω.

From equation 2, $|c|$ is then given. Finally equation 3 is used to specify ℓ. The frequency as a function of temperature is then of the form of figure 1.*

We expect any oscillator, whether with lumped or distributed parameters, to act similarly with temperature although in many cases the materials of the oscillator may disintegrate or melt before reaching the temperature at which the frequency is maximum.

The frequency may be made even less sensitive to temperature by the following procedure.

Let the feedback path length $\ell = \ell_1 + \ell_2 + \ldots \ell_n$.

One can choose ducts of length ℓ_1, ℓ_2, etc, each of a slightly different cross section so that for a given frequency, the speed of propagation reaches its maximum at a slightly different temperature for each length. The frequency will then be given by

$$\omega = \frac{2\pi}{\frac{\ell_1}{|c_1|} + \frac{\ell_2}{|c_2|} + \cdots + \frac{\ell_n}{|c_n|}} \qquad (5)$$

***Figures 1 through 8 appear on pages 12 through 19.**

A simpler procedure is to use a converging duct.

By use of this technique the curve can be flattened in the vicinity of its maximum.

Actually this procedure is not necessary because small ducts of uniform cross section act in many respects as converging ducts. In particular, because of the frictional effects, the Mach number, static pressure, and static temperature are functions of position along the duct; the Mach number increases and both the static pressure and the static temperature decrease in the downstream direction. As a result, the speed of wave propagation is a function of position in the duct and as the stagnation temperature changes, the speed of propagation increases in one part of the duct while decreasing in another part (if the parameters are properly chosen).

Equation 4 is adequate for determining the region of temperature insensitivity with A and p given; however, this may require excessively long feedback paths. It is therefore advantageous practically to start with a given length in which case the calculation is somewhat more cumbersome.

From (2) and (3) we obtain

$$\left(\frac{\omega \ell}{2\pi}\right)^4 = |c|^4 = \frac{a_1}{\frac{1}{T^2} + \frac{a_2 T^{3/2}}{\omega^2 A^2 p^2}}$$

or

$$\omega^2 = -\frac{a_2 T^{7/2}}{2A^2 p^2} + \frac{1}{2}\sqrt{\frac{a_2^2 T^7}{A^4 p^4} + \frac{4a_1 (2\pi)^4 T^2}{\ell^4}} \qquad (6)$$

The procedure is similar to that previously used; i.e., the temperature is found from equation 6 for which ω^2 is a maximum after which A and p are chosen for a given ℓ to make the temperature maximum (i.e., the region of insensitivity) occur in the vicinity of the temperature at which operation is desired.

2. A Pressure-Controlled Oscillator

Equation 6 shows that the oscillator may under certain conditions be forced to oscillate at a frequency approximately proportional to the pressure. To do this, it is necessary only to choose ℓ, A, and p so that

the second term under the radical of equation 6 is small compared with the first term, in which case

$$\omega^2 \cong -\frac{a_2 T^{7/2}}{2A^2 p^2} + \frac{a_2 T^{7/2}}{2A^2 p^2}\left[1 + \frac{2(2\pi)^4 a_1 A^4 p^4}{\ell^4 a_2^2 T^5}\right] \tag{7}$$

whence

$$\omega \cong \frac{(2\pi)^2 A a_1^{1/2}}{\ell^2 T^{3/4} a_2^{1/2}} p \tag{8}$$

which is the relation desired for a pressure-controlled oscillator. For maximum sensitivity the coefficient of p in equation 7 should be made as large as possible but with the restriction that the second term under the radical of equation 6 remain small compared with the first term. Since ℓ and A enter equation 6 as terms of the fourth degree but A is only of the first degree in equation 7 whereas ℓ is of second degree, it follows that a reduction of ℓ keeping the ratio of A/ℓ constant will result in a larger coefficient of p without a change in the accuracy of the approximation.

It is useful to normalize equation 7 as suggested by J. R. Keto. Returning to equation 1 and using the previously given values for R, L, etc, Keto obtains

$$\frac{\omega}{\omega_o} = \frac{1}{\eta\sqrt{2}}\left\{(1+4\eta^4)^{1/2} - 1\right\}^{1/2} \tag{9}$$

where

$$\omega_o = \frac{2\pi a}{\ell}$$

and

$$\eta = \frac{Aa}{4\ell\mu} \rho = \frac{Aa}{4\ell\mu R_g T} p$$

A plot of ω/ω_o as a function of η is shown in figure 2, where it is seen that the relationship is approximately linear for $\eta < 0.5$.

3. Experimental Results

The oscillator tested is shown in figure 3. A binary amplifier was used because of its higher gain. Appreciable gain is needed to make up for the attenuation that occurs in the feedback line. In spite of the fact that a binary amplifier was used, an output that was almost sinusoidal was obtained because of the filtering action of the feedback line.

Figure 4 shows the experimental curve in the vicinity of its maximum for the oscillator whose theoretical curve* is given in figure 1. As expected, the curve is flatter than the simple theory predicts probably for the reasons given; i.e., the Mach number in the feedback line, and consequently both temperature and pressure in the line are functions of position.

The temperature region at which the frequency peaks is shifted appreciably from the theoretical curve; however, error is to be expected because of the many variables not taken into account; these include the variations of Mach number with position, the capacitance of the amplifier itself, the switching time of the amplifier, and the nonlinear effects due to the waves being of large amplitude.

Figure 5 shows that with a feedback line of smaller cross-sectional area, the peak is shifted to lower temperatures as predicted, and the frequency then decreases with increasing temperature.

In figure 6, the theoretical frequency/pressure dependence is compared with the experimental values. The discrepancy between the curves is not so great as that between theoretical and experimental frequency peaks, but is undoubtedly due to the same causes.

In order to determine whether this effect occurs in lumped circuits, the oscillator of figure 7 was tested. It was found that the feedback resistance could be adjusted to obtain a frequency peak in the same temperature region. The curve obtained in this case (figure 8), however, is not as flat as when a duct is used in a distributed RC feedback oscillator.

---

*The curves of figures 1 and 6 are obtained using the equations given in this paper and with the assumption that the Mach number in the duct is unity; however, it should be noted that the Mach number may be appreciably different from unity at the duct entrance and reaches unity only at the exit. In addition, the assumptions under which equation 1 is derived do not hold (small signals, constant viscosity); hence, quantitative agreement is not to be expected.

FIGURE 1

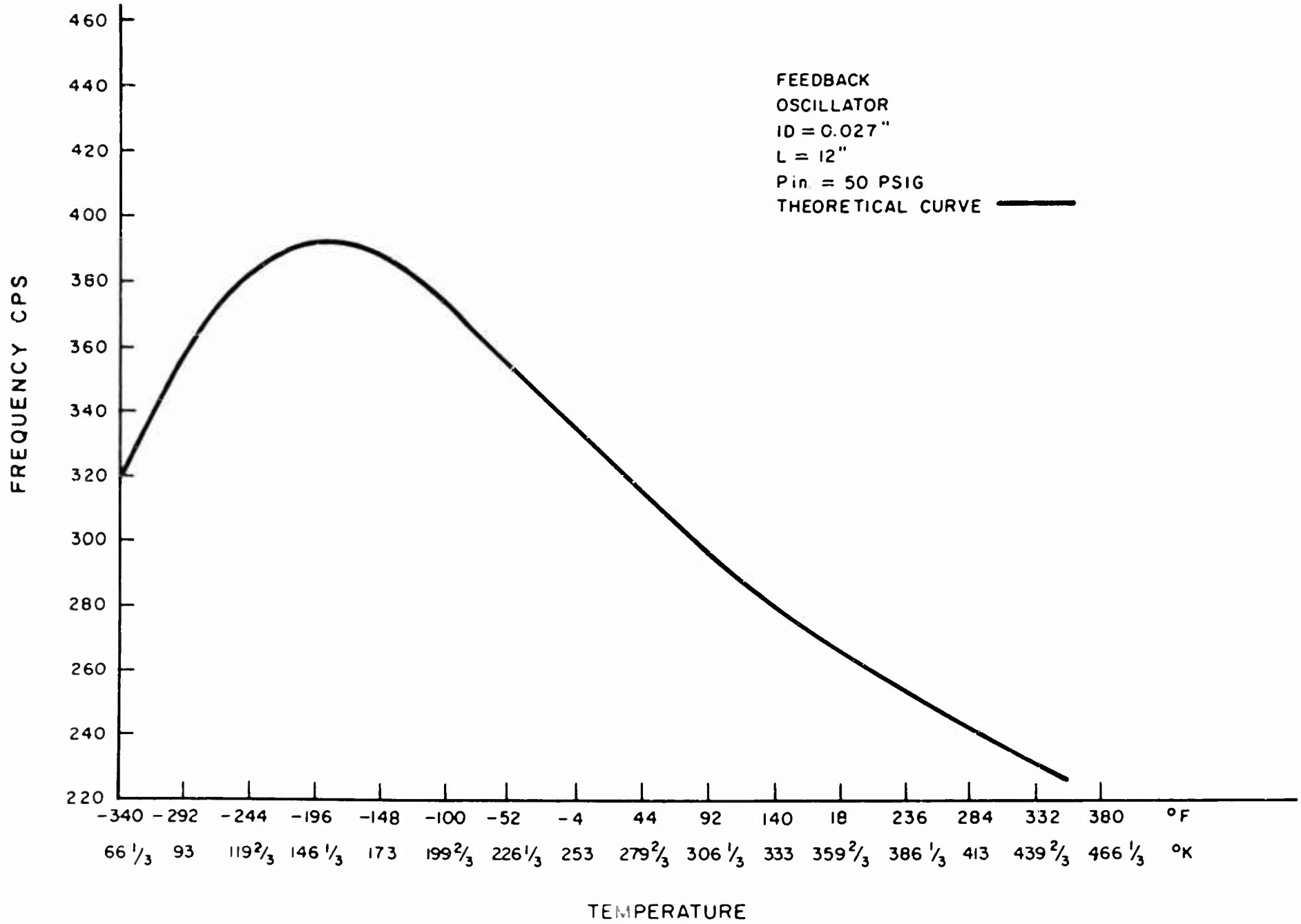
FEEDBACK
OSCILLATOR
ID = 0.027"
L = 12"
Pin = 50 PSIG
THEORETICAL CURVE
FREQUENCY CPS
460
440
420
400
380
360
340
320
300
280
260
240
220
-340 -292 -244 -196 -148 -100 -52 -4 44 92 140 18 236 284 332 380 °F
66 1/3 93 119 2/3 146 1/3 173 199 2/3 226 1/3 253 279 2/3 306 1/3 333 359 2/3 386 1/3 413 439 2/3 466 1/3 °K
TEMPERATURE

$$\frac{\omega}{\omega_o} = \frac{1}{\eta\sqrt{2}}\left\{-1+\sqrt{1+4\eta^4}\right\}^{1/2} \quad ; \text{WHERE} \quad \omega_o = \frac{2\pi a}{l}$$

$$\eta = \frac{A\sigma}{4l\mu}\,\rho = \frac{A\sigma}{4l\mu R_g T}\,\rho$$

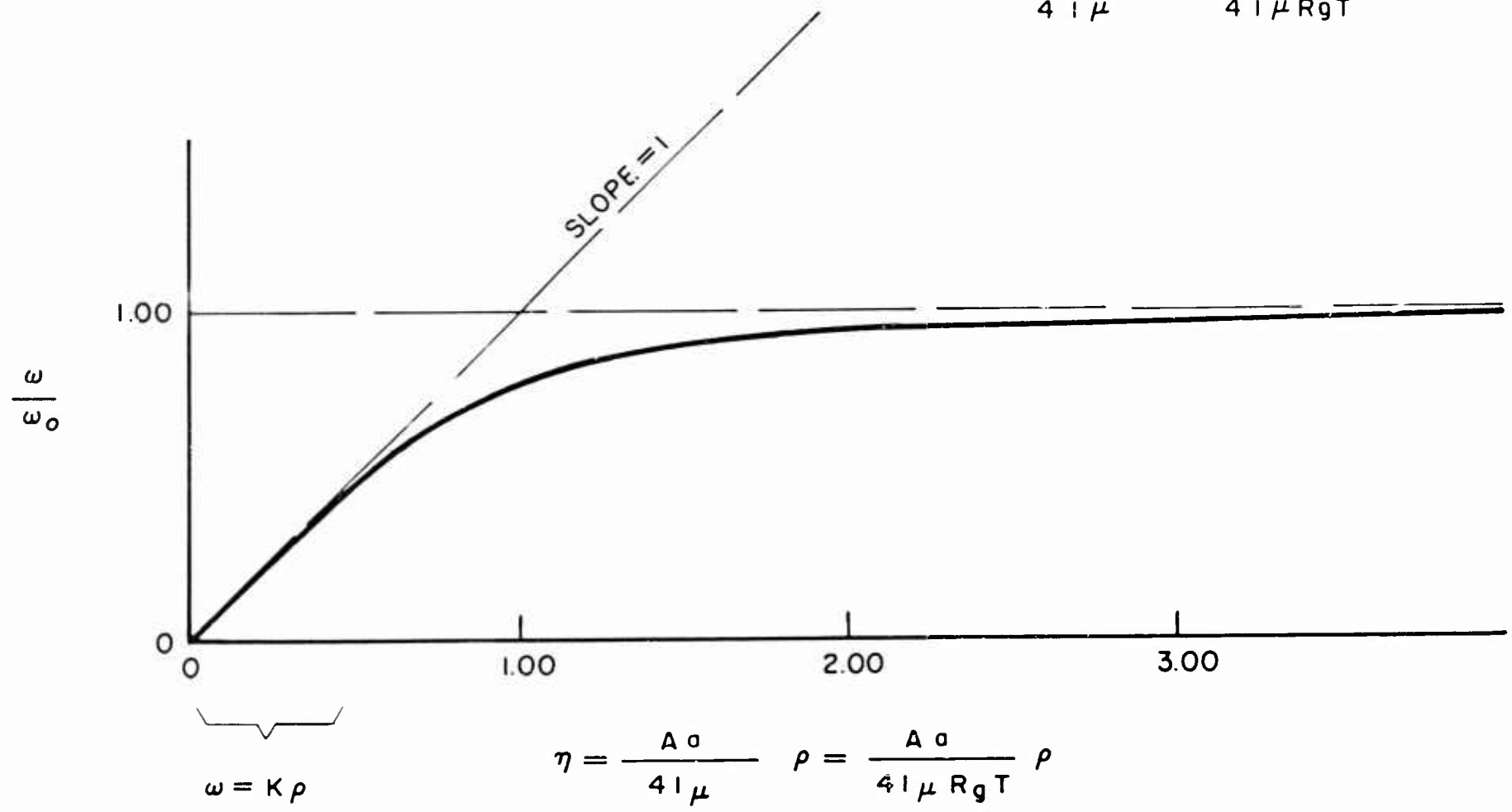

FIGURE 2 THEORETICAL CURVE FOR PRESSURE CONTROLLED OSCILLATOR

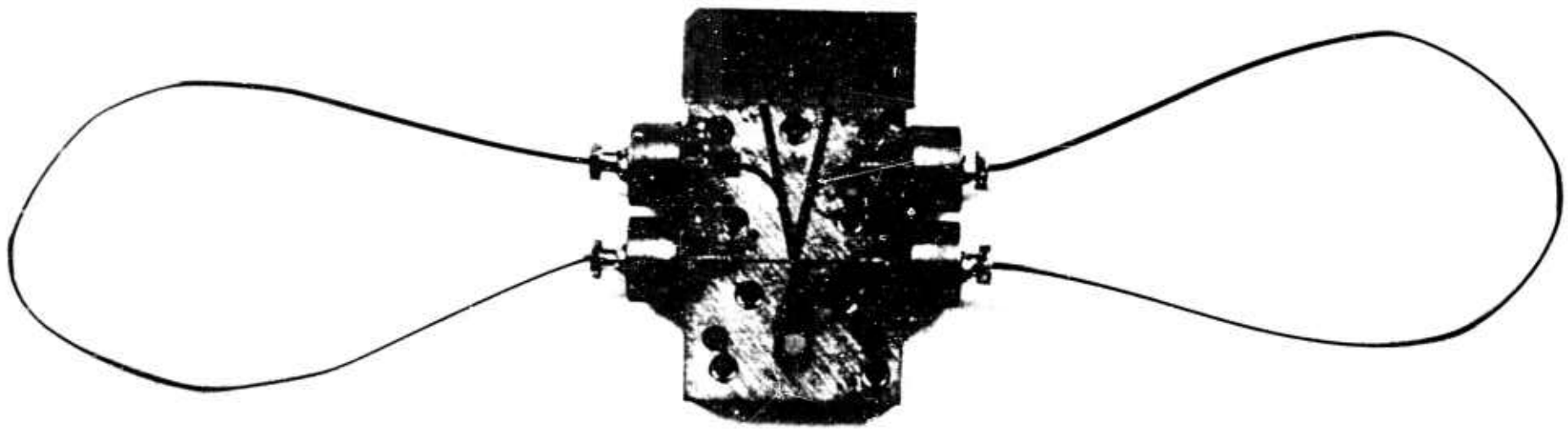

FEEDBACK OSCILLATOR USING DISTRIBUTED PARAMETER DUCT

FIGURE 3

FIGURE 4

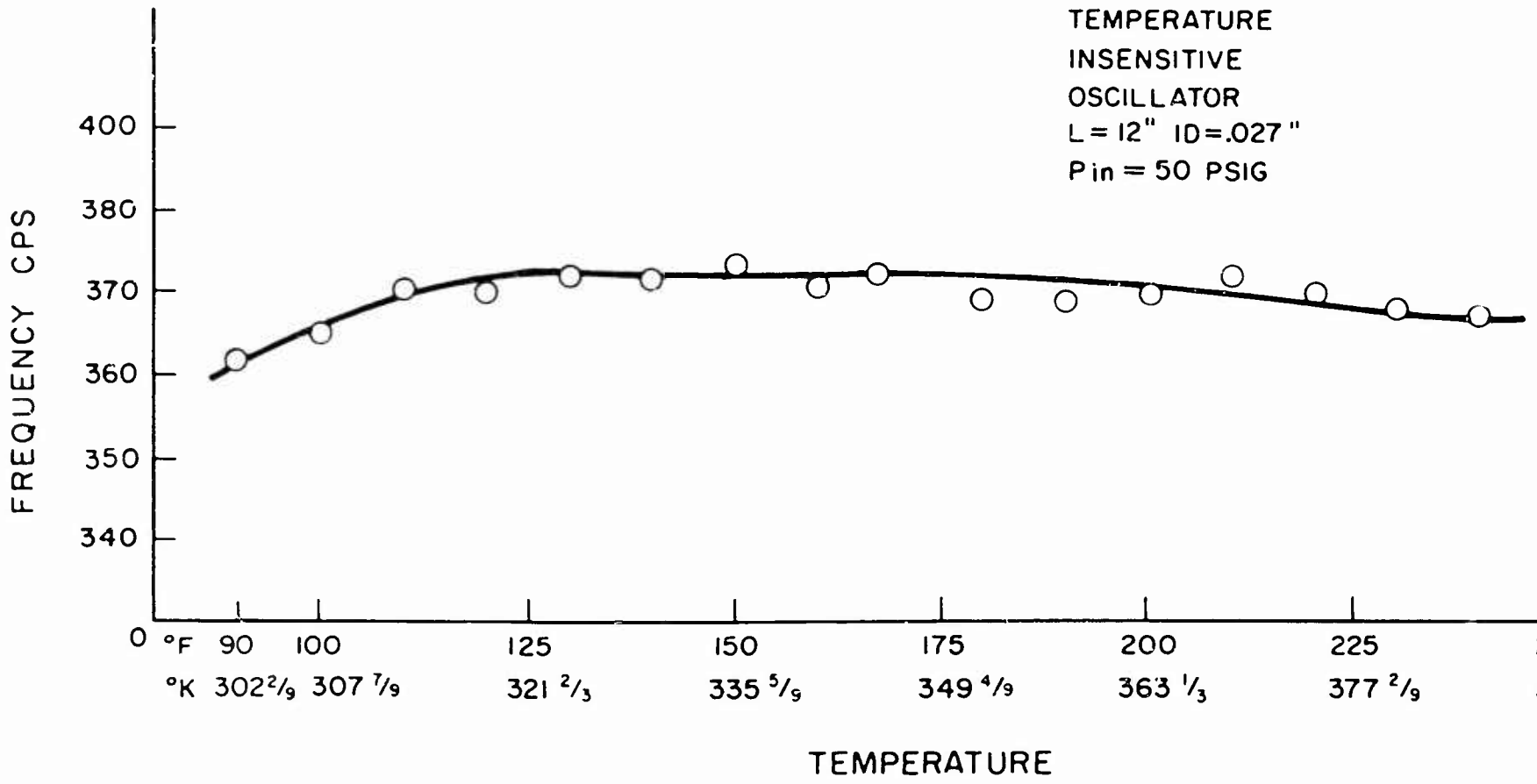
TEMPERATURE
INSENSITIVE
OSCILLATOR
L = 12" ID=.027"
Pin = 50 PSIG
FREQUENCY CPS
400
380
370
360
350
340
0
°F 90 100 125 150 175 200 225 250
°K 302 2/9 307 7/9 321 2/3 335 5/9 349 4/9 363 1/3 377 2/9 391 1/9
TEMPERATURE

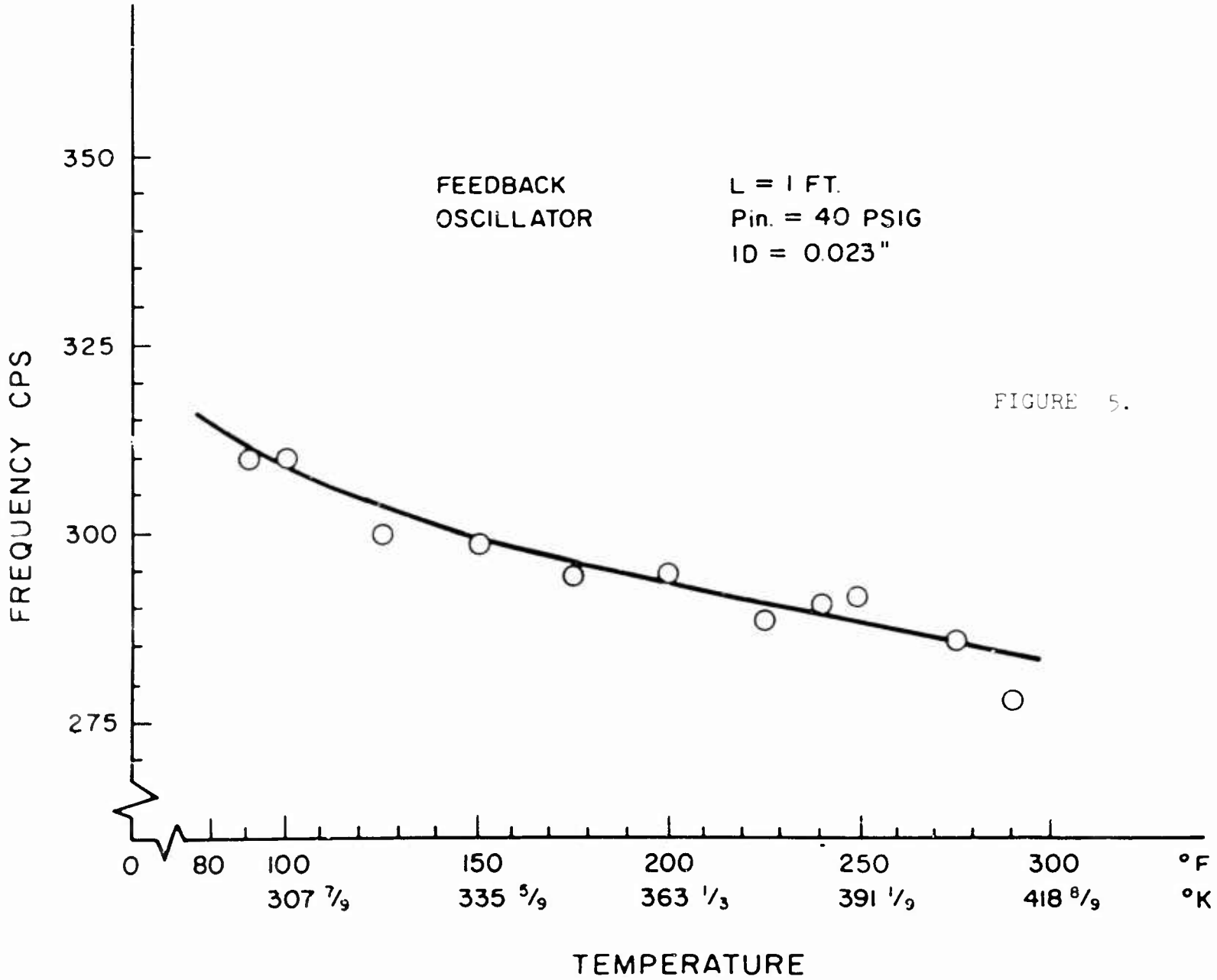
FEEDBACK
OSCILLATOR
L = 1 FT.
Pin. = 40 PSIG
ID = 0.023"
FREQUENCY CPS
350
325
300
275
0
80
100
150
200
250
300
°F
307 7/9
335 5/9
363 1/3
391 1/9
418 8/9
°K
TEMPERATURE

FIGURE 5.

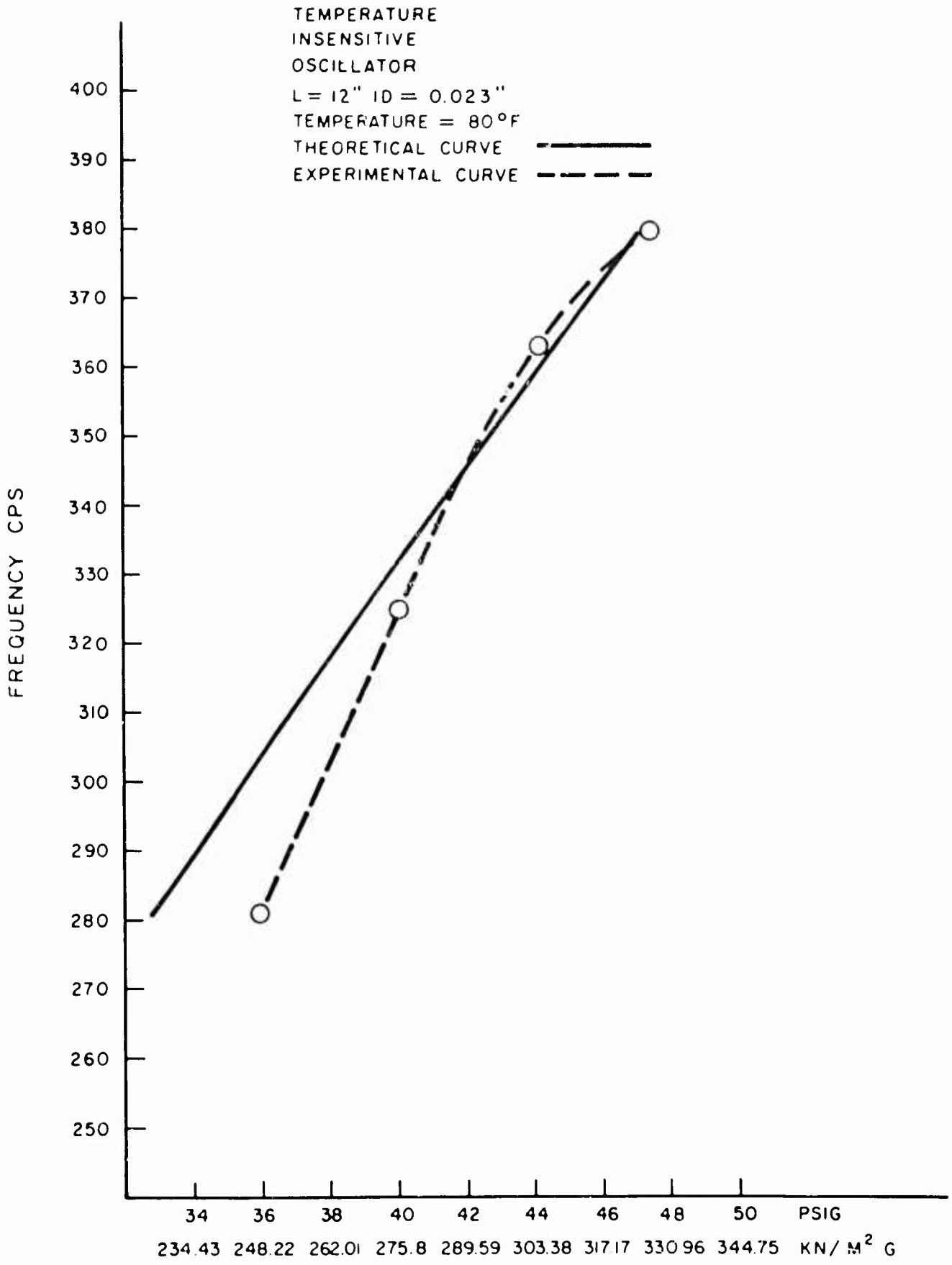
TEMPERATURE
INSENSITIVE
OSCILLATOR
L = 12" ID = 0.023"
TEMPERATURE = 80°F
THEORETICAL CURVE
EXPERIMENTAL CURVE
FREQUENCY CPS
400
390
380
370
360
350
340
330
320
310
300
290
280
270
260
250
34
36
38
40
42
44
46
48
50
PSIG
234.43
248.22
262.01
275.8
289.59
303.38
317.17
330.96
344.75
KN/M2 G
INPUT PRESSURE

FIGURE 6

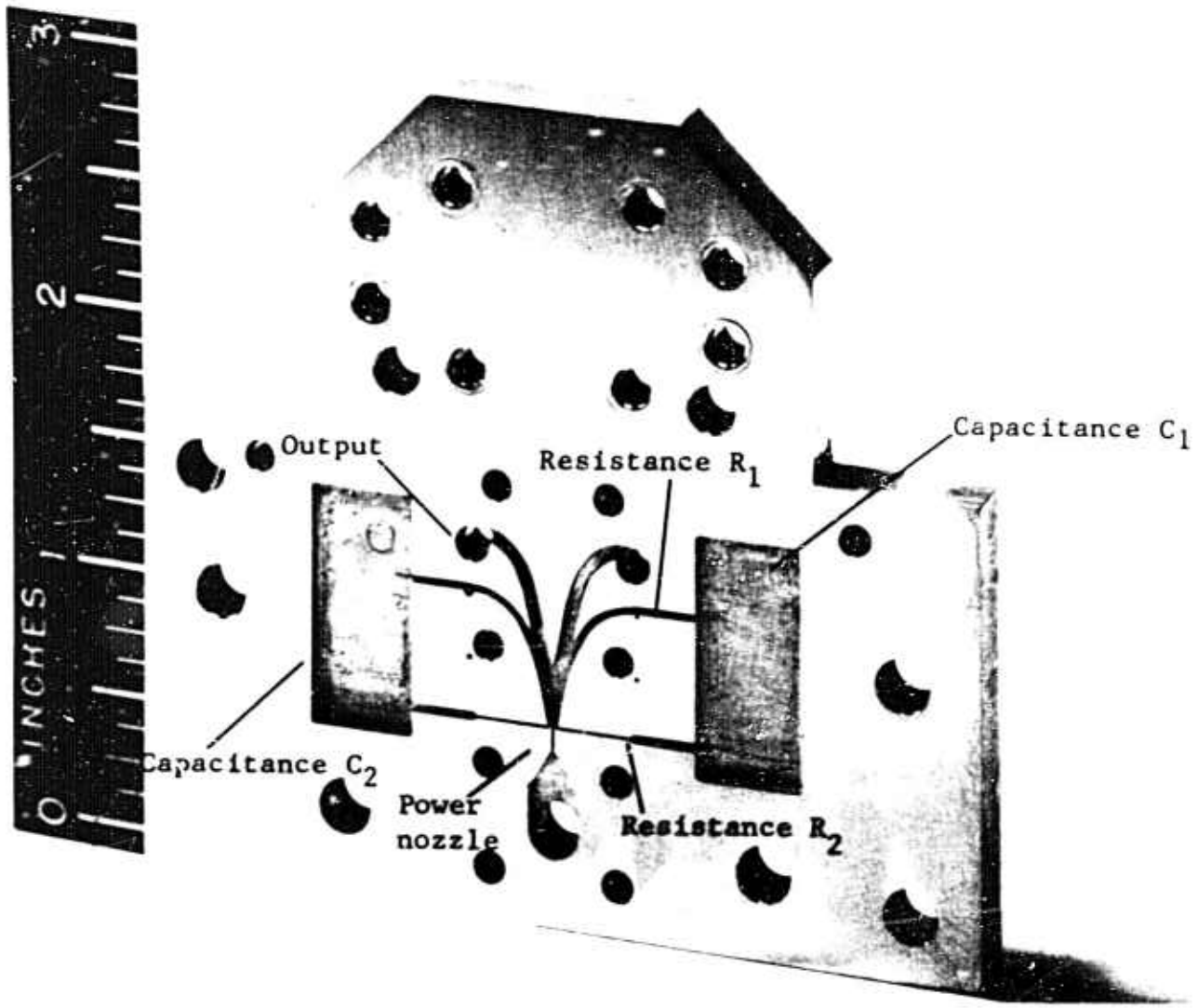

FIGURE 7. RELAXATION OSCILLATOR

FIGURE 8

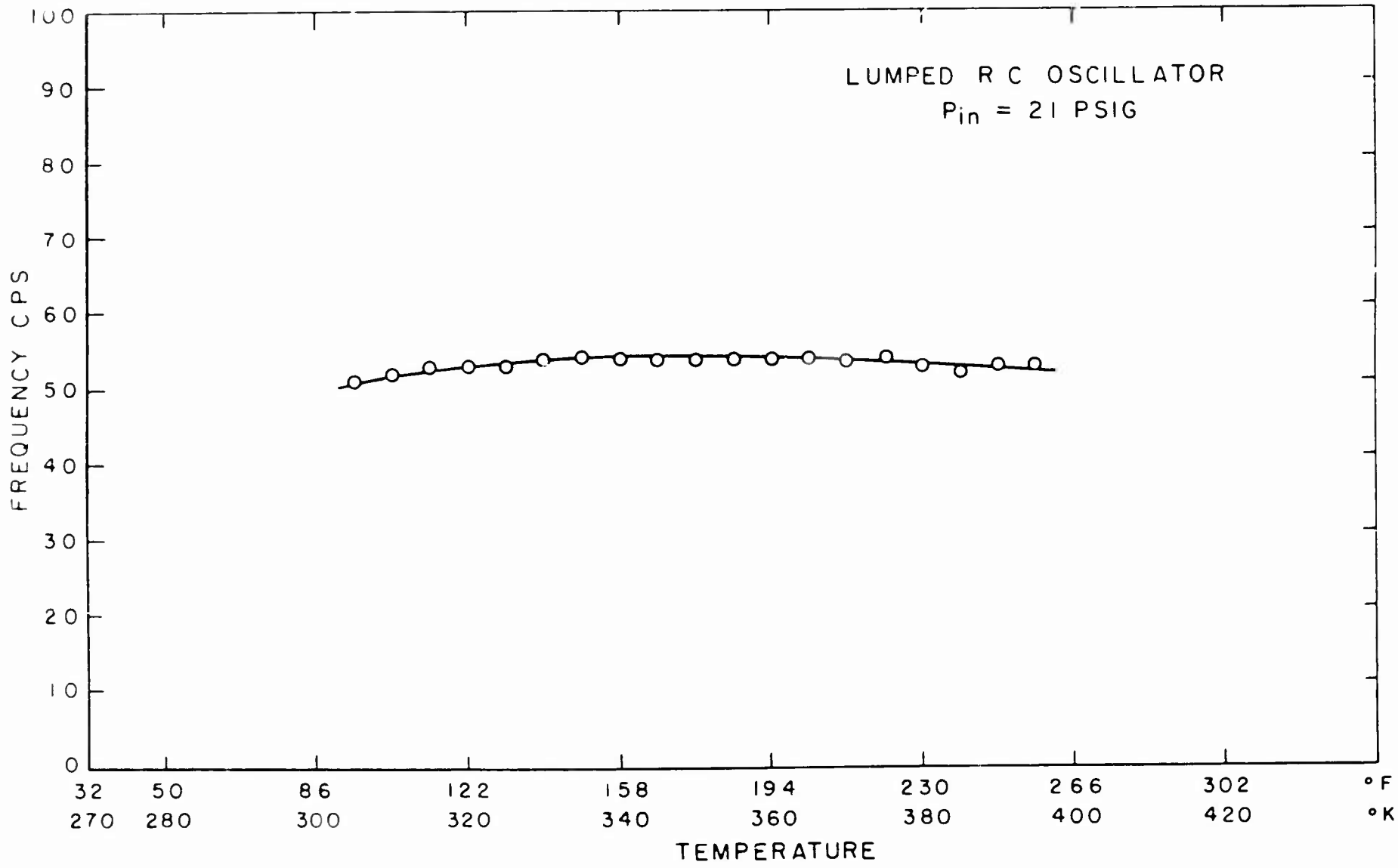
LUMPED R C OSCILLATOR
P_{in} = 21 PSIG
FREQUENCY CPS
100
90
80
70
60
50
40
30
20
10
0
32 50 86 122 158 194 230 266 302 °F
270 280 300 320 340 360 380 400 420 °K
TEMPERATURE

DEVELOPMENT OF A PRESSURE CONTROLLED OSCILLATOR FOR FM SYSTEMS

R-7-11-65

Francis M. Manion
Bowles Engineering Corporation

PRESSURE CONTROLLED OSCILLATOR

Summary

A primary component in the development of a frequency modulating system is the Pressure Controlled Oscillator which converts a pressure signal from a sensor into an equivalent frequency.

This section describes the development of a PCO. A schematic is shown with some performance test data in Figure 1.* This oscillator has a linear relationship between signal input pressure and output frequency with a conversion rate of over 800 cycles per second per psi and a useful range of 80 cps, (± 40 cps) when operating around 100 cps.

The oscillator is a feedback type that utilizes a change in jet transport time to change its frequency. This is accomplished by the design of a special feedback circuit to effect the necessary phase shift in the feedback loop to obtain the linear relationship. The development of this oscillator was preceded by a survey of the available types of pure fluid oscillators. The results of this survey indicated that the proportional feedback type was most promising. A conceptional model was then developed with the aid of some experiments. The mathematical study determined the design requirements for a linear characteristic.

Preliminary Evaluation

In the preliminary evaluation of oscillators, to determine which type was most suited as a pressure controlled oscillator, four different oscillator techniques were evaluated. These are

Feedback Oscillator
Coupled Control Oscillator
Load Sensitive Oscillator
Turbulence Oscillator

The operation of each of these oscillators is described below and is followed by an evaluation of their applicability as a pressure controlled oscillator.

Feedback Oscillator

The feedback oscillator is shown in Figure 2. This device is similar to the standard fluid amplifiers. The output signal is fed back and

*Figures start on page 33.

applied as a negative signal at the amplifier's control port. The amplifier car be either a digital (bistable) device or a stream interaction proportional element. In the case of the bistable element, the output signal is fed back to switch the jet. In a proportional element, the power stream is continually directed by the difference of the two control streams and, therefore, the output is essentially sinusoidal. The frequency of the feedback oscillator is determined by the transport time of the stream between the nozzle and the collectors and by the passive components in the feedback path. A bistable amplifier exhibits a sawtooth characteristic in its feedback path as the pressure builds up to the switch level and then decays after the device changes state. A proportional element has to have considerable phase lag in its feedback path in order to oscillate. This is because the transport time of the power jet from the nozzle to the output collectors is very small and for a given frequency the phase lag is small. As a result, the feedback impedance of this oscillator must include resistance, inductance, and capacitance components to obtain sufficient phase shift for the oscillation to occur. The variable frequency characteristics are obtained by using the transport time of the jet or its variance of entrainment which will cause different switch levels for the bistable device.

Coupled Control Oscillator

The coupled control oscillator is a bistable element, Figure 3. This element increases its frequency somewhat as the supply pressure is increased. The frequency of operation depends on the resistance and inductance and capacitance effects of the inter-connected control ports. When the pressure is applied, the resulting jet attaches itself to one of the sidewalls. This introduces, by aspiration, a negative pressure in the control port of this sidewall, and this pressure forces fluid to move toward the low pressure control port. The time required to establish flow to the level that will release the power jet from the sidewall is then determined by the sonic transport time and the response time of the passive network which couples the control ports. By raising the signal pressure, p_s , a decrease in the pressure in the attachment bubble occurs and as a result it increases the driving force in the interconnection line. This increased driving force is dominant and the time required to obtain the necessary flow tc switch the element is decreased for high pressure signals.

Load Sensitive Oscillator

The load sensitive oscillator shown in Figure 4 is, in a sense, the same type of oscillator as provided in the feedback device of Figure 2 except that the feedback path is along the sidewall of the output passageway. Again the power stream signal flow establishes itself on one sidewall and a negative pressure in the attachment bubble holds the

jet to the sidewall. However, in this element, as a pressure rises in the loaded output passage, the attachment bubble is broken and the power jet is released from the wall. The jet then attaches itself to the opposite sidewall and the sequence of events is repeated. In this type of element the time required for the pressure to break the attachment bubble is determined by the output leg volume and the flow rate into the volume. As a result, the time for a cycle of events to occur decreases as supply pressure increases.

Turbulence Oscillator

The turbulence or Bell amplifier is used as a bistable element and changes state by a transition from a laminar to a turbulent flow regime. This element is shown in Figure 5. These amplifiers can be made to oscillate by a simple feedback connection. In this arrangement the initial jet is laminar and the pressure recovery in the output is high. This output pressure is fed back as a control signal to cause the laminar jet to become turbulent. When the jet is turbulent, the output pressure is decreased. As the output pressure falls the control signal is reduced below a certain level, and the jet returns to its laminar flow condition. This device will change frequency somewhat as the signal jet's Reynolds Number is increased but the time required for the laminar condition to be re-established is the most significant part of the response time.

Evaluation

In evaluating all the possible variable frequency oscillator approaches, the classical feedback oscillator, shown in Figure 2, has demonstrated that it is sufficiently stable to perform the desired function. Each of the other approaches has definite drawbacks. The coupled control port oscillator is relatively insensitive to signal pressure variation. This is because the increased driving force obtained by the decrease in the bubble pressure with increasing pressure is for the most part compensated by a requirement for a high switching flow level. The result is that no significant change in frequency occurs with increasing supply. The load sensitive oscillator by its very nature is insufficiently stable, expecially when coupled to another element which varies its load. In the turbulence amplifier the switching cycle is primarily governed by the recovery time of the jet stream from the turbulent conditions. This is the predominant effect. The frequency of oscillations are far below any transport time that can be computed by the time constant of the feedback path. As a result, this element is rather insensitive to supply pressure changes. The evaluation concluded that the feedback oscillator provides the best method to obtain a stable oscillator which will convert a signal pressure into an equivalent frequency.

Feedback Oscillator

The feedback oscillator can make use of either the wall attachment phenomenon or the stream interaction principle to attain the gain necessary for oscillation. The stream interaction proportional amplifier was selected because of its stability and because the jet transport time could be used as a means to vary frequency. The bistable device seems to be more susceptible to random noise at the input. For example, if a fluctuation is in or out of phase with the returning control signal, the element will change state early or late.

After some study and a few tests, a method to obtain a proportional variable frequency oscillator was devised. The basic concept of this oscillator is a negative feedback in which the gain is greater than one and the oscillation frequency is determined by the frequency at which the phase shift around the feedback loop is 180 degrees as described by Bode's treatment of instability. The phase lag around the loop can be considered to be made up of the transport lag and the phase lag of the RLC components in the passive network. The transport lag is related to the velocity of the fluid and, therefore, this decreases as the pressure signal increases. Figure 6 shows graphically the phase angle frequency relationship for the transport lag and the feedback lag. Note that the phase shift of the transport lag increases with frequency and that the lag introduced by the RLC components increases up to 180 degrees and thereafter remains constant. If these two phase lags are summed, they will produce a phase shift curve which is zero at low frequencies and increases toward infinity as the frequency increases. At the point where the summed phase shift becomes 180 degrees the unit is unstable and this is the frequency of the oscillation.

If the pressure signal is increased, the transport lag decreases and hence at any specified frequency the transport phase lag also diminishes. In effect, therefore, the transport lag curve moves to the right with increasing supply pressure. Now, for the higher supply pressure, the phase lag components can be added and it will be found that the point at which the 180-degree phase shift occurs has moved to a high frequency. This is the mechanism of generating a frequency dependent upon supply signal pressure.

The next consideration is to determine the design which will yield a linear relationship between the supply pressure and the frequency. It can be seen that the shape of the transport lag curve does not change with supply pressure but moves only from the left to right. However, the RLC lag curve can be designed for various frequencies and slopes by choosing appropriate components of resistance, capacitance, and

inductance for the feedback path. A mathematical analysis was performed to determine the feedback network necessary to obtain a linear characteristic.

Analysis

In order to analyze the oscillator's performance, the equation for phase shift around the loop can be written:

$$\phi_1 + \phi_2 = \pi \tag{1}$$

and therefore differentiating with respect to frequency

$$\frac{d\phi_1}{d\omega} + \frac{d\phi_2}{d\omega} = 0 \tag{2}$$

ϕ_1 - transport phase angle

ϕ_2 - feedback phase angle

ω - frequency

The first equation is necessary for an oscillation to exist. The second equation is required if the oscillation is to have any frequency range and not exist only at a unique point.

Assume that

$$\phi_1 = l\sqrt{\frac{\rho}{2p}}\,\omega \tag{3}$$

$$\phi_2 = f(\omega) \tag{4}$$

where ϕ_1 is the phase shift contribution of the transport time and ϕ_2 is the phase shift due to the feedback network.

The phase lag due to the RLC feedback network increases with frequency. Therefore, the transport phase angle must decrease with increasing frequency to satisfy the condition of equation (1); the total shift around the loop is constant at 180°. Inspection of equation (3) indicates that the pressure must vary as frequency to a power greater than two if the transport lag is to decrease with increasing frequency. Since relationships between pressure and frequency other than linear were not of interest, the feedback network must be designed to have a decreasing phase angle with increasing

frequency. This can be accomplished by an RLC network with a lead-lag compensation. In the frequency range where the phase lead is effective, the network will have a decreasing phase angle with increasing frequency.

For a linear pressure controlled oscillator the transport phase angle will increase as $\sqrt{\omega}$. This can be shown by substituting into equation (3). This substitution results in equation (5).

$$\phi_1 = 1\sqrt{\frac{\rho}{2}}\sqrt{\frac{\omega}{A}} \qquad (5)$$

If the transport phase angle increases as square root of frequency , then the feedback lag must decrease as the square root of frequency to maintain the 180° phase shift around the loop. The design of the feedback phase angle—frequency relationship governs the relationship between the pressure and frequency.

The desired feedback network was obtained by using an RLC followed by a lead-lag circuit. The electrical analog can be shown as follows:

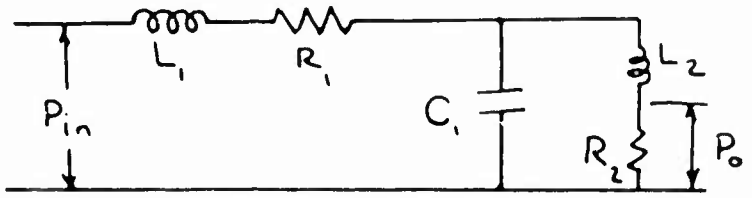

The network relationship between P_o/P_{in} is defined as:

$$\frac{P_o}{P_{in}} = \frac{\frac{R_2}{R_1+R_2}\left(\frac{L_2}{R_2}S+1\right)}{\left(\frac{L_1L_2C}{R_1+R_2}\right)S^3+\left(\frac{R_2L_1C}{R_1+R_2}+\frac{R_1L_2C}{R_1+R_2}\right)S^2+\left(\frac{R_1R_2C}{R_1+R_2}+\frac{L_1+L_2}{R_1+R_2}\right)S+1}$$

This can be simplified by actual values to the following:

$$\frac{P_o}{P_{in}} = \frac{\frac{R_2}{R_1+R_2}\left(T_2S+1\right)}{\left(\frac{S^2}{\omega_n^2}+\frac{2\rho}{\omega_n}S+1\right)\left(T_1S+1\right)}$$

Since the time constant T_1 is smaller than the time constant T_2, the phase relationship appears as in Figure 7.

The feedback network has a decreasing phase lag between the frequencies ω_1 and ω_3, as shown. Included on this plot are the phase lag-frequency characteristics for three input signal pressures: P_1, P_2, and P_3. The associated frequencies at which the sum of the phase lags are 180° are ω_1, ω_2 and ω_3, respectively.

A more general analysis can be performed to show how the functional dependency between pressure and frequency is determined by the feedback network. Equation (2) defines the condition for the oscillation to exist continuously at other frequencies. If the definitions of equation (3) and (4) are substituted into equation (2) the P vs ω functional dependency on feedback design is determined.

To perform this substitution, assume that f (ω) of equation (4) can be approximated by the function

$$\Phi_2 = \Phi_2 - K\omega^n \tag{6}$$

for the frequency range of interest.

Differentiating equations (3) and (6) with respect to frequency results in the following expressions

$$\frac{d\Phi_1}{d\omega} = l\sqrt{\frac{\rho}{2}}\left[P^{-\frac{1}{2}} - \frac{1}{2} P^{\frac{1}{2}} \omega \frac{dP}{d\omega} \right] \tag{7}$$

and

$$\frac{d\Phi_2}{d\omega} = -nK\omega^{n-1} \tag{8}$$

The sum of equations (7) and (8) is the definition of equation (2). Summing these equations and using the general pressure frequency relation,

$$P = A\omega^m \tag{9}$$

The dependency of m on n is obtained. This dependency is obtained by noting that the solution must be independent of frequency. The relationship between m and n is:

$$m = 2(1-n) \tag{10}$$

For linear pressure to frequency characteristics n must equal 1/2. This means the phase angle due to the feedback network depends on frequency in the following manner:

$$\phi_2 = \Phi_2 - K\sqrt{\omega} \qquad \text{(For the useful range of this device)} \qquad (11)$$

Equation (9) defines the other pressure-frequency relationships that can be obtained with a feedback network whose phase angle can be approximated by equation (6). These relationships are:

for $P = o\omega$ $n = 1/2$

$P = c\sqrt{\omega}$ $n = 3/4$

$P = c\omega^{-1}$ $n = 3/2$

The function $P = \omega^m$ where m is greater than 2 can be obtained by a feedback network whose phase angle frequency relationship is defined by the equation:

$$\phi_2 = K\omega^n$$

For the case, $P = A\omega^2$, the functional relationship cannot be obtained because the transport lag will remain constant, that is, independent of frequency. This function can be approached in the design of a constant frequency oscillator.

The linear P vs ω relationship has a gain or conversion rate given by

$$\frac{\omega}{2\pi P} = \frac{1}{2\pi A}$$

The constant A depends on the other system constants and a meaningful expression can be obtained by using equation (1). This expression is

$$\text{Gain} = \frac{1}{A} = \frac{2}{l\rho}\left(\frac{\pi - \Phi_2}{\sqrt{\omega}} + K\right)^2 \qquad (12)$$

The gain or conversion rate depends on K, l, Φ_2 and ω. K and n are related to the damping ratio. As the damping ratio increases n decreases. This increases the conversion rate but since n is defined for a linear pressure-frequency characteristic, the exponent n does not determine gain. These constants are related to the pressure range and distance between jet nozzle and receiver. In general, for a fixed l, the higher the operating frequency, which means the higher the pressure range, the less the conversion rate.

Development Tests

The experimental approach was pursued to obtain a linear pressure controlled oscillator with a useful range of 70 to 80 cps centered at 100 cycles per second. This operating frequency was selected because it can easily be handled by existing digital systems.

The experimental method was used as a means to determine the effects of the non-linearity in the oscillator characteristics. It also permitted some optimization to be performed. Several minor design variations such as collector widths, distance between power nozzle, and receivers were made to a silhouette that gave a nearly linear relationship. These models were designed in silhouettes and fabricated by means of the Optiform process. The elements were then tested by use of the hot wire anemometer and a frequency to DC voltage converter. The test arrangement is shown in Figure 8.

The test arrangement was designed to plot, on an X-Y recorder, the characteristic relationship between pressure and frequency. The input pressure to the oscillator was monitored by anemometer and a Statham pressure transducer. The output frequency was detected by means of a hot wire anemometer and displayed on the oscilloscope for visual monitoring. The anemometer signal was also fed into the frequency meter which gave a DC output voltage directly proportional to the input frequency. The output of the frequency meter provided the other input to the X-Y recorder. The typical X-Y plot of the performance of the oscillator is shown in Figure 9.

The exceptionally large noise is characteristic of the frequency-to d.c. converter. The noise is the same when the converter is driven by an electronic sine wave generator, so that this noise is definitely not due to the pressure controlled oscillator.

The characteristic of Figure 9 is linear. Figure 10 shows other characteristics that were recorded. In the first case the frequency pressure slope increases with increasing pressure, indicating that the effective phase angle-frequency relationship is too flat (high damping ratio). The second curve shows a decrease of slope as the pressure increases and this indicates that the damping is too low. Figure 11 shows still another characteristic. In this figure the slope of the curve increases, then remains constant, and then further increases. This effect is due to the non-linearity of the resistance. Increasing the stream velocity increases the resistance and thus increases the damping ratio. For a limited range the increase in resistance is compensated by the reduction of the damping ratio which results from the frequency increase, but in this case the damping ratio was not completely compensated for by frequency and therefore this characteristic resulted. This difficulty can

be avoided by carefully designing the other time constant in the feedback network. It is also important to remember the second time constant is somewhat coupled to the RLC circuit, and therefore this influences the performance of the oscillator.

Frequency response tests were not formally conducted but some tests were performed which showed that the oscillator is capable of following frequencies up to half its operating frequency with no difficulty.

Tests of frequency variation with temperature were conducted. Analysis shows that the frequency should increase as the square root of the total temperature but the test results indicated that the frequency increased in a manner somewhat less than this. This frequency temperature test data is shown in Figure 12. In the system it is anticipated that two oscillators will be used and both oscillators will be subjected to the same temperature environment. As a result changes in frequency due to temperature will not greatly influence the accuracy of the system.

Figure 13 shows a photograph of a PCO output trace. The upper trace is a wave of 550 cps and the lower trace is a wave of 45 cps. These traces were made with the same PCO element by reducing the size of the feedback capacitance. Figure 14 shows two traces of a linear pressure-controlled oscillator at 80 and 120 cycles. Both traces are essentially sinusoidal and very noise free. Figure 15 shows an oscillator performing at frequencies of 275 cps and 180 cps. The interesting part of this figure is that each trace was repeated 50 times in the photograph. This indicates the stability of the oscillator.

For a fixed oscillator element the feedback can be changed in order to select the operating frequency. But, with a fixed element, higher frequencies require higher input pressures. For example, the element shown in Figure 1 will oscillate at 80 cps for one inch of water pressure. This same element will also oscillate at 500 to 600 cycles for one psi input pressure, provided suitable resonant frequency changes were made the feedback network. In general, high frequencies can be obtained with low pressures provided smaller elements are used. And conversely, lower frequencies can be obtained with high pressures if larger elements are used.

Conclusion

In summary, the pressure controlled oscillator developed is an excellent analog to digital converter. The reason for its excellence is its high conversion rate, and noise free signal.

This element can be designed analytically and made to work in accordance with design theories. However, some testing is necessary because the fluid system is somewhat non-linear. The analysis presented shows that it is possible for this element to perform different functions. These functions are related to the feedback network design. In addition, if the feedback network quality factor is sufficiently high, a very stable frequency oscillator can be built. The one major advantage of this device is that it is an AC device and can operate at extremely low levels much more efficiently than DC or continuous flow devices.

For matching, this pressure controlled oscillator has an input pressure range which is compatible with the vortex rate sensor. Figure 1 shows that the gain of the oscillator is about 30 cycles per second for 1 inch of water change of input pressure, and the frequency response of this oscillator is at least half of its operating frequency; that is, about 50 cps.

Fig. 1

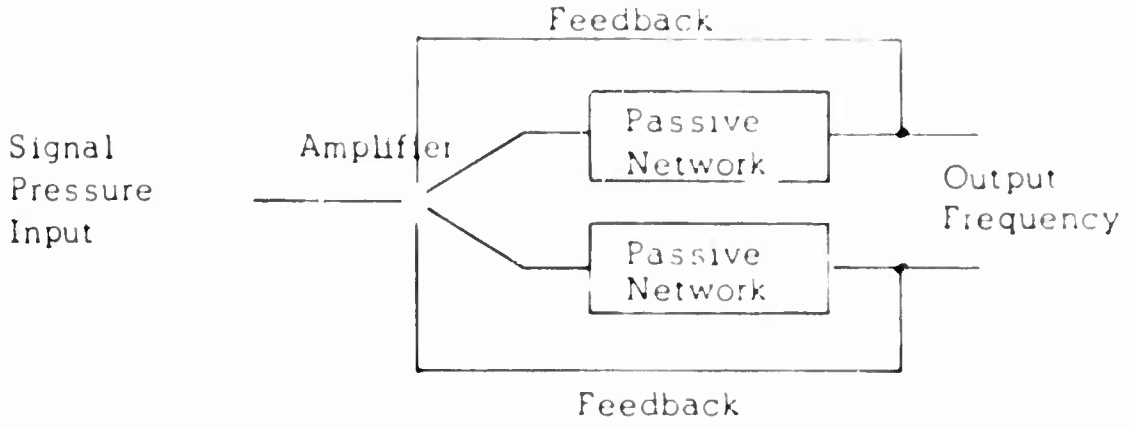

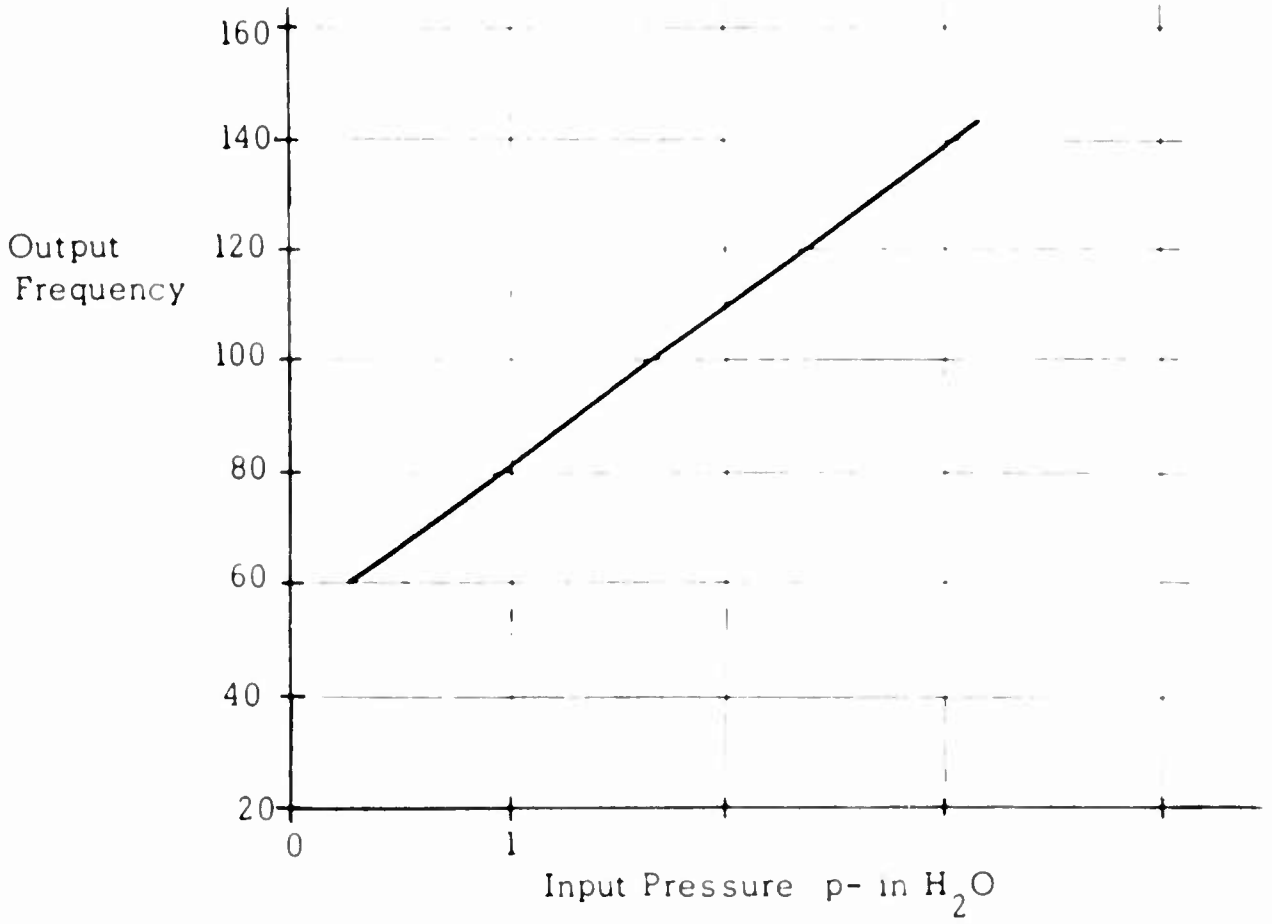

PRESSURE CONTROLLED OSCILLATOR
Schematic Diagram and Typical Test Data

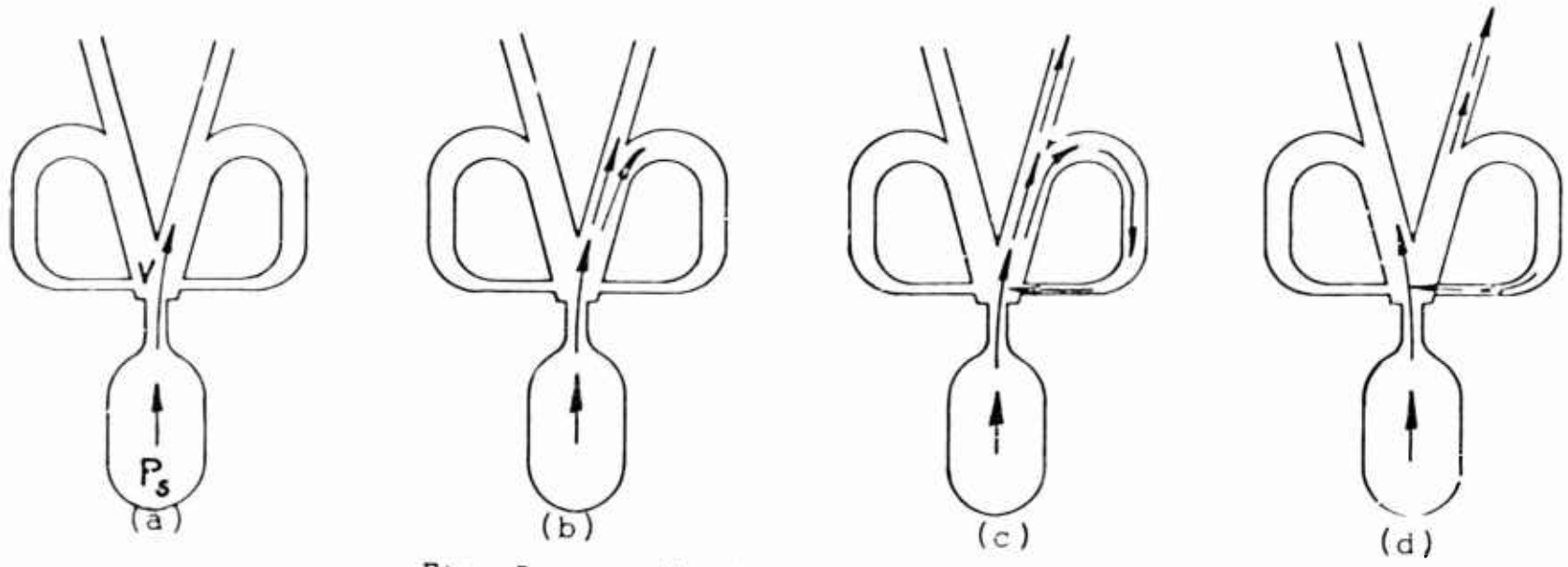

Fig. 2 Feedback Oscillator

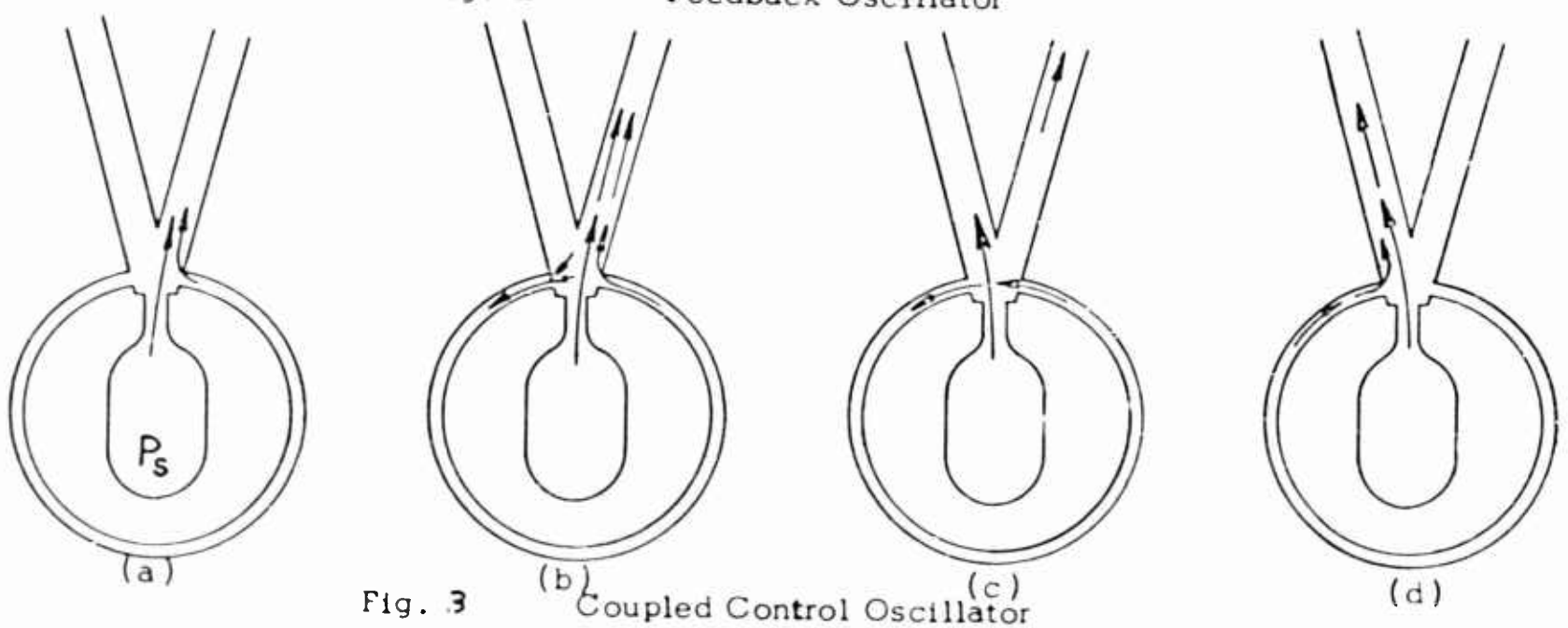

Fig. 3 Coupled Control Oscillator

FLUID OSCILLATORS
Operating Sequence Diagrams of Feedback Oscillator and Coupled Control Oscillator

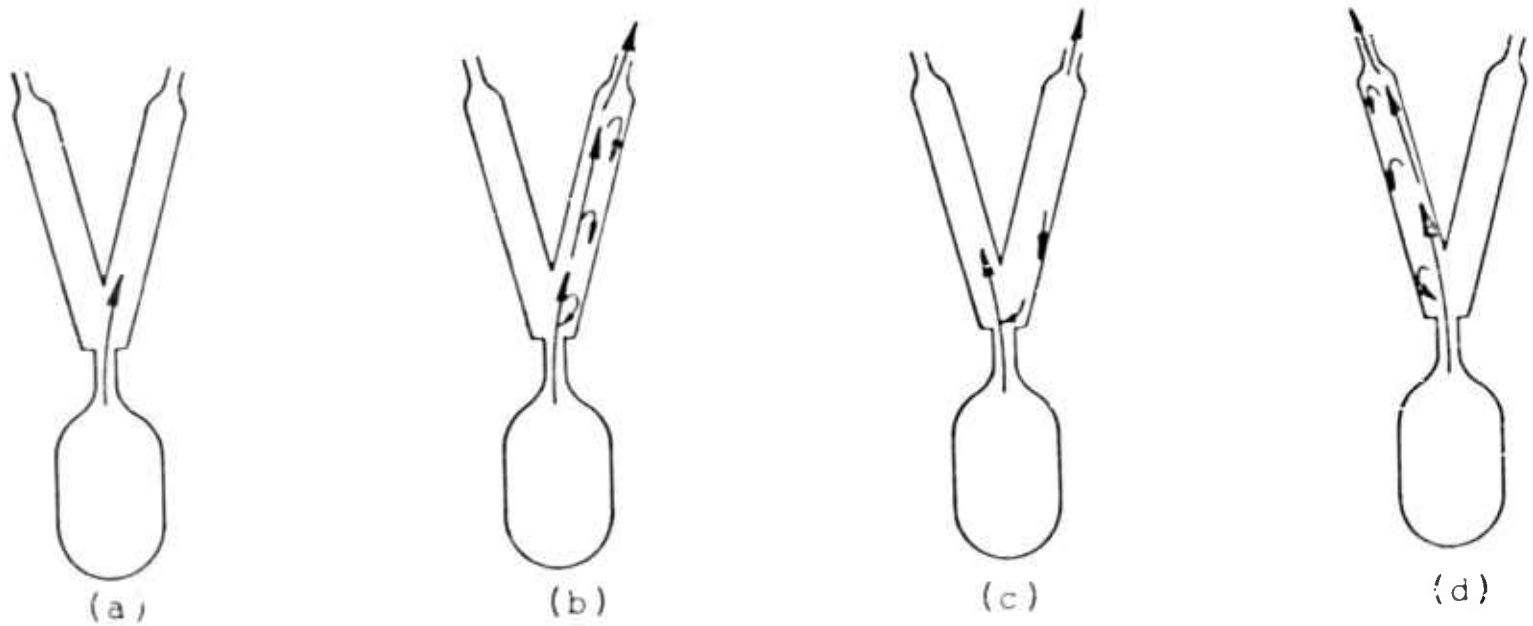

Fig. 4 Load Sensitive Oscillator

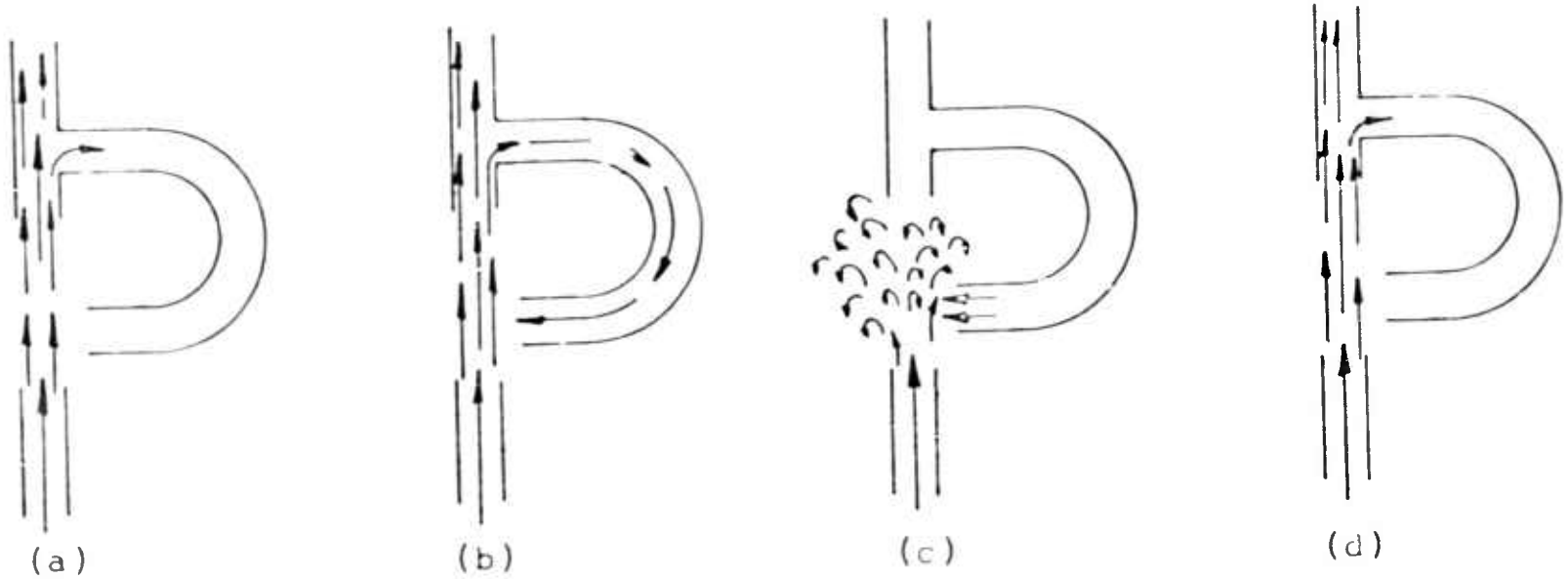

Fig. 5 Turbulence Oscillator

FLUID OSCILLATORS
Operating Sequence Diagrams of Load Sensitive Oscillator and Turbulence Oscillators

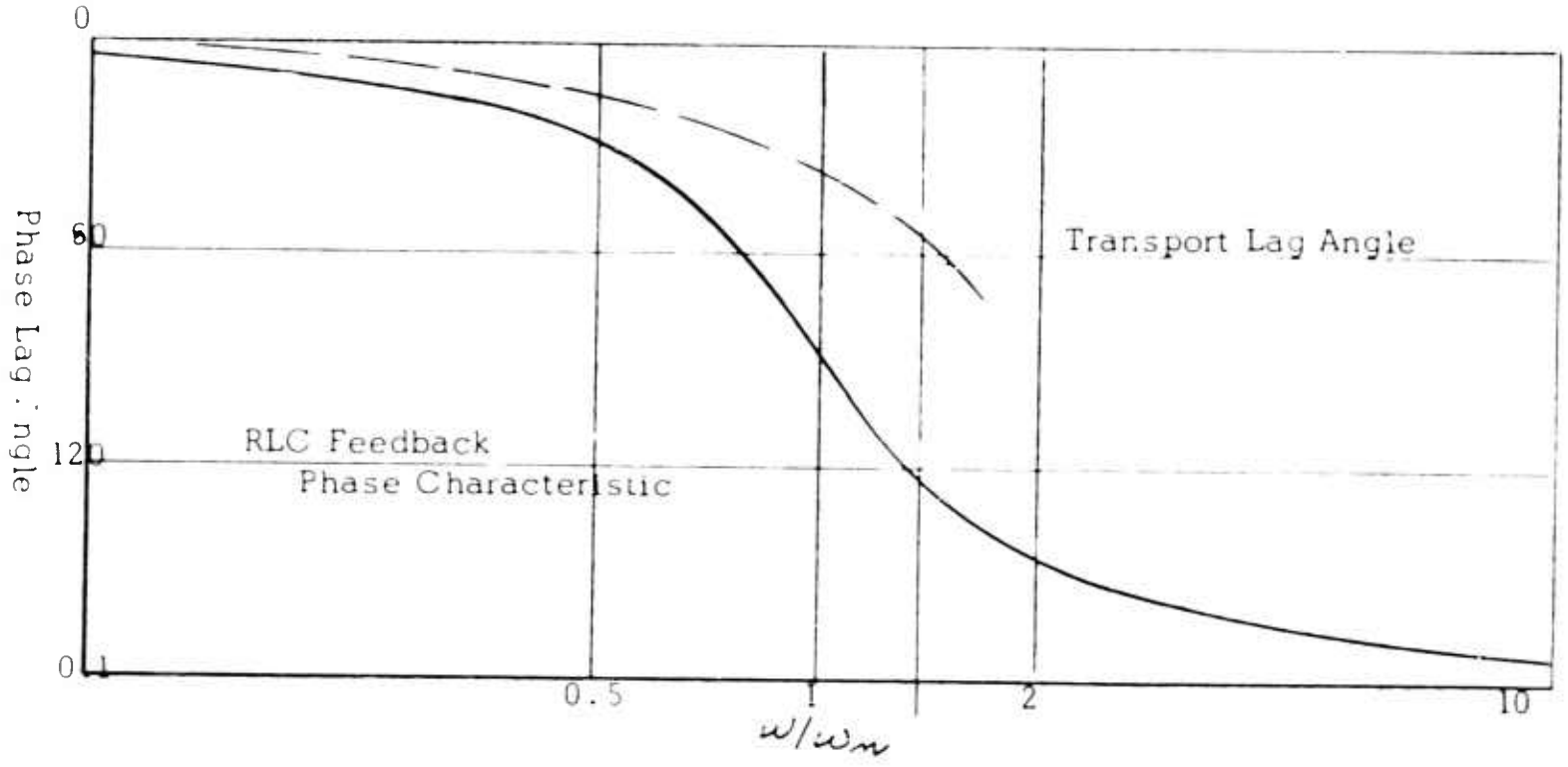

Frequency

Where $\omega_n = \frac{1}{\sqrt{LC}}$

Fig. 6

ω^* is frequency where the transport lag plus the RLC feedback lag sum to 180°

PRESSURE CONTROLLED OSCILLATOR
Phase Angle Characteristic due to Jet Transport and Feedback Network

Fig. 7

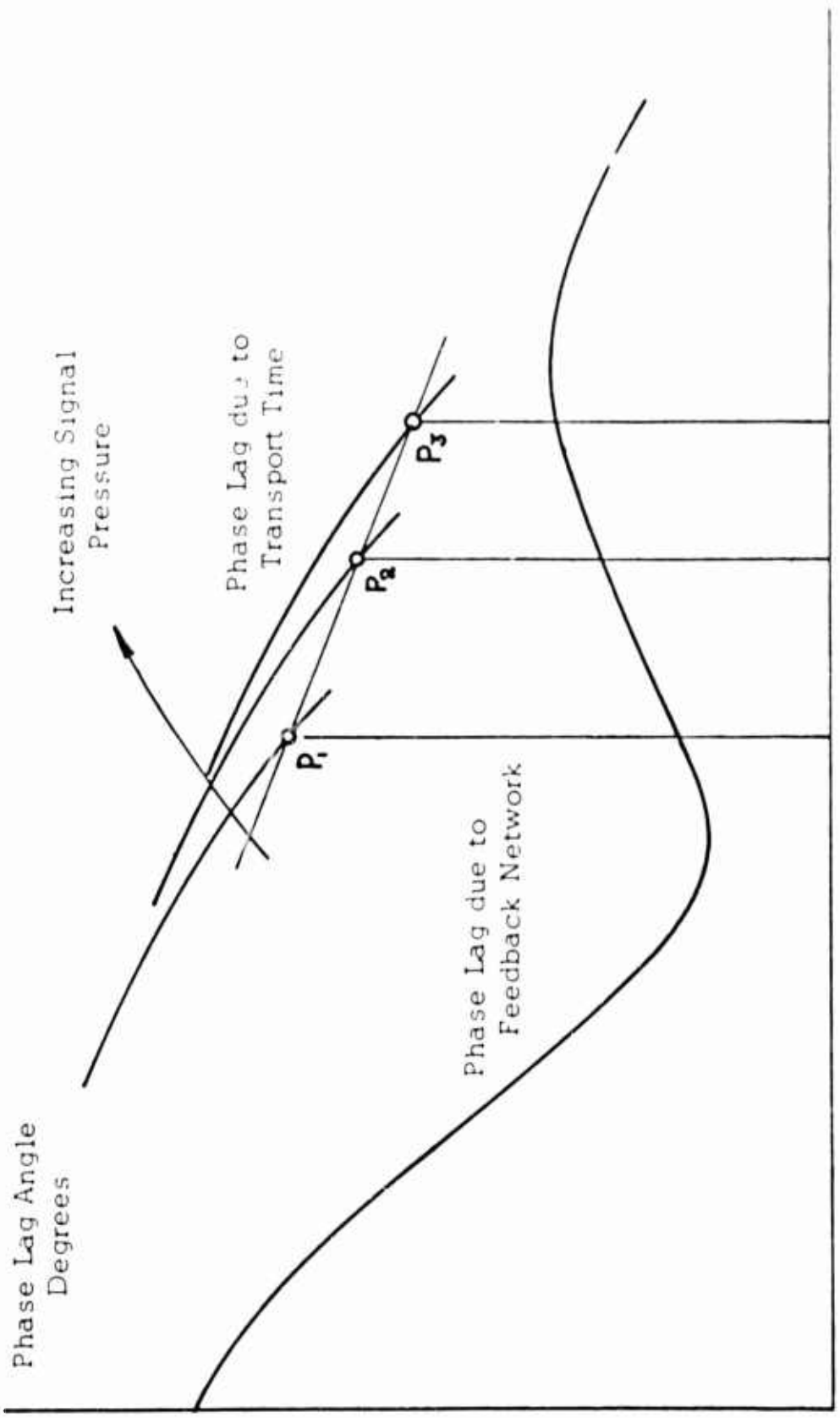

and are frequencies where associated with the signal pressures
where the sum of the transport lag and feedback phase lag is 180 degrees.

PRESSURE CONTROLLED OSCILLATOR

Graphical Determination of Resonant Frequency

Fig. 8

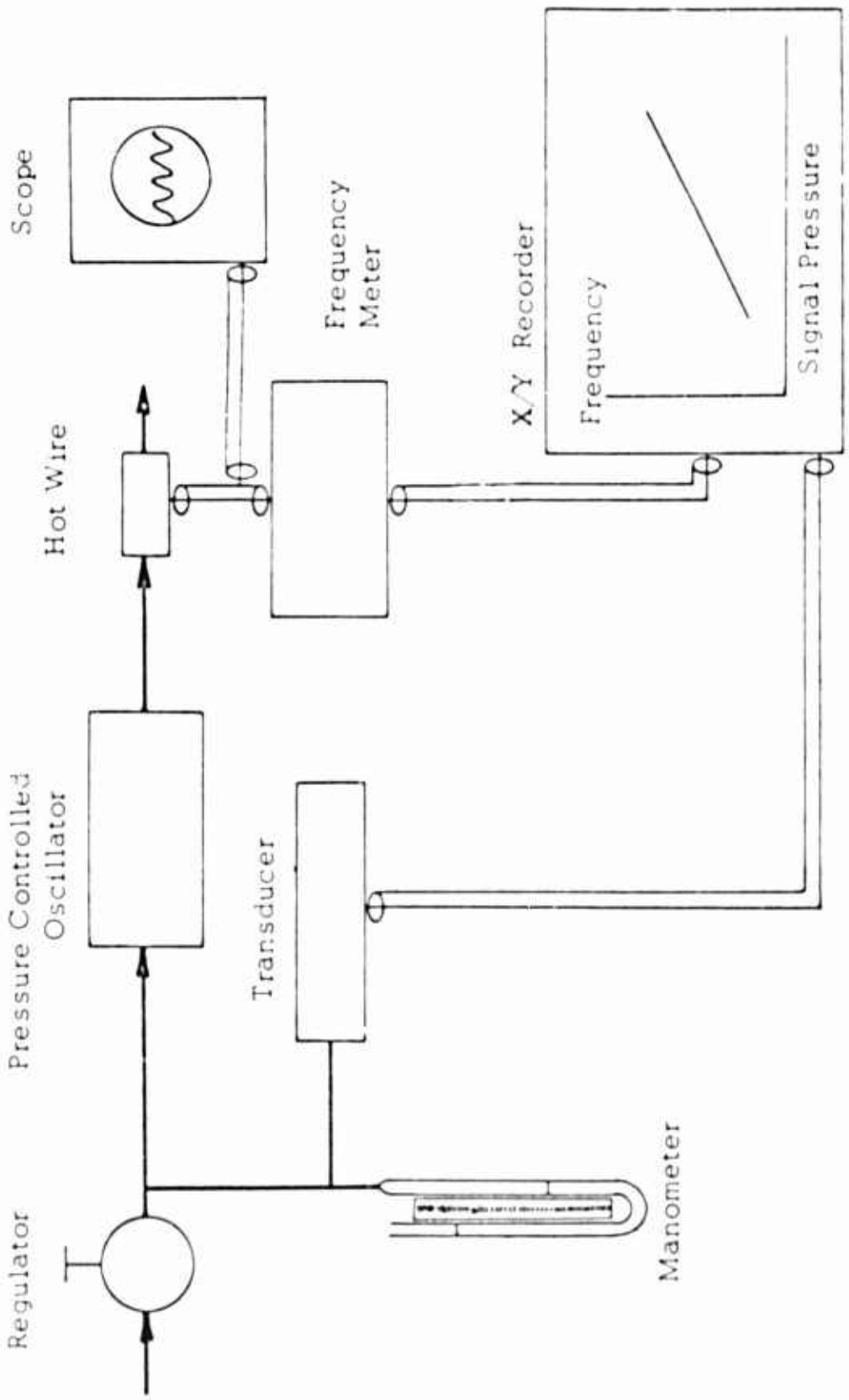

PRESSURE CONTROLLED
OSCILLATOR
Test Arrangement

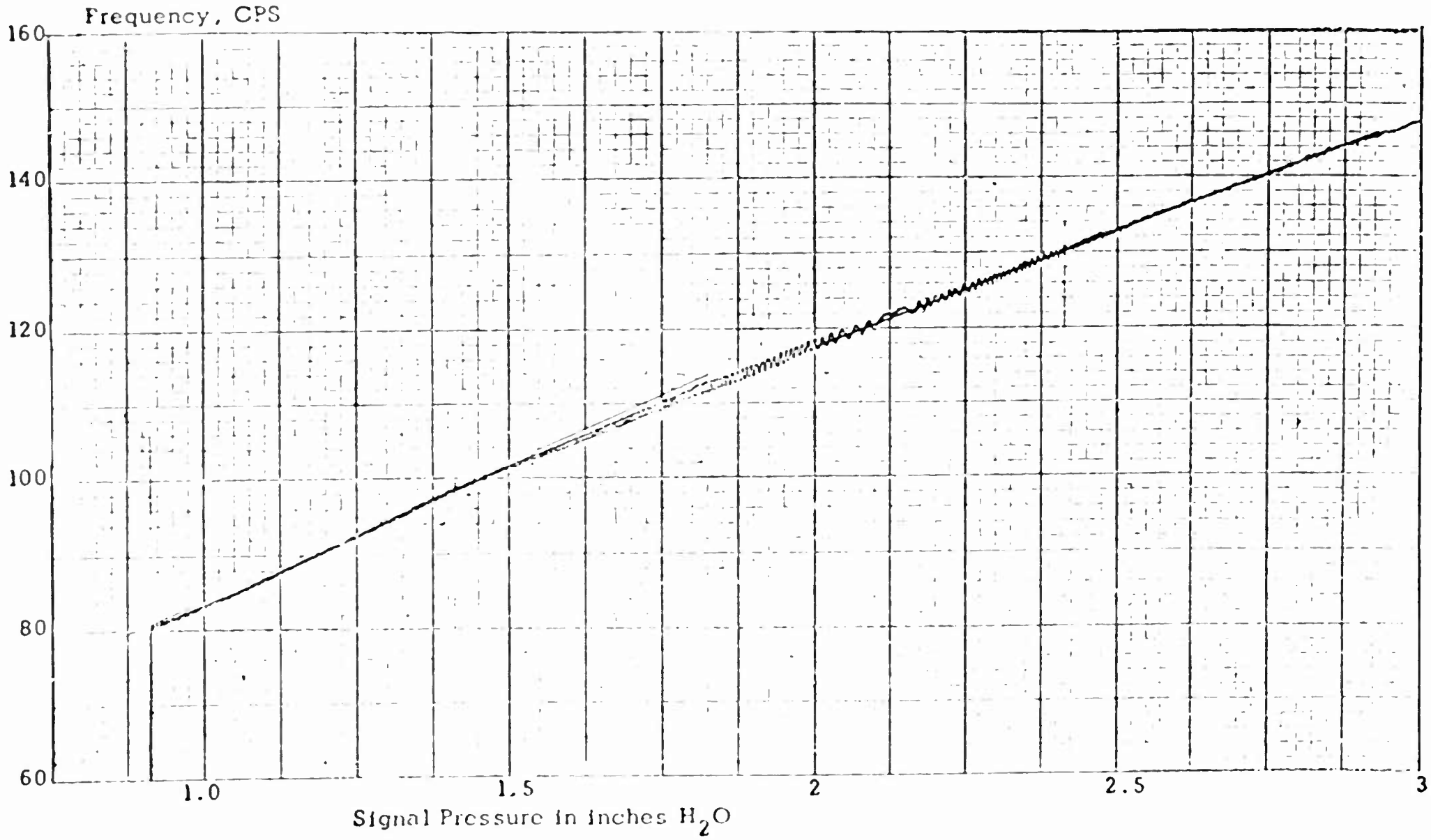

PRESSURE CONTROLLED OSCILLATOR
Test Results of Oscillator 2472B

Fig. 9

Fig. 10

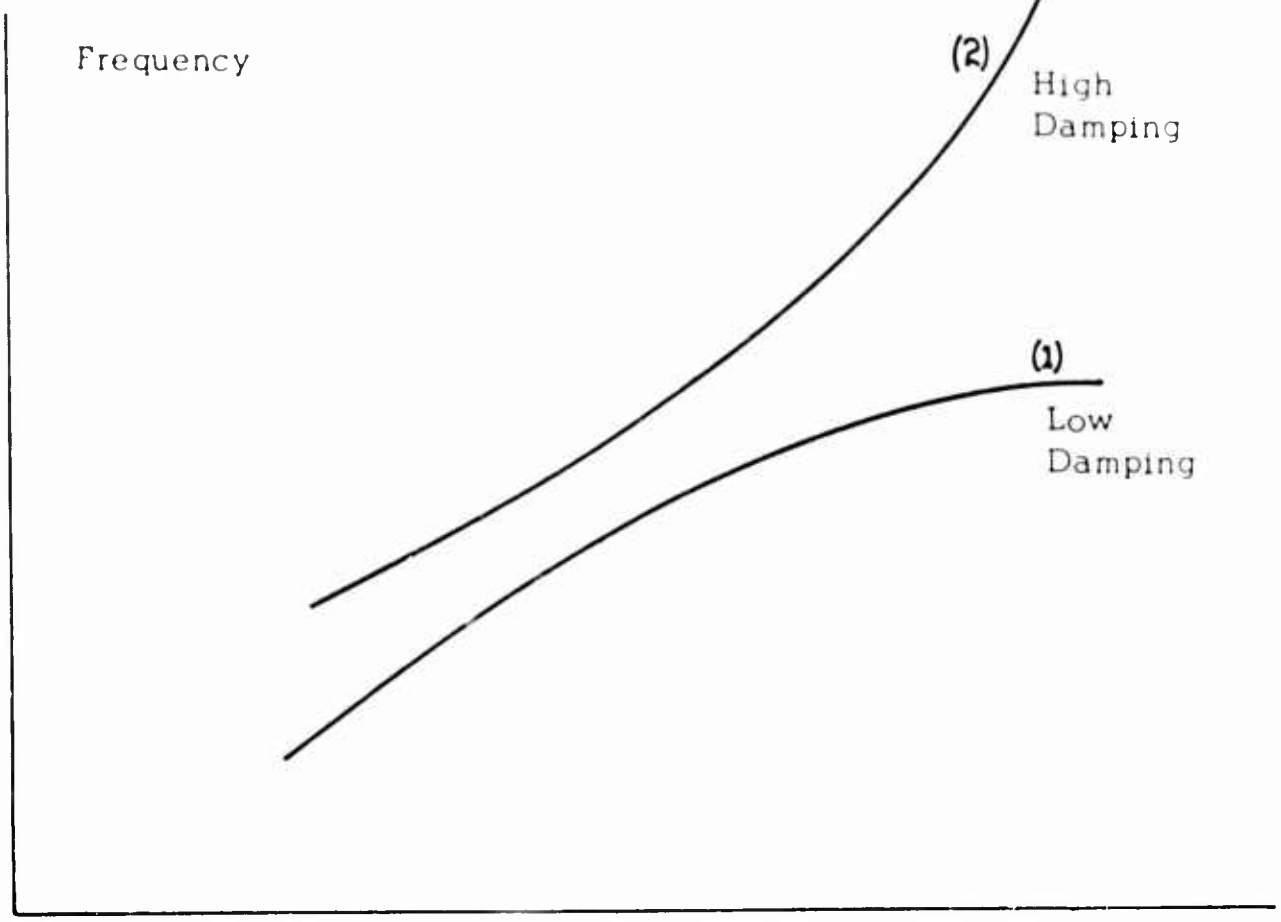

PRESSURE CONTROLLED OSCILLATOR

Signal Pressure - Frequency Relationships for
Feedback Circuits with High and Low Damping

Fig. 11

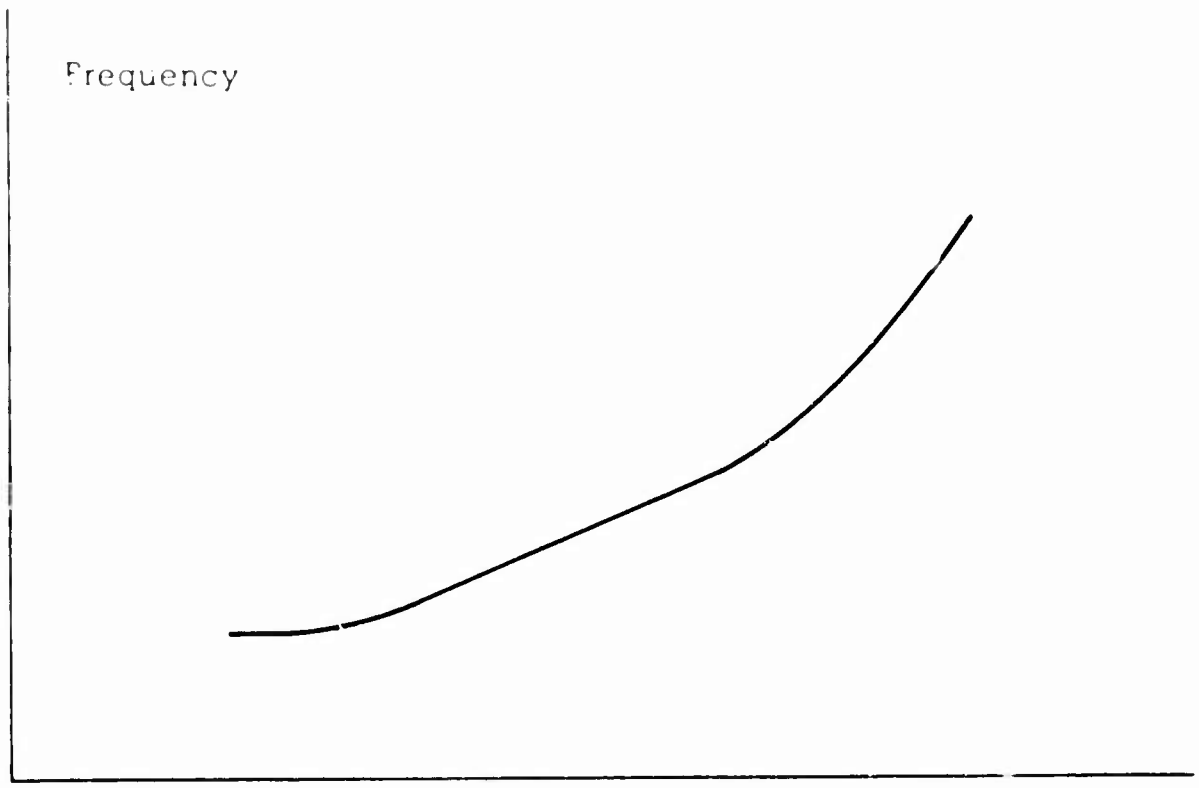

PRESSURE CONTROLLED OSCILLATOR

Effect of a Dominant Nonlinear Resistance
on the Signal Pressure - Frequency Characteristic

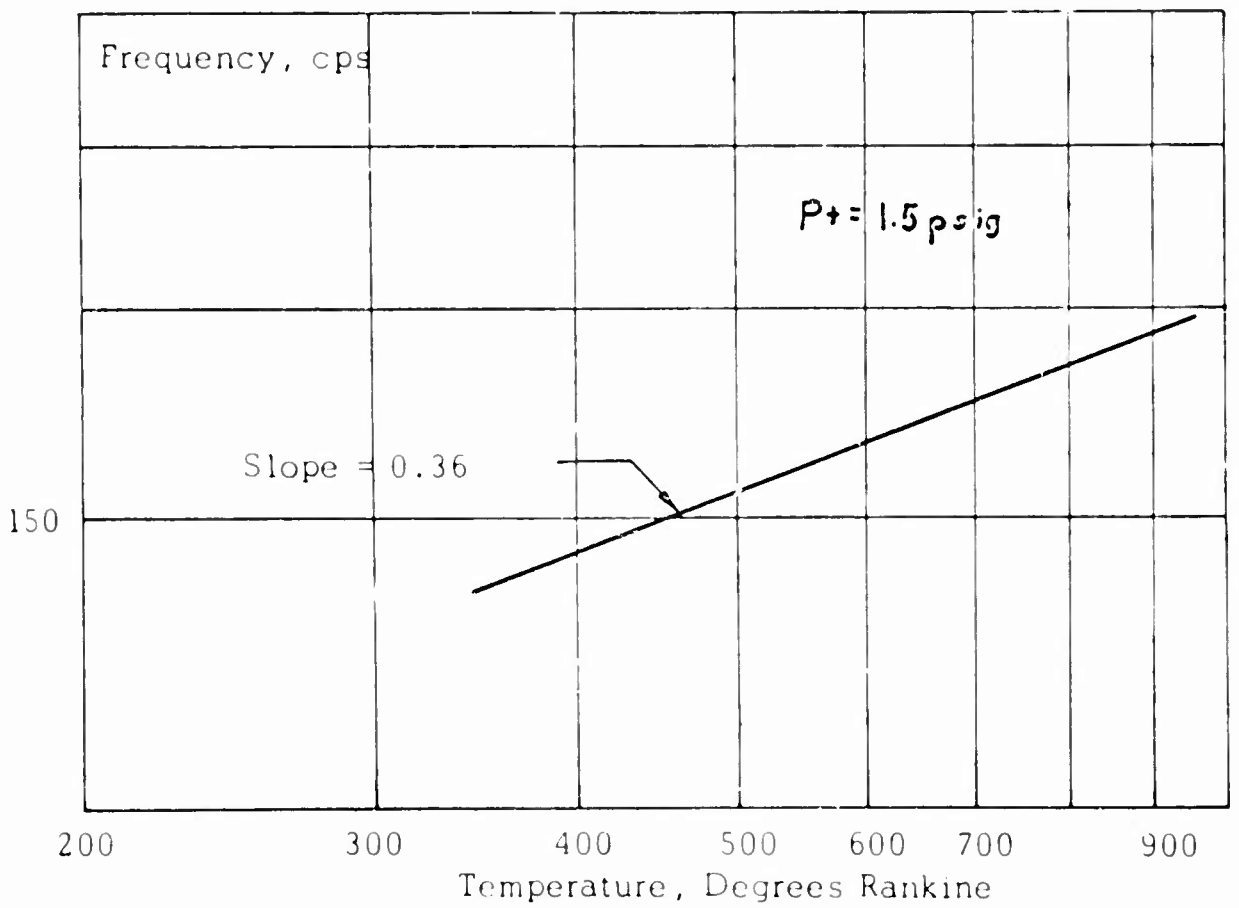

PRESSURE CONTROLLED OSCILLATOR
Temperature Effect on Frequency

Fig. 3

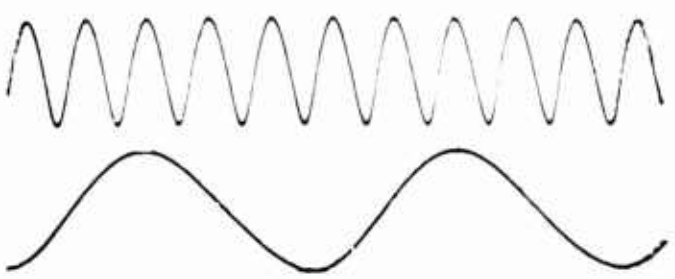

PRESSURE CONTROLLED OSCILLATOR
Frequency Adjusted to 45 and 550 cps with constant
Signal Pressure by Varying Feedback Capacitance

Fig. 14

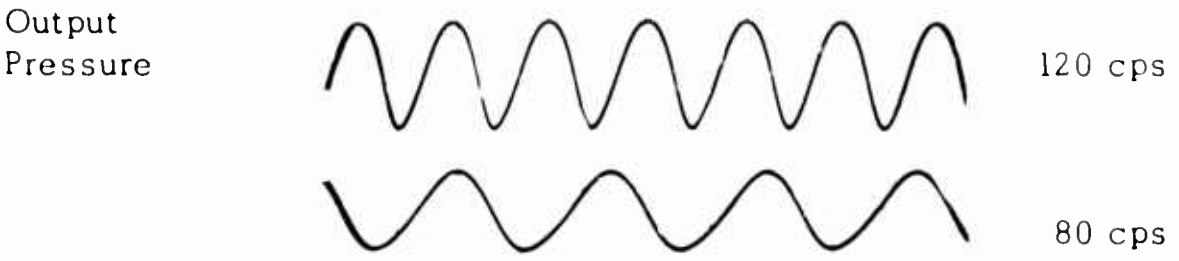

PRESSURE CONTROLLED OSCILLATOR
Oscilloscope Traces of the Output of Oscillator 2472 at 120 and 80 cps

Fig. 15

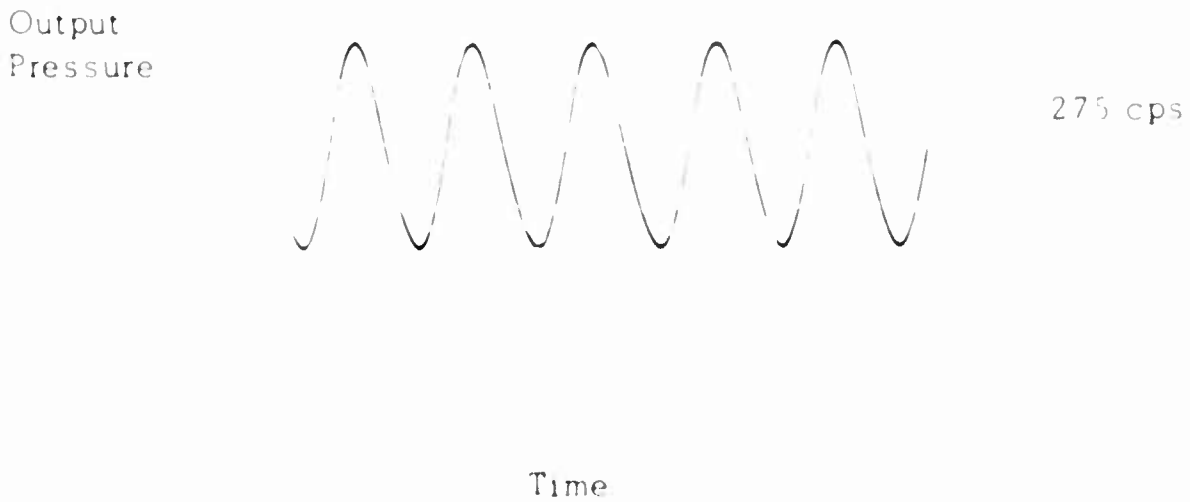

PRESSURE CONTROLLED OSCILLATOR

50 Superimposed Output Wave Traces at
180 and 275 cps

FLUID DYNAMIC EFFECTS OF LIQUIDS IN ELASTIC TUBES

R.W. Besant and V. Srinivas
Division of Control Engineering
University of Saskatchewan

PART A THEORY

ABSTRACT

In this paper a theoretical analysis is made of the frequency response of liquid flow in an elastic line for a load at one end and an input oscillator at the other end. Interaction, transverse and longitudinal wave modes are analysed for the system by linearizing the general partial differential equations of motion for the liquid and the elastic tube and by superimposing second order effects on the first order equations. The results yield different superimposed resonant frequencies for each wave mode and they should be valid within the bounds of the assumptions made.

1. INTRODUCTION

The dynamic operation of fluid state devices using liquids at high pressure may cause significant wave effects in the connecting elastic tubing. Excessive resonant oscillators could strongly influence the performance of digital, on-off and proportional systems. The phase lags associated with wave motion may cause instability in closed loop control systems since phase lags of 180 degrees or more are easily obtained. Finally, signal attenuation and dispersion that occurs in transmission lines will reduce the information conveyed and the power output.

With finite disturbances in liquid filled elastic tubes, waves may be transmitted in several modes; each mode has unique wave velocities and damping characteristics. Usually the dominant wave effect for an

---

List of Symbols

B = effective bulk moculus
c = phase velocity
$E = \lambda + 2\mu$ Young's modulus
$E_1 = \frac{4}{3}\eta$ viscoelastic damping modulus
$E_s = \mu$ shear modulus
$f(x, j\omega)$ = function defined in equation 18
$g(x, j\omega)$ = function defined in equation 21
$h(x, j\omega)$ = function defined in equation 27
$j = \sqrt{-1}$
$\kappa = (1+j)\sqrt{\frac{\omega}{2\nu}}$
L = load end subscript
p = pressure
$P(x)$ = pressure amplitude
p' = pressure perturbation

oscillating liquid in an elastic tube is due to the interaction of the inertia effect of the liquid and the capacitance effect of the tube. If the liquid is sufficiently compressible the combined capacitance effect of liquid compressibility and of tube compliance is used to analyze this type of wave motion. Other wave modes that have been observed in such systems are the transverse and the longitudinal waves in the elastic tube.

The problem of unsteady flow of viscous liquids in elastic tubes is not a new one. Thomson[1] investigated dynamic liquid waves in an infinite thin walled tube. Morgan and Kiely[2] analysed unsteady viscous flow in an infinitely long elastic tube. Womersley[3] re-examined and extended the work of Morgan and Kiely for viscous flow in an elastic tube and applied the results to the case of blood flow. Junger[4], interested in acoustical systems, analysed the motion of the surrounding fluid when pressure waves passed through an infinite tube. Dragos[5] showed the existance of a uniquely established solution for the movement of a viscous liquid in an elastic tube. Other authors concerned with minor elastic effects in fluid filled tubes have included the interaction type wave in their analyses.

In this paper linearized equations for the flow of a viscous incompressible liquid in an elastic tube are considered. The frequency response of loaded and unloaded lines are analysed by considering the wave modes separately. First, the interaction type wave is considered and then the transverse and longitudinal perturbations are included.

List of Symbols (Cont'd)

r = radial space coordinate
R = resistance coefficient
R' = resistance coefficient perturbation
R_i = internal tube radius
R_o = external tube radius
t = time
$U_r(xrt)$ = radial tube displacement
$u_r(x)$ = radial displacement amplitude
$U_x(xrt)$ = axial tube displacement
$u_x(x)$ = axial displacement amplitude
$V(x)$ = axial velocity amplitude
$V_r(xrt)$ = radial velocity
v_r = radial velocity perturbation amplitude
$V_x(xrt)$ = axial velocity
$v_x(xr)$ = axial velocity perturbation amplitude
$\bar{v}_x(x)$ = average axial velocity perturbation amplitude
x = axial spacial coordinate
$\alpha = \frac{j}{c}\sqrt{\omega^2 - \frac{jR\omega}{\rho}}$
η = viscoelastic damping term
λ = Lame's elastic coefficient
μ = Lame's elastic coefficient
υ = liquid kinematic viscosity

2. THE BASIC PRINCIPLES

2.1 Assumptions

For this analysis of dynamic flow of a viscous liquid in an elastic tube the following assumptions are made:

1. The motion is axially symmetrical.
2. The tube is elastic, homogeneous and isotropic with viscoelastic type damping characteristics.
3. The liquid is incompressible with constant properties.
4. The flow is laminar.
5. The body forces are neglected.

2.2 The Basic Differential Equations

Using the above assumptions the basic principles yield the following partial differential equations:

for fluid continuity

$$\frac{\partial V_x}{\partial x} + \frac{\partial V_r}{\partial r} + \frac{V_r}{r} = 0 \qquad (1)$$

for fluid momentum in the x direction

$$\frac{\partial V_x}{\partial t} + V_x \frac{\partial V_x}{\partial x} + V_r \frac{\partial V_x}{\partial r} + \frac{1}{\rho}\frac{\partial p}{\partial x} - \upsilon\left[\frac{1}{r}\frac{\partial}{\partial r}\left(r\frac{\partial V_x}{\partial r}\right) + \frac{\partial^2 V_x}{\partial x^2}\right] = 0 \qquad (2)$$

for fluid momentum in the r direction

$$\frac{\partial V_r}{\partial t} + V_x \frac{\partial V_r}{\partial x} + V_r \frac{\partial V_r}{\partial r} + \frac{1}{\rho}\frac{\partial p}{\partial r} - \upsilon\left[\frac{\partial}{\partial r}\left(\frac{1}{r}\frac{\partial}{\partial r}(rV_r)\right) + \frac{\partial^2 V_r}{\partial x^2}\right] = 0 \qquad (3)$$

for tube momentum in the x direction

$$\rho' \frac{\partial^2 U_x}{\partial t^2} = (\lambda + 2\mu)\frac{\partial^2 U_x}{\partial x^2} + (\lambda+\mu)\left(\frac{\partial^2 U_r}{\partial x \partial r} + \frac{1}{r}\frac{\partial U_r}{\partial x}\right) + \mu\left(\frac{\partial^2 U_x}{\partial r^2} + \frac{1}{r}\frac{\partial U_x}{\partial r}\right) + \text{DAMPING} \qquad (4)$$

List of Symbols (Cont'd)

ρ = liquid density

ρ' = tube density

σ = Poisson's ratio

$\phi = \omega\sqrt{\dfrac{\rho'}{E_s + j\omega E_s}}$

$\psi = \omega\sqrt{\dfrac{\rho'}{E + j\omega E_s}}$

ω = frequency

for tube momentum in the r direction

$$\rho' \frac{\partial^2 U_r}{\partial t^2} = (\lambda + 2\mu)\left(\frac{\partial' U_r}{\partial r^2} + \frac{1}{r}\frac{\partial U_r}{\partial r} - \frac{U_r}{r^2}\right) + (\lambda + \mu)\frac{\partial' U_x}{\partial r \partial x} + \mu \frac{\partial' U_r}{\partial x^2} + \text{DAMPING} \qquad (5)$$

These equations are simplified by neglecting terms of second order or higher (see Appendix 1) to give only

$$\frac{\partial V_x}{\partial t} + \frac{1}{\rho}\frac{\partial P}{\partial x} + \frac{R}{\rho} V_x = 0 \qquad (6)$$

where the linearized damping term R is theoretically predicted in Appendix 2.

3. FREQUENCY RESPONSE OF FLOW WITHOUT TRANSVERSE AND LONGITUDINAL TUBE WAVES

It can be shown[6] that the phase velocity c of a liquid disturbance in an elastic tube is governed by equation 6 and by the equation

$$\frac{1}{\beta}\frac{\partial P}{\partial t} + \frac{\partial V_x}{\partial x} = 0 \qquad (7)$$

where $C = \frac{\partial x}{\partial t} = \sqrt{\frac{\beta}{\rho}}$ is the wave velocity of the interaction of liquid inertia and tube compliance.

Combining equations (6) and (7) results in a damped wave equation

$$\frac{\partial^2 P}{\partial t^2} + \frac{R}{\rho}\frac{\partial P}{\partial t} = C^2 \frac{\partial^2 P}{\partial x^2} \qquad (8)$$

These two equations (7) and (8) determine the frequency response of wave disturbances assumed to be of the form

$$P(x\,t) = \mathcal{P}(x)\, e^{j\omega t}$$

$$V_x(x\,t) = V(x)\, e^{j\omega t}$$

Equations (7) and (8) may be rewritten in the form

$$\frac{\partial V}{\partial x} + \frac{j\omega}{\beta} P = 0 \qquad (9)$$

and

$$\frac{\partial^2 P}{\partial x^2} + \alpha^2 P = 0 \qquad (10)$$

where $$\alpha^2 = \frac{1}{C^2}\left(\omega^2 - \frac{jR\omega}{\rho}\right)$$

If the input and load end of the tube are denoted by the subscripts 0 and L respectively, the pressure and velocity responses are obtained as

$$\frac{p(L,j\omega)}{p(0,j\omega)} = \frac{1}{\cos(\alpha L) + \left[\frac{jB\alpha}{\omega}\,\frac{V_x(L,j\omega)}{p(L,j\omega)}\right]\sin(\alpha L)} \tag{11}$$

$$\frac{V_x(L,j\omega)}{V_x(0,j\omega)} = \frac{1}{\cos(\alpha L) + \left[\frac{j\omega}{\alpha B}\,\frac{p(L,j\omega)}{V_x(L,j\omega)}\right]\sin(\alpha L)} \tag{12}$$

where $\frac{p(L,j\omega)}{V_x(L,j\omega)}$ is defined as the load impedance which is an explicit function of load, inertia, capacitance and resistance as well as the frequency of oscillation. The method of theoretically estimating the load impedance for a linear second order system is given in Part B.

Two limiting cases can be deduced from equations (11) and (12). Load impedance is infinite for a closed end pipe and the velocity ratio given by (12) becomes zero leaving the pressure ratio

$$\frac{p(L,j\omega)}{p(0,j\omega)} = \frac{1}{\cos(\alpha L)}$$

Similarly for an open end pipe, load impedance is zero and only the velocity ratio is applicable, hence

$$\frac{V_x(L,j\omega)}{V_x(0,j\omega)} = \frac{1}{\cos(\alpha L)}$$

4. FREQUENCY RESPONSE OF FLOW DUE TO TRANSVERSE WAVES IN THE TUBE

In addition to the interaction wave of tube compliance and liquid inertia, transverse waves in the elastic tube may be induced in pulsatile flow. The first order terms for transverse waves with visco-elastic damping reduces equation (5) to[7]

$$\rho' \frac{\partial^2 U_r}{\partial t^2} = \mu \frac{\partial^2 U_r}{\partial x^2} + \frac{4\eta}{3}\frac{\partial^3 U_r}{\partial t\,\partial x^2} \tag{13}$$

If radial disturbances of the type

$$U_r(x,t) = u_r(x)\, e^{j\omega t}$$

are considered, equation (13) may be written in the form

$$\frac{\partial^2 u_r}{\partial x^2} + \phi^2 u_r = 0 \tag{14}$$

where $$\phi^2 = \frac{\rho' \omega^2}{E_s + j\omega E_v}$$

If the boundary conditions are taken to be[8]

$$u_r(0) = \frac{P_0}{E} \frac{R_1^3}{(R_0^2 - R_1^2)} \left[(1-\sigma) + (1+\sigma)\left(\frac{R_0}{R_1}\right)^2 \right] = K_1 P_0$$

$$u_r(L) = 0$$

then the solution of (14) is

$$u_r = K_1 P_0 \left[\cos(\phi x) - \cot(\phi L) \sin(\phi x) \right] \qquad (15)$$

These radial oscillations of the tube wall must be accompanied by small perturbations of the main axial flow. These perturbations in fluid flow may be estimated by using the appropriate form of equations (1), (2) and (3) in conjunction with equation (14) and its solution equation (15).

To predict the radial component of the velocity perturbation the second order terms of equation (3) are taken as

$$\frac{\partial V_r}{\partial t} - \upsilon \left[\frac{\partial^2 V_r}{\partial r^2} + \frac{1}{r} \frac{\partial V_r}{\partial r} - \frac{V_r}{r^2} \right] = 0 \qquad (16)$$

Considering disturbances of the type $V_r(xrt) = v_r(xr)e^{j\omega t}$ equation (16) transforms into

$$\frac{\partial^2 v_r}{\partial r^2} + \frac{1}{r} \frac{\partial v_r}{\partial r} - \left(\frac{1}{r^2} + \frac{j\omega}{\upsilon} \right) v_r = 0 \qquad (17)$$

where the boundary conditions for this equation are

$$v_r(x, r=0) = 0$$

$$v_r(x, r=R_1) = \frac{\partial u_r(x, r=R_1)}{\partial t}$$

The solution of (17) is

$$v_r = f(x, j\omega) I_1(\kappa r) \qquad (18)$$

where $$\kappa = (1+j)\sqrt{\frac{\omega}{2\upsilon}}$$

and $$f(x, j\omega) = \frac{j\omega K_1 P_0 \left[\cos(\phi x) - \cot(\phi L)\sin(\phi x)\right]}{I_1(\kappa R_1)}$$

From equation (1) and (2) the axial component of velocity perturbations due to transverse oscillations may be estimated. Rewriting equation (1) in the form

$$\frac{\partial v_x}{\partial x} = -\frac{\partial v_r}{\partial r} - \frac{v_r}{r}$$

and substituting equation (18) into this yields

$$v_x = \frac{j\omega K_1 P_0 K}{\phi I_1(\kappa R_1)}\left[\sin(\phi x) + \cot(\phi L)\cos(\phi x)\right] I_0(\kappa r) + \text{CONSTANT} \qquad (19)$$

For small oscillations of frequency ω equation (2) may be written in the form

$$\frac{\partial^2 v_x}{\partial r^2} + \frac{1}{r}\frac{\partial v_x}{\partial r} - \frac{j\omega}{\upsilon}\left[v_x + \frac{1}{j\omega\rho}\frac{\partial p}{\partial x}\right] = 0 \qquad (20)$$

The solution of this equation is

$$v_x = g(x, j\omega) I_0(\kappa r) - \frac{1}{j\omega\rho}\frac{\partial p}{\partial x} + \text{CONSTANT} \qquad (21)$$

where $$\kappa = (1+j)\sqrt{\frac{\omega}{2\upsilon}}$$

The boundary conditions for equations (19) and (21) are taken as

$$v_x(x, r = R_1) = 0$$

$$\frac{\partial v_x}{\partial r}(x, r = 0) = 0$$

Finally we get

$$v_x = -\frac{j\omega K_1 P_0 K\left[\sin(\phi x) + \cot(\phi L)\cos(\phi x)\right]\left[I_0(\kappa r) - I_0(\kappa R_1)\right]}{\phi I_1(\kappa R_1)\left[1 - I_0(\kappa R_1)\right]}$$

where the average axial perturbation velocity is

$$\bar{v}_x = \int_0^{R_1} \frac{2\pi r\, v_x}{\pi R_1^2}\, dr$$

$$\bar{v}_x = \frac{j\omega K_1 P_0 K \left[\frac{2}{KR_1} I_1(KR_1) - I_0(KR_1)\right]\left[\sin(\phi x) + \cot(\phi L)\cos\phi x\right]}{\phi \sin(\phi L)\, I_1(KR_1)\left[1 - I_0(KR_1)\right]} \tag{22}$$

The resulting axial pressure oscillations p' may be evaluated by re-writing equation (7) in the form

$$\frac{\partial \bar{v}_x}{\partial x} = -\frac{j\omega p'}{B} \tag{23}$$

hence

$$p' = \frac{B K_1 P_0 K \left[\frac{2}{KR_1} I_1(KR_1) - I_0(KR_1)\right]\left[\cos(\phi x) - \cot(\phi L)\sin(\phi x)\right]}{I_1(KR_1)\left[1 - I_0(KR_1)\right]}$$

The consequence of this equation is that the pressure response $p'_L/p_0 = 0$ Also from (23) it can be shown that the ratio of input velocity to input pressure is given by

$$\frac{V_0}{P_0} = -\frac{j\omega}{B\phi}\cot(\phi L)$$

hence equation (22) may be written as

$$\frac{\bar{v}_x}{V_0} = \frac{B K_1 K \left[\frac{2}{KR_1} I_1(KR_1) - I_0(KR_1)\right]}{\cos(\phi L)\, I_1(KR_1)\left[1 - I_0(KR_1)\right]}$$

5. FREQUENCY RESPONSE OF FLOW DUE TO LONGITUDINAL WAVES IN THE TUBE

Longitudinal tube waves may be induced by several causes such as viscous fluid shear on the tube wall or a load that is not fixed, etc. Proceeding as in section 4 the terms in equation (4) of second order for longitudinal tube waves are given by[7]

$$\rho' \frac{\partial^2 U_x}{\partial t^2} = (\lambda + 2\mu)\frac{\partial^2 U_x}{\partial x^2} + \frac{4\eta}{3}\frac{\partial^3 U_x}{\partial t\, \partial x^2} \tag{24}$$

For oscillations of frequency ω this equation may be rewritten in the form

$$\frac{\partial^2 u_x}{\partial x^2} + \psi^2 u_x = 0 \tag{25}$$

where $$\psi^2 = \frac{\rho' \omega^2}{E + j\omega E_1}$$

Considering only shear induced oscillations with the input end fixed and the load end free the distribution of shear forces may be estimated from equation (2) in the form

$$\frac{\partial V_x}{\partial t} + \frac{1}{\rho}\frac{\partial p}{\partial x} - \upsilon\left[\frac{\partial^2 V_x}{\partial r^2} + \frac{1}{r}\frac{\partial V_x}{\partial r}\right] = 0$$

where the term $\frac{\partial^2 V_x}{\partial x^2}$ is considered of third order. Considering oscillations of the form

$$V_x(x\,r\,t) = V(x\,r)\, e^{j\omega t}$$

this equation may be written

$$\frac{\partial^2 V}{\partial r^2} + \frac{1}{r}\frac{\partial V}{\partial r} - \frac{j\omega}{\upsilon} V - \frac{1}{\rho\upsilon}\frac{\partial p}{\partial x} = 0 \qquad (26)$$

The boundary conditions for this equation are taken as

$$\frac{\partial V}{\partial r}(x, r=0) = 0$$

$$V(x\ r=R_i) = 0$$

Hence the solution is

$$V_x(x, r, j\omega) = h(x, j\omega)\left[I_0(\kappa r) - I_0(\kappa R_i)\right]$$

where $$\kappa = (1+j)\sqrt{\frac{\omega}{2\upsilon}}$$

The function $h(x, j\omega)$ may be formed from equation (10) which gives

$$h(x, j\omega) = A_1 \sin(\alpha x) + B_1 \cos(\alpha x) \qquad (27)$$

The shear stress on the tube wall at $r = R_i$ is then

$$\rho\upsilon\frac{\partial V_x}{\partial r} = h(x, j\omega)\ \kappa I_1(\kappa R_i)\, e^{j\omega t}$$

hence the force on the tube per unit length is

$$2\pi R_i\, h(x, j\omega)\, \kappa I_1(\kappa R_i)\, e^{j\omega t}$$

If this forcing term is now included in the equation of motion of the tube we get

$$\frac{\partial^2 u_x}{\partial x^2} + \psi^2 u_x + \frac{2\pi R_i\, h(x, j\omega)}{\rho'\pi(R_o^2 - R_i^2)E}\kappa I_1(\kappa R_i) = 0 \qquad (28)$$

The boundary conditions for this equation are taken as

$$u_x(x=0, j\omega) = 0$$

$$\frac{\partial u_x}{\partial x}(x=L, j\omega) = 0$$

The solution of (28) with the above boundary conditions is

$$u_x = A_2 \sin(\psi x) + B_2 \cos(\psi x) + \frac{A_1}{\alpha^2-\psi^2} \sin(\alpha x) + \frac{B_1}{\alpha^2-\psi^2} \cos(\alpha x)$$

Finally the perturbation of the average axial flow velocity may be used in conjunction with equation (10) to give the frequency response of pressure and velocity for the longitudinal wave perturbation

$$\frac{\bar{v}_{x_L}}{V_0} = \frac{j\omega}{V_0}\left[A_2 \sin(\psi L) + B_2 \cos(\psi L) + \frac{A_1}{\alpha^2-\psi^2} \sin(\alpha L) + \frac{B_1}{\alpha^2-\psi^2} \cos(\alpha L)\right] \quad (30)$$

$$\frac{p'_L}{p_0} = \frac{\beta}{p_0}\left[A_2 \sin(\psi L) + B_2 \cos(\psi L) + \frac{A_1}{\alpha^2-\psi^2} \sin(\alpha L) + \frac{B_1}{\alpha^2-\psi^2} \cos(\alpha L)\right] \quad (31)$$

6. DISCUSSION OF THEORETICAL RESULTS

The theoretical results show that the frequency response of an oscillating viscous flow in an elastic tube, including a load, can be analysed, subject to the assumptions of Appendix 1 using a linearized approach to the basic equations of motion. The resistance term of the basic equation of axial flow (2) was linearized in the form given as it was thought that this approach could be readily extended to turbulent flow or to non-Newtonian laminar flow provided the resistance coefficient R could be theoretically or experimentally evaluated. Since Womersley's solution gives the same variation of R with frequency it was felt that the approach used in the analysis of the resistance coefficient R was a valid one. Both the interaction and the transverse waves must be used for the evaluation of the resistance coefficient. Also, it should be noted that the main flow equations (7) and (8) have a simpler form than those of the other authors, but, some of this advantage is lost when considering the resistance coefficient or the other wave perturbations. It would appear that the analytical approach used in this may have some slight advantage over other authors because of its simplicity and generality.

The solution in this paper yields the same result as Womersley for the phase velocity of the interaction wave. That is the phase velocity of this wave tends to zero directly with frequency or indirectly with viscosity. For zero viscosity or infinite frequency, the solution yields the same result as Lamb[9]. Thomson in his paper has the phase velocity of this wave tending to a finite constant. It is not known which result is correct as experimental verification is very difficult, but it is believed that the results are valid for $\frac{\omega R_i^2}{\upsilon}$ greater than one as confirmed by the experimental tests in Part B.

APPENDIX I

ORDER OF MAGNITUDE OF BASIC TERMS

Rewriting the basic equations and giving the order of magnitude of the terms of the equations we have:

1. For continuity

$$\frac{\partial V_x}{\partial x} + \frac{\partial V_r}{\partial r} + \frac{V_r}{r} = 0$$

the terms are of order ω

2. For x momentum of the fluid in the form

$$\frac{\partial V_x}{\partial x}\frac{\partial x}{\partial t} + V_x \frac{\partial V_x}{\partial x} + V_r \frac{\partial V_x}{\partial r} + \frac{1}{\rho}\frac{\partial p}{\partial x} - \upsilon\left[\frac{1}{r}\left(\frac{\partial}{\partial r}\left(r\frac{\partial V_x}{\partial r}\right)\right) + \frac{\partial^2 V_x}{\partial x^2}\right] = 0$$

the terms are of order ωC except the convective acceleration terms which are of order $\omega V_{o\,max}$

3. For r momentum of the fluid in the form

$$\frac{\partial V_r}{\partial x}\frac{\partial x}{\partial t} + V_x \frac{\partial V_r}{\partial x} + V_r \frac{\partial V_r}{\partial x} + \frac{1}{\rho}\frac{\partial p}{\partial r} - \upsilon\left[\frac{\partial}{\partial r}\left(\frac{1}{r}\frac{\partial}{\partial r}\left(rV_r\right)\right) + \frac{\partial^2 V_r}{\partial x^2}\right] = 0$$

the terms are of order $\frac{c}{R_i}\left(\frac{\partial u_r}{\partial t}\right)_{max}$ except the convective acceleration terms which are of order $\frac{V_{o\,max}}{R_i}\left(\frac{\partial u_r}{\partial t}\right)_{max}$

4. For the axial and radial momentum equations for the tube the radial derivatives are considered negligible, that is

$$\frac{\left(\frac{\partial u_r}{\partial r}\right)_{MAX}}{\left(\frac{\partial u_r}{\partial x}\right)_{MAX}} \doteq \frac{\left(\frac{\partial u_x}{\partial r}\right)_{MAX}}{\left(\frac{\partial u_x}{\partial x}\right)_{MAX}} \ll 1$$

5. For fluid flow the following assumption is made;

$$1 \gg \frac{V_{0\,MAX}}{C} \gg \frac{1}{C}\left(\frac{\partial u_r}{\partial t}\right)_{MAX}$$

APPENDIX 2

ESTIMATION OF THE RESISTANCE COEFFICIENT

The damping effects of shear forces in the main flow and of radial perturbations of the transverse waves are estimated in this section by considering the main flow and the perturbations separately. Longitudinal waves in the tube should not change the resistance coefficient appreciably. The main oscillatory flow is considered to be without a radial velocity component, whereas, the radial velocity perturbations are considered to be induced by the tube wall oscillations.

Similar to the case of longitudinal wave perturbations in the tube section the main flow is given by

$$V_x = h(x, j\omega)\left[I_0(Kr) - I_0(KR_i)\right]$$

A comparison between equations (2) and (6) show that the average velocity $\bar{V}_x$ over a cross section is related to the average viscous term in the equations by

$$\frac{R}{\rho}\bar{V}_x = -\nu\left[\frac{\partial^2 V_x}{\partial r^2} + \frac{1}{r}\frac{\partial V_x}{\partial r}\right]$$

It may be shown that the resistance coefficient is given by

$$R = \frac{2j\omega\rho I_1(KR_i)}{KR_i\left[\frac{2}{KR_i}I_1(KR_i) - I_0(KR_i)\right]}$$

Similarly for the perturbation velocity given in the form as given in the section on transverse waves

$$v_x = g(x, j\omega)\left[I_0(Kr) - I_0(KR_i)\right]$$

Hence

$$R' = \frac{j2\omega\rho I_1(kR_i)}{kR_i\left[\frac{2}{kR_i}I_1(kR_i) - I_0(kR_i)\right]}$$

When the perturbation resistance coefficient is related to the main flow the combined resistance coefficient becomes for no end effects

$$R = \frac{2\omega^2\rho^2 I_1(kR_i)\,I_0(kR_i)}{\frac{\partial\bar{p}}{\partial x}\,kR_i\left[\frac{2}{kR_i}I_1(kR_i) - I_0(kR_i)\right]}\left\{\frac{\frac{\partial\bar{p}}{\partial x}}{j\omega\rho I_0(kR_i)} - \frac{jk_1 p_0 kc\cos(\omega\frac{x}{c})}{I_1(kR_i)\left[1 - I_0(kR_i)\right]}\right\}$$

Acknowledgment

The authors would like to express their appreciation for support of this project under DRB 9550-15, NRC A-1080 and NRC A-2754 research grants.

REFERENCES

1. Thomson, W.T., "Transmission of Pressure Waves in Liquid Filled Tubes", Proc. 1st U.S. National Congress of Applied Mechanics, 1951, p.927.

2. Morgan, G.W. and Kiely, J.P., "Wave Propagation in a Viscous Liquid contained in a Flexible Tube", J. Acoust. Soc. Amer., 27, 1954, p. 323.

3. Womersley, J.R., "Oscillatory Motion of a Viscous Liquid in a Thin-Walled Elastic Tube - I: The Linear Approximation for Long Waves", Phil. Mag., 46, 1955, p.199.

4. Junger, M.C. "The Effect of a Surrounding Fluid on Pressure Waves in a Fluid-Filled Elastic Tube", J. of App. Mech., 22-23, 1955, p.227.

5. Dragos L., "Sur le Mouvement d'un fluide visqueux dans un tube élastique", Compt. Rend. Acad. Sci. Paris, 254, 1962, p.417.

6. Rich, G.R., "Hydraulic Transients", Dover, 1963, p.5.

7. Ivey, D.G., Mrowca, B.A. and Gath, E., "Propagation of Ultrasonic Bulk Waves in High Polymers", J. of App. Phys. 20, 1949, p.486.

8. Den Hartog, J.P., "Advanced Strength of Materials", McGraw-Hill, 1952, p.57.

9. Lamb, H., "On the Velocity of Sound in a Tube as Influenced by the Elasticity of the Walls", Mem. Manchester Lit. and Phil. Soc., 42, 1898, No. 9.

FLUID DYNAMIC EFFECTS OF LIQUIDS IN ELASTIC TUBES

R.W. Besant and V. Srinivas
Division of Control Engineering
University of Saskatchewan

PART B EXPERIMENTAL AND COMPUTED RESULTS

ABSTRACT

In this paper experimental results are presented for an oscillating liquid flow in a long elastic tube with and without load. The frequency response of pressure and velocity for each case is compared to the computed results based on the theory of Part A. In addition the phase lags are also presented. Two different wave modes were observed in the experimental results, interaction and transverse. These waves showed strong attenuation and dispersion with frequency as indicated by the theory. Results are presented in dimensional and non-dimensional form.

1. INTRODUCTION

The analysis of an oscillating viscous flow of a liquid in an elastic tube is discussed in Part A.

In this paper results are presented for the frequency response of pressure, velocity and phase lag of a no load and a loaded elastic transmission line using water as transmission fluid. The experimental set-up is described. The experimental results are presented in both dimensional and non-dimensional form and they are discussed as compared to the computed results predicted by the theoretical analyses of Part A.

A great number of workers have done experiments on transmission lines, but very few have reported observing more than one type of elastic wave. Only one group, D'Souza and Oldenburger[1], has reported observing resonance with a second wave effect. Due to the type of load they selected, an orifice, they got a longitudinal wave resonance in the tube. This was analysed by neglecting wall shear forces on the tube and by including damping at the orifice but not in the tube. Taylor[2] experimented with oscillating viscous liquids in a long rubber tube terminating in a constant pressure reservoir. No resonance effects were observed in his system since, at high frequencies (up to 28 c/s), waves were attenuated and at low frequencies the termination was modified to eliminate reflection. McDonald[3] in his book, Blood Flow in Arteries, discusses the measurements of several workers who have tried to measure longitudinal extensions and radial extentions in arteries. While radial extensions are significant, it is difficult to draw definite conclusions about longitudinal strains. Bassett[4] experimentally tested the no load case.

2. EXPERIMENTAL TEST SETUP

The experimental test setup used is schematically illustrated in Figure 1 for the no load case and in Figure 2 for the load case. The power supply was the same for both cases. An hydraulic servo-mechanism using a linear hydraulic cylinder for a load was used to actuate a piston that oscillated saline water in an elastic tube.

Figure 1 illustrates the no load case where the elastic tube discharged fluid to and from a reservoir at constant pressure. For this case a natural rubber tube 24.2 feet long, 3/16 inches and 5/16 inches inside and outside diameters, respectively, was used.

Figure 2 illustrates the load case where the saline water was used to actuate a column of mercury in a U-tube as shown. This simulates a typical second order load. A 10.8-feet tygon tube was selected for this case with inside and outside diameters of 3/16 inches and 5/16 inches, respectively.

The instrumentation was the same for both cases; velocity and pressure were measured at input and output. The input velocity was measured by a fixed induction coil with a moveable iron core attached to the hydraulic ram. The output velocity was measured by a full flow electromagnetic flowmeter. Both pressures were measured by strain gage type transducers. Transducer signals were amplified and recorded on a strip chart. Static and dynamic calibration of all the transducers indicated that they had sufficient accuracy, sensitivity and bandwidth for all the test runs.

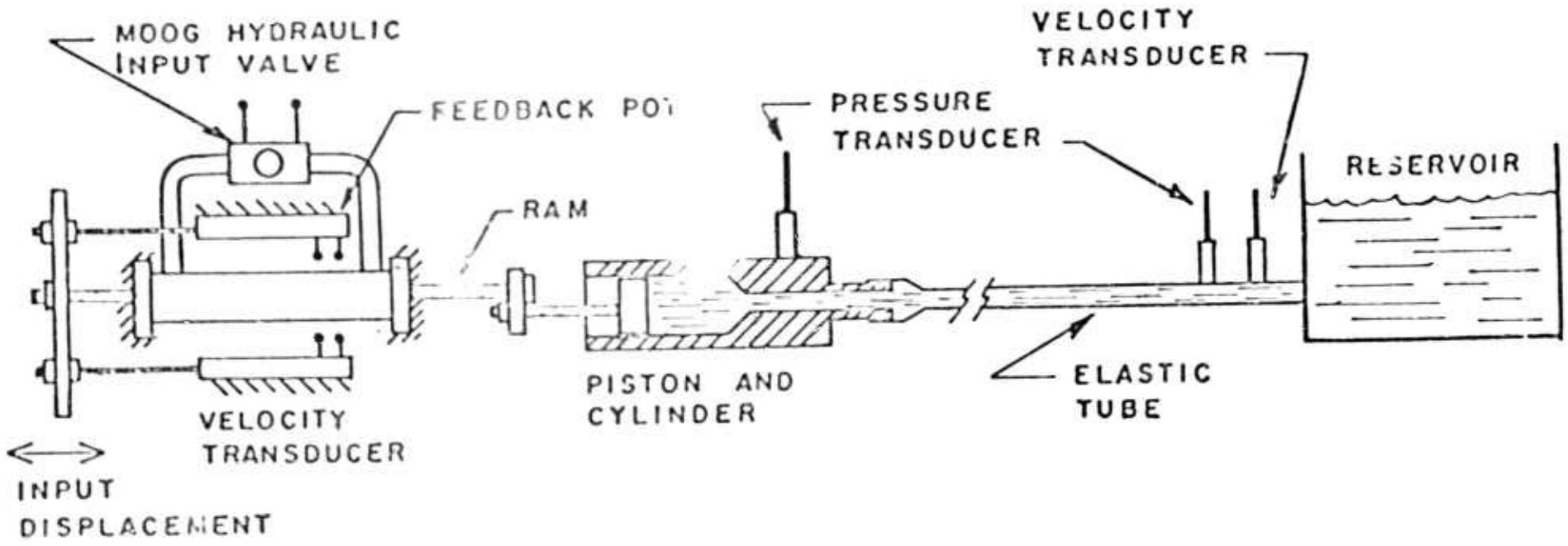

SCHEMATIC OF THE SYSTEM (NO LOAD)

FIGURE 1

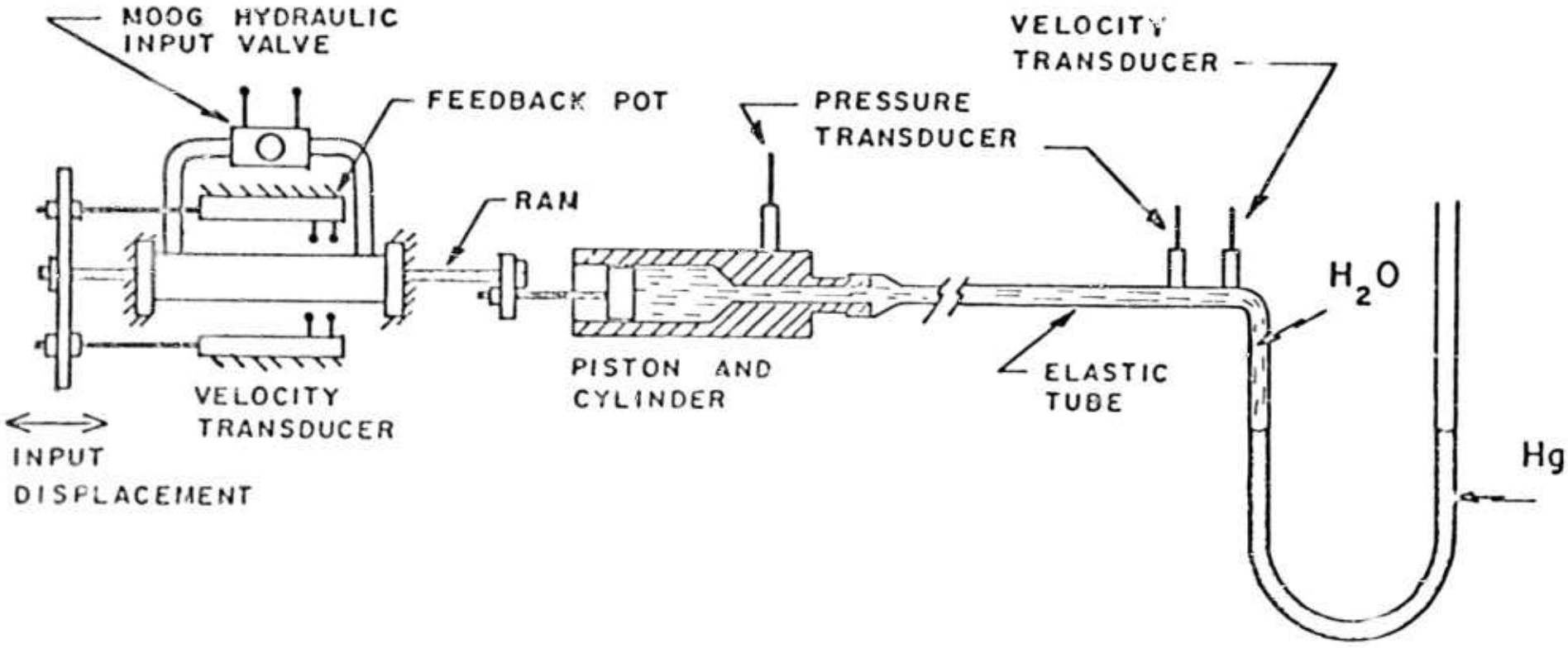

SCHEMATIC OF THE SYSTEM (LOAD)

FIGURE 2

3. THE NO LOAD RESULTS

Figures 3 and 4 present the computed and the experimental test results for the no load case. Two experimental runs were conducted for this case; one for low amplitude oscillations and another for high amplitude oscillations. The amplitude of oscillation was held constant within 5 percent for each test run. The experimental pressure response was zero for the no load case, as predicted by the theory; hence it is not presented. The theoretical velocity frequency response for the no load case is presented for various resistance coefficients in Figure 3 by using zero load impedance. The phase lag for velocity with the no load case are presented in Figure 4. The experimental results for phase lag are within 5 percent of the computed results for both test runs.

The effective bulk modulus for this case is estimated in Appendix 1.

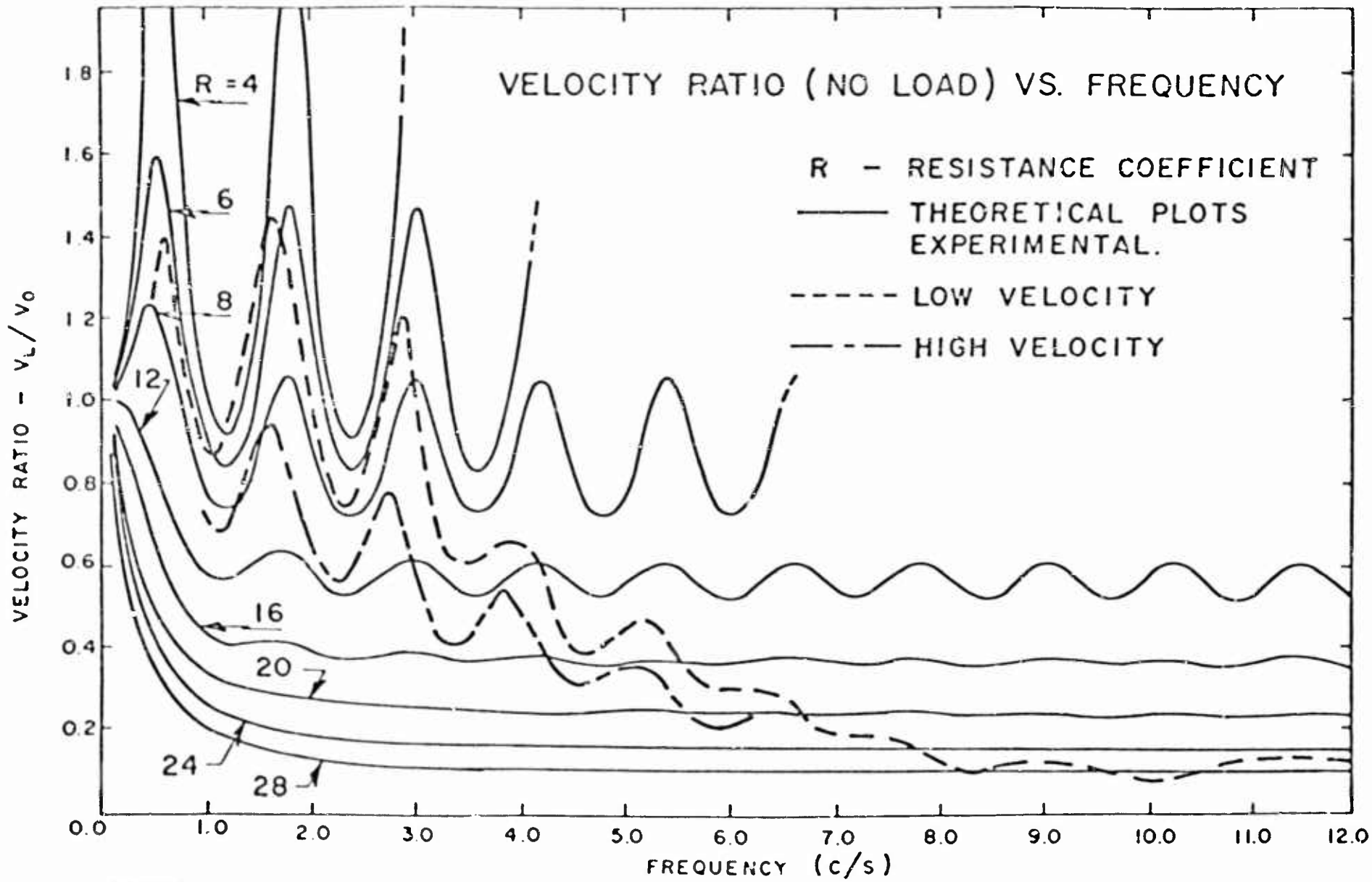
VELOCITY RATIO (NO LOAD) VS. FREQUENCY
R - RESISTANCE COEFFICIENT
THEORETICAL PLOTS
EXPERIMENTAL.
LOW VELOCITY
HIGH VELOCITY
R =4
6
8
12
16
20
24
28
VELOCITY RATIO - V_L / V_0
FREQUENCY (C/S)
0.0
1.0
2.0
3.0
4.0
5.0
6.0
7.0
8.0
9.0
10.0
11.0
12.0
0.2
0.4
0.6
0.8
1.0
1.2
1.4
1.6
1.8

FIGURE 3

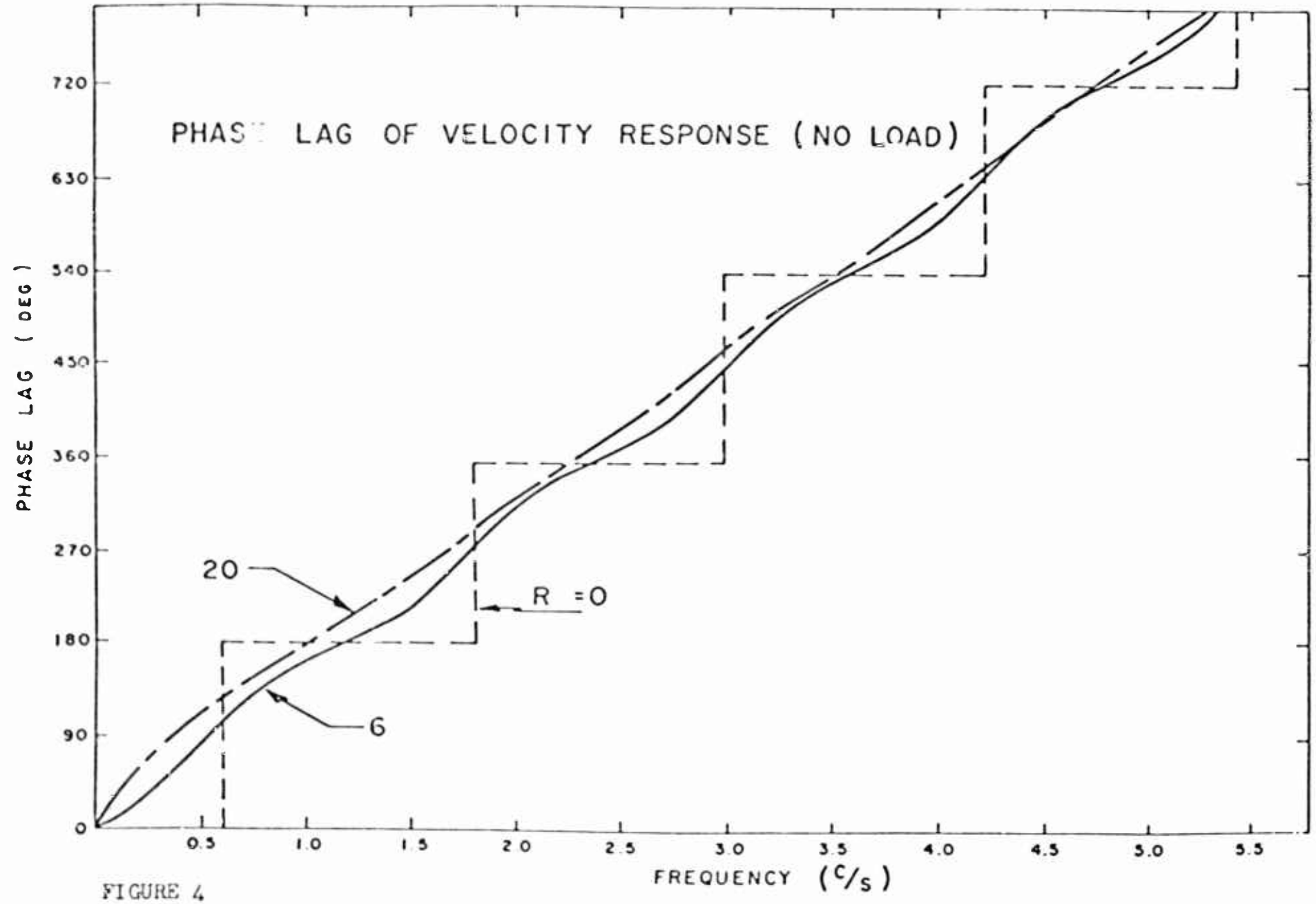
PHASE LAG OF VELOCITY RESPONSE (NO LOAD)
PHASE LAG (DEG)
720
630
540
450
360
270
180
90
0
20
R =0
6
0.5
1.0
1.5
2.0
2.5
3.0
3.5
4.0
4.5
5.0
5.5
FREQUENCY (C/S)

FIGURE 4

4. THE LOAD RESULTS

Figures 5,6 and 7 present the experimental and computed results for the load case. An estimation of the second order linear load is given in Appendix 2. Results are presented in dimensional and non-dimensional form in Figures 5 and 6. The non-dimensional terms are presented in Appendix 3. Figure 5 presents the pressure frequency response from the test results and from results computed for various resistance coefficients. Figure 8 estimates how the resistance coefficient should vary with frequency for this case. The velocity response is presented in Figure 6 for the load case in the same form as Figure 5. The phase lag is presented for only one resistance coefficient for both pressure and velocity in Figure 7. Other resistance coefficients would result in similar phase lag results.

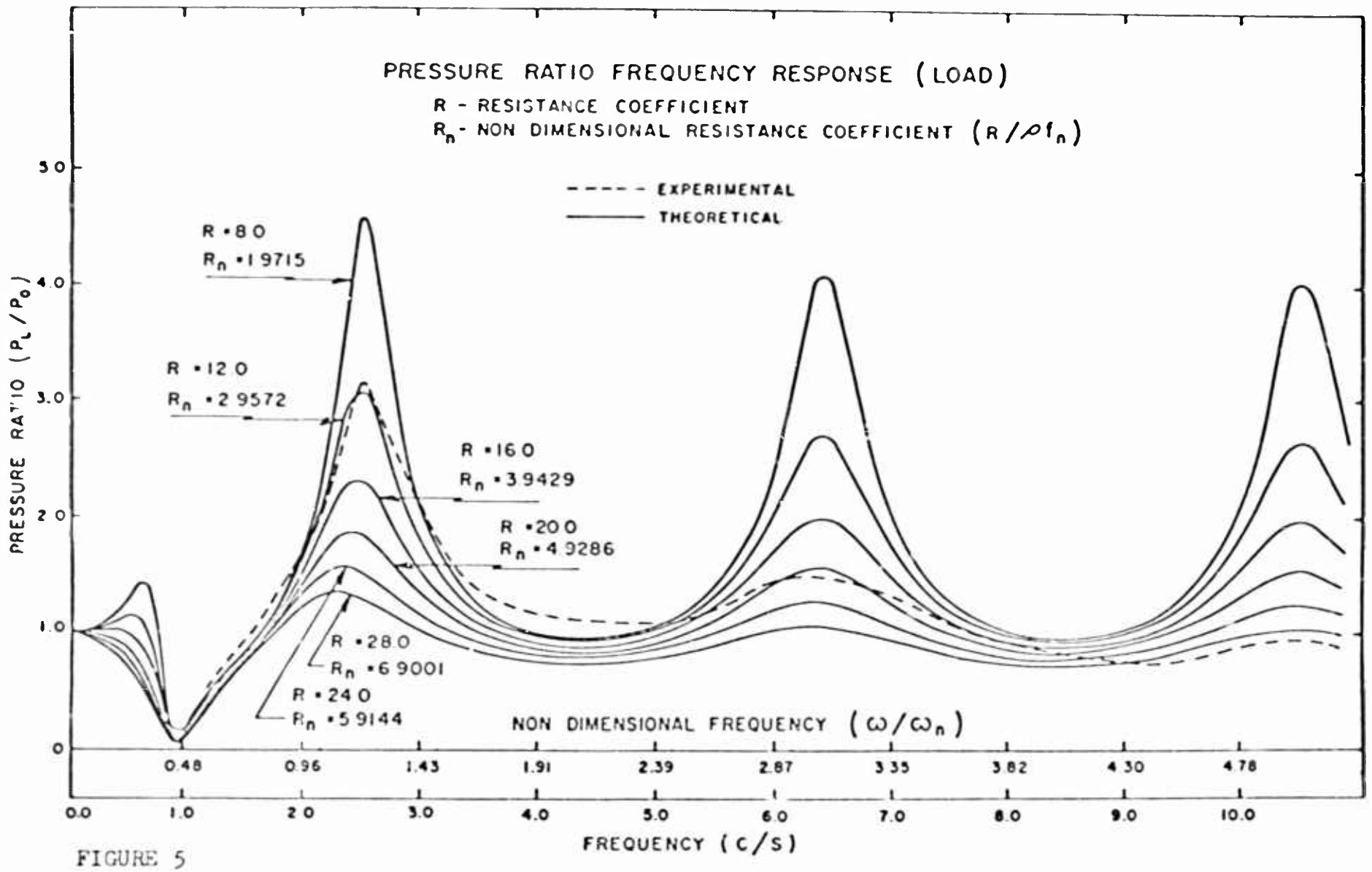
PRESSURE RATIO FREQUENCY RESPONSE (LOAD)
R - RESISTANCE COEFFICIENT
R_n - NON DIMENSIONAL RESISTANCE COEFFICIENT ($R/\rho f_n$)
EXPERIMENTAL
THEORETICAL
R = 8.0
R_n = 1.9715
R = 12.0
R_n = 2.9572
R = 16.0
R_n = 3.9429
R = 20.0
R_n = 4.9286
R = 28.0
R_n = 6.9001
R = 24.0
R_n = 5.9144
PRESSURE RATIO (P_L/P_o)
0
1.0
2.0
3.0
4.0
NON DIMENSIONAL FREQUENCY (ω/ω_n)
0.48
0.96
1.43
1.91
2.39
2.87
3.35
3.82
4.30
4.78
0.0
1.0
2.0
3.0
4.0
5.0
6.0
7.0
8.0
9.0
10.0
FREQUENCY (C/S)

FIGURE 5

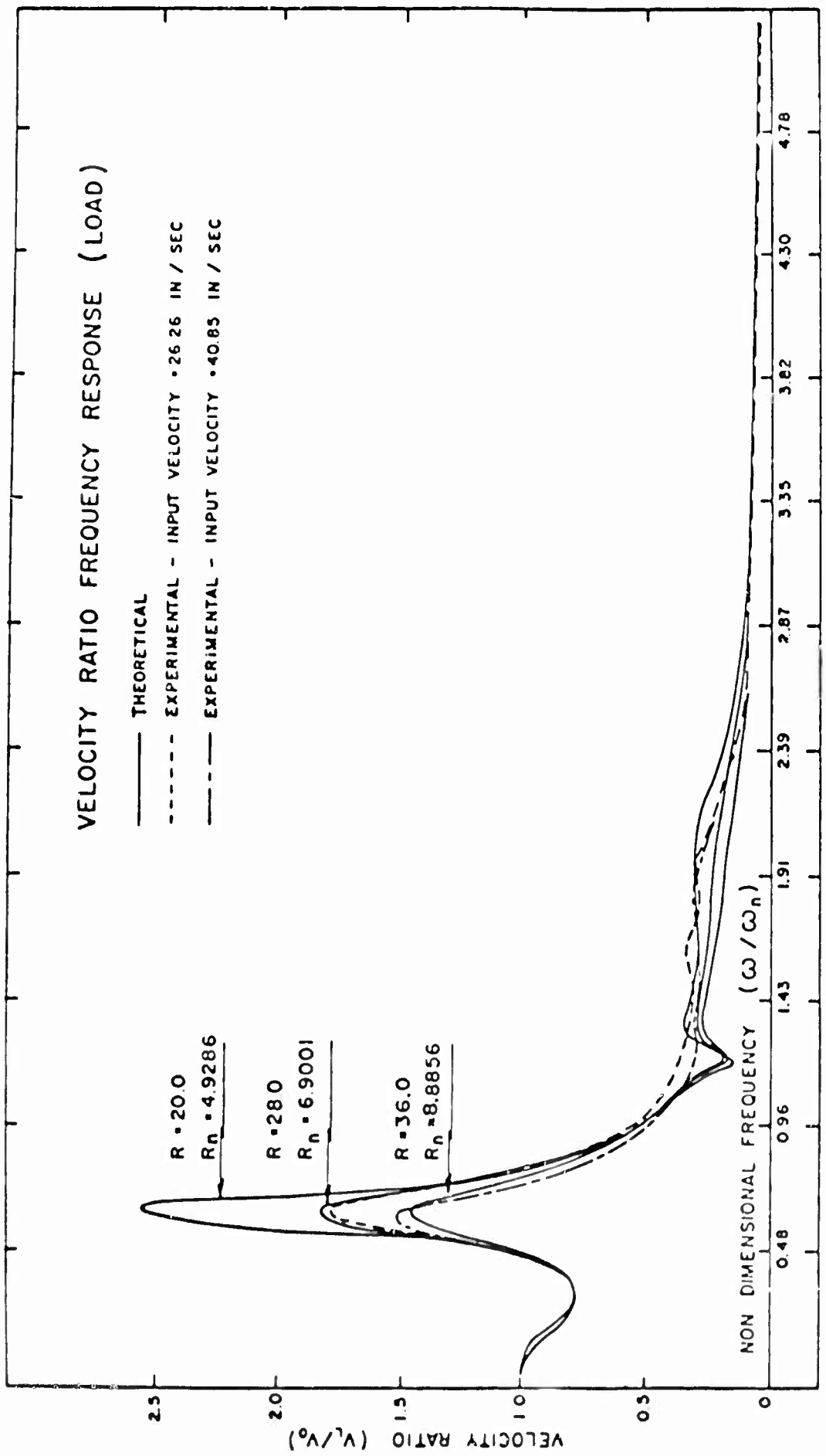
VELOCITY RATIO FREQUENCY RESPONSE (LOAD)
THEORETICAL
EXPERIMENTAL - INPUT VELOCITY •26 26 IN / SEC
EXPERIMENTAL - INPUT VELOCITY •40.85 IN / SEC
R • 20.0
Rn • 4.9286
R •28 0
Rn • 6.9001
R • 36.0
Rn •8.8856
VELOCITY RATIO (VL/Vo)
NON DIMENSIONAL FREQUENCY (ω/ωn)
FREQUENCY (C/S)

FIGURE 6

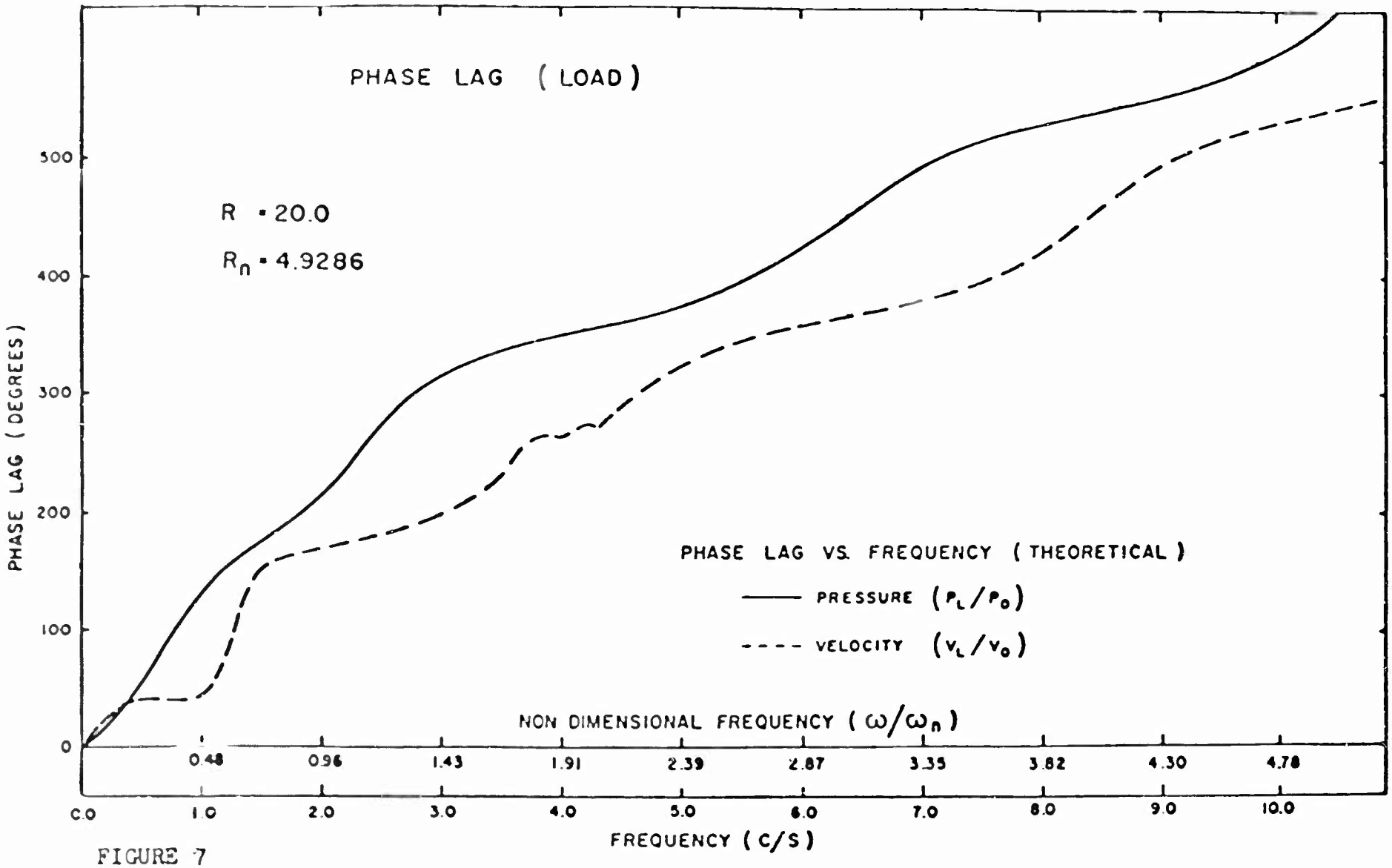
PHASE LAG (LOAD)
R = 20.0
R_n = 4.9286
PHASE LAG (DEGREES)
500
400
300
200
100
0
PHASE LAG VS. FREQUENCY (THEORETICAL)
PRESSURE (P_L/P_0)
VELOCITY (V_L/V_0)
NON DIMENSIONAL FREQUENCY (ω/ω_n)
0.48
0.96
1.43
1.91
2.39
2.87
3.35
3.82
4.30
4.78
0.0
1.0
2.0
3.0
4.0
5.0
6.0
7.0
8.0
9.0
10.0
FREQUENCY (C/S)

FIGURE 7

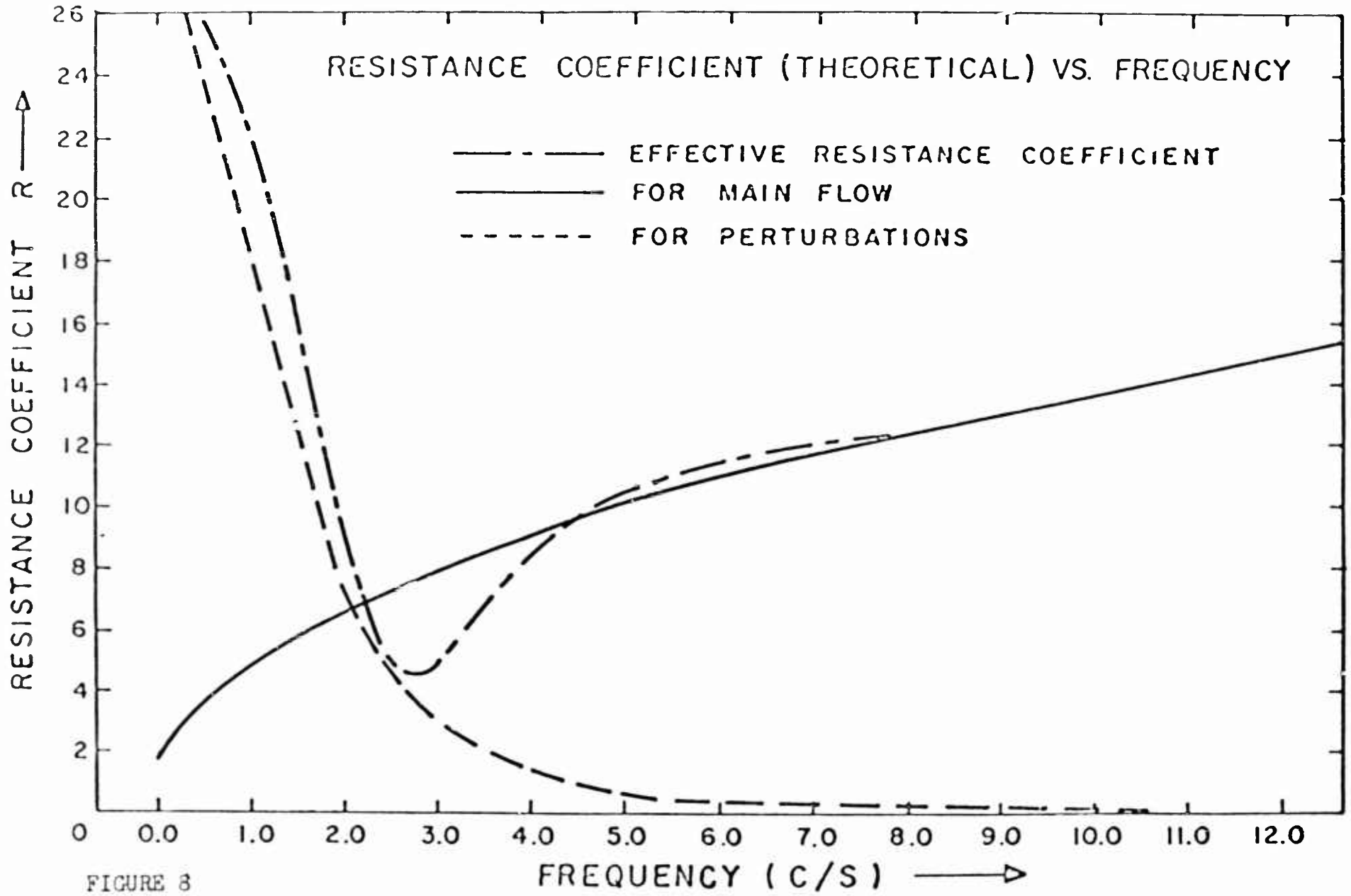
RESISTANCE COEFFICIENT (THEORETICAL) VS. FREQUENCY
EFFECTIVE RESISTANCE COEFFICIENT
FOR MAIN FLOW
FOR PERTURBATIONS
RESISTANCE COEFFICIENT R
FREQUENCY (C/S)
0
2
4
6
8
10
12
14
16
18
20
22
24
26
0.0
1.0
2.0
3.0
4.0
5.0
6.0
7.0
8.0
9.0
10.0
11.0
12.0

FIGURE 8

5. DISCUSSION OF RESULTS

The results presented in this paper tend to justify the theoretical analyses of Part A; however, a number of important limitations should be noted. The flow was essentially laminar, the tubes were relatively long, and the frequency range considered was slightly above zero and of moderate bandwidth. In addition, a number of disturbances may tend to cause some discrepancy between the computed and the experimental results. End effects were considered small in the long tubes used. Nonlinear elastic behaviour could be present but it should be slightly different in the two different types of tubes used, natural rubber and tygon. Figure 9 in Appendix 1 shows how the bulk modulus varies with pressure for the tygon tube. Flow disturbances such as periodic turbulence or cavitation could have been the greatest cause of irregularities. These two effects may cause increased resistance and capacitance. Cavitation was not observed during test runs, but, it could have existed to a small extent at the input end where the flow could not be observed. No tests were conducted for turbulence, but maximum Reynolds numbers were kept below 5000 for the maximum velocity test run and 3000 for the lower velocity amplitude test run.

The no load test results showed several interesting points. The resistance coefficient increased with frequency and with amplitude of oscillation. These effects are predicted by the theory although no computed results are presented for this case. The experimental results indicate that only the interaction type wave gave rise to any measureable resonance effects and that the phase velocity of this wave remained nearly constant over the frequency range considered. The theory also predicts the phase velocity nearly constant over this frequency range. Further studies of tube properties will be necessary before additional transverse or longitudinal wave resonance effects can be predicted accurately; however, the theory does predict the resonance frequencies accurately when they do exist as in the load case.

The load case indicated similar results to the no load case. The resistance coefficient increased with frequency amplitude as predicted by the computed results in Figure 8. The slight discrepancy between the two may be partially accounted for by the fact that damping was not included in the load. The results obtained here are similar to those of Taylor. The test results indicate that only the interaction type wave resonance is present for the pressure response, whereas, both the interaction and the transverse wave resonance were measured for the velocity response in Figure 6. The test results show that the phase velocity of the transverse wave has increased measureably as indicated by the viscoelastic damped wave results computed for this case. Longitudinal wave resonance, which would have occurred at a much higher frequency, gives no measureable result. The high damping coefficients indicated in Figure 8 would tend to predict this result.

The computed results presented in all graphs are thought to be very accurate except for a very small region where ω tends to zero. Some of the Bessel function ratios were indeterminate at $\omega = 0$.

APPENDIX 1

THE EFFECTIVE BULK MODULUS

It is well known that when liquid is used in pipe lines, the elastic nature of the pipe lines decreases the effective bulk modulus of the liquid. Here a method is shown to estimate the effective bulk modulus of the liquid using the equation for tube expansion as applicable to thick cylinders under constant pressure without end effect. The radial expansion Δu_r of the inner radius R_i of the tube when subjected to an internal pressure change Δp is given by

$$\Delta u_r = \frac{\Delta p}{E} \frac{R_i^3}{R_o^2 - R_i^2} \left[(1-\sigma) + (1+\sigma)\left(\frac{R_o}{R_i}\right)^2 \right] = \frac{m}{E} \Delta p = K_1 \Delta p$$

If a unit length of tube is considered, the change in fluid volume per unit length resulting from the pressure p_o is given by

$$\Delta V = \pi \left[(R_i + \Delta u_r)^2 - R_i^2 \right]$$

$$= 2\pi \Delta u_r R_i \qquad \text{FOR} \quad R_i >> \Delta u_r$$

$$= 2\pi p_o \frac{m}{E} R_i$$

The volumetric strain in the fluid and internal volume of the tube is

$$\frac{\Delta V}{V} = \frac{\Delta V}{\pi R_i^2} = \frac{\Delta p}{B'} + \frac{2m}{E R_i} \Delta p$$

Hence the effective bulk modulus is

$$\frac{1}{B} = \frac{1}{B'} + \frac{2m}{E R_i}$$

Figure 9 shows the theoretical effective bulk modulus of the water in the tygon tube for the load case. Curve A shows the linear case, Curve B shows the nonlinear case with load pressure applied from zero to p_o in one increment and finally Curve C shows the effect of small increments. Curve A was used for calculations.

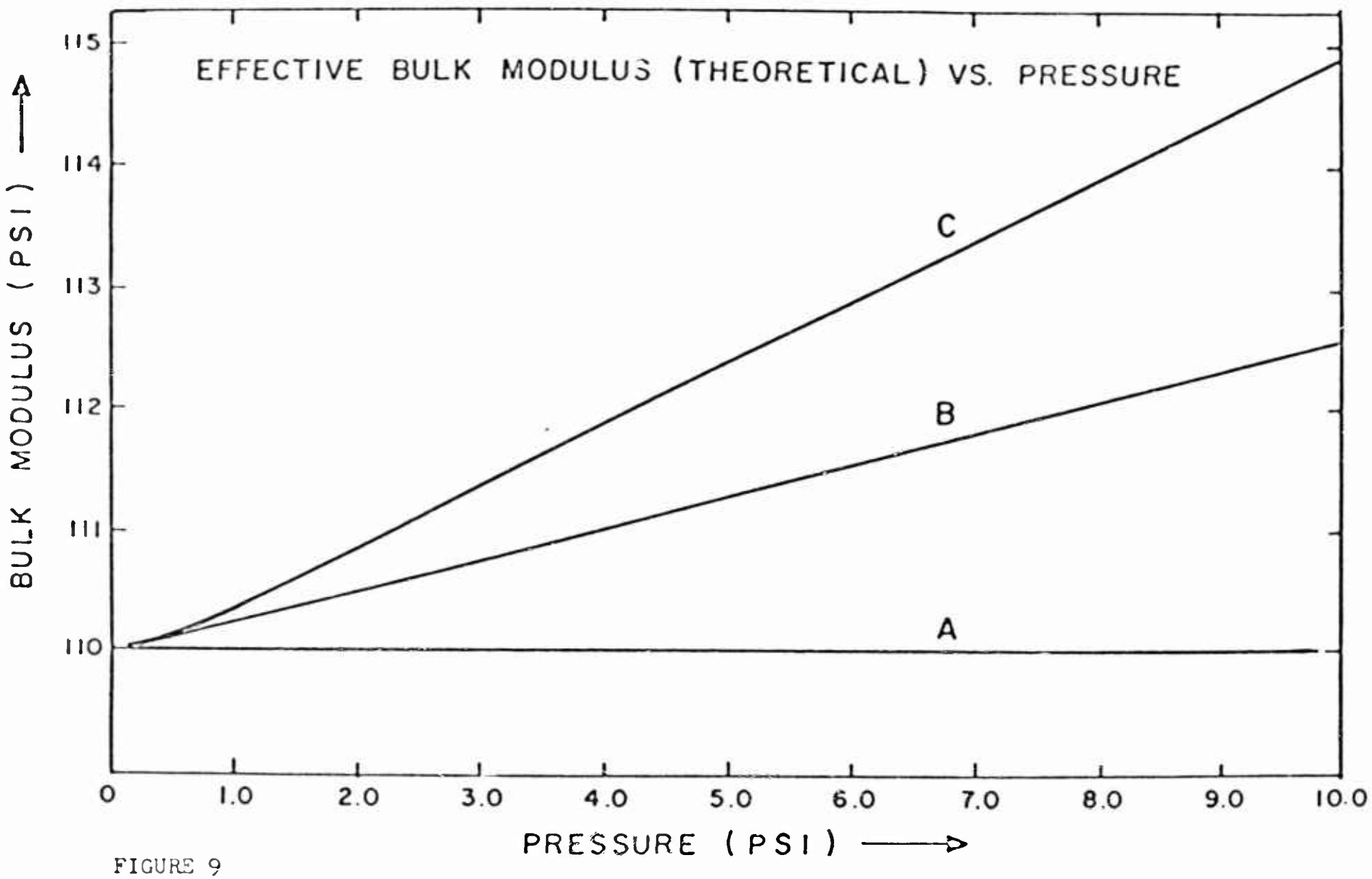
EFFECTIVE BULK MODULUS (THEORETICAL) VS. PRESSURE
BULK MODULUS (PSI) ⟶
115
114
113
112
111
110
C
B
A
0
1.0
2.0
3.0
4.0
5.0
6.0
7.0
8.0
9.0
10.0
PRESSURE (PSI) ⟶

FIGURE 9

APPENDIX 2

LOAD IMPEDANCE

Neglecting the damping effects of mercury in a glass tube, the forces acting on the mercury are water pressure and gravity.

$$P_L A_L = m_L W_L + K_s A_L \int W_L \, dt$$

For oscillating disturbances this can be rewritten

$$P_L(j\omega) = \frac{1}{A_L}\left[m_L j\omega + \frac{K_s A_L}{j\omega}\right] W_L$$

The velocity ratio of the elastic tube to glass tube is given by the area ratio

$$\frac{W_L}{V_L} = \frac{A_p}{A_L}$$

Hence the load impedance is

$$\frac{P_L(j\omega)}{V_L(j\omega)} = j\left[m_L \frac{A_p}{A_L^2}\omega - \frac{K_s A_p}{\omega A_L}\right]$$

APPENDIX 3

NONDIMENSIONAL TERMS

The interaction phase velocity C gives a resonant frequency $\omega_n = \frac{2\pi C}{4L}$. Using ω_n as a reference frequency we get the following non dimensional terms

$$\frac{\omega_n L}{C} \qquad \frac{\omega}{\omega_n} \qquad \frac{B}{\rho C^2} \qquad \frac{R}{\rho \omega_n} = R_n$$

Since the load must be matched to the tube for each case in which the wave velocity and length are varied, the results should not be construed as universal. However, if the load is matched to the tube conditions as required by the pressure and velocity response equations, then the nondimensional theory could be applied.

List of Symbols

A_L = area of glass U-tube

A_p = elastic tube flow area

B = effective bulk modulus

B' = bulk modulus of water

C = phase velocity of interaction wave

E = Young's modulus

$J = \sqrt{-1}$

L = tube length

m_L = mass of mercury load

P = pressure

P_L = pressure at load

P_o = pressure at input to tube

R = resistance coefficient

K_s = gravitational spring constant

R_n = nondimensional resistance coefficient

R_i = inner radius of elastic tube

R_o = outer radius of elastic tube

t = time

U_r = radial tube displacement

V = volume

W_L = load velocity

σ = Possion's ratio of elastic tube

ρ = water density

ω = frequency

ω_n = resonant frequency

V_L = Velocity at load end of elastic tube

V_o = velocity at input to elastic tube

Acknowledgement

The authors would like to express their appreciation for support of this project under DRB 9550-15, NRC A-1080 and NRC A-2754 research grants.

References

1. D'Souza, A.F. and Oldenburger, R., "Dynamic Response of Fluid Lines", Trans ASME Sec. D. Sept. 1964, p. 589.

2. Taylor, M.G., "An Experimental Determination of the Propagation of Fluid Oscillations in a Tube with a Visco-elastic Wall; together with an Analysis of the Characteristics Required in an Electric Analogue", Phys. Med. Biol., 4, 1959, p.63

3. McDonald, D.A., "Blood Flow in Arteries", Ch. IX, Edward Arnold, 1960.

4. Bassett, D.A., "Frequency Response of an Elastic Tube", B.Sc. Thesis, University of Saskatchewan, 1965.

HARRY DIAMOND LABORATORIES
WASHINGTON, D. C. 20438

TRANSIENT RESPONSE OF A FLUID LINE WITH AND WITHOUT BLEEDS

by

WILLIAM H. WALSTON, JR.

ARMY MATERIEL COMMAND

DEPARTMENT OF THE ARMY

CONTENTS

ILLUSTRATIONS

LIST OF SYMBOLS

a	speed of sound
A	cross-sectional area
d	subscript, upstream of nozzle
e	subscript, exit conditions
G	gap width
L	duct length
n	subscript, entrance conditions
o	subscript, stagnation conditions
P	Riemann variable
Q	Riemann variable
r	subscript, atmospheric or reference conditions
s	specific enthalpy
t	time coordinate
u	flow velocity
x	distance coordinate
γ	ratio of specific heats
θ	form of Riemann variable
ξ	nondimensional space coordinate
τ	nondimensional time coordinate
ϕ	form of Riemann variable

ABSTRACT

The theory of characteristics is applied to determine the transient response of rectangular ducts to a step input. The step input is generated by a unique film-snatching apparatus. The output pulse of the duct is shaped by a nozzle termination and by the addition of side branches to the duct. Only subsonic flow is considered. Experimental results that confirm the theoretical predictions are presented.

I INTRODUCTION

In order to design fluid amplifiers that will meet certain performance specifications, it is necessary to know the dynamic characteristics of the units. If the amplifier is a proportional device operating on small amplitude signals, the dynamic properties can be determined satisfactorily using linearized equations and the static performance curves. However, bistable devices generally operate on large amplitude signals, which cause sizeable reflections at discontinuities and terminations. These reflections have been noted by Keto [1] and by Katz, Winston, and Hawes [2]. This type of disturbance is present both in the amplifier proper and in the connecting lines or ducts. Therefore it is especially important to consider large amplitude waves when bistable units are being staged.

The mass flow required to switch a bistable amplifier is an important parameter. Generally this flow passes through a nozzle or an orifice at the control input. In a static experiment the pressure and flow at the control on the attached side is slowly increased until a switch is obtained. Dynamic experiments at HDL have shown that switching can be accomplished at a lower steady-state control pressure if the control input is applied suddenly instead of gradually. The sudden application of a signal is similar to the condition that exists when one bistable unit is being switched by the output of another bistable device. In such cases there can be periods when the transient flow through the control port is greater than the steady-state level. This difference is, however, not large enough to account for the difference between static and dynamic switching.

The ultimate purpose of this investigation is to obtain a better understanding of the dynamic performance of bistable amplifiers. This preliminary work, however, is concerned only with the effects of reflections of finite amplitude waves in fluid lines. A rigorous analysis of the problem is not feasible. However, by

making suitable assumptions, the problem can be treated by the method of characteristics.

In many cases, bleeds or side branches are used in fluid amplifier systems. These have been discussed by Warren (3) as steady-state load decoupling devices. The effect of bleeds on dynamic signals is not so well known, however. In this paper, a study is made of the effect of bleeds on the output velocity of a duct when the input pressure is a step function. The flow out of the bleed itself is also considered. The analysis presented here is restricted to subsonic flow.

II WAVES AND REFLECTIONS IN DUCTS

Finite amplitude waves and reflections are treated extensively by Rudinger (4), Foa (5), Shapiro (6), and others. Much of the background for this report is taken from their works. In some fluid amplifier applications, reflected waves may be used to advantage while in other instances it may be desirable to eliminate them. One objective of this study is to determine the effect of geometric changes on the shape of the output pulse.

The manner in which waves of finite amplitude are reflected depends upon three major factors—(1) the termination geometry, (2) the environment into which the wave is propagating, and (3) the properties of the wave itself. If the end of the duct is closed, waves are reflected in a like sense, i.e., compression as compression and expansion as expansion. If the duct is completely open at the end, the waves are reflected in an unlike sense. Now consider the duct to be terminated by a nozzle. In this case both types of reflections are possible depending upon the nozzle ratio and the strength of the incident wave. The nozzle ratio is defined as the smallest cross-sectional area of the nozzle divided by the cross-sectional area of the duct. It is apparent that by a proper matching of these parameters, there may be no reflection at all from the termination. The duct is then said to be matched.

The equations associated with nonsteady fluid flow are complex and are difficult to solve by analytical procedures. Fortunately there is available a graphical or numerical technique adaptable to this type of problem. This method, known as the theory of characteristics, is used in solving differential equations.

When writing fluid equations, one may select which of several variables to use. In this case, it has been found advantageous to use the local speed of sound, a, and the local particle speed relative to the duct, u. Having chosen the variables it is now necessary to write the pertinent equations in terms of them.

The following assumptions are made:

1. one-dimensional flow in the duct,
2. ideal gas,
3. isentropic flow,
4. area unvarying with time, i.e., rigid walls.

Using these assumptions, the continuity equation may be written in terms of a and u as:

$$\frac{2}{\gamma-1}\frac{\partial a}{\partial t} + \frac{2}{\gamma-1}u\frac{\partial a}{\partial x} + a\frac{\partial u}{\partial x} = -au\frac{\partial \ln A}{\partial x} \quad . \tag{1}$$

where A is the cross-sectional area of the duct.

The momentum equation is

$$\frac{\partial u}{\partial t} + u\frac{\partial u}{\partial x} + \frac{2}{\gamma-1}a\frac{\partial a}{\partial x} = 0 \quad . \tag{2}$$

These equations may be combined to give

$$\frac{\partial}{\partial t}\left(\frac{2}{\gamma-1}a \pm u\right) + (u \pm a)\frac{\partial}{\partial x}\left(\frac{2}{\gamma-1}a \pm u\right) = -au\frac{\partial \ln A}{\partial x} \quad . \tag{3}$$

It is desirable to nondimensionalize these equations. This is accomplished through multiplication by $L_r a_r^2$ (Rudinger, 4), where L_r is the length of the duct and a_r is the ambient speed of sound. We obtain

$$\frac{\partial}{\partial \tau}\left(\frac{2}{\gamma-1}\frac{a}{a_r} \pm \frac{u}{a_r}\right) + \left(\frac{u}{a_r} \pm \frac{a}{a_r}\right)\frac{\partial}{\partial \xi}\left(\frac{2}{\gamma-1}\frac{a}{a_r} \pm \frac{u}{a_r}\right) = -\frac{au}{a_r^2}\frac{\partial \ln A}{\partial \xi} \qquad (4)$$

where

$$\xi = \frac{x}{L_r} \qquad (5.a)$$

and

$$\tau = \frac{a_r t}{L_r} \cdot \qquad (5.b)$$

It is convenient to group the variables in equation 4. The new variables thus formed are called the Riemann variables. They are defined as

$$P = \frac{2}{\gamma-1}\frac{a}{a_r} + \frac{u}{a_r} \qquad (6.a)$$

and

$$Q = \frac{2}{\gamma-1}\frac{a}{a_r} - \frac{u}{a_r} \cdot \qquad (6.b)$$

Equations 4 may now be written as

$$\frac{\partial P}{\partial \tau} + \left(\frac{u}{a_r} + \frac{a}{a_r}\right)\frac{\partial P}{\partial \xi} = -\frac{au}{a_r^2}\frac{\partial \ln A}{\partial \xi} \qquad (7.a)$$

and

$$\frac{\partial Q}{\partial \tau} + \left(\frac{u}{a_r} - \frac{a}{a_r}\right)\frac{\partial Q}{\partial \xi} = -\frac{au}{a_r^2}\frac{\partial \ln A}{\partial \xi} \quad . \tag{7.b}$$

These two equations enable us to solve some unsteady flow problems. By choosing

$$\frac{d\xi}{d\tau} = \frac{u}{a_r} + \frac{a}{a_r} \tag{8.a}$$

and

$$\frac{d\xi}{d\tau} = \frac{u}{a_r} - \frac{a}{a_r} \quad , \tag{8.b}$$

equations (7.a) and (7.b) become

$$\frac{dP}{d\tau} = \frac{\partial P}{\partial \tau} + \frac{\partial P}{\partial \xi}\frac{d\xi}{d\tau} = -\frac{au}{a_r^2}\frac{\partial \ln A}{\partial \xi} \tag{9.a}$$

and

$$\frac{dQ}{d\tau} = \frac{\partial Q}{\partial \tau} + \frac{\partial Q}{\partial \xi}\frac{d\xi}{d\tau} = -\frac{au}{a_r^2}\frac{\partial \ln A}{\partial \xi} \quad . \tag{9.b}$$

Equations (8.a) and (8.b) designate the P-characteristics and the Q-characteristics. Equations (7.a) and (7.b) describe the behavior of the P and Q waves along these curves or characteristics. This will be of considerable benefit in solving wave reflection problems.

Consider the problem shown in figure 1.

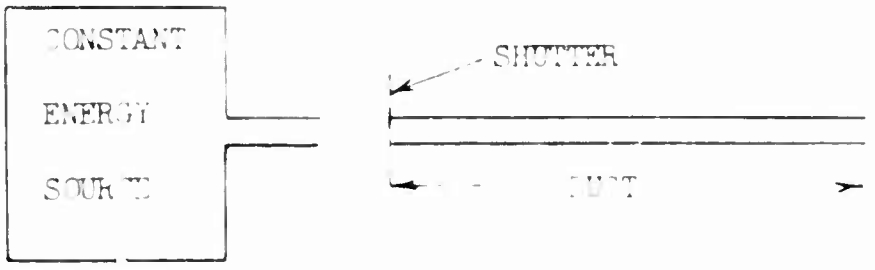

Figure 1. Schematic Drawing of Nonsteady Flow Problem under Consideration

The duct is separated from the source by a shutter. The shutter is moved instantly, allowing a step function pulse to enter the duct. To solve this problem, it is necessary to specify the boundary conditions at the entrance and at the exit of the duct. A constant energy source is assumed at the duct entrance. This assumption leads to a unique relation between the P and Q variables at the entrance to the duct. To obtain this relation the energy equation is written in the form

$$\frac{1}{2}\left(\frac{P}{a_r}\right)^2 + \frac{1}{\gamma-1}\left(\frac{a}{a_r}\right)^2 = \frac{1}{\gamma-1}\left(\frac{a_o}{a_r}\right)^2 \quad . \tag{10}$$

The definition of the Riemann variables given in equations (9) and the energy equation (10) may now be combined. When this is done for a specific heat ratio of $\gamma = 1.4$, the result is

$$P_n = \frac{2Q_n \pm \sqrt{150\left(\frac{a_o}{a_r}\right)^2 - 50Q_n^2}}{3} \tag{11}$$

where the subscript n refers to the entrance conditions. Equation (11) represents the constant energy ellipse for the entrance to the duct in terms of the Riemann variables. This may be nondimensionalized by setting

$$\phi = \frac{P}{\frac{a_o}{a_r}} \tag{12.a}$$

and

$$\Omega = \frac{Q}{\frac{a_o}{a_r}} \tag{12.b}$$

Now

$$\phi_n = \frac{2\omega_n \pm \sqrt{150 - 5\omega_n^2}}{3} \quad . \tag{13}$$

This equation represents the constant energy level for any stagnation pressure, so we need to plot only one ellipse for all conditions. Figure 2 illustrates this curve.

The boundary condition at the duct exit must also be specified. Thermodynamic relations yield

$$\frac{p}{p_r} = \left(\frac{a}{a_r}\right)^{2\gamma/\gamma-1} e^{-\frac{1}{R}(s - s_r)} \tag{14}$$

where p is pressure, s is specific entropy, and the subscript r denotes reference conditions, which in this case are the ambient conditions. Since an isentropic process is assumed, $s = s_r$, or

$$\left(\frac{p}{p_r}\right)^{(\gamma-1/2\gamma)} = \frac{a}{a_r} \quad . \tag{15}$$

The boundary condition chosen is that the exit pressure, p_e, is equal to the atmospheric pressure, p_r. Thus

$$\frac{a_e}{a_r} = 1 \tag{16}$$

where a_e is the speed of sound at the duct exit. The exit relation is obtained by combining equations (6) and (11) for $\gamma = 1.4$ to yield

$$P_e + Q_e = 10 \tag{17}$$

where the subscript e denotes exit conditions. Equation (17) is

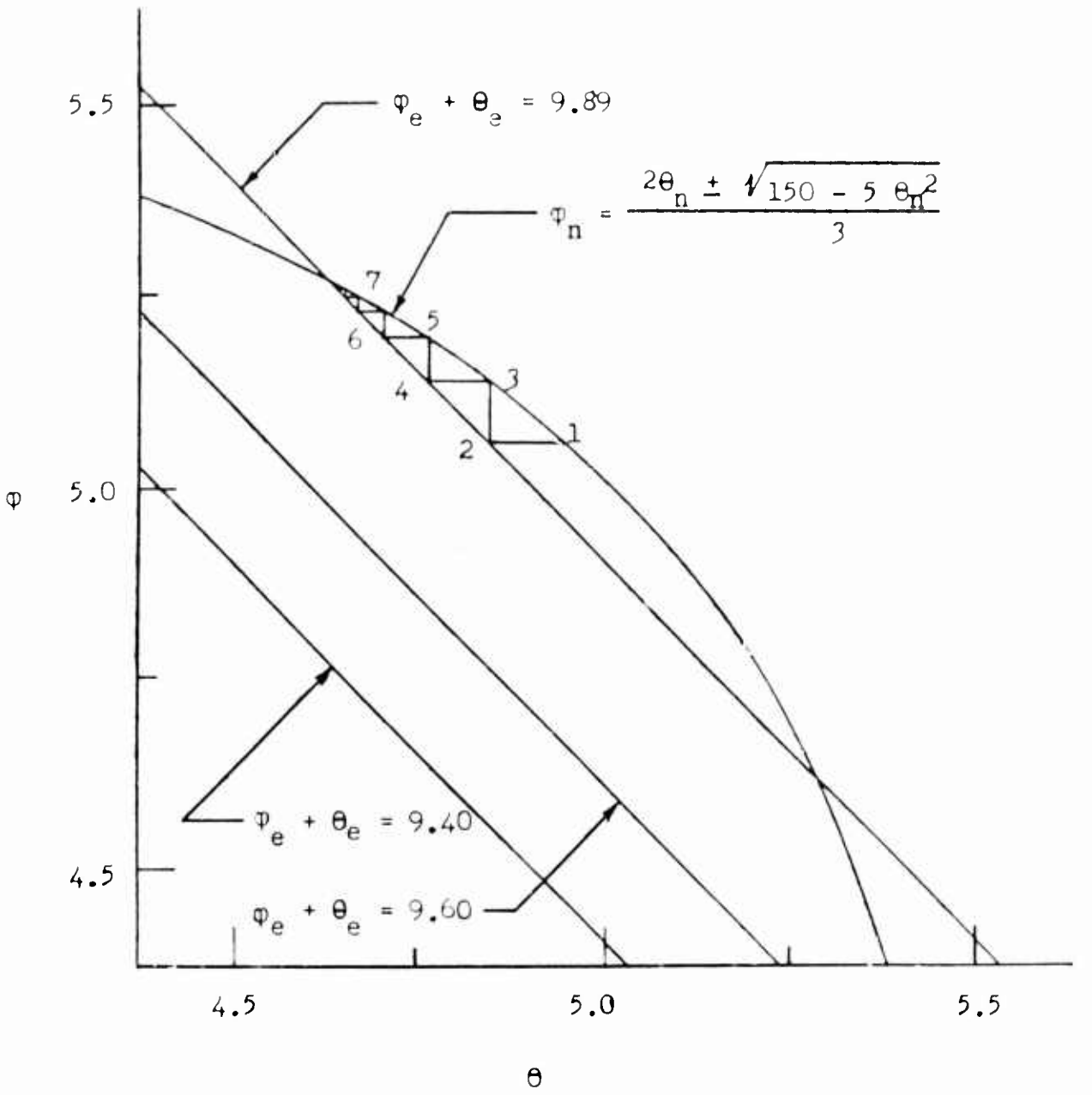

FIGURE 2. BOUNDARY CONDITIONS AT ENTRANCE AND EXIT OF DUCT.

then the boundary condition at the duct exit in terms of the dimensionless variables. It may be rewritten as

$$\theta_e + \phi_e = \frac{10}{\frac{a_o}{a_r}} \qquad (19)$$

which is also plotted for several values of a_o/a_r in figure 2, where a_o is the stagnation speed of sound. Given a particular energy level at the source, the transient flow at the open end of the duct may now be determined from figure 2.

For example, if the stagnation pressure at the duct entrance is $p_o = 1.17$ psig, the stagnation speed of sound is given by

$$\frac{a_o}{a_r} = \left(\frac{p_o}{p_r}\right)^{1/7} = (1.0796)^{1/7} = 1.011 \quad . \qquad (17)$$

Now calculate the strength of the initial pressure wave into the duct which is filled with motionless air, $u = 0$. To do this the starting point, denoted by subscript 1, on the ellipse must be obtained. From equation (6.b),

$$\theta_1 = \frac{Q_1}{\left(\frac{a_o}{a_r}\right)} = \frac{5}{1.011} = 4.9455 \qquad (20)$$

which locates point 1 on the ellipse. As the pressure wave propagates down the duct, ϕ remains constant. Now it must be determined which of the exit condition lines is applicable to this case. Equation (18) gives

$$\theta_2 + \phi_2 = \frac{10}{\left(\frac{a_o}{a_r}\right)} = \frac{10}{1.011} = 9.8910 \qquad (21)$$

which determines the location of point 2 in figure 2. Point 3 is now reached by moving along a constant θ line to the energy ellipse. Point 4 is determined by moving along a constant ϕ line to the exit condition $\phi + \theta = 9.891$. This procedure is continued until steady state is reached at the intersection of the two boundary condition lines. Since both ϕ and θ are known at each point, the exit velocity, u_e, may be easily calculated at each point also. Figure 3 shows the time distance representation of the analysis described above. This particular type of plot is often referred to as a wave diagram. The values of ϕ and θ are shown for any point along the duct at any given time. As one proceeds up the time axis, the flow approaches steady state and ϕ and θ approach constant values.

The experimental apparatus designed to test the theory is shown in figure 4. A strip of film covers the entrance of the duct as the pressure in the source is raised to the desired level. Air flows out of the source and is exhausted at the gap between the source and the duct entrance. The film strip is then brought into contact with the motor-driven friction wheel, which pulls the film through the film guide at a high speed. Typical film speed is approximately 75 fps. This means that the entrance to the duct is uncovered in 0.25 to 0.30 msec. This sudden opening allows a step pressure wave to start down the duct. The flow at the exit is measured by a hot-wire anemometer. Since the voltage-velocity plot is nonlinear for the type of instrument used, one must consider this when observing the experimental oscilloscope plots. The duct is a 0.50- by 0.25-in. rectangular channel, which was varied in length from 1.25 to 27.25 in. in the experiments.

To supply a duct of this size with constant energy requires a source with a very low impedance. Since this was not available,

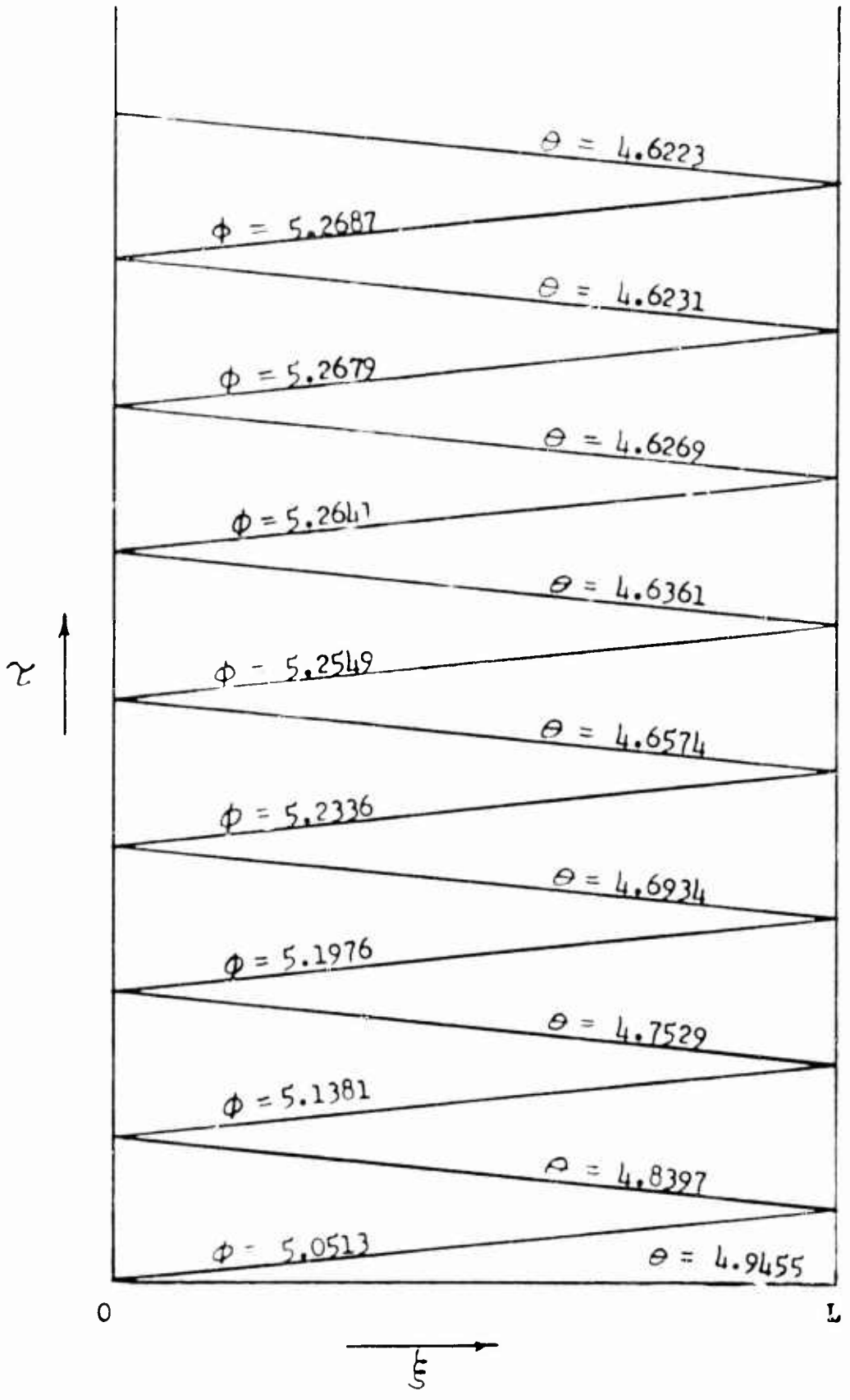

FIGURE 3. REFLECTIONS OF CHARACTERISTICS IN THE OPEN-ENDED DUCT.

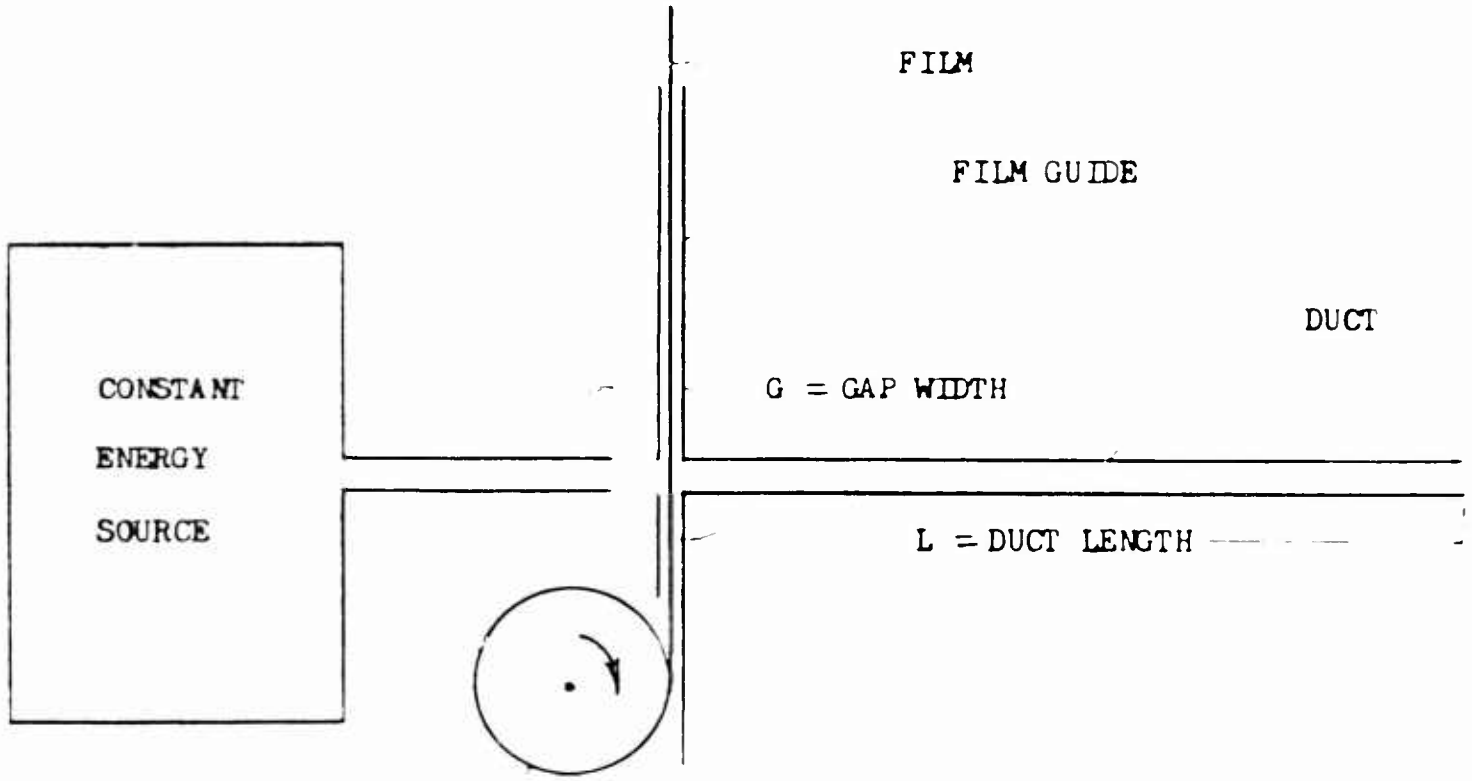

FIGURE 4. EXPERIMENTAL APPARATUS.

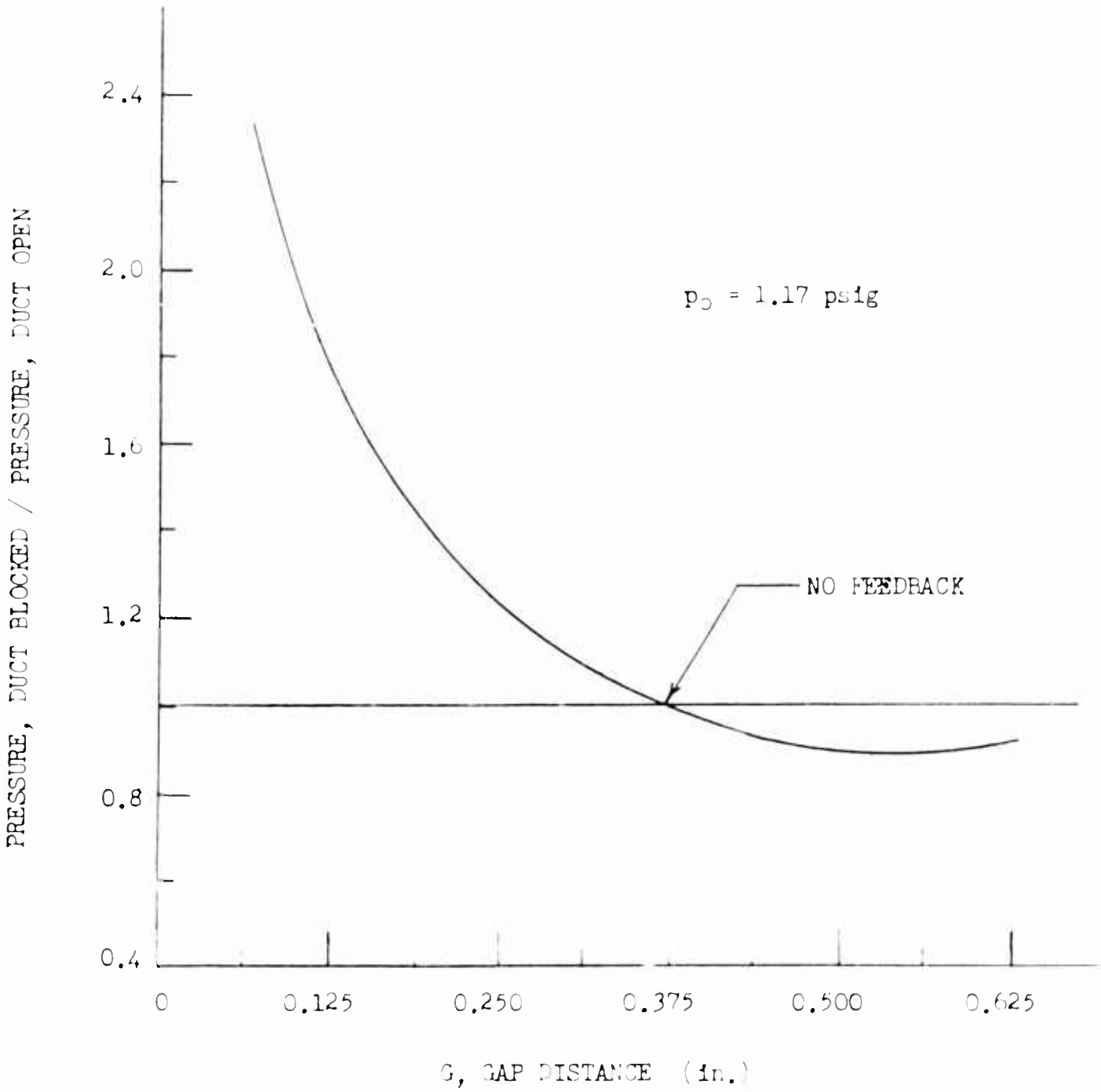

FIGURE 5. FEEDBACK AS A FUNCTION OF GAP DISTANCE

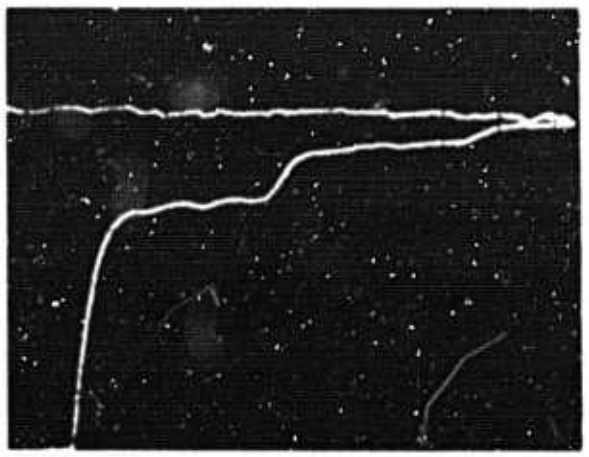

(1 V/DIV)

(1 MSEC/DIV)

a) OSCILLOSCOPE PLOT

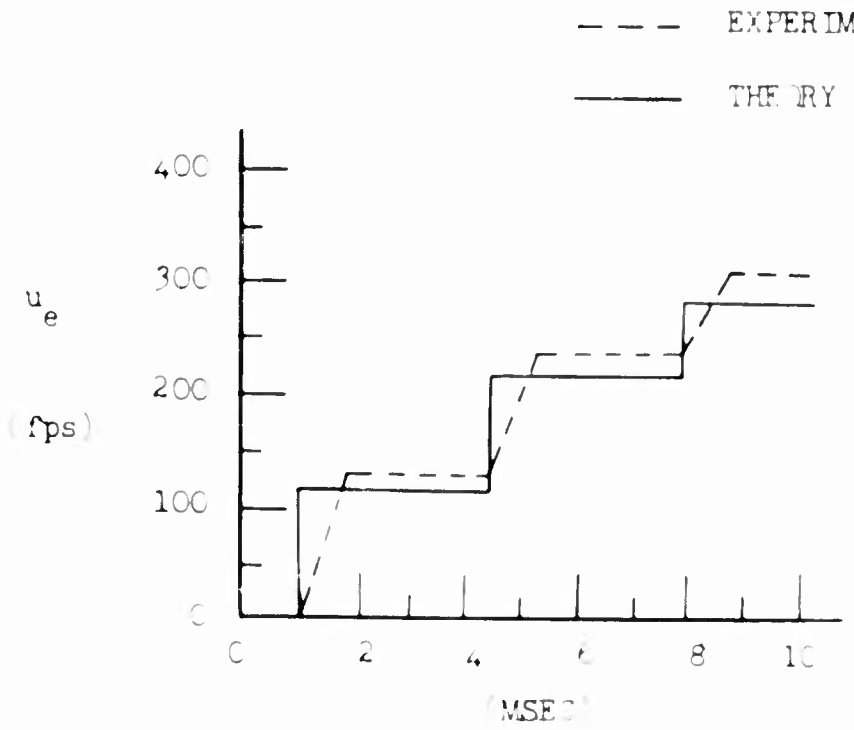

b) COMPARISON OF THEORY AND EXPERIMENT

FIGURE 4. TYPICAL RESULTS FOR OPEN-ENDED DUCT.

the width of the gap, δ, became a critical adjustment. The gap must be large enough so that no feedback from reflections within the duct will affect the source, i.e., the gap must isolate the source from any feedback. If the gap is too short, the source pressure will drop as the duct entrance is sealed. The gap must be large enough to present a fixed load to the source. Experiments were performed to determine the optimum gap width. Typical results are shown in figure 7. From these results, a gap width of 0.375 in. was chosen. The negative feedback depicted at width just above 0.37 in. is similar to results found by Chen [7].

Figure 8a shows the oscilloscope plot of voltage against time for a typical experiment. Experiment is compared with theory in figure 8b. The theoretical amplitude of the pulse agrees well with the experimental results. Since the hot wire is used to measure only the midstream velocity, the experimental results exceed the theoretical predictions. Even better agreement is obtained in the time coordinate. The theoretical time required for a reflection to travel from the exit to the source and return to the exit is calculated to be approximately 3.9 msec for a 24-in. duct. This corresponds to the experimental results of between 3.4 and 3.7 msec as seen in figure 8.

III DUCTS WITH NOZZLE TERMINATIONS

Now consider the duct to be terminated by various nozzle ratios as shown in figure 9.

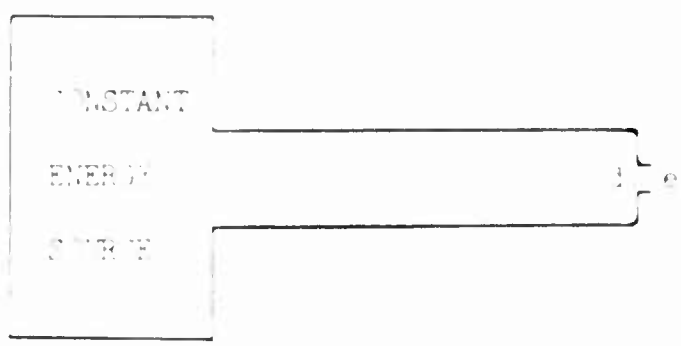

Figure 9. Schematic of Duct Terminated by Nozzle

It is convenient to consider the nozzle as a discontinuous change of cross-section area at the exit of the duct. It is therefore assumed that the fluid properties change instantaneously at the nozzle and that the nozzle length is short so that i and e may be treated as coincident points. Let i denote the conditions upstream of the nozzle and e those downstream, which are also the exit conditions.

The steady-state energy equation (1) when referred to conditions at the duct exit is written as

$$\frac{a_o}{a_e}^2 = 1 + 0.2 \frac{u_e}{a_e}^2 \qquad 22)$$

since $a_r = a_o$ and $\gamma = 1.4$.

From equation (11) the initial P-wave at the exit is calculated to be

$$P_e = \frac{10 + \sqrt{150 \frac{a_o}{a_e}^2 - 125}}{3} \qquad 23)$$

since $Q_e = 5,000$ initially. Now if the duct is perfectly matched, the initial P-wave will equal the steady-state P-wave. This gives

$$P_i = P_e = \frac{10 + \sqrt{150 \left(1 + 0.2 \frac{u_e}{a_e}^2\right) - 125}}{3} \qquad 24)$$

for the steady-state or matched conditions at the duct exit. This is plotted as the steady-state curve in figure 8.

The conservation of mass between points i and e gives the relation

$$\frac{\rho_i}{\rho_e} \frac{u_i}{u_e} = \frac{A_e}{A_i} \quad . \qquad 25)$$

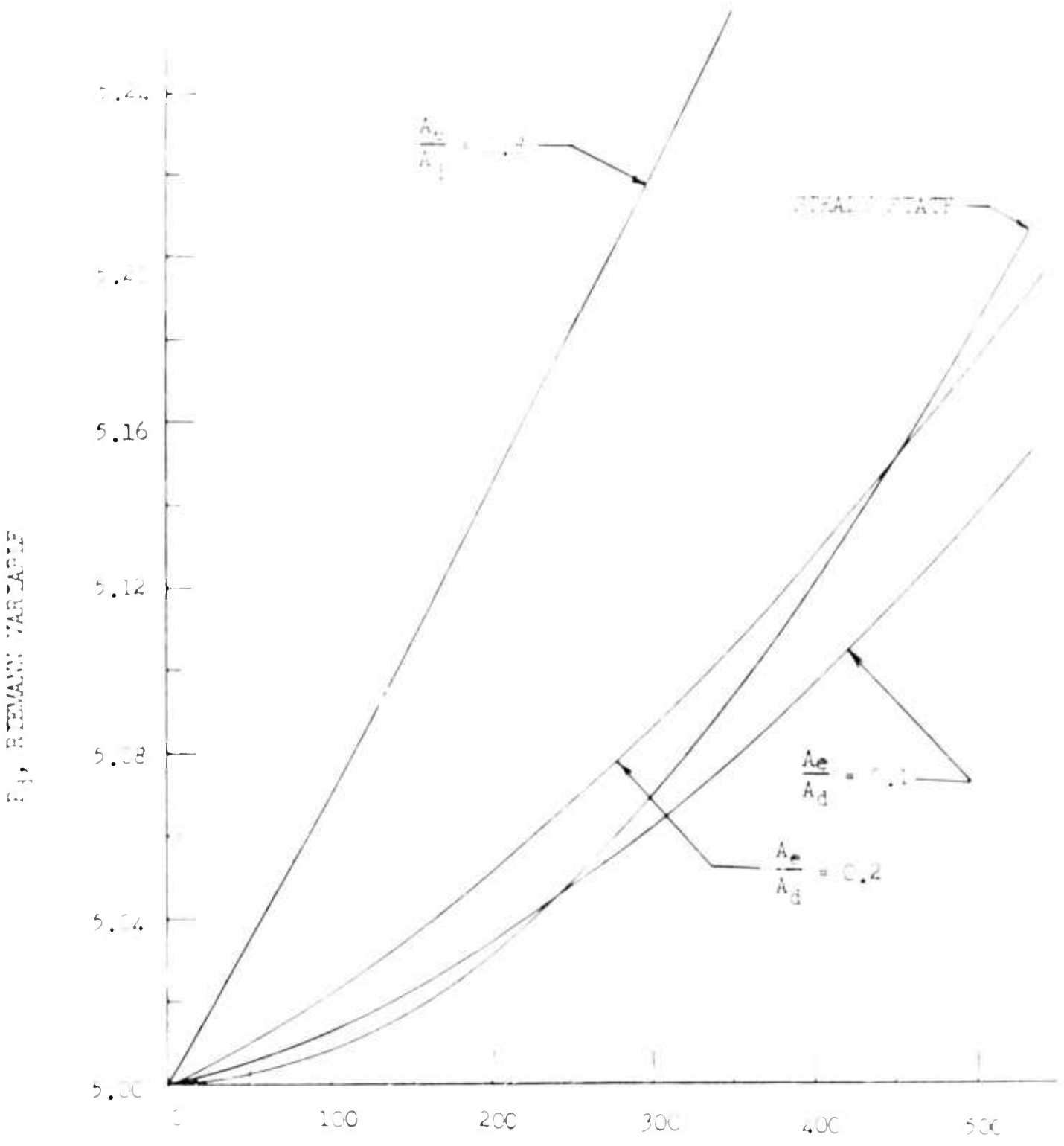

P_d, REMAIN VARIABLE

V_e, EXIT VELOCITY (fps)

FIGURE 8. EXIT VELOCITY AS A FUNCTION OF P_d

For isentropic flow of an ideal gas with $\gamma = 1.4$, this becomes

$$\frac{A_*}{A_1} = \frac{1}{u_1} \left(\frac{a_1}{a_*} \right)^3 . \tag{26}$$

The energy equation (1) across the nozzle may be written as

$$\frac{a_1^2}{a_e^2} + 0.2 \left(\frac{u_1}{a_e} \right)^2 = 1 + 0.2 \left(\frac{u_e}{a_e} \right)^2 \tag{27}$$

which may be combined with equation 26) to yield

$$\left(\frac{u_1}{a_e} \right)^2 = \frac{5 \left(\frac{a_1}{a_e} \right)^2 - 5}{\left(\frac{a_1}{a_e} \right)^{10}} \tag{28}$$

$$\frac{\left(\frac{A_e}{A_1} \right)^2}{\left(\frac{A_e}{A_1} \right)^2} - 1$$

Equation 7.a gives

$$P_1 = 5 \frac{a_1}{a_e} + \frac{u_1}{a_e} \tag{29}$$

across the nozzle. Equations (28) and (29) may be solved for the unknowns u_1/a_e and a_1/a_e, given the parameters A_e/A_1 and P_1. The nozzle ratio fixes A_e/A_1, and P_1 may be determined from the energy ellipse. The exit velocity, u_e, is obtained from equation 27. This is plotted as a function of P_1 and A_e/A_1 in Figure 8.

Now the theoretical solution for the velocity at the end of a duct terminated with a nozzle can be determined. For example, figure 7 illustrates the three possible transient flow conditions at the nozzle exit. In figure 7.a the initial P-wave is less than the value required for matching, and the exit velocity approaches the steady-state in a stair-step manner. The wave reflected at the

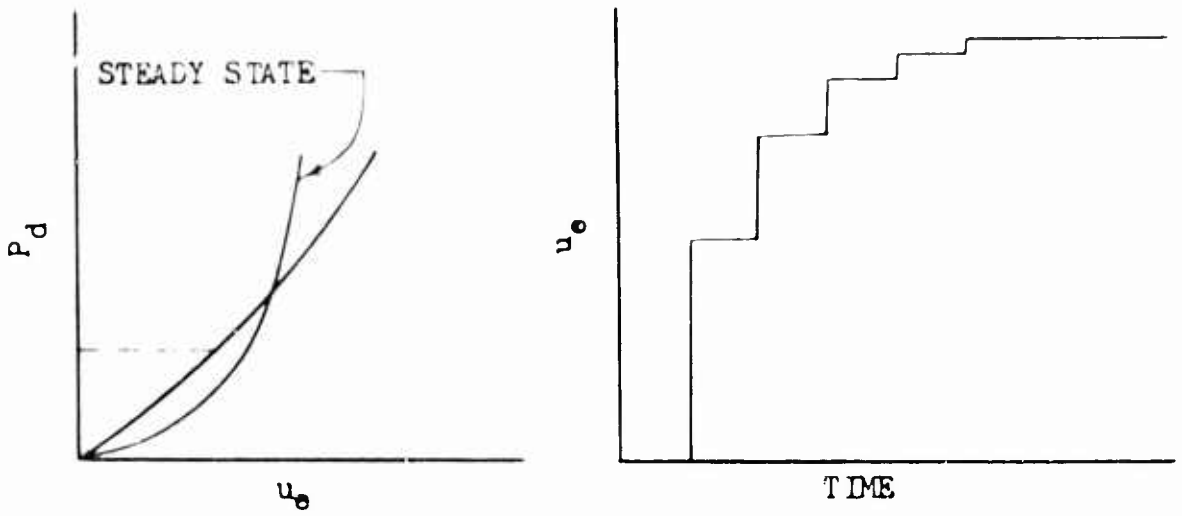

a) P-WAVE LESS THAN REQUIRED FOR NO REFLECTION

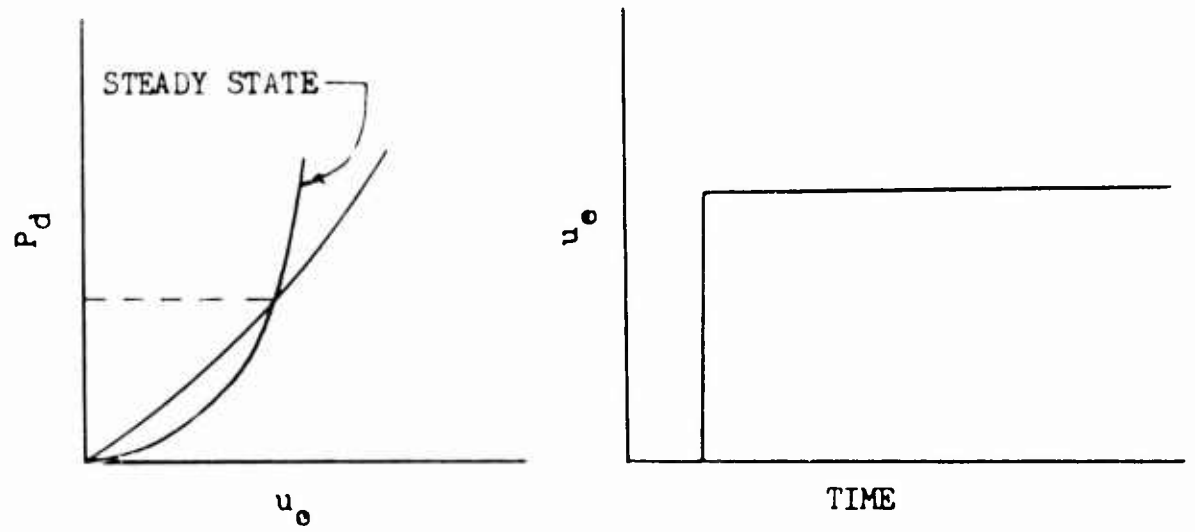

b) P-WAVE EXACTLY AS REQUIRED FOR NO REFLECTION

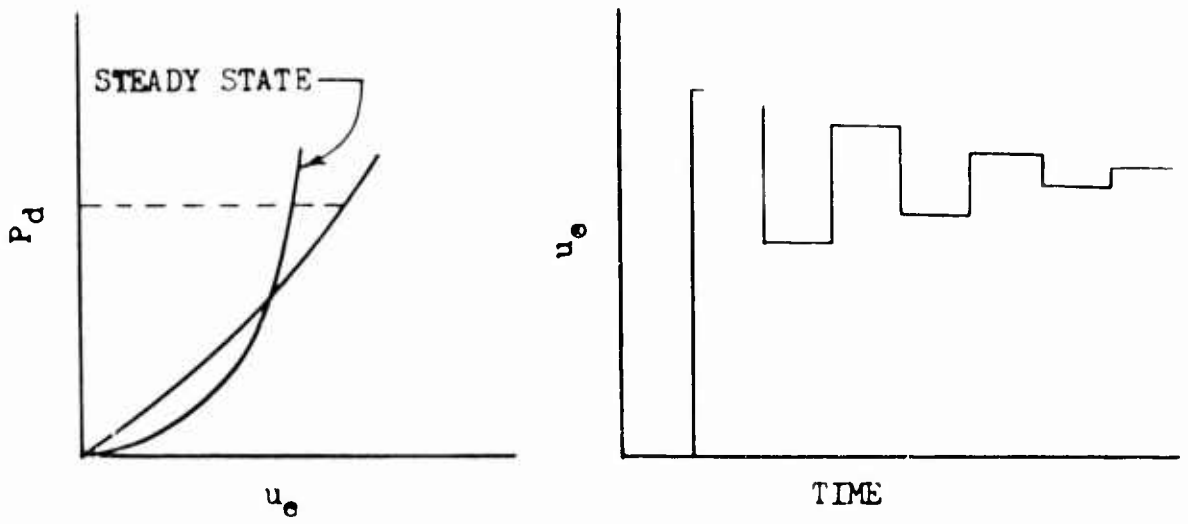

c) P-WAVE GREATER THAN REQUIRED FOR NO REFLECTION

FIGURE 9. POSSIBLE TRANSIENT FLOW CONDITIONS AT EXIT OF DUCT TERMINATED WITH A NOZZLE

nozzle is an expansion wave. Figure 9.b shows the case where the P wave is exactly equal to the matching value; i.e., it corresponds to the intersection of the steady-state velocity line and the transient velocity line for the given nozzle ratio. The duct is therefore matched, and no reflection takes place. The expansive reflections are equal to and cancel out the compressive reflections. Figure 9.c illustrates an initial P-wave that is greater than required. The output velocity initially exceeds the steady-state level, and then oscillates about the steady-state value as the transient conditions damp out. This is the case where a compression wave reflects initially from the nozzle termination.

Figure 10 illustrates these cases with experimental plots. A typical comparison of theory with experiment is given in table I. These particular examples are for a P-wave large enough to produce overshoot and oscillation to steady state.

The length of each step or level is dependent on the time required for the reflection to travel twice the length of the duct. Thus one is able to lengthen or shorten these as desired, Figure 11 shows two plots taken under exactly the same conditions except for duct length. However, as the duct is lengthened, friction becomes more important. Since this theory was obtained neglecting friction, the experimental results deviate farther from the theory as the duct is lengthened.

IV TERMINATED DUCTS WITH SIDE BRANCHES

The effect of bleeds on the wave reflections in ducts is of concern since it is important to be able to predict the shape of a pulse at the duct exit. Bleeds exert considerable influence on both the shape and the magnitude of these pulses.

To simulate a bleed in a fluid amplifier, a terminated duct with a side branch was used. These branches were placed at either of the two positions shown in figure 12. Only one bleed was used in any one experiment. Two sizes of side branches were used; each

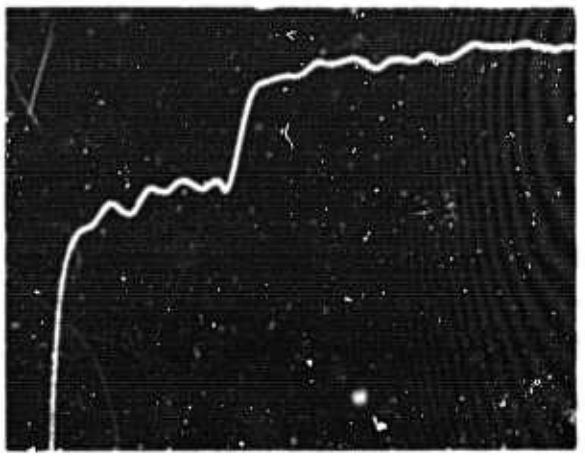

a) P-WAVE LESS THAN REQUIRED FOR NO REFLECTION

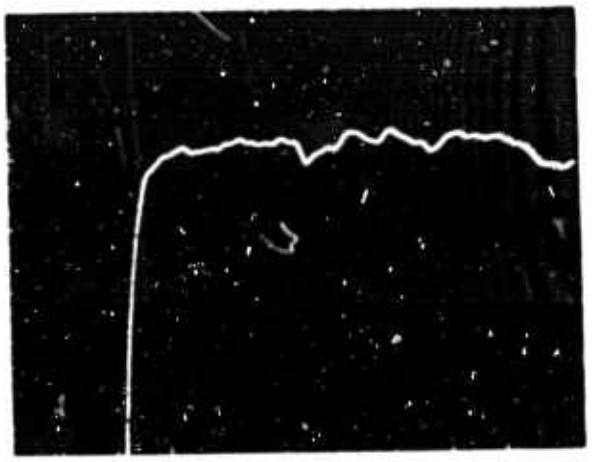

b) P-WAVE EXACTLY AS REQUIRED FOR NO REFLECTION

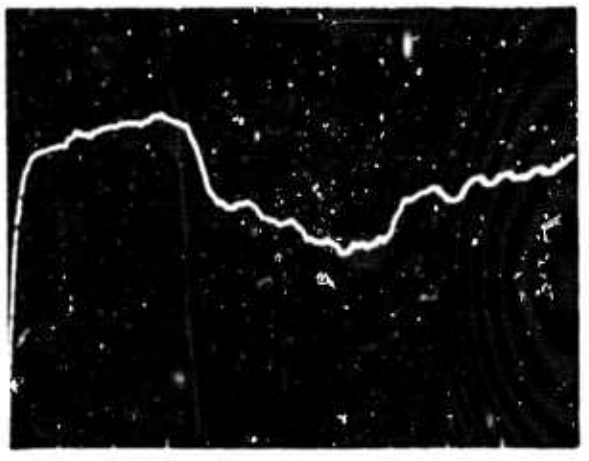

c) P-WAVE GREATER THAN REQUIRED FOR NO REFLECTION

FIGURE 10. EXPERIMENTAL RESULTS DEPICTING VARIOUS FLOW CONDITIONS AT EXIT OF DUCT TERMINATED WITH A NOZZLE.

TABLE I. COMPARISON OF THEORETICAL AND EXPERIMENTAL TRANSIENT EXIT VELOCITIES FROM THE INITIAL OUTPUT TO THE STEADY-STATE VALUE.

u_e , EXIT VELOCITIES (fps)

	CASE 1		CASE 2	
STEP	THEORY	EXPERIMENT	THEORY	EXPERIMENT
1	397	400	430	446
2	324	314	341	360
3	365	388	394	409
4	345	330	365	378
5	356	390	382	403
6	350	348	372	372
7	353	372	378	403
8	352	353	374	383
.				
.				
.				
STEADY STATE	351	372	375	400

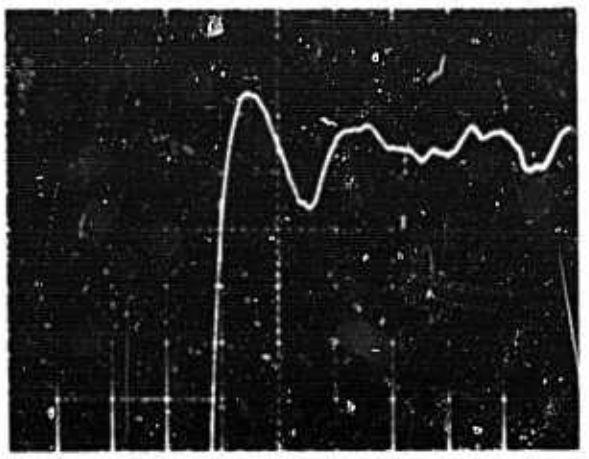

a) DUCT LENGTH OF 6 INCHES

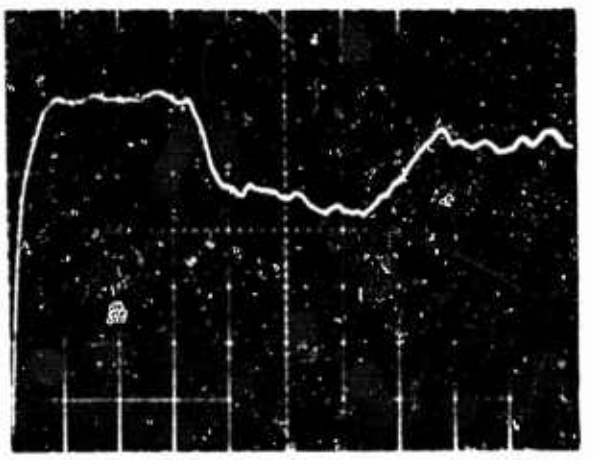

b) DUCT LENGTH OF 24 INCHES

FIGURE 11. EXPERIMENTAL PLOTS TAKEN WITH ALL CONDITIONS IDENTICAL EXCEPT THE LENGTH OF THE DUCT.

was 3 in. long and 0.5 in. wide with a depth of either 0.25 in.

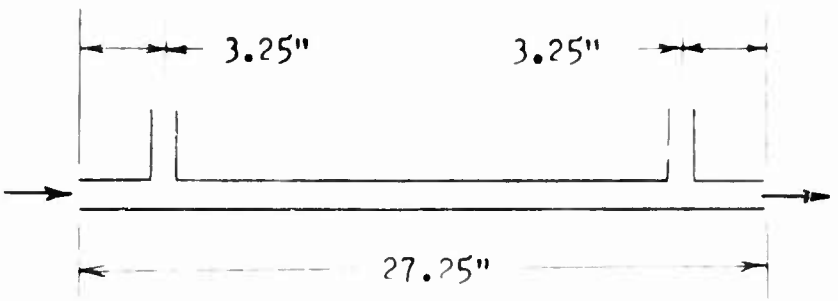

Figure 12; Location of Bleeds in Duct

or 0.0625 in. The larger the bleed, the more the flow level is lowered at the duct exit. As a result, energy levels change and the assumption of constant energy is no longer valid. A mathematical analysis of the flow therefore was not attempted. However, by consideration of the waves and reflections, the general shape of the pulse at both the duct exit and the bleed exit may be predicted.

Figure 13 shows theoretical predictions and experimental results for the case when the bleed is located near the entrance of the duct. It should be emphasized that no attempt was made to predict quantitatively the amplitude of the pulses. Only the relative magnitudes were considered. Figure 13.a shows the predicted output of the duct. The initial large pressure pulse resulting from the step input is followed by a series of successively smaller pressure waves emanating from the duct entrance and the bleed. As these damp out, the rarefaction wave resulting from the initial large pressure pulse returns to the entrance and its reflection now appears at the exit as a large compression wave. This cycle is repeated until steady state is reached. Figure 13.b shows the oscilloscope plot of this case.

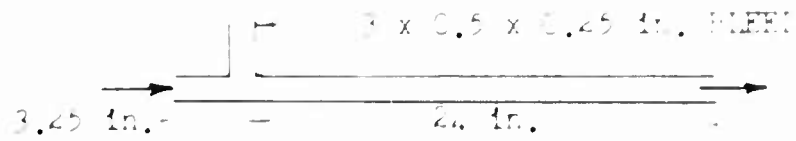

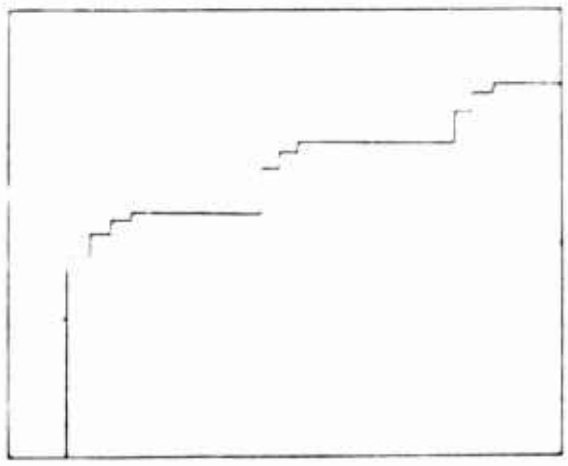

a) PREDICTED DUCT OUTPUT

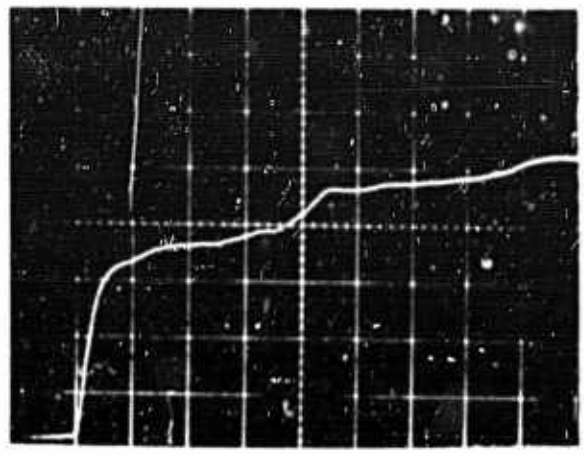

b) EXPERIMENTAL DUCT OUTPUT

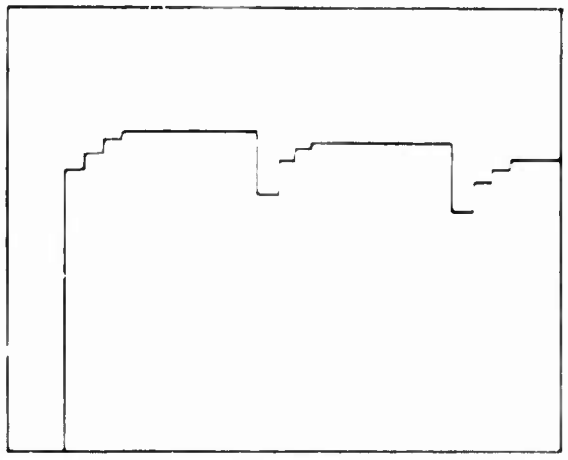

c) PREDICTED BLEED OUTPUT

p_o = 1.17 psig

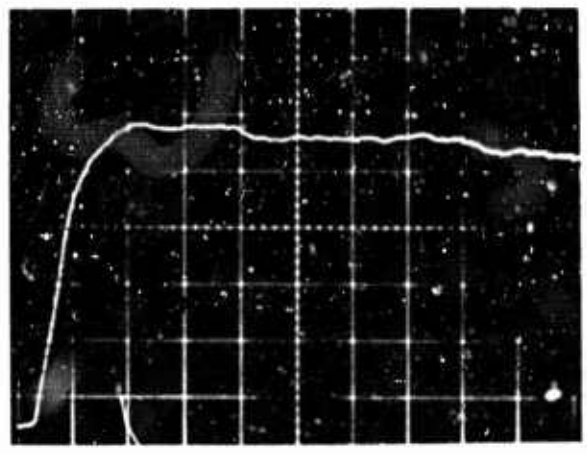

d) EXPERIMENTAL BLEED OUTPUT

TIME SCALE = 1 MSEC

FIGURE 13. FLOW CONDITIONS WITH BLEED NEAR DUCT ENTRANCE.

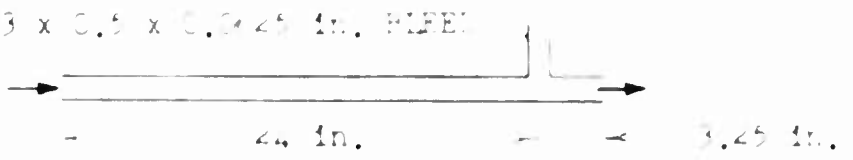

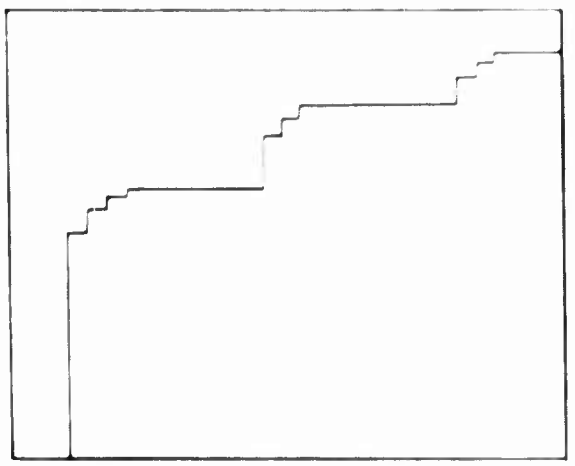

a) PREDICTED DUCT OUTPUT

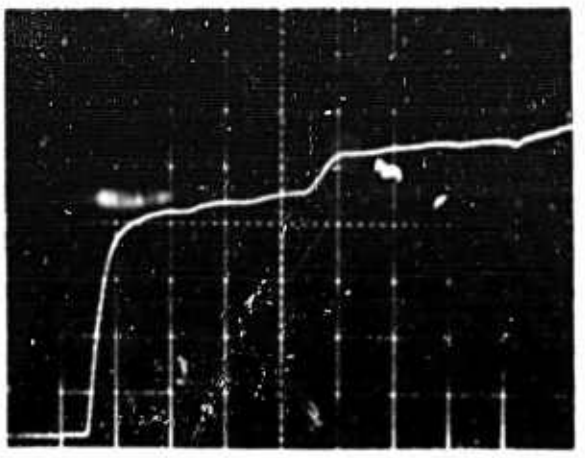

b) EXPERIMENTAL DUCT OUTPUT

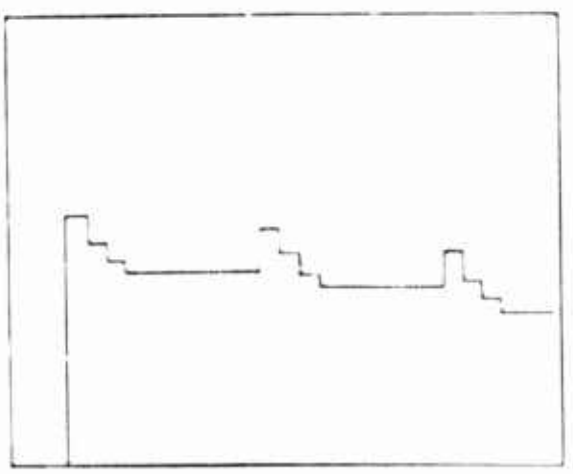

c) PREDICTED BLEED OUTPUT

p_o = 1.17 psia

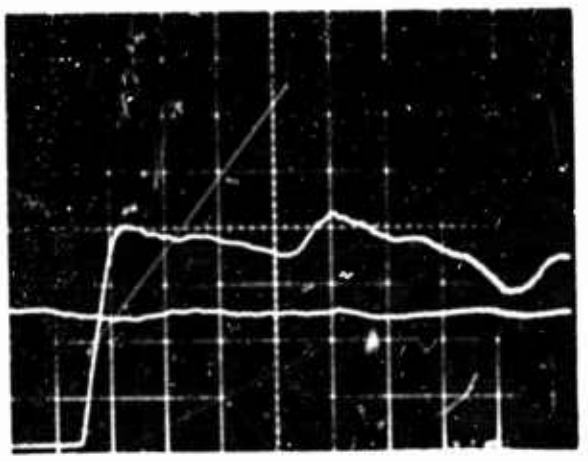

d) EXPERIMENTAL BLEED OUTPUT

TIME SCALE = 1 MSEC

FIGURE 14. FLOW CONDITIONS WITH BLEED NEAR DUCT EXIT.

Figure 14.3a [illegible] the predicted output at the duct exit. The first large compression wave resulting from the step input is followed by smaller compression waves resulting from reflections at the [illegible] branch. This [illegible] compression wave is reflected as a [illegible] from the [illegible] entrance. This rarefaction wave eventually returns from the duct exit, and lowers the velocity considerably. A pressure is reflected from the duct entrance, and this cycle is repeated until steady state is attained. Figure 14.3b is the experimental result for this condition.

Figure 14.4 shows theoretical predictions and experimental results for the case where the branch is placed near the duct exit. Figure 14.4a shows the theoretical output at the exit of the duct. The explanation for this parallels that of figure 14.3a. Figure 14.4b is the corresponding experimental plot.

Figure 14.5a is the prediction for the output of the bleed located near the exit. Note that this branch has a smaller area than the bleed in figure 14.4. The larger initial compression wave is followed by smaller rarefaction waves coming from the bleed. Then the large pressure wave returns from the entrance. This cycle is repeated until steady state is reached. Figure 14.5b is the oscilloscope plot for this case.

Thus the shape of the pulse can be qualitatively predicted by considering the effects of waves and reflections in a duct. Further considerations are necessary to determine the magnitude of the pulses.

Conclusion

In the [illegible], even with the implification [illegible], [illegible] provide [illegible] with the [illegible] to a step input. The initial flow from the [illegible] may be greater than, equal to, or less than the steady-state flow. The governing parameters are the strength of the incident wave, the environment into which the wave is propagating, and the [illegible] termination.

The introduction of bleeds into the unit lowers the flow level of each step as well as the steady-state value. Thus by proper selection of the step input, the bleed termination, and size and location of bleeds, the output pulse can be shaped to a desired form. The output of the bleed itself can be made, by proper adjustment, to correspond roughly to the derivative of the flow input.

Further investigation is required to determine the effect of step inputs at the control of bistable fluid amplifiers. A wider range of experiments is also necessary to ascertain the importance of bleeds as pulse shapers.

[illegible]

1. [illegible], [illegible], [illegible]

2. [illegible], [illegible], [illegible]

3. [illegible], [illegible], [illegible]

4. [illegible], [illegible], [illegible]

5. [illegible], [illegible], [illegible]

6. Shapiro, A. H., [illegible]

7. Stodola, [illegible]

ABSTRACT

Frequency selective acoustically controlled fluid dynamic switches are discussed in terms of Reynolds number, Strouhal number, and geometric parameters. The successful operation of such a device depends on the simultaneous conditions that:

1. The stream, which is basically controlled by the boundary, is in the monostable region of operation.
2. That stream operation takes place in the region of flow where it is most sensitive to small disturbances. Such a flow region is specified in terms of Reynolds and Strouhal numbers.
3. An acoustic resonator is coupled to the orifice to increase the frequency selectivity and also act as a velocity amplifier which controls the flow at the orifice of the jet. It is important that the resonator be tuned to the frequency for which the flow is most sensitive.

A stream, which is stable along one nozzle boundary in the undisturbed state, may be switched acoustically to a second stable condition along the opposite boundary, during the period that the flow is disturbed, when only the first two conditions set forth above are present; however, greater sensitivity and frequency selectivity may be achieved when the third condition simultaneously is present. When the disturbance is removed, the stream returns to its original stable state.

Operating conditions have ranged from a Reynolds number (based on stream thickness and average velocity) of 300 to 4,000 and a Strouhal number (based on stream thickness, average velocity and control frequency of 0.07 to 0.3. Input signal levels range from .5 to 50 dynes/cm . Response time and sensitivity of the device depends primarily on how close the operating monostable point is to the region where operation would be bistable. Experimental results from a study of nozzle geometry on the hysteresis phenomenon for bistable operation are of prime importance and hence emphasized along with the importance of the sound sensitive characteristics of fluid jets.

Introduction

The acoustically activated fluid switch depends primarily on the sound sensitive characteristics of laminar jets and on boundary layer control or the Coanda effect. First, the laminar jet is operated in the region of flow where it is most unstable to small disturbances at the designed switching frequency. Second, the nozzle exit boundaries are adjusted so that the undisturbed stream is monostable on one boundary, and in the disturbed state it is conditionally stable on the opposite boundary. The primary flow is the jet itself which sets up a secondary flow. When acoustically disturbed, the free boundary of the stream develops into a vortex flow which increases entrainment and sufficiently adjusts the secondary flow to cause switching.

Jet Instability Characteristics

The sound sensitive jet needs no introduction to those working in the field of fluid amplification for it is now well recognized how important jet instability characteristics are in the development of fluid jet devices. Although a mathematical description of the flow itself, especially in the well developed vortex flow region, is neither implementor easy to work with, the physical characteristics of the jet are known from the large amount of experimental work that has been done.

It was originally expected that if the jet was free for several slit widths downstream of the orifice before reattaching to a boundary, that it would be sensitive to sound in essentially the same region of the Reynolds-Strouhal plane as that of the free jet. This expectation has seemingly been fulfilled by our experimental work.

Figure 1* shows the region of operation for free laminar plane jets having an exit parabolic velocity profile. The solid line represents the assumed region of maximum sensitivity. The R-S region shown encompasses the operation region for the edgetone without a resonator. (Resonators broaden the operating region considerably.) Data taken by this author under the direction of Professor Alan Powell at the Aerosonics Laboratory was later published in references 1 and .

Although for the work described in this paper the channel length was sufficiently long to ensure a parabolic velocity profile at the highest expected Reynolds number, many other devices use short channels with the exit velocity described more closely by a square velocity profile. Following the approach found applicable in boundary layer flows, a modified momentum thickness has been considered. We define the "jet momentum thickness" as:

$$\theta = \delta - 2\int_0^{\delta} \frac{u(y)}{U_{oo}}\left[1 - \frac{u(y)}{U_{oo}}\right] dy$$

where δ is the jet width and U_{oo} is the centerline velocity. For a square profile (which can only be approximated in practice) the jet momentum thickness is simply the channel thickness δ. For a parabolic profile, $\theta = .67\delta$. Using the jet momentum thickness as the characteristic length in the dimensionless Reynolds and Strouhal number appears to offer better dynamic similarity. It also helps to adjust for the increased instability found for the square velocity profile compared to the parabolic flow.

It may be noted that the line describing the region of maximum sensitivity does not lie in the center of the region of operation primarily because the spacial gain is profoundly influenced by the convected wavelength. At low Reynolds number the jet is considerably more stable than at higher Reynolds number. This is partly due to the stabilizing influence of viscosity. We can expect the jet to become stable, or at least neutrally stable, for small Strouhal numbers because the

*Figures start on page 121.

wavelength is sufficiently long that the disturbance is convected out of the region of interest before any gross amplification can take place. Furthermore, the jet is stable for large Strouhal numbers because when the convected wavelength reaches the order of magnitude of the jet width, the induced velocity effect becomes incoherent and the process of vortex coalescence, the mechanism responsible for the developing vortex flow, is reduced. For fluid switching applications as herein described the operating point is selected on the line representing the region of maximum sensitivity. In the event that the switch is to respond to either of two input frequencies, the operating points are suitably chosen symmetrically about the line of maximum sensitivity. For fluid controlled devices where instability is a problem it is wise to operate above or well below the indicated region of operation.

Boundary Layer Control

Boundary layer control in a viscous flow field is possible due to the regenerative action of fluid entrainment. We employ this phenomenon to control the directional stability condition of the jet. For our application we want the stream to be normally stable on one boundary, but of course, not too stable for we must be able to switch. Hence, we want the condition which yields the jet just barely stable on one boundary, but near the stable flow region for the opposite boundary.

Let us consider a few flow examples and then it will be apparent why the fluid switch geometry is employed. Figure 3a illustrates a symmetrical nozzle where the flow could attach to either boundary. Assume the flow to be on the left boundary as shown. Now as we withdraw the left nozzle wall the jet follows and remains attached as long as fluid entrainment is sufficient to keep the cavity pressure sufficiently low to overcome the centrifugal force on the stream. Note that as the wall is withdrawn the influence of the right wall is rapidly being reduced. When the centrifugal force becomes dominant the jet swings free from the left wall and immediately becomes trapped by the regenerative flow field between the jet and the right wall so that the jet becomes attached to the right wall. If we now move the left wall toward the jet until the boundaries are symmetrical we find the jet remains attached to the right wall. If we move the left boundary further toward the jet we find a condition where the regenerative pressure area on the left again dominates the balance of forces and the jet again becomes attached to the left wall. Figure 3b shows a plot of the overall action which we call the hysteresis phenomenon. We could get a similar hysteresis effect if we were to make the variable the cavity pressure or input control jet volume flow instead of nozzle wall position. A jet which has a hysteretic history as shown is called a bistable jet. It is obvious that the hysteresis effect should not be dominant in our application. To reduce the hysteresis action we can adjust the nozzle walls so that the critical ratio $(x/s)_c$ is almost met; then the jet is always on the verge of switching. With the area under the curve tending to zero we approach the condition where oscillation is possible or we might say that the jet is unstable.

As long as the boundaries are symmetrical the jet can only be bistable (a special case is where it oscillates). In fluid amplifiers the usual technique is to bias the main jet with a control jet. In our case, we do not employ a second jet so that the biasing is accomplished by making the boundaries asymmetrical.

Let us next consider an asymmetrical configuration as shown in Figures 3 and 4. For small values of d the jet is deflected from the left boundary toward the right boundary and ultimately attaches along the right boundary. The jet is stable on the right only (SRO). As d is increased the jet becomes bistable, but more stable on the right than on the left (BS + R). As d is further increased the modes of operation are respectively; bistable (BS), bistable with greater attraction on the left (BS + L), and stable on the left only (SLO). As d becomes very large the jet is unable to attach to the left wall and the sequence reverts to BS +L, BS, BS +R, and finally SRO.

The general slope of the regions results from the fact that in laminar flow the jet breadth does not increase as rapidly with downstream distance as the Reynolds number is increased, while as impending turbulence is approached, the jet spreads more rapidly and at higher Reynolds numbers the flow is essentially independent of Reynolds number. This plot is somewhat idealistic for in a real situation the flow regions are not as well defined as indicated due to the onset of oscillation.(This is of a different nature from the oscillations previously mentioned which result from an essentially zero hysteresis. These oscillations are of the edgetone class and their particular behavior depends on the construction of the device)

The cross-hatched region is the one of particular interest to us. Here the jet is stable on the left, but not too stable. We call it monostable since a suitable disturbance can change its stability condition. The closer we operate to the boundary between SLO and BS + L, the more sensitive will the device become. The regions SRO and SLO are the only ones which do not possess hysteresis.

Now as the ratio c/a approaches unity the SLO region becomes vanishingly small so that the modes with increasing d are SRO, BS + R, BS, and SRO.

Dimension c is chosen to be smaller than the distance at which the stream could oscillate at its highest working velocity whereas dimension a is chosen to be as large as the distance required for full vortex development at the lowest working velocity. Dimensions b and d are then selected so that the broadest operating region is possible or for maximum sensitivity.

Boundary wall length also plays an important roll. In general, hysteresis is increased for long walls and the monostable region diminishes slightly. On the other hand, for extremely short walls the boundary influence vanishes.

Manufacturing tolerances require that the monostable region be sufficiently broad; and furthermore, for operation over a large range of stream velocity it is advantageous for the region to be parallel to the abscissa.

As mentioned, figure 4 is somewhat idealistic because the plot is generally more complex due to various regions of self-excited oscillation. Quite often it is found that the SLO region is completely closed. The double cross-hatched area is the one where acoustically activated switching is most sensitive.

Description of the Switching Mechanism

A typical configuration is shown in figure 3. The large cavity on the right of the jet is a resonator of the Helmholtz type. For low frequency switching the Helmholtz type resonator (lumped parameter) is used, whereas for higher frequencies (above 1 or 2 kcps) longitudinal standing-wave resonators are more practical. Figures 5a through 5c illustrate the process of switching. With the jet adjusted to be sensitive to small disturbances and operating in the monostable flow region, we have the jet attached to the left boundary wall. Fluid entrainment establishes the secondary flow illustrated. When an acoustic signal at the resonant frequency of the resonator enters the switch from the downstream side, the jet becomes disturbed with the resulting developed vortex flow illustrated in figure 5b. The vortex flow increases entrainment (thus lowering the pressure in cavity V_1) and tends to increase the secondary flow, thereby lowering the pressure on the right boundary. Within a few cycles, assuming the external acoustic disturbance continues, the vortex flow developes to a sufficient magnitude to suppress the secondary flow and switching is accomplished with the ultimate turbulent reattachment of the jet on the right boundary. The pressure gradient from cavity V_1 to the ambient atmosphere tends to counterbalance the centrifugal force on the jet, and it stays reattached to the right boundary as long as the acoustic disturbance exists. When the disturbing signal ceases, the jet returns to the left boundary thereby allowing automatic reset.

Input Signal Impedance

The switch can be driven at a low acoustic impedance point as illustrated in figure 6, or a high acoustic impedance location in the cavity V_1 as shown in figure 7. Of course intermediate driving impedances are available and for longitudinal standing wave resonators the impedance-space characteristics are more amenable mathematically than for the Helmholtz resonator. The configuration illustrated as figure 6 has two prominent modes. The lowest frequency mode is one where the acoustic flow is in phase in both cavities, whereas the high frequency mode is one with a phase reversal between the two side cavities. This higher frequency mode is extremely attractive since it allows the most effective drive to the jet with the disturbance predominantly transverse to the stream. On the other hand, the system is not only responsive to two frequencies but it also implies a reduction in jet sensitivity since the two operating points in the R_s

plane must straddle the region of maximum sensitivity.

When driving the switch through the cavity as shown in figure 7, the equivalent circuit shows the resonator to be in parallel resonance thus offering a maximum impedance at resonance. This requires the source impedance to be large so that the resonant response is not damped.

Frequency Selective Response and Sensitivity

Acoustic resonators have been included to improve the frequency selectivity of the switch thus allowing more channels in a given frequency space. The resonator also augments the acoustic particle velocityin the vicinity of the jet orifice thereby increasing sensitivity. Figure 8 illustrates the sensitivity and frequency selective response for two different switches which are spaced nearly an octave apart in frequency space. The curve is for the minimum acoustic pressure needed at a particular frequency to activate switching. The SPL measurements were taken in an anechoic chamber. The ordinate is the free field SPL which existed in the space location of the switch with the switch removed.

Channel separation is on the order of 25 to 30 db as illustrated. The expected control over input signal level and frequency determines the required channel separation level, and the Q (quality factor) of the chambers specifies the frequency spacing required for multiple channel operation.

In practice we have successfully operated acoustically activated switches from 400 cps to 4 kcps. At the lower frequencies the resonators become quite large so that space limitations must be considered and at the higher frequencies, say at 4 kcps, the nozzle adjustment is more critical and poses high-production manufacturing limitations. In addition, at the higher frequencies the radiation resistance as seen by the resonator is becoming large and hence the Q of the resonator is decreasing. The largest Q are found for the low frequency resonators. One major advantage the Helmholtz type resonator has over the longitudinal standing wave type is that the overtones are not harmonically related and the second mode is generally several octaves above the fundamental resonance.

The ratio of flow power at the channel exit to the acoustic power entering the switch has been found to be as high as half a million for the most sensitive switches. For models capable of operating over a 50% change in stream velocity, this power ratio is generally on the order of .1 to .3 million. Of course power recovery at the nozzle exit depends on the turbulence level of the jet. Momentum recovery for fully developed vortex flow is on the order of one half since the rotational momentum is not generally recoverable.

It is interesting to note that when the device is operated in a regenerative manner it has phenomenal sensitivity which depends primarily on the noise level of the channel flow. In the regenerative

mode, the "c" dimension is adjusted so that the device is on the verge of edgetone type oscillation. Then only an extremely small acoustic signal is needed to supplement the feedback to enhance oscillation. Once in oscillation, the switch generates its own signal for switching. Of course this type of operation is difficult to control. It requires extremely good control of the channel velocity and a quiet entrance flow.

Switching Response Time

This device is not considered to have a quick response. The number of acoustic cycles necessary for switching depends on the input signal level and on how close the operating point is to the boundary between LLO (monostable region) and LL + L; ie, how close the system is to having a little hysteresis. Since the pressure in the chamber builds up exponentially as

$$P_c(t) = P_0 Q\left[1 - e^{-\frac{t}{2Q/\omega}}\right]$$

where P_0 is the driving free field pressure, the response time is primarily dependent on the Q of the chamber and the frequency. As an example, the switch whose response is shown in figure 3 requires on the order of 50 cycles to switch with an input signal at 70 db and 1 kcps. For much higher input signal levels the minimum number of cycles is reduced to 5. Hence, for a 1-kcps switch response times ranging from 5 to 50 ms can be expected. For lower frequency switches the response time will be longer.

Summary

Acoustic switching of sound sensitive laminar jets has been described in some detail. The mechanism for switching is quite clear. The sensitivity of the device depends on the quietness of the flow, how close the operating point is to the monostable boundary, and on the Q of the associated resonator. Frequency selectivity depends primarily on the Q of the resonator. Switching time depends on the input level, the Q of the resonator, the frequency, and again the nearness of operation to the monostable boundary. The number of available channel depends primarily on the channel separation or "cross talk" allowable, as well as many other factors that have been mentioned. The device was originally developed as a low cost substitute for an electronic microphone-amplifier-relay circuit, but it is expected that many other useful fluid controlled circuitry applications will be found especially where frequency discrimination is essential.

References;

1. A. Lowell, J. Acoust. Soc. Am. vol. 33, p. 795 (1961)
2. A. Lowell & W. Unfried, Univ. Calif. at Los Angeles Dept. Engr. Rept. 64-49, (1964)

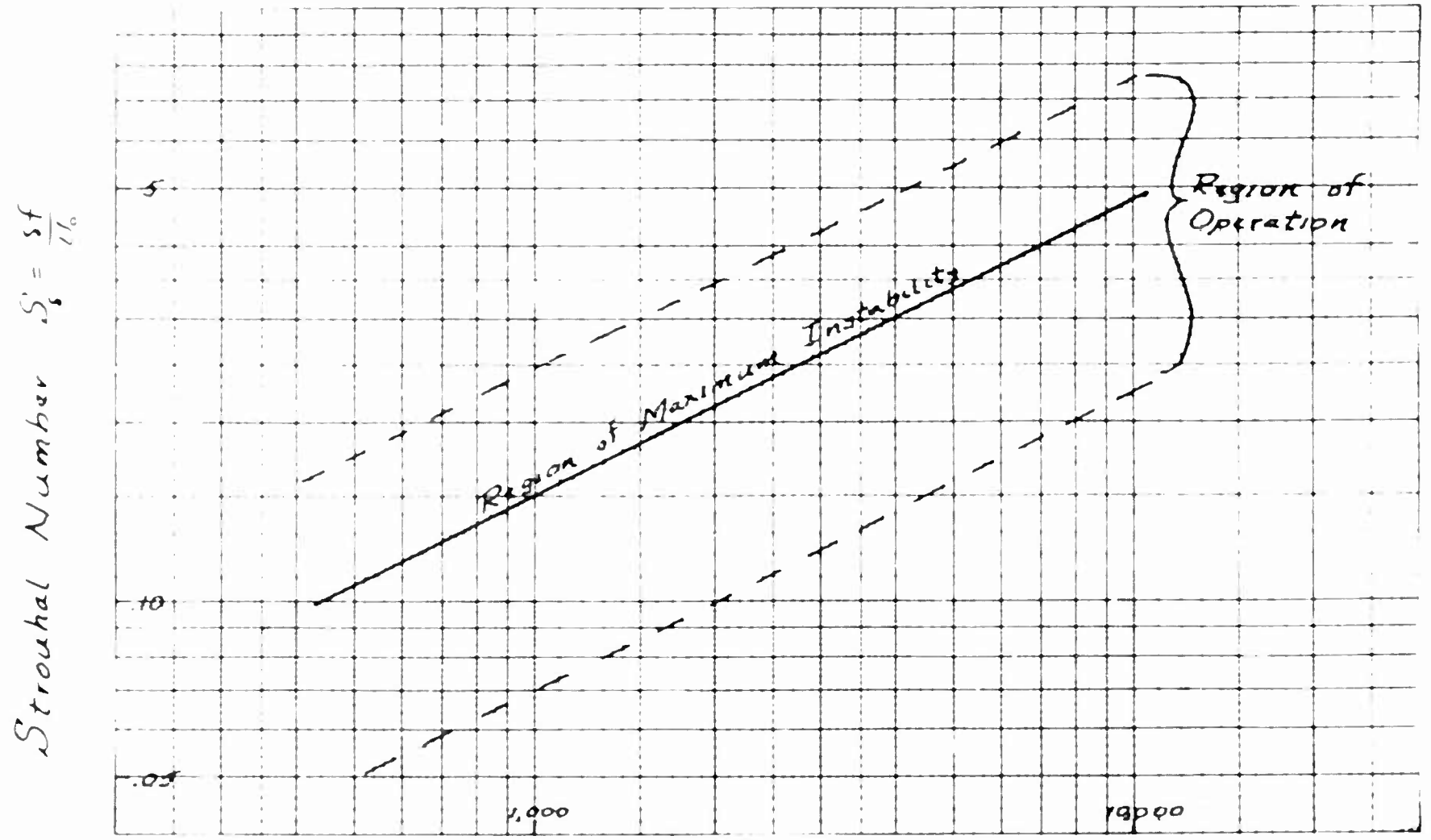

Reynolds Number $R_s = \frac{SU_o}{\nu}$

Region of Instability for Plane Free Jets

FIG 1

Hysteresis Phenomenon of Bistable Jet

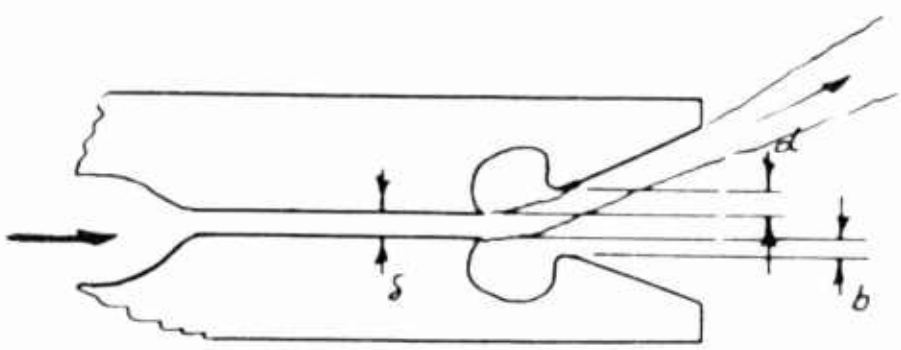

Fig 2a

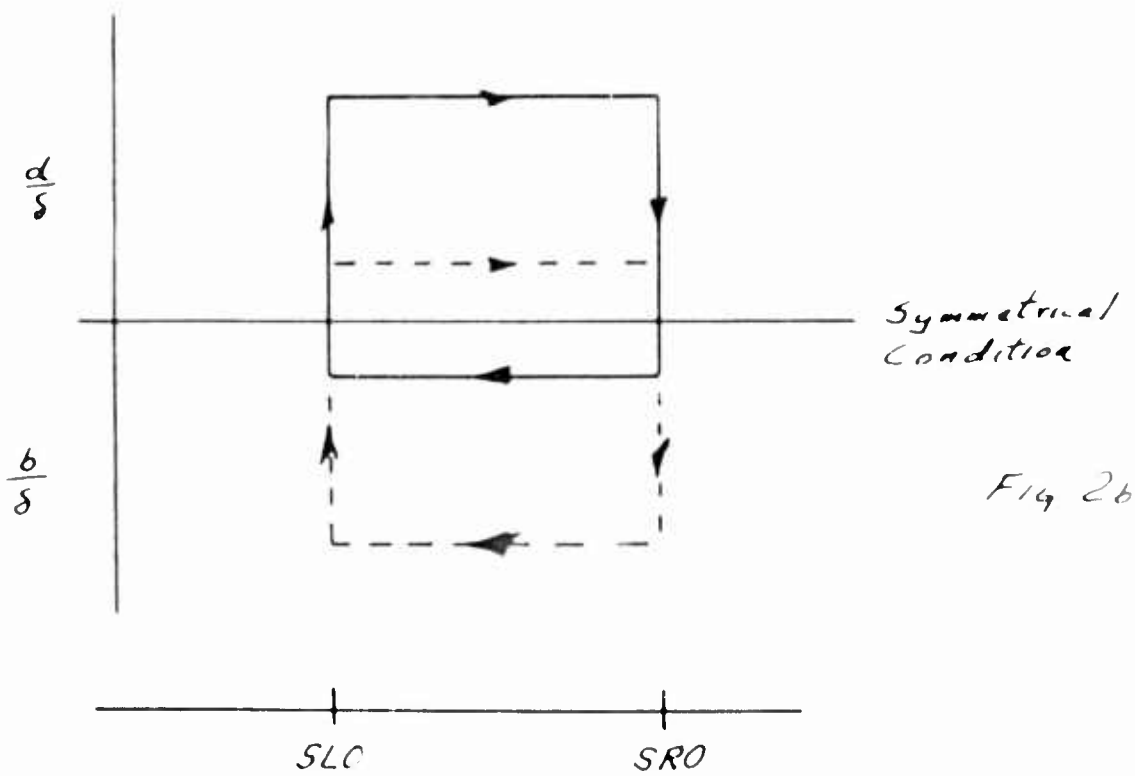

Fig 2b

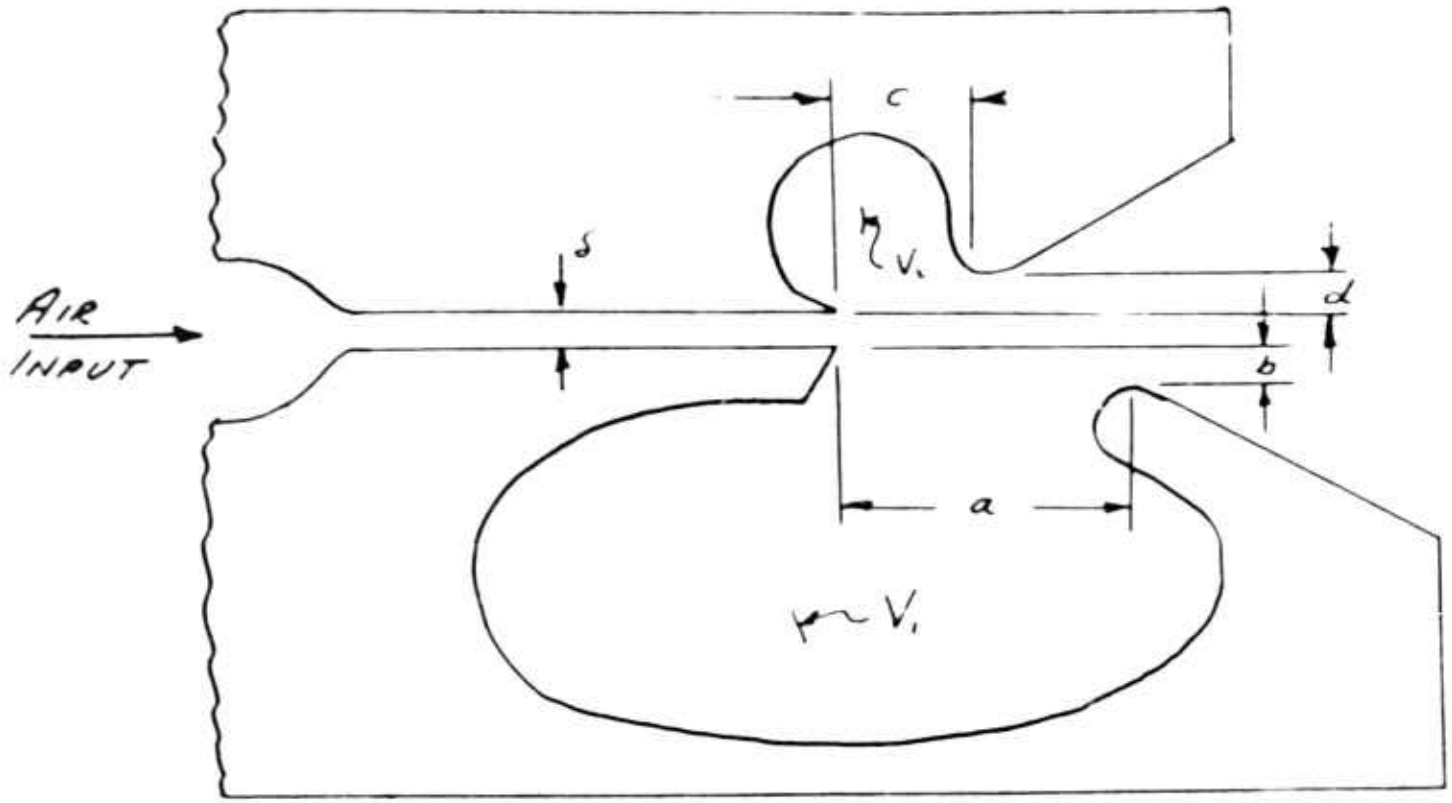

VIEW OF NOZZLE BLOCK SHOWING
DESCRIPTIVE SYMBOLS

FIG. 3

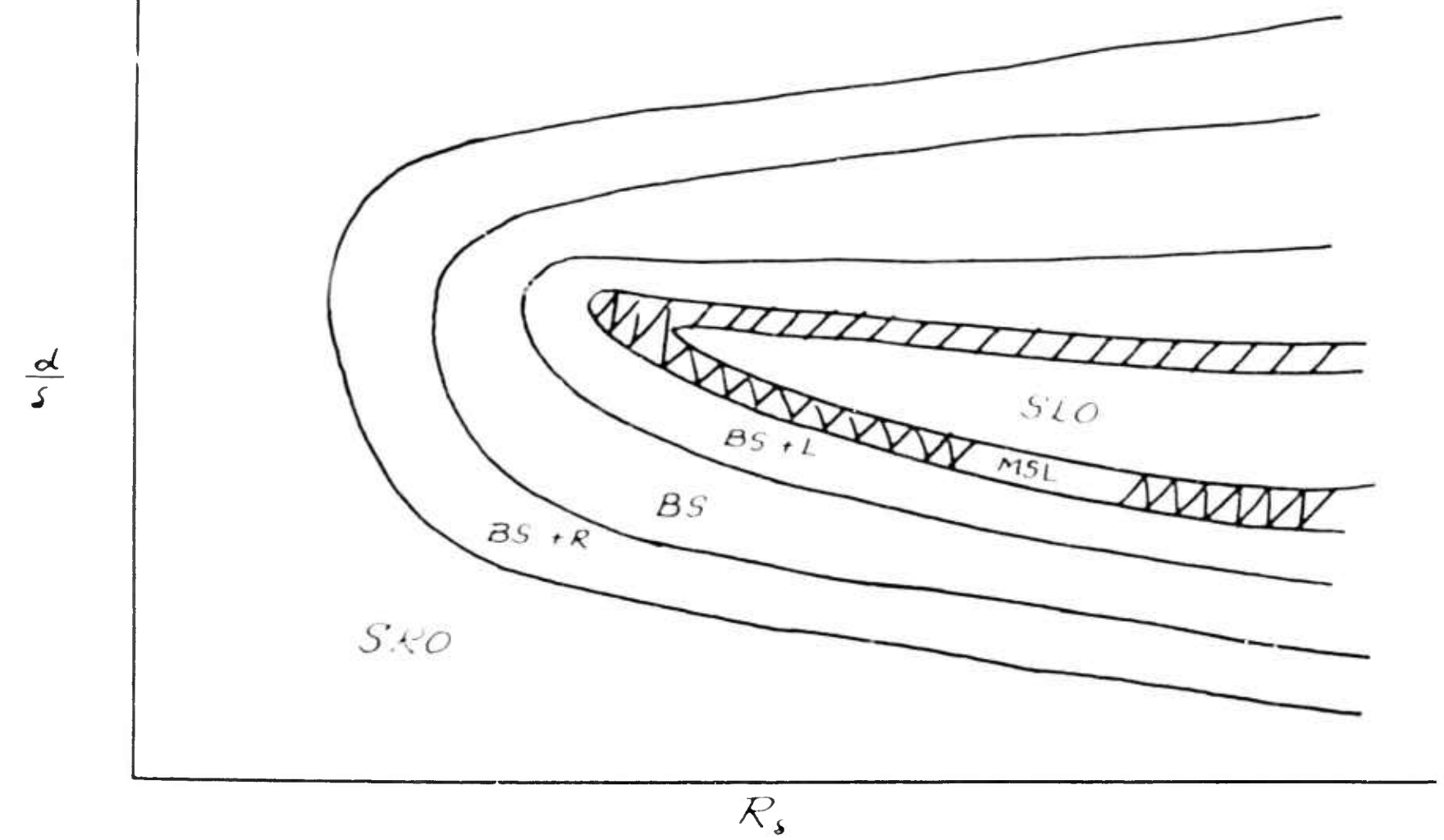

Operating Modes for Boundary Layer Controlled Plane Jet

Fig 4

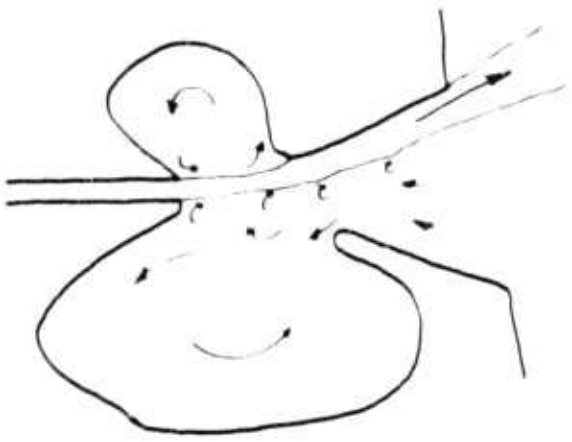

Fig. 5a

Flow undisturbed.
Fully developed
secondary flow.

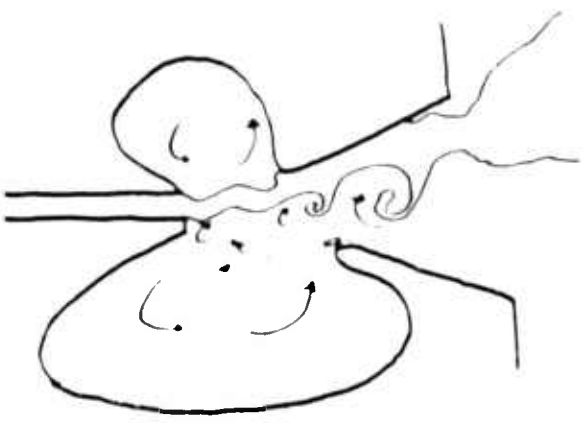

Fig. 5b

Flow slightly disturbed.
Vort. flow developing and
altering secondary flow.

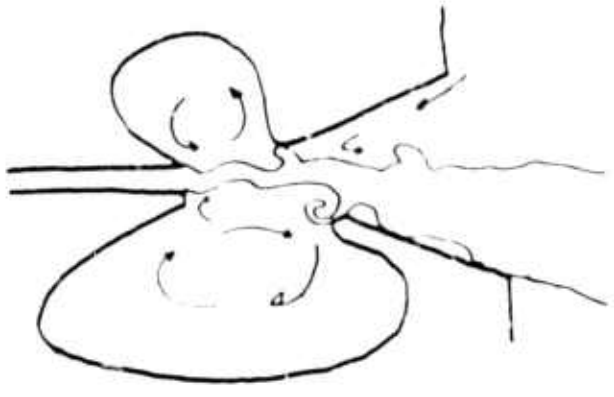

Fig. 5c

Switching has transpired
after vortex flow stopped
secondary flow on
right hand boundary

Sequence of events during act of switching

Fig 6a

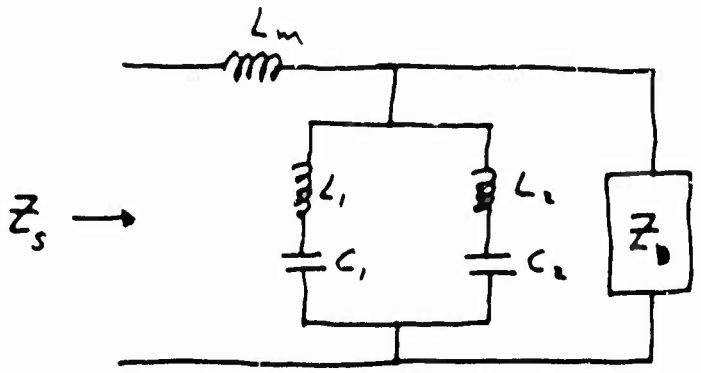

Fig 6b

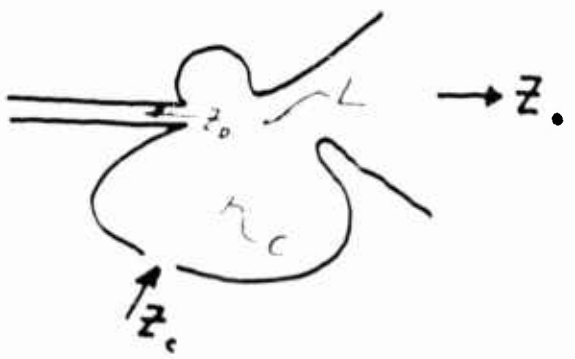

Fig 7a

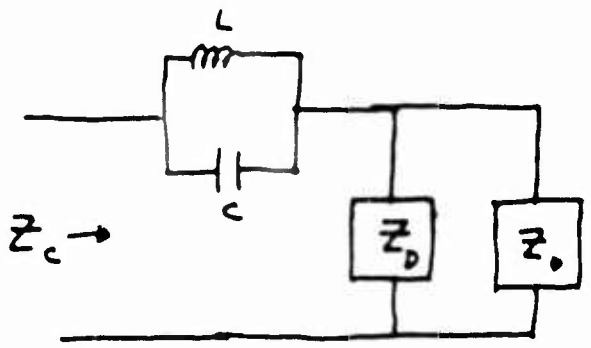

Fig 7b

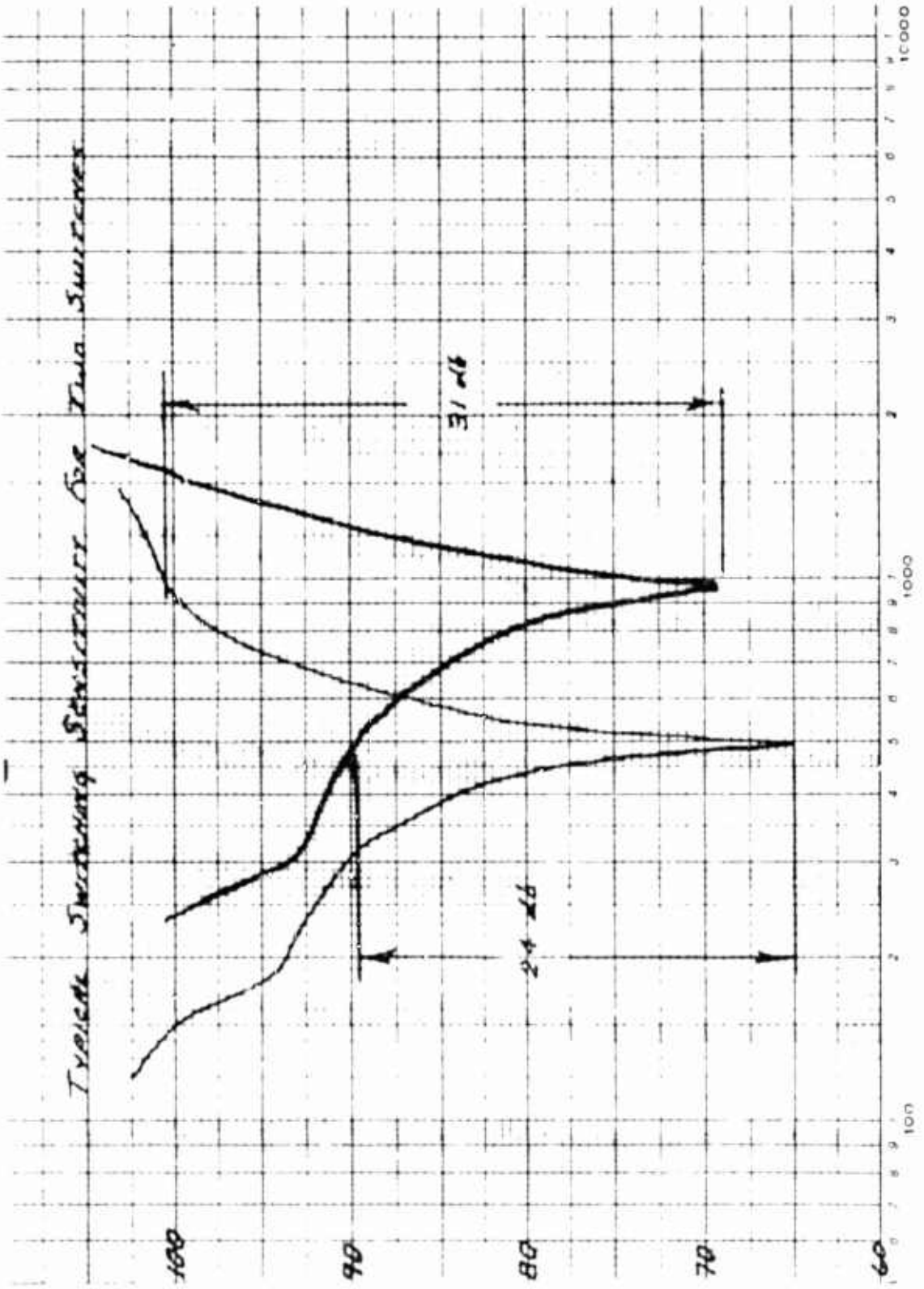

Fig 8

Free Field Acoustic Pressure
Required for Switching
SPL dB [ref 0.002 dynes/cm²]

SOME INFLUENCES OF TURBULENCE ON THE NOISE OF PROPORTIONAL FLUID AMPLIFIERS

by

Dennis W. Prosser

and

Michael J. Fisher

IIT Research Institute
Chicago, Illinois
June, 1965

To be presented at the
Third Symposium on Fluid Amplification
at the Harry Diamond Laboratories
Washington, D. C.
October 26, 27, 28, 1965

The work presented herein was supported by the Harry Diamond Laboratories of the U. S. Army Materiel Command under Contracts No. DA-49-186-AMC-101-C(D) and DA-49-186-AMC-192(D)

SOME INFLUENCES OF TURBULENCE ON THE NOISE OF PROPORTIONAL FLUID AMPLIFIERS*

by

Dennis W. Prosser
and
Michael J. Fisher

IIT Research Institute
Chicago, Illinois

I. INTRODUCTION

In this paper we discuss the "noise" problem associated with proportional fluid amplifiers. The word "noise" refers to the undesirable pressure fluctuations which turbulence superimposes on the mean pressure signal measured at a receiver placed in the fluid jet.

We now consider how noise can adversely affect the performance of a proportional fluid amplifier. A simplified version of such a device is depicted in Fig. 1. A main jet, which of its own accord would by-pass the receiver, is deflected by a control jet. A portion of the main jet is "collected" by the receiver. The momentum of the collected portion of the jet is converted into pressure within the receiver.

To perform accurately functions such as computing or controlling, changes in input stimuli (control port pressure) must be reproduced faithfully as changes in the output signal (receiver pressure). Furthermore, the relation between input and output must necessarily be known.

Ideal conditions for relating input to output exist if the jet flow is not accompanied by turbulence. In that case, the receiver pressure will remain constant so long as the input

*The work presented herein was supported by the Harry Diamond Laboratories of the U. S. Army Materiel Command under Contracts No. DA-49-186-AMC-101-C(D) and DA-49-186-AMC-192(D).

stimuli are constant. Analytical relations between input and output have been established for this idealized steady-state situation.[1,2,3]** Unfortunately, in an actual fluid amplifier the jet stream is turbulent. Thus, even when the mean (or average) input conditions are held constant, there will be some fluctuations in the output. As stated, these fluctuations will be referred to as noise.

One adverse effect of noise is its tendency to mask-out changes in output signals. When small but rapid changes are made in the input stimuli, corresponding changes should result in the output. With turbulence present, however, additional fluctuations (noise) in the output will also exist. Under certain conditions it will be difficult, if not impossible, to distinguish between variations that reflect the changing stimuli and the noise. It is equally possible that the noise might be interpreted as a variation in the stimuli, even when none occurs.

It is possible, of course, to lessen or even completely eliminate the effects of noise by properly designing the receiver. This possibility exists because fluctuations in the jet velocity field give rise to pressure fluctuations at the receiver entrance, where the fluid is stagnated (Fig. 1). It is the pressure in the receiver chamber, however, that represents the output signal. By providing the proper combination of entrance resistance and chamber volume (capacitance) comparatively high frequency fluctuations at the entrance can be prevented from reaching the chamber. It must be emphasized, however, that this attenuation can only be obtained at the expense of a reduced frequency response of the device as a whole. Quite obviously, then, the characteristics of the turbulent fluctuations must be known if their effects are to be damped out without unduly limiting the sensitivity of the receiver. This work represents a step toward understanding and evaluating the effects of turbulence on the operation of proportional fluid amplifiers.

** Superscripts denote references.

NOTE: Figures start on page 152.

The literature contains many relatively successful attempts to predict analytically the mean values associated with turbulent jets, e.g., the mean velocity field. These analytical "solutions" are obtained by employing the Navier-Stokes equations for turbulent flow and incorporating standard phenomenological laws to relate the correlation of fluctuating velocities to the gradient of the mean velocity. On the other hand, no attempt has been made to determine the fluctuating velocity field itself. The complexity of the problem makes this readily understandable, and no attempts were made along these lines during this work. Rather, since the statistical properties of the velocity field can be obtained readily using hot-wire anemometry, we set out to establish a suitable statistical description of the pressure fluctuations at the receiver entrance in terms of the statistical characteristics of the velocity field of the jet.

II. THE BASIC EQUATIONS

Refer to Fig. 2 which depicts a receiver in a two-dimensional jet. The instantaneous pressure, p_I, at any point on the receiver entrance (such as point B) is given by the expression

$$p_I = \frac{1}{2}\rho u_I^2$$

where u_I is the instantaneous velocity just upstream from the point under consideration. If both the pressure and velocity are expressed in terms of their time averaged components (P and U) and their turbulent components (p and u) as $p_I = P + p$ and $u_I = U + u$, then employing the fact that $\bar{u} = 0$ it is easily shown that

$$P = \frac{1}{2}\rho U^2(1 + I^2) \qquad (1)$$

and

$$p = \frac{1}{2}\rho(2Uu + u^2 - \overline{u^2}) \tag{2}$$

where

$$I = \sqrt{\overline{u^2}}/U \tag{3}$$

is the local turbulent intensity and overbars ($\overline{\ }$) denote time averages.

The time averaged and turbulent pressure components, averaged spatially over the entrance of the receiver, are then obtained from the expressions

$$P_f = \frac{1}{(y_2 - y_1)} \int_{y_1}^{y_2} P(x_o, y)dy \tag{4}$$

and

$$p_f(t) = \frac{1}{(y_2 - y_1)} \int_{y_1}^{y_2} p(x_o, y, t)dy \tag{5}$$

where $y_1 = y_o$ and $y_2 = y_o + \ell$.
The quantity P_f is what we will refer to as the signal, whereas $\sqrt{\overline{p^2}}$ is referred to as the noise.

Later we will show that quantities such as U/U_o and $\sqrt{\overline{u^2}}/U_o$, at various axial locations, collapse to a single curve when plotted against the similarity parameter, η, defined as

$$\eta = \frac{y - w/2}{x} \tag{6}$$

where w is the width of the nozzle. Therefore, it is convenient to write Eqs. (4) and (5) in terms of η. The resulting expressions are:

$$P_f = \frac{1}{(\eta_2 - \eta_1)} \int_{\eta_1}^{\eta_2} P(\eta)d\eta \qquad (7)$$

and

$$p_f(t) = \frac{1}{(\eta_2 - \eta_1)} \int_{\eta_1}^{\eta_2} p(\eta, t)d\eta \qquad (8)$$

Note that η_1 is the line from point A (Fig. 2) through point (x_o, y_o) and η_2 is the line from point A through point $(x_o, y_o + \ell)$. Furthermore, since Eqs. (7) and (8) are independent of x_o, the results hold for any receiver whose edges lie on these two lines. Thus, the single integration yields results for a family of receivers of different sizes located at different axial stations. There is a limitation to the above statement; namely, the receiver whose edges lie on the two lines must also lie wholly above the center line of the jet. This is necessitated by the fact that the definition of η (Eq. (6)) is valid only when $y \geq 0$. When $y \leq 0$, a new set of η lines, originating from the lower lip of the jet, is required.

Although we have extended this work to include receivers that span the center line of the jet, we will restrict this presentation to receivers which lie wholly above the axis. This restriction is necessitated by the fact that we presently have numerical results for only thirty-five receivers of different sizes located at various positions in the jet. Of these thirty-five, only seven that lie above the jet axis lend themselves to a systematic presentation of results. An additional 165 receivers, 79 of which span the axis, are presently being evaluated by a computer program.

The restriction to receivers above the x-axis does have the advantage that the mathematics are a little less complex and hence easier to present. Indications are that some quantities change sharply as the receivers begin to span the x-axis.

Some mention will be made of these facts later in the section entitled "Discussion of Results".

To obtain an expression for $\overline{p_f^2}$ we write

$$p_f^2(t) = \frac{1}{(\eta_2 - \eta_1)^2}\left[\int_{\eta_1}^{\eta_2} p(\eta, t)d\eta\right]^2$$

which is equivalent to

$$p_f^2(t) = \frac{1}{(\eta_2 - \eta_1)^2}\int_{\eta_1}^{\eta_2} p(\eta, t)d\eta \int_{\eta_1}^{\eta_2} p(\xi, t)d\xi$$

since the variables of integration are "dummy" variables, that is, can be represented by any symbols; this latter expression can be written as

$$p_f^2(t) = \frac{1}{(\eta_2 - \eta_1)^2}\int_{\eta_1}^{\eta_2}\int_{\eta_1}^{\eta_2} p(\eta, t)\ p(\xi, t)d\eta d\xi \qquad (9)$$

Assuming that time and space averages can be interchanged on the right-hand side of Eq. (9), we obtain

$$\overline{p_f^2(t)} = \frac{1}{(\eta_2 - \eta_1)^2}\int_{\eta_1}^{\eta_2}\int_{\eta_1}^{\eta_2} \overline{p(\eta, t)p(\xi, t)}d\eta d\xi \qquad (10)$$

It should be noted that ξ and η are different symbols for the same thing, namely, a measure of the position of points on the receiver entrance. Thus, when $\xi = \eta$, the integrand is $\overline{p^2(\eta, t)}$, the mean square pressure at "point" η. When $\xi \neq \eta$, the integrand is the correlation of pressure between "points" ξ and η.

To a close approximation we can write Eqs. (1) and (2) as

$$P = \frac{1}{2}\rho U^2, \qquad p = \rho U u \tag{11}$$

Thus, if we use the shorthand notation U_η for $U(\eta)$, we can write Eqs. (7) and (10) as

$$P_f = \frac{\rho}{2(\eta_2 - \eta_1)} \int_{\eta_1}^{\eta_2} U_\eta^2 d\eta \tag{12}$$

and

$$\overline{p_f^2} = \left(\frac{\rho}{\eta_2 - \eta_1}\right)^2 \int_{\eta_1}^{\eta_2}\int_{\eta_1}^{\eta_2} U_\eta U_\xi \, \overline{u_\eta u_\xi} \, d\eta d\xi \tag{13}$$

Next, we introduce the correlation coefficient which is normally defined as

$$R(\xi,\eta) = \frac{\overline{u_\eta u_\xi}}{\sqrt{\overline{u_\eta^2}}\sqrt{\overline{u_\xi^2}}} \tag{14}$$

Then Eq. (13) can be written as

$$\overline{p_f^2} = \left(\frac{\rho}{\eta_2 - \eta_1}\right)^2 \int_{\eta_1}^{\eta_2}\int_{\eta_1}^{\eta_2} U_\eta U_\xi \sqrt{\overline{u_\eta^2}}\sqrt{\overline{u_\xi^2}} \, R(\eta,\xi) d\eta d\xi \tag{15}$$

Since we will present the values of U/U_o and $\sqrt{\overline{u^2}}/U_o$ later in this paper, we write Eqs. (12) and (15) in the dimensionless forms:

$$\frac{P_f}{\frac{1}{2}\rho U_o^2} = \frac{1}{(\eta_2 - \eta_1)} \int_{\eta_1}^{\eta_2} \left(\frac{U_\eta}{U_o}\right)^2 d\eta \tag{16}$$

and

$$\frac{\overline{p_f^2}}{\frac{1}{4}\rho^2 U_o^4} = \frac{4}{(\eta_2 - \eta_1)^2} \int_{\eta_1}^{\eta_2}\int_{\eta_1}^{\eta_2} \frac{u_\eta}{U_o}\frac{u_\xi}{U_o}\sqrt{\frac{\overline{u_\eta^2}}{U_o}}\sqrt{\frac{\overline{u_\xi^2}}{U_o}}\, R(\eta,\xi)\,d\eta\,d\xi \tag{17}$$

Relations Between Signal and Noise

Eqs. (16) and (17) are the basic expressions for signal and noise, respectively. Their numerical values are of some interest and importance in themselves, however, certain interrelations between these quantities shed more light on the receiver noise problem. For example, the noise-to-signal ratio, $I_f(p)$, defined as

$$I_f(p) = \frac{\sqrt{\overline{p_f^2}}}{P_f} \tag{18}$$

is useful in evaluating the performance of an amplifier with the receiver positioned in a jet held stationary by the control jets. It would probably be even more useful as a means of evaluating the performance of each proportional amplifier in a chain of such devices, under quasi-steady state conditions, where the noise is possibly amplified at each stage.

To evaluate the influence of noise on a proportional amplifier when the control stimuli are varied (so that the main jet deflects) a more appropriate relation would be the "coefficient of noise", C_f, defined as

$$C_f = \frac{\left(\sqrt{\overline{p_f^2}}\right)_a}{\left(\frac{\partial P_f}{\partial \eta}\right)_a \Delta\eta} \tag{19}$$

The subscripts "a" indicate that the quantities in parentheses are to be evaluated when the receiver is stationed in position "a" relative to the jet center line. The numerator

is simply the noise at position "a". The denominator represents tne change in signal for a small deflection, $\Delta\eta$.

It should be noted that mathematically it is immaterial whether $\Delta\eta$ represents the amount of deflection the jet undergoes while the receiver remains stationary, or if the receiver is considered to move by amount $\Delta\eta$ in a stationery jet. Under normal conditions, one would hope tnat C_f is small for a given deflection, indicating that the change in signal is large in comparison to the noise so that it can be detected as something distinct from the noise.

We realize that there are other relations between signal, noise, stimuli, etc., which would be more appropriate under certain circumstances. For example, one might wish to combine Eq. (19) with the relation between the amount of control stimuli required to produce the deflection $\Delta\eta$. We have chosen Eqs. (18) and (19) as the most obvious and possibly most useful to consider

III. EXPERIMENTAL RESULTS

In order to evaluate the expressions presented above, it was necessary to measure the pertinent statistical quantities associated with the velocity field of a two-dimensional jet. We made an assumption commonly employed in fluid amplifier work, namely, that the velocity field of an unobstructed jet will be but slightly altered by the presence of a sharp-edged receiver. Thus, measurements made in an unobstructed jet are assumed to apply when a receiver is introduced in the stream. Should this assumption introduce excessive errors, when comparison is made with experimental data, the basic approach presented here can still be applied. However, the actual velocity field in front of the receiver would have to be used in the subsequent calculations.

Employing a hot wire anemometer, measurements were made of the mean velocity, U, and the root mean square value of the turbulent component, $\sqrt{\overline{u^2}}$, in the x-direction (see Fig. 2 for

nomenclature). These measurements were made in the lateral direction (y) at various axial stations (x). The width of the nozzle, w, was 1/2 inch, and the axial stations chosen were x = 1.5", 2", 3", 4", 6" and 8".

The values of U were nondimensionalized by dividing by the nozzle exit velocity U_o. The results are plotted in Fig. 3. The values of $\sqrt{\overline{u^2}}$ were also divided by U_o and are plotted together with U/U_o in Figs. 4, 5, and 6 for x = 2", 4" and 8", respectively. It should be noted that the maximum value of $\sqrt{\overline{u^2}}/U_o$ always occurs near the inflection point of the corresponding curve for U/U_o. Thus, $\sqrt{\overline{u^2}}/U_o$ is maximum where $\frac{\partial}{\partial y}\left(\frac{U}{U_o}\right)$ is maximum. We shall see later that this is a consequence of the fact that $\sqrt{\overline{u^2}}$ and $\frac{\partial U}{\partial y}$ are very nearly linearly related.

The Similarity Parameter η

It is well known that the mean velocity profiles of both circular and two-dimensional jets exhibit self-similarity. To demonstrate this fact it has become common practice to plot $\frac{U}{U_m}$ against $\frac{y}{y_{0.5}}$, where U is the mean velocity at a point distance y from the jet axis, U_m is the maximum velocity, found on the jet axis, and $y_{0.5}$ is the distance from the jet axis at which the velocity is $0.5U_m$. There is no doubt that such a method of collapsing various velocity profiles is extremely useful, particularly for axial locations far downstream from the jet. It is not applicable, however, for the first few diameters of the flow where the potential core is still present. Also, it should be pointed out that basically three pieces of information are required for the use of such a plot in a practical application. These are:

a) the graph of $\frac{U}{U_m}$ vs. $\frac{y}{y_{0.5}}$

b) the locus of $y_{0.5}$ as a function of axial location

c) the variation of U_m with axial location.

The work of Ref. (4) has indicated that for a circular jet, velocity profiles of the first 10 diameters of the flow will collapse when $\frac{U}{U_o}$ is plotted against the parameter η_c, where U_c is the jet exit velocity. For the circular jet, η_c is defined

$$\eta_c = \frac{y - D/2}{x}$$

where y is the radial distance from the jet axis
x is the axial distance from the jet lip
D is the jet diameter.

This method of plotting has the advantage that, not only does it cover the potential core region, but in addition, all the required information is contained in one graph.

In fluid amplifier work, we shall be concerned primarily with only the first five to fifteen slit widths of the power jet flow. It therefore seemed of prime interest to examine whether a similar parameter will collapse the profiles of Fig 3 For this purpose we have defined η as presented earlier in Eq. (6). The resulting plot of U/U_o against η is shown in Fig. 7. The degree of collapse obtained is, in general, within the accuracy of the measurements in the range of five to fifteen slit widths downstream. Succeeding discussions will be based on the results for this range, which is represented by the mean line drawn in Fig. 7.

In addition to U/U_o, the values of $\sqrt{\overline{u^2}}/U_o$ were also plotted against η. The results are shown in Fig. 8. Once again, a good collapse is obtained for the range of five to fifteen slit widths as represented by the curve in Fig. 8.

The values of U/U_o and $\sqrt{\overline{u^2}}/U_o$ as a function of η, taken from the curves in Fig. 7 and 8, are presented in columns (3) and (5) of Table I. The significance of the remaining columns of this table will become apparent later in this paper.

Table I

CALCULATED AND MEASURED VALUES OF U/U_o AND $\sqrt{\overline{u^2}}/U_o$

(1)	(2)	(3)	(4)	(5)
y	Calculated	Measured	Calculated	Measured
	$\frac{U}{U_o}$	$\frac{U}{U_o}$	$\frac{\sqrt{\overline{u^2}}}{U_o}$	$\frac{\sqrt{\overline{u^2}}}{U_o}$
10	.981	.999	.00393	.045
-.075	.958	.975	.0536	.075
-.05	.900	.910	.0964	.107
-.025	.810	.815	.128	.134
0	.700	.695	.147	.146
.025	.581	.57	.152	.146
.05	.465	.465	.145	.140
.075	.354	.35	.129	.126
.10	.260	.25	.108	.109
.125	.183	.185	.086	.09
.150	.124	.125	.0645	.072
.175	.081	.09	.0462	.055
.20	.05	.07	.0311	.038

IV. RELATION BETWEEN MEAN SHEAR AND TURBULENT INTENSITY

In the case of a circular jet, the work of Ref. (4) indicates that a relation of the form

$$\sqrt{\overline{u^2}} = -Kx \frac{\partial U}{\partial y}$$

exists. Alternatively, this can be written as

$$\sqrt{\overline{u^2}} = -K\frac{\partial U}{\partial r} \qquad (20)$$

Table II presents the results of an attempt to establish a similar relationship for the two-dimensional jet employed in this work. The values in column (2) represent the gradient of the velocity profile in Fig. 7 as a function of η. These values when divided into $\sqrt{\overline{u^2}}/U_o$ yield the values of K in Eq. (20). Over a wide range of η values, a value of K of the order of .031 is indicated. This compares favorably with the equivalent value of the order of .026 found for a circular jet. The increase in K for $|\eta| > 0.1$ indicates a breakdown of the relationship as expected. For example, on the jet axis (y = 0), $\frac{\partial U}{\partial y}$ is zero, but a finite value for $\sqrt{\overline{u^2}}$ is observed.

V. EMPIRICAL EXPRESSIONS

To facilitate the evaluation of Eqs. (16) and (17) we developed empirical expressions to represent the velocity field data. The expression for U/U_o was assumed to have the form

$$\frac{U_\eta}{U_o} = e^{-(A\eta^2 + B\eta + C)} \qquad (21)$$

Choosing the values of A, B and C to fit the curve in Fig. 7, we obtained:

$$A = 32.6, \quad B = 6.64, \quad C = 0.357 \qquad (22)$$

Table II

MEAN SHEAR AND TURBULENT INTENSITY

(1) r_i	(2) $\frac{1}{U_o}\frac{\partial U}{\partial r}$	(3) $\frac{\sqrt{\overline{u^2}}}{U_o}$	(4) $k = \frac{(3)}{(2)}$
-.10	0.4	.045	.11
-.075	1.8	.073	.045
-.05	3.4	.107	.031
-.025	4.2	.134	.032
0	4.6	.146	.032
+.025	4.7	.146	.031
.05	4.8	.140	.029
.075	4.3	.126	.029
.10	3.6	.109	.030
.125	2.8	.09	.032
.15	1.8	.072	.040
.175	1.0	.055	.055
.20	.54	.038	.070

The values obtained from Eqs. (21) and (22) appear in column (2) of Table I, and compare favorably with the measured values in column (3) over the entire range of η.

Next we employed Eq. (20) together with Eq. (21) to obtain an empirical expression for $\sqrt{\overline{u^2}}/U_o$. The values calculated from this expression appear in column (4) of Table I and compare favorably with the measured values in column (5) for the range $\eta \geq -.075$, i.e., almost the full η range.

Although we have not made any correlation measurements, the experimental work of Laurence[5] is very closely approximated by the following relation

$$R(\xi,\eta) = e^{-H|\xi - \eta|} \qquad (H \simeq .24) \tag{23}$$

Hence, we have empirical expressions for all of the terms in the integrands of Eqs. (16) and (17).

VI. ANALYTICAL EVALUATIONS OF SOME OF THE BASIC EQUATIONS

If Eq. (21) for U/U_o is placed in Eq. (16) and some simple transformations of variables are made, it can be shown that

$$\frac{P_f}{\frac{1}{2}\rho U_o^2} = \frac{e^{-2C + \delta^2}}{\alpha(\eta_2 - \eta_1)} \left[\int_0^{\alpha\eta_2+\delta} e^{-s^2} ds - \int_0^{\alpha\eta_1+\delta} e^{-s^2} ds \right] \tag{24}$$

where C is the value given in Eq. (22) and α and δ are obtained from Eq. (22) through the relations

$$\alpha = \sqrt{2A} \qquad \delta = B/\sqrt{2A} \tag{25}$$

Equation (24) can now be evaluated by the use of standard tables since the integrals appearing in that expression are simply the error function (erf).

Now we introduce the symbol η_w for the "η width", that is

$$\eta_w = \eta_2 - \eta_1 \tag{26}$$

Solving Eq. (26) for η_1 and substituting into Eq. (24) we obtain an expression for $P_f/\frac{1}{2}\rho U_o^2$ in terms of η_2 and η_w. Differentiating this expression partially with respect to η_2 gives the rate of change of the signal as the receiver position changes, while the receiver width is maintained constant. This is the differential required in the denominator of Eq. (19). The result of this differentiation is

$$\frac{\partial}{\partial\eta}\left(\frac{P_f}{\frac{1}{2}\rho U_o^2}\right) = \frac{e^{-2C+\delta^2}}{\eta_w}\left[e^{-(\alpha\eta_2+\delta)^2} - e^{-(\alpha\eta_1+\delta)^2}\right] \tag{27}$$

Note that we have dropped the subscript 2 from $\partial/\partial\eta_2$ because the same result can be obtained by expressing Eq. (24) in terms of η_1 and η_w or any other η, such as the mid-point value, and differentiating appropriately.

The only other expression that must be evaluated in order to calculate $I_f(p)$ (Eq. (18)) and C_f (Eq. (19)) is the expression for $\sqrt{\overline{p_f^2}}$, as represented by Eq. (17). Unfortunately, we have been unable to evaluate Eq. (17) in terms of tabulated functions. Consequently, a simple computer program was written to evaluate this expression numerically. Furthermore, an upper bound on $\overline{p_f^2}$ is obtained by considering the completely correlated case, i.e., $R(\xi,\eta) = 1$. In that case, Eq. (17) integrates to yield the simple result:

$$\frac{\overline{p_f^2}}{\frac{1}{4}\rho^2 U_o^4} = \left(\frac{K}{\eta_2 - \eta_1}\right)^2\left[\left(\frac{U_{\eta_2}}{U_o}\right)^2 - \left(\frac{U_{\eta_1}}{U_o}\right)^2\right]^2 \tag{28}$$

VII. POINT RECEIVERS AND FINITE RECEIVERS

A most appropriate consideration of the expressions given above is to examine the limiting situation as the receiver width, η_w, approaches zero. This will lead to expressions for "point" receivers, i.e., receivers of infinitesimal width. Such a receiver could be approached practically by an extremely small pitot tube.

Starting with Eq. (24), the result of such a limiting process is the indeterminate quantity, 0/0. However, by application of L'Hospital's rule for handling such indeterminate forms, it can easily be shown that the limit is

$$\frac{P_f}{\frac{1}{2}\rho U_o^2} = \left(\frac{U_\eta}{U_o}\right)^2 \tag{29}$$

This is exactly what one would expect, since it can be directly obtained from the first of Eqs. (11).

A similar limiting process when applied to Eqs. (17) and (27) leads to the following results:

$$\frac{\overline{p_f^2}}{\frac{1}{4}\rho^2 U_o^4} = \frac{4U_1^2\overline{u_\eta^2}}{U_o^4} \tag{30}$$

Once again these results can be more easily obtained from the second of Eqs. (11) and the first of Eqs. (11), respectively.

From Eqs. (30) and (29) it follows that, for a point receiver, $I_f(p)$ (Eq. 18)) becomes

$$I_f(p) = 2\sqrt{\frac{\overline{u_\eta^2}}{U_\eta}} = 2I \tag{32}$$

where I is the local turbulent intensity (see Eq. (3)). Dividing the values in column (4) of Table I by the corresponding values in column (2) yields I. Then Eq. (32) can be plotted as shown in Fig. 9.

From Eqs. (30) and (31) it follows that, for a point receiver, C_f (Eq. (19)) becomes

$$C_f\Delta^{\prime} = \frac{\sqrt{\overline{u_{\eta}^2}}}{\frac{\cdot U_{\eta}}{\delta^{**}}}$$

which in view of Eq. (30) can be written as

$$-C_f\Delta^{\eta} = K \qquad (K \cong .031) \tag{33}$$

This latter relation is plotted as a horizontal line in Fig. 10

Finally, the graphical results are completed by using the expressions for finite receivers to plot the results when $\eta_w = .05$ and $\eta_w = .10$. These results also appear on Figs. 9 and 10. We explained earlier that a limited amount of numerical results are presently available. Hence, the results represented by Figs. 9 and 10 are somewhat tentative. However, they do appear consistent, in that the point receiver results are approached as η_w becomes smaller.

Actually, we do not have enough results to absolutely guarantee that the lines for finite η_w are perfectly straight as depicted in Fig. 9. Furthermore, the lines for finite η_w in Fig. 10 are not perfectly horizontal as is the one for the point receiver. More complete results might even show that these lines are not straight but might be somewhat curved. More is said concerning these points in the following section.

VIII. DISCUSSION OF RESULTS

Even though a limited number of results are presently available, we feel that their apparent consistency lends weight to accepting them as indicators of the i. fluence of noise on proportional amplifiers when the receivers are located entirely above the jet axis.

Assuming that the results are accurate, let us consider their physical significance. First, however, let us write the defining equation for η, Eq. (6), in the form

$$y = \eta x + w/2.$$

Referring to Fig. 11 we see that this expression represents a family of straight lines emanating from the upper lip of the nozzle ($x = 0$, $y = w/2$) with slope equal to η. Thus, the line $\eta = 0$ is parallel to the x axis. The outer edge of the jet (line bd) is approximately $\eta = .20$, while the edge of the potential core (line bc) is $\eta = -.10$. The line from point b through any point on or above the x axis, and between the edges of the jet and the potential core, corresponds to a value of η in the range $-.10 \leq \eta \leq .20$.

Now consider a receiver located at a value of $x < 5w$ (Fig. 11) and between the edges of the jet and the potential core. As the lower edge of this receiver approaches the potential core ($\eta = -.10$), Fig. 9 indicates that the noise-to-signal ratio $I_f(p)$ approaches zero regardless of its width. This appears logical because once the receiver is completely embedded in the potential core $I_f(p)$ should essentially be zero.

Next consider a receiver located at $x = 10w$. In this case the η line passing through $x = 10w$, $y = 0$ is $\eta = -.05$. Thus, as the receiver approaches the x-axis, $I_f(p)$ becomes smaller; however, it will never become zero because the lower limit on η at this x location is $-.05$.

As a matter of fact, the results obtained from a few receivers spanning the x-axis indicate that the curves for $I_f(p)$ depart from their straight-line form when the spanning begins. To be more specific, the curves tend to flatten out, i.e., become horizontal to the η axis. The complete results will be discussed in a future paper.

We see then, that Fig. 9 indicates that, independent of the receiver width, the noise-to-signal ratio is smallest when the receiver is near the edge of the potential core or near the x-axis, depending upon its x location. Furthermore, for any given x and y position of the receiver midpoint, i.e., for any given value of η (midpoint) the curves in Fig. 9 indicate that the noise-to-signal ratio, $I_f(p)$, becomes smaller as the width of the receiver (η_w) is made larger.

Next, let us consider the results depicted in Fig. 10. Note first that C_f is always negative since $\partial P_f/\partial\eta$ is negative. This occurs because as η increases the receiver moves to a region where the dynamic pressure, $\frac{1}{2}\rho U^2$, and hence P_f, becomes smaller. Our interest, then, centers on $|C_f|$.

We recall that C_f is essentially the noise to change-in-signal ratio, due to a small deflection, $\Delta\eta$, of the main jet. Consequently we would hope to find positions within the jet where the receiver can be placed so as to minimize $|C_f|$ for a given value of $\Delta\eta$, just as we have seen how to minimize $I_f(p)$. It is clear from the nearly horizontal character of these curves, however, that independent of the receiver position, one obtains essentially

$$C_f = -\frac{\text{constant}}{\Delta\eta} \tag{34}$$

where the "constant" depends upon the receiver width, η_w. This would tend to indicate that there is no position that minimizes C_f for a given deflection $\Delta\eta$. However, the results obtained for a few receivers spanning the x-axis indicate that the curves for $-C_f\Delta\eta$ begin to rise rapidly once the receiver begins to span the center line. As a matter of fact, since $\partial P_f/\partial\eta$ can be shown to be zero when the midpoint of the receiver is on the x-axis, it is apparent that $-C_f\Delta\eta$ goes to infinity under these conditions. In a sense, then, $|C_f|$ is minimized by keeping the receiver from spanning the center line of the jet.

Returning now to Fig. 10, and restricting the discussion to receivers which lie wholly above the x-axis, we see that the "constant" in Eq. (34) becomes smaller as the receiver width increases. Thus, for a given value of $\Delta\eta$, we see that $|C_f|$ becomes smaller as the receiver width increases.

Consider a simple numerical example of the significance of C_f. When $\eta_w = .10$, the constant in Eq (34) is approximately .023. It can easily be shown that $\Delta\eta$ is approximately equal to the deflected angle $\Delta\theta$ of the jet center line; thus, if $|C_f|$ is to be, say, 0.50, a deflection of the amount

$$\Delta\theta = \Delta\eta = \frac{\text{constant}}{|C_f|} = .046 \text{ radians} \cong 2.5°$$

is required.

Based upon the above discussion, the primary results of this work are that, for receivers above the x-axis, both $I_f(p)$ and $|C_f|$ become smaller as the receiver width increases. Furthermore, results based upon a few receivers spanning the x-axis indicate that $I_f(p)$ does, indeed, become a minimum when the receiver midpoint lies on the x-axis, whereas $-C_f\Delta\eta$ approaches infinity under these conditions. Hence, $I_f(p)$ is minimized by having the receiver on the x-axis, whereas $|C_f|$ is minimized by having the receiver stay entirely above the x-axis.

Acknowledgements

We wish to acknowledge the support and encouragement extended to us by personnel of the Harry Diamond Laboratories under whose auspices this work was performed.

REFERENCES

1. Peperone, S. J., S. Katz and J. Goto, "Gain Analysis of the Proportional Fluid Amplifiers", Proceedings of the Fluid Amplification Symposium, Harry Diamond Laboratories, October, 1962, 319.

2. Wuerer, J., "Experiments on the Control of Flane Jets by Auxiliary Flows", UCLA. Report No. 63-31, July, 1963.

3. Moynihan, F. A. and R. J. Reilly, "Deflection and Relative Flow of Three Interacting Jets", Proceedings of the Fluid Amplification Symposium, Vol. 1, Harry Diamond Laboratories, Army Materiel Command, Washington, D. C., May, 1964, 123-146.

4. Davies, P. O. A. L., and M. J. Fisher, "Statistical Properties of the Turbulent Velocity Fluctuations in the Mixing Region of a Round Subsonic Jet", AGARD Report 451, April, 1963. (Appears in part on pages 337 - 367 of J. Fl. Mech., 15, pt. 3, 1963).

5. Laurence, J. C., "Intensity, Scale and Spectra of Turbulence in Mixing Region of Free Subsonic Jet", NACA Report 1292, 1956.

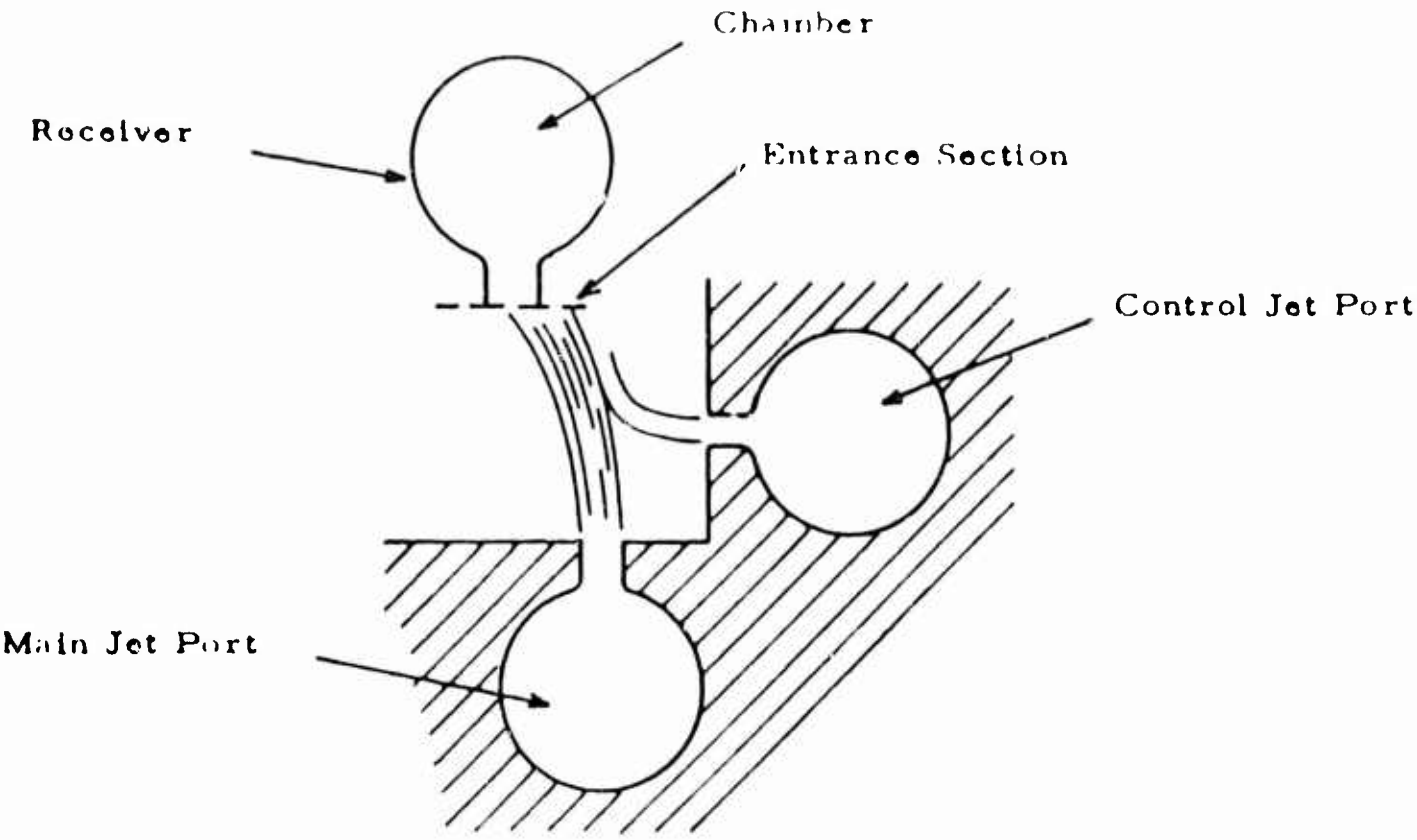

Fig. 1. SIMPLE PROPORTIONAL AMPLIFIER

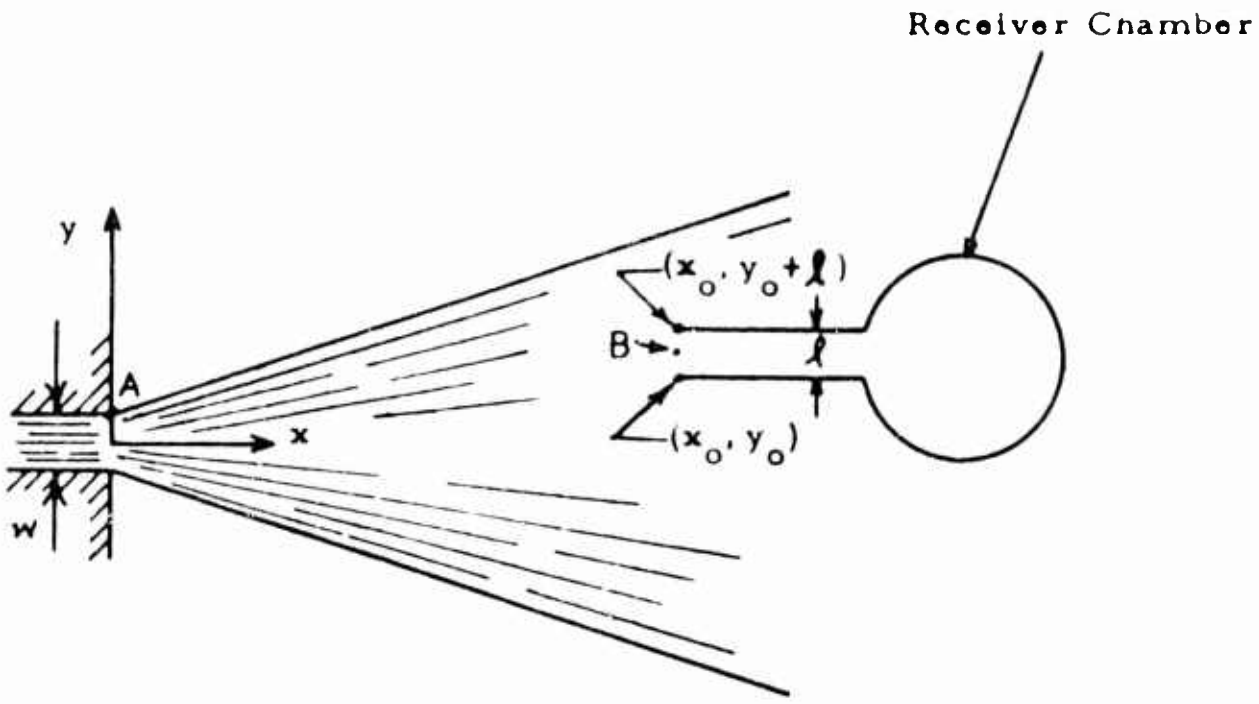

Fig. 2. FINITE RECEIVER

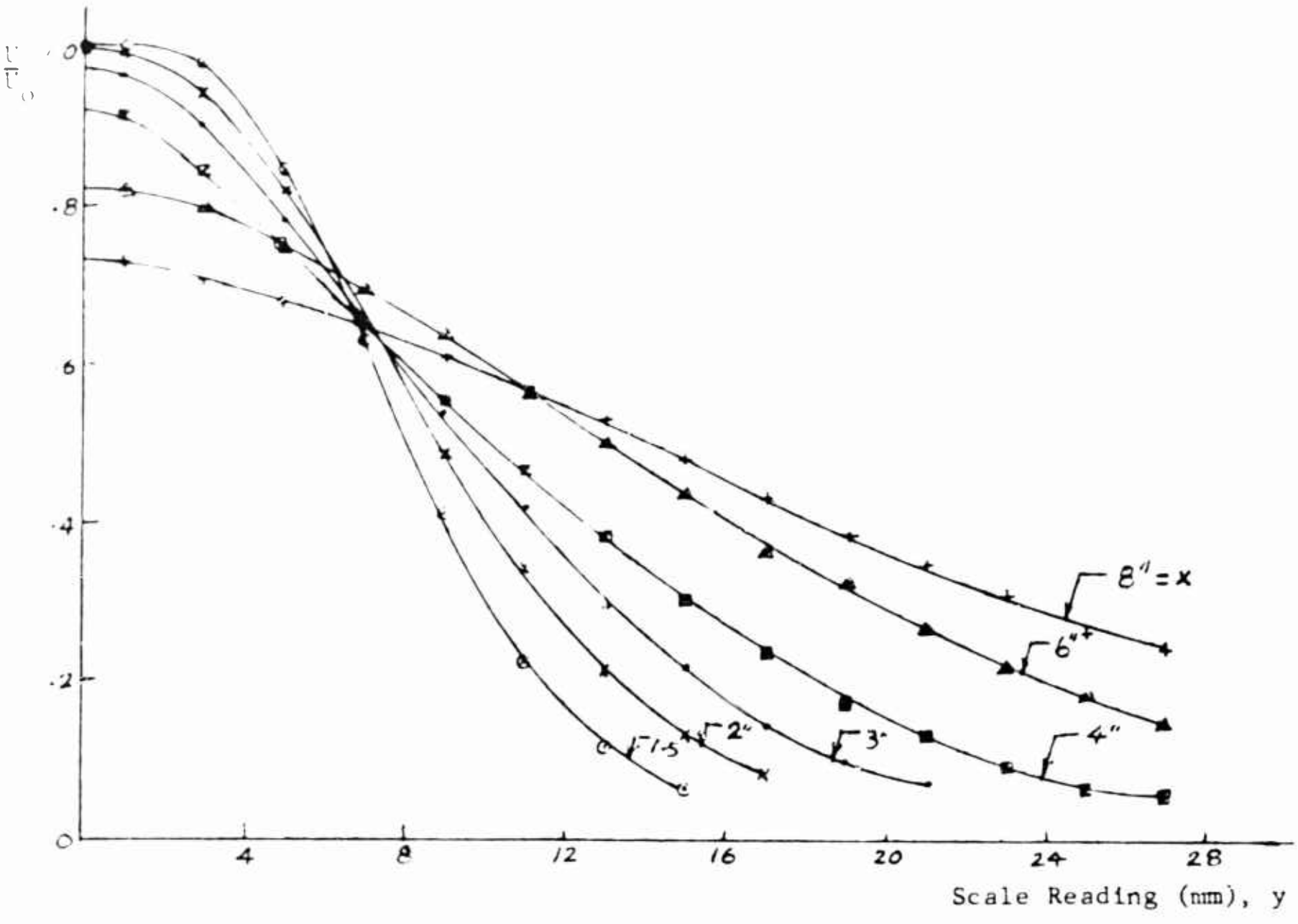

Fig. 3. MEAN VELOCITY PROFILE AT VARIOUS AXIAL STATIONS

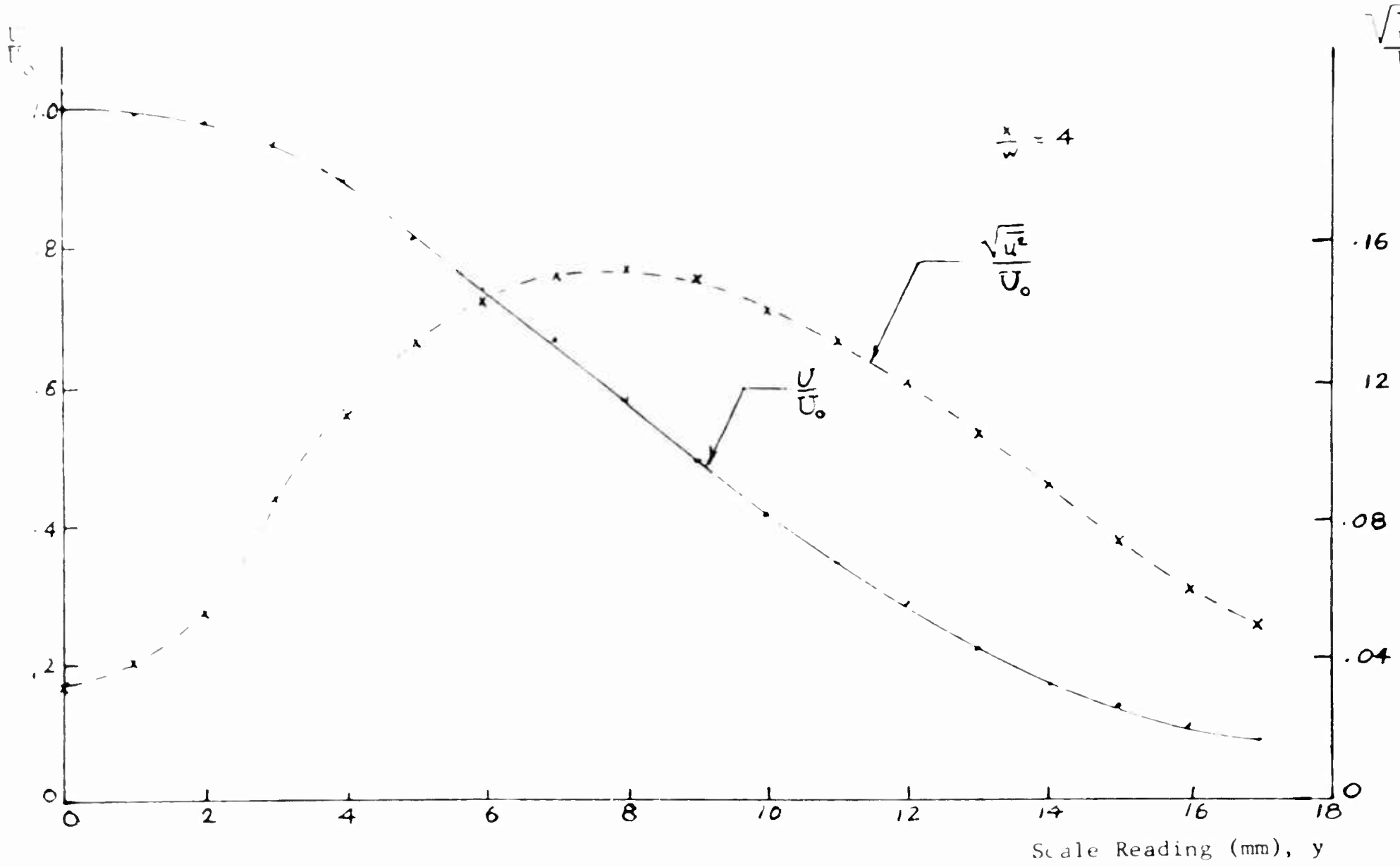

Fig. 4. MEAN AND TURBULENT VELOCITIES AT x = 2"

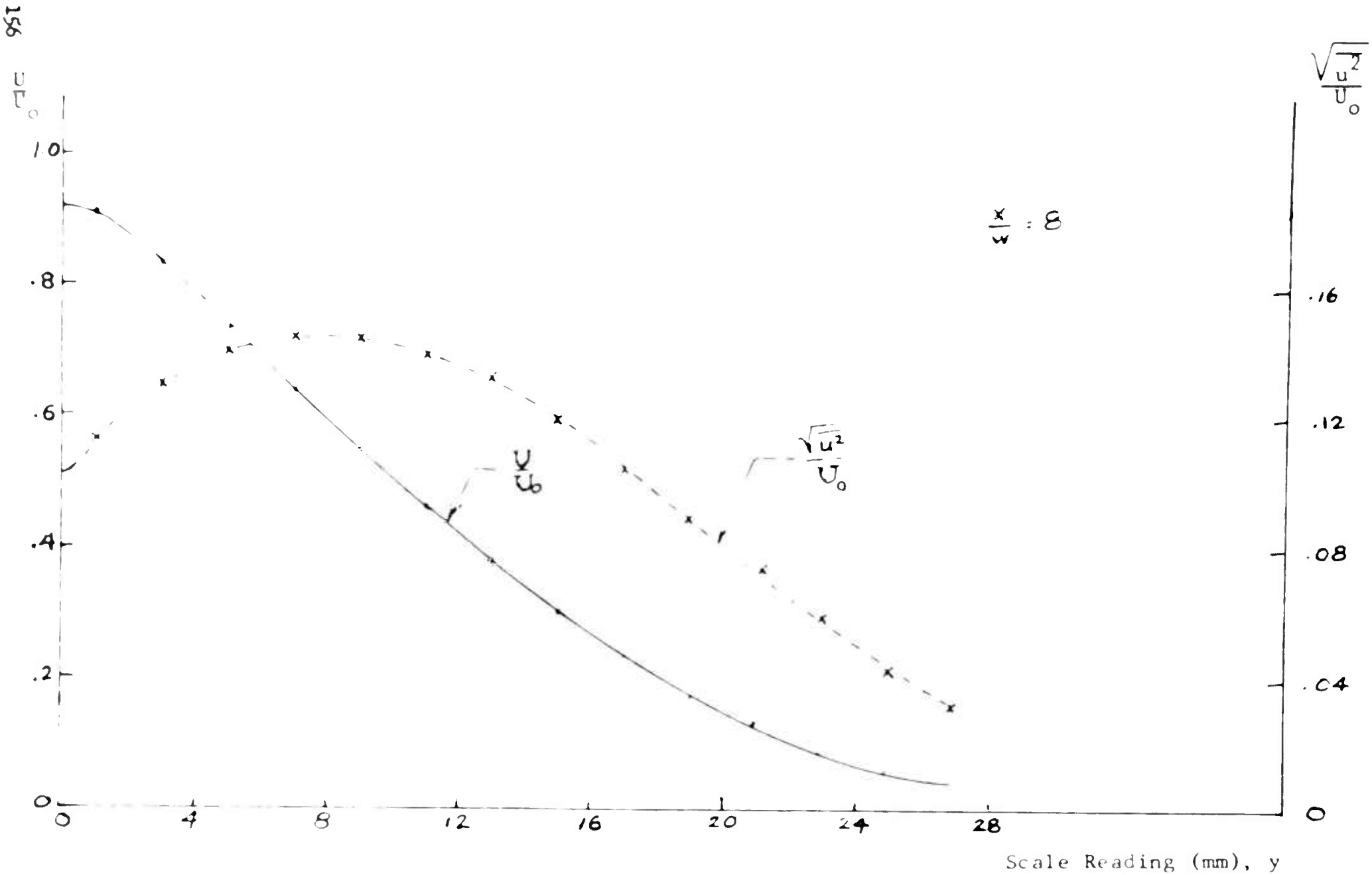

Fig. 5. MEAN AND TURBULENT VELOCITIES AT x = 4"

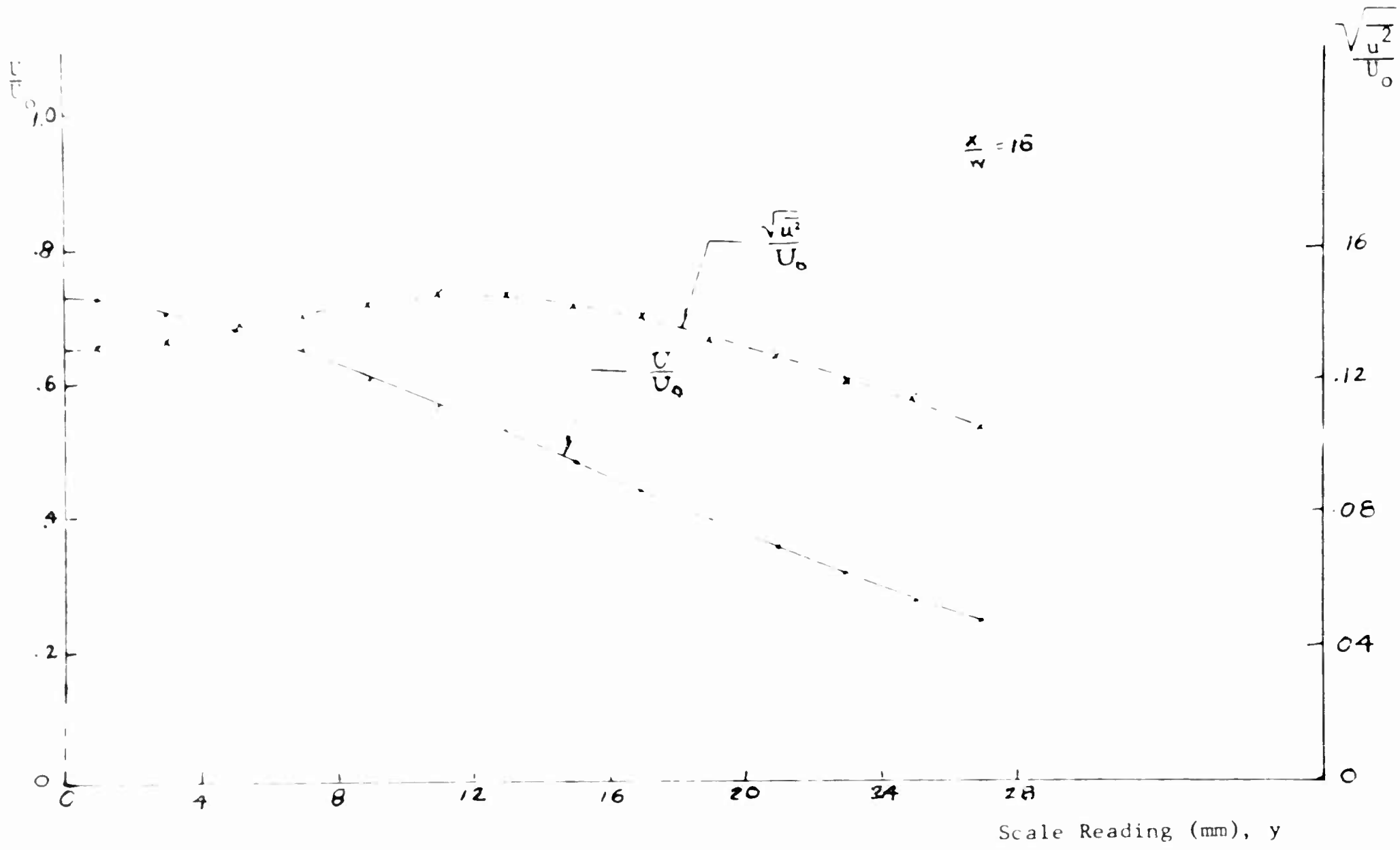

Fig. 6. MEAN AND TURBULENT VELOCITIES AT x = 8"

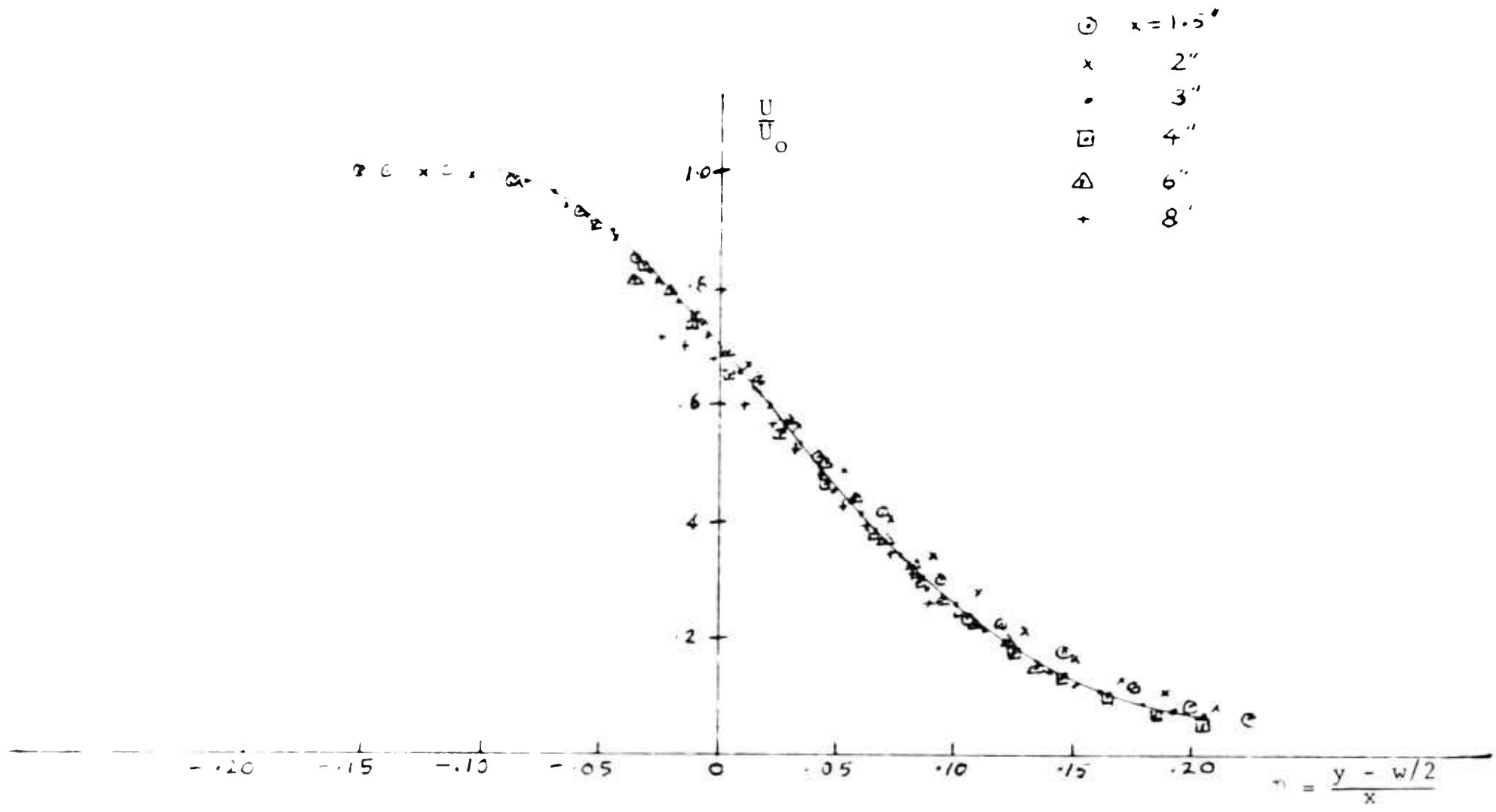

Fig. 7. MEAN VELOCITY PLOTTED AGAINST SIMILARITY PARAMETER

Fig. 8. TURBULENT VELOCITY PLOTTED AGAINST THE SIMILARITY PARAMETER

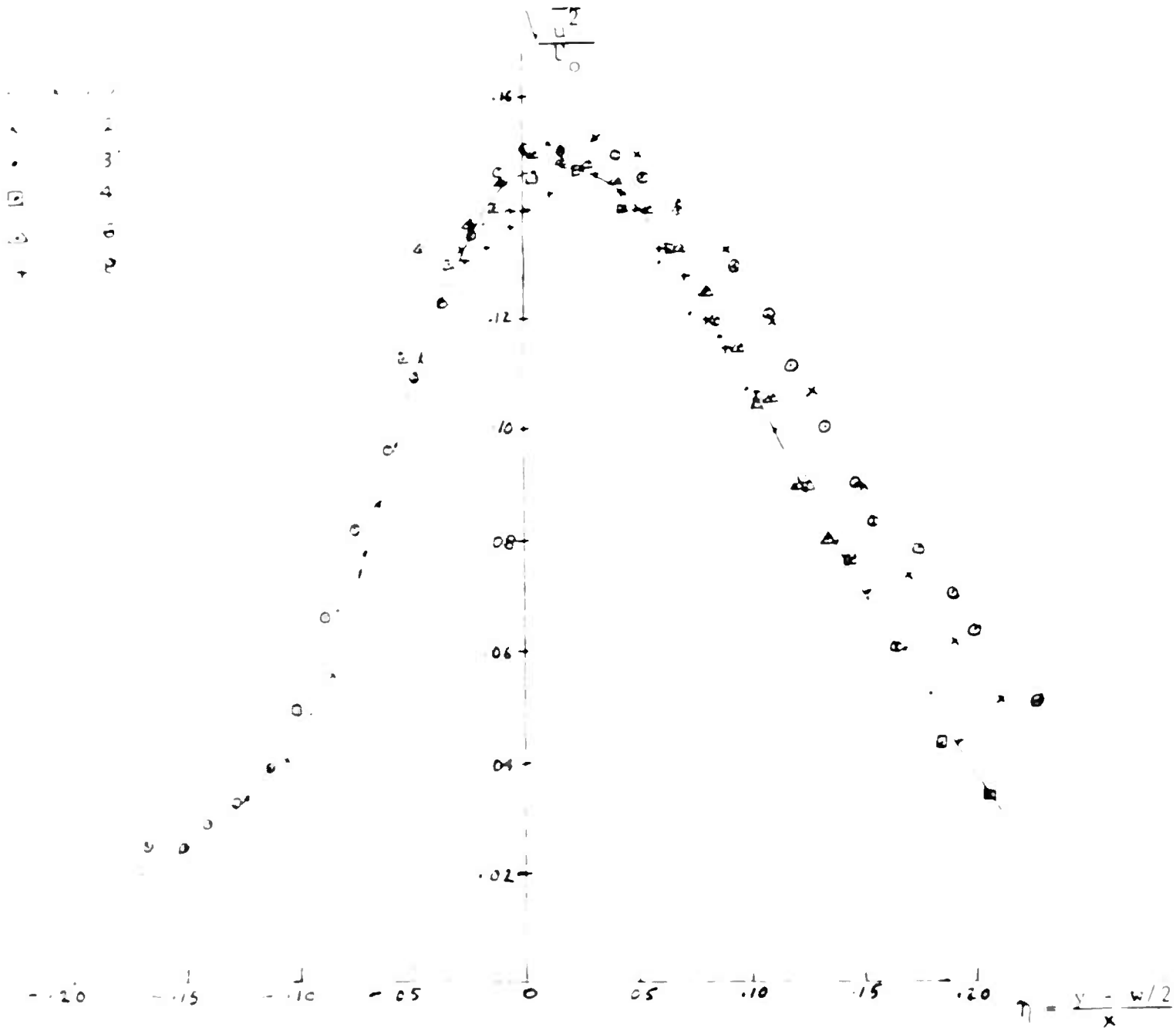

Fig. 9. NOISE TO SIGNAL RATIO VS. POSITION OF MID-POINT OF RECEIVER

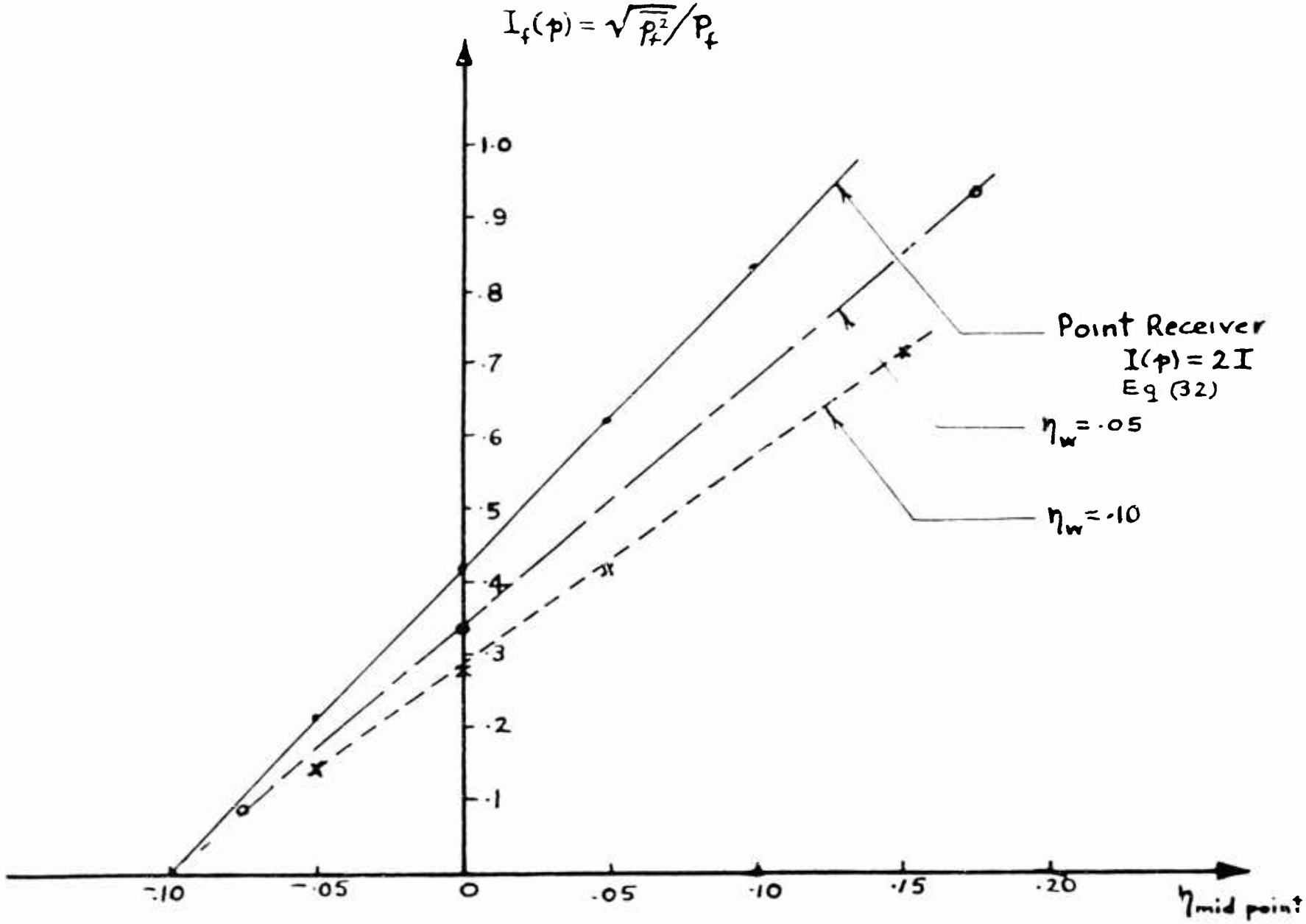

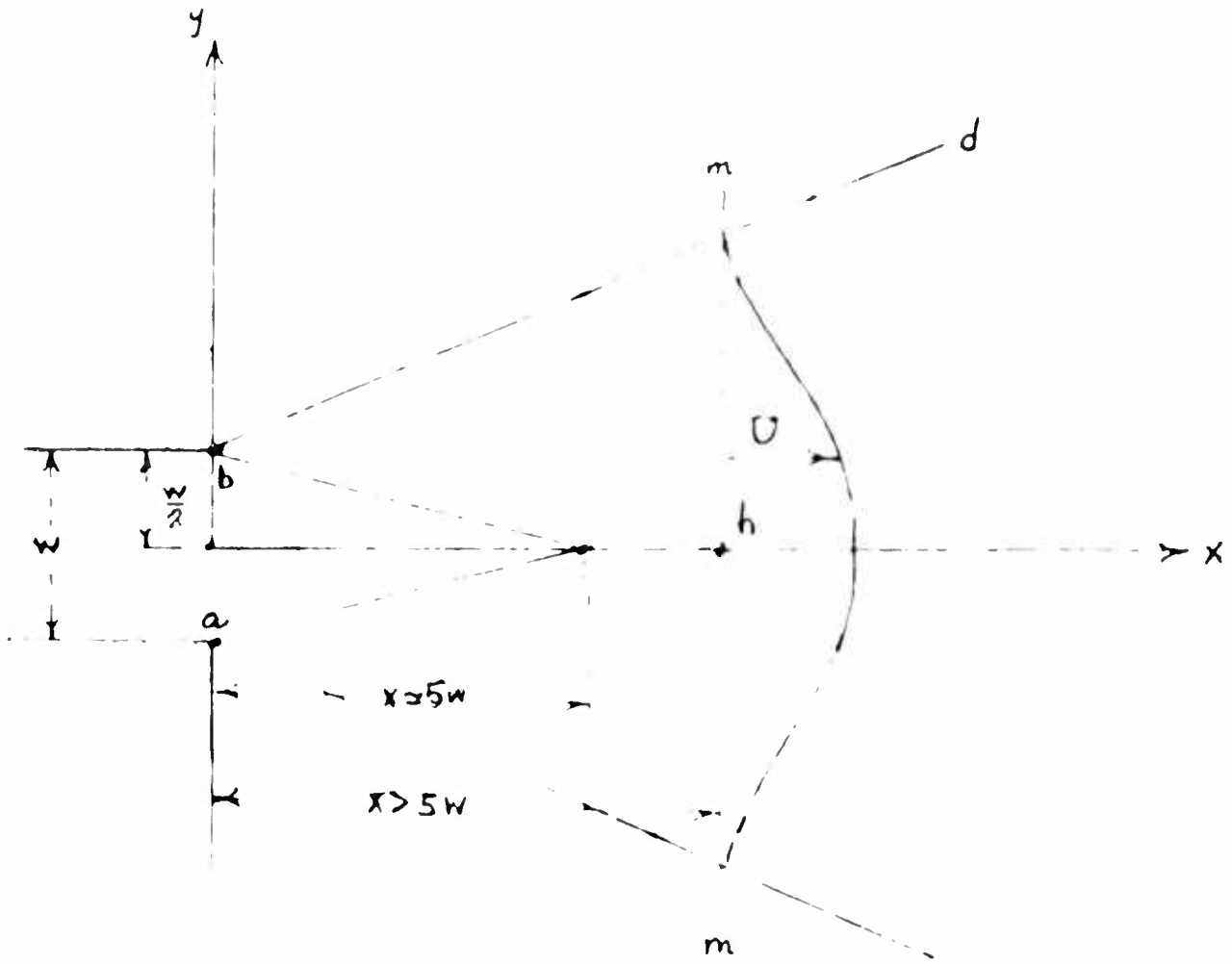

Fig. 11. LIMITATION ON [illegible]

Fig. 10. NOISE COEFFICIENT VS. RECEIVER POSITION

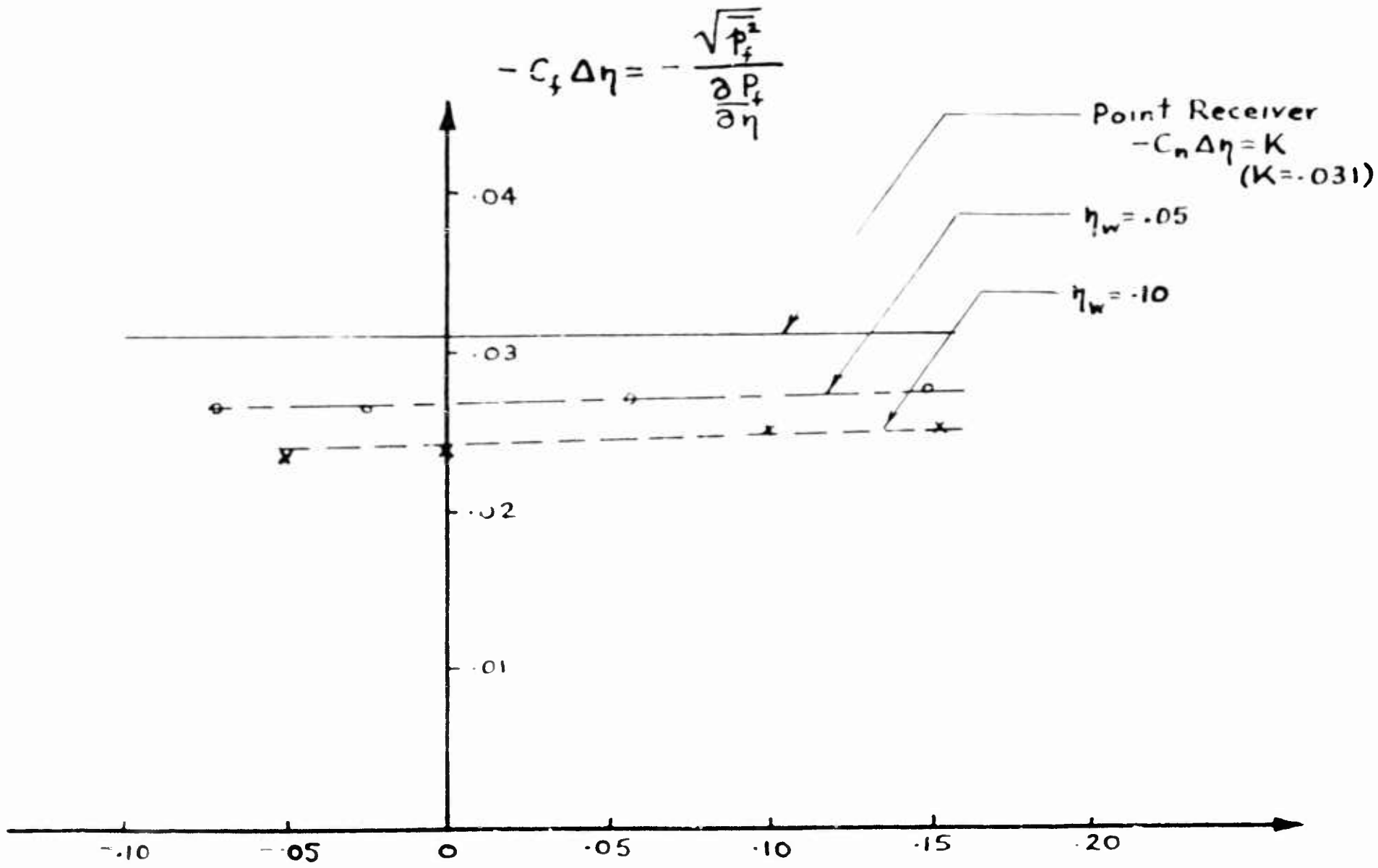

Effect of Receiver Design on Amplifier Performance and Jet Profile of a Proportional Fluid Amplifier

By
John A. Kallevig
Honeywell Inc.

ABSTRACT

Experimental data taken using a proportional amplifier with a one-half inch power nozzle is presented to show the effects of receiver geometry on the upstream velocity and total pressure profiles and amplifier performance. The work has two major sections. The first part covers the extreme case where the outlets are completely blocked and all of the flow exits through the vents. The second part consists of a survey of the pressure distribution and velocities within the amplifier having no vents, i.e., all of the flow exiting through the receiver. These data were taken using four different receivers and bellmouth configurations.

Introduction

One of the major concerns of the fluid amplifier designer has been whether the receiver geometry will seriously alter the flow in the interaction region and change the gain and pressure recovery that can be expected. Moynihan, Reference 2, has shown that the optimum receiver width can be calculated to maximize the gain. However, this assumes that the receiver does not disturb the upstream flow. Although we regularly made this assumption, its validity was always questionable so that it seemed appropriate that tests be made to determine just how important these effects would be. This paper reports the results of experiments which were conducted to accurately determine the effect of the receiver design on the amplifier performance and the jet profile of a proportional fluid amplifier.

Description of Apparatus

The experiments were performed on a large jet-interaction apparatus (Figure 1)* which has a central power jet and two perpendicular control jets with velocities in the power nozzle varying from 40 to 90 feet per second. Total pressure of the power nozzle was limited to approximately one to two inches of water gage, with a power nozzle width equal to 1/2 inch. Reynolds number, based on power nozzle width, ranged from 12,000 to about 25,000. The aspect ratio, which is the power jet height divided by the power jet width, was held constant at six. The control port width was four times the power nozzle width.

The first series of experiments were performed with a barrier placed across the width of the amplifier normal to the power jet centerline. It was placed at a distance equal to 8 power nozzle widths downstream of the exit of the power nozzle as shown in Figure 2. For the second series of experiments, the barrier was replaced by receivers which were machined from aluminum blocks. Figures 7 to 15 show the configuration used. A total pressure probe, attached to the movable upper plate, was used to survey the total pressure at various locations in the amplifier. Corresponding static pressure measurements were made (simultaneously) using a static tap in the upper plate.

Discussion

To establish basic data for comparison, the apparatus was set up without any receiver geometry installed. The projected offset was fixed at 1/4 the control port width and $W_c/W_p = 4.0$. Total and static pressure surveys were taken at $x/W_p = 4.5$ and 8.5. Figure 3 shows the velocity profile at these two stations. At $x/W_p = 4.5$ it is still possible to detect the outlines of the control jets on either side of the power jet velocity. However, at $x/W_p = 8.5$ the jets have combined to form a typical free jet with the control jets forming an integral part of the smooth velocity profile. Comparison of the two curves is allowed by making the total pressure dimensionless, dividing it by the power-jet total pressure and multiplying it by a factor to make the centerline value equal to the theoretical centerline value of a free jet. Figure 4 shows this dimensionless profile (circles) superimposed on the theoretical free-jet total-pressure profile as derived by Albertson (Reference 1). This comparison shows that the theoretical free jet is an excellent approximation of the measured values.

The control jets are still discernible but the survey was taken just downstream of the control port exits, at $x/W_p = 4.5$, so this is expected. Further downstream, the similarity to the free jet is even greater.

*Figures start on page 170.

One extreme condition occurs when the receivers are completely blocked and all of the flow must go out through the vents. This was simulated by installing a wall or a barrier across the width of the amplifier at $x/W_p = 8.0$. This is shown in Figure 2. Once again, the static and total pressures were measured at $x/W_p = 4.0$ and the static pressure was measured along the barrier. The squares in Figure 4 indicate the dimensionless total pressure profile at $x/W_p = 4.0$. The curve shows that the barrier had negligible effect on the total pressure profile at this station.

Figure 5 shows the effect of the barrier on the velocity profile at $x/W_p = 4.0$. The pressure difference at the centerline with the barrier is due to the data being taken further upstream at the exits of the control ports. This gave a slightly greater centerline velocity, and the control flow effects are more apparent. Despite these differences, the velocity distributions are quite similar and the barrier's effect is minimal.

Figure 6 shows the static pressure distribution measured along the barrier. The static pressure distribution expected along the barrier can be calculated using potential theory (Reference 4). The velocity at any point in the flow against a barrier is given by

$$V^2 = A^2 (x^2 + y^2)$$

Substituting this expression into Bernoulli's equation

$$P^o - P = 1/2 \rho V^2$$

gives

$$P^o - P = 1/2 \rho A^2 (x^2 + y^2)$$

Since we are only interested in the pressure distribution along the wall, $x = 0$. Also, since the flow is symmetrical about the x-axis and the y term is squared, only positive values of y are used. Thus, solving for the static pressure gives

$$P = P^o - 1/2 \rho A^2 y^2$$

where A is a real constant which depends on the free-stream conditions and y is the distance from the center of symmetry. At the stagnation point the velocity is zero so the static pressure equals the total pressure. For this particular geometry, A = 772 cycles per second. This includes a factor to make the static pressure at the centerline equal to the measured static pressure. The parabola in Figure 6 shows this prediction is accurate at the stagnation point and at high velocities. But, since it fails to account for viscosity and, hence, boundary layer effects, it is not valid farther away from the centerline of the jet.

Fraessling (Reference 3) presents the velocity as a function of the free-stream velocity for axially symmetrical flow with a stagnation point. Using Bernoulli's equation, we can calculate the static pressure distribution along the barrier. Figure 5 shows this expression to be a much better prediction than that given by potential theory.

Since the barrier has minimal effect on the upstream flow and the flow corresponds closely to free-jet flow in the plane of the downstream edge of the control ports, first experiments with receivers positioned the splitter at this plane. The sides of the outlegs were extended downstream from this plane, parallel to the 20-degree splitter. Movnihan's method (Reference 2) for estimating amplifier gain predicts a pressure gain of about seven for this setup. Figures 7 and 8 show the velocity and total pressure profiles at various places in the amplifier. With this configuration, the pressure gain was 17.1 with a flow gain of 1460. However, the flow through the receiver of this amplifier never becomes fully developed because the large flow gradient between the splitter centerline and the outer edge of the receiver is accentuated by the diffuser. This leads to significant losses in pressure recovery because of the large velocity gradients. Some form of receiver bellmouth seemed to be the logical answer to make the velocity distribution more uniform.

The first change consisted of reducing the offset from 1/4 to 3/16 of the control port width. This also reduced the receiver width from 5/8 to 1/2 inch. Figures 9 and 10 show the velocity and total pressure profiles at various places in the amplifier. The pressure gain remained constant at about 17 but the flow gain was reduced to about 325. The velocity profile and total pressure profile have about the same shape as before.

For the next series of tests the receiver was modified with curved inlets followed by a short converging portion. This caused the flow along the outer wall to be accelerated and still allowed slower flow around the corner of the control ports into the receiver. Figures 11 and 12 show the velocity and total pressure profile for this condition. The flow improvements, which were experienced due to the converging sections, were counteracted by the diverging sections so that the net gain was negligible, except for the reduction in velocity around the corner from the control ports into the receiver. Also, although the flow gain advanced from 325 to about 535, the pressure gain dropped to 13.3.

There is a limit to how far the offset can be reduced, especially with large control ports. If, for instance, the offset were reduced to 1/8 the control width, the downstream edge of the control port will peel off part of the power flow on one side so that flow will leave through that control port rather than enter through both, as is more customary. This could lead to difficulties in staging amplifiers and is not desirable for most applications. It could also cause other difficulties such as attachment, etc.

The last step was to round off the receiver ports even more and reduce the outleg width to 0.20 inch. This gave an indeterminate projected-offset. Also, no diffuser section was used. Several additional pressure measurements were made at various places in the outlegs. Figures 13 and 14 show that as far upstream as $x/W_R = 8.0$ the flow is already fully developed so that the bellmouth is very efficient. Therefore, in this configuration, the diffuser could probably start this far upstream. However, the diffuser should start on both sides rather than just on the outside as has been done in the past. Then, if necessary, the whole channel could curve outward from the centerline. The flow and pressure gains could not be measured because the control velocities were too small to be measured with our existing instrumentation.

Two small amplifiers with geometry similar to Figures 7 and 13 were constructed. Both have aspect ratios of 2.0 with power nozzle widths equal to 0.050 inch. The projected offset is 1/4 the control port width, which is four times as wide as the power nozzle. The receivers for the first one (Figure 6) are 2.050 inch wide and are 0.040 inch wide for one similar to Figure 13. The data has not yet been fully analyzed but the pressure gain for the first model varies between 5 and 15, depending on the operating conditions. The pressure gain for the second model is slightly less but the linear range appears to be greater.

One of the problems encountered in testing these small amplifiers was in measuring the static pressures in the interaction regions. Several pressure surveys taken in the large amplifier showed that this pressure is the same as the total pressure in the control ports, provided there are no leaks from one channel to another or to the atmosphere. See Figure 15.

Conclusions

The interaction data indicates that downstream geometry, except for raising the pressure level of the amplifier, does not affect the velocity and total pressure profiles upstream. Thus, the receivers can be positioned at the downstream edge of the control ports, eliminating the need for a crossover channel, reducing noise, increasing the linear range and making the amplifier easier to build.

Giving the receiver a bellmouth shape is advantageous in that it makes the flow fully-developed sooner. This helps to reduce losses and makes it possible to shorten the outlegs, thus, reducing the size. However, these tests show that gain is also sacrificed because the bellmouth shape has a large projected offset and yet the receivers are small. Moynihan (Reference 2) shows that there is an optimum receiver size and projected offset for maximum gain. In using the bellmouth shape, we can no longer keep these optimum sizes. If the offset size is optimum, the offset is too large. The pressure gain decreased from 17 to 13.3.

Two small amplifiers have been built, the first with geometry similar to that shown in Figure 7, and the second similar to that shown in Figure 13. The power and control ports are identical. The main difference is in the receiver geometry. Preliminary tests indicate that the amplifier with bellmouth-shaped receiver has poorer pressure gain but slightly better linear range. No noise data has been taken.

Acknowledgement

I wish to acknowledge Mr. Frederick Moynihan's help and advice throughout the conduct of this work. In addition, I wish to acknowledge Mrs. Albert Preston's help in editing the paper and preparing the figures.

References

1. Albertson, M. L., et al, "Diffusion of Submerged Jets", Paper 2409, Transaction of ASCE, Pg. 639-664.

2. Moynihan, F. A., "Fluid Amplifier Basic Studies, Receiver Design", MR8485, October 11, 1963.

3. Schlichting, Hermann, "Boundary Layer Theory", Pergamon Press, New York, 1955, Pg. 73.

4. Streeter, Victor L., "Fluid Dynamics", McGraw-Hill Book Company, New York, 1948, Pg. 96, 102.

Symbols

MR	Mass Ratio	$MR = \frac{\Sigma Q_c}{Q_p}$
P	Static Pressure	
P^o	Total Pressure	
$\overline{P}$	Average Pressure	
Q	Mass Flow (equivalent volume flow at standard conditions)	
s	Control Port Switch	
V	Velocity	
W	Port Width	
x	Distance downstream from the power nozzle exit	
y	Distance from the centerline of the power nozzle	
θ	Deflection angle of the power jet	
ρ	Mass Density	

Subscripts

c	Control Stream
p	Power Stream
1, 2	Denotes particular control or outlet

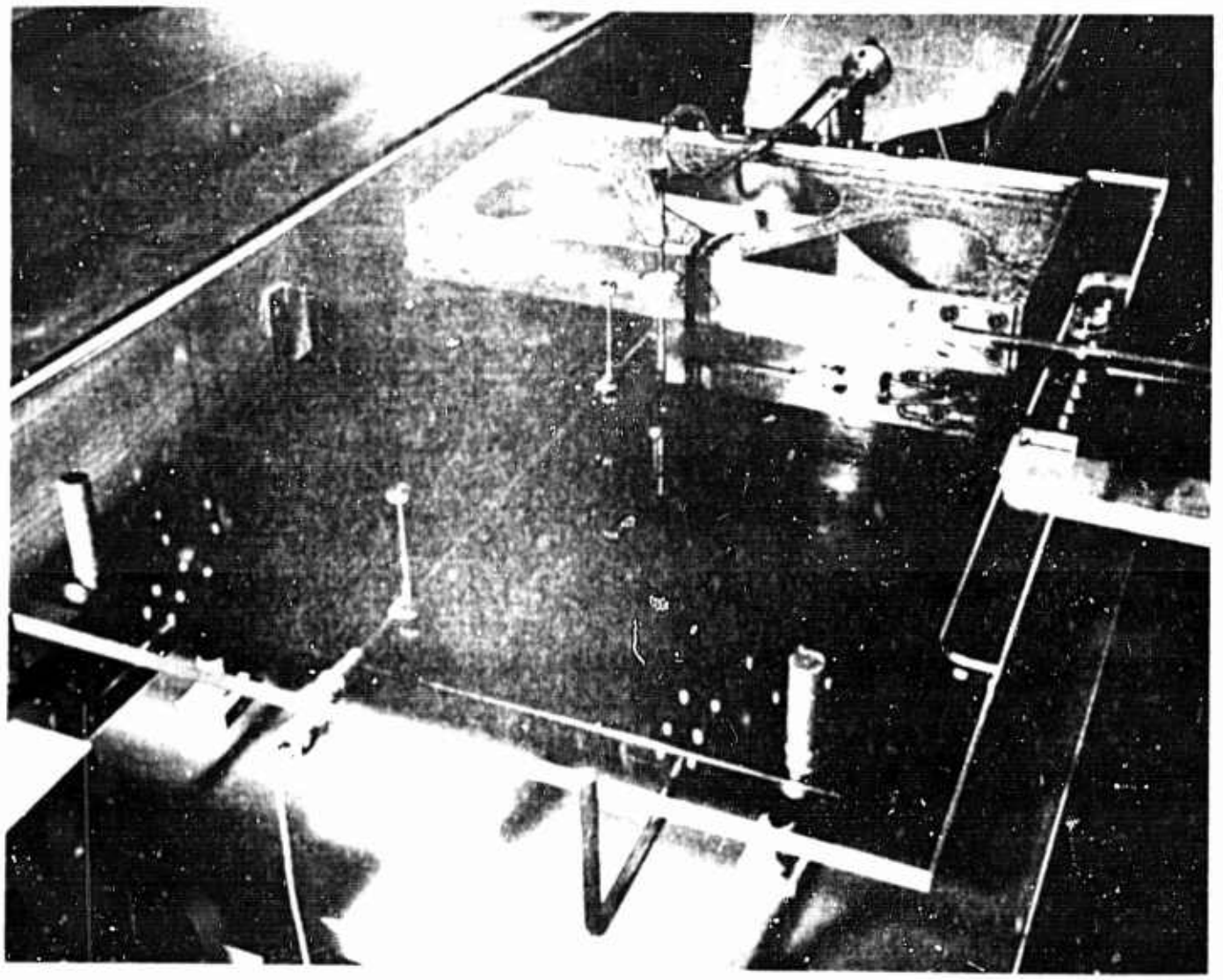

Figure 1. Jet Interaction Experimental Apparatus

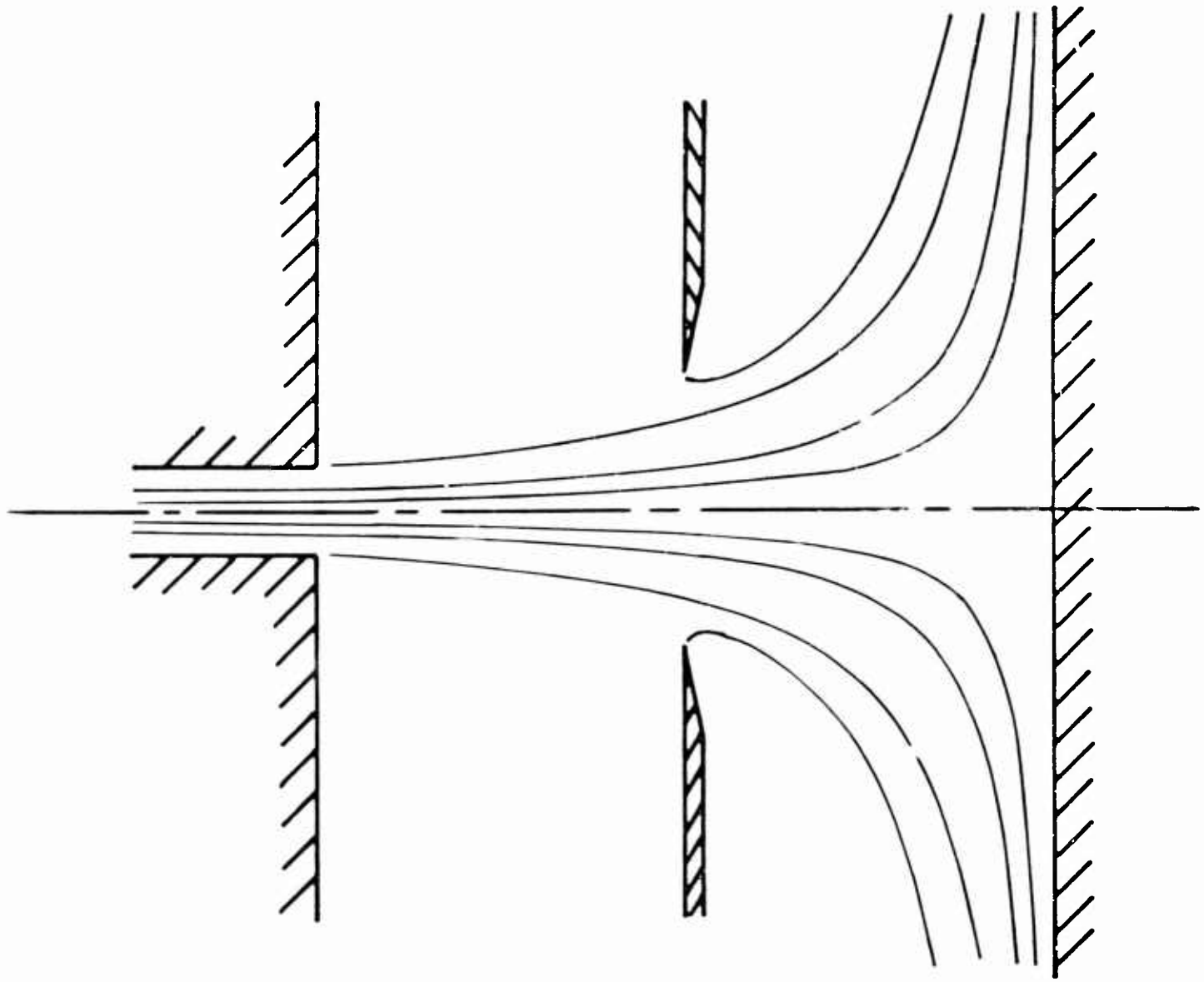

Figure 2. Flow from Jet Interaction Apparatus with Barrier in Place at $X/W_c = 8.0$

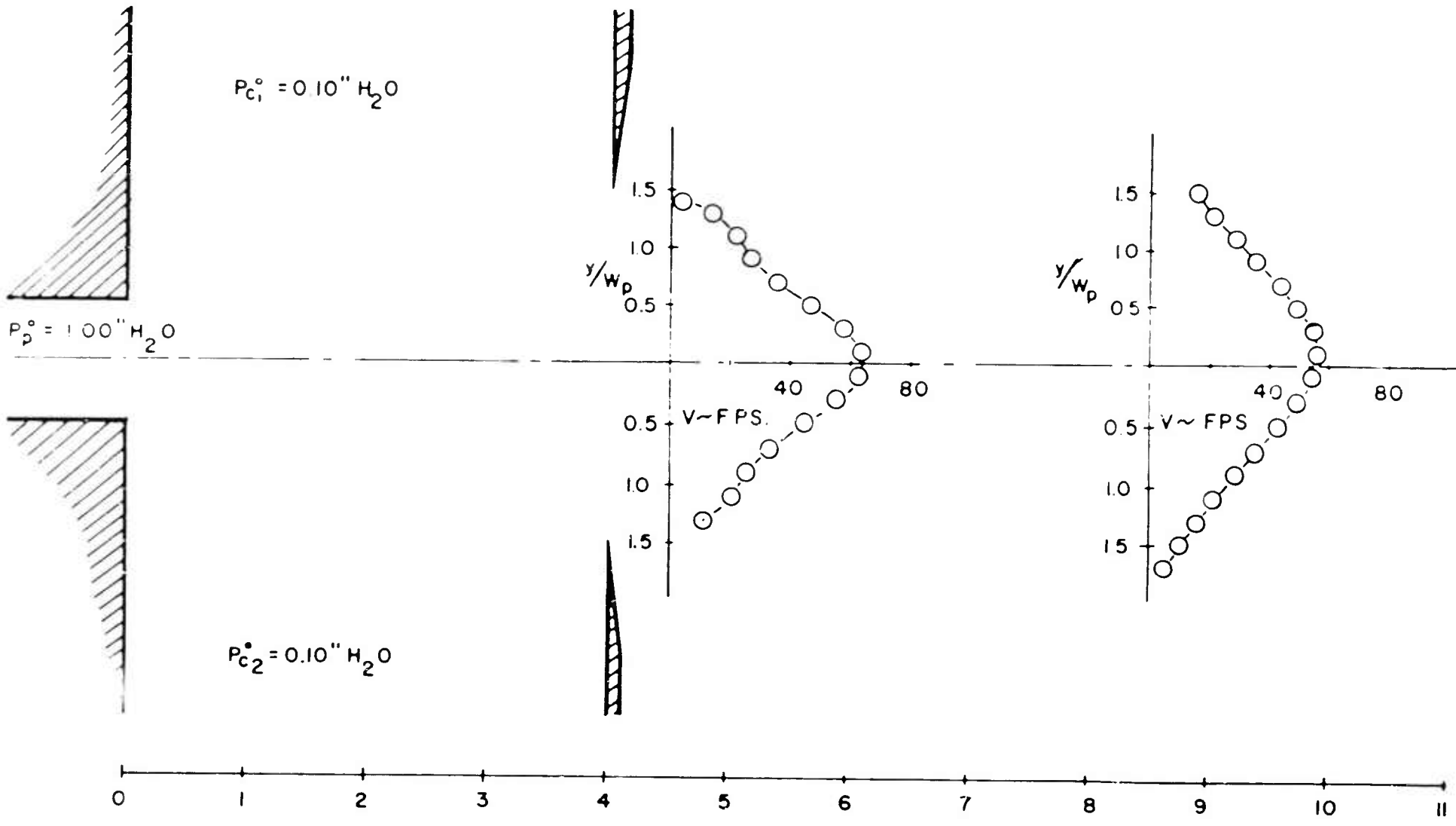

Figure 3. Velocity Profiles at x/W_p = 4.5, 8.5. W_c/W_p = 4.0, s/W_c = 0.25, $\bar{P}_c^{\circ}/P_p^{\circ}$ = 0.10, ΔP_c° = 0.00, Aspect Ratio = 6.0, Mass Ratio = 0.20

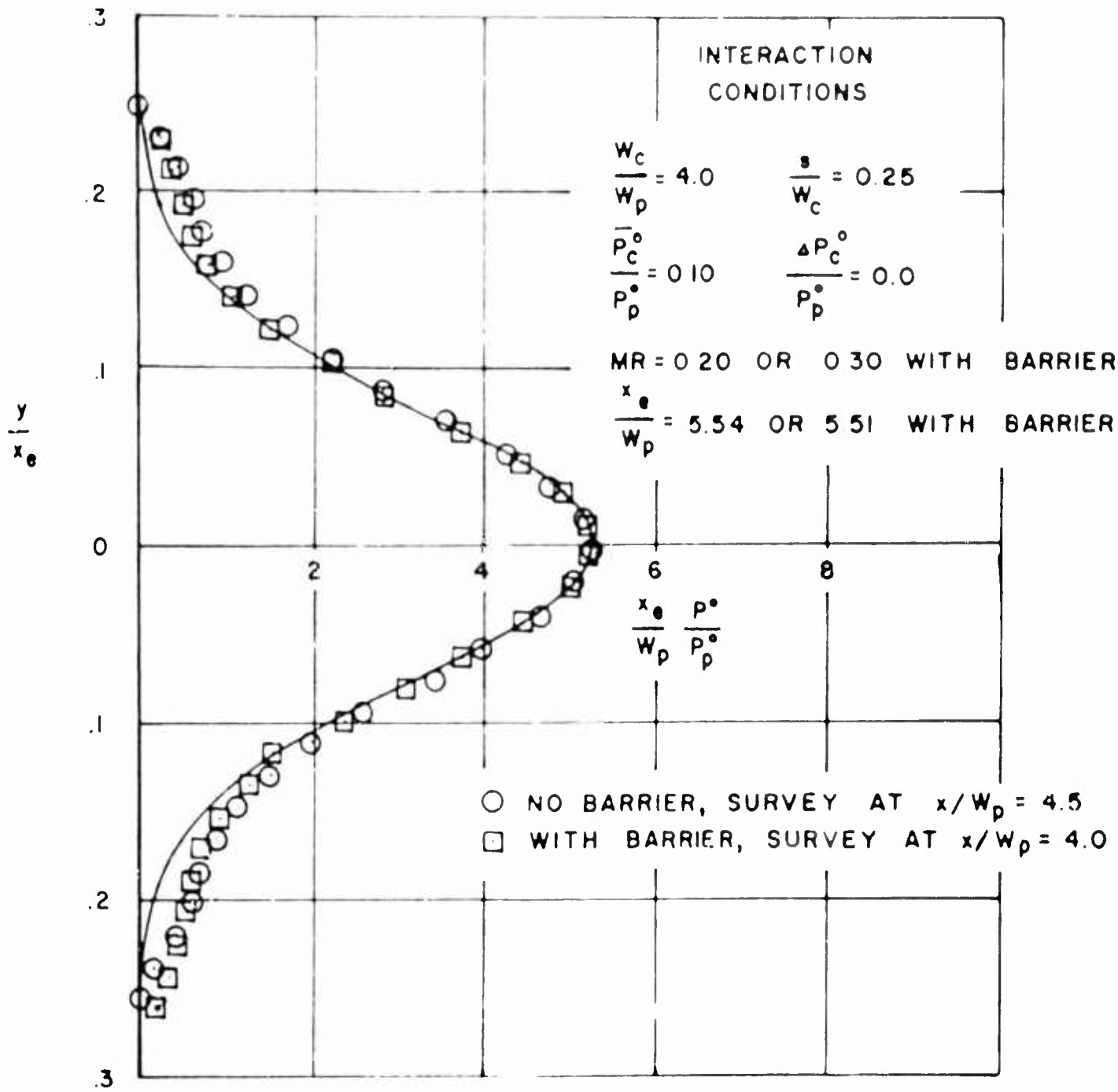

Figure 4. Comparison of Interaction with Theoretical Free Jet Total Pressure Profile, with and without a Barrier

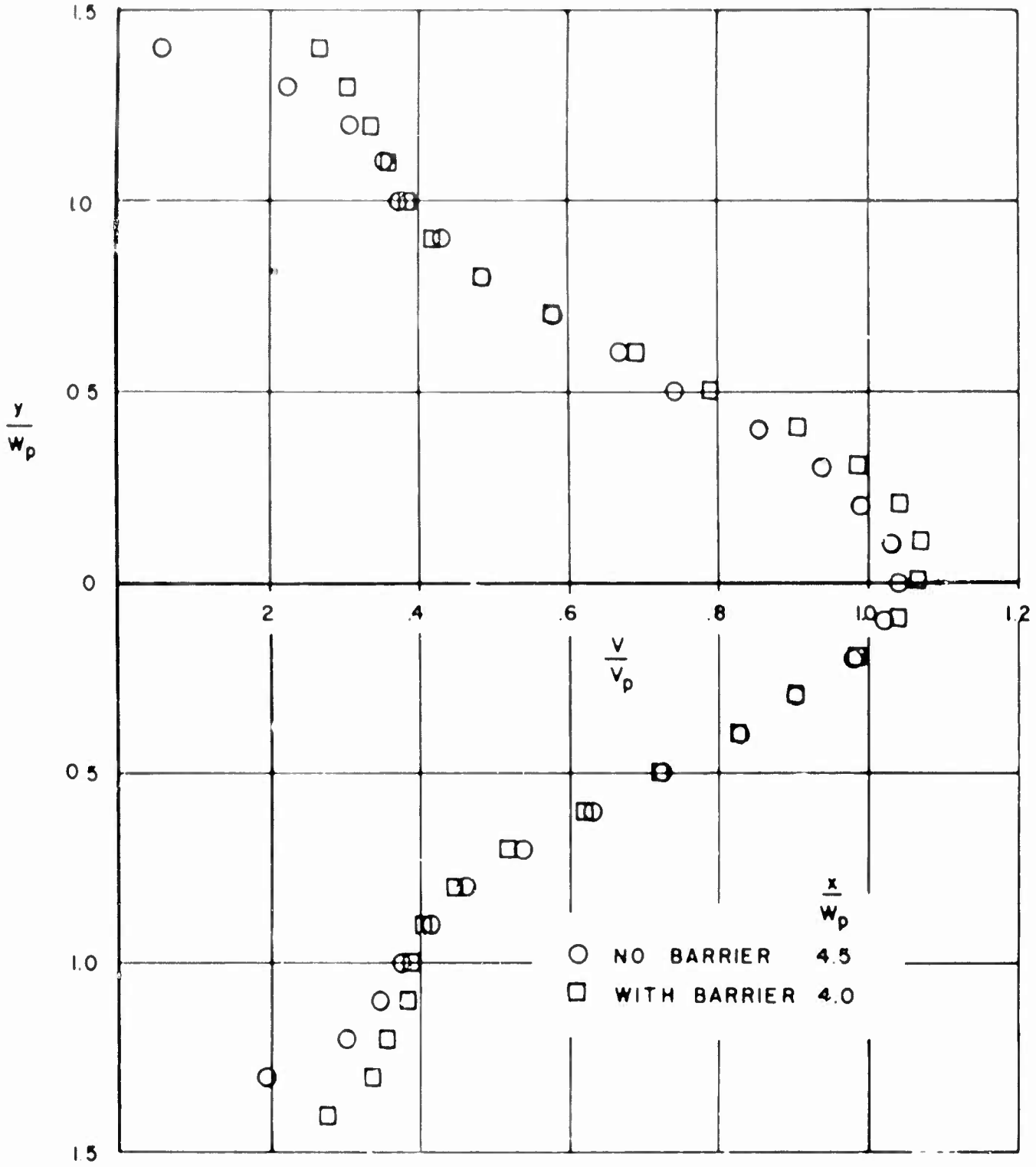

Figure 5. Effect of Barrier at $x/W_p = 8.0$ on Velocity Profile at $x/W_p = 4.0$

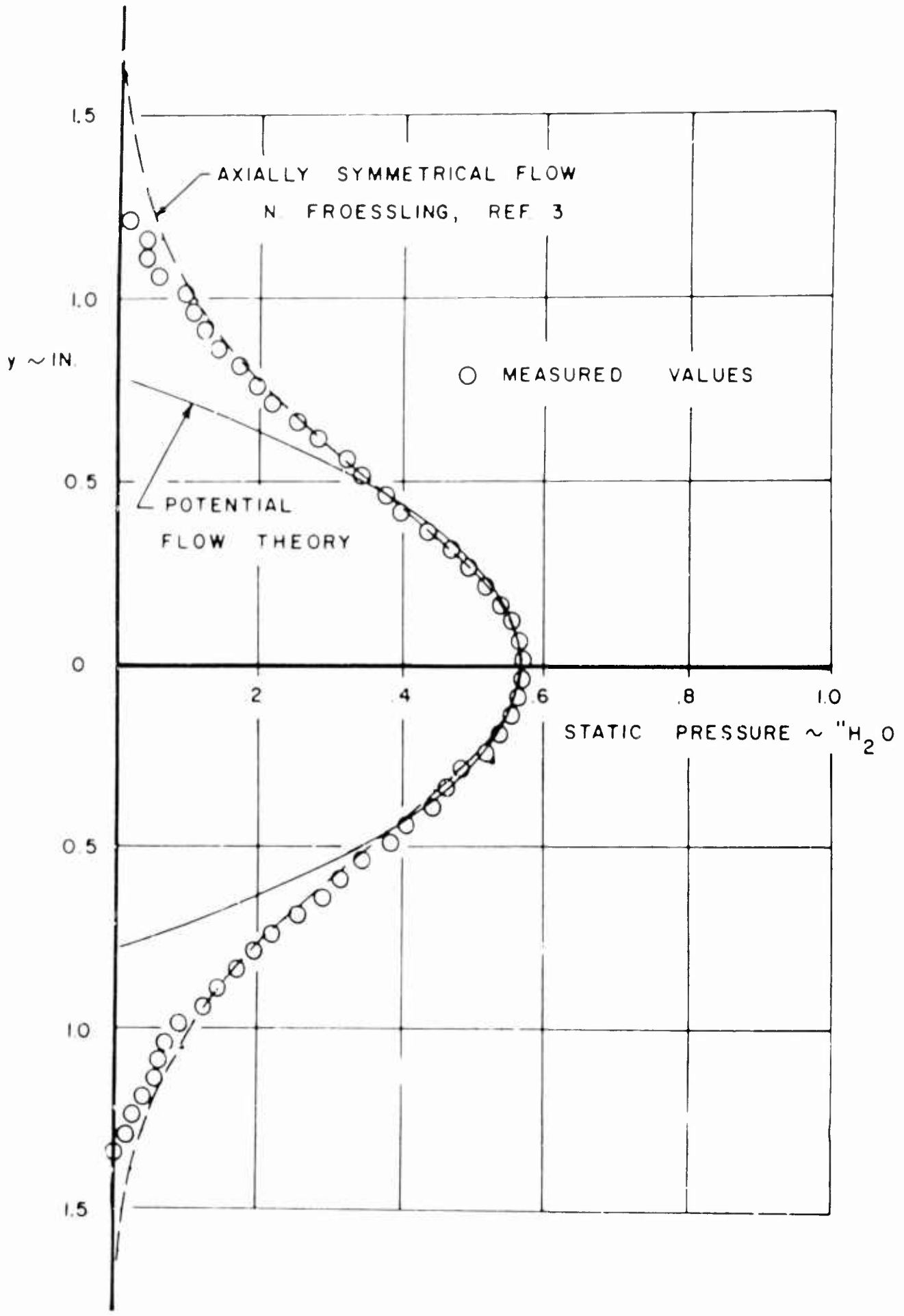

Figure 6. Static Pressure Distribution Along a Barrier

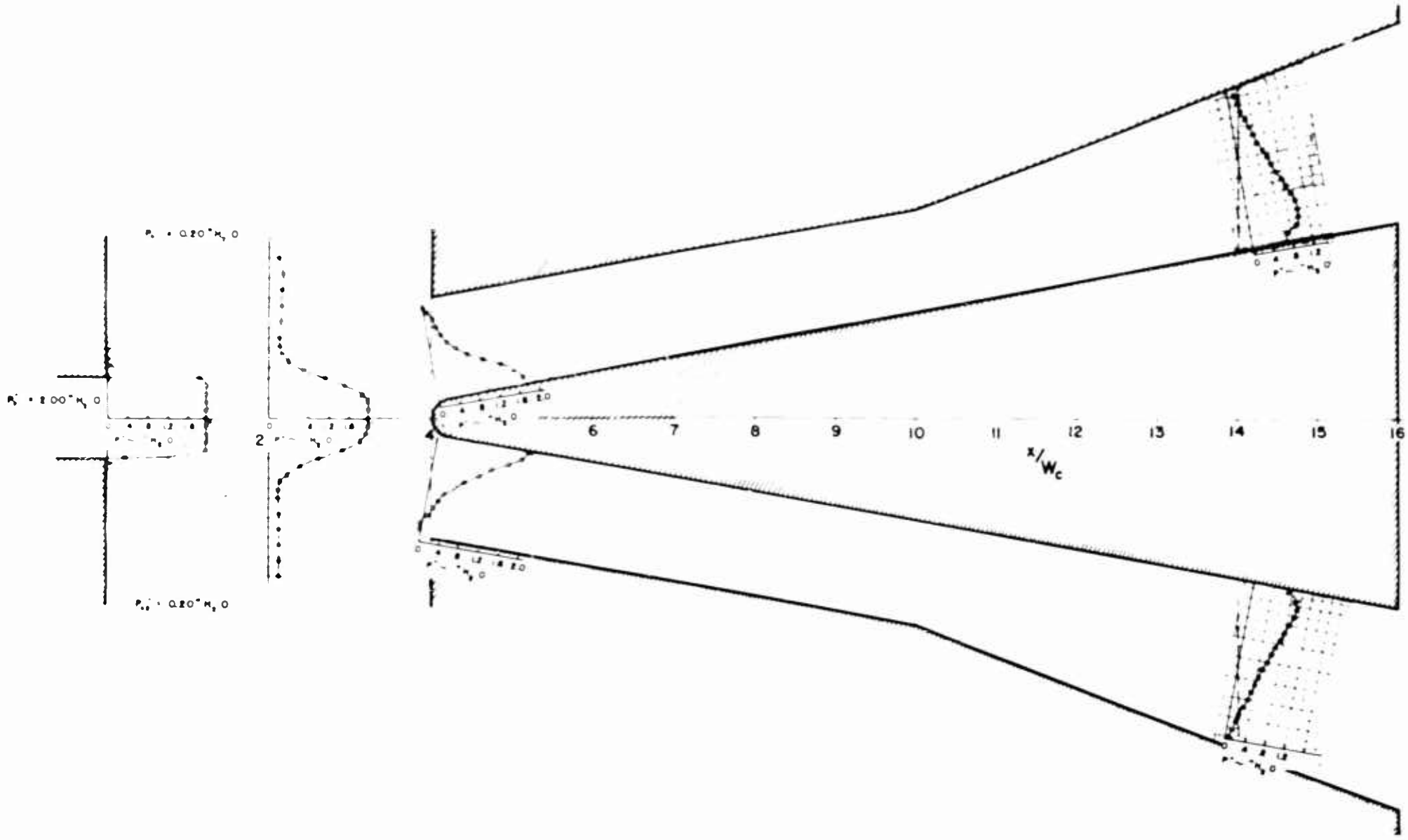

Figure 7. Total Pressure Distribution at Various Stations in a Proportional Amplifier

$\frac{W_c}{W_p} = 4.0 \quad \frac{s}{W_c} = 0.25 \quad A.R. = 6.0 \quad \frac{\bar{P}_c}{P_p} = 0.10 \quad \frac{\Delta P^o_c}{P^o_p} = 0.0$

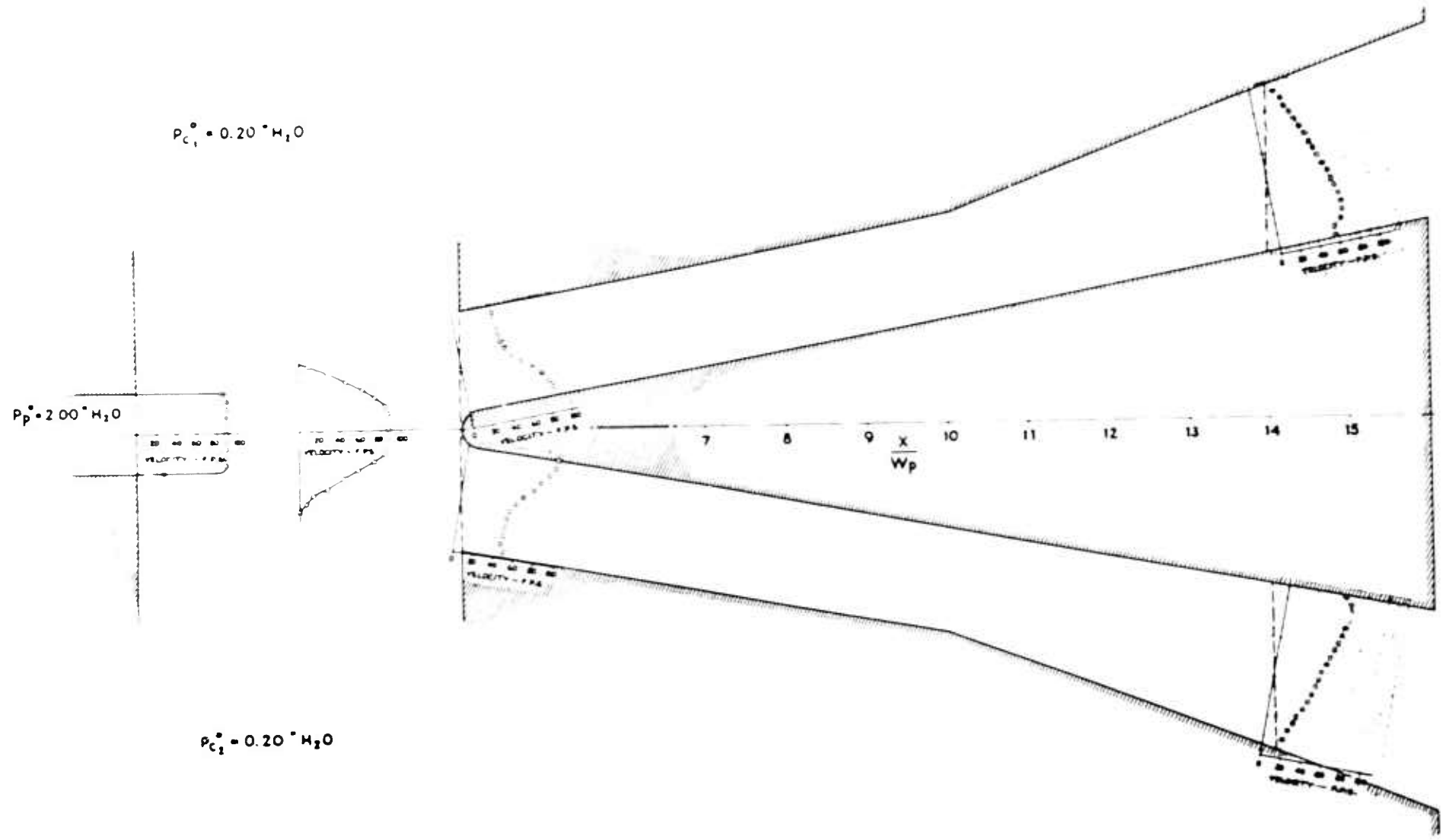

Figure 8. Velocity Distribution at Various Stations in a Proportional Fluid Amplifier

$\frac{W_c}{W_p} = 4.0$ $\frac{S}{W_c} = 0.25$ A.R. = 6.0 $\frac{\bar{P}_c^{\circ}}{P_p^{\circ}} = 0.10$ $\frac{\Delta P_c^{\circ}}{P_p^{\circ}} = 0.0$

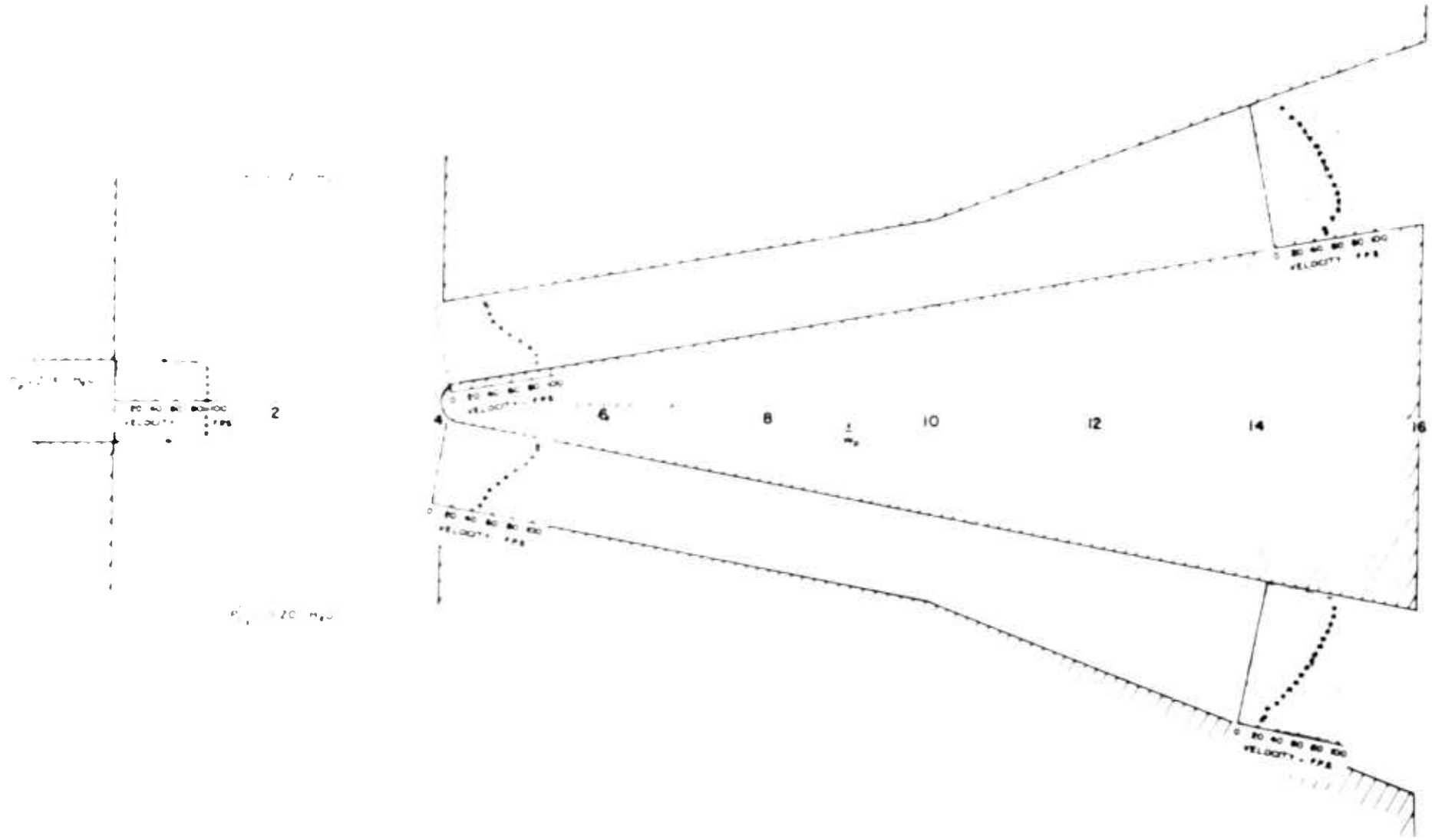

Figure 9. Velocity Distribution at Various Stations in a Proportional Fluid Amplifier

$$\frac{W_c}{W_p} = 4.0 \quad \frac{S}{W_c} = 0.188 \quad A.R. = 6.0 \quad \frac{P^\circ_c}{P^\circ_p} = 0.10 \quad \frac{\Delta P^\circ_c}{P^\circ_p} = 0.0$$

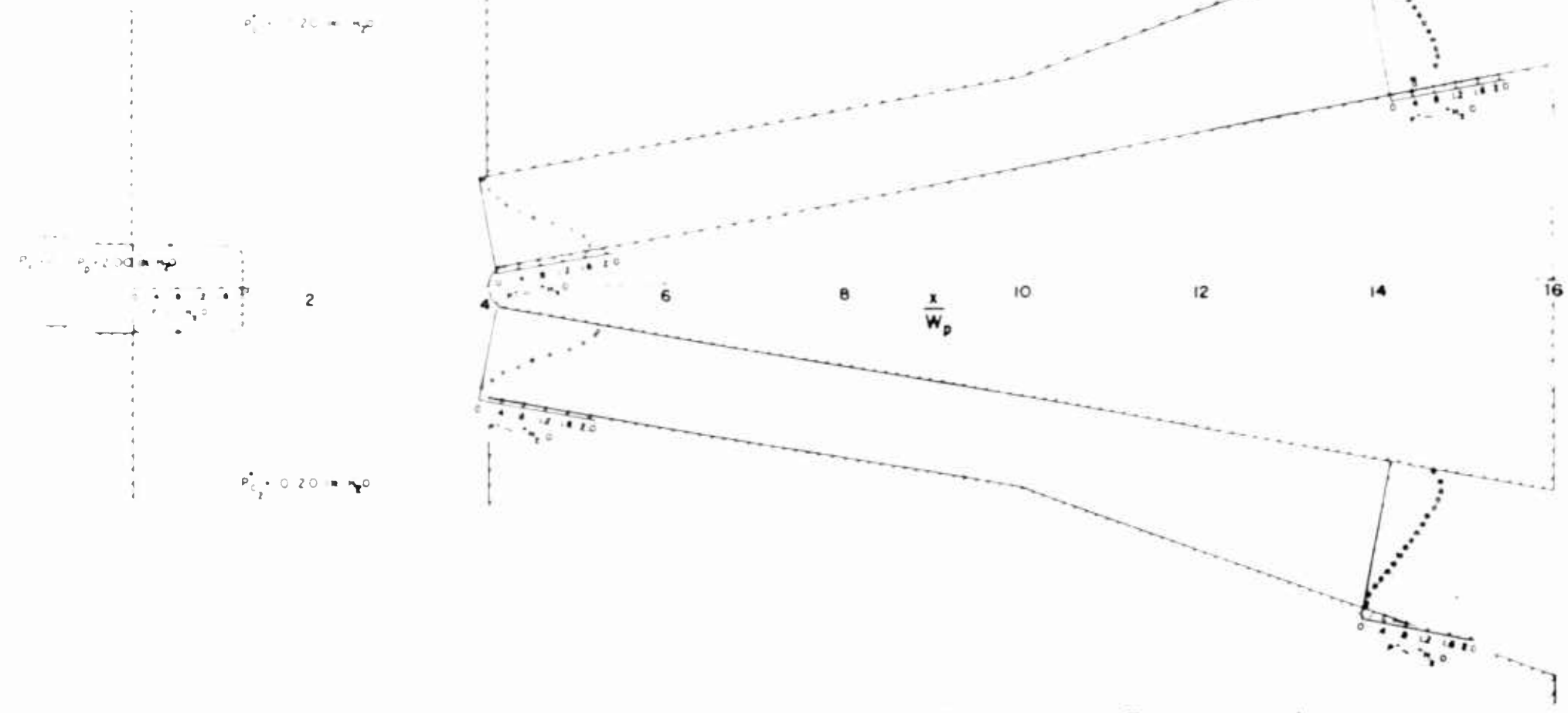

Figure 10. Total Pressure Distribution at Various Stations in a Proportional Fluid Amplifier

$$\frac{W_c}{W_p} = 4.0 \qquad \frac{S}{W_c} = 0.188 \qquad A.R. = 6.0 \qquad \frac{\bar{P}^\circ_c}{P^\circ_p} = 0.10 \qquad \frac{P^\circ_c}{P^\circ_p} = 0.0$$

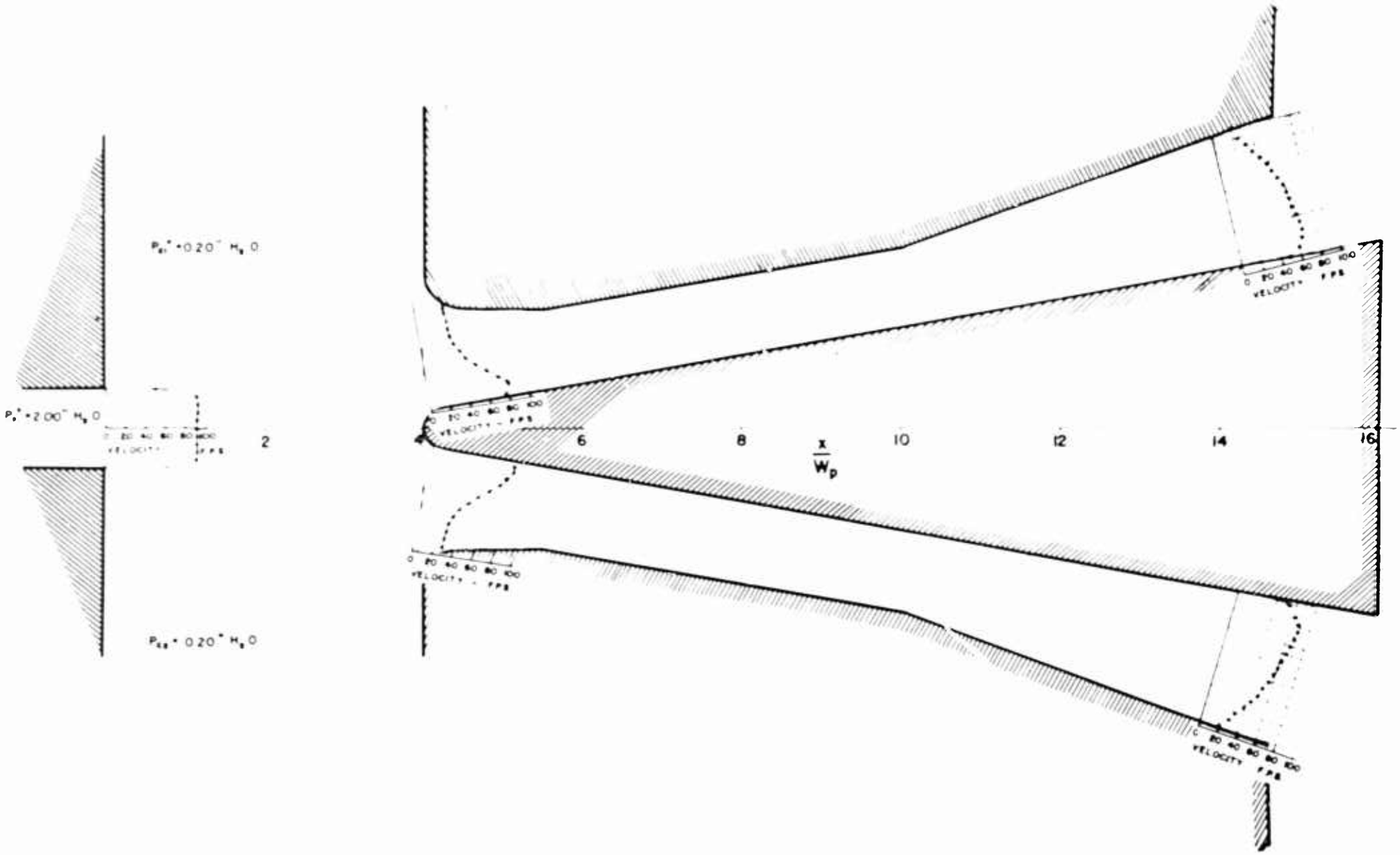

Figure 11. Velocity Distribution at Various Stations in a Fluid Proportional Amplifier

$$\frac{W_c}{W_p} = 4.0 \quad \frac{s}{W_c} = 0.25 \quad A.R. = 6.0 \quad \frac{P^\circ_c}{P^\circ_p} = 0.10 \quad \frac{\Delta P^\circ_c}{P^\circ_p} = 0.0$$

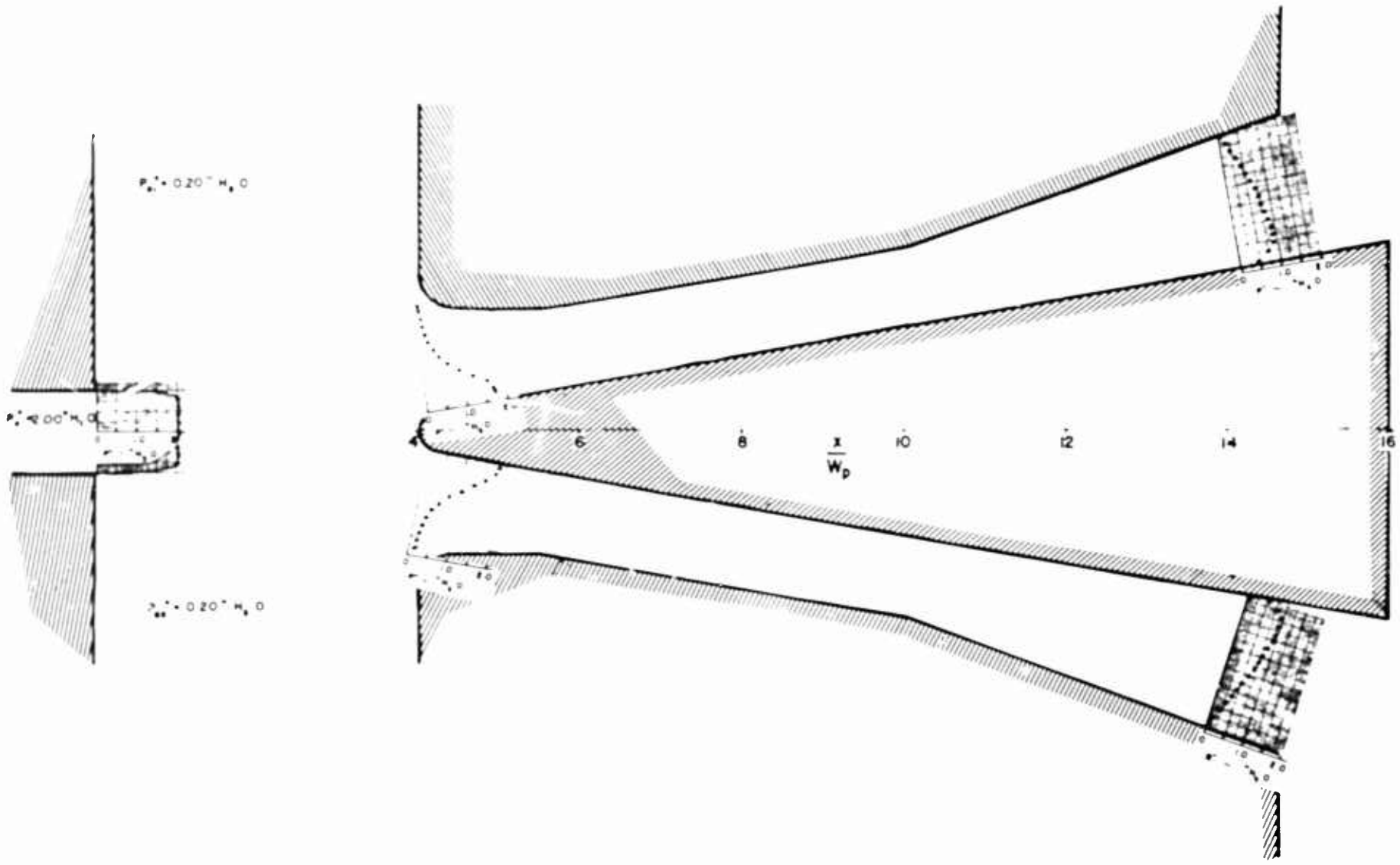

Figure 12. Total Pressure Distribution at Various Stations in a Proportional Fluid Amplifier

$$\frac{W_c}{W_p} = 4.0 \quad \frac{s}{W_c} = 0.25 \quad A.R. = 6.0 \quad \frac{\bar{P}^\circ_c}{P^\circ_p} = 0.10 \quad \frac{\Delta P^\circ_c}{P^\circ_p} = 0.0$$

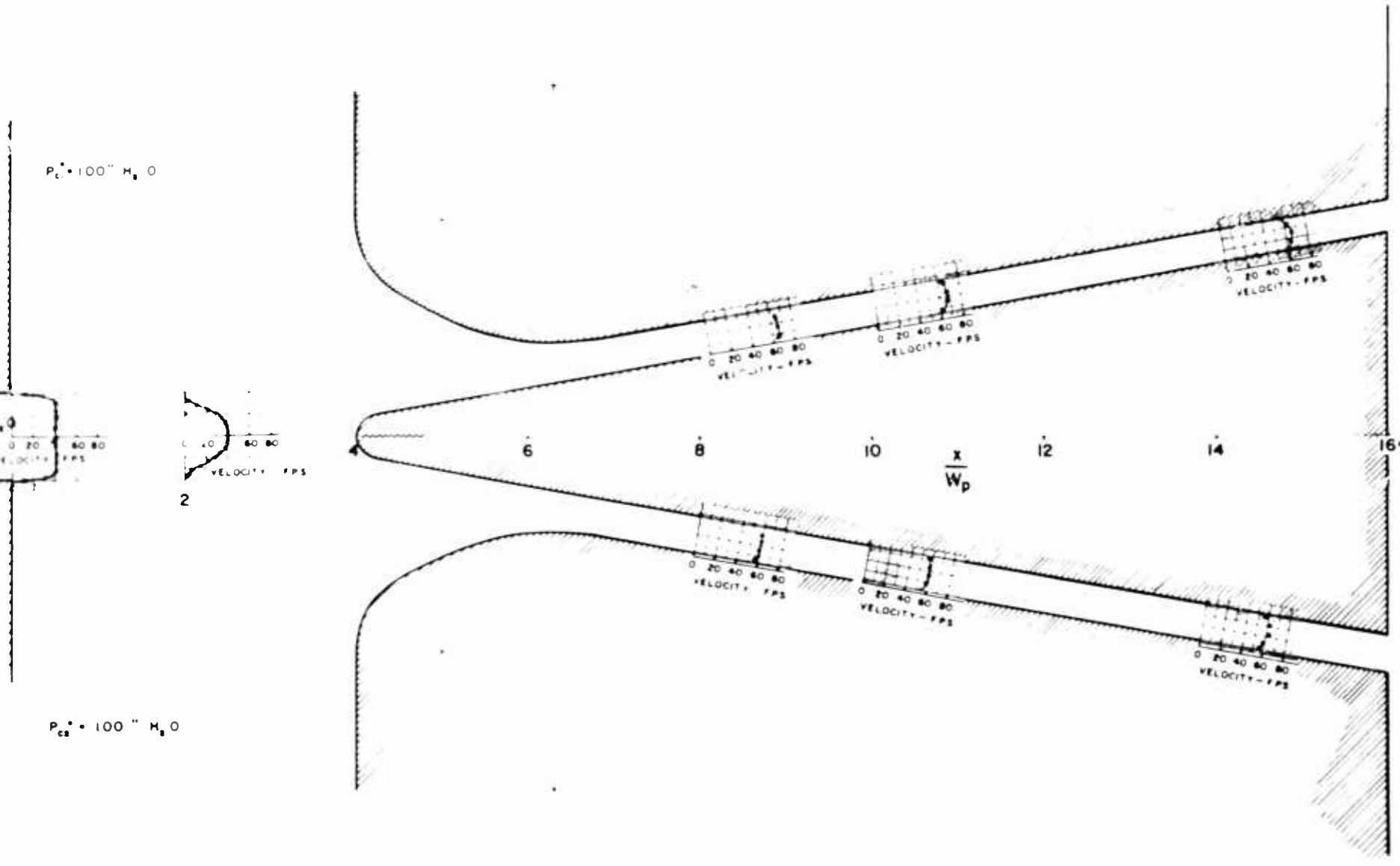

Figure 13. Velocity Distribution at Various Stations in a Proportional Fluid Amplifier

$\frac{W_c}{W_p}$ = 4.0 $\frac{s}{W_c}$ = A.R. 6.0 $\frac{P^\circ_c}{P^\circ_p}$ = 0.71 $\frac{\Delta P^\circ}{P^\circ_p}$ =

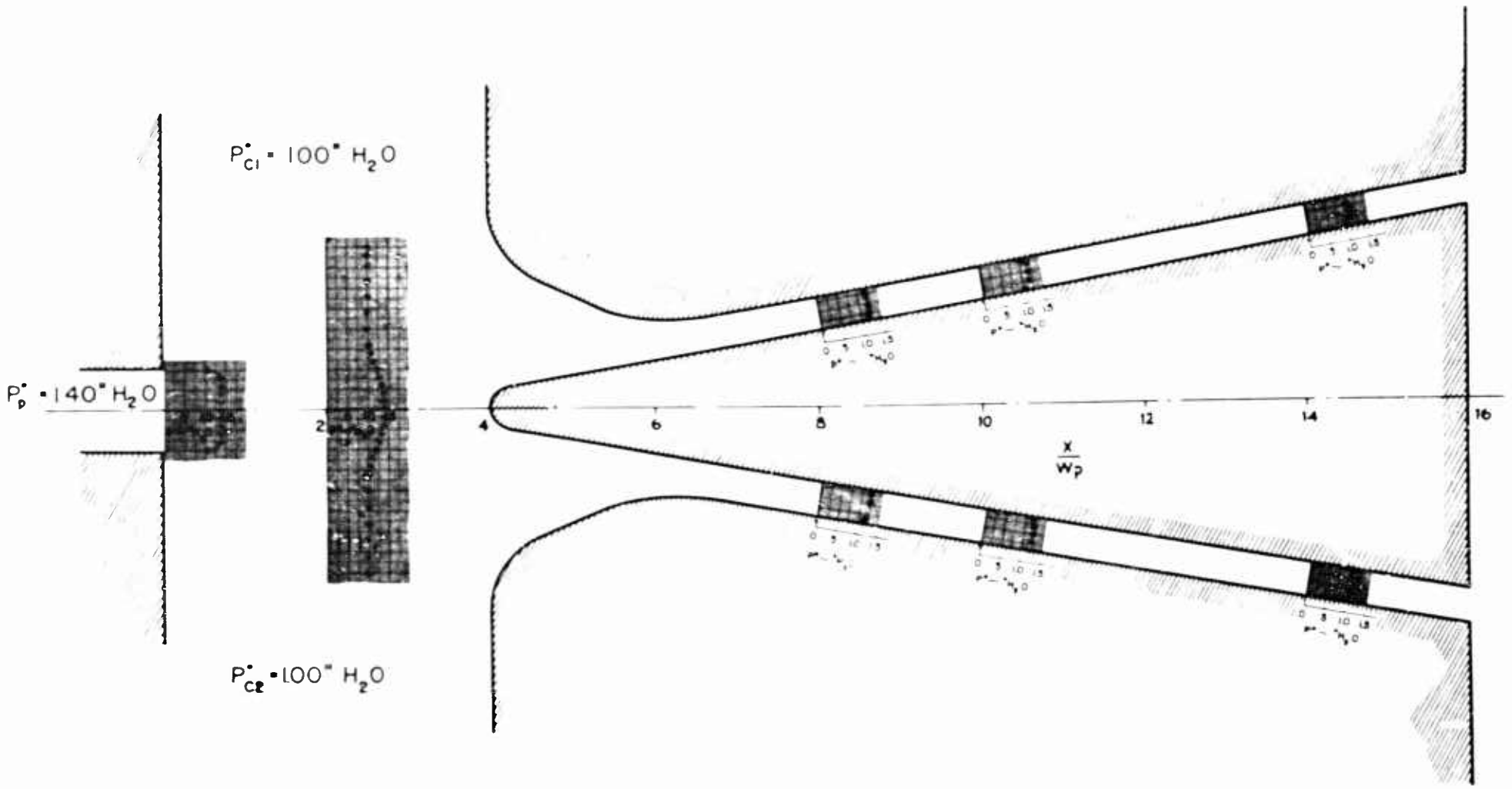

Figure 14. Total Pressure Distribution at Various Stations in a Proportional Fluid Amplifier

$\frac{W_c}{W_p} = 4.0$ $\frac{S}{W_c} =$ A.R. $= 6.0$ $\frac{\bar{P}^{\circ}}{P_p^{\circ}} = 0.71$ $\frac{\Delta P_c^{\circ}}{P_p^{\circ}} = 0.0$

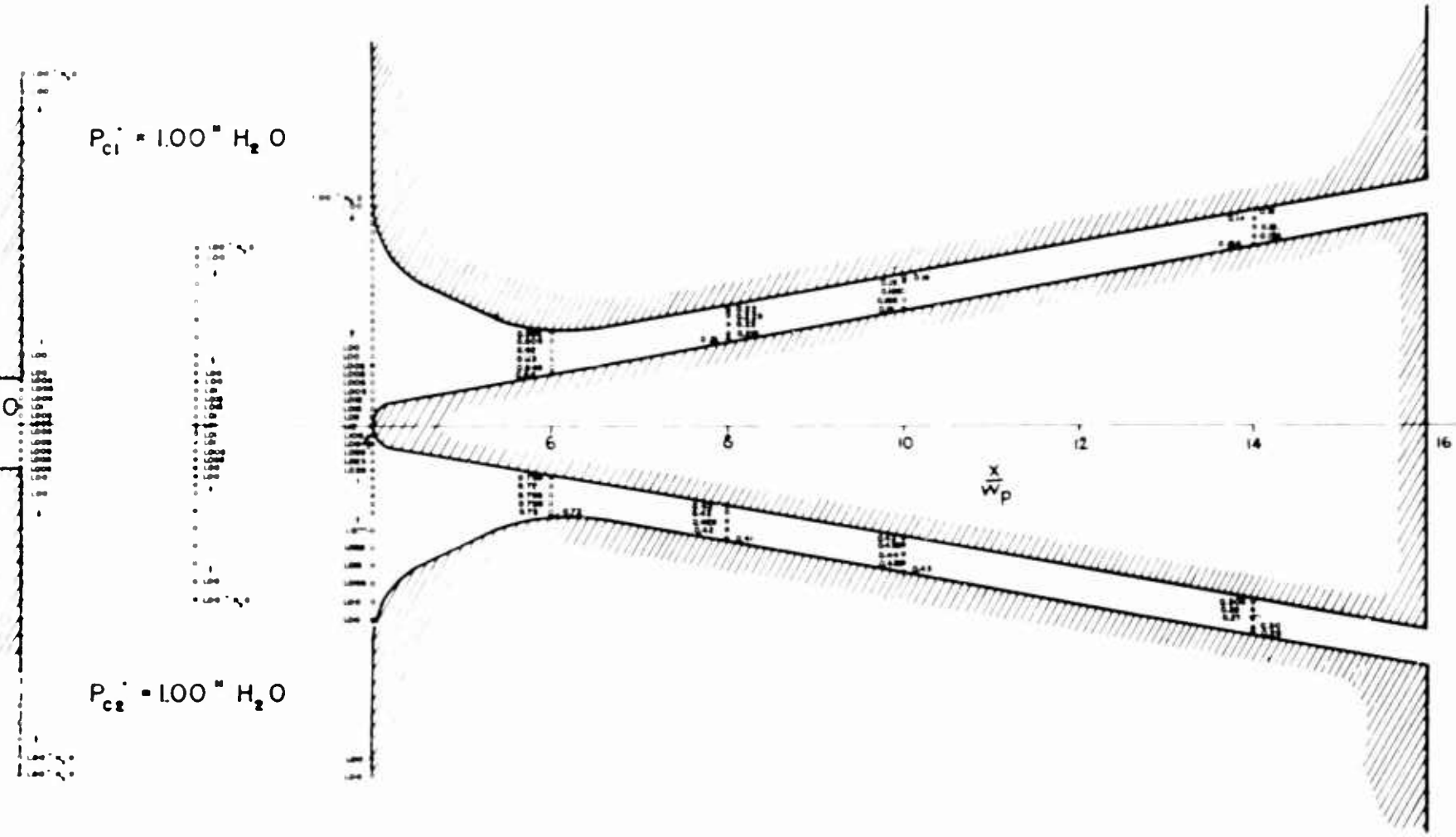

Figure 15. Static Pressure Distribution at Various Stations in a Proportional Fluid Amplifier

$$\frac{W_c}{W_p} = 4.0 \qquad A.R. = 6.0 \qquad \frac{\bar{P}^\circ}{P^\circ_p} = 0.71 \qquad \frac{\Delta P^\circ_c}{P^\circ_p} = 0.0$$

STEADY AND TRANSIENT BEHAVIOR OF A BISTABLE AMPLIFIER WITH A LATCHING VORTEX*

by

Turgut Sarpkaya
University of Nebraska

Reported herein is an investigation of the steady and transient behavior of an unvented, cusped, bistable amplifier. Experiments were conducted with air and water as the working fluids. The evolution of the latching vortex and the variation of pressure at about 15 critical points in the interaction region were studied for two types of switching: (a) by restricting the on-side load port, and (b) by applying a signal to the on-side control port. Each type of switching was investigated under quasi-steady and transient conditions. The pressure perturbations in the interaction region, evolution of pressure in the attachment bubble, formation of vortices at the two sides of the cusp, the differences between the transient and quasi-state switching, and the propagation of shock waves are discussed with the help of normalized curves and motion pictures.

INTRODUCTION

The primary objectives of this investigation are the understanding of the mechanism of switching of a cusped bistable amplifier, exploration of the pressure and flow fields, and the formulation of analytical techniques which will allow the prediction of the steady and transient behavior of the amplifier in terms of its relevant parameters. The experimental data and visual observations constitute the backbone of the first part of the investigation, for it is the characteristics of the amplifier that permit the design of a working model and the understanding of the internal mechanism of the fluid motion.

In addition, this investigation is concerned with several other areas of interest which are related to or come as by-products of the main investigation described above. These include design optimization,

---

*The financial support of the Harry Diamond Laboratories, U. S. Army Materiel Command is gratefully acknowledged.

generalization of results to vented amplifiers, scaling effects, and prediction and control of pressure perturbations.

DESCRIPTION OF THE AMPLIFIER

The geometrical characteristics of the amplifier chosen for the investigation are shown in Fig. 1*. It has evolved at the end of extensive qualitative and semi-quantitative studies with the use of a water table. No vents were provided and no special attempt was made to prevent the spillover of flow from one load port to the other. It should, however, be noted that the data obtained with the present model disclosed characteristics which made possible the design of a vented and an unvented amplifier whose performances appear to be quite satisfactory. It should further be noted that the conclusions presented herein concerning the mechanism of fluid motion are dependent upon the general form of the amplifier rather than on its specific dimensions.

The location of static pressure taps are also shown in Fig. 1. Each pressure tap was connected to a Sanborn-2678 differential-pressure transducer and the pressures were recorded simultaneously on a multi-channel recorder.

Pictures were taken with a modified high-speed motion picture camera using the flow visualization technique described elsewhere+.

PERFORMANCE TESTS

Closed Controls - Active Port Loading

The test set-up used for the experiments in the closed control mode is shown in Fig. 2. Once the particular supply pressure was set, the

---

*This amplifier was used only for the tests with water. The one used with air was geometrically similar to and one half the size of the water model.

+T. Sarpkaya and C. J. Garrison, "Vortex Formation and Resistance in Unsteady Flow," Trans. ASME, Jour. Appl. Mechs., Vol. 30, ser. E, No. 1, March, 1963, pp: 16-24.

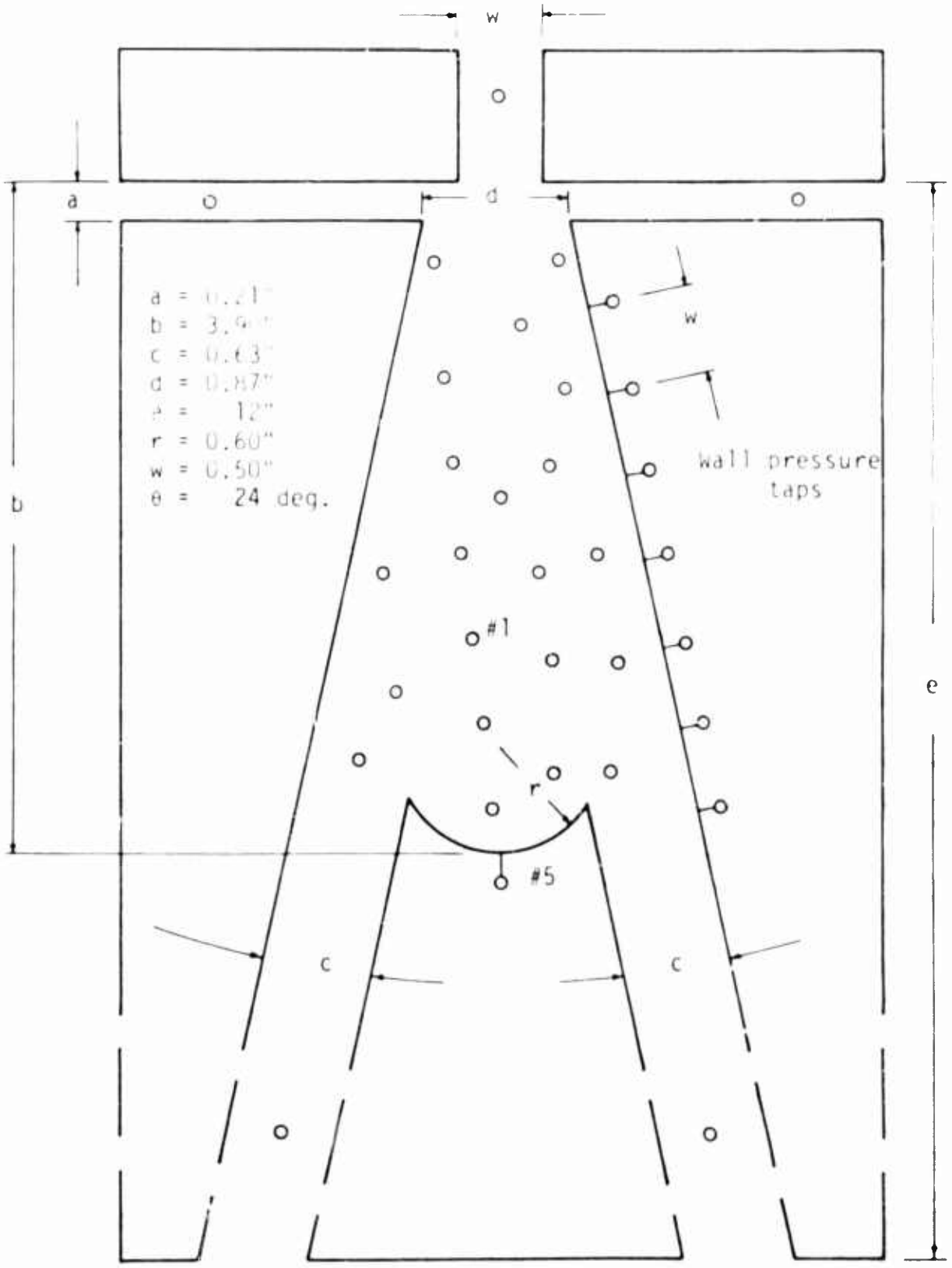

Fig.1 Cusped Bistable Amplifier

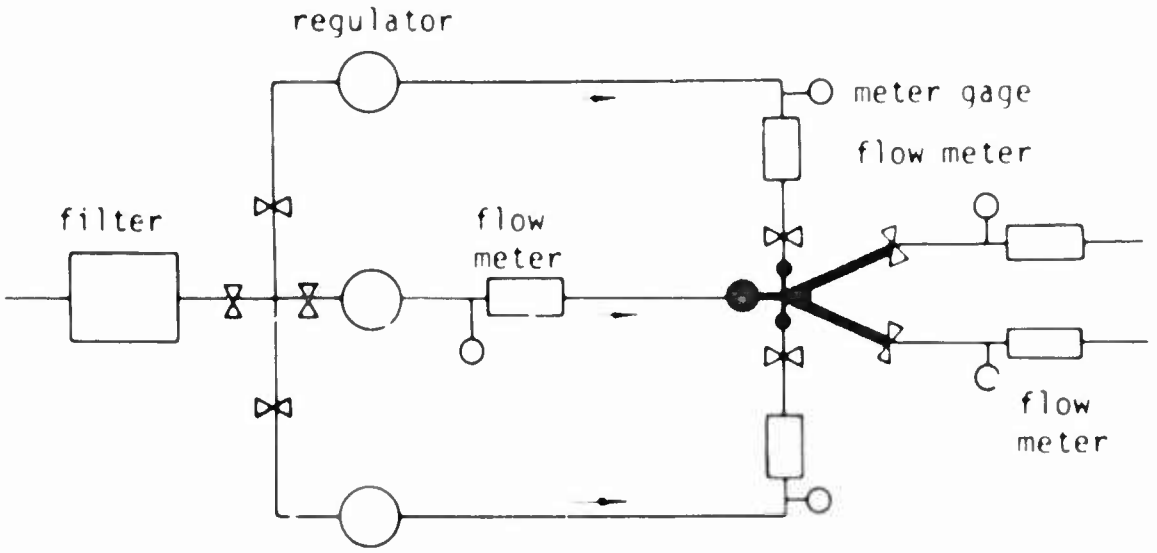

Fig. 2 Schematic Diagram of the Test Circuit

test procedure was first to adjust the load restrictor valve to the desired value. Then the flow rates and the pressures at the points noted were recorded. Once the measurements were completed, the load restrictor valve was re-set to a new value. Data points were taken with the load restrictor valve at settings ranging from wide-open to nearly shut. It is clear that as far as the flow and pressure recovery characteristics are concerned the most unfavorable condition corresponds to the wide-open setting of the valve at the off-side load port. However, to avoid any ambiguity in the interpretation of the results it must be noted that during each test the setting of the off-side load-port valve was varied within wide limits*, and it was found that the two load ports are quite effectively decoupled.

The results are shown in Fig. 3 in terms of pressure and flow recovery factors. It is evident that for two different fluids and a wide range of velocities the load pressure recovery remained at about 80 per cent for flow recovery factors below 50 per cent and gradually decreased for higher output flows. The maximum flow recovery varied from 90 per cent down to 80 per cent as the supply pressure was increased within the limits used in the tests. The power recovery factor is

---

*The state of critical closure (nearly shut-off) at which the jet will switch from one side to another must be excluded. As long as the setting of the valve is above the critical-setting, the active and passive ports are effectually decoupled. Had vents been used this restriction could have been easily removed.

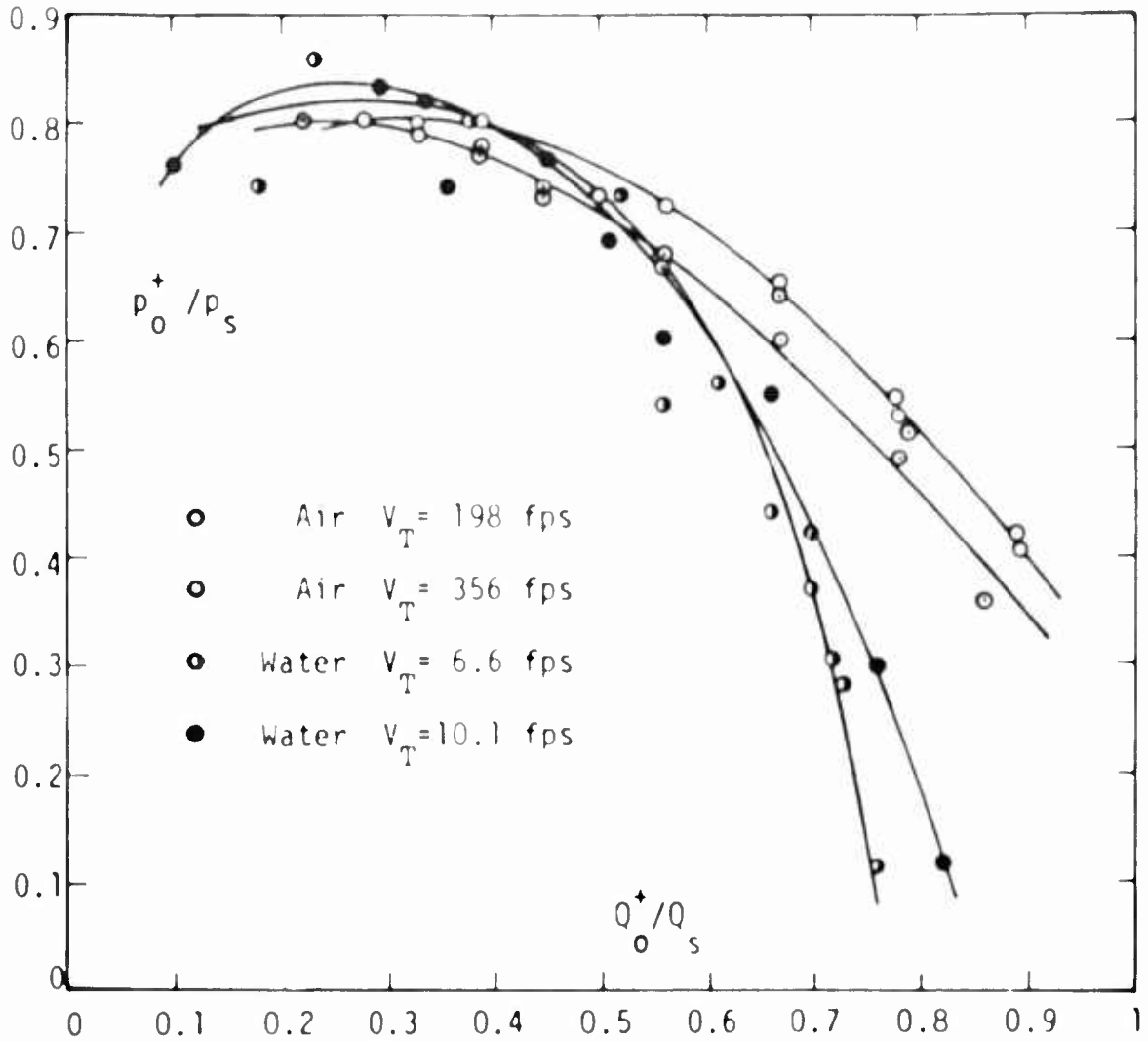

Fig. 3 Normalized Pressure and Flow Characteristics

shown in Fig. 4 as a function of p_o^+/p_s. The peak efficiency is about 42 per cent and occurs at $p_o^+/p_s = 0.60$.

Other related steady-state characteristics of the amplifier concern the differential pressures at the control and load ports and the pressure distributions in the interaction and wall attachment regions. Figure 5 shows the normalized differential pressure between the two control ports as a function of Q_o^+/Q_s. The relationship between these two parameters appears to be almost linear, $\Delta p_c^+/p_s$ varying from 0.20 at the highest active port flow rate to 0.10 near the point of switching.

Figure 6 shows the normalized differential pressure between the two load ports as a function of the normalized differential control port pressures. When the load restrictor valve is wide-open, the differential

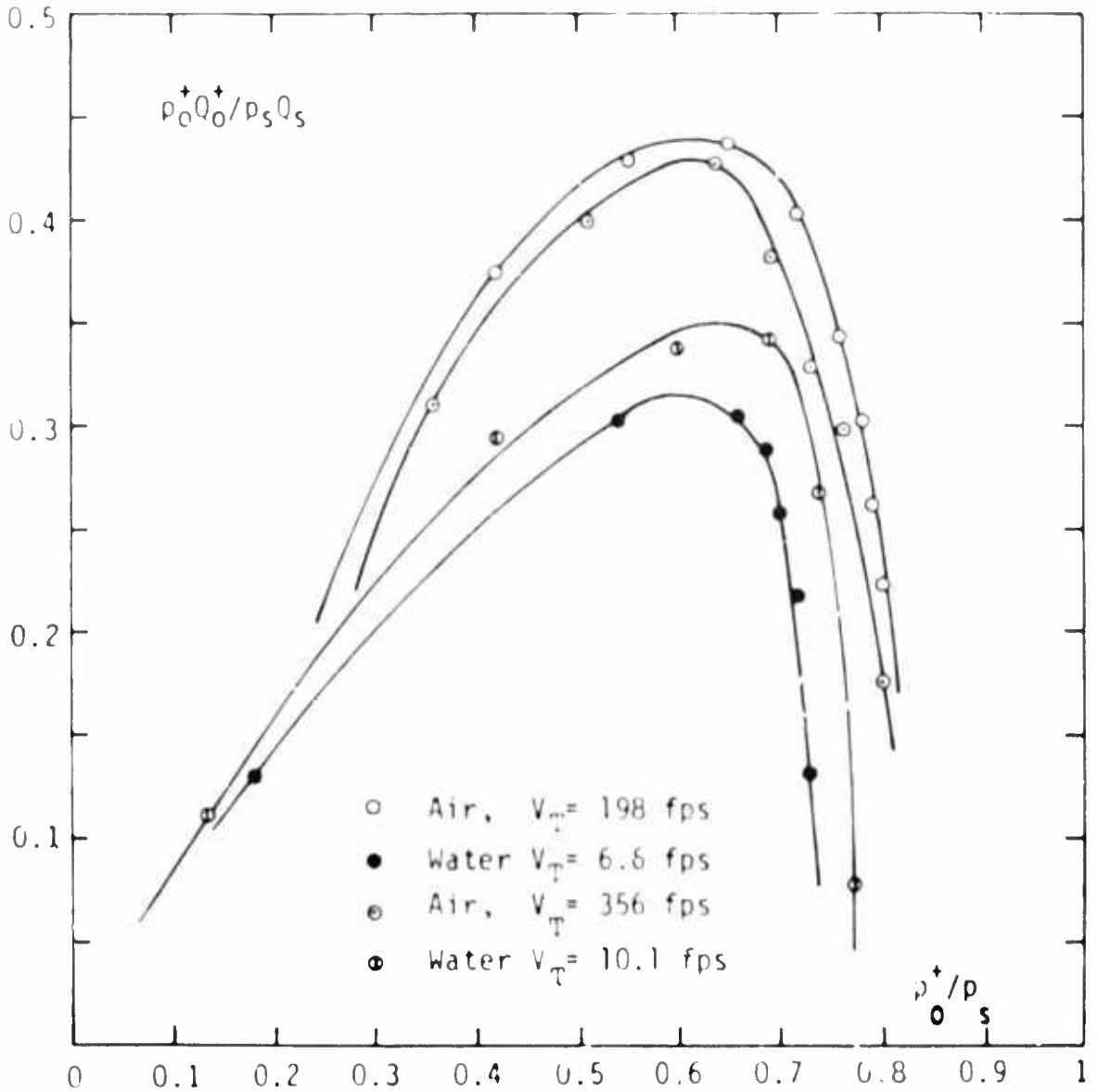

Fig. 4 Normalized Power and Pressure Characteristics

load pressure is naturally quite small. As the amplifier is loaded the differential pressure increases rapidly to about 0.60.

The characteristics of the interaction region cannot be fully evaluated without considering the associated pressure field. It is not, on the other hand, practicable to present the variation of pressure at every point shown in Fig. 1. For this reason only two points (No. 1 and No. 5) are selected for the present discussion. Figure 7 shows the variation of the corresponding normalized pressures as a function of Q_o^+/Q_s. The pressure in front of the cusp (point No. 5) increases with increasing load at the active port and, during the period of switching, almost reaches the stagnation pressure; i.e. $p_5 \approx p_s$. For a similar amplifier but with wider receiving ports the rate of rise of pressure at the cusp with Q_o^+/Q_s would be somewhat smaller until the time of switching and quite rapid thereafter. The pressure at point No. 1 shows a similar

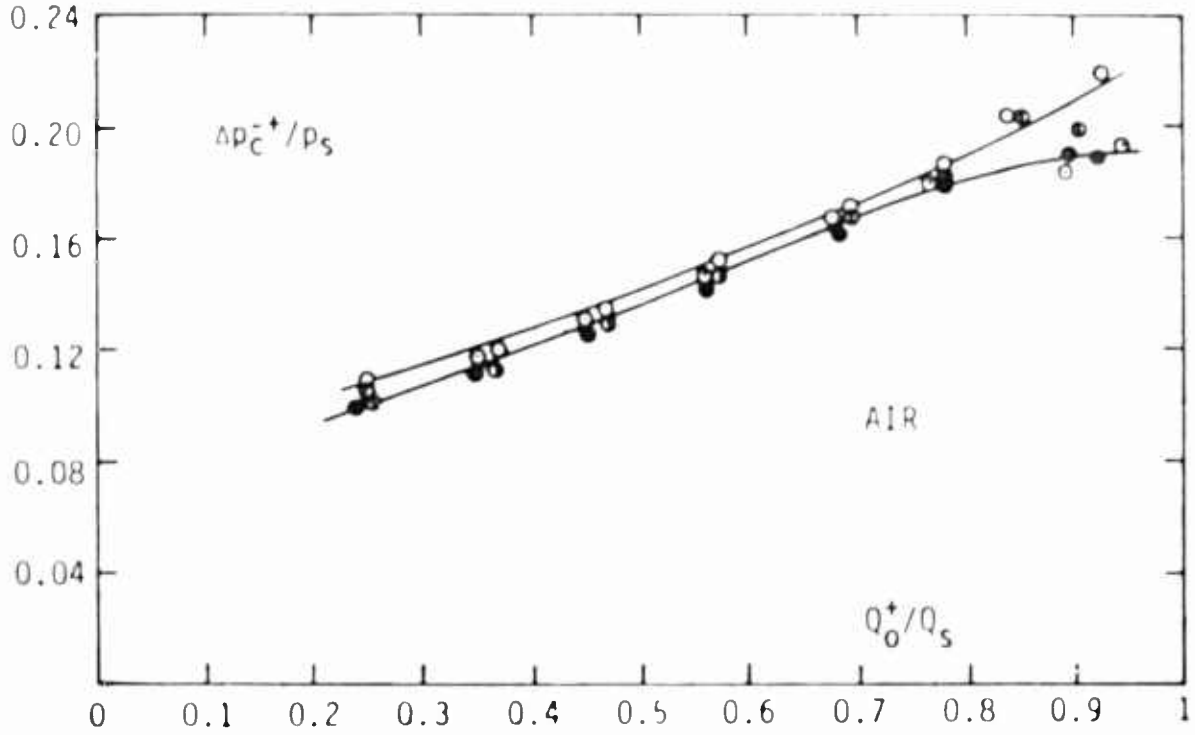

Fig. 5 Normalized Differential Control-Port Pressure Versus Flow Recovery Factor

variation. Its maximum value, however, is considerably lower than that of point No. 5 because of the larger velocities prevailing there.

Figure 8 shows the evolution of pressure along the wall in the jet attachment region for a quasi-steady state loading of the active port. When the active port is full-open, the jet attaches at about x/w = 2.5. With increasing loads the point of attachment moves downstream and the pressure in the bubble gradually increases*. The configuration of the power jet and the formation of vortices in the attachment region and at the two sides of the cusp are clearly visible in the pictures shown in Fig. 9. It is observed that although the vortex on the active-port side of the cusp effectively blocks the power jet and precipitates switching, the vortex on the passive-port side of the cusp delays switching by choking the flow into the passive side. It appears that streamlining the edges of the cusp will improve the performance of the amplifier.

---

*It will be seen later that when the power jet is switched with the control jet, the pressure in the bubble gradually decreases until the time of switching.

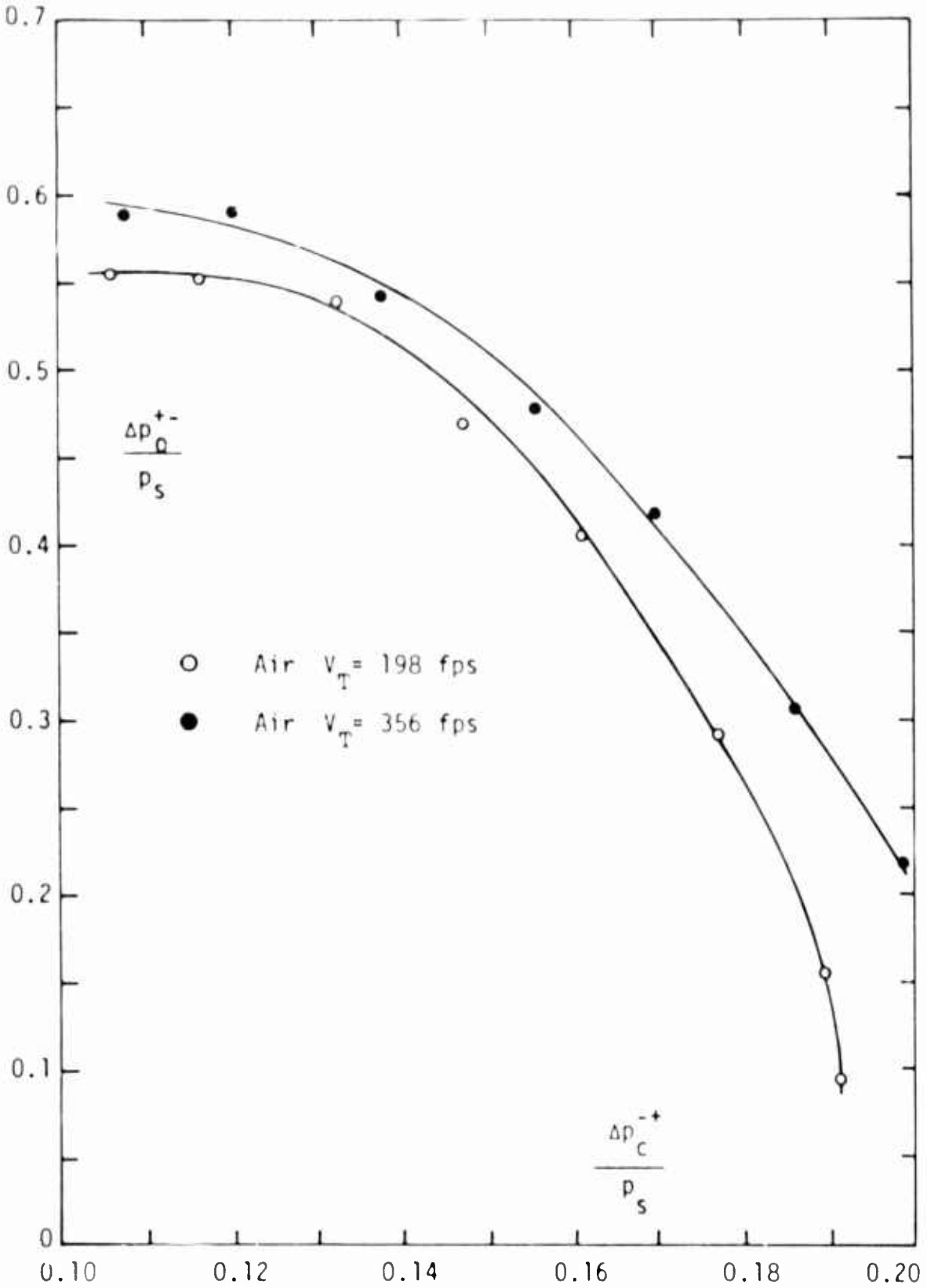

Fig. 6 Normalized Load-Port and Control-Port Differential-Pressure Characteristics

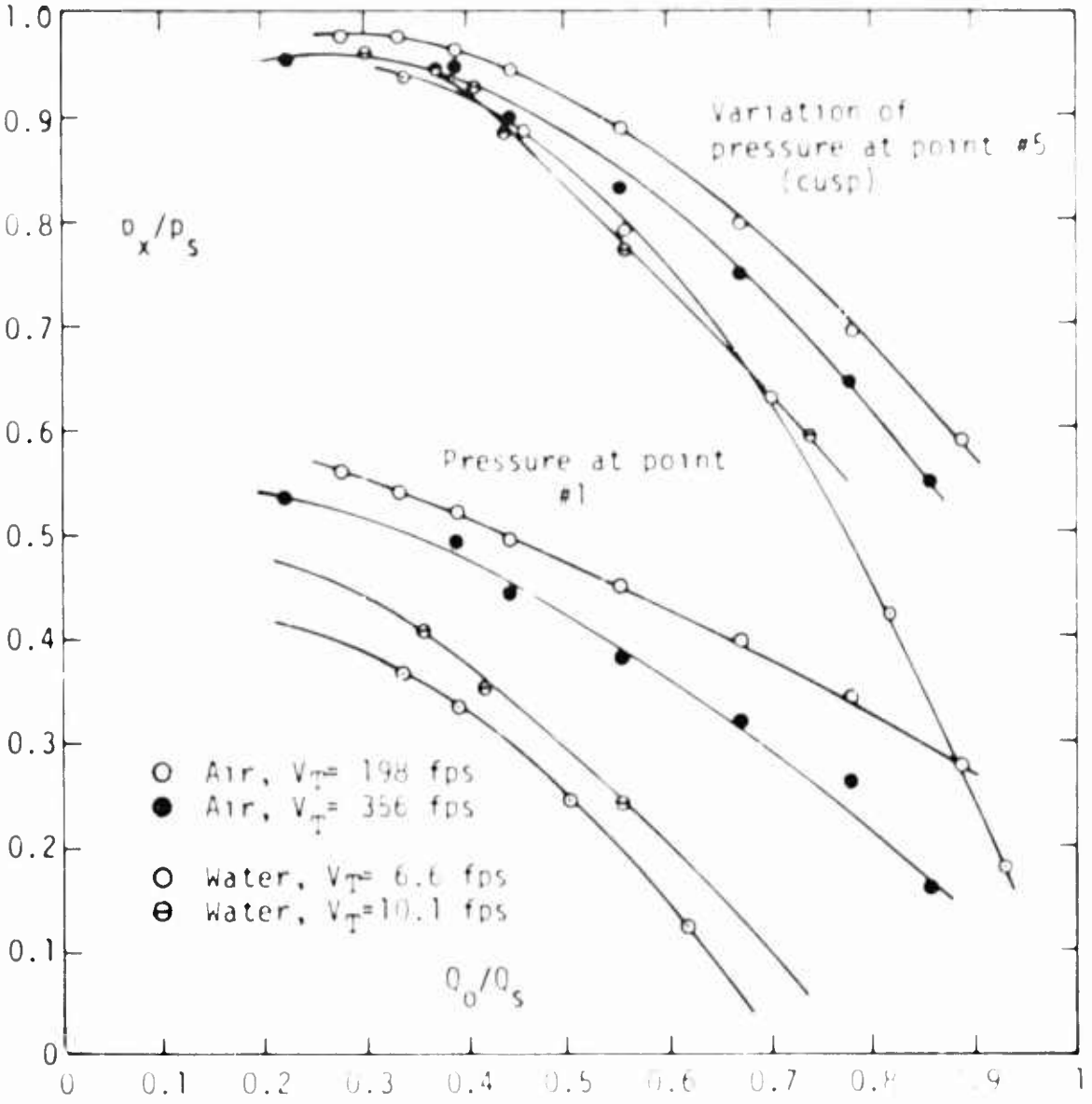

Fig. 7 Variation of Pressure at Points No. 1 and No. 5

Closed Controls - Control Port Loading

The test procedure was quite similar to that described for the active port loading. Once the particular supply pressure was set, the load restrictor valve was adjusted to the desired value and the flow rates and pressures at various points were recorded. Then the flow into the control port, on the active side, was turned on and increased at regular increments. The pressures at all points of interest as well as the flow rate into the control port were recorded at the end of each increment. The results are presented in Fig. 10 in terms of p_o^+/p_s and Q_c^+/Q_s for various initial settings of the load restrictor valve, i.e. for various initial values of p^*. The envelope curve (dotted line) corresponds to the control flow rates necessary to switch the power

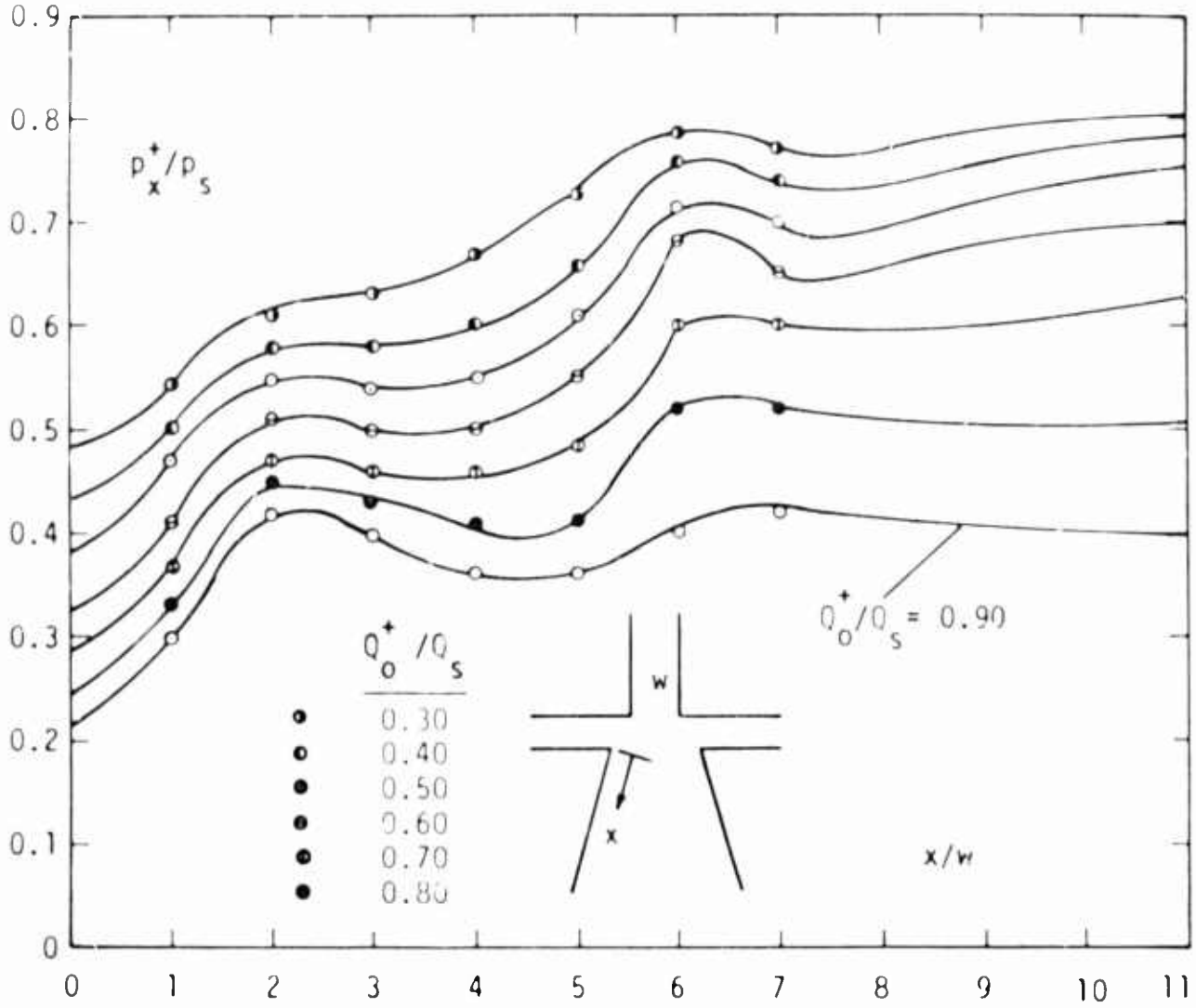

Fig. 8 Variation of Pressure Along the Wall on the Active Side of the Amplifier

jet. It is observed that p_o^+/p_s decreases only slightly as the intensity of the control jet is gradually increased. The variation of the control supply pressure with the control flow rate for various initial loadings of the active load-port is shown in a similar plot in Fig. 11.

The variation of pressure in the attachment bubble is shown in Fig. 12. This figure points out several interesting features of the switching mechanism. In the absence of control flow the jet attaches at about $x/w = 2.5$*. Between the point of attachment and near the entrance into the load port the pressure remains fairly constant and then

---

*A theoretical analysis, based on the free streamline theory, for the prediction of the point of attachment in terms of the relevant parameters of the amplifier will be reported separately.

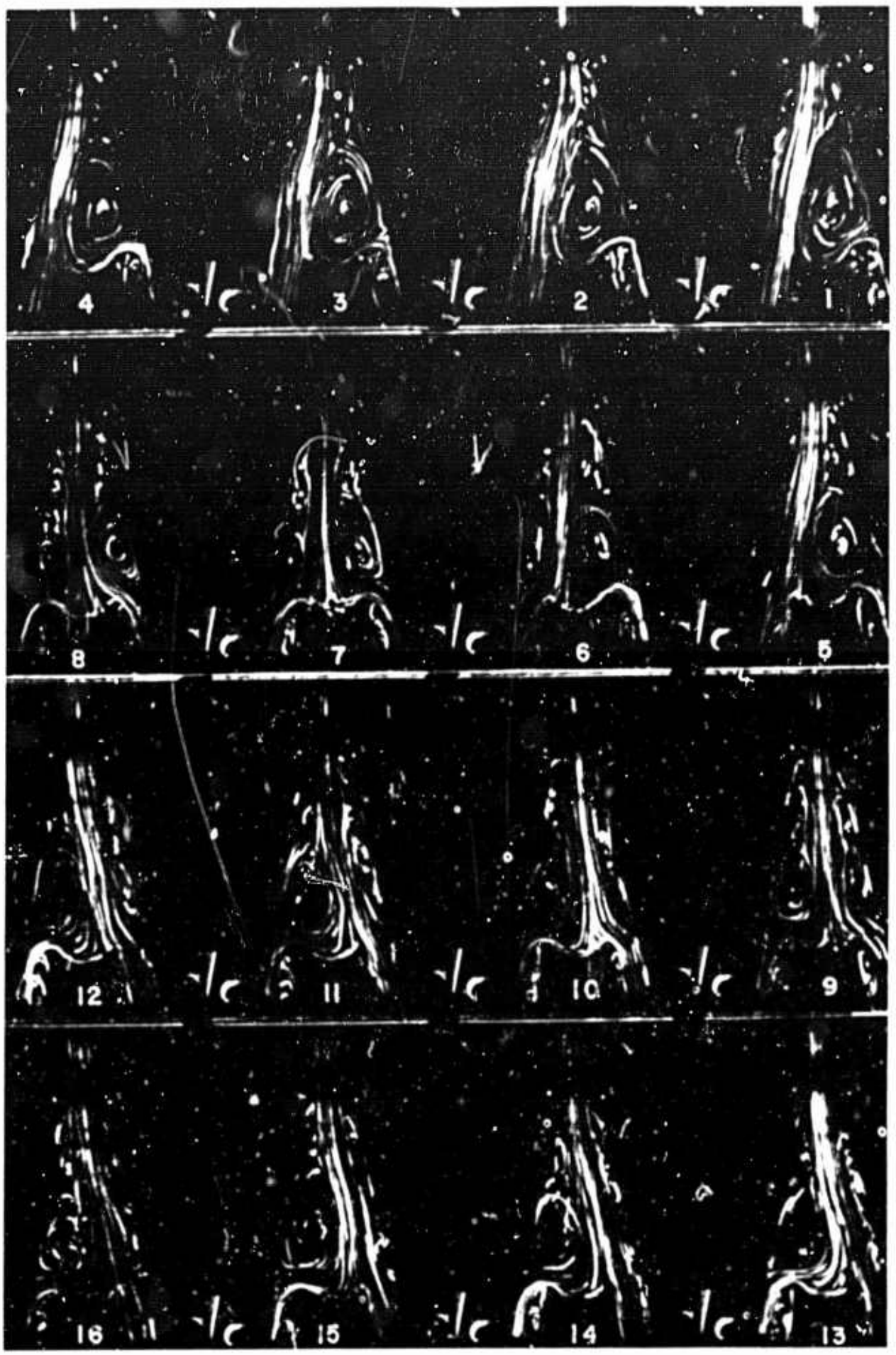

Fig. 9 Switching With Active Port Loading

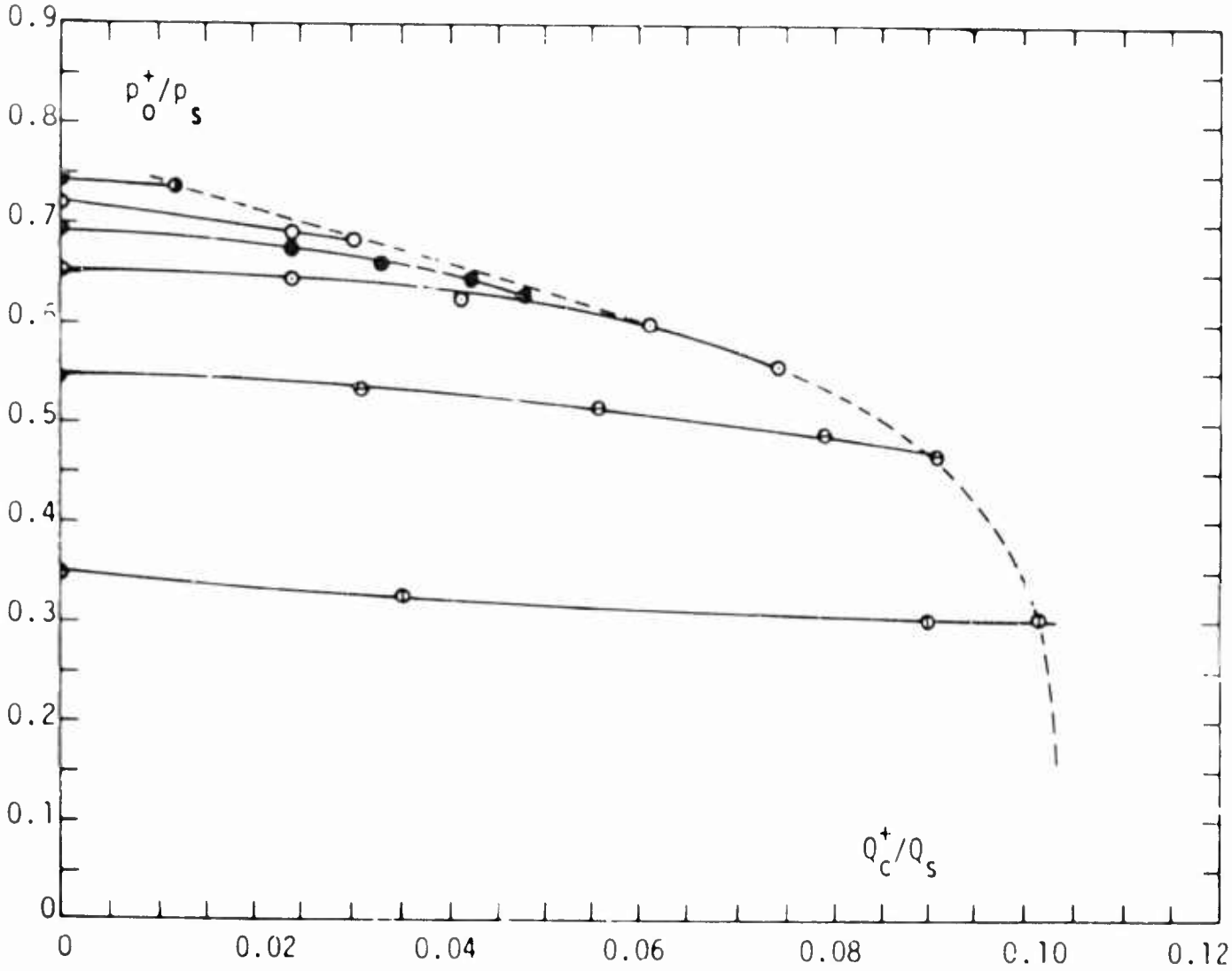

Fig. 10 Normalized Pressure and Control Flow Characteristics

increases rapidly as the power jet proceeds into the load port. When the control flow is turned on and gradually increased, the attachment point moves further downstream and the pressure in the bubble rapidly decreases. It should, however, be noted that in the zone a short distance beyond the point of attachment the pressure increases slightly and near the entrance into the load port it decreases once again, as one would have expected. One may, therefore, conclude on the basis of the above observations that switching is not due to a build up of pressure in the attachment bubble. The analysis of the pressure field and visual observations (see Figs. 13 and 14) show that the control flow plays a twofold role in the switching mechanism. When the control flow is turned on, its momentum deflects the power jet away from the attachment bubble and in the meantime its mass satisfies the entrainment of the attachment zone. The pressure in the bubble decreases as the intensity of the vortex increases with increasing control flow rates. As the jet is deflected away from the active side the latching vortex gradually flattens out between the jet and the passive-side wall and subsequently breaks up into smaller vortices as

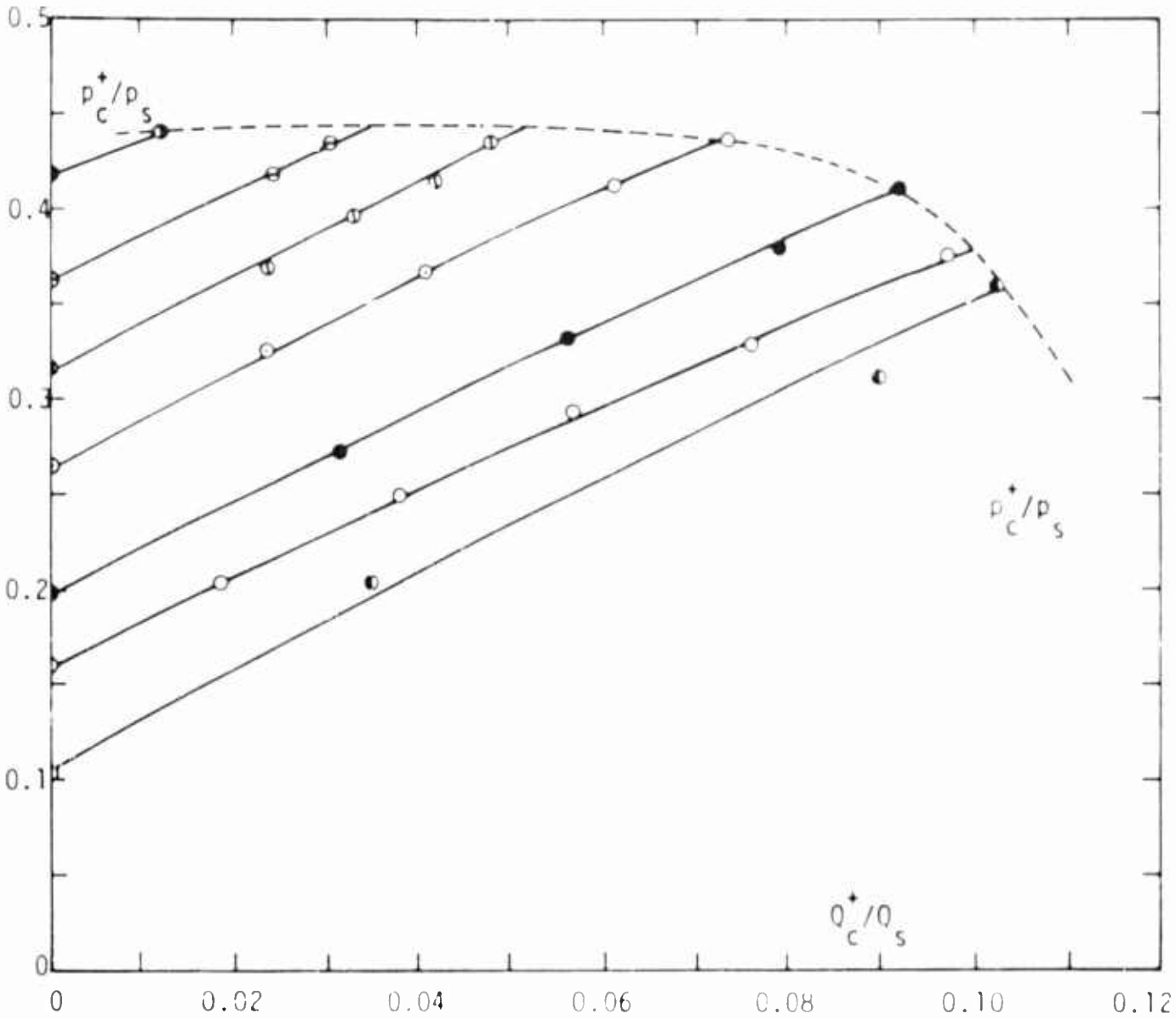

Fig. 11 Normalized Control Port Supply Pressure and Control Flow Characteristics

seen in Fig. 4. This action reduces the pressure along the wall (passive side) and not only compensates for the decrease of pressure in the original attachment zone but also provides a net pull on the power jet. Hence, switching is accomplished in part by the momentum imparted by the control jet and in part by the positive differential suction provided by the latching vortex. Needless to say the latter could not have come into existence if it were not due to the triggering action of the momentum of the control jet.

The intensity of the latching vortex is determined primarily by the amount of that portion of the power jet which is diverted and deflected by the cusp in front of the splitter plate. Consequently, the smaller the width of the load port relative to the power nozzle, the larger is the intensity of the latching vortex and vice versa.

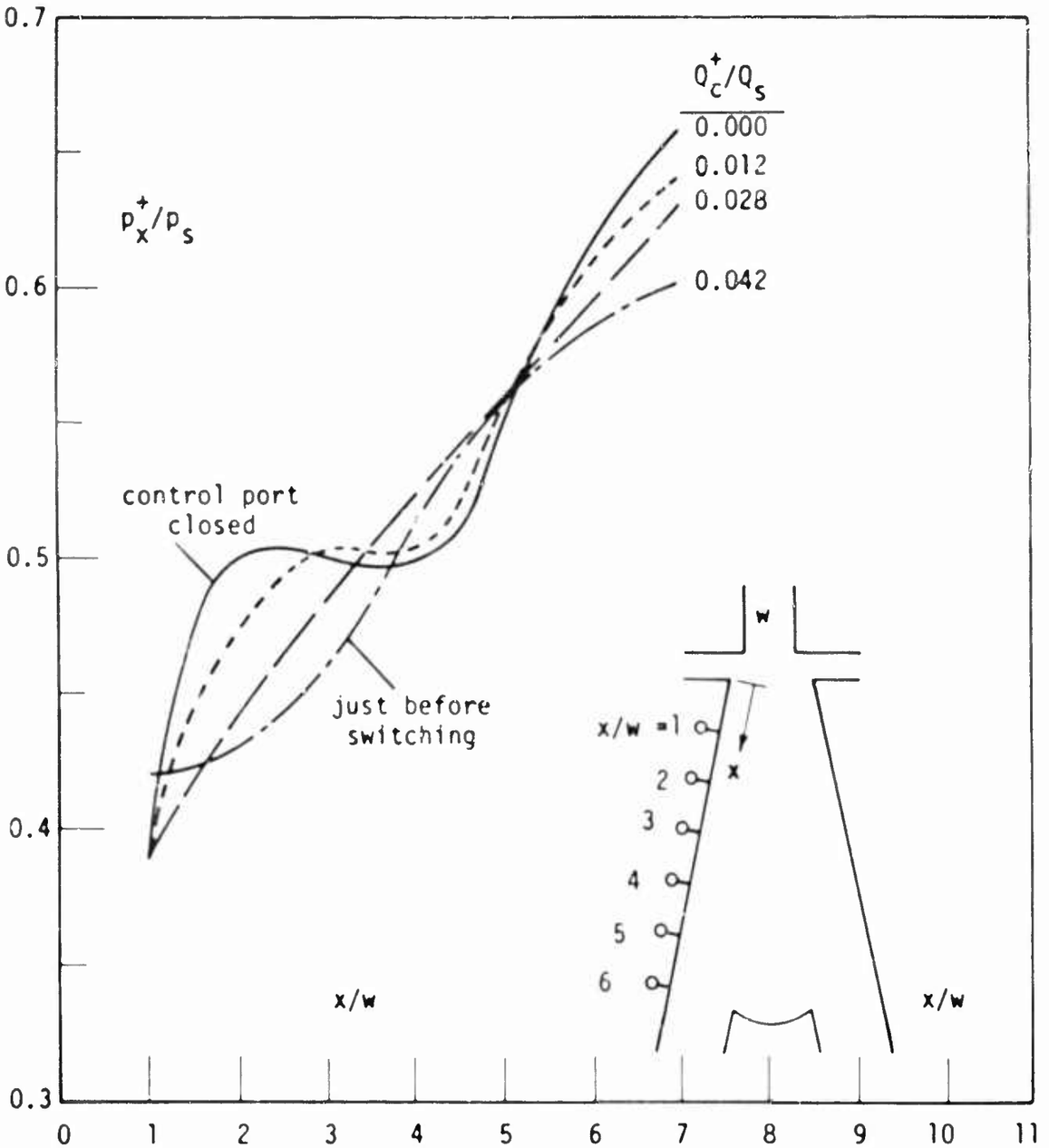

Fig. 12 Variation of Pressure Along the Wall During Switching

However, it is clear that increasing the vortex strength by decreasing the area of the receiving port reduces the effectiveness of the amplifier and causes excessive energy loss. The optimum of the ratio of the width of the receiving port to the power nozzle appears to be about 1.6.

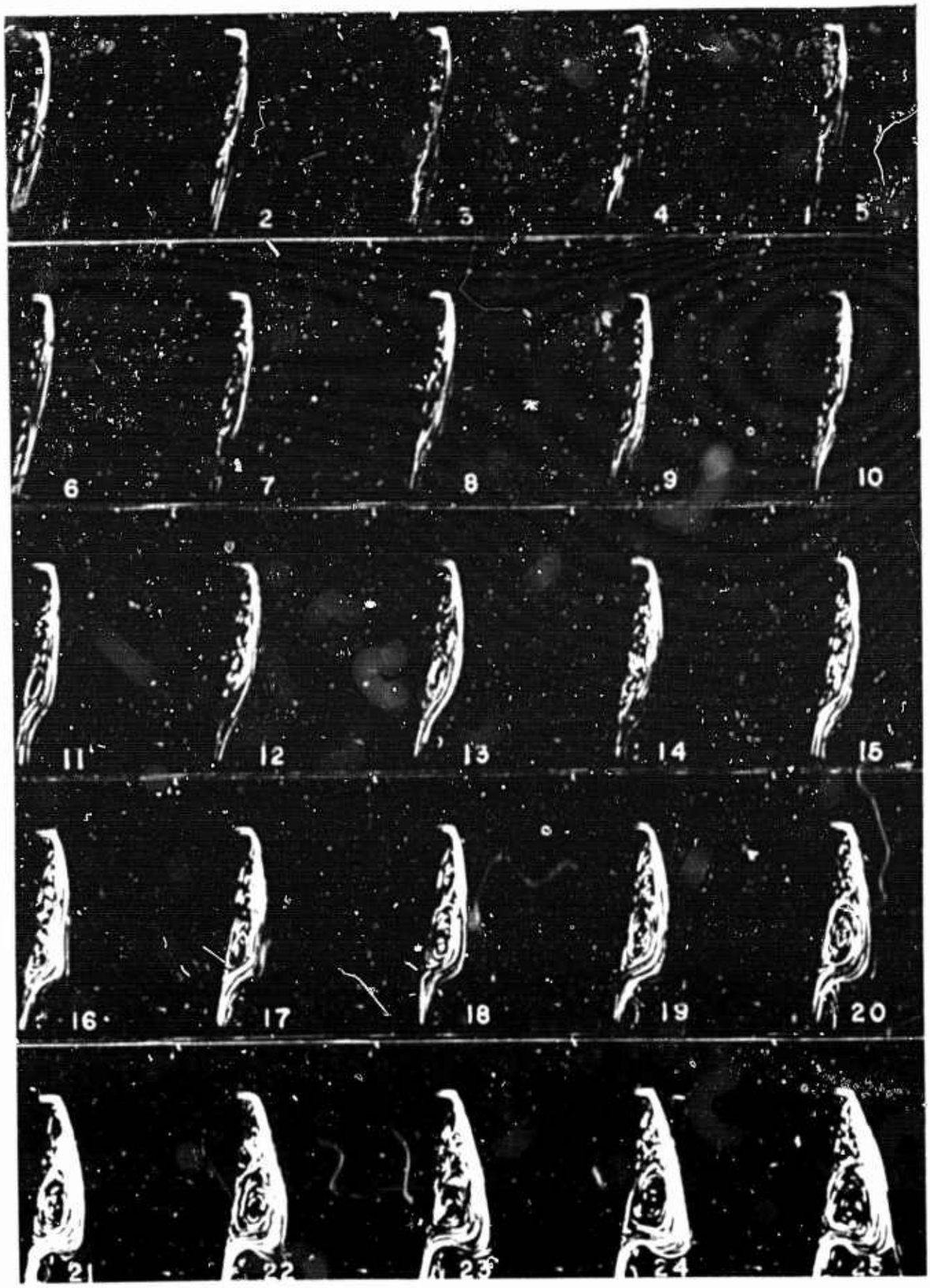

Fig. 13 Switching With Control Port Loading

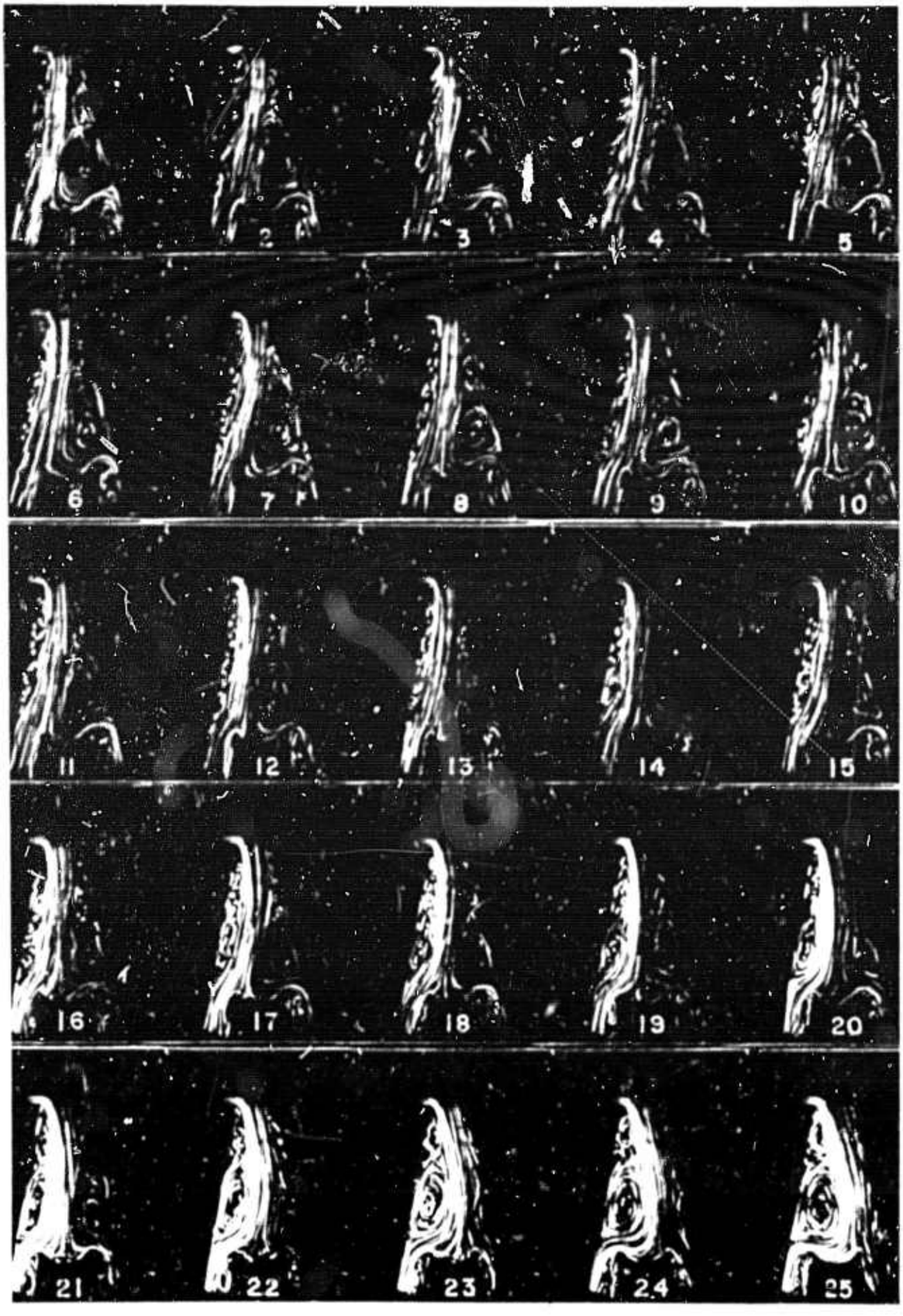

Fig. 14 Switching With Control Port Loading

Transient Switching of the Power Jet

Upon the completion of the tests with quasi-steady state switching, experiments were conducted to determine the transient characteristics of the amplifier and to explore the differences between the steady and transient states. For this purpose the load restrictor valve was set at various values and after a steady state was achieved, a control signal was applied impulsively at the control port on the active side of the amplifier. A sample recording of the variation of pressure at various representative points is shown in Fig. 15. The comparison of these recordings with those obtained with quasi-steady state switching shows that in the amplifier there are two types of pressure oscillations. The first which is an oscillation of very high frequency is due to turbulence created during the penetration and expansion of the power jet into the interaction region and the entrainment of flow in the passive side of the amplifier. The second type of pressure oscillations is due to the compression and rarefaction waves created during impulsive switching. These waves are most apparent in the active and passive load ports immediately after the start of switching. The major frequency of these oscillations is determined solely by the inertance and capacitance characteristics of the receiving lines. The intensity of the waves is determined by the velocity of sound, the change of local velocity of fluid in the amplifier and in the receiving lines, and the density of fluid, i.e. $\Delta P = \rho C \Delta V$. The propagation of the expansion and compression waves and their complex interaction with time is shown in Fig. 16. This figure shows that when the control jet is turned on impulsively, a compression wave is created. This wave is partly reflected as a rarefaction wave and partly transmitted as a compression wave into the opposite control port, power jet (if subsonic), and into the receiving ports. The compression waves in the load ports are reflected as rarefaction waves back to the interaction region. In the meantime the waves in the control ports, interaction region, and the power jet reflect back and forth and in an extremely short time create a very complex wave pattern. The relative strength and position of these waves as well as the transient switching of the amplifier depend on the length of the associated circuits or in other words on the acoustical characteristics of the entire system. It is evident from this discussion that under the right circumstances the compression and rarefaction waves in the separation bubble and in the off-side load port may be sufficient to switch the amplifier.

Returning to the discussion of the comparison of pressures at various points just before switching in the steady and transient cases, it should be noted that the data taken for both cases was analyzed and plotted in Fig. 17 in terms of Q_o^+/Q_s and the ratio of the corresponding transient and steady-state pressures at representative points. It is observed that the mean of the said pressure ratio is about unity and that the quasi-steady state characteristics of the amplifier are

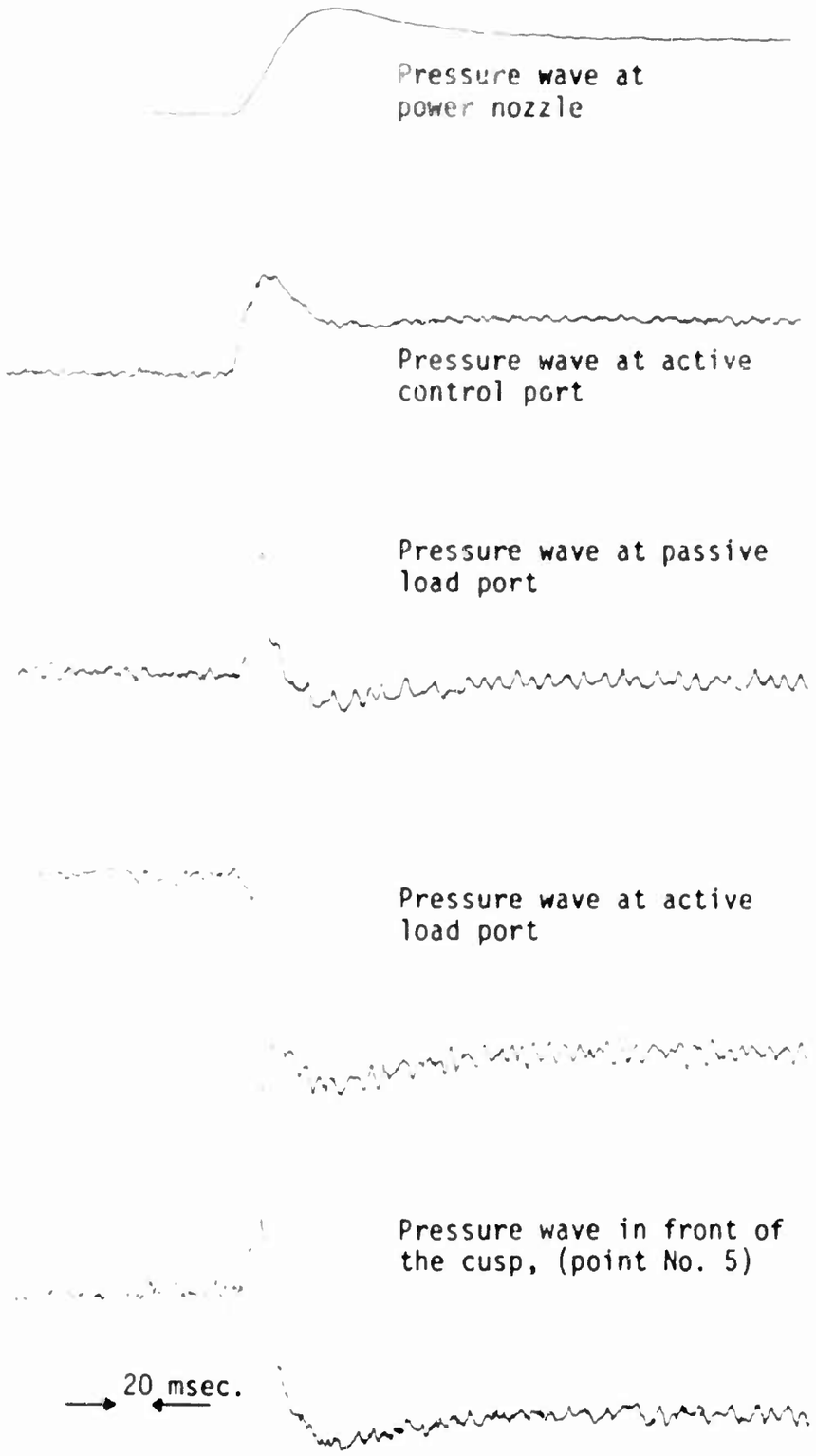

Fig. 15 Sample Recordings of Pressure Waves at Various Points for Impulsive Control Flow Switching

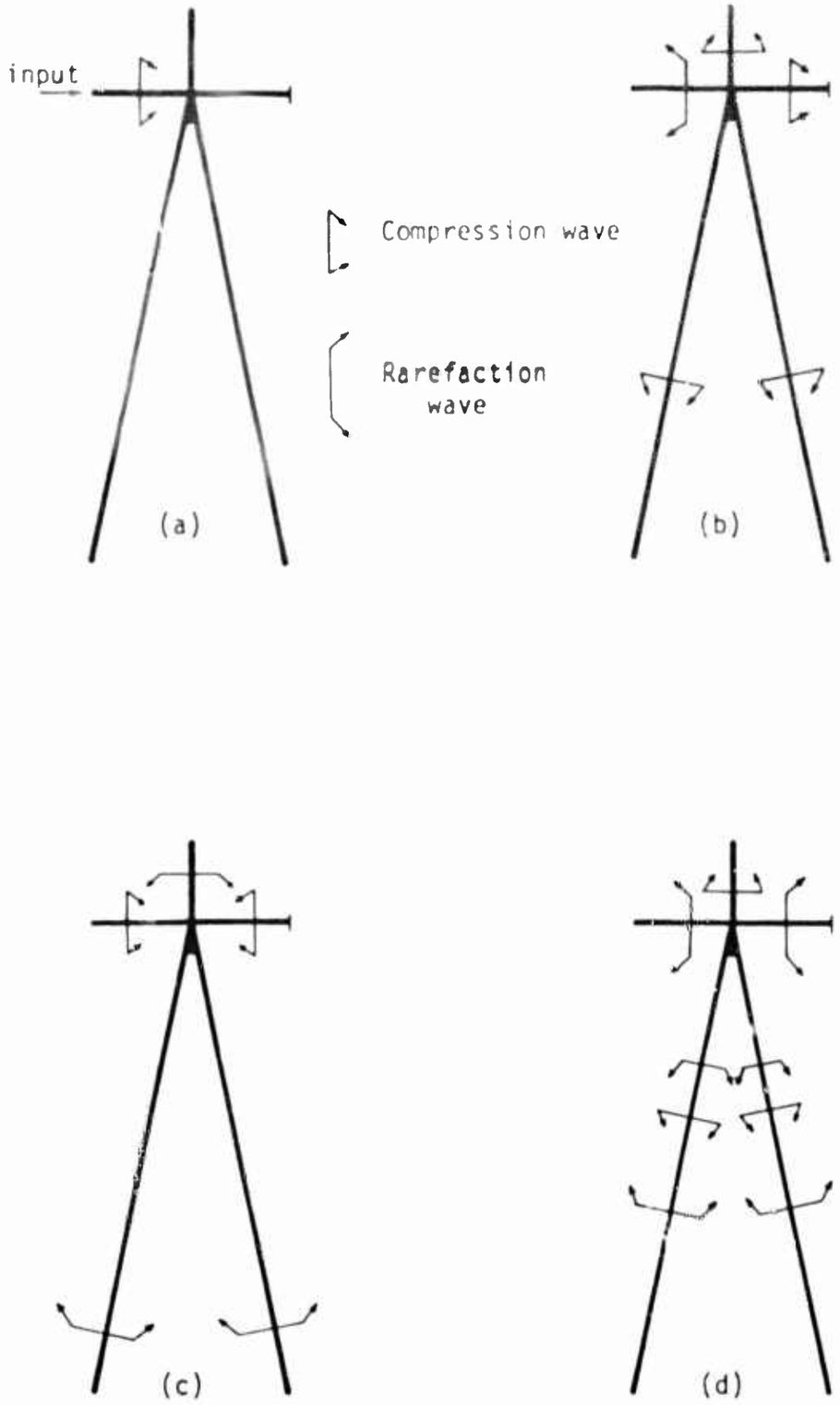

Fig. 16 Propagation of Compression and Rarefaction Waves

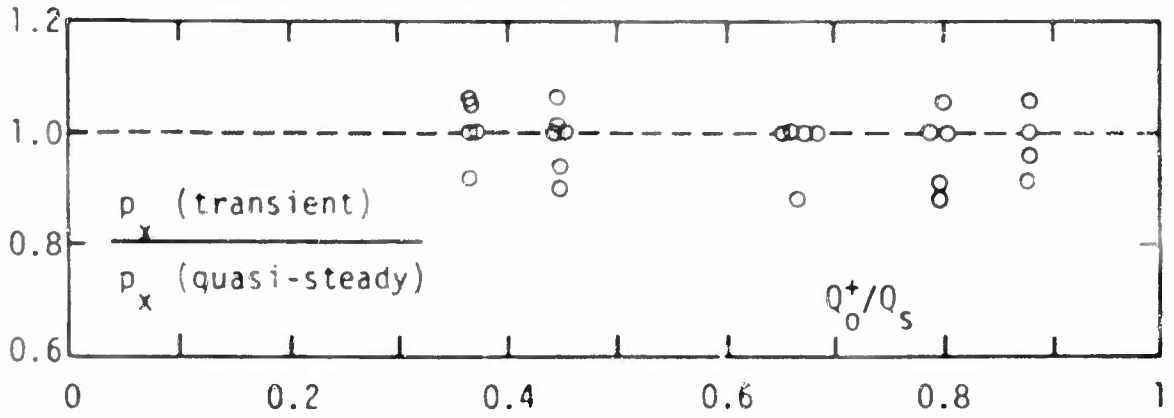

Fig. 17 Comparison of Transient and Quasi-Steady State Pressures

identical with those of the transient state with the exception of the shock waves which during switching completely alter the pressure pattern in the amplifier and render impossible the discussion of an average pressure field.

CONCLUSIONS

The investigation of the steady and transient behavior of an unvented, cusped, bistable amplifier has shown that:

a. the pressure, flow, and power recovery factors of the amplifier are considerably increased by the cusp in front of the splitter plate or in other words by the presence of a latching vortex;

b. as the flow into the control port is increased, the point of attachment moves downstream and the pressure in the attachment bubble decreases rapidly;

c. the stagnation point on the splitter plate moves from the sharp edge of the cusp into the circular arc portion of the cusp and this in turn creates a vortex at the active as well as passive-load port sides of the cusp; the vortex in the active load-port side effectively blocks the flow but the vortex in the passive load-port side delays switching by choking the flow just beginning to enter into the passive leg;

d. the latching vortex is pushed toward the wall on the passive side and as a result of this the pressure along the wall (passive side) is rapidly decreased. This in part compensates for the decrease of pressure in the attachment bubble in the active side and in part provides

suction or pull on the power jet. Hence, switching is accomplished in part by the momentum imparted by the control jet and in part by the positive differential suction provided by the latching vortex;

e. the mean transient characteristics of the amplifier are very nearly identical with the steady-state characteristics with the exception of the shock waves created by the impulsive loading of the control jet;

f. the propagation of the shock waves in the amplifier and in the connecting lines may be analyzed by considering a particular amplifier and the characteristics of the incident and reflected expansion and compression waves. The main drawback of such an analysis comes from the difficulty of determining or estimating the wave transmission and reflection coefficients of the interaction region. It is clear that the sharp corners at the end of control ports, power nozzle, and the cusp set up secondary shock wave fronts and render the determination of that portion of the incident wave which is transmitted into the load ports rather difficult;

g. the flow visualization technique employed in the present investigation is quite satisfactory for understanding qualitatively the switching mechanism and for quick evaluation of the streamline pattern of an amplifier before its actual testing.

ACKNOWLEDGEMENTS

The financial support of the Harry Diamond Laboratories, U. S. Army Materiel Command is gratefully acknowledged.

The author wishes to express his appreciation to Messrs. J. M. Kirshner, K. R. Scudder, and R. Keto for their invaluable comments and t Mr. A. A. Sutko for diligently carrying out the experiments.

NOMENCLATURE

c	velocity of sound
p	pressure (psig)
p_x	pressure at point x
Q	flow rate, (cfm)
V_T	throat velocity
w	width of power nozzle
ρ	density of fluid

Superscripts:

+	active, (on-side)
-	passive, (off-side)

Subscripts:

c	control port
s	supply
o	load port
x	point x

Bendix Report No. BPAD - 863 - 16608R

PERFORMANCE CHARACTERISTICS OF VORTEX AMPLIFIERS

G. R. Howland

Bendix Products Aerospace Division
South Bend, Indiana

To be submitted to
Harry Diamond Laboratories
Washington D. C.

For inclusion in the Proceedings of the
Third Fluid Amplification Symposium
October 1965

PERFORMANCE CHARACTERISTICS OF VORTEX AMPLIFIERS

G. R. HOWLAND
BENDIX PRODUCTS AEROSPACE DIVISION
SOUTH BEND, INDIANA

With the introduction of the concept of controlling and amplifying a fluid flow by use of secondary control flows, an entire family of fluid interaction devices has been, or are, being developed. A large percentage of these devices is based on the jet-on-jet configuration in which the control fluid intersects the power jet at right angles and causes the combined flow to deflect from one receiver to a second receiver.

The purpose of this paper is to present recent developments of a different version of fluid amplification, namely, the vortex amplifier. Although the concept of the vortex amplifier is not new, the development of this device has not received the attention which potential applications warrant. It is hoped that this paper will help to draw attention to the vortex amplifier addition to the family of fluid interaction devices.

THE VORTEX AMPLIFIER

The basic vortex valve or amplifier is shown schematically in Figure 1. The device consists of a cylindrical chamber with a wide slot cut into the periphery of the chamber radially, and a smaller slot cut along a tangent to the periphery. A hole is provided through the end wall concentric with the chamber diameter. The device is usually constructed from three plates. One plate, containing the circular chamber and milled slots, is sandwiched between the two end plates which contain the outlet or outlets and the appropriate fittings. Figure 2 (a) shows three vortex chambers made from plastic, and Figure 2 (b) shows an assembled unit.

A supply flow is introduced to the radial slot and allowed to leave the chamber by the center hole. Usually the dimensions of the chamber and inlet are such that the outlet hole represents the predominant restriction. The entire chamber, therefore, is at essentially supply pressure. If a second flow is introduced into the chamber by the tangential slot, the interaction of the two flows will cause a rotational motion to occur at the periphery of the chamber. The combined flow will follow a spiral path to the exit hole. By the conservation of angular momentum, the tangential velocity of the fluid will increase rapidly as the radius of rotation reduces. The centrifugal force generated by the high rotational swirl near the exit is reflected on the radial incoming flow as a high impedance. Therefore, the impedance of the vortex valve is greatly increased by the tangential injection of a small control flow.

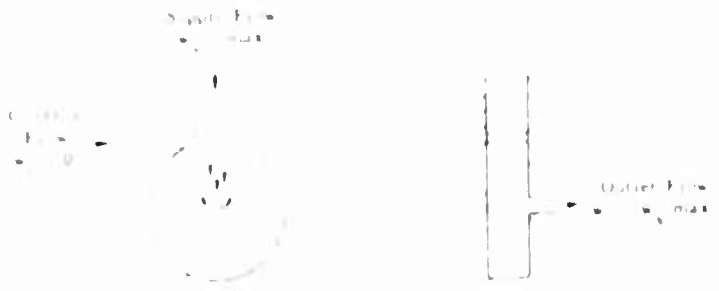

MINIMUM IMPEDANCE

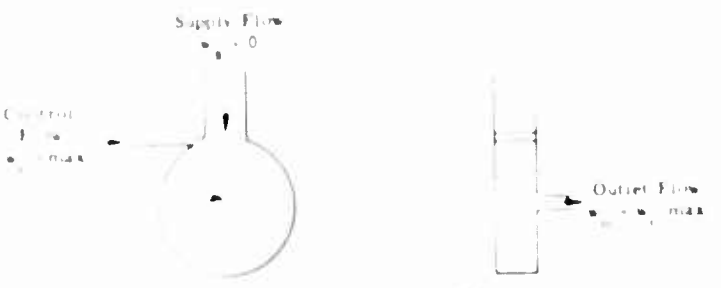

MAXIMUM IMPEDANCE

Figure 1

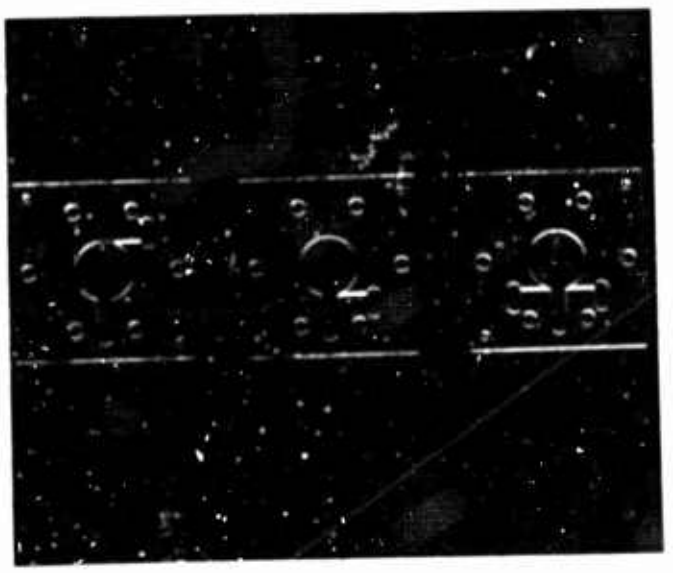

(a)

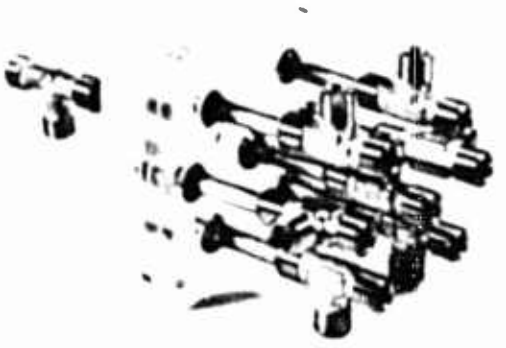

(b)

Figure 2

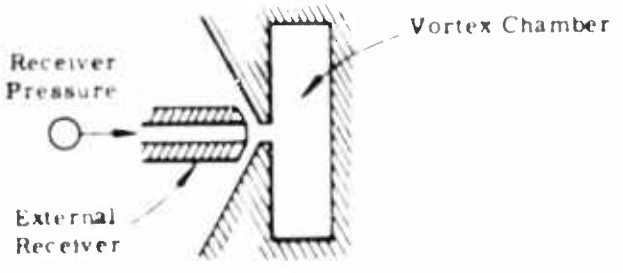

(a)

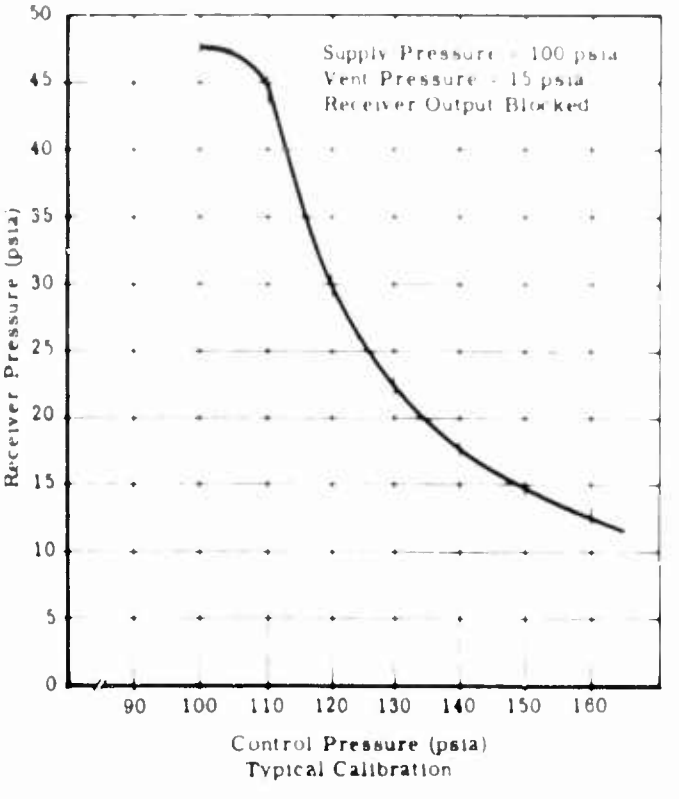

(b)

Figure 3

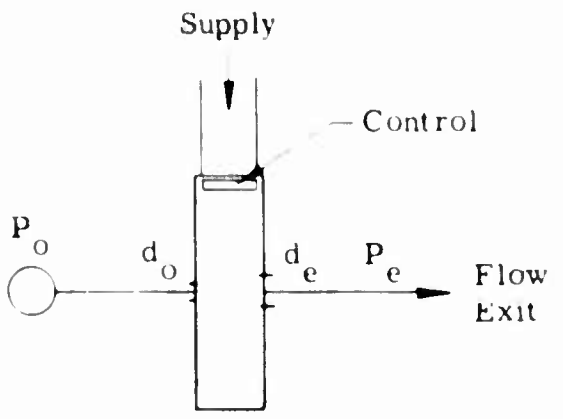

(a)

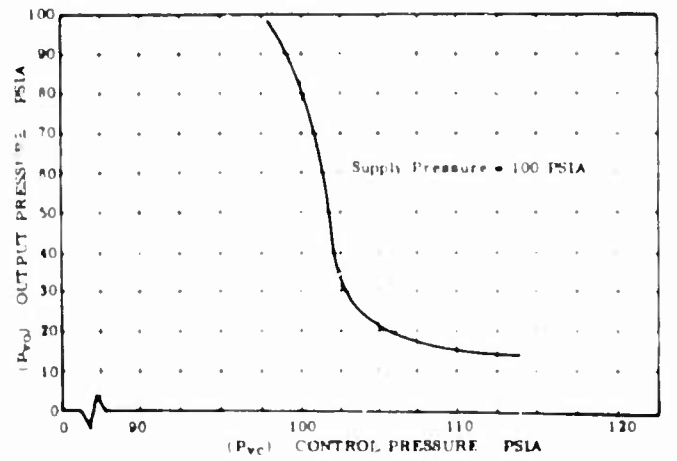

(b)

Figure 4

Typical Performance Characteristics

Since the required control flow is less than the maximum supply flow (for a given supply to exit pressure differential), flow amplification results. The amount of swirl generated in the chamber depends on the interchange of momentum. Therefore, large flow reduction can be obtained by using a small control port area. The maximum to minimum exit flow ratio is then dependent on the control port to exit hole area ratio. However, large flow amplification factors are obtained at the expense of higher control to supply pressure differentials. A trade-off is then obtained between flow and pressure amplification.

Load Pressure Pickoffs

As the vortex amplifier is a fluid interaction device and depends on the reaction of control and power flows, it is not possible to reduce the output flow to zero. For certain applications where a zero load flow is required, one of two receiver configurations can be employed. In Figure 3 (a) an external receiver is inserted downstream of the vortex chamber outlet. When the chamber is at full flow condition, the flow leaves the exit hole in a solid jet and is collected in the receiver. In the full turndown or maximum swirl condition, the flow leaves the chamber and fans out in a conical spray, completely bypassing the receiver. The high velocity of the conical flow can cause aspiration in the receiver. This aspiration is indicated in the calibration shown in Figure 3 (b) by the negative portion of the load pressure characteristic curve.

A second method of reducing the load flow to zero is shown in Figure 4 (a). In this configuration, the load flow is taken from a hole on the opposite wall and concentric with the exit hole. This internal receiver will be referred to as the "P_o tap". Although the maximum load pressure obtainable in the external receiver configuration is limited by the losses inherent in the recovery of a high velocity jet, the maximum dead ended pressure obtainable at the P_o tap is close to the supply pressure. The minimum P_o pressure obtained at full swirl condition is dependent on the ratio of the P_o tap diameter (d_o) to the exit hole diameter (d_e). A calibration of P_o against control pressure P_c is shown in Figure 4 (b).

Figure 5 shows the relationship between the P_o pressure to valve downstream pressure (P_e) ratio, and the diameter ratio for a supply pressure of 50 psia. The P_o pressure is less than the downstream exhaust pressure if the P_o tap diameter is less than 80% of the exit hole diameter.*

The P_o tap can be useful in the following ways:

1. It provides a method of calibrating and comparing the performance of various vortex valve configurations, without the necessity of measuring flows.

2. It provides an output receiver which is particularly useful when the load impedance is essentially infinite (such as a bellows or spring-loaded piston).

3. The P_o tap can be used to obtain an adjustable gain amplifier stage.

*It has been recognized that the relationship shown in Figure 5 is dependent on the supply to exhaust pressure ratio; and that maximum and minimum P_o P_e ratios exist. These conditions and limits have not, to date, been fully evaluated.

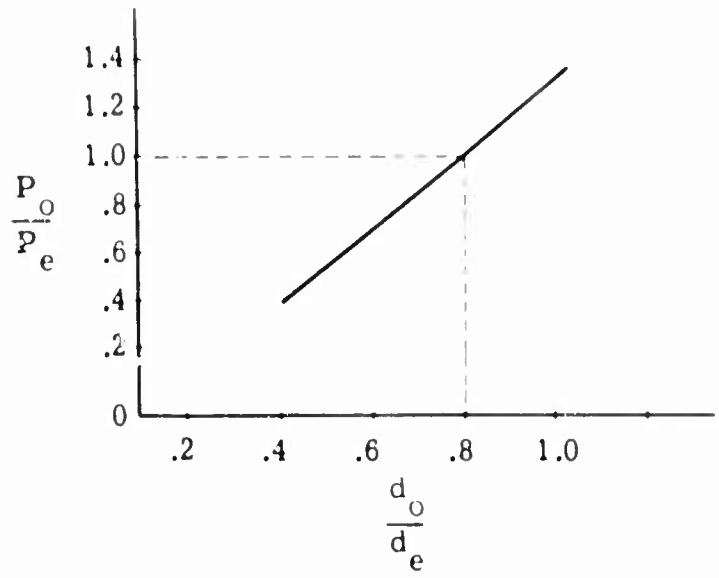

Figure 5

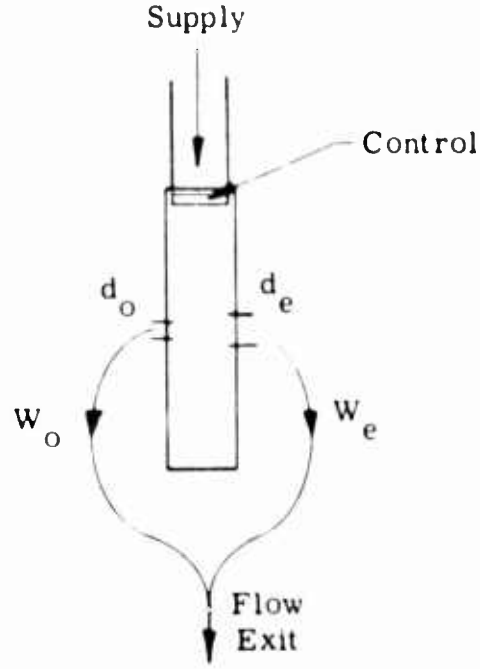

(a)

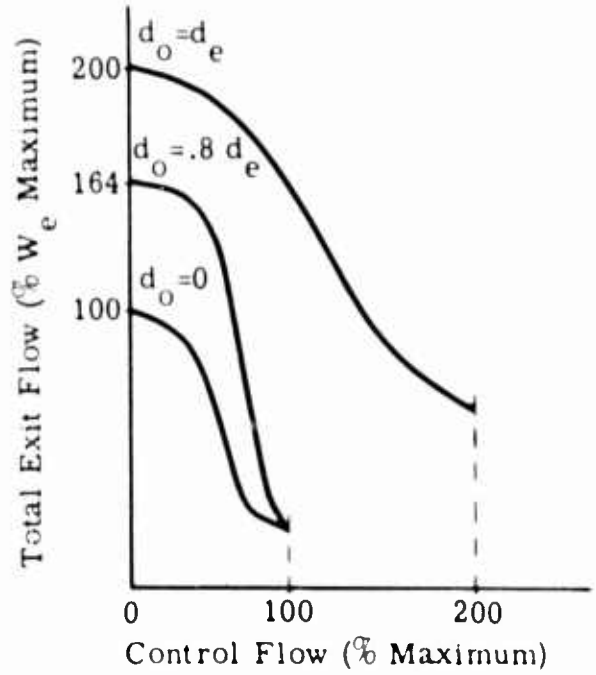

(b)

Figure 6

Items 1. and 2. are self-explanatory. Item 3. probably requires further explanation. If the vortex amplifier exit and P_o tap are connected externally as shown in Figure 6 (a), the total outlet flow (w_t) is equal to the sum of the flows from the exit hole and the P_o tap. Therefore, $w_t = w_o + w_e$.

If $d_o\ d_e = .8$, then at maximum flow condition the pressure upstream of both exits is essentially supply pressure and $w_{omax} = (.8)^2\ w_{emax}$.

Thus $w_{tmax} = w_{emax} + .64\ w_{emax} = 1.64\ w_{emax}$. However, at the full turndown condition $P_o\ P_e = 1$ and therefore $w_{omin} = 0$.

Thus, $w_{tmin} = w_{emin}$.

The maximum valve output flow has been increased by 64%, while the minimum output is unchanged. The corresponding increase in flow amplification is illustrated in Figure 6 (b). If a variable restrictor is placed in the P_o tap line, the range in flow amplification can be adjusted between the limits shown.

Multiple Inputs and Bias Control

The vortex valve can become a more useful device by using multiple control ports. Although the schematic of Figure 1 shows the control port interacting directly with the inlet supply flow, experimental evidence has proven that the control can be injected along any tangent line to the chamber periphery. Multiple control ports which generate a swirl in the same direction have additive effects. Control flows which tend to oppose each other are subtractive.

The latter effect can be used to obtain negative calibration characteristics. That is, an increasing control flow in a biased valve causes a reduction in the valve impedance. A typical calibration of a biased vortex valve is shown in Figure 7.

The effect of summing and subtracting control inputs can be useful in servo systems where it is necessary to compare command and feedback signals with a minimum of cross impedance. Multiple control ports can also be used to obtain dynamic compensation. A lead network, shown in Figure 8, consists of two opposing control ports connected from a common input signal. One control line contains a resistance (orifice) and capacitance (volume). The opposing control line contains only a resistance. For any quiescent input signal, the two control ports are balanced and the output flow or pressure is independent of the input signal level. For a changing input signal pressure, the time required to compress the gas in the volume capacitance causes the pressure at one port to lag the pressure at the opposing port. A swirl is then generated, and the output pressure will reduce by an amount proportional to the rate of change or time derivative of the input signal.

It can be seen that a lag circuit is obtained if the two control ports are additive.

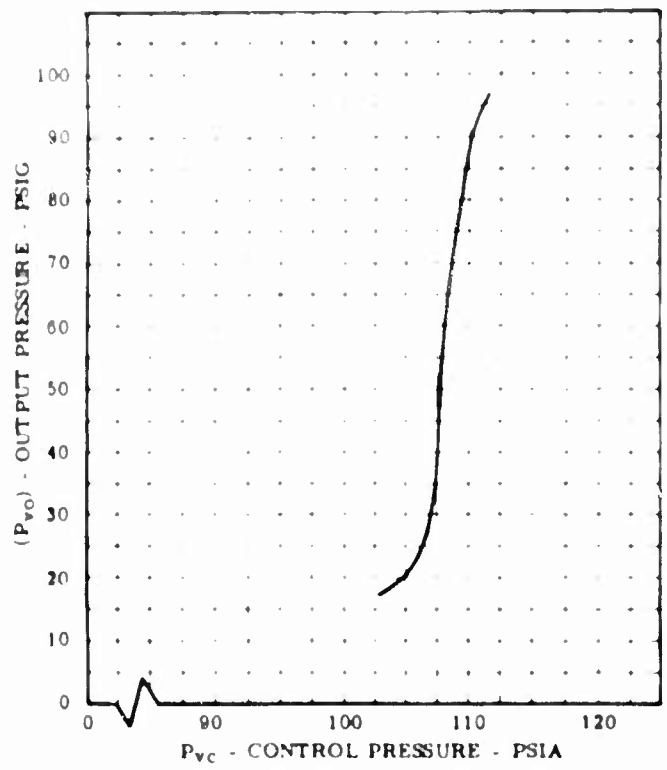

Figure 7

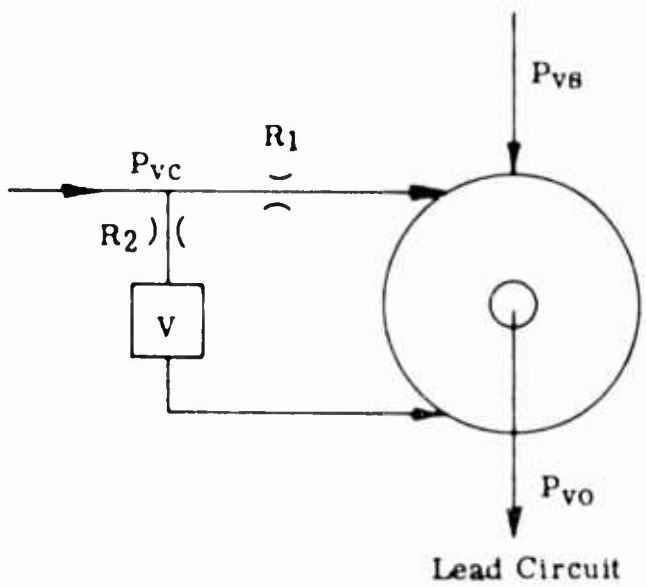

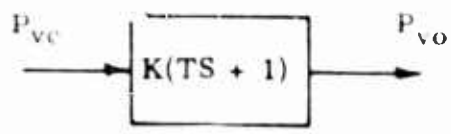

Figure 8

Dynamic Response Characteristics

A digital computer program was developed to calculate both the steady state performance of a vortex valve and the response to a step change in control pressure. Figure 9 shows the comparison between computer and measured data for a one inch diameter vortex chamber. The valve response consists of a transportation delay and a single order lag. For this particular valve, the delay is 2 milliseconds and the lag time constant is 8 milliseconds. For smaller valves of the same configuration, the response is much faster, and for larger valves the response is slower. The transportation delay can be approximated by the equation:

$$t_d = \frac{\left[\left(\frac{D_o}{d_e}\right)^2 - 1\right] L}{13.44\ N\ \sqrt{RT}}$$

where D_o = valve peripheral diameter (inch)

d_e = exit hole diameter (inch)

R = gas constant (in.lb. lb. degree)

T = gas temperature (degrees)

N = average flow turndown ratio at the test condition $\left(\frac{w_o - w_{omin}}{w_{omax} - w_{omin}}\right)$

L = chamber depth (inches)

AMPLIFIER STAGING

Single Ended Circuit

Vortex valves can be used in series to obtain high amplification factors, by attaching the output of one valve to the control port of the second valve. A schematic and typical amplification curve is shown in Figure 10. In this configuration, a 1 2 inch diameter valve was used to drive a one-inch diameter valve. An overall pressure gain (ΔP_{o2} ΔP_{c1}) of 40 was obtained. The linear pressure gain of each stage was 7.

One of the main advantages of staging with vortex devices is the fact that all of the flow introduced at the various supply and control ports is available at the outlet of the power stage. This is not possible when a constant flow amplifier is used.

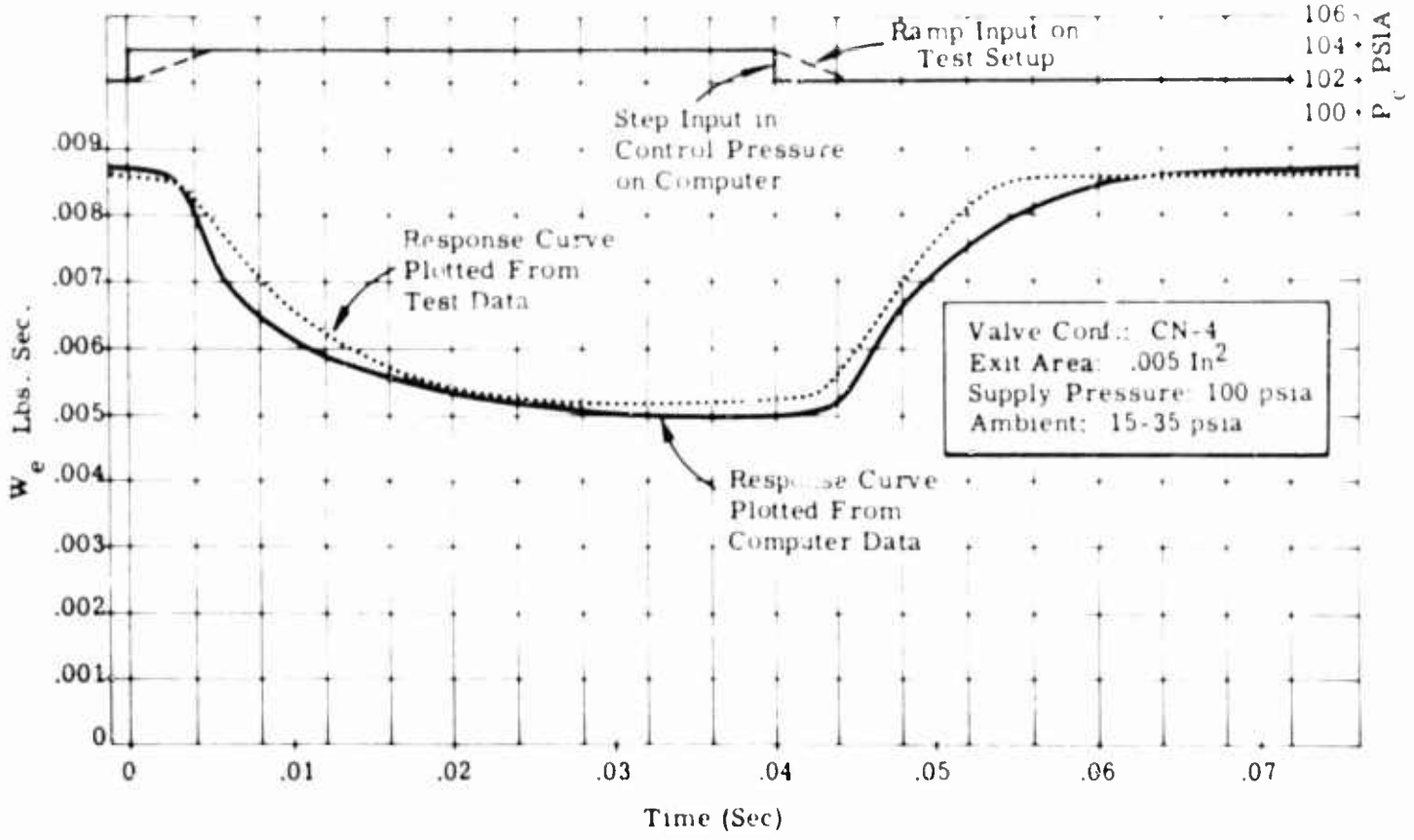

Figure 9

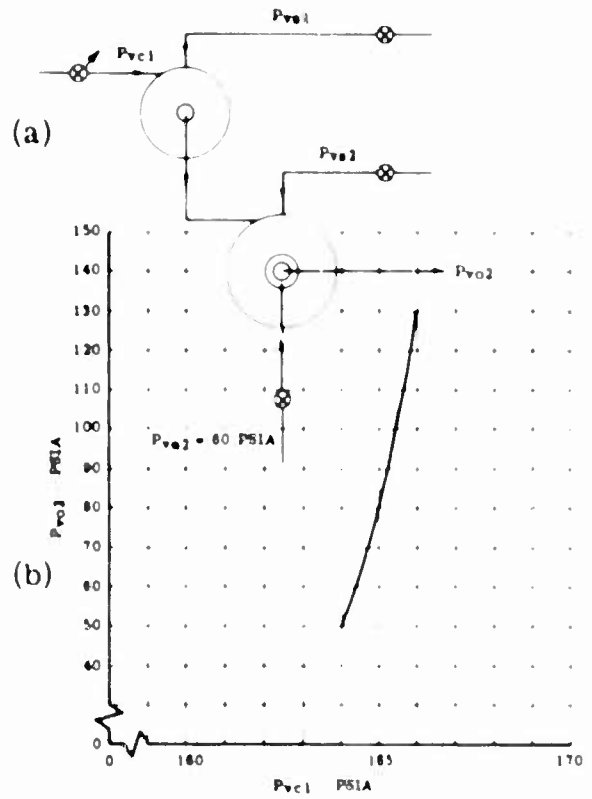

Figure 10

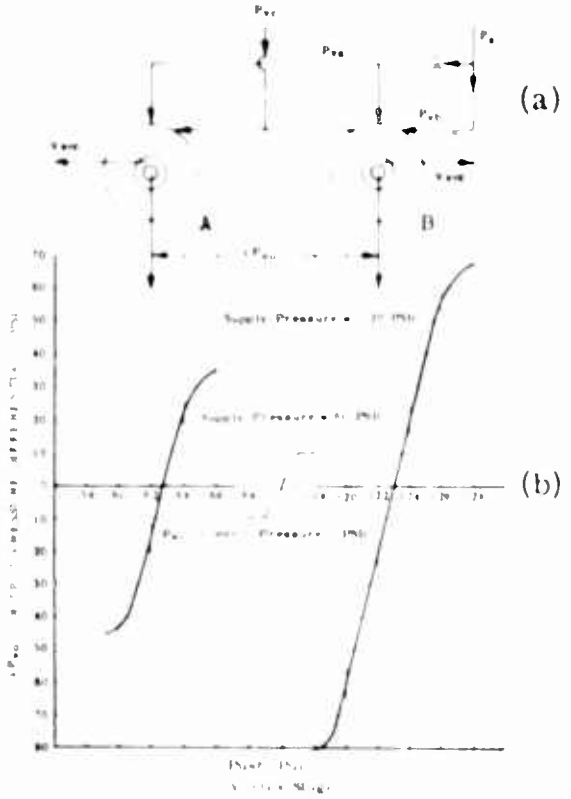

Figure 11

Push-Pull Circuit

Since the control pressure applied to a vortex amplifier is of a higher level than the corresponding output pressure, it is necessary, when staging valves, to slightly reduce the supply pressure to each consecutive stage. Therefore, a separate pressure regulator would be required for each stage, if the valves are staged as shown in Figure 10. This is not desirable in a practical system. In order to eliminate this problem and for other reasons which will be discussed later, it is desirable to copy the electrical practice of operating amplifier stages in push-pull. Figure 11 (a) indicates schematically the method of obtaining a push-pull circuit.

When a single control input is used, the control is applied to both valve A and valve B. An increasing control pressure will cause the impedance of valve A to increase and, since valve B is biased, its impedance will decrease. If valves A and B are identical and symmetrical, the total impedance to supply flow will be independent of the control signal level. The common supply pressure to the two valves can then be set by a fixed restriction from the source pressure level. High amplification factors can be obtained by staging the outputs to control inputs in the conventional manner. No further biasing is required in the other stages, since the inputs are in push-pull from the preceding stage. The supply pressures to each stage can be maintained at the required level by suitable restrictors from the source pressure. Figure 11 (b) shows the output pressure differential (ΔP_O) against input control pressure (P_C) obtained from a single stage push-pull circuit. This figure indicates the good linearity obtained over a large percentage of the useful range. The comparison of the test data at two supply pressure levels (60 psig and 120 psig) shows that although the range of differential pressure output is proportional to supply pressure, the gain of the circuit is independent of the pressure level. By deliberately unbalancing the impedance match of the two valves, the common supply pressure can be made to increase or decrease, with an increasing control flow. In this manner, the control impedance reflected at the input can be varied from essentially zero to a high value. This variation in input impedance can be useful in matching a sensor output to an amplifier input for optimum circuit performance.

If a push-pull control input is obtained such as from a torque motor flapper, no bias is required on the first stage of the amplifier.

Some of the advantages of employing a push-pull circuit include reduced sensitivity to supply pressure level and supply noise, insensitivity to both gas temperature and material thermal expansion effects, and ease of obtaining the required stage supply pressures.

APPLICATIONS

In this section, two applications for the vortex amplifier are described. These applications are sufficiently different in concept to provide examples of the adaptability of the device.

Amplifier and Compensation Network

Figure 12 shows an amplifier and compensation network for a pneumatic actuator, which has been developed for NASA-Marshall Space Flight Center. The amplifier consists of four stages of vortex valves in push-pull operation, which provide an uncompensated gain

of 1400. An input pressure differential at the torque motor flapper of approximately 1 3 psi provides an output load pressure differential of 410 psi. The supply fluid is hydrogen at 800 psi.

The output stage, consisting of four vortex valves in a bridge arrangement, replaces the conventional spool type servo valve. The load pressure and flow power a pneumatic vane motor. The vane motor, through a planetary transmission and ball lead screw, produces a high force linear stroke output for gimballing a rocket engine.

Position feedback is obtained from pressure pickoffs from a linear cam attached to the output shaft. A position command caused by motion of the torque motor flapper generates a pressure differential at the input to the amplifier. The resulting motion of the output shaft changes the position pickoff bleed areas. The amplifier input pressure differential will reduce to zero when the bleed areas of the position pickoff balance the bleed areas of the torque motor.

Dynamic compensation is obtained by summing a motor speed signal and load pressure differential at the input stage to the amplifier.

A breadboard version of the amplifier is shown in Figure 13.

Commutation Circuit

Figure 14 shows a commutation circuit for a new concept in pneumatic actuator. The circuit is basically a logic circuit which increases or reduces the pressures applied to eight bellows. To operate the actuator, it is necessary to pressurize the bellows sequentially in groups of four. To do this, the sixteen selector valves accept as inputs the directional signal from a bistable amplifier and the actual position of the output member (obtained as the upstream pressures of four variable bleed orifices). The combination of inputs causes one pair of vortex selector valves to operate in push-pull and provide control signals to two of the eight power valves. The P_o tap of the power valves is connected directly to the bellows. The relationship between the position pickoff pressures and the corresponding pressurized bellows is such that continuous sequencing of the bellows occurs in a manner similar to the brush commutation of an electric motor. The pressure error valve output applies a bias to the power valves which is inversely proportional to the absolute value of the input error signal. This bias dictates maximum bellows pressure (and therefore output torque) obtained.

This circuit is an example of the analog logic functions which can be performed without the use of mechanical valving. The actuator has been developed under a NASA Lewis Research Center Contract.

Other Applications

In the area of controls for gas turbine engines, the necessity for multiple closed loop controls leads to requirements for simple and reliable sensors, logic circuits, amplification and power devices. Operation of one or more vortex valves as speed sensors, temperature sensors, pressure ratio sensors, logic sequencing and amplification have been demonstrated. The insensitivity of the circuits to supply pressure level allows use of the compressor discharge pressure as an unregulator source.

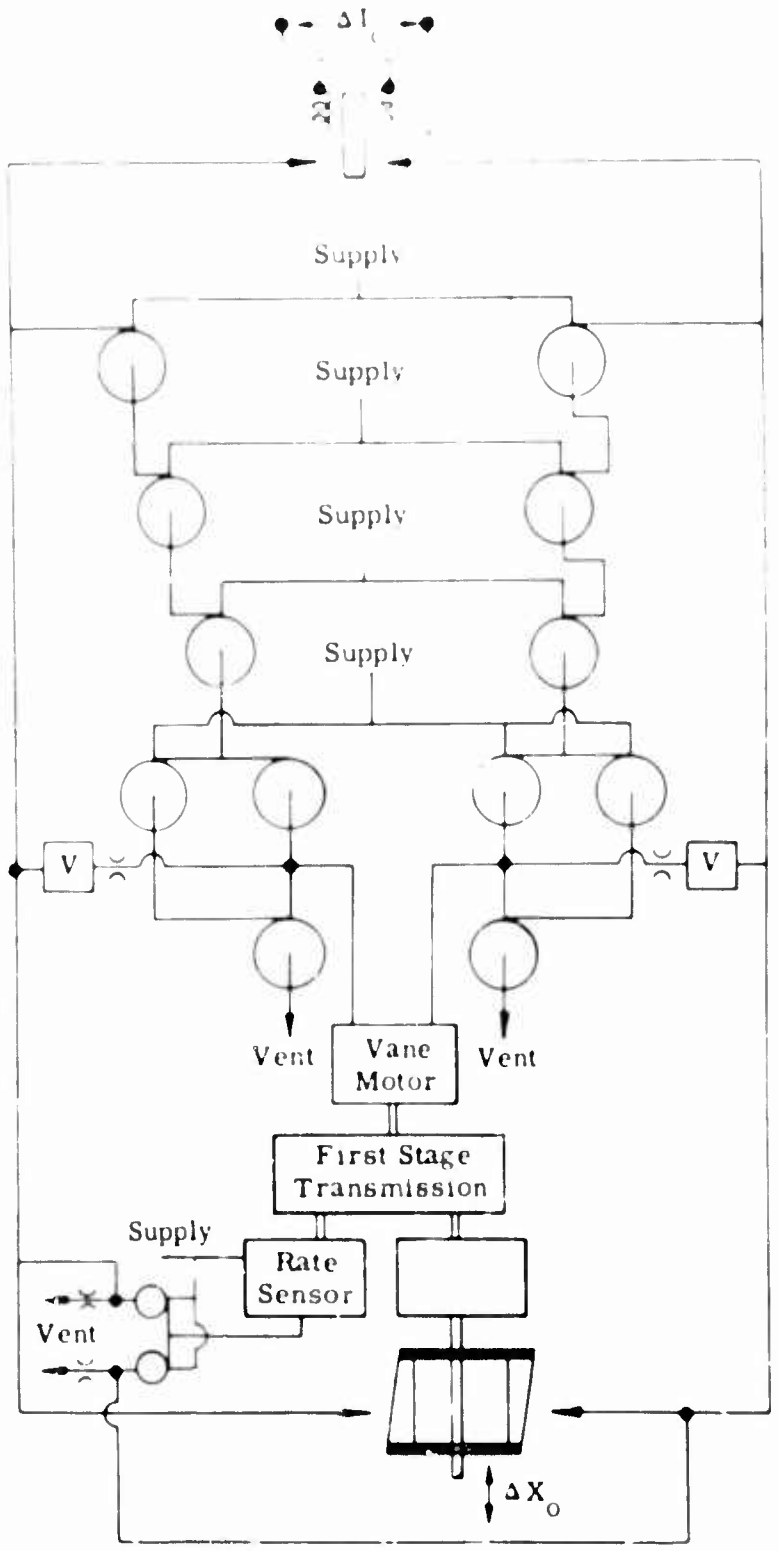
Supply
Supply
Supply
Supply
V
V
Vent
Vane Motor
Vent
First Stage Transmission
Supply
Rate Sensor
Vent
ΔX_o

Figure 12

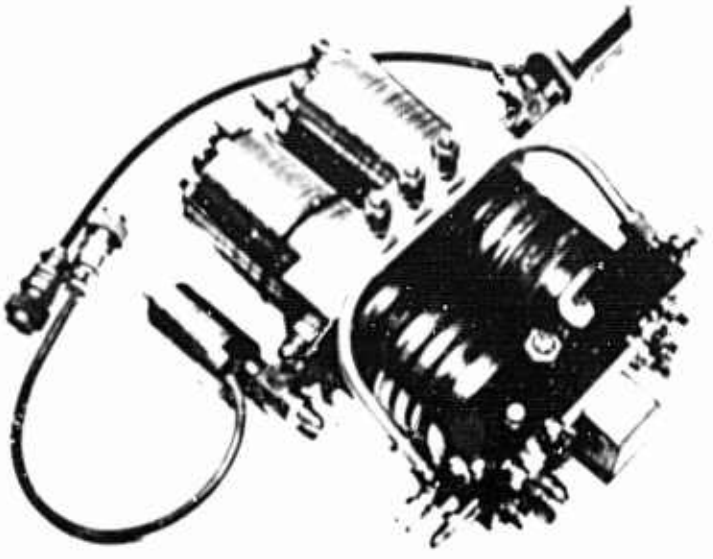

Figure 13

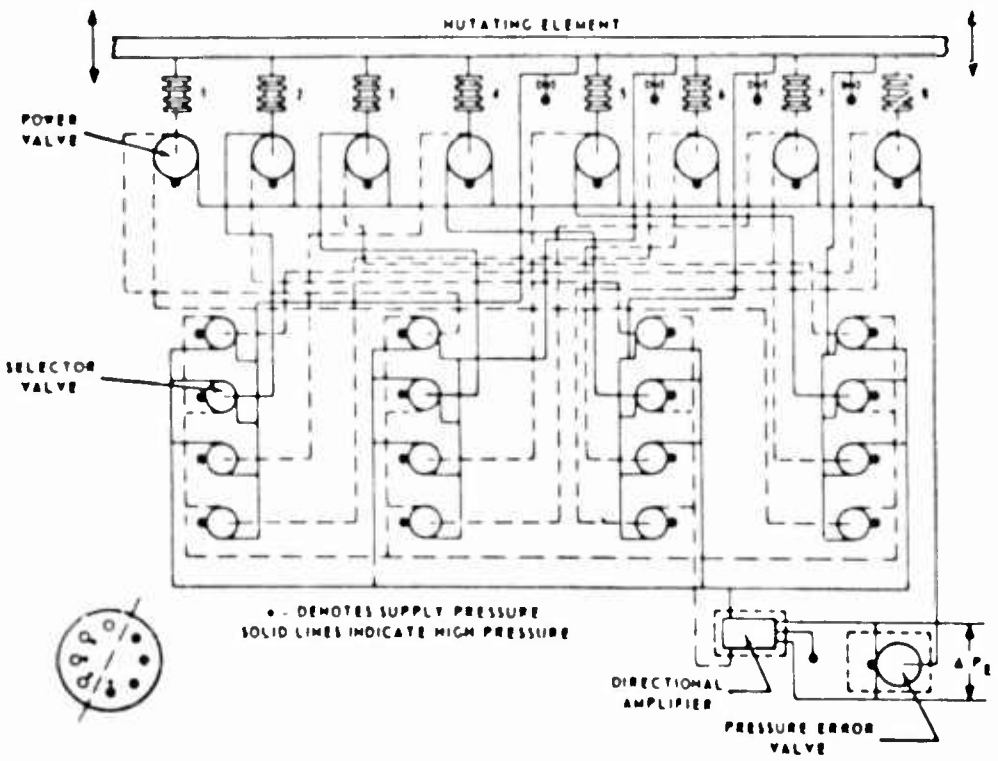

Figure 14

SUMMARY AND CONCLUSIONS

The vortex valve as an amplifying device offers unique advantages over other concepts of "pure fluid" devices. The basic amplifier is easy to fabricate by conventional machining techniques, it is capable of operating reliably and predictably over a virtually infinite range of pressure differentials, and it does not contain any splitters, receivers or other critical geometric shapes. The vortex valve can be scaled from a minimum dictated by dirt sensitivity and fabrication techniques to the largest size capable of providing the required dynamic response.

The pressure available at the output ranges from the supply pressure to a pressure less than the vent pressure. Employing push-pull circuits materially broadens the potential usefulness of the device, and the conservation of flow in multiple staging provides high power efficiency.

FLUID VORTEX AMPLIFIER OPTIMIZATION

by

I. Greber, P. E. Koerper, C. K. Taft

Abstract

A vortex amplifier is designed to obtain maximum flow shutoff capability. Empirical relations are established which describe the maximum flow conditions of the amplifier. They are used to predict the shutoff capability as a function of the amplifier outlet and inlet areas, and consequently to design for maximum shutoff. The optimized amplifier produced a flow shutoff of less than 9 percent maximum flow and was a bistable, hysteretic device.

A non-hysteretic amplifier was designed by modifying the hysteretic amplifier. Its shutoff capability is less than 14 percent of maximum flow.

This research was supported in part by a grant from the ARO Corporation, Bryan, Ohio and in part by the National Aeronautics and Space Administration under NAS Contract 8-11267.

Introduction

The vortex amplifier described herein is a pure fluid device in which a radial main flow is controlled by an tangential control flow. Without viscosity and with azimuthal symmetry the streamlines in the main part of the device would be spirals, and can be regarded as the superposition of a vortex flow and a source flow; hence, the name "vortex amplifier". The device described is geometrically and operationally relatively simple. Its geometry can be completely described by only four non-dimensional parameters. Its maximum and minimum flow limits follow a simple functional behavior, experimentally determined. From this functional behavior one can predict the geometrical parameters at which maximum shutdown capability of the amplifier occurs. This paper discusses the establishment of the flow limit functional behavior and the design of an amplifier for a maximum ratio of maximum to minimum flow rate. The ratio of maximum to minimum flow rate will henceforth be called the "turndown ratio".

Optimization Procedure

The method of optimization of the amplifier is as follows:

1. A geometrical design is chosen based on knowledge of the

characteristics desired in the amplifier. This choice of design will be discussed.

2. Flow through the vortex chamber is described mathematically for the maximum and minimum flow conditions. The equations for these extremes originate from an empirical relation for minimum flow (i.e. when all flow is through the tangential control ports), and viscous orifice flow equations for maximum flow (i.e. when all flow is introduced through the supply inlet annulus).
3. The optimum amplifier is defined as one which maximizes the ratio of maximum flow to minimum flow out of the chamber. This ratio is called the "turndown ratio" and is denoted by $\bar{Q}$.
4. From the above mentioned equations, an expression for the outlet diameter in terms of the supply inlet area at which $\bar{Q}_{max}$ occurs is obtained.
5. Experimental data is used to determine the detrimental effect of the supply inlet annulus area on vortex flow.
6. Tasks 3 and 4 are combined to yield the optimized values of the outlet diameter and inlet area at which $\bar{Q}_{max}$ will occur.
7. Experimental data is used to find the value of $\bar{Q}_{max}$.
8. The effect of the tangential control port area on $\bar{Q}_{max}$ and the shape of the total flow versus control pressure curves is determined experimentally.

Geometrical Design

The geometrical design to be optimized is presented in Figure 1. Supply flow enters through the axial inlet annulus and exits through the two outlet holes whose centers are located at the center of the vortex chamber. Two control ports are used and are spaced 180° apart.

1. The inlet annulus. To obtain maximum flow through the amplifier it is essential that the inlet supply port be as large as possible. The inlet annulus has the advantage of providing a large flow area for relatively small annulus thickness (d_s). Note that in this design only one annulus was used. This was for ease in fabrication. It is possible that two inlets on both sides of the chamber might further increase the turndown ratio. Although there are many advantages to the annular entrance, there is the disadvantage that increasing the annulus opening decreases the effectiveness of the control jet. This effect is crucial in the optimization of the amplifier.

2. The two outlet holes. Two outlet holes are used (instead of the one hole pictured in most conceptual drawings). This is because the restrictive effect of the vortex is almost entirely a function of d_o/d_1. Adding a second hole to the chamber does not alter this ratio in any way but does increase the outlet area considerably. Thus, for a given outlet diameter, twice the flow area is obtained which increases the maximum flow through the amplifier while effectively not changing the minimum flow conditions.
3. Control Ports. Two inlet control ports were used. Tests indicate that the only advantage in more control ports is that of providing an azimuthally more uniform flow pattern. However, the additional uniformity obtained with more than two control ports does not noticeably increase the turn-down ratio. The total control port area appears to be the final determining factor in the control pressure (as shown later), not necessarily the number of control ports.

Empirical Vortex Model and Minimum Flow Rate

The behavior of the amplifier can be described by using the behavior of a non-viscous amplifier to show how the parameters should group, then correcting experimentally for the effects of viscosity. The non-viscous fluid must satisfy conservation of mass and Euler's equation of motion

$$\frac{\partial \rho}{\partial t} + \operatorname{div}(\rho \bar{V}) = 0 \tag{1}$$

$$\frac{\partial \bar{V}}{\partial t} + \bar{V}\frac{V^2}{2} \bar{V} \times (\bar{V} \times \bar{V}) + \frac{1}{\rho} \bar{V} p = 0 \tag{2}$$

Assuming constant density, these equations, with appropriate boundary conditions, are sufficient to determine the flow. Additionally assuming a steady two-dimensional azimuthally symmetric flow, that is

$$\frac{\partial}{\partial t} = \frac{\partial}{\partial \theta} = u_z = 0 \tag{3}$$

one finds that the flow can be regarded as the superposition of a source and a vortex. The pressure difference between any two radii is then given by

$$\frac{2}{\rho}(p_1 - p_2) = \left[\left(\frac{d_1}{d_2}\right)^2 - 1\right]\left[I_{v1}^2 + U_{r1}^2\right] \tag{4}$$

Assuming the flow into the chamber is through only the tangential control ports (this is the condition for minimum flow rate) and using an inlet geometry as pictured in Figure 1,* where the outer wall varies in radius as $r = r_1 - \frac{Wθ}{π}$, and assuming vortex flow pattern is correct up to the outlet hole, the final equation can be written;

$$\left[\frac{2}{\rho} (p_1 - p_o) \right] = V_{in}^2 \left[\frac{1}{\bar{D}^2} - 1 \right] \left[\left(\frac{2Wh}{\pi d_1} \right)^2 + 1 \right] \tag{5}$$

where $\frac{2Wh}{\pi d_1} << 1$ for condition tested.

Taking the pressure difference between the chamber outer radius and the outlet and neglecting $(\frac{2Wh}{\pi d_1})^2$ with respect to unity, equation (5) can be rewritten non-dimensionally as

$$\bar{\Delta P} = 1 \tag{6}$$

To correct the above result, equation (6), for viscous effects, qualitative considerations suggest that

$$\bar{\Delta P} = f \left[\left(\frac{Q}{vh} \right) \left(\frac{w}{d_1} \right) \left(\frac{d_1}{d_o} \right)^{1/2} \right] \tag{7}$$

The right-hand side of (7) is a stretched Reynolds number. Figure 2 shows the experimental data plotted according to equation (7). The experimental data is seen to be well correlated when plotted in this manner, and appears to approach the non-viscous result, $\Delta P = 1$, as the stretched Reynolds number goes to infinity, as one expects.

For later work, it is useful to rewrite equation (7) as a formula for Q_{min}. Noting that Q is equation (7) is Q_{min}, it can be rewritten as

$$Q_{min} = \left[\frac{2Wh}{\sqrt{\bar{\Delta P}}} \right] \left[\frac{\bar{D}^2}{1-\bar{D}^2} \right]^{1/2} \left[\frac{2}{\rho} (p_{ch} - p_o) \right]^{1/2} \tag{8}$$

It is also important to note that $p_{ch} = p_s$ when all flow comes from the control ports; that is, when $Q = Q_{min}$, then also $p_{ch} = p_s$.

Equations (7) and (8) and Figure 2 are valid when there is no entrance annulus. When an entrance annulus is present but there is no entrance supply flow, equation (8) must be replaced by

$$Q_{min} = g(\bar{D}_s) \left[\frac{2Wh}{\sqrt{\bar{\Delta P}}} \right] \left[\frac{\bar{D}^2}{1-\bar{D}^2} \right]^{1/2} \left[\frac{2}{\rho} (p_s - p_o) \right]^{1/2} \tag{9}$$

*Figures start on page 234.

The function $g(\bar{D}_s)$ accounts for the effect of the entrance annulus on the "vortex" flow. Its effect it to increase the throughflow for a given pressure difference. This is equivalent to decreasing the effectiveness of control flow in producing vortex-like motion. A plot of $g(\bar{D}_s)$ is shown in Figure 3.

Maximum Flow Through Chamber

Flow through the chamber is maximum when tangential control flow is zero. Then flow enters only axially through the annulus and may be described by orifice flow equations for two orifices in series.

$$Q_s = \left[\frac{(K_o A_o)^2 (K_s A_s)^2}{(K_c A_o)^2 + (K_s A_s)^2} \right]^{1/2} \left[\frac{2}{\rho} (p_s - p_o) \right]^{1/2} \qquad (10)$$

Note that it is fallacious to talk about a single orifice and that two orifices in series must be used. This becomes obvious later. Rewriting equation (10) in terms defined by Figure 1:

$$Q_s = Q_{max} = (K_s \pi d_1 d_s) \left[\frac{2}{\rho} (p_s - p_o) \right]^{1/2} \left[\frac{\bar{D}^4}{\bar{D}^4 + \left(\frac{2K_s \bar{D}_s}{K_o} \right)} \right]^{1/2} \qquad (11)$$

Optimization of Turndown Ratio

The turndown ratio $\bar{Q} = Q_{max}/Q_{min}$ is obtained by dividing equation (11) by equation (8), and noting that at Q_{min}, $p_{ch} = p_s$. One obtains

$$\bar{Q} = \left(\frac{K_s \pi d_1 d_s}{2wh} \right) \frac{(\sqrt{\Delta P})}{g(\bar{D}_s)} \left[\frac{\bar{D}^2 - \bar{D}^4}{\bar{D}^4 + 4\left(\frac{K_s}{K_o}\right)^2 \bar{D}_s^2} \right]^{1/2} \qquad (12)$$

One can now find $\bar{D}$ such that $\bar{Q}$ is a maximum by setting $\partial\bar{Q}/\partial\bar{D} = 0$, where all quantities other than $\bar{D}$ are held fixed in the differentiation. This means that the optimization is made at a fixed, but unspecified, value of stretched Reynolds number. It remains for a posteriori experiments to demonstrate that the optimum geometry so chosen remains optimum over a suitable Reynolds number range. The result is

$$\bar{D}^2_{opt} = -4\left(\frac{K_s}{K_o}\right)^2 \bar{D}_s^2 + 2\frac{K_s}{K_o}\bar{D}_s\left[1 + 4\left(\frac{K_s}{K_o}\right)^2 \bar{D}_s^2\right]^{1/2} \tag{13}$$

Since $2\frac{K_s}{K_o}\bar{D}_s$ is small, one has the useful approximation

$$\bar{D}_{opt} = \left[2\frac{K_s}{K_o}\bar{D}_s\right]^{1/2} \tag{14}$$

Equation (13) is equivalent to the statement

$$K_o A_o = K_s A_s \tag{15}$$

so that, roughly speaking, the inlet and outlet areas should be about the same size.

Having found now the inlet and outlet areas should be related, the optimization can be continued by putting this relation back into the expression for the turndown ratio $\bar{Q}$, equation (12), and again seeking a maximum of $\bar{Q}$. Using equation (14), equation (12) becomes

$$\bar{Q} = \frac{K_o \pi d_1^2}{4Wh}\sqrt{\Delta\bar{P}}\left\{\frac{\left[\frac{K_s}{K_o}\bar{D}_s - 2\left(\frac{K_s}{K_o}\right)^2\right]^{1/2}}{g(\bar{D}_s)}\right\} \tag{16}$$

Now holding all quantities other than $\bar{D}_s$ fixed, a maximum of $\bar{Q}$ occurs at a maximum of the factor in the braces $\{\}$ in equation (16). This factor is shown in Figure 4, for $K_s = K_o$. Under these conditions a maximum value of $\bar{Q}$ occurs where $\bar{D}_s = 0.045$.

Correspondingly,

$$\bar{D} = \left[2\frac{K_s}{K_o}\bar{D}_s\right]^{1/2} = 0.3$$

Summarizing:

$$\begin{aligned} \bar{D}_{s\ opt} &= 0.045 \\ \bar{D}_{opt} &= 0.3 \end{aligned} \tag{17}$$

An optimum choice of $\bar{H}$ requires a Reynolds number study similar to that which was made for the no-supply-flow limit. This was not

done. Qualitative tests indicated that a range of $\bar{H}$ values could be used without seriously changing the operation of the amplifier. For the final amplifier built, $\bar{H} = 0.1875$ was used.

Experimental Results for "Optimum Amplifier"

A vortex amplifier was then built to the optimized specifications ($\bar{D} = .3$, $\bar{D}_s = .045$ and $\bar{H} = .1875$). The control port widths w were designed to be adjustable. Then a series of tests were run with air at low supply pressure (p_s=1.5 psig) to determine the total turndown ratio of the amplifier and the effects of $\bar{W}$ on $\bar{Q}$ and $\bar{P}$ and the shape of the of the Q_T versus P_c curves. The results of these curves are given in Figures 5,6, and 7.

A turndown ratio of 10 was obtained for the amplifier with a pressure ratio $\bar{P} = 2$. As the control port area $2\bar{W}\bar{H}$ was decreased the turndown ratio increased slightly, but the $\bar{P}$ ratio increased dramatically. An increase in the area $2\bar{W}\bar{H}$ caused the opposite effect. Since the amplifier is much more useful with $\bar{P}$ close to 1, it is recommended that relatively large control port areas be used. This will, of course, depend on the actual use of the amplifier and it is suggested that Figures 5,6, and 7 be used as a guide for obtaining the operation desired.

Extension of Theory to One Outlet Hole Amplifier

The derivation of a single outlet hole amplifier is identical to the double case with one exception.

$$A_o = \left[2 \frac{K_c w d_o^2}{4} \right]_{2 \text{ holes}} = \left[K_o \frac{w d_o^2}{4} \right]_{1 \text{ hole}} \tag{18}$$

By going through the same procedure as before the identical results are obtained, that is

$$K_o A_o = K_s A_s \text{ and } \bar{P}_{1\,\text{hole}} = 0.045 \tag{19}$$

This leads to the result that

$$\bar{D}_{1\,\text{hole}} = 0.425$$

No experimental tests were made with this geometry. However, the resulting turndown ratio can be predicted from 2 hole data.

$$\left(\frac{Q_{max}}{Q_{min}}\right)_{1\ hole} \approx \left(\frac{\bar{D}_2}{\bar{D}_1}\right)\left[\frac{Q_{max}}{Q_{min}}\right]_{2\ holes}$$

$$Q_{max} \approx \left(\frac{.3}{.425}\right)(11.5) = 8.1\ \text{(Predicted)} \qquad (20)$$

Development of Nonhysteresis Vortex Amplifier

The amplifier just optimized was designed to obtain maximum turndown with little consideration of the shape of the Q_T versus p_c operating curve. As a result a high turndown device was designed but it had an unstable hysteretic area in its operating range (see Figure 5).

Increasing the control port area decreases but does not eliminate the hysteretics (see Figure 5). It was necessary to reduce the size of the outlet hole to achieve the desired non-hysteretic amplifier.

Tests were made to determine the maximum outlet hole size allowable with no hysteresis, with a chamber diameter of one inch and with air at p_3 = 3 psig. It was found that the maximum outlet hole diameter ratio $\bar{D}$ (for two outlet holes) was roughly 0.15. Above a value of $\bar{D}$ = 0.15 hysteresis could not be removed by increasing the control port area. Figure 9 shows how the hysteresis varies with increasing $2\bar{W}\bar{H}$, for $\bar{D}$ = 0.14 (i.e. near the upper limit of useful $\bar{D}$).

A maximum turndown ratio for the nonhysteretic amplifier was found to be 7:1. The pressure ratios, $\bar{P}$, were always less than 2 and for large control port areas approached 1.

It is worthwhile to note that the limiting case for a useful non-hysteretic amplifier is not necessarily lack of hysteresis. Noise in the amplifier is present in the high gain region of the operating curve.

If this amplifier is to be a highly sensitive device as in the case of rate sensors, this noise, which is greater at larger diameter ratios, will make the higher turndown ratio amplifiers difficult to use.

Figure 10 presents the final design arrived at for the non-hysteretic amplifier.

LIST OF SYMBOLS

A	area
d	diameter
d_s	supply annulus width
$\bar{D}$	$= \frac{d_o}{d_1}$
$\bar{D}_s$	$= \frac{d_s}{d_1}$
$g(\bar{D}_s)$	experimental function of $\bar{D}_s$
h	height of chamber
$\bar{H}$	$\frac{h}{d_1}$
K	orifice coefficient
K_Q	$\frac{K_c \bar{H}}{K_o \bar{W}}$
M	arbitrary constant
p	pressure
$\bar{P}$	$\frac{P_c}{P_s}$
$\overline{\Delta P}$	nondimensional pressure function
Q	volumetric flow rate
Q'	flow normalized by flow across an orifice
$\bar{Q}$	$= \frac{Q_{max}}{Q_{min}}$
r	radius
R_e	$= \frac{Q}{\nu h}$, Reynolds number
U	= velocity component
$\bar{V}$	total velocity vector
w	control port width
$\bar{W}$	$= \frac{w}{d_1}$
∇	gradient vector
θ	angle

ρ	mass density
$()_c$	measurement at the control port
$()_{ch}$	measurement at the chamber outer radius
$()_N$	normalising quantity
$()_{in}$	measurement at inlet
$()_o$	measurement at outlet
$()_s$	measurement at supply port
$()_1$	measurement at radial boundary (1)
$()_2$	measurement at radial boundary (2)
$\bar{()}$	dimensionless quantity

REFERENCES

1. Koerper, P. E.,M.S. Thesis Dissertation, Case Institute of Technology, 1965.

2. Koerper, P. E., Progress Report to the ARO Corp., Case Institute of Technology, September, 1964.

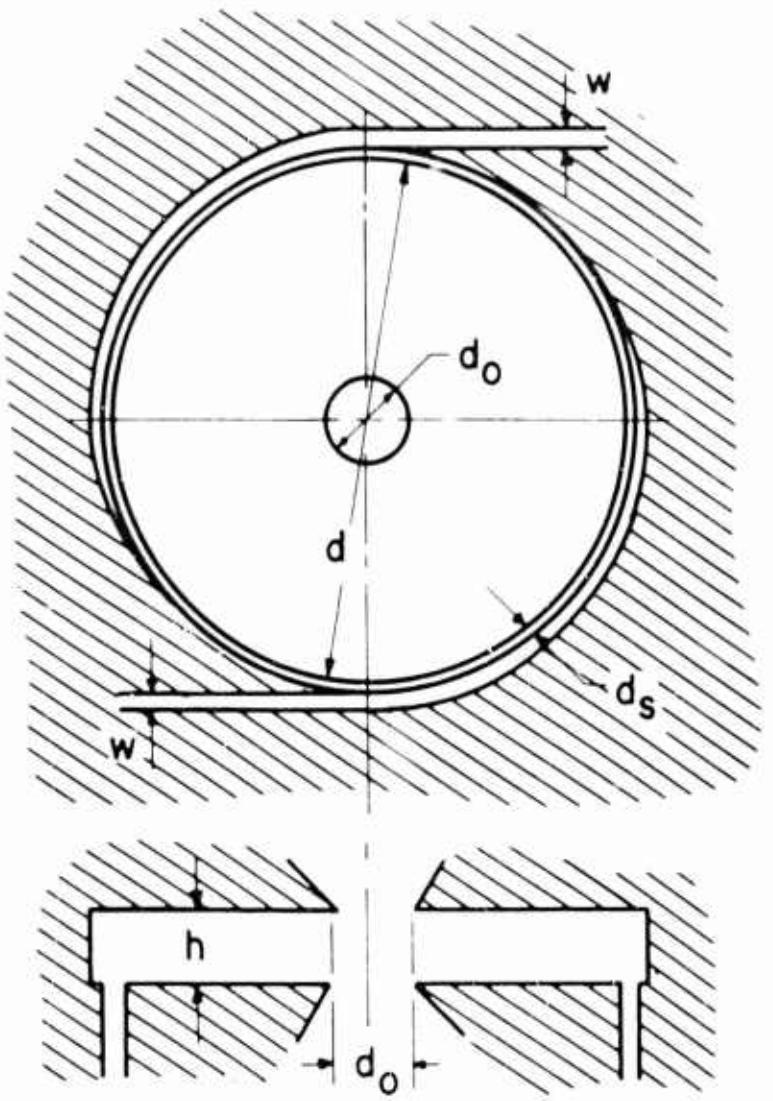

WHERE

$$\overline{D} = \frac{d_o}{d_1} \quad , \quad \overline{D_s} = \frac{d_s}{d_1} \quad , \quad \overline{H} = \frac{h}{d_1} \quad , \quad \overline{W} = \frac{w}{d_1}$$

FIGURE 1, PROPOSED VORTEX AMPLIFIER DESIGN TO BE OPTIMIZED

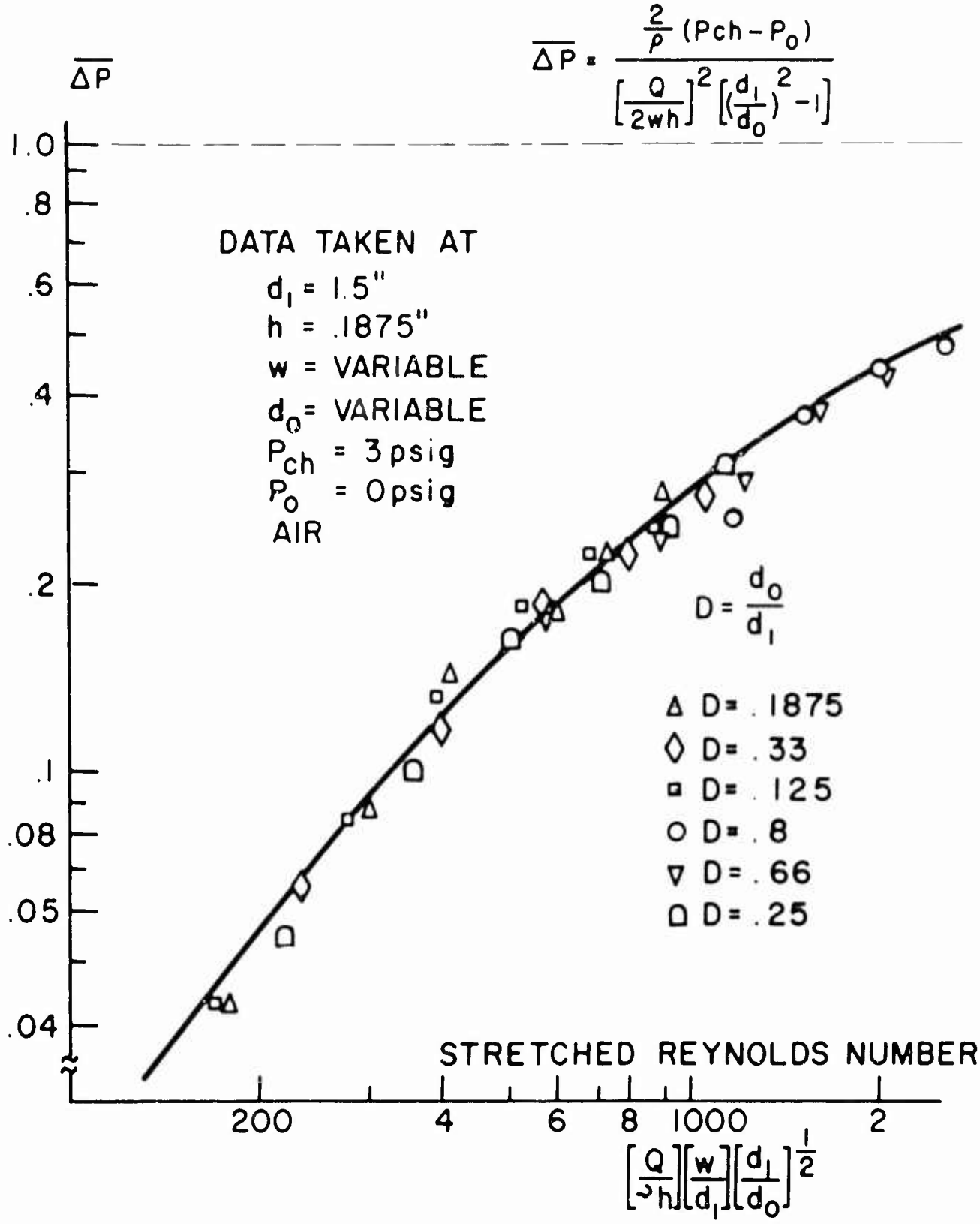

FIGURE 2, EXPERIMENTAL DATA SHOWING NONDIMENSIONAL $\overline{P}$ VERSUS THE STRETCHED REYNOLDS NUMBER

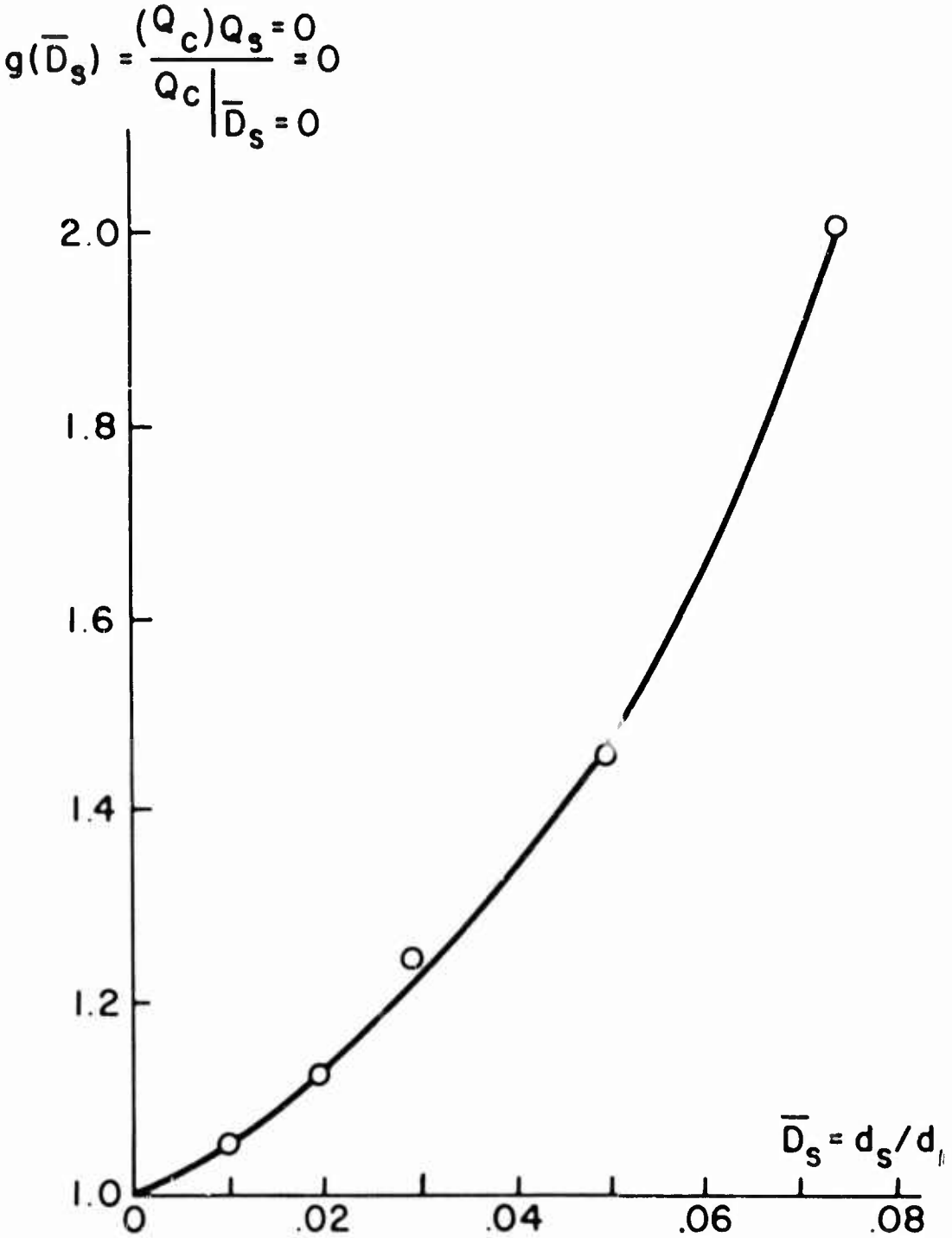

FIGURE 3, EFFECT OF INLET ANNULUS ON VORTEX FLOW

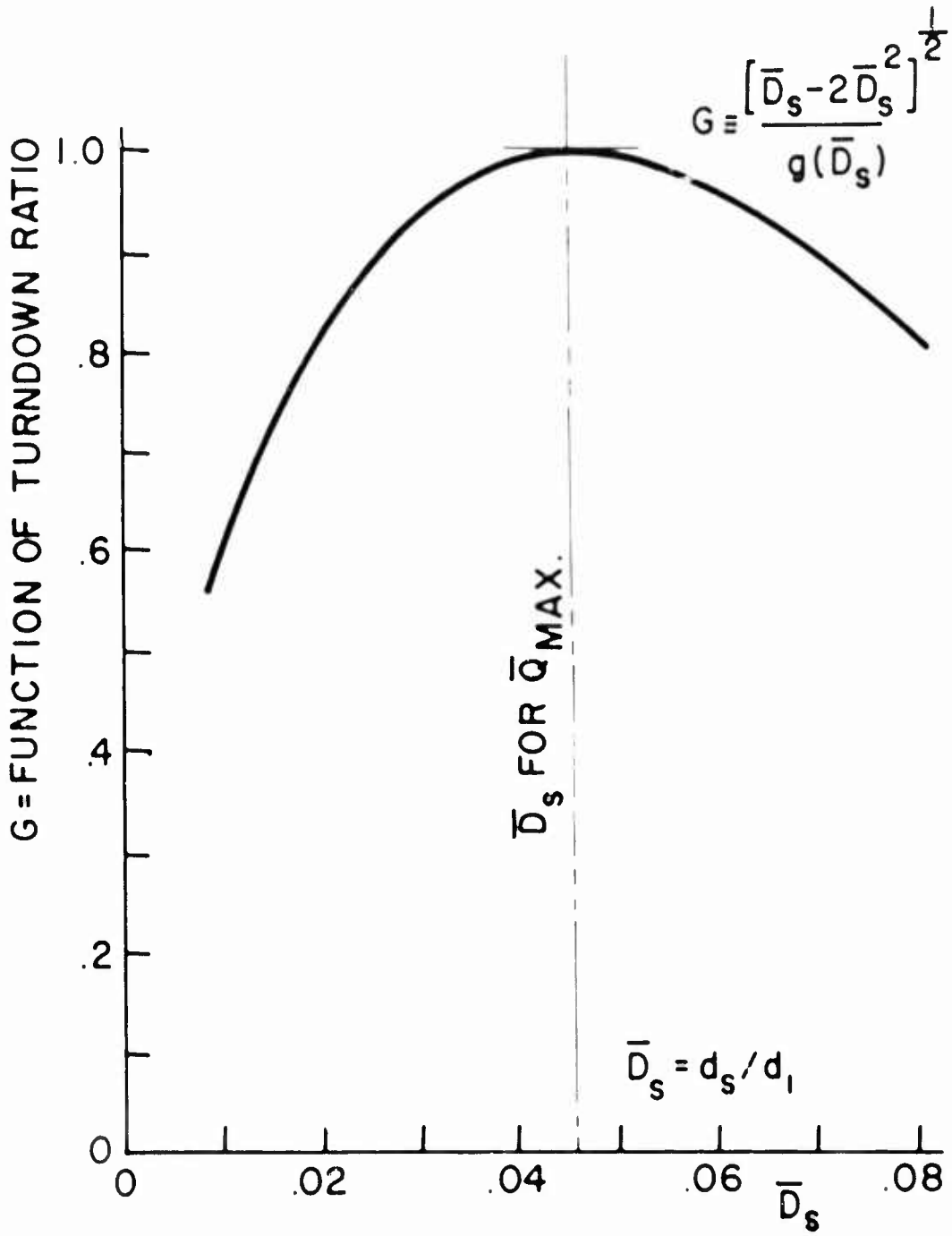

FIGURE 4, EFFECT OF $\bar{D}_s$ ON TURNDOWN RATIO HOLDING $K_o A_o = K_s A_s$ & $K_o = K_s$

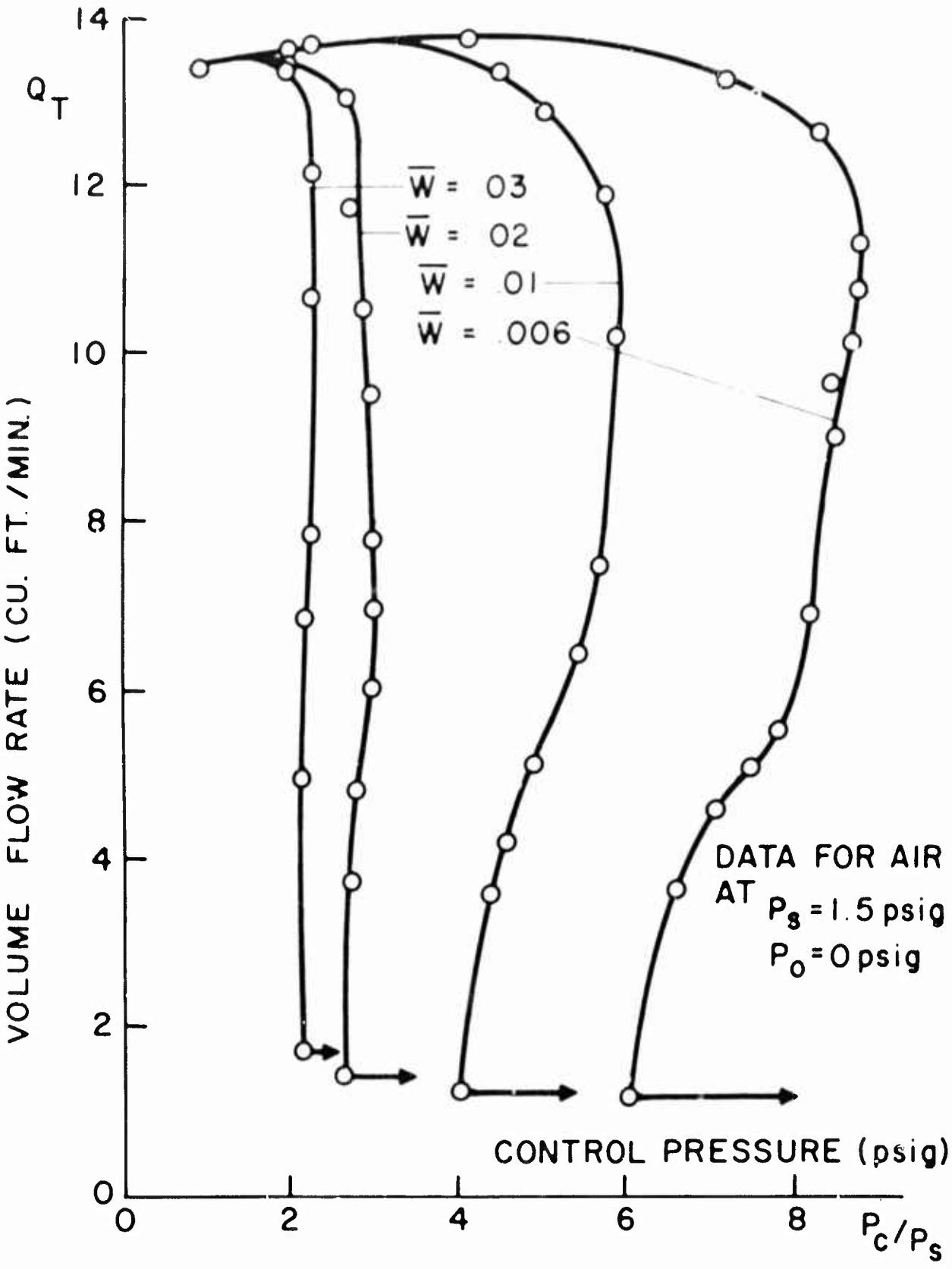

FIGURE 5, FLOW VERSUS PRESSURE CURVE WITH AIR FOR FINAL OPTIMIZED AMPLIFIER AS SHOWN IN FIGURE 8

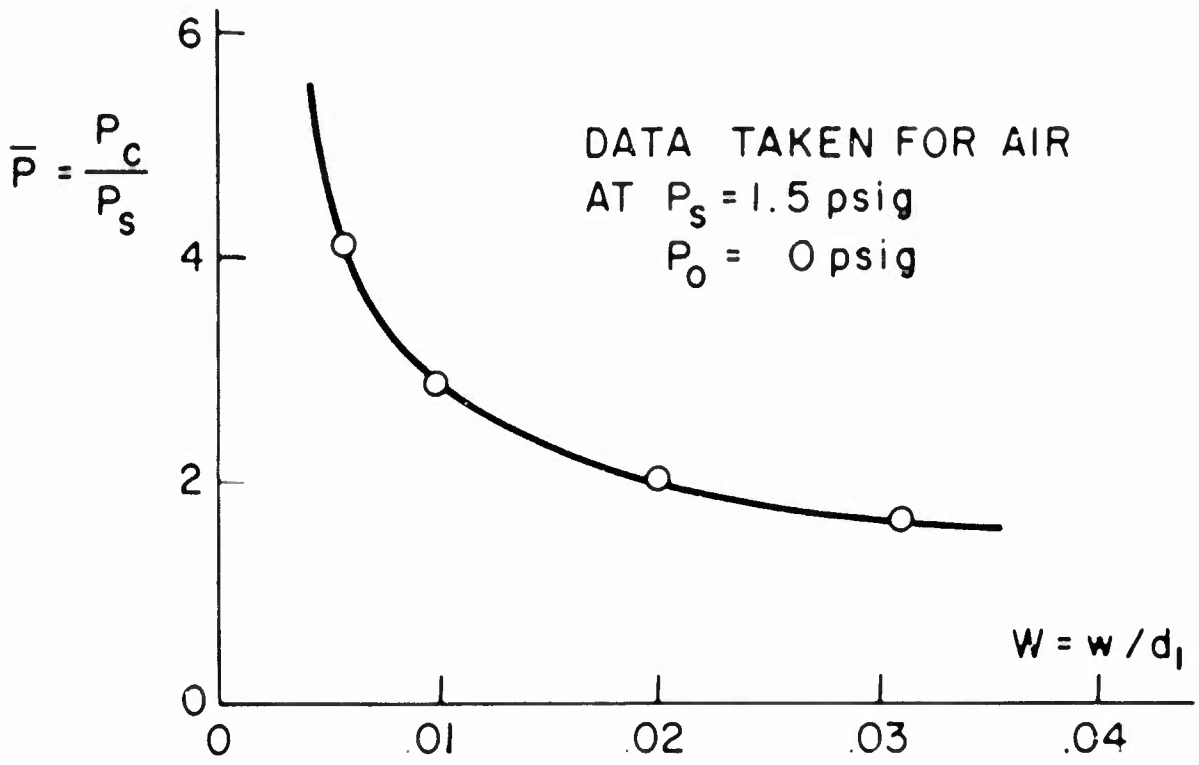

FIGURE 6, $\bar{P}$ VERSUS W FOR AMPLIFIER DESIGN SHOWN ON FIGURE 8

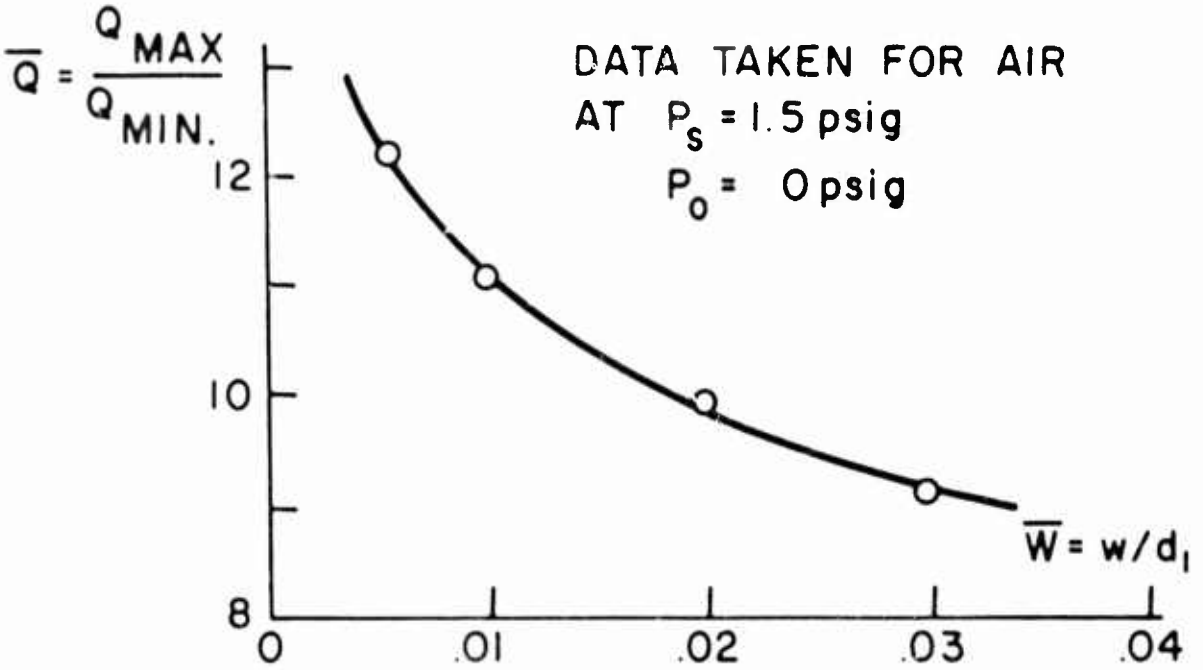

FIGURE 7, $\bar{Q}$ VERSUS W FOR AMPLIFIER DESIGN SHOWN ON FIGURE 8

DATA TAKEN AT

$d_1 = 1"$

$h = .1875"$

NOTATION

$\bar{D} = \frac{d_o}{d_1}$

$\bar{W} = \frac{w}{d_1}$

$\bar{H} = \frac{h}{d_1}$

$\bar{Q} = \frac{Q_{MAX}}{Q_{MIN}}$

$\bar{D}_s = \frac{d_s}{d_1}$

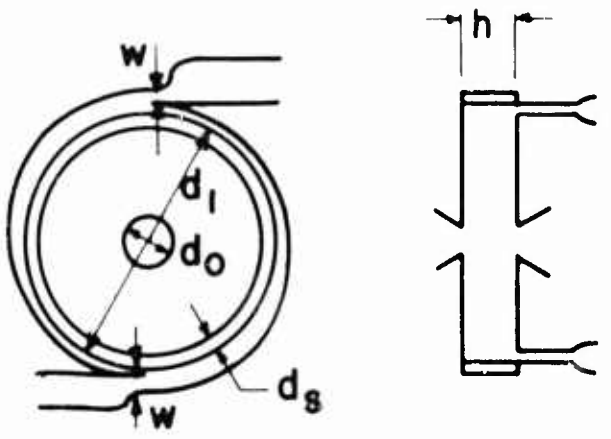

PARAMETER	TWO HOLE CONFIRMED	ONE HOLE
$\bar{D}$	.3	.425
$\bar{D}_s$	.045	.045
EXPERIMENTAL	EXPERIMENTAL	PREDICTED
$\frac{K_s}{K_o}$	1	1
$\bar{Q}$	11.5:1	8:1

FIGURE 8, FINAL VORTEX AMPLIFIER DESIGN OPTIMIZED FOR MAXIMUM TURNDOWN (HYSTERETIC)

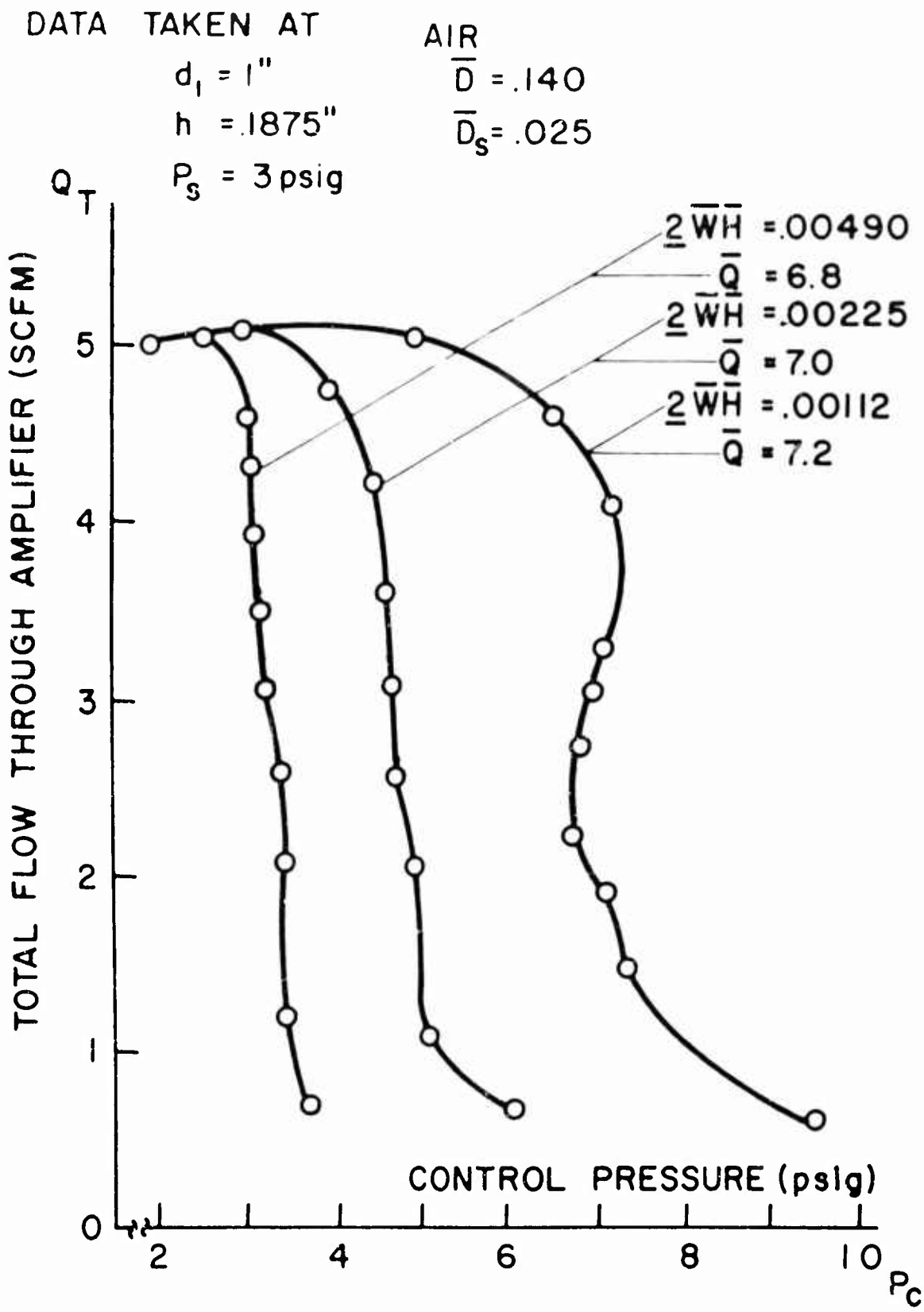

FIGURE 9, LIMITING CASE OF USEFUL NONHYSTERETIC AMPLIFIER

NOTATION

$$\bar{D} = \frac{d_o}{d_1}$$

$$\bar{D}_s = \frac{d_s}{d_1}$$

$$\bar{H} = \frac{h}{d_1}$$

$$\bar{W} = \frac{w}{d_1}$$

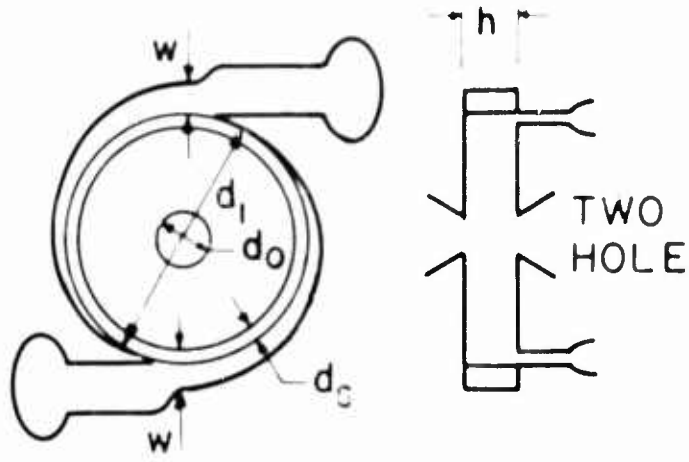

DATA TAKEN AT

$d_1 = 1"$

$h = .1875"$

PARAMETER	DESIGN
$\bar{D}$	.11 – .14
$\bar{D}_s$	.045
$\bar{Q}$	6.4 7.0
$2\bar{W}\bar{H}$	.0025

FIGURE 10, FINAL DESIGN FOR NONHYSTERECTIC VORTEX AMPLIFIER

CHARACTERISTICS OF A VORTEX DEVICE AND THE VORTEX-BREAKDOWN PHENOMENON

by

Turgut Sarpkaya

University of Nebraska, Lincoln, Nebraska

The results of an investigation of the forced and periodic breakdown of a confined vortex by another vortex rotating in the opposite direction are presented. The vortex tube consists of two chambers connected by a short conduit through streamlined transitions. The upstream end is closed by a plain wall and a circular orifice is provided at the downstream end. The swirling flow and the breaker-vortex are generated by introducing varying proportions of air or water through tangential ports located near the upstream and downstream walls of the unit. The cases of single-breakdown and periodic-breakdown are explored and typical data are presented for each case.

Possible applications of the device are several—switching, binary counting, pressure modulation, and speed governing. The key to the device's versatility lies in its ability to produce a sharp and strong signal at the time of vortex breakdown. When a counter jet is applied or when the device is rotated, and the circulation created by the jet or the rotation reaches the critical value required, the flow through the orifice switches from the subcritical, hollow-cone regime to supercritical power-jet regime and as such the device works as a reed switch or signal generator for a speed governor system. The output remains locked in position until the intensity of the counter jet or the rate of rotation is decreased. When the downstream tangential port is connected to a Helmholtz resonator, a periodic vortex breakdown is achieved and in this case the device works as a binary counter or pressure modulator. The frequency of oscillation is determined by the inertance of the feedback path and the capacitance of the resonator system.

INTRODUCTION

The vortex breakdown phenomenon, an abrupt change of flow structure at some position along the axis of a longitudinal vortex, and the periodic oscillations associated with it have been observed both in separated flow above sweptback lifting surfaces and in confined swirling flows in "vortex whistles"[1] and cyclone separators.[2] The present interest in the development of nuclear rocket propulsion using gaseous-core nuclear reactors[3], electrical power generation using magnetohydrodynamic

effects[4], vortex-valves[5], and pure fluid pressure modulators for pneumatic-amplifier systems[6] have provided an added incentive for research on confined steady vortex flows in general and on swirling flows with temporal and/or spatial periodicity in particular.

Although the theoretical understanding of the vortex breakdown phenomenon is still lacking, an increasing number of experimental observations of isolated studies are being reported in the literature. Vonnegut[1] was probably the first to describe this phenomenon. He constructed simple whistles that produced sound "by the escape of a vortex from the open end of a tube." He found that the frequency of the sound depended almost linearly on the rate of flow. Subsequently, studies were reported by Suzuki[7], Smith[8], Lambourne and Bryer[9], Harvey[10], Chanaud[11], and Gore and Ranz[12]. Theoretical studies, based essentially on small perturbation analysis of the inviscid equations of motion, were carried out by Michelson[13], Squire[14], Howard and Gupta[15], and Gartshore[16]. These analyses suggested that the vortex breakdown may be caused by spatial amplification of small disturbances and that it is a gradual rather than an abrupt change in the flow structure. Benjamin[17, 18], departing radically from previous theories, considered the breakdown to be an abrupt and unidirectional transition of finite magnitude between two dynamically conjugate states of flow and thus analogous to the hydraulic jump in open-channel flow. Although Harvey's[10] observations of flow reversal on the tube axis indicate the inception of a critical phenomenon and thus lend some experimental support to Benjamin's[17] analysis, the recent and rather comprehensive work of Chanaud[11] on temporally periodic motion in a vortex whistle and cyclone separator suggests that both the flow reversal and the amplification of small disturbances contribute to the hydrodynamic instability of confined swirling flows. This suggestion is, as pointed out by Chanaud[11], in conformity with that made earlier by Gartshore[16] on theoretical grounds.

In the present study the vortex breakdown, solitary or periodic, is initiated and controlled by another vortex rotating in the opposite direction. It is hoped that the information obtained from the controlled or forced-breakdown, as opposed to natural-breakdown, of the swirling flows will shed further light on this complex, time-dependent, three-dimensional phenomenon.

EXPERIMENTAL ARRANGEMENT

A schematic diagram of the confined swirling flow apparatus is shown in Fig. 1. Units of various sizes were built of plexiglass and carefully polished inside and out. The upstream end of the unit was closed by a plane wall and a hypodermic needle was attached at the center for the purpose of introducing a dye filament or dense smoke. A circular, sharp-edged orifice was provided at the center of the downstream wall. The swirling flow and the breaker-vortex were generated

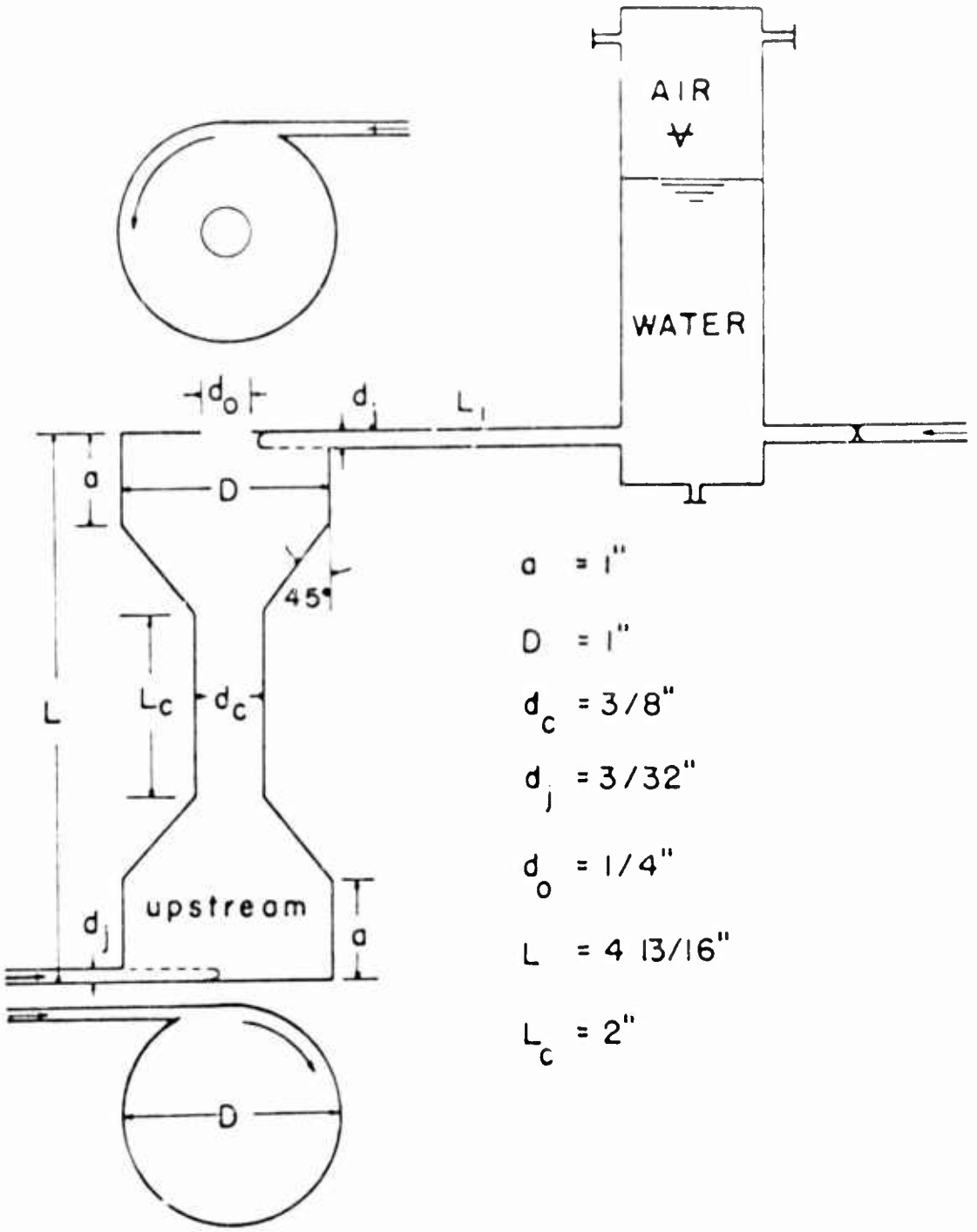

FIG. 1 SCHEMATIC DRAWING OF THE TEST APPARATUS

by introducing varying proportions of air or water through tangential ports located near the upstream and downstream walls of the unit.

The system, as described so far, was sufficient for the exploration of the first phase of the study, namely the forced vortex breakdown. The surge-chamber shown in Fig. 1 was incorporated into the system only during the study of the periodic vortex breakdown. It consisted of a fluid inductance (long, low resistance path) in series with a fluid capacitance (volume), capable of holding varying amounts of air. Such a chamber is referred to ordinarily as a Helmholtz resonator.

The flow rates were determined by means of calibrated rotameters. The pressures on the wall of the upstream and downstream chambers and in the resonator were measured by pressure transducers and recorded simultaneously by means of an amplifier-recorder assembly.

Experimental Procedure and Observations

The first case explored in the experimental study was that of the "forced vortex breakdown". For this purpose the downstream port was connected directly to the rotameter, i.e. the surge-chamber was taken out of the system. In order to create a swirling flow the upstream jet was turned on and the downstream inlet was kept closed. When a very small swirl was produced, its existence could be detected easily by means of the dye filament introduced through the hypodermic needle. For very small Reynolds numbers* (Re $\sim$ 400), the dye filament proceeded downstream along the axis of the unit in the form of a spiraling sheet as shown in Figs. 2a and 2b. As the intensity of the swirl was increased, a tiny air core formed at the orifice and the end of the air core darted irregularly short distances back and forth. The emergent jet diverged in the form of a smooth hollow cone (angle of divergence = 82 deg.). With a further increase of the swirl, the end of the air core moved upstream and attached to the center of the upstream wall. The air core did not remain in the form of a long smooth tube coincident with the axis of the vortex tube, but developed spiraling standing waves. These waves and the shape of the emerging hollow jet may be seen in Fig. 3.

Following the establishment of a swirling flow, the downstream jet was turned on slightly and the upstream and downstream wall pressures and the flow rate were recorded. The downstream pressure decreased slowly but the upstream pressure remained nearly constant. The dye introduced into the downstream supply line was captured by the main swirling flow as depicted schematically in Fig. 4a. As the velocity of the downstream jet was increased in small steps, the intensity of the swirl in

---

*Reynolds number is based on the diameter of the connecting tube and the average axial velocity.

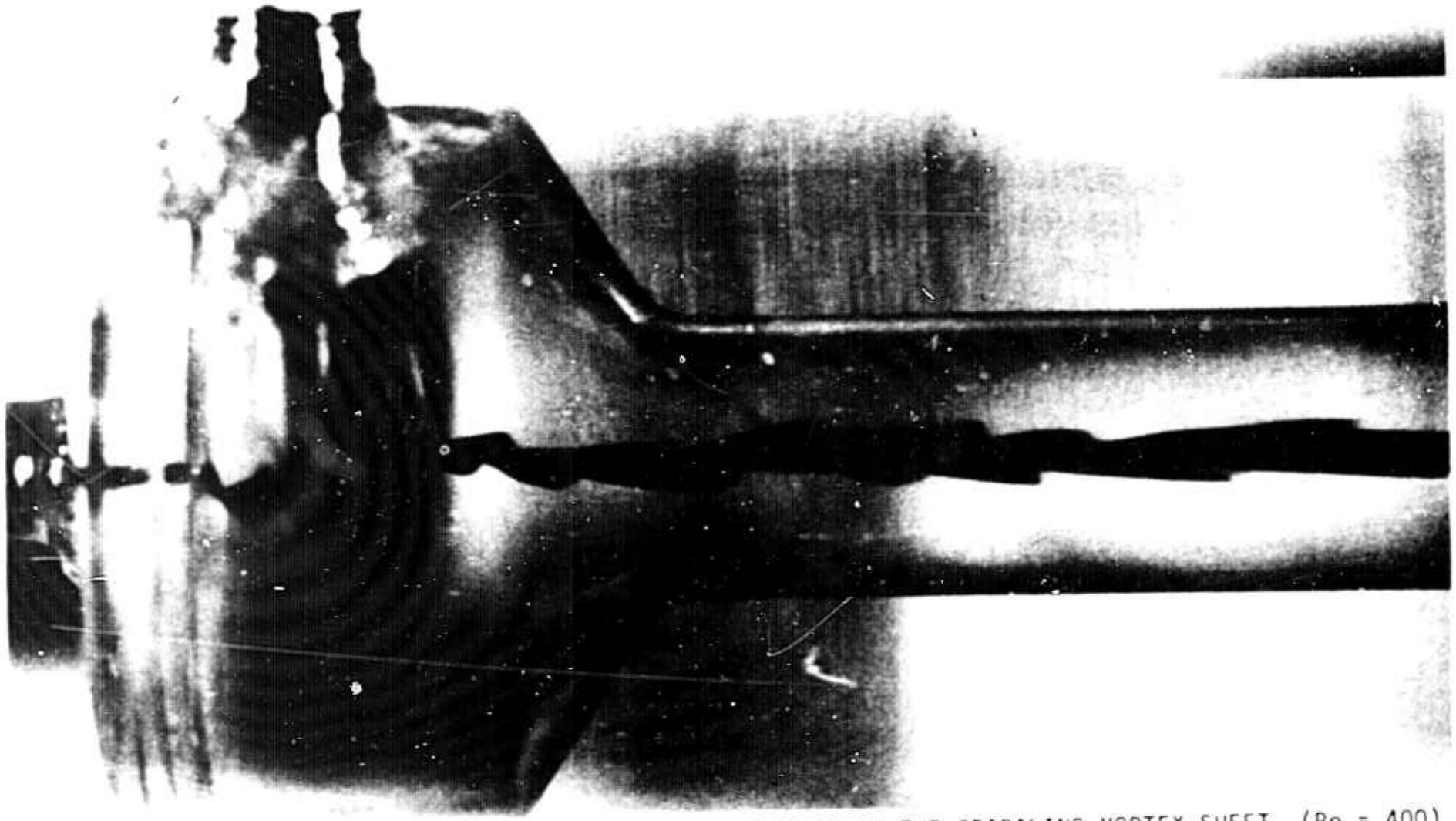

FIG. 2A PICTURE OF THE SPIRALING VORTEX SHEET, (Re = 400)

FIG. 28 PICTURE OF THE SPIRALING VORTEX SHEET, (Re = 600)

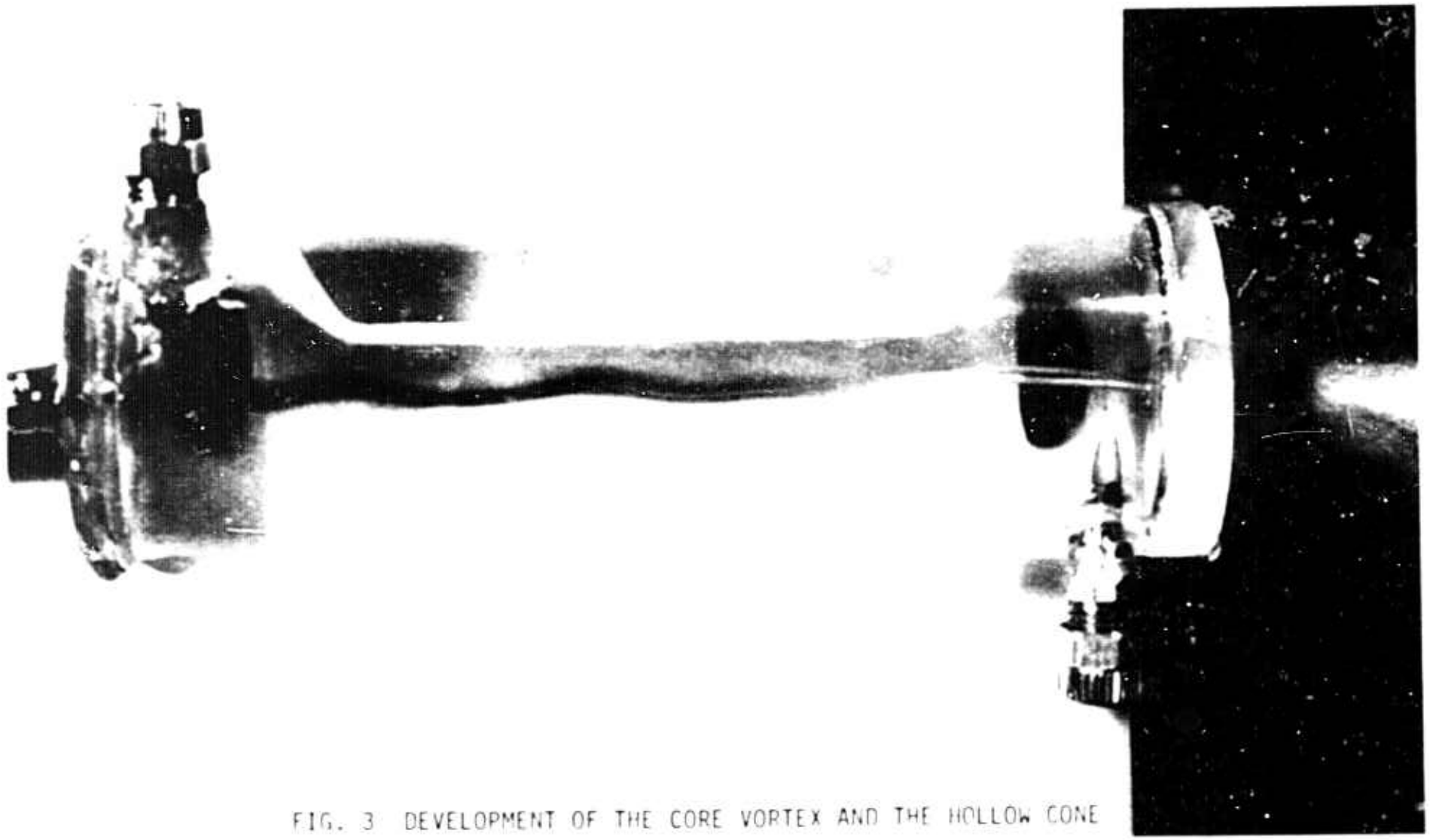

FIG. 3 DEVELOPMENT OF THE CORE VORTEX AND THE HOLLOW CONE

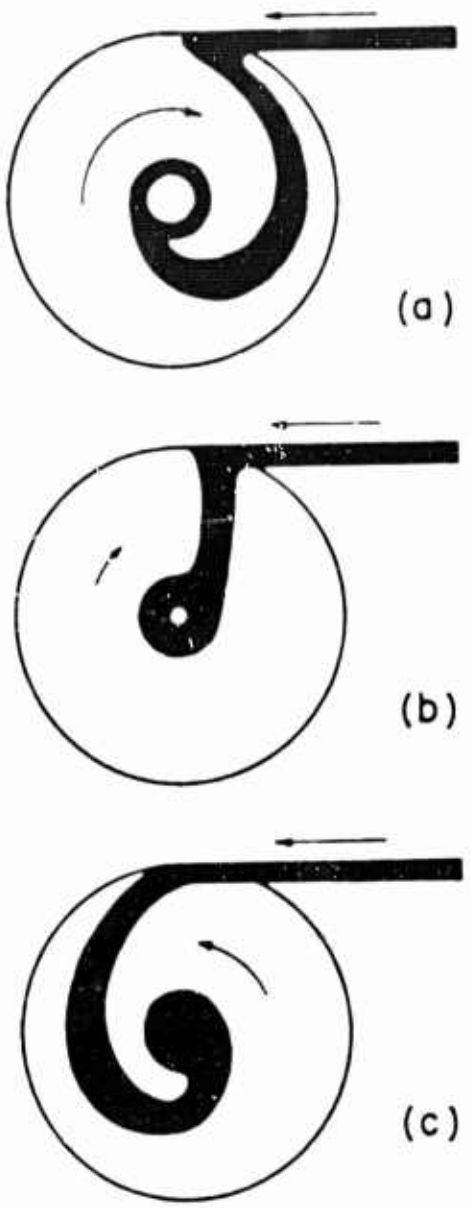

FIG. 4 EVOLUTION OF THE DOWNSTREAM VORTEX PRECEDINC VORTEX BREAKDOWN

the downstream chamber decreased and the dye filament reached the air core more quickly and along a line closer to the radial line joining the axis of the unit and the downstream inlet port as shown in Fig. 4b. With a further slight increase in downstream jet velocity, the flow pattern in the downstream chamber changed abruptly. This change, aside from momentarily producing a sharp noise, eliminated the air core and the hollow cone, sharply lowered the wall pressure in the downstream chamber to a minimum, and rendered the emergent jet fully turbulent (see Figs. 4 and 5). Despite this abrupt and rather drastic change the upstream wall pressure remained nearly constant. Further increase of the downstream jet velocity increased the downstream wall pressure and created a vortex in the downstream chamber whose rotation was in the opposite direction to that of the upstream vortex. When the downstream wall pressure was made identical to that which prevailed at the start of motion (downstream jet closed), by increasing the intensity of the counter vortex, neither the upstream pressure nor the turbulent jet showed any observable changes. In short, a new flow condition has been established which was identical, as far as the two wall pressures were concerned, with that obtained originally by the main swirling flow, but drastically different from the original state as far as the emergent jets and flows in the downstream chamber were concerned.

The second case explored was that of the "periodic vortex breakdown". For this purpose the downstream port was connected to the outlet of the Helmholtz resonator and the valves on top of the air chamber and on the inlet line of the resonator were closed. Once again a swirl was created in the vortex tube and an emergent hollow jet was established. During this time the water coming from the downstream port partly filled the resonator and reached a constant level.

Following the establishment of a steady-state, the flow into the resonator was turned on and increased in small increments. The incoming flow increased the pressure in the air chamber and forced the downstream jet to inject a weak current into the downstream chamber. This current was carried to the exhaust hole with a spiraling motion. As the valve leading to the resonator was opened gradually, the secondary current joined the orifice in a more nearly radial direction and at a critical state, stopped abruptly the vortex motion in the downstream chamber. The events following this abrupt change were similar to those described previously in connection with the single-breakdown. The sudden and significant drop in pressure in the downstream chamber increased the pressure gradient between the resonator and the downstream port. Consequently, the velocity of the downstream jet and hence the intensity of the counter-vortex in the downstream chamber increased rapidly. This in turn decreased both the discharge coefficient of the orifice and the pressure in the air chamber. It is significant to note that during these and subsequent changes, the pressure and the flow rate at the upstream chamber and the flow into the surge tank remained nearly constant*. The

---

*The change in P_1 was approximately 3%. The change in the flow rate into the resonator was approximately 2%.

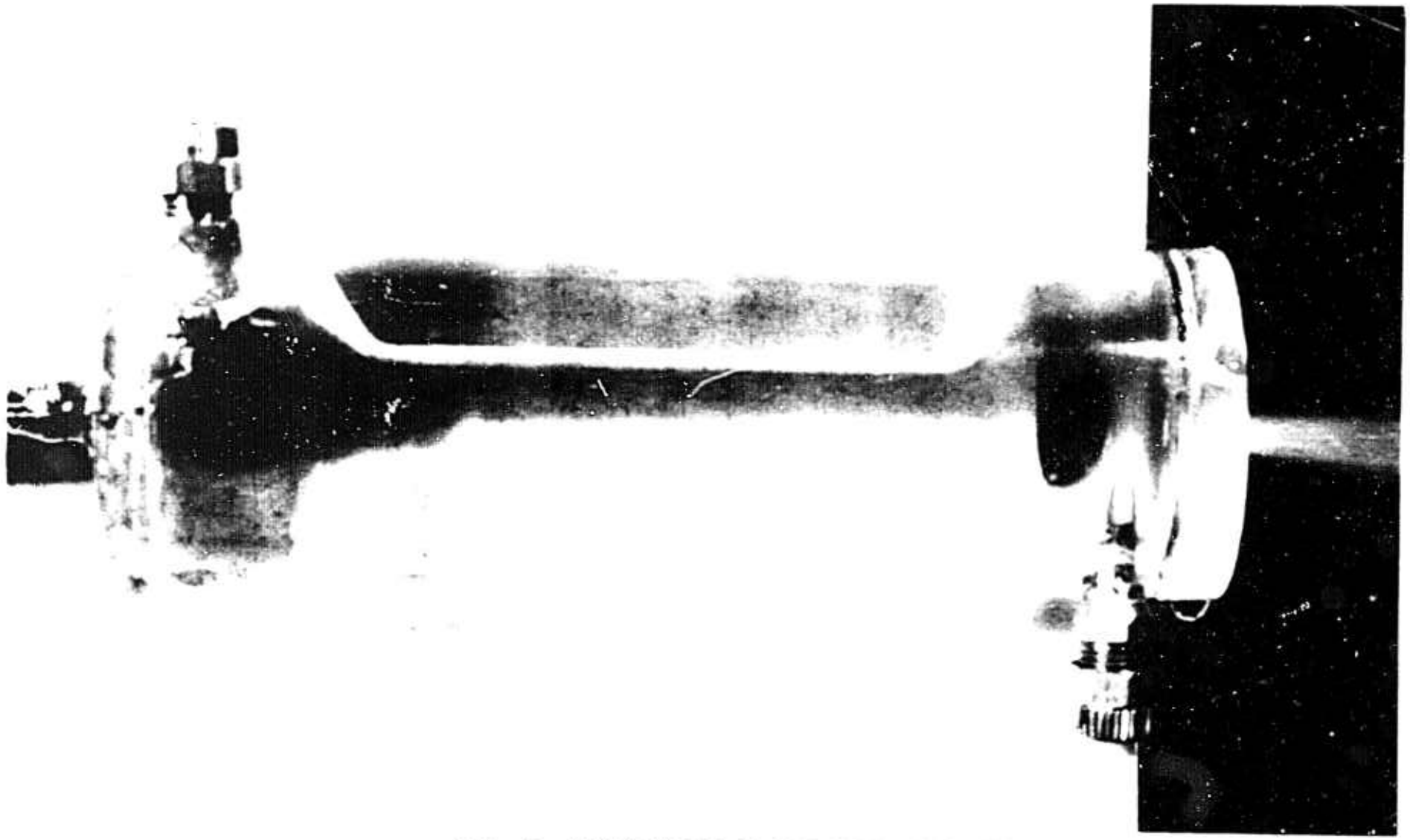

FIG. 5 DEVELOPMENT OF THE TURBULENT JET

gradual increase of the downstream pressure and the decrease of pressure in the air chamber reduced the velocity of the downstream jet. When a critical state was reached, the flow in the vortex tube changed abruptly to its initial form. The sense of rotation of flow in the downstream chamber became identical with that of the original swirling flow. This increased the stagnation pressure at the downstream port above the pressure in the air chamber and developed a reverse flow in the tube connecting the vortex tube to the resonator. The reverse flow as well as the flow entering the resonator at a constant rate from its upstream inlet increased the pressure in the air chamber. When a critical maximum pressure was reached, the fluid rushed from the surge tank to the downstream port through the connecting tube and once again charged the flow and pressure in the downstream chamber of the vortex tube. This action completed the end of a cycle of the periodic oscillation. To change the frequency of this oscillation, everything was kept constant except that some air was let out of the air chamber through the valve previously provided. With this, oscillatory motion automatically resumed and continued with clock-like regularity (see Fig. 6). To decrease the frequency, an inverse procedure was followed, i.e. some compressed air was introduced into the air chamber.

The experiments described above were repeated with air as the working fluid. It suffices to note that everything was kept the same except that the inlet and outlet near the top of the resonator were used for obvious reasons and that the frequency was changed by admitting or removing some water into or out of the resonator through the valve at the bottom of it. Once again an oscillation of constant frequency was obtained.

DISCUSSION OF RESULTS

a. Forced Vortex Breakdown

The experimental data obtained through the procedure described previously was plotted in various dimensionless forms. In the following, the relationships between the pressure, flow rate, and the discharge coefficient of a typical vortex-tube are discussed*.

Figure 7 shows, as an example, the normalized downstream wall pressure $\bar{P}$ as a function of the normalized downstream flow rate $\bar{Q}$. It is observed that as $\bar{Q}$ increases, $\bar{P}$ decreases slowly at first and then abruptly when the vortex in the downstream chamber breaks down and the

---

*The characteristics of various other vortex-tubes are discussed in an internal report presented to Harry Diamond Laboratories, Report No. 2, July, 1964.

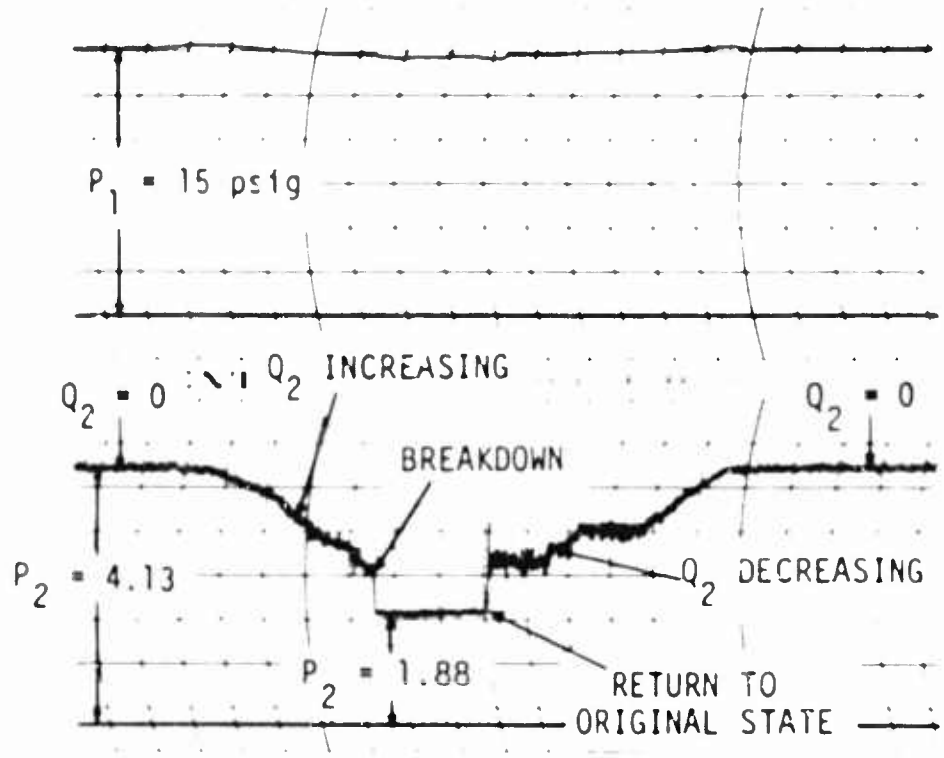

FIG. 6a VARIATION OF THE DOWNSTREAM WALL PRESSURE IN THE CASE OF SINGLE VORTEX-BREAKDOWN

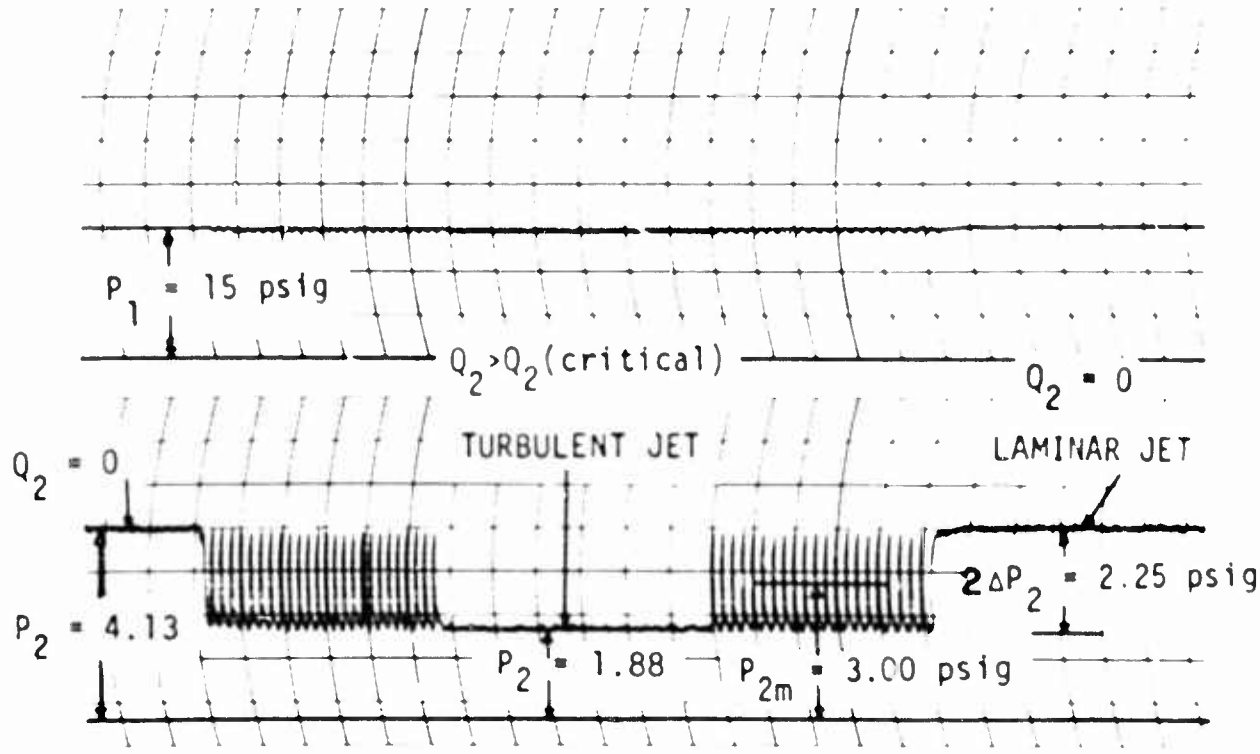

FIG. 6b VARIATION OF THE DOWNSTREAM WALL PRESSURE IN THE CASE OF PERIODIC VORTEX-BREAKDOWN

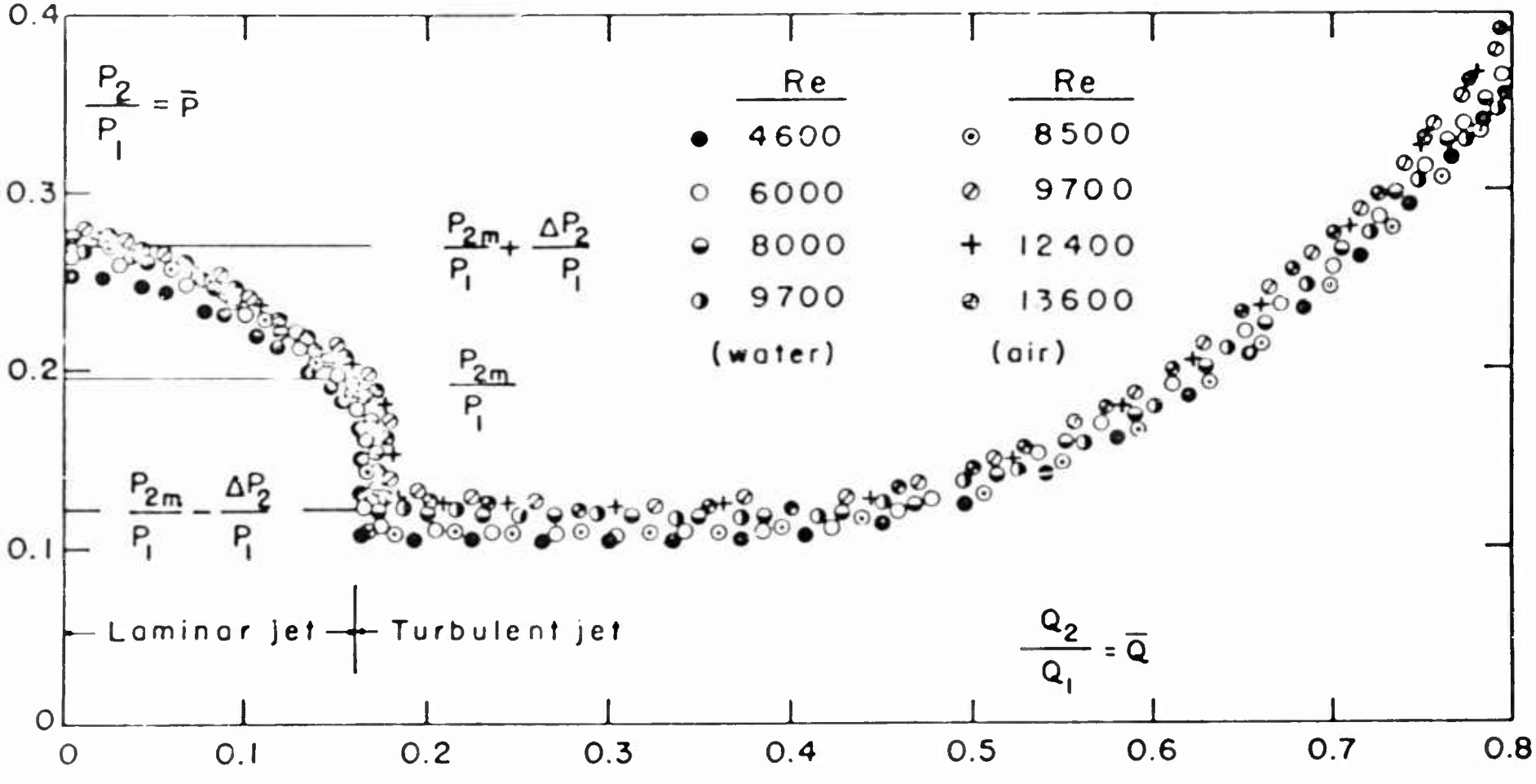

FIG. 7 VARIATION OF THE NORMALIZED DOWNSTREAM PRESSURE WITH NORMALIZED DOWNSTREAM FLOW RATE

emergent jet becomes turbulent. For values of $\bar{Q}$ between 0.16 and 0.4, $\bar{P}$ remains fairly constant. This range of $\bar{Q}$ values corresponds to a special state of flow in the downstream chamber. The observations of the dyed jet have shown that following the breakdown of the vortex motion in the downstream chamber the flow is essentially axial with a radial component superimposed on it. For larger values of $\bar{Q}$, the intensity of the counter vortex increases and as will be noted later the discharge coefficient decreases. Consequently, the pressure in the downstream chamber increases with increasing values of $\bar{Q}$.

Figure 8 shows, for the same vortex tube, the discharge coefficient as a function of $\bar{P}$. It is noted that at the start of motion, i.e. for $\bar{Q} = 0$, the flow is throttled and the discharge coefficient is at its minimum. As $\bar{Q}$ increases, the intensity of the swirl in the downstream chamber decreases. This in turn increases the discharge coefficient quite rapidly. Near the point of vortex breakdown, C_D reaches its maximum value*. Following the vortex breakdown and for a small range of $\bar{P}$ values, C_D remains fairly large. Subsequently, as the intensity of the counter vortex increases, the discharge coefficient decreases gradually toward its initial value. It is noted that for $\bar{P} < 0.25$, C_D is a double valued function of $\bar{P}$. The upper branch of the C_D—$\bar{P}$ curve corresponds to the state of the turbulent jet and the lower branch to the state of the laminar jet. Furthermore, it is noted that, within the range of Reynolds numbers encountered in the tests, neither C_D versus $\bar{P}$ nor $\bar{P}$ versus $\bar{Q}$ show any dependency on the Reynolds number.

b. Periodic Vortex Breakdown

A series of tests was conducted not only with the particular vortex tube discussed herein but also with fifteen other vortex tubes of various sizes and characteristic length ratios using the procedure described previously. It was firmly established that for a given vortex tube, only the unique combinations of pressures at the two vortex chambers produce periodic oscillations of constant amplitude; the amplitude of the pressure oscillations in the upstream chamber is insignificantly small (about 3%); the amplitude of the pressure oscillations in the downstream chamber is large in magnitude and independent of the frequency of oscillation; the frequency of oscillation for each vortex tube depends on the inertance and capacitance characteristics of the unit and of the external conduit-resonator system; and that no oscillatory motion can be obtained in a rigid system with an incompressible fluid, i.e. the vortex tube requires a capacitance provided either by the compressibility of the fluid in the flow system or by the distensibility of the conduit walls.

---

*This maximum is nearly equal to the theoretically predicted discharge coefficient for this orifice, i.e. $C_D = 0.62$.

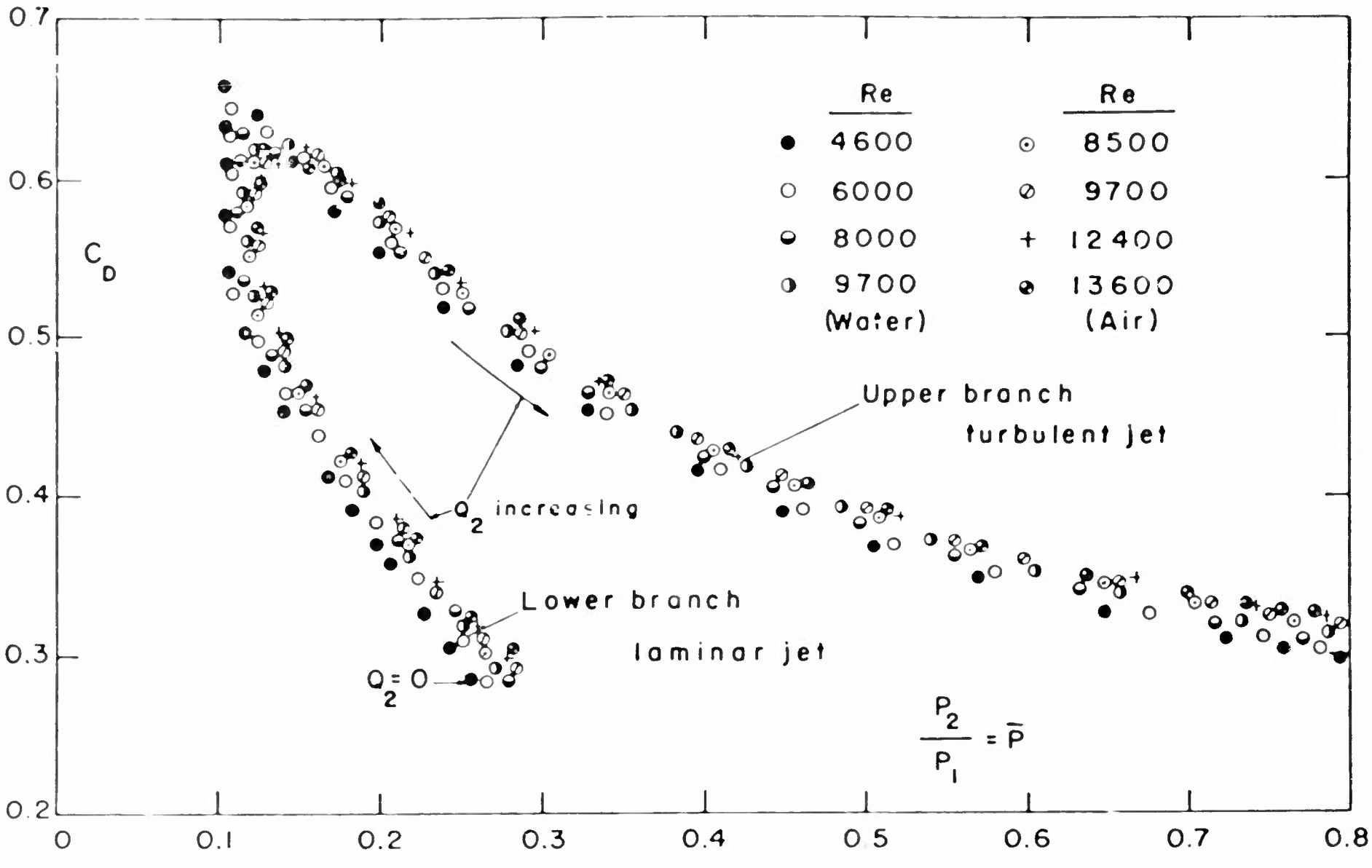

FIG. 8 VARIATION OF THE DISCHARGE COEFFICIENT WITH NORMALIZED DOWNSTREAM PRESSURE

Figures 9 and 10 show in dimensional form the relationship between P_1, P_{2m} and ΔP_2 and P_1. Each data point in these figures was checked with all possible frequencies of oscillation by varying the air volume in the resonator. It is apparent that for a given vortex tube a linear relationship exists between P_1 and P_{2m} and P_1 and the amplitude of the pressure oscillations in the downstream chamber.

In order to determine the relationship between the single and periodic vortex breakdown, the slopes of the two curves shown in Figs. 9 and 10 were calculated and marked on Fig. 7. It is clear that the normalized median pressure corresponds to the pressure at the inception of the single vortex breakdown, the maximum of the oscillating pressure corresponds to the pressure at $\bar{Q} = 0$, and the minimum of the oscillating pressure corresponds to the pressure at the completion of the breakdown, i.e. when the hollow laminar jet becomes turbulent. It may, therefore, be concluded that the amplitude of the oscillations as well as the normalized median pressure may be predicted from the relationships obtained for the case of single vortex breakdown.

A close examination of the data obtained for all vortex tubes used in the experiments has shown that for a given unit larger orifices require a smaller pressure P_{2m} or, in other words, a smaller P_{2m}/P_1 ratio to produce oscillations. The diameter of the upstream or downstream chamber does not seem to affect either the P_1 versus P_{2m} or P_1 versus ΔP_2 relationships. On the other hand, the length of the connecting tube between the upstream and downstream chamber materially affects the vortex motion and hence the relationships between the pressures and pressure fluctuations.

c. Frequency of Oscillations

It has been pointed out previously that a vortex tube requires either a compressible fluid and/or an elastic system to produce an oscillatory motion. A critical analysis of the variables involved in the phenomenon shows that if the viscous effects are ignored and the total temperature T is kept constant then the frequency is determined by

$$f_{th} = \frac{1}{2\pi}\sqrt{\frac{1}{C\,I}} \qquad (1)$$

where C and I represent the capacitance and inertance of the elastic system and are given by*

---

*The summation in I includes the discrete elements comprised of the tangential port, connecting tube, and the portion of the resonator which contains the working fluid. The summation in C includes only those elements which contain air.

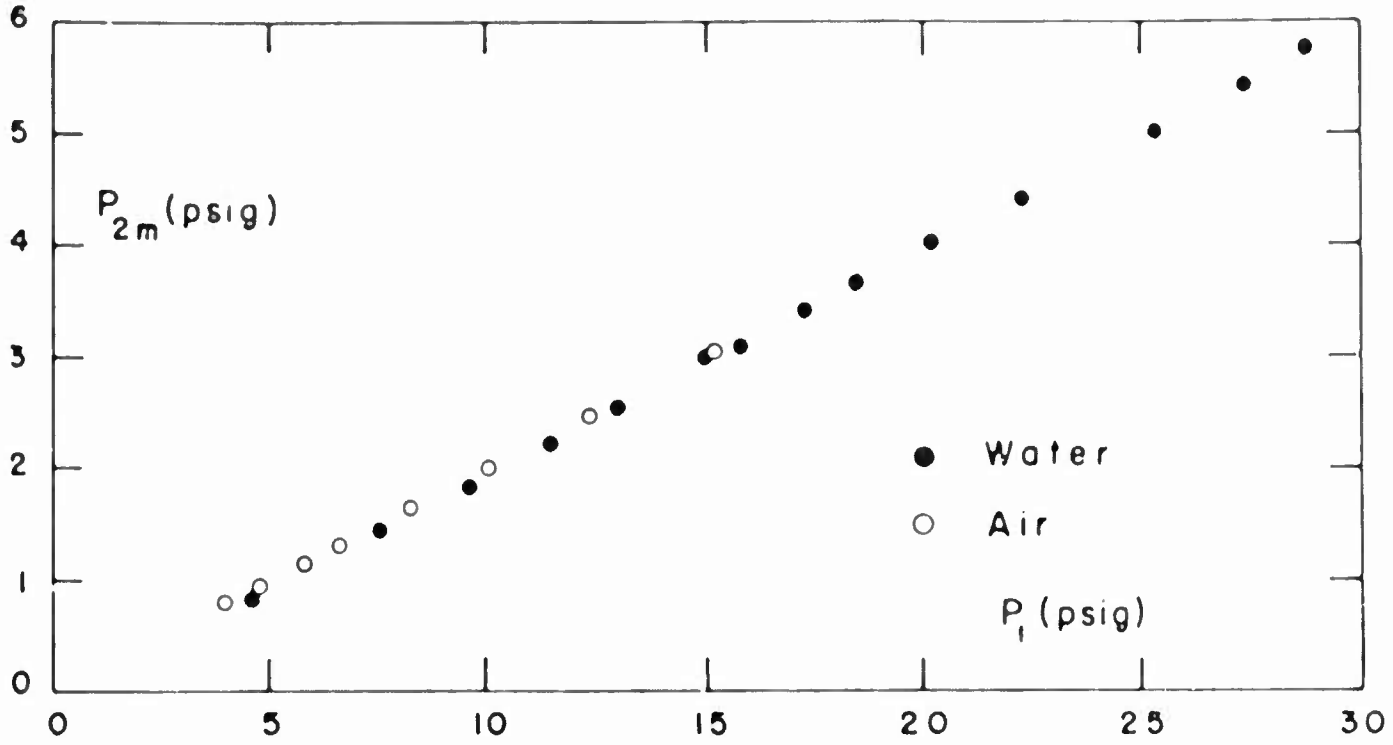

FIG. 9 VARIATION OF THE MEDIAN OF THE DOWNSTREAM PRESSURE WITH UPSTREAM PRESSURE, (PERIODIC VORTEX-BREAKDOWN)

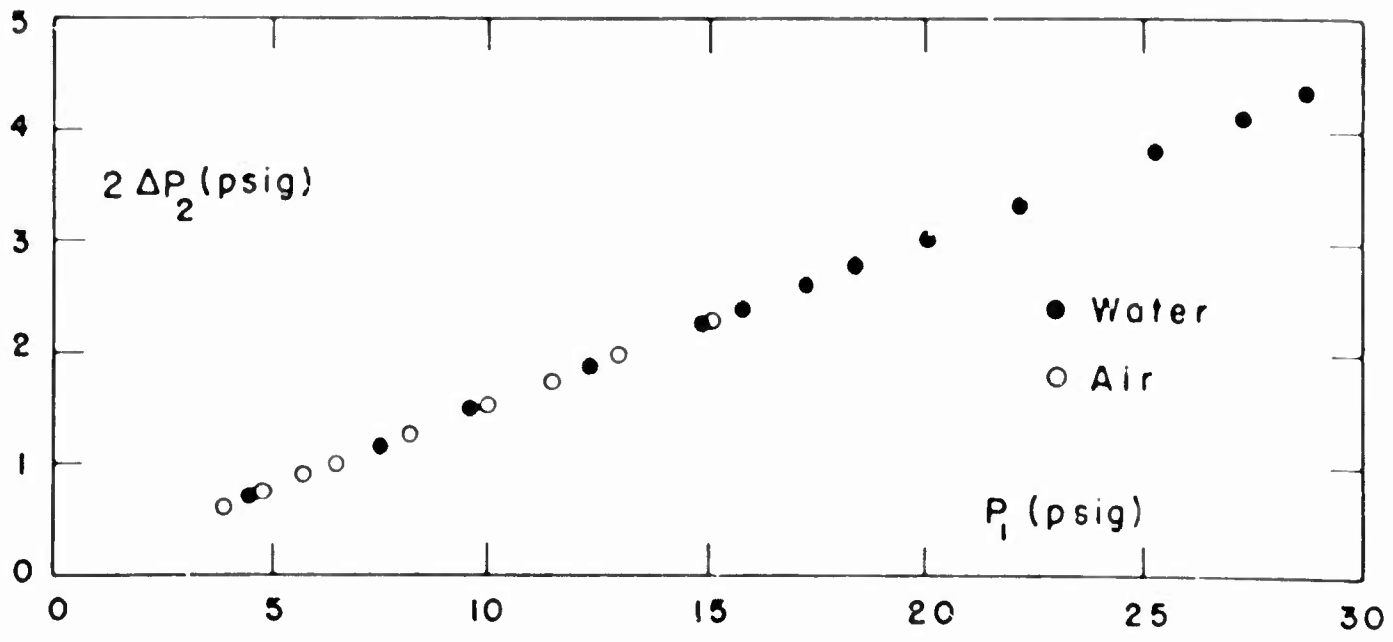

FIG. 10 VARIATION OF THE DOWNSTREAM PRESSURE FLUCTUATION WITH UPSTREAM PRESSURE, (SEE ALSO FIG. 6B)

$$C = \frac{1}{\rho_a c^{*2}} \sum_{k} (L_k A_k) \quad \text{and} \quad I = \rho_f \sum_{k} L_k / A_k \qquad (2)$$

In the experiments described herein the working fluid, the length and cross-sectional area of the conduit between the unit and the resonator, the volume of air in the resonator, and the upstream pressure were varied and the frequency of oscillation was determined from the oscillograph records. Figure 11 shows the variation of the measured frequency as a function of the theoretically calculated frequency. The correlation of the two frequencies is good but the theoretical frequencies are about 3 times larger than the measured frequencies. This is not entirely unexpected in view of the fact that the contribution of the mass of fluid within the unit and the viscous and form resistances were completely ignored. It is apparent that the inclusion of these terms will be equivalent to increasing the effective length of the tube between the unit and the resonator and will yield theoretical frequencies closer to those observed experimentally. The reason the aforementioned corrections were not incorporated into the analysis is because the energy losses can at best be predicted only approximately. It was, therefore, preferred to present the analysis as given above instead of reducing it to the prediction of the effective conduit lengths.

d. Experiments Concerning the Applications of the Device

A series of experiments were conducted with the unit described herein to explore the potential applications of the device. These experiments consisted of (a) single and periodic switching of a biased amplifier; and (b) sensing the change in the rate of rotation of a shaft.

In order to switch a biased amplifier, the control port at the side of the initial jet attachment was connected to the collector placed in front of the orifice as shown in Fig. 12. The Helmholtz resonator was taken out of the system and the counter-vortex flow Q_2 was increased gradually. When $\bar{Q}$ reached the critical value of 0.16, the jet emerging from the orifice abruptly became a fully developed turbulent jet and flowed directly into the collector. The resulting control flow switched the power jet in the amplifier and kept it locked in its new position. When Q_2 was reduced slowly and $\bar{Q}$ reached once again the critical value of 0.16, the turbulent jet abruptly changed to laminar hollow-cone regime and at the same time the power jet in the amplifier switched back to its original position.

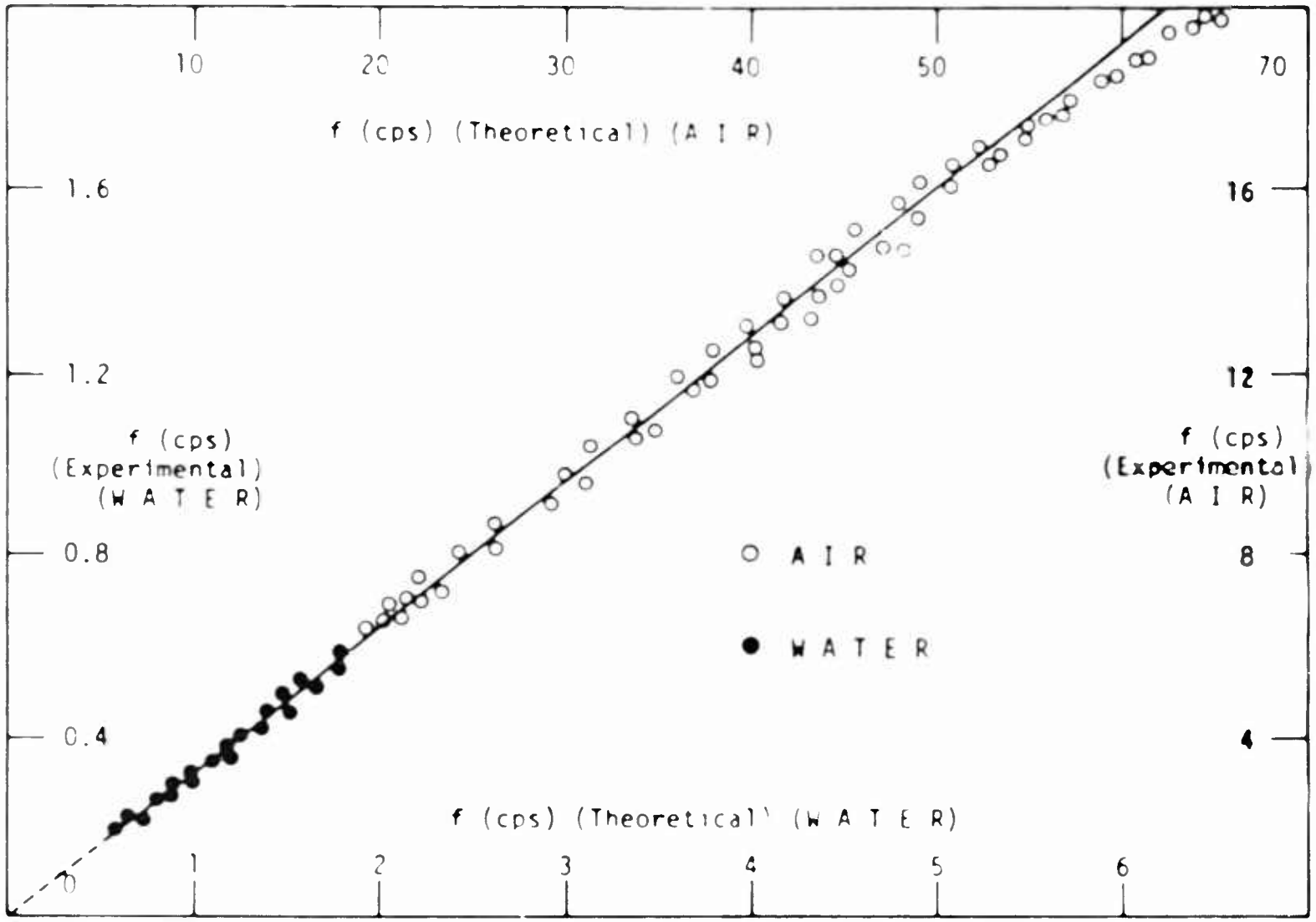

FIG. 11 VARIATION OF THE FREQUENCY OF OSCILLATION

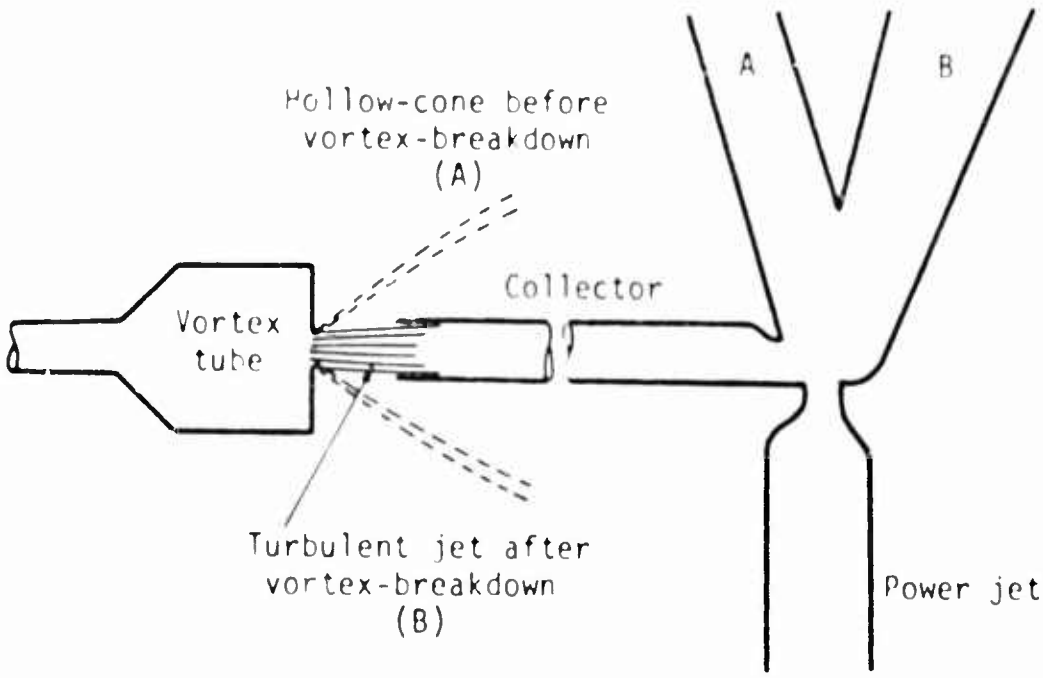

Figure 12

Upon the completion of experiments with single switching, the resonator was put back in the system and a periodic vortex-breakdown with desired frequency was established. When the collector was once again placed in front of the orifice, the power jet in the amplifier switched back and forth with the set frequency. This experiment established the potential use of the device as a binary counter.

In order to explore the ability of the device to secure a change in the rate of rotation of a shaft, the device was connected to the shaft of a variable speed motor. The flow rates Q_1 and Q_2 were adjusted so that $\bar{Q}$ was slightly under 0.16. Then the tube was rotated in the direction of the downstream tangential jet. This rotation increased the circulation of the counter vortex in the downstream chamber and decreased the circulation of the vortex in the upstream chamber. When the rate of rotation of the shaft reached a critical value, the jet emerging from the orifice abruptly became a straight turbulent jet and flowed into the collector and switched the power jet in the amplifier. When the speed of the motor was slowly reduced 4% below its existing value, the signal into the collector abruptly stopped and the power jet in the amplifier returned to its original state. This phase of the investigation was found to be extremely encouraging and the research is being continued with increased intensity to establish the design characteristics of a rate sensing vortex tube for the purpose of angular speed control.

CONCLUSIONS

The experiments described herein have shown that the swirling fluid motion in an axially symmetrical tube comprised of two chambers and a connecting tube may be subjected to an abrupt change by another vortex rotating in the opposite direction. This change produces a large pressure drop in the zone of vortex breakdown. For a given set of upstream and downstream wall pressures there are two different states of flow through the vortex tube. The location of the breakdown is determined by the conditions prevailing in the downstream section of the tube, in the same way that location of a hydraulic jump on a supercritical stream in an open channel is determined by the backwater conditions. Moreover, just as some sort of obstruction in the channel is necessary to precipitate a hydraulic jump on a supercritical stream, the vortex breakdown requires one or more triggering agencies such as the counter vortex motion and/or the adverse pressure gradient created by the divergence of the connecting tube into the downstream chamber. Coupled with a Helmholtz resonator, the vortex tube works like a hydrodynamic oscillator. The energy of the oscillator is derived from the hydrodynamic instability of the fluid within a reversed-flow region in the downstream chamber.

Preliminary investigations show that the vortex-breakdown phenomenon will be of significant value in the development of pressure modulators and angular rate sensing pneumatic devices.

ACKNOWLEDGMENT

The author wishes to express his appreciation to the Harry Diamond Laboratories, U. S. Army Materiel Command, Washington, D. C., for its generous support which has made this investigation possible and to Messrs. Joseph Kirshner and Kenneth R. Scudder for their encouragement and valuable suggestions.

REFERENCES

1 B. Vonnegut, "A Vortex Whistle," J. Acoust. Soc. Amer. vol. 26, 1954, p. 18.

2 J. L. Smith, "An Analysis of the Vortex Flow in Cyclone Separator," J. Basic Engr. vol. 84, 1962, p. 609.

3 J. L. Kerrebrock and R. V. Meghreblian, "Vortex Containment for the Gaseous Fission Rocket," J. Aerospace Sci. vol. 28, 1961, p. 710.

4 W. S. Lewellen, "Magnetohydrodynamically Driven Vortices," Proceedings of the Heat Transfer and Fluid Mechanics Institute, Stanford Univ. Press, Stanford, Calif., 1960, p 1.

5 E. M. Dexter, "Vortex Valve Development," A Report by General Electric Laboratory, Schenectady, New York, April 17, 1961.

6 T. Sarpkaya, "Characteristics of Counter Vortex Oscillators," Proceedings of the Fluid Amplification Symposium, Harry Diamond Laboratories, Washington, D. C., vol. II, May, 1964, p. 147.

7 M. Suzuki, "Theoretical and Experimental Studies on the Vortex Tube," Sci Pap. Inst. Phys. Chem. Res., Tokyo, vol. 54, 1960, p. 43.

8 J. L. Smith, "An Experimental Study of the Vortex in the Cyclone Separator," J. Basic Engr. vol. 84, 1962, p. 602.

9 N. C. Lambourne and D. W. Bryer, "The Bursting of Leading Edge Vortices—Some Observations and Discussion of the Phenomenon," Aero. Res. Counc., U. K., R & M. 3282, 1962.

10 J. K. Harvey, "Some Observations of the Vortex Breakdown Phenomenon," J. Fluid Mech. vol. 14, 1962, p. 585.

11 R. C. Chanaud, "Observations of Oscillatory Motion in Certain Swirling Flows," J. Fluid Mech. vol. 21, 1965, p. 111.

12 R. W. Gore and W. E. Ranz, "Backflows in Rotating Fluids Moving Axially Through Expanding Cross Sections," Amer. Inst. Chem. Engrs. J. vol. 10, 1964, p. 83.

13 I. Michelson, "Theory of the Vortex Whistle," J. Acoust. Soc. Amer. vol. 27, 1955, p. 930.

14 H. B. Squire, "Analysis of the 'Vortex Breakdown' Phenomenon, Part I," Imperial Coll. Sci. Tech., London, Rep. No. 102, 1960.

15 L. N. Howard and A. S. Gupta, "On the Hydrodynamic and Hydromagnetic Stability of Swirling Flows," J. Fluid Mechs. vol. 14, 1962, p. 463.

16 I. S. Gartshore, "Recent Work in Swirling Incompressible Flow," Nat. Res. Counc. (Canada) Aero. Rep. LR-343, 1962.

17 T. B. Benjamin, "Theory of the Vortex Breakdown Phenomenon," J. Fluid Mech. vol. 14, 1962, p. 593.

18 T. B. Benjamin, "Significance of the Vortex Breakdown Phenomenon," ASME Paper No. 64-WA/FE-18, 1964.

NOMENCLATURE

A_1 cross sectional area of the tube between the unit and the resonator

a length of the vortex chambers

C capacitance

c* velocity of sound

C_D discharge coefficient, $Q_T/\pi d_o^2/4\sqrt{2\,P_{2m}/\rho_w}$ (for water), and

$W_T/Y Y_a \pi d_o^2/4\sqrt{2P_{2m}/\rho_a}$ (for air)

D diameter of vortex chamber

d_c diameter of the connecting tube, (see Fig. 1)

d_j diameter of targential jets

d_o orifice diameter

f frequency of oscillation

I inertance

k summation index

L total length of the vortex-tube (see Fig. 1)

L_1 length of the tube between the unit and the resonator

L_c length of the connecting tube (see Fig. 1)

$\bar{P}$ = P_2/P_1, (psig/psig)

P_1 upstream wall pressure

P_2 downstream wall pressure

P_{2m} median of downstream wall pressure

ΔP_2 amplitude of downstream wall pressure

$\bar{Q}$ = Q_2/Q_1, (cfs/cfs for water) and (lb/sec/lb/sec for air)

Q_1 upstream port flow rate, (cfs for water and lb/sec for air)

Q_2 downstream port flow rate, (cfs for water and lb/sec for air)

Q_T = $Q_1 + Q_2$

Re Reynolds number, $\rho V_1 d_c/\mu$

V_1 average axial velocity in the connecting tube

W_T air flow rate (lb/sec)

Y	expansion factor
γ_a	specific weight of air
μ	dynamic viscosity of fluid
ρ_a	density of air
ρ_w	density of water
ρ_1	density of fluid in the tube between the unit and the resonator

EXPERIMENTAL PROFILES OF VELOCITY COMPONENTS AND RADIAL PRESSURE DISTRIBUTION IN A VORTEX CONTAINED IN A SHORT CYLINDRICAL CHAMBER

(AN ABRIDGED VERSION)

by Joseph M. Savino and Edward G. Keshock

Lewis Research Center
Cleveland, Ohio

TECHNICAL PREPRINT prepared for

Third Fluid Amplification Symposium
sponsored by the U.S. Army Materiel Command
Washington, D.C., October 26-28, 1965

NATIONAL AERONAUTICS AND SPACE ADMINISTRATION

EXPERIMENTAL PROFILES OF VELOCITY COMPONENTS AND RADIAL PRESSURE DISTRIBUTIONS IN A VORTEX CONTAINED IN A SHORT CYLINDRICAL CHAMBER*

by Joseph M. Savino and Edward G. Keshock

Lewis Research Center
National Aeronautics and Space Administration
Cleveland, Ohio

ABSTRACT

The chamber was formed by two 11.72-inch-diameter disks spaced 1.25 inches apart. A high swirl was imparted to the fluid (air) as it entered the chamber through 48 tangentially alined vanes. A 2-inch-diameter tube at the center of one disk served as the exhaust port. Static pressure and the profiles of the radial and tangential velocity components were measured at 8 radial stations. All the radial inflow took place close to the disk surfaces, while a slow outward flow existed in midchannel. The tangential velocities were used to predict the static pressures which agreed well with the measured values.

INTRODUCTION

With the advent of the nuclear cavity reactor concept in 1957 and 1958 there developed a wide-spread interest in the further possible applications of vortex fluid motion in magnetohydrodynamic (MHD) generators and fluid amplification devices. Many studies, both analytical and experimental, have been conducted into the fluid dynamical characteristics (such as the velocity components and pressure profiles) of vortex motions that were generated inside cylindrical chambers. Most of these investigations were

*This work is a condensed version of an NASA TN now in preparation.

undertaken primarily because the nature of confined vortex motions inside stationary containers was poorly understood, and this understanding is essential to the development of any device that utilizes the vortex flow. The study we are reporting here was among these many investigations.

In most applications that employ vortex motion, the fluid is injected tangentially at one or more ports on the cylindrical surface and exhausted though a hole in the center of one or both of the circular end walls. These end walls are usually stationary and are now known to exert a great influence on the motion. Heretofore, the nature and extent of this influence was unknown and was the subject of investigation.

Until recent years no literature was available that reported what the influence of the end walls would be on a confined vortex. Some results were reported by Kelsall (ref. 1), in which he made measurements of the radial, tangential, and axial velocity components inside a hydrocyclone separator. His experiments revealed the existence of large secondary motions with most of the mass movement occurring close to all walls where the centrifugal force was lowest. Interestingly enough, the loci of constant tangential velocities were concentric cylinders everywhere except very close to the walls. Thus, Kelsall's work pointed out the importance of stationary surfaces on the motion of confined vortices.

Williamson and McCune (ref. 2) and Donaldson (ref. 3) conducted experiments, in the same apparatus, on short cylinders ($0.133 \leq L/D \leq 0.2$). In both references are reported axial traverses of the total pressure only and radial distributions of the tangential velocity calculated from these measurements. The latter data in reference 2 (and presumably in ref. 3

also) was evaluated by differentiating the measured static wall pressure and equating this radial pressure gradient to the centrifugal force. The total pressure profiles in both references were quite uniform except for a slight depression in the region far from the end walls.

Ragsdale (refs. 4 and 5) made measurements with a pitot tube in a vortex chamber (length to diameter ratio = 0.5) at two radial stations and several axial stations and deduced in reference 5 that the motion was essentially tangential with very little axial variation in the magnitude. Radial distributions of the static pressure were also determined.

Beverloo, et al. (ref. 6) made radial traverses of the total pressures only with a pitot tube at three axial stations and two angular stations downstream from the single injection slot in short vortex chambers for a variety of injection port and outlet sizes and length to diameter ratios L/D. Their measurements resulted in the radial distributions of the tangential velocities only.

The most revealing experiments on the distribution of velocities inside vortices have been reported by Kendall (ref. 7) and Donaldson and Williamson (ref. 8). Kendall experimented with a vortex that was generated inside a rotating porous cylinder that imparted a swirl to the fluid as it passed through the cylinder into the cavity. The chamber was 6 inches in both length and diameter. The end containing the exit was fixed to the porous cylinder and rotated with it, while the other end was fixed.

Kendall used a flattened pitot tube (which is not normally used for direction measurements because it is not sensitive to yaw angles up to at least $\pm 5^{\circ}$) to traverse the boundary layer on the fixed end wall for both

the total pressure and the local fluid direction. He assumed that at a distance far from the wall the radial velocity was zero and the motion was one of pure tangential velocity. These measurements resulted in profiles of the radial and tangential velocity components. The tangential profile was essentially flat with a slight depression outside the boundary layer. The radial component, on the other hand, was a maximum at the closest measuring station to the wall and decreased monotonically to zero outside the boundary layer. Thus radial profiles showed that the stationary end walls alter the vortex motion considerably and produce a flow pattern in which a sizable inflow occurs in the boundary layer adjacent to stationary end wall.

More recently Donaldson and Williamson (ref.) made measurements of the tangential and radial components and the turbulence in a short cylinder whose inner and outer radii and length were 1.573, 4.484, and 0.75 inches respectively. The fluid (air) was injected through a rotating porous outer cylinder and removed through stationary porous inner cylinder. A sensitive yaw probe consisting of two beveled tubes was first used to map the local flow directions. Then a pitot tube was inserted and oriented with the local streamlines to measure the local velocity magnitude. A hot wire was employed to determine the mean and fluctuating tangential velocities on the center plane between both end walls. Velocity components were determined at eight axial positions at each of three radial stations for various flow rates and turbulence levels. Because of the manner in which the yaw probe was constructed complete traverses from one end wall to the other were not possible. The resulting profiles revealed the radial inflow was a maximum very close to the end wall and a minimum far from the end walls. A reversal

of flow outside the end wall boundary layer region was indicated, but it was assumed to be due to measurement difficulties and therefore nonexistent. The tangential profiles were fairly uniform although several did have a slight depression in the center region of the profile. These results showed that the velocity distributions in a short vortex chamber are quite similar to those found in Kendall's where the length to diameter ratio was unity.

The theoretical work on confined vortex flows in the presence of end walls has been concerned with the influence exerted by the end wall flow on the main vortex field for both laminar and turbulent conditions. The approach applied is the momentum integral technique where some reasonable form for the velocity profiles in the boundary layer and the wall skin function laws are assumed. Mack (ref. 9) studied the laminar boundary layer on a finite disk in a rotating flow where a variety of radial distributions of tangential velocity in the freestream were specified. He found that a sizable mass flow occurred in the boundary layer. Rott (ref. 10) examined the sensitivity of the mass flow in a turbulent boundary layer to the assumed form of the shear law and noted that the sensitivity was small. The mutual interaction between the main flow and the boundary layer flow were analyzed by Anderson (refs. 11 and 12) and Rosenzweig, Lewellen, and Ross (ref. 13). For strong vortex flow with high swirl the interaction caused the existence of secondary motion with radial outflow motion in the primary flow for vortex flows of high swirl. Thus, these analytical studies showed that under certain conditions a part or all of the net flow into a vortex passes through the end wall boundary layers.

It was the object of this study, to determine (1) detailed experimental

profiles of the velocity components and radial pressures of a vortex confined in one particular geometry, a short cylinder with plane end walls, and (2) which factors are responsible for the resulting profiles. A cylindrical chamber 11.72 inches in diameter and 1.250 inches in length (L/D = 0.107) was used as the vortex container. Air was injected tangentially into the chamber through a series of 48 guide vanes all around the periphery and discharged through a 2.000-inch-diameter exhaust tube that was located at the center of one end wall. This chamber was somewhat similar to that used in references 2, 3, and 5. Axial traverses (24 points) were made at seven radial stations (r = 1.0, 1.5, 2.0, 2.5, 3.0, 3.5, and 4.5 in.) with a probe that sensed both the magnitude and direction of a velocity vector at a point. From these traverses were evaluated the profiles of the radial and tangential velocity components, and the streamline pattern. An additional traverse was made with a pitot tube at the injection radius. Static pressures were also measured at the same radial positions and in addition at r = 5.81 inches. The results are presented for only one mass flow rate of 0.209 pound mass per second at an absolute pressure of 42 inches of mercury at r = 5.81 inches and temperature of 80° F, although data at higher and lower flows yielded similar results. Therefore, the conditions were essentially for the incompressible regime.

APPARATUS

The short, cylindrical vortex chamber is shown schematically in figure 1.* The 48 guide vanes imparted a high swirl to the air as it passed inward from the inlet plenum chamber. The wire-gauze damping screen aided in producing angular symmetry around the periphery. The end wall opposite the exhaust

*Figures start on page 293.

was fabricated with static wall taps and seven probe ports, each fitted with a removable plug that was flush with the inside surface of the end walls To make a traverse at a given radial station the plug was removed and the probe holder assembly fastened in its place. Static wall taps 0.010-inch in diameter were drilled at the same radial positions as the probe ports. These taps were located 1 or more inches ahead of the probe station in the angular upstream direction to avoid interference due to the presence of the probe.

It was realized after some preliminary experiments that the velocity component profiles could only be determined with an instrument that was sensitive to the direction as well as the magnitude of any local velocity vector. The conventional pitot tubes that are fabricated from small round tubes are rather insensitive to the yaw and pitch angles up to $\pm 5^{\circ}$ or more (ref. 14). This is also true of flattened pitot tubes such as the one used in reference 7. Hence, the 3-tube pitot-yaw probe shown in figure 2 was finally chosen because it is very sensitive to yaw in the plane of the three tubes but not to pitch. These two characteristics made the probe quite suitable for this experiment where the axial velocity component was expected to be small. The choice was based on the work of Bryer, Walshe, and Garner (ref. 15).

A second important factor for consideration in the probe selection was its size. Any probe regardless of its size will exert a drag that tends to slow down the vortex. Obviously, the velocities indicated by the probe will differ from those of the undisturbed vortex; the difference increasing with increasing probe size. In addition to slowing down the vortex, the probe

size can produce another undesirable effect. If it is used in a region where the motion is very nearly circular, the probe wake will be convected in a circular path so that the probe could be in its own wake. Here again the indicated velocities will differ from those of undisturbed vortex if the wake is too large to be dissipated before it comes back on the probe. Thus, it is seen that disturbances by the probe cannot altogether be avoided, but they can be minimized. To insure the greatest possible accuracy in this experiment, the probe was made as small as possible consistent with reasonable response times and strength.

For these experiments a special holder was made for the 3-tube probe. With it the probe could be positioned axially and rotated into any angular orientation while the tip was always at the same radius. To establish the reference angle the entire assembly was alined in a 4-inch-diameter unidirectional airstream of uniform velocity. The airstream was produced by a special jet tunnel that was specifically designed for calibrating and alining probes. The reference angle was chosen to be zero when the probe was alined with a radial line and directed toward the vortex center.

A special pitot tube was made to determine the distribution of the velocity magnitude of the air leaving the injection vanes. No provisions were made to measure the angle of injection with this probe. The probe is shown in figure 3 along with the measured profiles. The total pressure was measured relative to a static wall tap at $r = 5.61$ inches. The true static pressure at the vane outlet was determined by extrapolating the radial static pressure data from $r = 5.61$ to $r \approx 5.9$ inches.

The mass rate of flow through the test section was measured with a

calibrated orifice plate that was accurate to within 1/2 percent.

The radial static pressures were measured relative to each other on a group of water manometers the legs of which were all connected to a common well at the lower end. The pressure sensed at the outermost radius, r = 5.61 inches, was measured relative to atmosphere on a mercury "U-type" manometer. Water "U-type" manometers were used to measure the difference between (1) the total pressure sensed by the center tube of the pitot-yaw probe and the local static wall pressure at the same radius, (2) the pressures sensed by the beveled yaw tubes of the pitot-yaw probe, (3) the orifice plate pressure difference, and (4) the total pressure of the probe at the vane tips and the wall tap at r = 5.61 inches.

The accuracy of the final results depends on the accuracy of the instruments used. All manometers were easily readable to within 0.02 inch. The flow rate was maintained steady within ±1/2 inch of water out of an overall Δp of 50 inches. The protractor was equipped with a vernier that was readable to 5 minutes and the zero reference was established to within 5 minutes. The micrometer head had a least count of 0.001 inch.

TEST PROCEDURE

To make a typical run, the probe holder was installed in a port at a radius where an axial traverse was desired. The flow of air was started and increased until the desired rate was reached. About 15 minutes were allowed for all manometers to achieve steady-state values. A typical traverse was started with the probe tip completely withdrawn from the flow and touching the wall on which the probe is mounted. The probe was rotated until the pressure difference between the two beveled tubes was zero. The angle was

recorded along with the difference between the total pressure sensed by the center tube and the static pressure sensed by the wall tap ahead of it. Then the probe was moved out into the fluid stream to a new position and the procedure was repeated. This was done repeatedly until a complete traverse from one wall to the other was made.

Radial distributions of the static pressures were made both when the probe extended all the way across the channel and when it was completely withdrawn. This was done to note whether the probe exerted any appreciable drag on the vortex.

RESULTS

Velocity Profiles

The velocity traverse made at a typical vane injection slot is shown in figure 3. Velocity directions could not be read with the probe; therefore the plot is only of the velocity magnitude. Figure 3 shows that velocity magnitude was quite uniformly distributed. Because the air was injected through thin rectangular slots formed by the flat vanes, it is believed that uniform injection was achieved for both the radial and tangential velocities.

The traverse made with the pitot-yaw probe yielded the magnitude V and direction θ' of the local velocity vector. The local radial and tangential velocity components were calculated from relations $u' = V \cos \theta'$ and $v' = V \sin \theta'$. The corrected profiles of the nondimensional radial velocities $u/u_{av,om}$ are given in figure 4, and the dimensional tangential velocities v in figure 5. All the data is given in greater detail in table I of reference 14. The streamline pattern depicted in figure 6 was

calculated from the definition $\psi(z) = \int_0^z u r\,dz$ and normalized by the average value $\psi = \pi r u_{av,om}$. The axial components w were quite small in comparison to the other components over the region where measurements were made. These were calculated from the relation $w = -\frac{1}{r}\frac{\partial}{\partial r}\psi(z)$, but are not shown here. The axial components are probably comparable to u_o near the vane where the incoming fluid is diverted toward the end walls as indicated by the dotted streamlines.

Figures 3 to 5 reveal several prominent features. The first is the abrupt change in the profile of the radial velocity from a uniform distribution shown in figure 3 to that of figure 4(g). Secondly, figure 4 clearly shows that all of the incoming fluid moves along the end wall toward the exhaust region with the maximum radial velocity occurring very close to the wall. The radial velocities adjacent to the wall are increasing quite rapidly with decreasing radius while away from the walls the radial velocities are small and outward (positive) in direction. The nondimensionalization of u values by the average value $u_{av,om}$ in figure 4 obscures these facts on the one hand, but reveals a similarity of the profile in the boundary layer region on the other. The third feature is that the tangential velocities increase with decreasing radius and that the profiles develop a depression in them. These profiles show the same general features that were independently found in the experiments by Kendall (ref. 7) and Donaldson and Williamson (ref. 8). One significant difference between profiles of references 7 and 8 and those reported here is the presence of the radial outflow in the mainstream. It is quite possible that the outflow questioned in reference 8 was actually present.

The velocity profiles are [illegible] v_i/v_o is imparted to the fluid, the [illegible] the end wall, and the interaction of the [illegible] with the rotating velocity component. The [illegible] approximately by [illegible] where the influence of variable v_o/u_o ratio was investigated. The [illegible] with vortex motion, the [illegible] that was always [illegible] For $v_o/u_o \leq 1.5$, the radial inflow [illegible] the vortex and the tangential velocities were distributed approximately like the [illegible] v_o/u_o was increased, $v_o/u_o > 1.5$, the fluid was unable to penetrate the centrifugal field as far, and it turned to move axially at [illegible] the center of larger radii. Finally, at $v_o/u_o \geq 1.8$ the fluid turned sharply from radial to axial motion immediately upon entering the vortex chamber, and the tangential motion approached solid-body rotation. From these findings it is apparent that in the present vortex, where $v_o/u_o = 1.8$, that the air entering the chamber was quickly diverted axially solely to raise the centrifugal force imparted to it was substantially higher than its inward momentum. The diverted air exited the narrow boundary region $\bar{r} > 0.1$ adjacent to the end wall where it [illegible] move radially inward more easily because of the reduced centrifugal force field and increased radial momentum in these regions. The reduced centrifugal force was produced by the no-slip condition on the end walls, and the inward momentum was increased because the effective flow area was reduced and the local velocity increased. However, for all of the vortex motion approaching solid-body rotation such as was found in reference 1 for $v_o/u_o > 1.8$, the

tangential velocities approached those of an inviscid vortex. The reason is the fact that some radial inward flow was forced to exist in the present apparatus because two end walls were present whereas such was not the case in reference 17. It is shown in references 17 and 18 that solid body motion results when no radial velocities exist, and that the presence of a negative radial velocity in viscous and turbulent vortices interact with the tangential motion causing the motion to depart from solid body rotation and tend toward the inviscid vortex where $v \sim 1/r$ as $-u$ becomes larger in magnitude. In other words, the negative radial velocities tend to preserve angular momentum with complete preservation almost being achieved in the experiment reported here at $\bar{z} = 0.03$ and $\bar{z} = 0.47$. The high centrifugal force field of the boundary regions is then transmitted by tangential turbulent shear to the region away from the boundaries. There a small radial outflow is induced that tends to decrease the angular momentum and cause the depression in the tangential velocity profiles (fig. 5).

The existence of a higher radial mass flow along the end wall opposite the one containing the exhaust port was somewhat unexpected at first glance. A plausible explanation for this situation is the fact that the greatest drag on the vortex by the probe occurred when making traverses on the end wall with the exhaust port. On the other hand, two other factors that influence the vortex motion could be the cause. They are the radius and the length of the exhaust tube. Some unpublished data and observations were recorded on the present vortex chamber when the radius and length of the exhaust tube were varied. The radial pressure distributions inside the exhaust radius were significantly affected by the geometry of the exhaust tube.

Static Pressure Distributions

The measured static pressures are presented in normalized form in Figure [illegible] and in both dimensional and normalized form in Table II of reference [illegible]. The tangential velocity at the vane tips v_o appearing in the normalization factor ρv_o^2 was extrapolated from the measured values as will be explained.

Also presented for comparison are two curves that were calculated in a simple, frequently used, model with the aid of the measured tangential profiles. It has been common practice in the study of cyclone separators and other vortex devices to evaluate the radial distribution of the tangential velocities from the measured radial distribution of the static pressure under the basic assumption that the radial pressure gradient is provided by the centrifugal force of the fluid. The validity of this assumption can be checked for the present application because both tangential velocities and static pressures were measured.

If in the radial momentum equation for incompressible turbulent flow

$$\rho\left[u\frac{\partial u}{\partial r} + w\frac{\partial u}{\partial z} - \frac{v^2}{r}\right] = -\frac{\partial p_s}{\partial r} + \begin{pmatrix}\text{Turbulent}\\ \text{shear}\\ \text{terms}\end{pmatrix} \tag{1}$$

the following conditions are met

$$u\frac{\partial u}{\partial z} \ll \frac{v^2}{r} \tag{2a}$$

and

$$w\frac{\partial u}{\partial z} \ll \frac{v^2}{r} \tag{2b}$$

$$\text{turbulent shear terms} \ll \frac{\partial p_s}{\partial r} \tag{2c}$$

then the equation reduces to

$$\rho \frac{v^2}{r} = \frac{dp_s}{dr} \tag{3}$$

The tangential and radial velocity profiles in figures 4 and 5 show that in the midchannel region away from the end walls, the conditions of equations (2a) and (2b) are met because $\partial u/\partial z \approx 0$, $w \approx 0$, and u and $\partial u/\partial r$ are both small; condition of equation (2c) is assumed to hold because the gradients of u and v in the z-direction are small. As is frequently done, let

$$\frac{v}{v_o} = \left(\frac{r}{r_o}\right)^{-n} \tag{4}$$

where n is an experimentally determined exponent. For an inviscid vortex, the equation of motion for the tangential velocity component yields the well known distribution $v \sim 1/r$; that is, $n = 1$.

When equation (4) is substituted into equation (3) and then equation (3) is integrated, the following nondimensional expression for the static pressure results

$$\frac{p_s(\bar{r}) - p_{s,o}(\bar{r} = 1)}{\rho v_o^2} = \frac{1}{2n}\left[1 - \left(\frac{1}{\bar{r}}\right)^{-2n}\right] \tag{5}$$

Before equation (5) can be applied, a value for n must be chosen from the experimental tangential profile data, and it must be fit reasonably well with equation (4). Two choices suggest themselves, one for the v at midchannel ($\bar{z} = 0.5$) where the equations (2a), (2b), and (2c) are satisfied, and the other for the integrated average tangential velocity v_{av}. The best fit

through each allowed the data to be extrapolated to $\bar{r} = 1.0$ to give v_0 ($\bar{r} = 1$, $\bar{z} = 0.$) and $v_{av,0}$ and the exponent n. The resulting curve fits ...

$$\frac{v\ \bar{r},\ \bar{z} = 0.)}{v_0\ \bar{r} = 1,\ \bar{z} = 0.)} = \left(\frac{r}{r_0}\right)^{-0.}$$ (.)

.)

$$\frac{v_{av}\ \bar{r})}{v_{av,0}} = \left(\frac{r}{r_0}\right)^{-0.}$$ (.)

... $v_0\ \bar{r} = 1,\ \bar{z} = 0.\ ) = .1$ and $v_{av,0} = .$ feet per second. ...quations (.) and (.) and the data from which they were derived are given ...figure .. The agreement between equations (.) for both equations (.) and (.) and the experiment pressures in figure . is seen to be very good. The maximum deviation of about 13 percent occurred at $r/r_0 = 0.1$ where the pressure gradients were greatest.

An attempt was made to check equation (3) by differentiating the experimental pressure distribution as was done by Williamson and McCune (ref. 2), but it was not as successful as the preceding approach because of the inherent inaccuracies in differentiating experimental data.

The agreement achieved herein between experimental data and the model verifies the usual assumption that in the body of fluid away from the end walls, the radial pressure gradient is balanced largely by the centrifugal force. Also the average v_{av} at any r is approximately equal to the value away from the end walls.

Accuracy of Results

The accuracy of the measurements was examined carefully. The static

wall pressure data were valid because the wall taps were small (0.010 inch-diam), and they were carefully made with square edges free of burrs. The reproducibility of the static pressure data is evidenced in figure 7 and table II of reference 1 where these data were recorded after each velocity traverse.

There was no doubt about the accuracy of the pitot (center) tube of the probe because of its insensitivity to yaw and its long established reliability for velocity measurements in various shear flows. The velocity head readings were repeatable to within a maximum deviation of 1.2 percent. However, because the beveled yaw tubes were used in a field where there were radial as well as axial gradients of the total pressure, each beveled tube was generally exposed to a slightly different local total pressure, even though the spacing between them was small (0.060 in.). As a result the probe could have been yawed relative to the local streamline, when the Δp between them was zero. For this reason a check was made on the accuracy of the θ measurements, and a detail discussion of it is given in reference 1.

A slight azimuthal asymmetry existed in the flow pattern in spite of the precaution to avoid it. Two identical traverses at r = 2.0 inches but 180° removed from each other revealed the asymmetry which is shown in figures 4(c) and 5 and table I. These two profiles are similar and differ by a small amount. Yet, the integrated mass rates for the uncorrected data of the two traverses at r = 2.0 inches (fig. 4(c)) were 0.230 and 0.144, respectively, compared to the true value of 0.204 pounds per second as measured by the orifice meter. The large errors in the integrated mass rate

occurred because each profile of the radial velocity component in Figure 4 has two spikes; the value of integrated mass rate is quite sensitive to small variations in the profile magnitudes. Although it would have been desirable to have close agreement between the integrated and measured mass flows as a check on the accuracy of the profiles, the shape of the profile make this agreement difficult. It appears that agreement between the integrated mass flow, and the orifice meter value is not a good method to test the accuracy of the radial velocity profile data. Hence to present a consistent set of graphs the velocity profile data for five out of seven traverses were corrected for the asymmetry by shifting the profile of the measured angles an amount necessary to bring the integrated mass flow to within about 2 percent of the measured profile. The absolute magnitude of the angle correction varied from 0.3 to 1.4 degrees. The correction could have been made on the velocity, or on a combination of angle and velocity. However, since there appeared to be no factor affecting the choice of correction, the choice was arbitrary. One additional observation merits comment and that is the discovery of the asymmetry is additional evidence that the yaw probe was quite sensitive to flow direction.

The presence of the probe exerted a drag on the vortex tending to slow it down. This was evidenced by a shifting of the radial distribution of the static pressure readings as the probe was extended into the stream. The slowdown depended somewhat on the radial location of the probe, the greatest slowdown occurring at the smallest radii, where the velocities were highest, and when the probe was fully extended across the vortex. The maximum shift in the radial pressure distribution amounted to one part in six of the radis-

turbed distribution that is shown in figure 3. On the average for most of the data the effect of the drag was considerably less. No attempt was made to correct the velocity profiles for the effects of probe drag because it appeared impossible to do accurately.

An attempt was made to assess the effect of the probe wake by injecting helium into the vortex with a probe-like injection tube and recording Schlieren photos. It appeared that any disturbance created by the probe was dissipated so that the probe wake did not seem to propagate back on itself. The Schlieren photos also confirmed that the motion was turbulent everywhere. Hence, it was concluded that the presence of the probe wake was producing at most a second-order effect on the profiles.

The extrapolated value of v_o and $v_{av,o}$ were 94.1 and 88.7 feet per second as compared with an average of about 104.5 feet per second measured at the vane tip shown in figure 3. This variation was expected because there exists local mixing of the jets as they emerge from the vane injection slots.

CONCLUSIONS

The purpose of this study was to make accurate measurements of the radial and tangential velocities throughout the vortex and of the radial static pressures and to determine the factors that influence the motion. This goal was achieved, and from the results presented herein and those of the investigators cited, the following conclusions are drawn concerning the factors that influence confined vortex motion. In particular, these conclusions apply to cylindrical chambers that have stationary planar end walls

with an exhaust hole, much smaller in diameter than the cylinder, in one (or possibly both) of them, and a L/D ratio less than approximately 2.

The amount of swirl (the ratio of tangential-to-radial velocities) imparted to the fluid as it is injected into the chamber alone determines what fraction of the total mass flow will be forced to flow inwardly within the end wall boundary layers. When the swirl is low, a tangential-to-radial velocity ratio less than approximately 1 to 2, the radial inflow will have enough inward momentum to penetrate the centrifugal field, and inflow will exist at all axial and radial positions away from the walls. When the swirl is high as it was in the present work with velocity ratios above roughly 10, the radial inflow is diverted axially; and if two stationary end walls are present, all the fluid leaves the chamber by way of the boundary regions adjacent to these end walls. However, if at least one of the chamber is wide open, the fluid would discharge immediately out of this end. Because the centrifugal force field near the walls is reduced due to the no-slip condition on the surface, inward radial velocities exist there, and they tend to conserve angular momentum. This accounts for the approximate inviscid-like vortex motion.

The simple model whereby the centrifugal forces are balanced only by the radial pressure is valid in regions far removed from the end walls.

NOMENCLATURE

D vortex chamber outer diameter, $2r_o$

L vortex chamber length

n exponent appearing in eq. (4)

p pressure, lb. ft.

r dimensional radial coordinate

$\bar{r}$ dimensionless radial coordinate, r/r_o

u radial velocity component

V velocity vector magnitude

v tangential velocity component

w axial velocity component

z dimensional axial coordinate

$\bar{z}$ dimensionless axial coordinate, z/L

δ angle measured from radial line to local velocity vector

ρ fluid density

ψ stream function

Subscripts:

av average value

i integrated value

om value calculated from orifice meter flow rate

o value at outer vortex radius, r_o = 2.00 in.

s static pressure

' indicated values

REFERENCES

1. Kelsall, D. F.: "A Study of the Motion of Solid Particles in a Hydraulic Cyclone." Trans. Instn. Chem. Engineers, v. 30, 1951, pp. 87-103.

2. Williamson, J. S., and McCann, J. P.: "A Preliminary Study of the Structure of Turbulent Vortices." AMAP Report No. 42, Aero. Res. Assoc. Princeton, Inc., Princeton, New Jersey, July 1951.

urements ... Turbulent Vortex Flow..." AIAA Journal, Vol. [illegible], No. [illegible], February [illegible], pp. [illegible].

9. Rom, J.: "Application of Mixing Length Theory to Turbulent Vortex Flows." NASA TM [illegible], April [illegible].

10. Rott, N., Lewellen, W. S., and Whitelaw, J. A. H.: "Incompressible Non-Axisymmetric Vortex Flow." British Aeronautical Council, Vol. [illegible], No. [illegible], Oct. [illegible], pp. [illegible].

7. Kerrebrock, J. L., Jr.: "Experimental Study of a Compressible Viscous Vortex." Tech. Report No. 32-[illegible], Jet Propulsion Laboratory, California Institute of Technology, June 5, 1962.

8. Donaldson, C. duP., and Williamson, G. G.: "An Experimental Study of Turbulence in a Driven Vortex." Aero. Res. Assoc., Princeton, Princeton, New Jersey. ARAP Tech. Memo. No. 64-1, July 1964.

9. Mack, L. M.: "The Laminar Boundary Layer on a Disk of Finite Radius in a Rotating Flow." Tech. Report No. 32-111, Jet Propulsion Laboratory, California Institute of Technology, May 10, 1961.

10. Rott, N.: "Turbulent Boundary Layer Development on the End Walls of a Vortex Chamber." Rept. No. ATN 62 (3302)-1. Aerospace Corp. El. Segundo, Calif., July 30, 1962.

11. Anderson, O. L.: "Theoretical Solutions for the Secondary Flow on the End Wall of a Vortex Tube." United Aircraft Corp. Res. Lab. Rept. R-2404-1, Nov. 1961.

12. Anderson, O. L.: "Theoretical Effect of Mach Number and Temperature Gradient on Primary and Secondary Flows in a Jet-Driven Vortex." United Aircraft Corp. Res. Lab. Tech. Documentary Rept., RTD-TDR-63-1098, Nov. 1963.

13. Rosenzweig, M. L., Lewellen, W. S., and Ross, D. H.: "Confined Vortex Flows with Boundary-Layer Interactions." AIAA Jour., vol. 2, no. 12, Dec. 1964, pp. 2127-2134.

14. Gracey, W., Letko, W., and Russell, W. R.: "Wind-Tunnel Investigation of a Number of Total-Pressure Tubes at High Angles of Attack. Subsonic Speeds." NACA TN 2331, April 1951.

15. Bryer, D. W., Walshe, D. E., and Garner, H. G.: "Pressure Probes Selected for Three-Dimensional Flow Measurements." Aero. Res. Council Report R and M No. 3037, 1956.

16. Savino, Joseph M., and Keshock, Edward G.: "Experimental Profiles of Velocity Components and Radial Pressure Distributions in a Vortex Contained in a Short Cylindrical Chamber." NASA TN now in preparation.

17. Donaldson, C. duP., and Snedeker, R. S.: "Experimental Investigation of the Structure of Vortices in Simple Cylindrical Vortex Chambers." ARAP Report No. 47, Aero. Res. Assoc. Princeton, Princeton, New Jersey, December 1962.

18. Donaldson, C. duP.: "Solutions of the Navier-Stokes Equations for Two and Three-Dimensional Vortices." Ph.D. Thesis Princeton Univ., 1957.

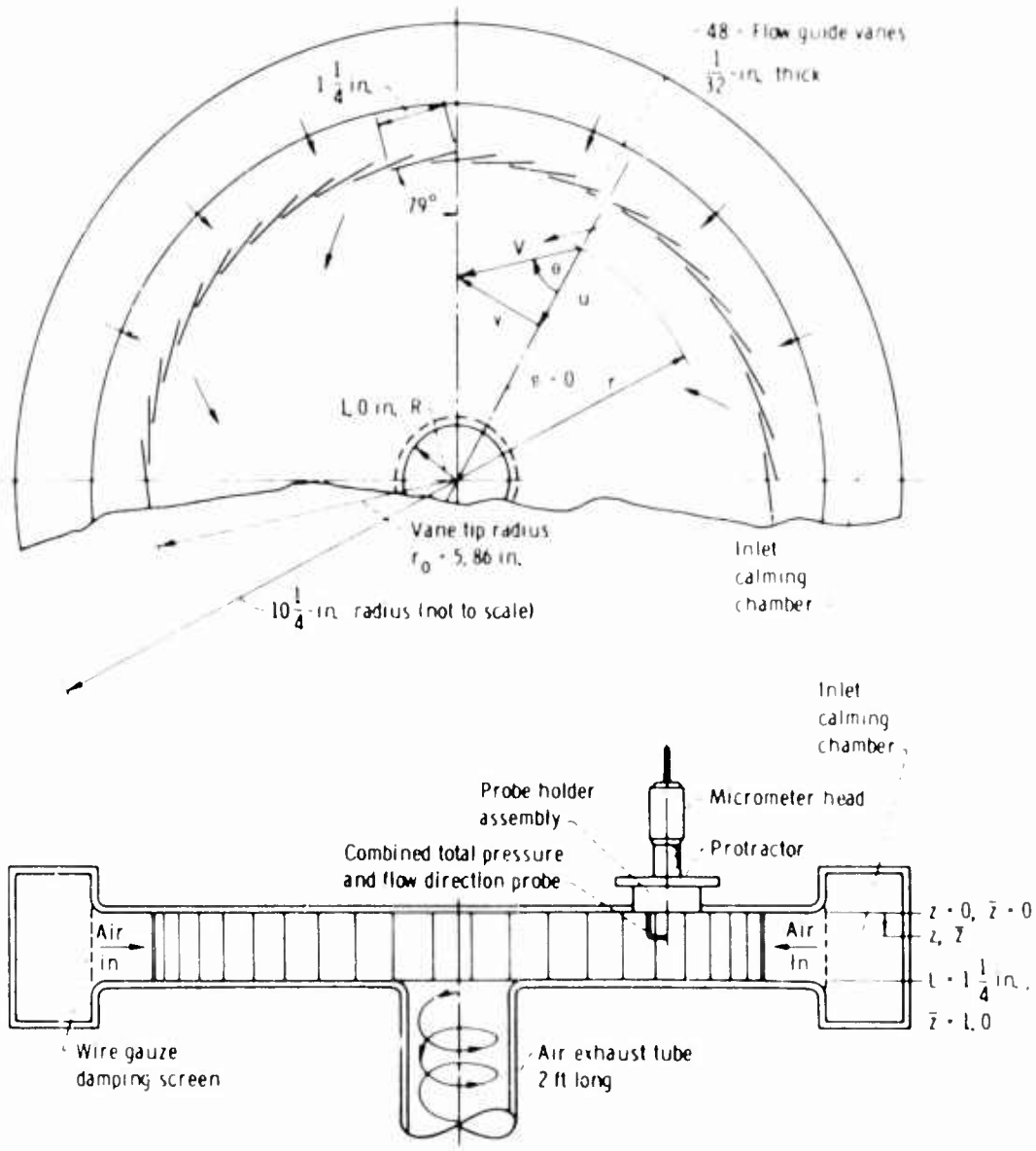

Figure 1. - Schematic arrangement showing essential features of vortex chamber.

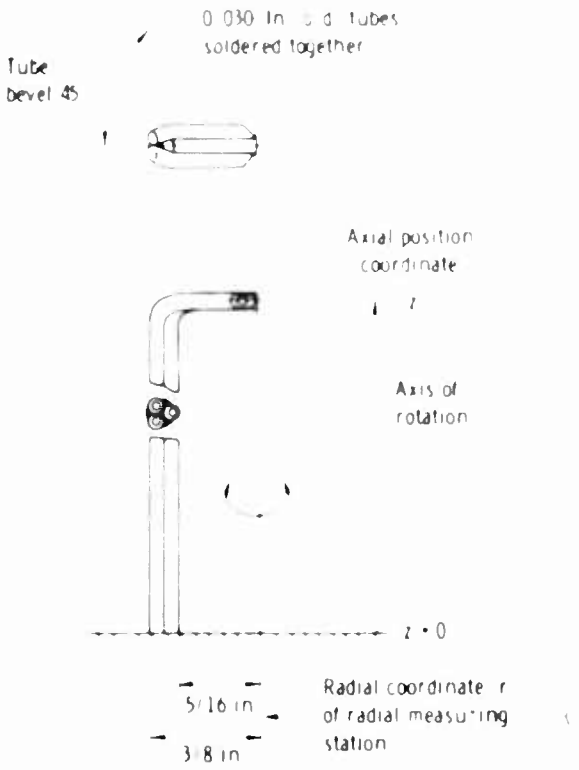

Figure 2 - Three-tube probe for measuring velocity vector magnitude and angular direction

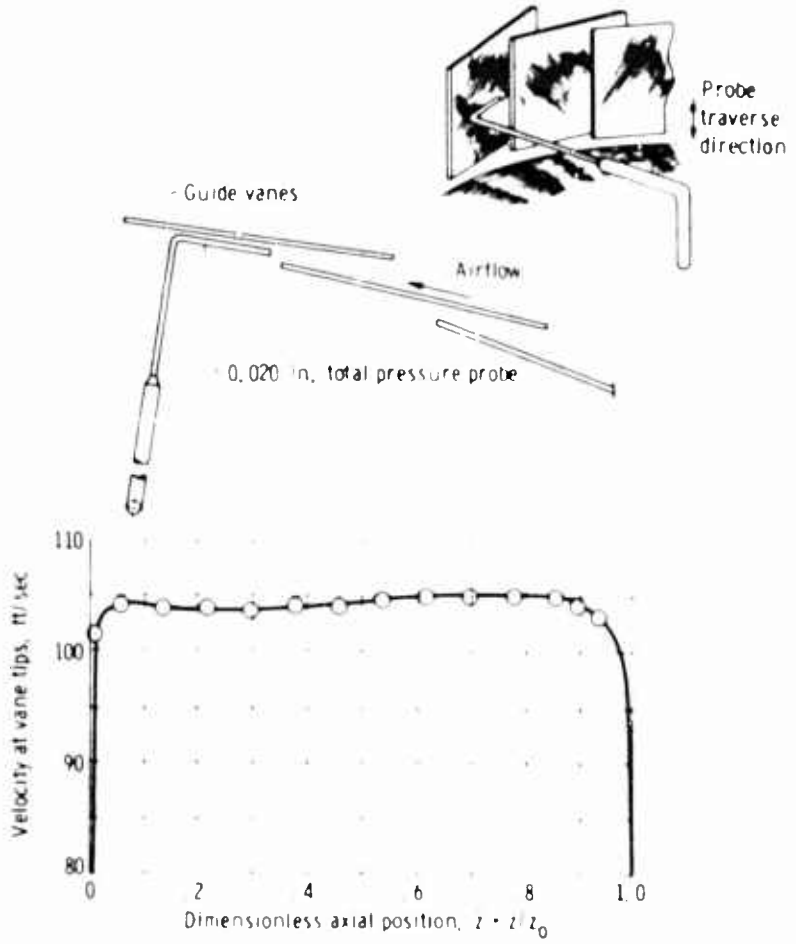

Figure 3 - Velocity profile at guide vane with measuring technique illustrated. Dimensionless radial coordinate, $\bar{r} = 1.0$, mass flow rate = 0.206 lb/sec.

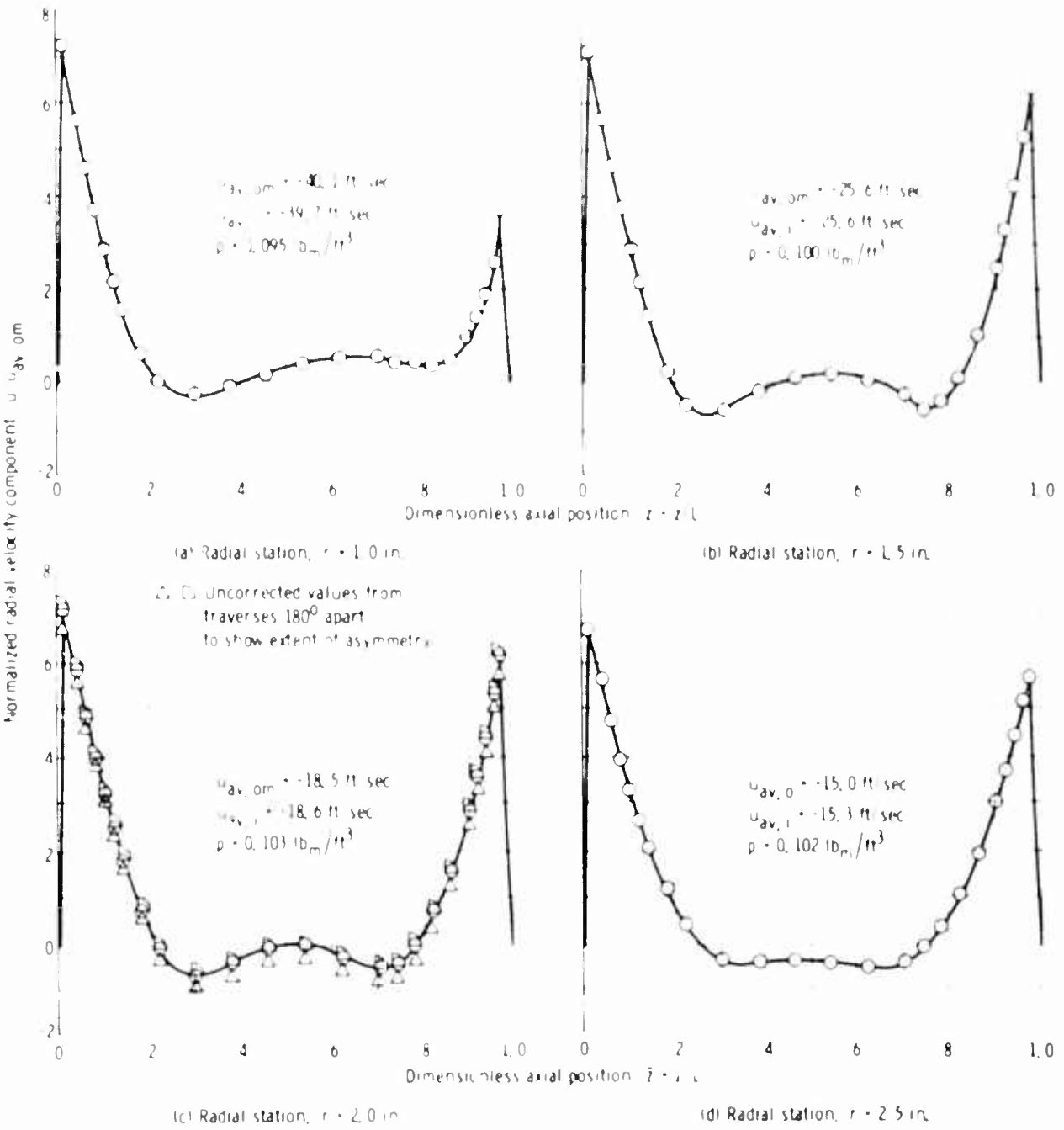

Figure 4. - Dimensionless radial velocity distributions at various radial positions (corrected for asymmetry).

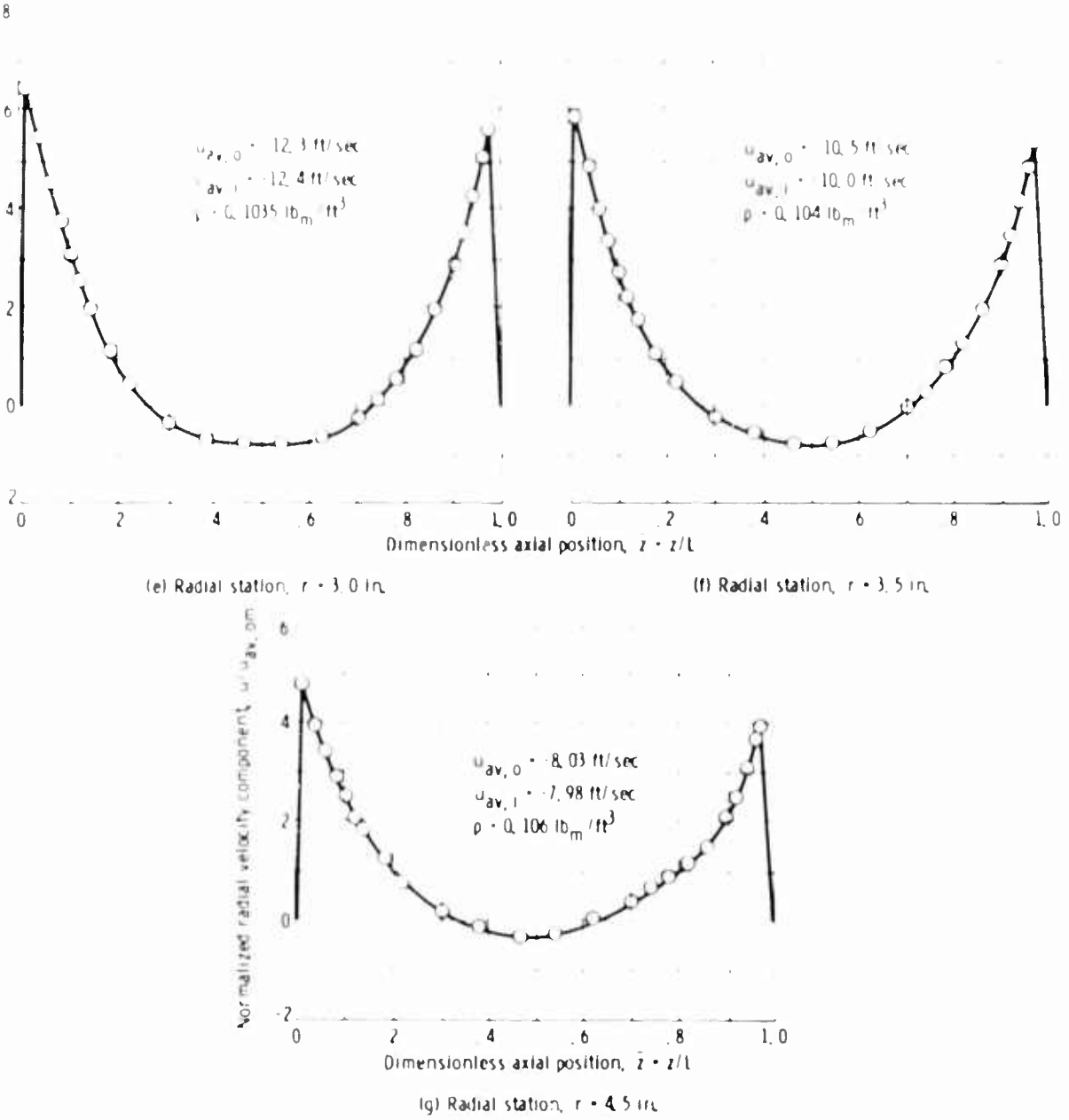

Figure 4. - Concluded. Dimensionless radial velocity distributions at various radial positions (corrected for asymmetry).

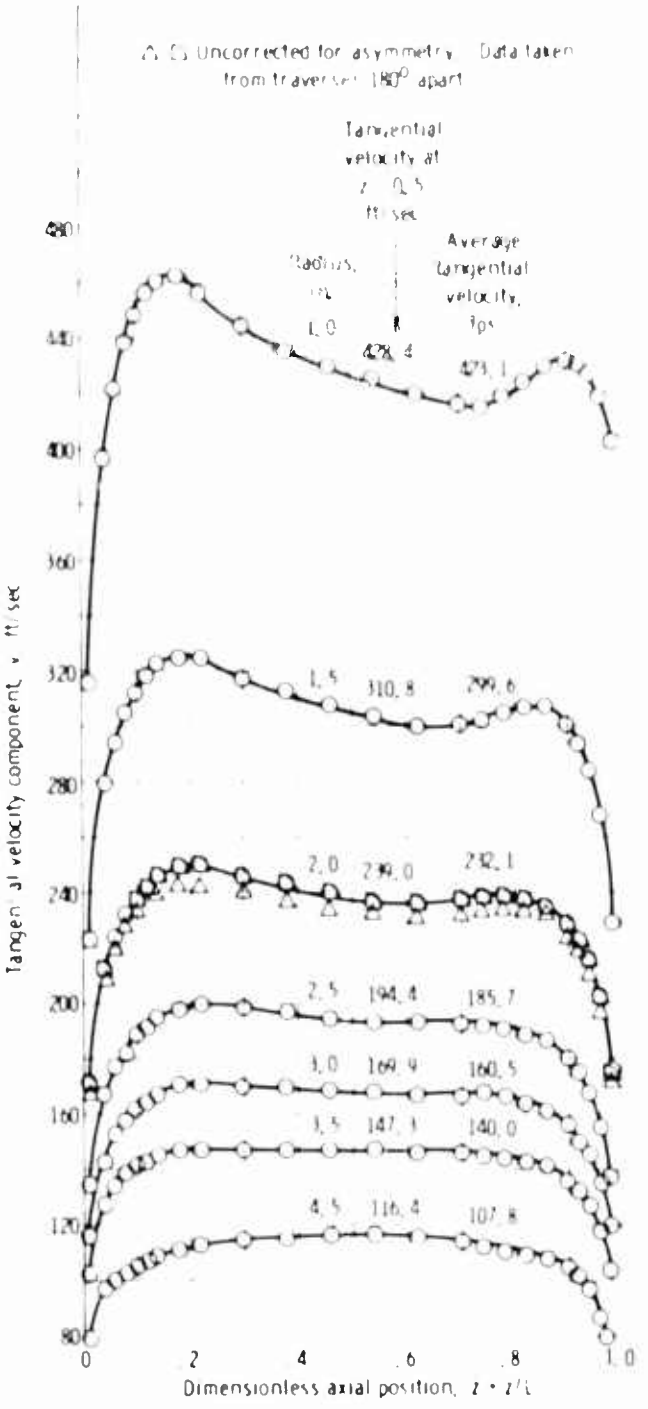

Figure 5. - Dimensional tangential velocity distributions at various radial positions (corrected for asymmetry).

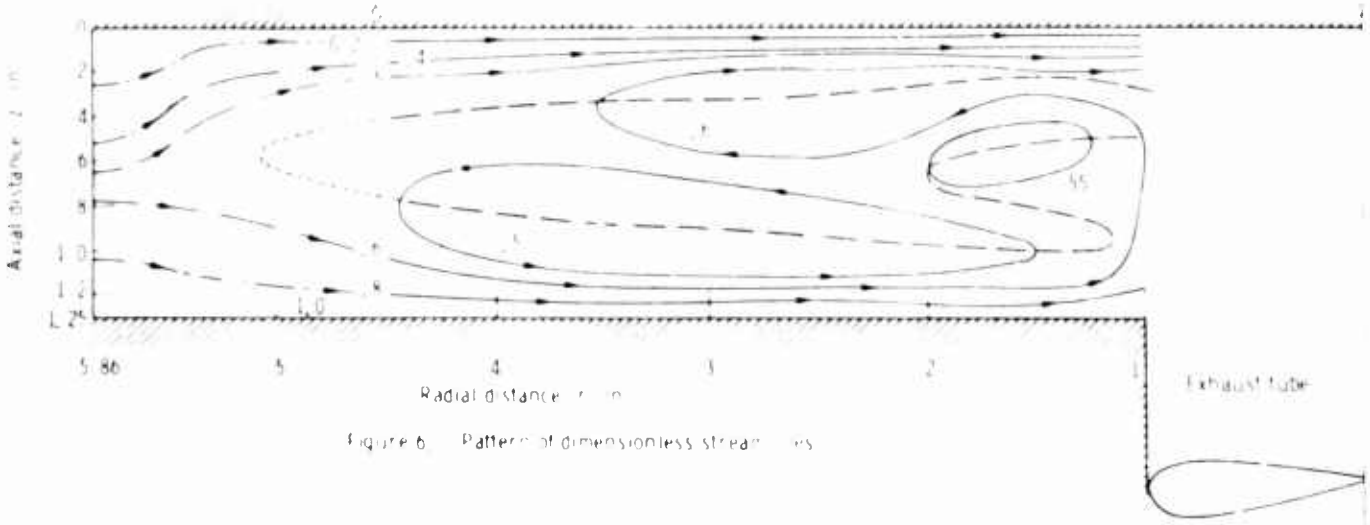

Figure 6 Pattern of dimensionless stream lines

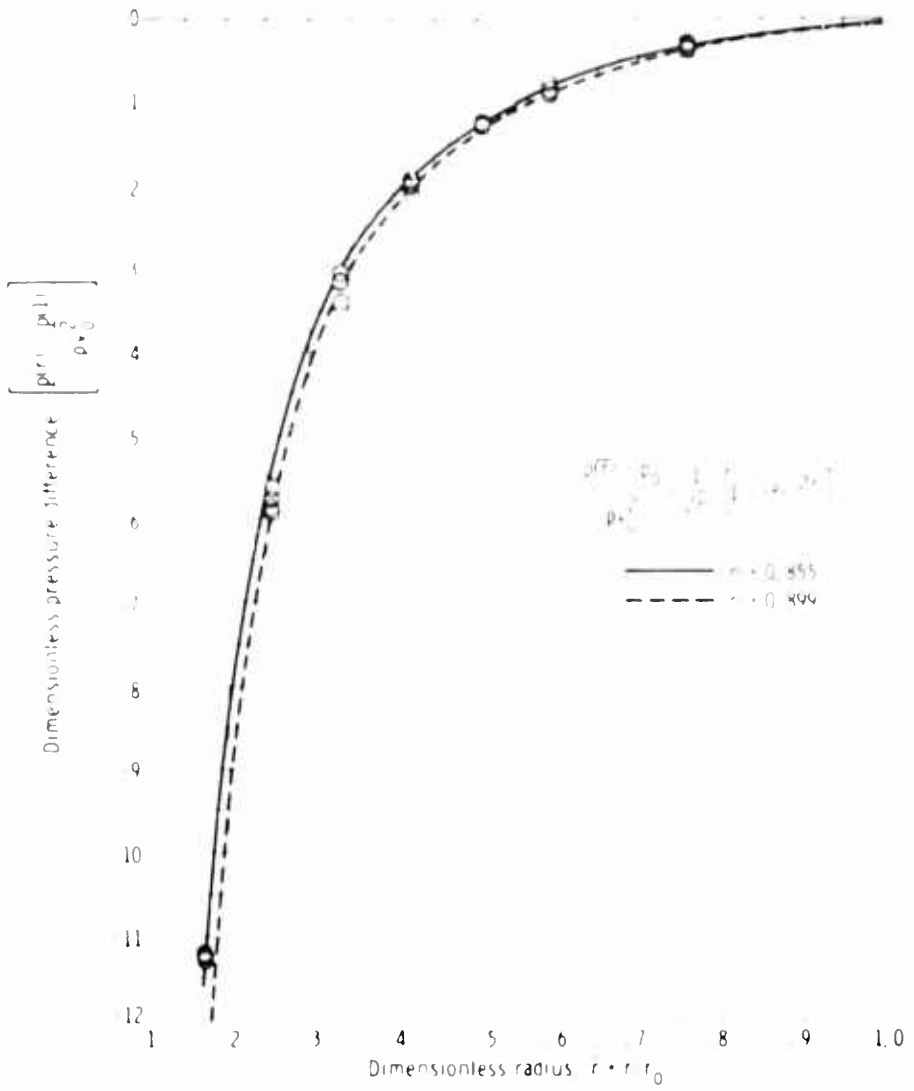

Figure 7 Comparison of experimentally and analytically determined radial distribution of static pressure

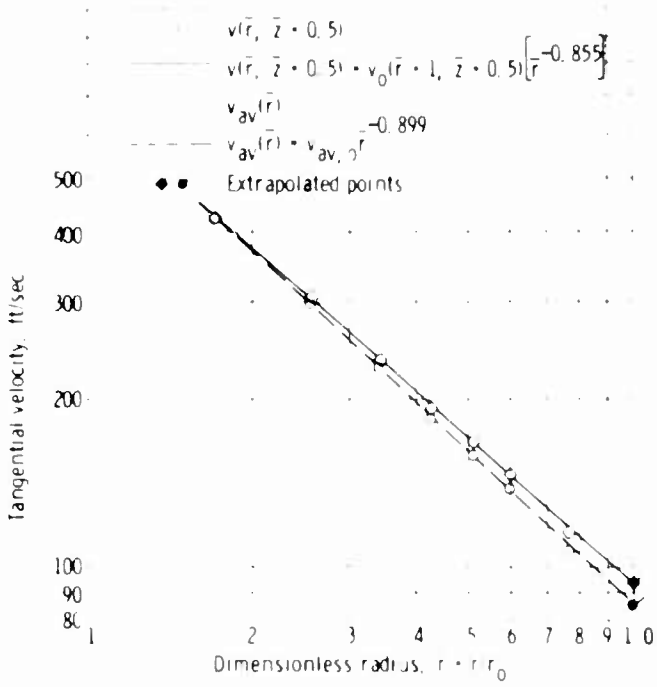

Figure 8 - Radial dependence of experimentally tangent velocities and best-fit curves through data

A THEORETICAL AND EXPERIMENTAL INVESTIGATION OF THE VORTEX-SINK ANGULAR RATE SENSOR

by

Turgut Sarpkaya

University of Nebraska, Lincoln, Nebraska

ABSTRACT

This paper describes the characteristics of flow of a viscous fluid between two rotating coaxial disks separated by a porous cylindrical wall. The sensitivity of the device to rotational motion has been determined for various flow rates, angular velocities, and types of pickoffs. The viscous efficiency of the sensor has been determined theoretically and compared with that obtained experimentally. It is found that the device as well as the pickoff may be designed for a given range of operation and maximum rate detection through a combination of theoretical and experimental studies.

INTRODUCTION

The purpose of the theoretical and experimental investigation described herein is to determine the characteristics of an angular rate sensor. This study falls in the general category of developing sensors, without moving parts, which utilize the properties of fluid flow to sense the changes in the state of motion of an object to which the sensor is rigidly attached and give a mass flow and pressure output proportional to the rate at which the change in motion occurs. The output of such a device may then be magnified to actuate other components in the system which will preserve with their reactions the original or the desired state of motion.

The vortex-sink angular rate sensor consists basically of an ideal sink flow between two coaxial disks and a vortex created by the rotation of the unit about its axis of symmetry. The strength of the ideal vortex is proportional to the rate of rotation. Hence, the determination of the rate of rotation reduces to the determination of the vortex strength either directly or indirectly through the measurement of certain dynamic characteristics of fluid motion. The direct measurement of the vortex strength is often difficult and requires the use of moving elements. On the other hand, the determination of mass and pressure output through non-moving elements or pickoffs provides only an indirect means

of evaluating the vortex strength or the rate of rotation. The use of indirect pickoff elements necessarily adds theoretical difficulties to the understanding of the rate sensor. To begin with, both the sink and the vortex flow are modified by the viscous forces. Consequently, the intensity of the vortex motion does not remain constant as it progresses through the u it. Secondly, the pickoff itself introduces secondary boundary-layer effects, reduces the effective flow area, and increases the noise level because of the vortices shed behind it. Thirdly, the presence of any object, however small, such as a pickoff in a region of high tangential velocity or large tangential shear causes large energy dissipation and reduces the intensity of the vortex created by the rotation of the rate sensor. Consequently, the angular momentum which the fluid retains at the sampling zone of the pickoff becomes an unknown fraction of the angular momentum imparted to the fluid by the sensor. It is for this reason that a theoretical and experimental study of the vortex-sink motion of a viscous fluid is undertaken herein.

EXPERIMENTAL EQUIPMENT AND PROCEDURE

The apparatus consisted of a compressor, filter, pressure regulator, metering pressure gage, rotameter, supply lines, a test chamber or a slip-ring mechanism, rate sensor, pickoff, pressure transducer, and an amplifier-recorder assembly. Figures 1, 2, and 3 show the general layout and two of the several sensors used.

Filtered and metered air was supplied to the porous coupling either by a test chamber enclosing the sensor as shown in Fig. 1, or by a slip-ring mechanism as shown in Fig. 2. The latter method permitted access to the sensor and made possible the installation of numerous pressure taps on one of the two coaxial disks.

The rate of rotation was determined by connecting the event marker on the recorder to an electrical wiper-contact on the sensor wall. For very slow rotations, in the order of 0.5 deg/sec, an electric timer was used to determine the angular velocity. The output of the rate sensor was determined through the use of several pickoffs. The size and location of each pickoff and the material used in its construction is shown in Fig. 4. The output of the pickoff was fed into a pressure transducer and recorded with the help of an amplifier-recorder assembly.

Experimental procedure consisted of the following steps:

a. setting the pressure regulator and the metering pressure gage;
b. setting the desired flow rate on the calibrated rotameter;
c. recording the pickoff signal (if any) without rotation;
d. rotating the sensor uniformly with the variable speed motor and recording the output of the pickoff;
e. increasing the flow rate to a new desired value, repeating step (c), and rotating the sensor at previously set angular velocity;

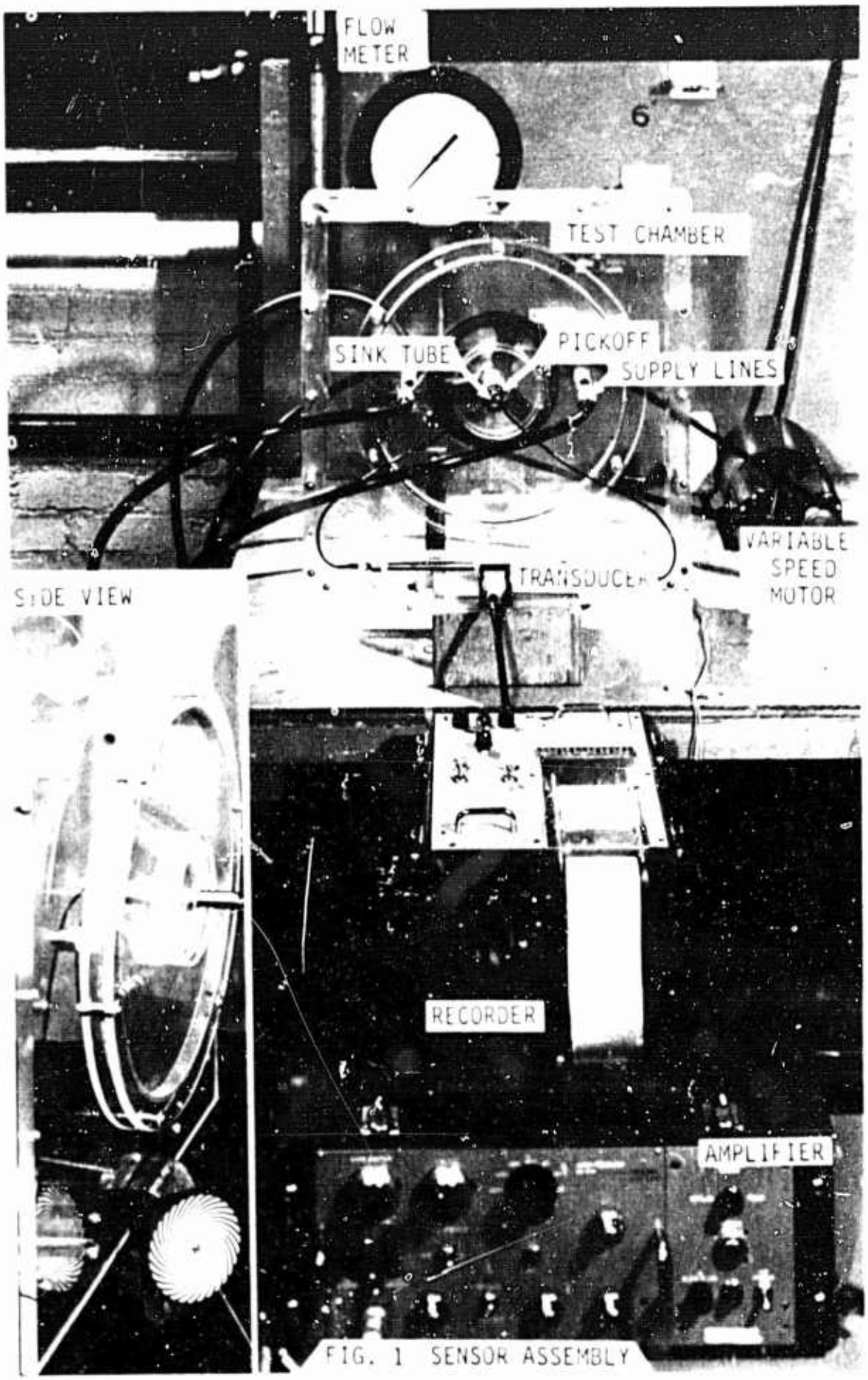

FIG. 1 SENSOR ASSEMBLY

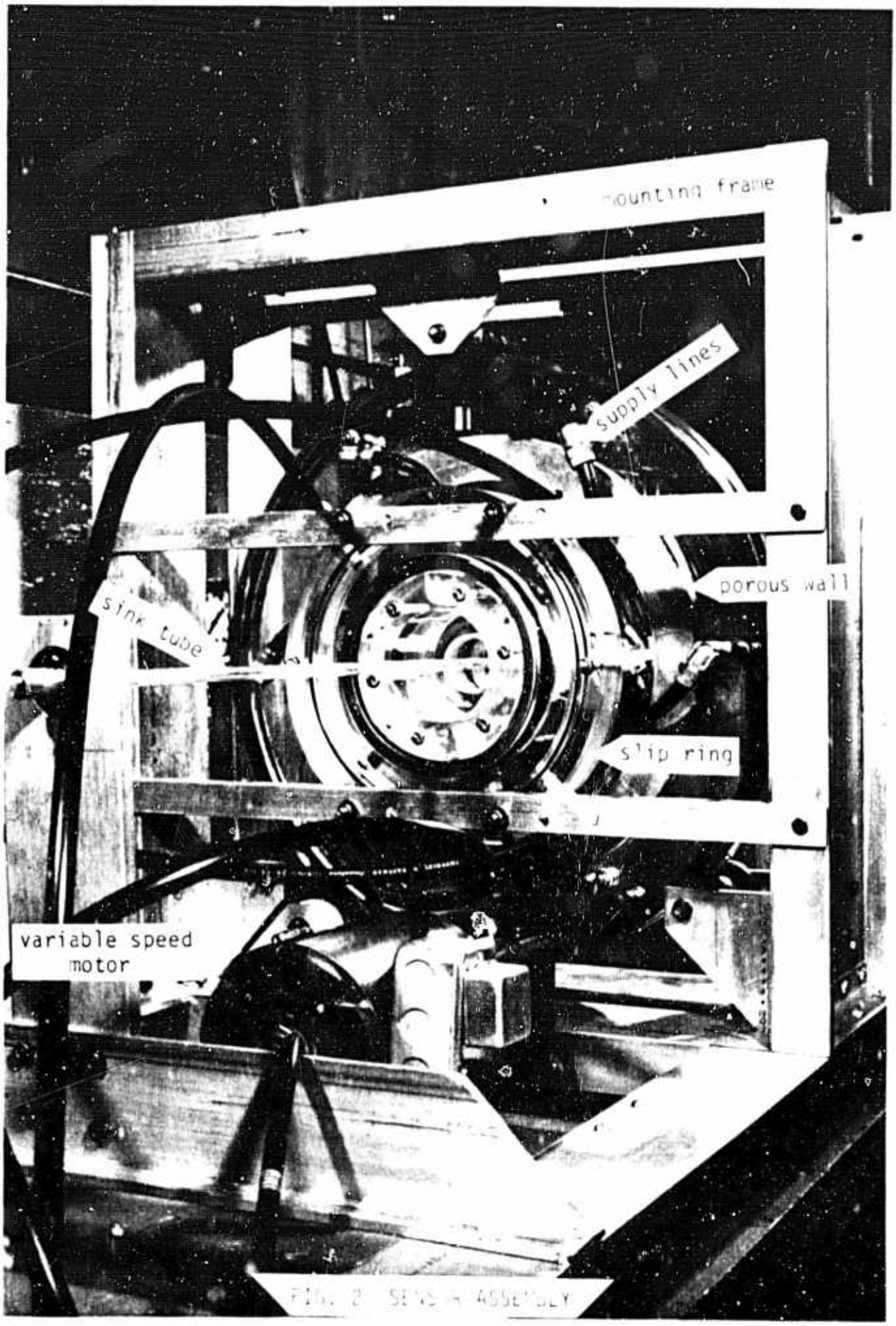

FIG. 2 SENSOR ASSEMBLY

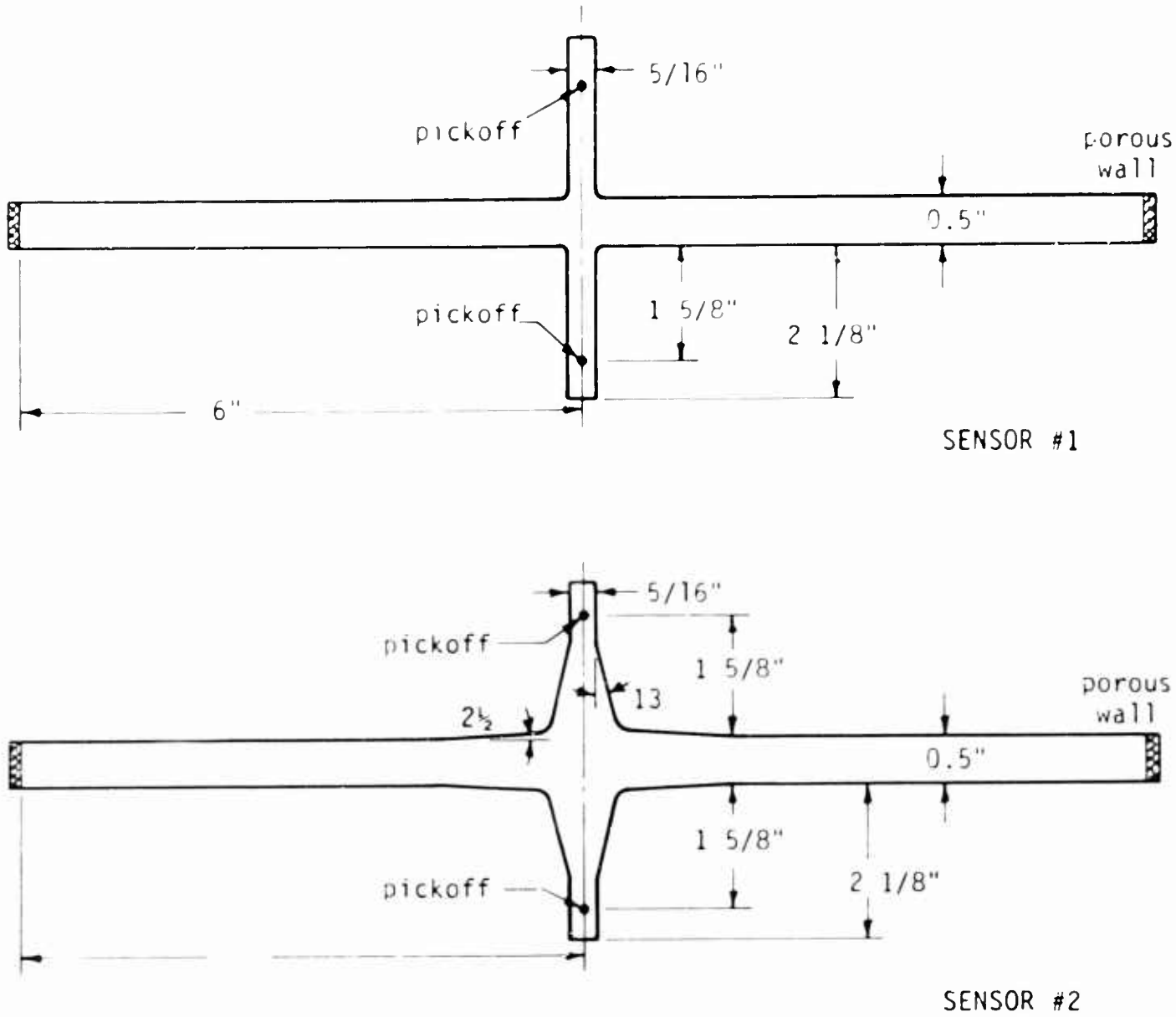

FIG. 3 GEOMETRICAL CHARACTERISTICS OF THE SENSORS

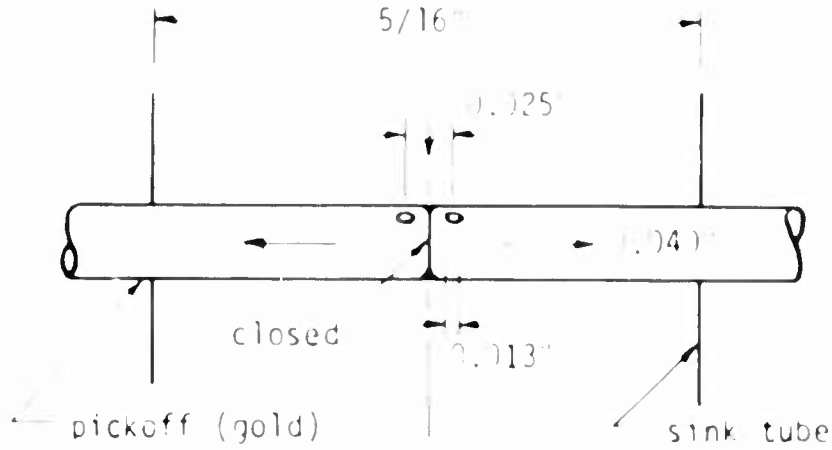

PICKOFF #1

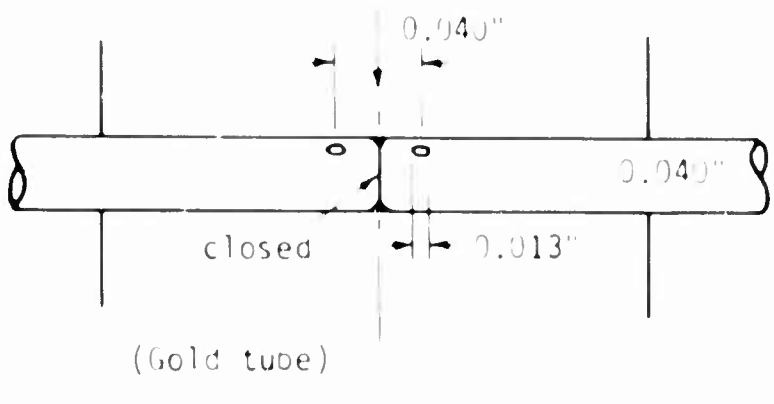

PICKOFF #2

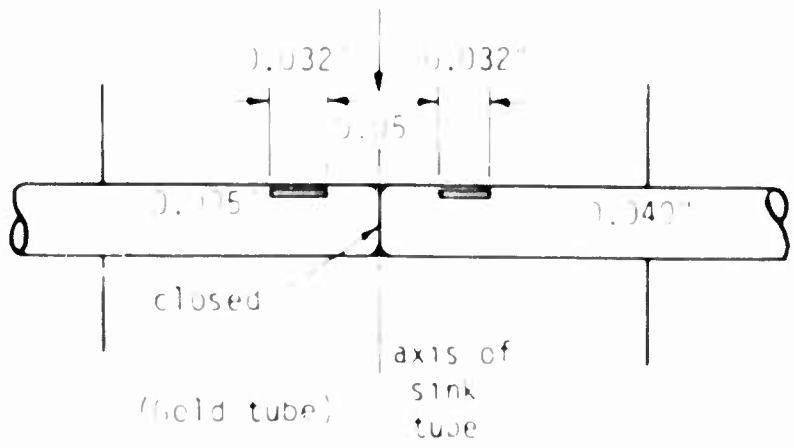

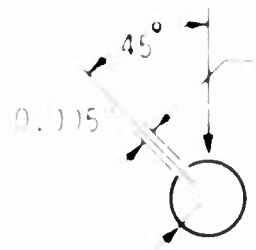

PICKOFF #3

FIG. 4-a GEOMETRIC CHARACTERISTICS OF PICKOFFS

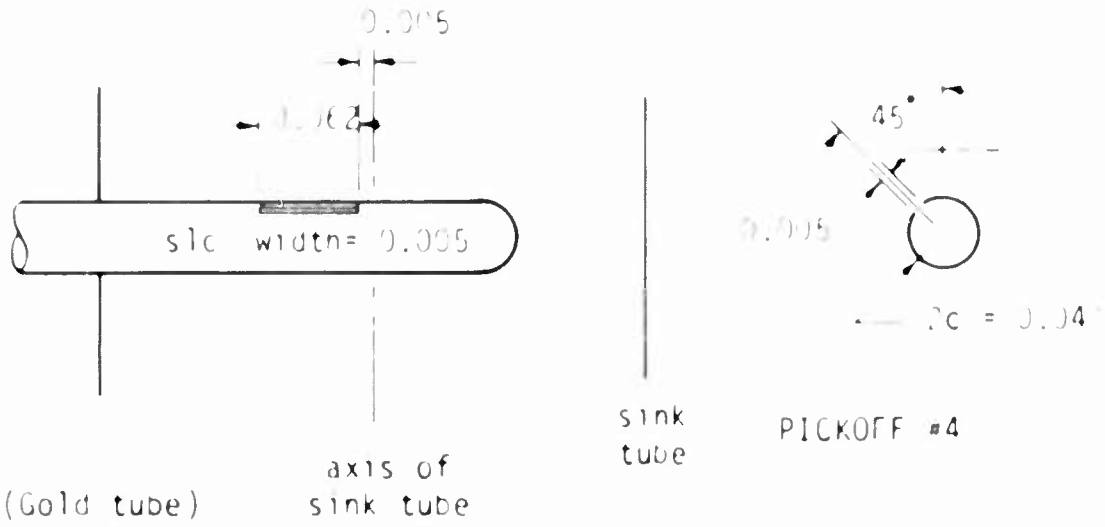

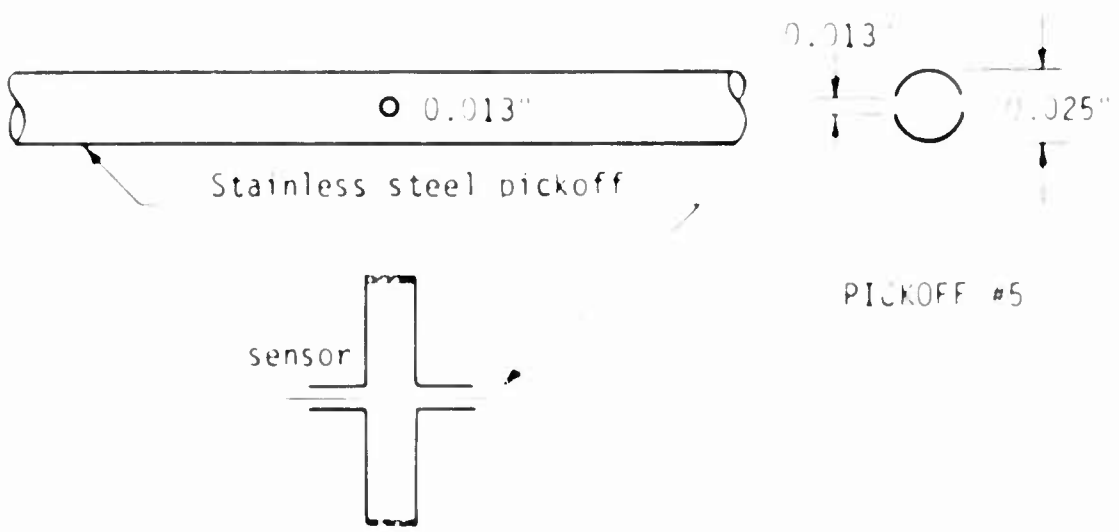

FIG. 4-6 GEOMETRIC CHARACTERISTICS OF PICKOFFS

f. repeating the above procedure for all flow rates, and finally,
g. beginning once again with the smallest flow rate and increasing the rate of rotation to a new constant value.

The data obtained through the procedure described above is evaluated and plotted in terms of the parameters devised theoretically.

THEORETICAL ANALYSIS OF VORTEX-SINK FLOW

The present study considers the type of flow shown in Fig. 5, where the fluid enters the region of interest through a porous wall, spirals radially inward, and exits axially at some smaller radius. Since the radial and tangential Reynolds numbers are in general within the subcritical range and since the radial and relative tangential velocities are required to be zero on the walls, viscosity generally plays an important part in determining the flow, at least in some neighborhood of the walls. Consequently, the present study is concerned with the motion of a viscous fluid.

It is well known that solving the full Navier-Stokes equations for a confined vortex is a formidable problem. A useful method of attack is to analyze the radial nonrotating flow through the use of the boundary layer equations and extend the resulting solution to flows with weak swirl through perturbation methods.

The influence of rotation on the fluid motion may be indicated by the Rossby number, $U_o b/\omega R_o^2$, which represents the ratio of linear momentum to angular momentum. When the Rossby number is large, the influence of rotation is small, and it is possible to consider perturbations about any of the simple, known solutions of the axially symmetric Navier-Stokes equations. Examples of this type have been given in the literature for other types of vortex flows.(1)

Analysis of the Radial Flow

In the case of two-dimensional steady motion of an incompressible viscous fluid, the boundary layer equations and their boundary conditions are given by:

$$u \frac{\partial u}{\partial x} + w \frac{\partial u}{\partial y} = U \frac{dU}{dx} + \nu \frac{\partial^2 u}{\partial y^2} \qquad (1)$$

---

(1) W. S. Lewellen, "Linearized Vortex Flows," AIAA Journal, vol. 3, No. 1, January, 1965, pp: 91-98.

and

$$\frac{\partial u}{\partial x} + \frac{\partial w}{\partial y} = 0 \tag{2}$$

with

$$y = 0, \quad u = 0, \quad w = 0, \quad y = \delta, \quad u = U(x) \tag{3}$$

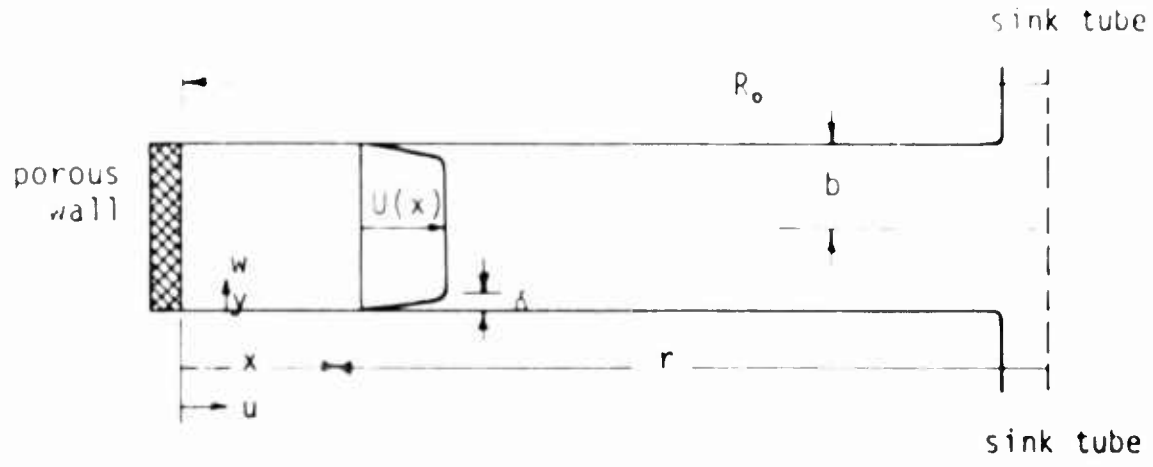

Fig. 5 Coordinate axes

We begin by writing the equation of continuity

$$\int_0^b u \, dy = U_o b \tag{4}$$

Introducing the displacement thickness δ^* as

$$\int_0^b (U - u) dy = U \delta^* \tag{5}$$

and noting that near the inlet section the boundary layer develops in the same way as on a flat plate at zero incidence in an unaccelerated flow, we have[2]

$$\frac{\delta^*}{b} = 1.72 \sqrt{\frac{\nu x}{b^2 U_o}} = K_1 \varepsilon \quad , \quad \varepsilon = \sqrt{\frac{\nu x}{b^2 U_o}} \tag{6}$$

[2] Boundary Layer Theory, Herman Schlichting, 4th Ed. McGraw-Hill, 1960, Translated by: J. Kestin.

Hence, the velocity of the potential flow outside the boundary layer becomes

$$U(x) = \frac{U_o R_o}{R_o - x}(1 + K_1\varepsilon + K_2\varepsilon^2 + \ldots) \tag{7}$$

in which K_2, K_3, ... remain to be determined as part of the solution. witnout the effect of the boundary layer, the velocity of the potential flow would have been

$$U(x) = \frac{U_o R_o}{R_o - x}$$

Now introducing the similarity transformation,

$$n = \frac{y}{R_o - x}\sqrt{\frac{U_o R_o}{\nu}} \tag{8}$$

and the stream function

$$\Psi(x,y) = \frac{U_o b \sqrt{R_o}}{\sqrt{x}}\{\varepsilon f_o(n) + \varepsilon^2 f_1(n) + \ldots \varepsilon^n f_n(n)\} \tag{9}$$

we obtain the velocity components u and w as

$$u = \frac{\partial \Psi}{\partial y} = \frac{U_o R_o}{R_o - x}(f_o' + \varepsilon f_1') \tag{10}$$

and

$$-w = \frac{\partial \Psi}{\partial x} = \sqrt{U_o R_o \nu}\{f_o' \frac{y}{(R-x)2}\sqrt{\frac{U_o R_o}{\nu}} + \frac{1}{2}\sqrt{\frac{\nu}{b^2 U_o x}} f_1 + \varepsilon f_1' \frac{y}{(R-x)^2}\sqrt{\frac{U_o R_o}{\nu}}\} \tag{11}$$

wnere f_o' , f_1' , etc. denote the derivatives of f_o , f_1 , ... with respect to n.

In order to make sure that the equation of continuity is satisfied it is necessary to determine the derivatives of the velocity components as

$$\frac{\partial u}{\partial x} = \frac{U_o R_o}{(R_o - x)^2}\left(f_o' + \varepsilon f_1'\right) + \frac{U_o R_o}{R_o - x}\left\{f_o'' \frac{y}{(R_o - x)^2}\sqrt{\frac{U_o R_o}{\nu}} + \right. \tag{12}$$

$$\left. \frac{1}{2} f_1' \sqrt{\frac{\nu}{b^2 U_o x}} + \varepsilon f_1'' \frac{y}{(R_o - x)^2}\sqrt{\frac{U_o R_o}{\nu}} + \cdots \right\}$$

and

$$-\frac{\partial w}{\partial y} = \frac{U_o R_o}{R_o - x}\sqrt{\frac{U_o R_o}{\nu}}\frac{y}{(R_o - x)^2} f_o'' + \frac{U_o R_o}{(R_o - x)^2} f_o' + \frac{1}{2}\sqrt{\frac{U_o \nu}{b^2 x}}\frac{1}{R_o - x} f_1' + \tag{13}$$

$$U_o R_o \sqrt{\frac{U_o R_o}{\nu}}\,\varepsilon \frac{y}{(R_o - x)^3} f_1'' + \varepsilon \frac{U_o R_o}{(R_o - x)^2} f_1' + \cdots$$

Introducing Eq. (12) and (13) into Eq. (2), it is easy to verify that the equation of continuity is satisfied.

Now introducing the velocity components and their derivatives into the equation of motion, Eq. (1), we obtain for the first approximation, i.e. for $\varepsilon \cong 0$, the differential equation*

$$f_o'^2 = 1 + f_o''' \tag{14}$$

which is to be solved with the boundary conditions

$$\begin{aligned} \eta = 0 &: \quad f_o' = 0 \,, \quad f_o = 0 \\ \eta = \infty &: \quad f_o' = 1 \end{aligned} \tag{15}$$

Multiplying Eq. (14) with f_o'' and integrating, one has

---

*This equation is identical with that obtained for the exact solution of viscous flow in a convergent channel (see Ref. 2, page 144). The similarity, at least for the first approximation, between the radial flow in a sensor and the flow in a convergent channel is apparent.

$$f_o''^2 - \frac{2}{3}(f_o' - 1)^2 (f_o' + 2) = C \tag{16}$$

Since $\eta \to \infty$ $f_o'' = 0$, $f_o' = 1$, $C = 0$, we have

$$f_o'' = \frac{df_o'}{d\eta} = \left\{\frac{2}{3}(f_o' - 1)^2 (f_o' + 2)\right\}^{1/2} \tag{17}$$

or

$$\eta = \sqrt{\frac{3}{2}} \int \frac{df_o'}{\sqrt{(f_o' - 1)^2 (f_o' + 2)}} \tag{18}$$

Upon performing the indicated integration, we nave

$$\eta = \sqrt{2}\left\{\tanh^{-1}\frac{\sqrt{2 + f_o'}}{\sqrt{3}} - \tanh^{-1}\sqrt{\frac{2}{3}}\right\} \tag{19}$$

Solving for f_o', we have

$$f_o' = \frac{u}{U(x)} = 3\,\tanh^2\left(\frac{\eta}{\sqrt{2}} + 1.146\right) - 2 \tag{20}$$

Combining Eq. (20) with Eq. (10) and remembering that for the first approximation $\epsilon = 0$, we have

$$\frac{u}{U_o} = \frac{3}{1 - \frac{x}{R_o}} \tanh^2 \frac{y\sqrt{\frac{U_o}{2R_o\nu}}}{1 - \frac{x}{R_o}} + 1.146 - \frac{2}{1 - \frac{x}{R_o}} \tag{21}$$

Althougn it was possible to obtain a second order solution for u/U_o by making use of Eq. (20), this was found to be unnecessary particularly for small rates of rotation.

A careful examination of Eq. (20) shows that at $\eta = 3$, the boundary layer merges with the potential flow. Hence, the boundary layer thickness becomes (see Eq. 8)

$$y = \delta = 3(R_o - x)\sqrt{\frac{\nu}{U_o R_o}} \tag{22}$$

which shows that δ is maximum near the porous wall and it decreases as the flow approaches the sink tube.

It should first be noted that there is no possibility of the boundary layer thickness increasing toward the sink and choking the potential flow. Secondly, in order to reduce the effect of viscosity on the performance of the sensor one must gently converge the sensor walls from the porous coupling toward the sink tube instead of diverging them. At present a sensor is being built with converging side walls and short streamlined entrances into the sink tubes.

Returning to Eq. (22), it is noted that the maximum value of δ is given by

$$\delta_m = 3\sqrt{\frac{\nu R_o}{U_o}} \tag{23}$$

In general the half width b of the sensor is larger than δ_m (with the possible exception of that portion near the porous coupling) and the theoretical analysis based on the boundary conditions used herein ($y = 0$, $u = 0$, $w = 0$, $y = b$, $u = U(x)$), is as precise as the one which would have been obtained by using the boundary conditions $y = 0$, $u = 0$, $y = b$, $u = U(x)$.

Flow with Weak Swirl

In the foregoing, the development of the boundary layer and the velocity components for only the radial sink flow were discussed. It is appropriate at this time to determine the tangential component of velocity due to axial rotation as well as the ever present radial flow.

For large values of the Rossby number, i.e. for weak swirls, the inclination of the relative streamlines within the boundary layer with respect to the radial direction—if the wall is imagined at rest and the fluid is taken to rotate at a large distance from the wall—may be written equal to the inclination of the relative streamlines outside the boundary layer. This procedure yields

$$v_{rt} = \frac{\omega R_o}{U_o}\left(\frac{r_r}{r_o} - \frac{r^2}{R_o^2}\right) u \tag{24}$$

in which Γ_r and Γ represent the strength of the vortex at radial distances r and R_o respectively and u is given by Eq. (21). Figure 6 shows the variation of the tangential component of velocity.

If the strength of the vortex were not diminished by the shear stress on the walls, the ratio Γ_r/Γ_o would have been equal to unity. Obviously, Γ_r/Γ_o represents the ratio of the angular momentum which the fluid retains at a radial distance r to that imparted at the coupling, i.e. the viscous efficiency of the sensor.

Viscous Efficiency of the Sensor

In order to determine the ratio of the circulation or the angular momentum which the fluid retains at the pickoff to that imparted at the coupling it is necessary to determine the circumferential component of the shear stress.

Writing

$$\tau_{Ot} = \mu \left|\frac{\partial v_{rt}}{\partial y}\right|_{y=0} = \mu \frac{\omega R_o}{U_o} \left(\frac{\Gamma_r}{\Gamma} - \frac{r^2}{R_o^2}\right) \left|\frac{\partial u}{\partial y}\right|_{y=0} \qquad (25)$$

and

$$\left|\frac{\partial u}{\partial y}\right|_{y=0} = \frac{U_o R_o}{r} \left|f_o''\right|_{y=0} \frac{1}{r} \sqrt{\frac{U_o R_o}{\nu}} \qquad (26)$$

through the use of Eqs. (8) and (10), one obtains

$$\tau_{Ot} = \rho \omega \frac{R_o^2}{r^2} \left(E - \frac{r^2}{R_o^2}\right) \left|f_o''\right|_{y=0} \sqrt{U_o R_o \nu} \quad \text{with} \quad \Gamma_r/\Gamma_o = E \qquad (27)$$

Since $y = 0 \rightarrow n = 0 \rightarrow f_o' = 0$, Equation (17) yields $\left|f_o''\right|_{y=0} = 2/\sqrt{3}$.

The strength, $\Gamma_r/2\pi$, of the vortex at a radial distance r may be written as

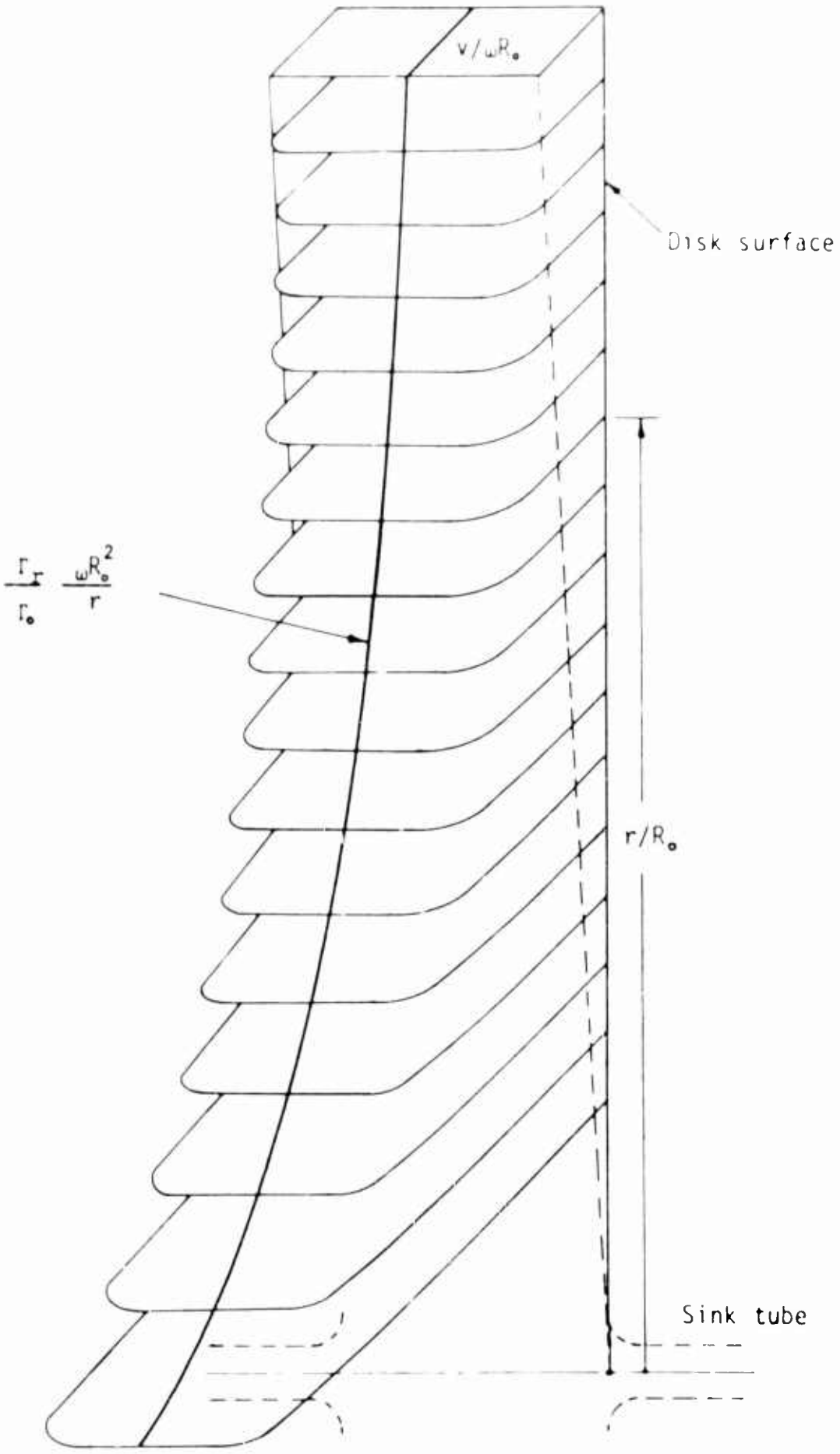

Fig. 6 Tangential Velocity Distribution

$$\frac{\Gamma_r}{2\pi} = \frac{r}{b}\int_0^b v\,dy \tag{28}$$

The torque acting on the two sides of an annulus of fluid mass dM ($dM = 4\pi\rho br dr$) is given by

$$dT = 4\pi r^2 \tau_{0t} dr \tag{29}$$

Since

$$\frac{dT}{dM} = \frac{\partial(\Gamma_r/2\pi)}{\partial t} = \frac{\partial(\Gamma_r/2\pi)}{\partial r}\frac{dr}{dt} \tag{30}$$

we have

$$\frac{\partial(\Gamma_r/2\pi)}{\partial r} = \frac{r}{b}\frac{\tau_{ot}}{u} \tag{31}$$

If there were no effect of viscosity, the vortex strength $\Gamma_r/2\pi$ would obviously have been equal to ωR_0^2. In order to evaluate the effect of viscosity on the reduction of circulation, the ratio of circulation actually present at a given distance r to the ideal circulation ωR_0^2 is defined as the viscous efficiency E. Hence, we have

$$E = \frac{\Gamma_r}{\Gamma_o} = \frac{1}{\rho b\omega R_o^2}\int_{r_{po}}^{R}\frac{\tau_o r}{u}\,dr \tag{32}$$

or by replacing u by the average radial velocity U_0R_0/r and combining with Eq. (27), one obtains

$$\frac{dE}{dr} = \frac{2}{\sqrt{3}}\frac{1}{b}\sqrt{\frac{\nu}{U_o R_o}}\left(E - \frac{r^2}{R_o^2}\right)$$

Writing

$$r/R_o = \zeta \ , \quad r_{po}/R_o = \zeta_{po}, \quad Q = 4\P R_o b U_o$$

$$Re = \frac{Q\, b}{\nu\, R_o^2} \ , \quad \text{and} \quad K = 4\sqrt{\frac{\P}{3}}\sqrt{\frac{1}{Re}}$$

we have

$$\frac{dE}{d\zeta} = K\,(E - \zeta^2) \tag{33}$$

Integrating Eq. (33) and noting that for $\zeta = 1$, $E = 1$, one obtains

$$E = \zeta_{po}^2 + \frac{2\,\zeta_{po}}{K} + \frac{2}{K^2} - \left(\frac{2}{K} + \frac{2}{K^2}\right) e^{K(\zeta_{po}-1)} \tag{34}$$

Although we are interested with the value of E at the pickoff, i.e. at $\zeta = \zeta_{po}$, in general ζ_{po} is extremely small and for all practical purposes it may be taken as zero. Hence, Eq. (34) reduces to

$$E = \frac{3\ Re}{8\ \P} - \left(\frac{1}{2}\sqrt{\frac{3}{\P}}\sqrt{Re} + \frac{3}{8}\frac{Re}{\P}\right) e^{-4\sqrt{\frac{\P}{3}}\sqrt{\frac{1}{Re}}} \tag{35}$$

The results obtained from this equation are compared later with those obtained experimentally.

The Output of the Pickoff

The pressure distribution around a cylinder of radius c located in a uniform flow of U_s is given by

$$p = p_o + \frac{\rho U_s^2}{2}\,(1 - 4\sin^2\theta) \tag{36}$$

in which P_∞ is the ambient pressure.

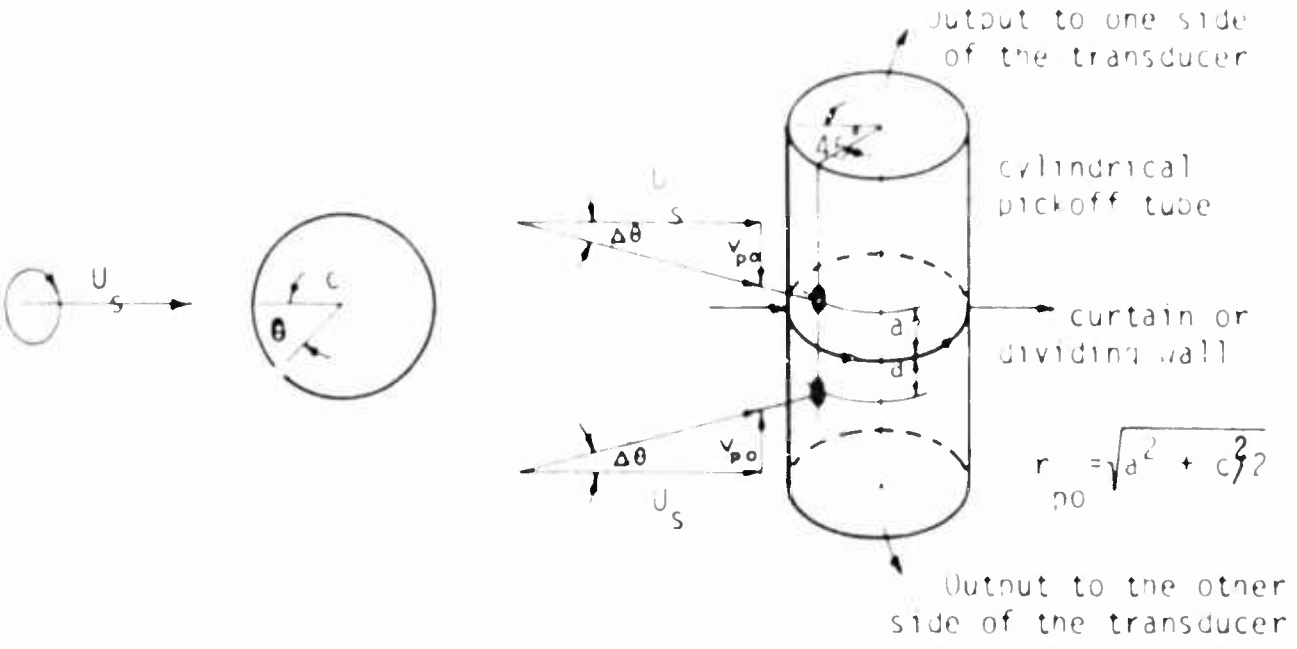

Fig. 7

In order to find the maximum of $\partial p/\partial\theta$, we write

$$\frac{\partial p}{\partial \theta} = -8 \frac{\rho U_s^2}{2} \sin\theta \cos\theta \tag{37}$$

and

$$\frac{\partial^2 p}{\partial \theta^2} = -8 \frac{\rho U_s^2}{2} \cos 2\theta \quad , \quad \theta = \pi/4 \tag{38}$$

Consequently, the holes on the pickoff must be located at $\theta = \pm \pi/4$ in order to get the largest response. Hence from Eq. (37) we have

$$|\Delta p| = 4 \frac{\rho U_s^2}{2} \Delta\theta \quad \text{(for one hole)} \tag{39}$$

The angle $\Delta\theta$ must be determined in terms of U_s and the tangential velocity prevailing at the point (actually a finite sampling area) of output.

With reference to Fig. 7, one finds that

$$U_s = V_{r_{po}} / U_s \tag{40}$$

Combining Eqs. (35), (39), and (40), we have

$$\frac{\Delta p}{\rho U_s^2/2} = 4 \frac{\omega R_o}{U_s} \frac{R_o}{r_{po}} E \tag{41}$$

It must be noted that the pickoff, because of its finite dimension, reduces the effective area in the sink tube. The effective velocity around the probe is determined by writing

$$Q = (\pi r_s^2 - 2 c . 2r_s) U_s \tag{42}$$

or

$$U_s = \frac{Q}{\pi r_s^2 - 4 c r_s} \tag{43}$$

Eq. (43) is used together with Eq. (41) in calculating the dimensionless parameter $\Delta p/\rho U_s^2/2$.

In closing the theoretical analysis the following observations must be recorded:

a. when two pickoff holes are used as in the case of pickoffs # 1, 2, and 3, the right side of Eq. (41) must be multiplied by 2, i.e.,

$$\frac{\Delta p}{\rho U_s^2/2} = 8 \frac{\omega R_o}{U_s} \frac{R_o}{r_{po}} E \tag{44}$$

since the differential pressure is twice the pressure obtained through one hole or slot;

b. the energy loss near the entrance into the sink tube and within the sink tube is not taken into consideration in the determination of E;

c. the points (actually holes or slots of finite size) on the pickoff indicate the average pressure over the sampling area rather than the pressure at a theoretical point. A better approximation could easily be obtained by performing a double integration with respect to r and θ over the sampling area. This was done for the pickoff # 2, and it was found that the use of a radial distance r_{po} (see Fig. 7) to the

center of the pickoff hole is more than satisfactory for the calculation of the actual average pressure;

d. it is obvious that the theoretical efficiency of the sensor would be higher than that predicted experimentally because of the energy losses not included in the analysis.

Although the theoretical analysis presented in the foregoing is fairly complete and quite satisfactory for small to moderate rates of rotation, studies are underway to extend the analysis to higher orders of approximation to make it applicable to larger rates of rotation.

DISCUSSION OF RESULTS AND CONCLUSIONS

A matter of considerable interest is the comparison of the measured pickoff output with that determined theoretically. Before doing so, however, the results of the exploratory measurements made with various pickoffs will be presented.

Figure 8 shows the data obtained with pickoff # 5 and sensor # 1 for various flow rates. It is apparent that this particular pickoff does not sense the direction of rotation and that its output at low values of ω is not satisfactory. It may, however, be used successfully for moderate values of ω to detect the changes in a unidirectional rotation. Under these circumstances it will be found that the output of the pickoff # 5 (psi/deg/sec) is quite high.

Extensive exploratory measurements were made with the pickoff # 4. Figure 9 shows the pressure distribution around the pickoff for three different flow rates with no rotation. This particular experiment was conducted for the sole purpose of determining the effect of the sink tube on the characteristics of flow around a circular cylinder protruding only half way into the pipe flow. The results show conclusively that if the diameter of the pickoff is small compared with the diameter of the sink tube, the pressure distribution around the pickoff area of the probe is not significantly different from that around the circular cylinder immersed in an unbounded uniform flow. Figure 10, which was obtained with probe # 4 and sensor # 2, shows the output as a function of the rate of rotation for $\theta = \pi/4$. It is clear that the output of the pickoff increases considerably with the increasing flow rates. At high rates of rotation, however, the output levels off and the pickoff becomes rather ineffective. The significance of this result lies in the fact that one needs different types of probes for small or moderate angles of rotation in order to obtain the optimum output.

Upon completion of the preliminary investigation, probes # 1, 2, and 3 were designed and built using a gold tube available commercially. Figure 11 shows the results obtained with probe # 2 and sensor # 2 in terms of pressure (psi) and rotation (deg/sec, clockwise or counter-clockwise)

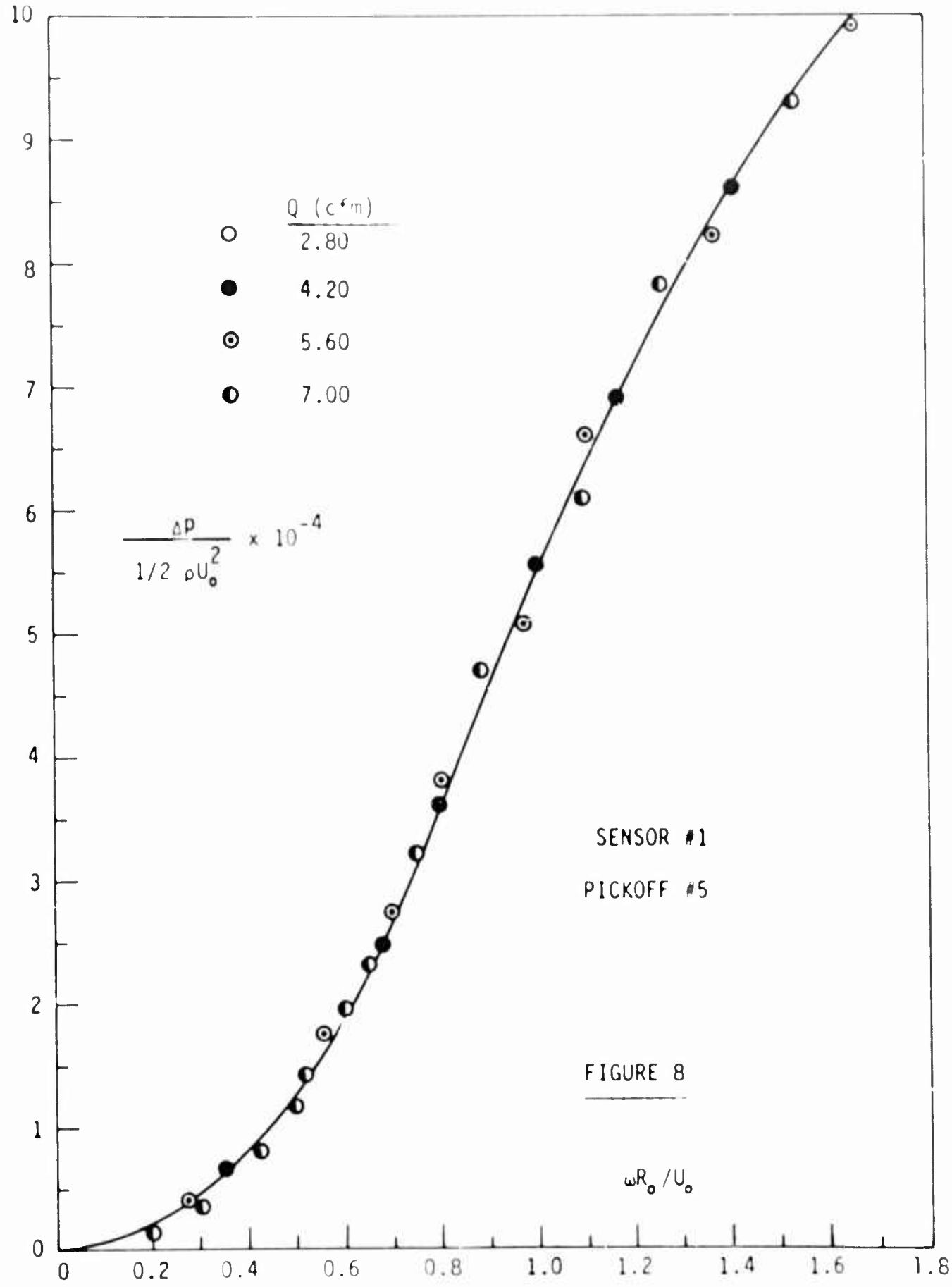
Q (c'm)
2.80
4.20
5.60
7.00
$\frac{\Delta p}{1/2\ \rho U_o^2} \times 10^{-4}$
SENSOR #1
PICKOFF #5
$\omega R_o / U_o$
0
1
2
3
4
5
6
7
8
9
10
0
0.2
0.4
0.6
0.8
1.0
1.2
1.4
1.6
1.8

FIGURE 8

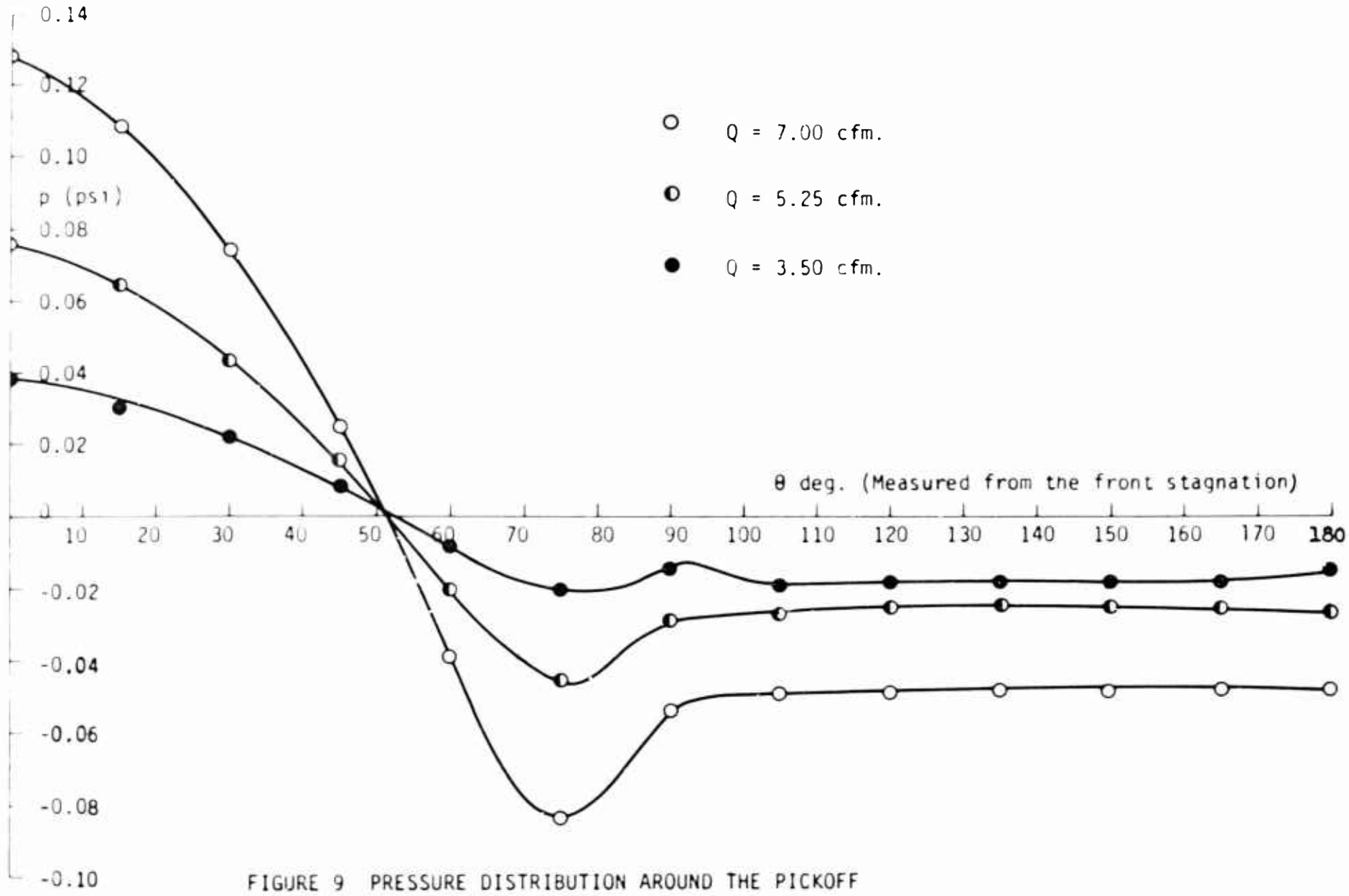

FIGURE 9 PRESSURE DISTRIBUTION AROUND THE PICKOFF

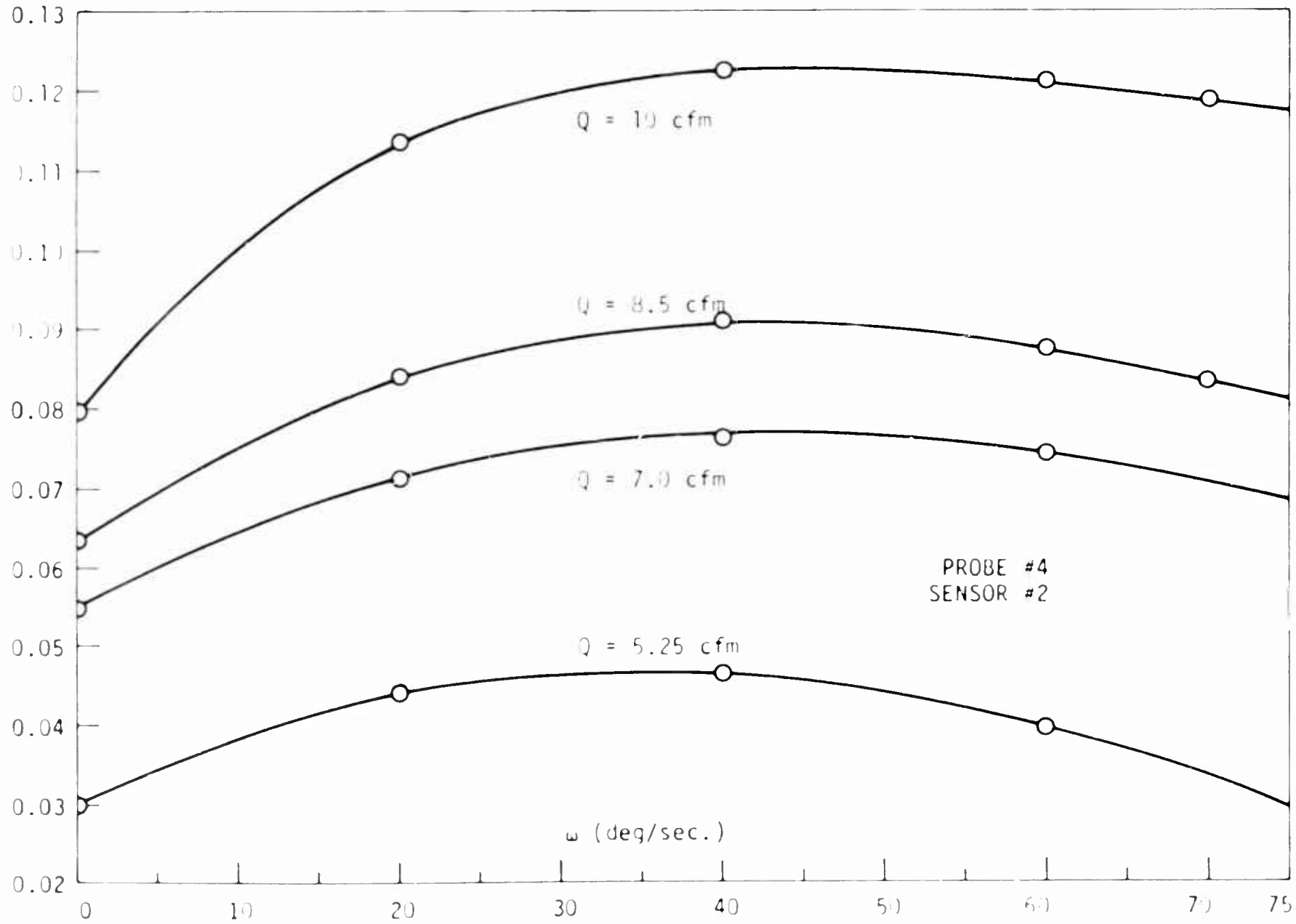

FIG. 10 OUTPUT AS A FUNCTION OF ROTATION FOR VARIOUS FLOW RATES

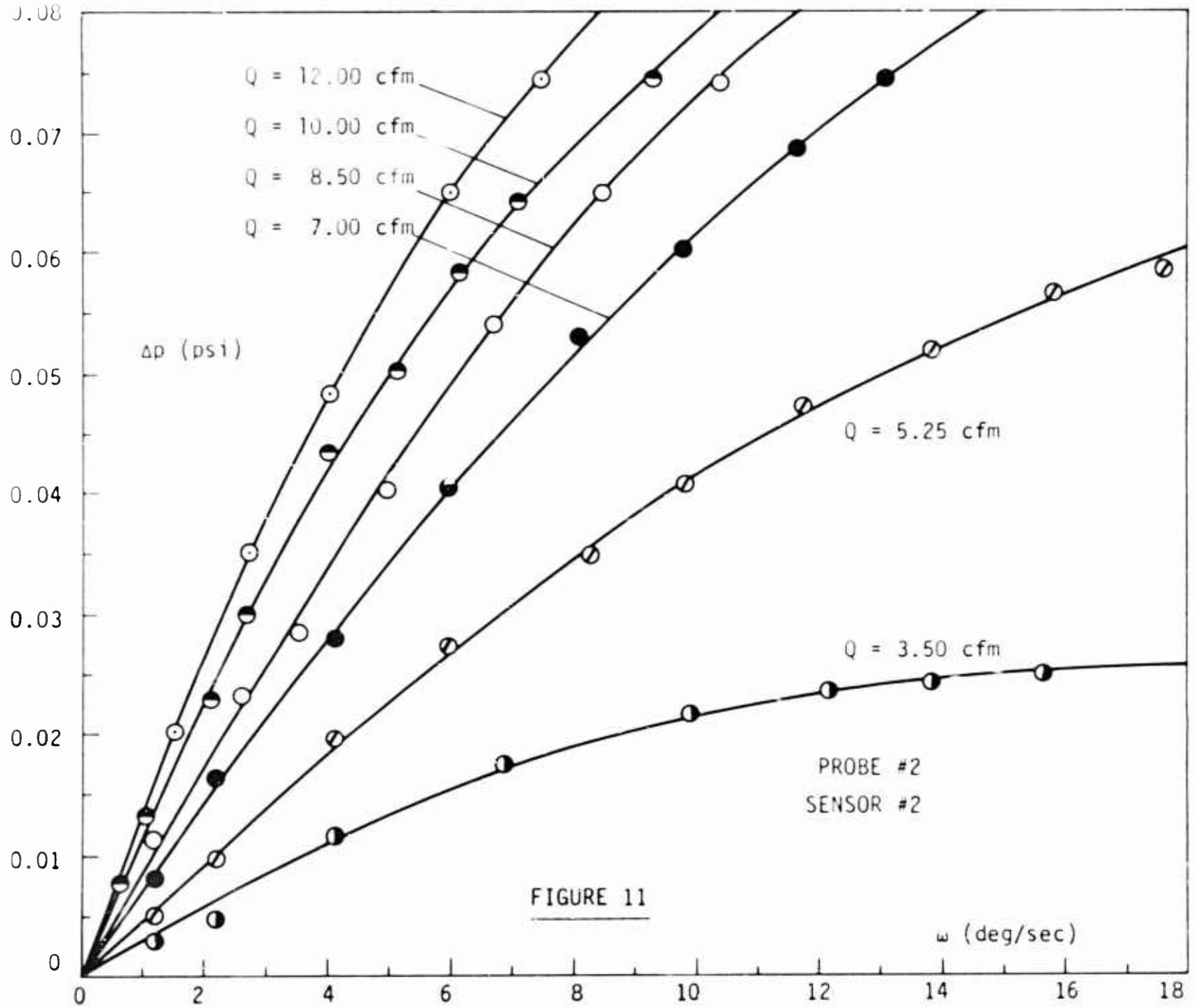
0.08
0.07
0.06
0.05
0.04
0.03
0.02
0.01
0
Δp (psi)
Q = 12.00 cfm
Q = 10.00 cfm
Q = 8.50 cfm
Q = 7.00 cfm
Q = 5.25 cfm
Q = 3.50 cfm
PROBE #2
SENSOR #2
0
2
4
6
8
10
12
14
16
18
ω (deg/sec)

FIGURE 11

for various flow rates. A brief examination of this figure shows that the output is quite linear for small values of ω and that it increases with increasing flow rates.

Probe # 2 gives a zero signal in the absence of rotation regardless of the flow rate through the sink tube. The reason for this is that the holes on the pickoff are situated symmetrically (at the same side of the probe) with respect to the center of the sink tube. Furthermore, it is clear that the flow output of the pickoff may be increased four times when used with a low input impedance amplifier. For this purpose it is sufficient to use two pickoffs and to connect their outputs as shown in Fig. 12.

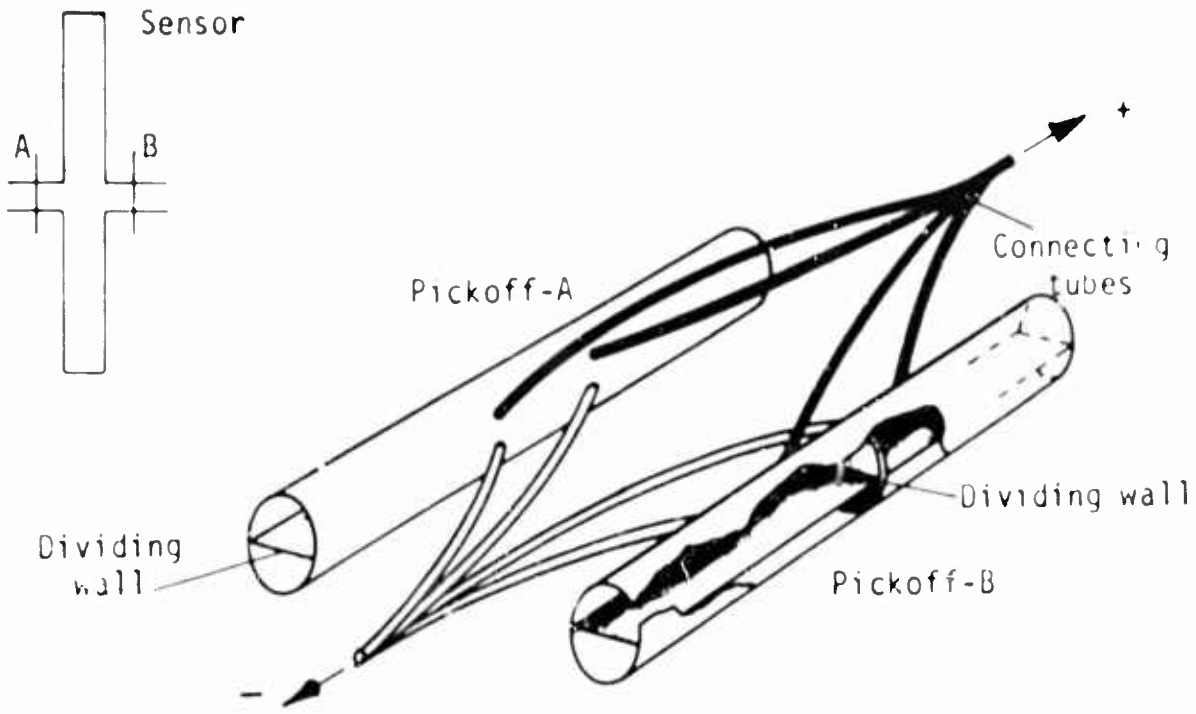

Fig. 12 Interconnection of two active pickoffs

For high input impedance devices the use of one pickoff is sufficient and probably more advantageous.

It is important to note the significant difference between the outputs of a probe like probe # 2 and the probe # 4. In the case of the former the static pressure difference is always zero while in the latter it changes with the flow rate. Consequently, the output of a probe like probe # 4 is more susceptible to fluctuations in the flow rate than probe # 2. Measurements similar to that presented in Fig. 11 were obtained with probes # 1 and 2, and with sensors # 1 and 2. The results have shown that the two holes on probe # 1 were too close and that the flow

around the two pickoff points interacted and reduced the output. The slots on the pickoff # 3, on the other hand, were spaced too far apart and the output was likewise lower than that obtained with probe # 2. It appears that there is an optimum distance between the two holes on the probe which will give the maximum output. This point will be explored separately in the future. In closing the discussion of the characteristics of probe # 2 it should be noted that the spanning of the probe across the entire sink tube, unlike probe # 4, reduced separation, prevented probe vibration, and lowered the noise level of the pickoff output. It is sufficient to say that in view of the various advantages cited above the use of a probe similar to probe # 2 is highly recommended.

The climax of the discussion presented herein is certainly the comparison of the various efficiencies obtained theoretically and experimentally. The theoretical viscous efficiency is calculated from Eq. (35) and plotted in Fig. 13. The experimental viscous efficiency of the sensor # 2 and pickoff # 2 is determined by using the data presented in Fig. 11. For this purpose Eq. (44) is rewritten as

$$E = \frac{\frac{\Delta p}{\rho U_s^2/2}}{8\frac{\omega R_o^2}{U_s r_{po}}} = F\left(\frac{Q\,b}{\nu R_o^2}, \frac{R_o}{r_{po}}\right)$$

and the values of E are calculated for each value of the modified Reynolds number $Q\,b/\nu R_o^2$. The results are plotted in Fig. 13 for the purpose of comparison. It is apparent that the experimental values, although quite consistent among themselves, are lower than those predicted theoretically. This is partly due to the exclusion, from the theoretical analysis, of the energy losses occurring in the sink tube and partly due to the interference of the vortex core with the pickoff. It is believed that with the design of smaller pickoffs and modifications of the sensor geometry the efficiency of the sensor may be increased considerably. The significance of Fig. 13 lies in the fact that the efficiency of a vortex-sink device can be calculated theoretically and that the experimental values follow the same trend as the theoretical values.

It is appropriate at this time to note briefly the several observations made during the experiments:

a. The sensor was rotated about the other two axes perpendicular to its axis of symmetry and no signal was recorded;
b. The sensor was given translational motion in several directions and once again no signal was observed;
c. The rotations in the clockwise as well as in the counter-clockwise direction gave identical pressure signals;
d. Although during each test a dummy probe was mounted inside the

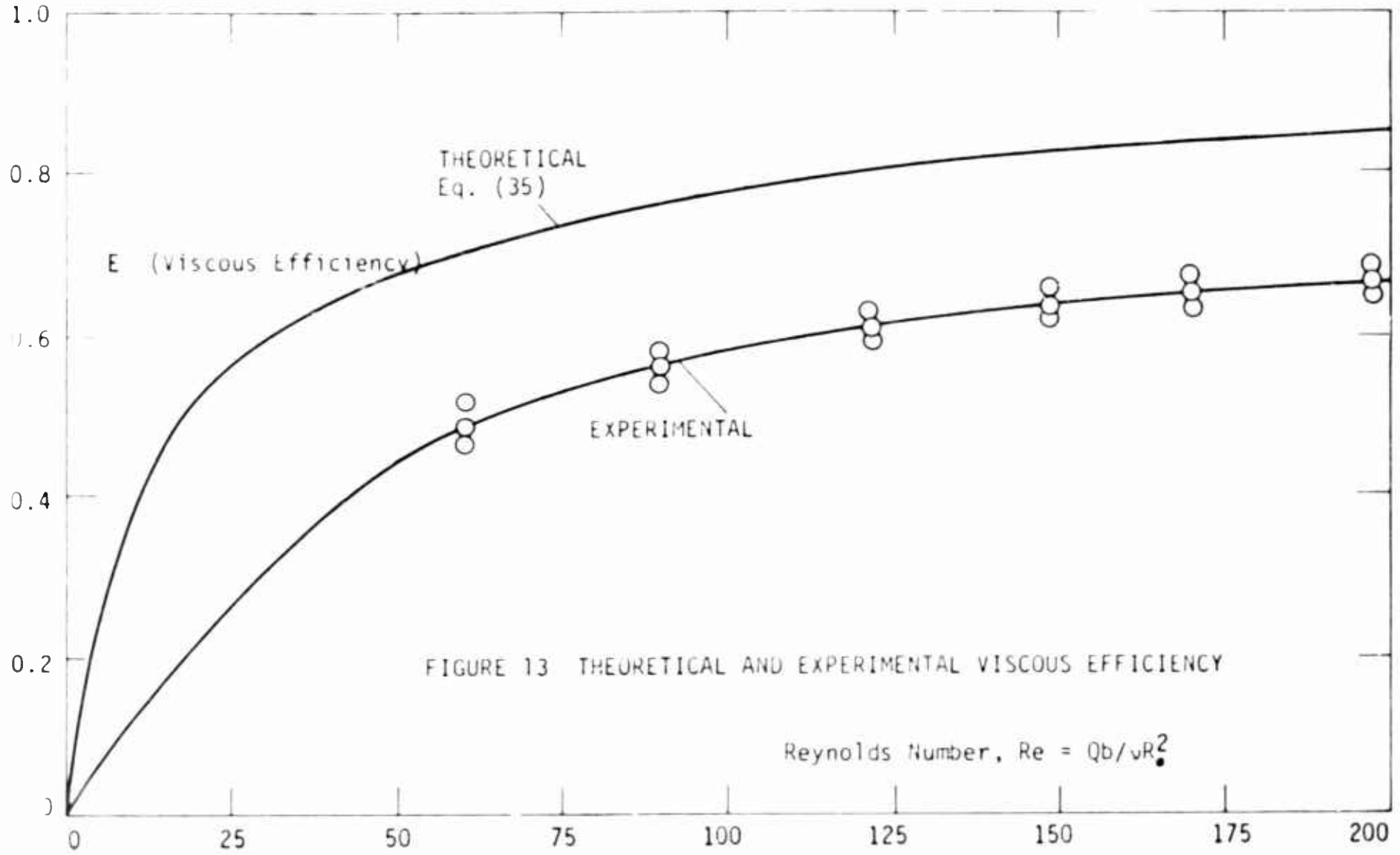

FIGURE 13 THEORETICAL AND EXPERIMENTAL VISCOUS EFFICIENCY

opposite sink tube, during several exploratory measurements the dummy probe was removed to see if the output of the active pickoff would vary. The results have shown that for small values of ω and Q the absence of the dummy probe does not change the output of the active probe. For larger flow rates, however, the use of a dummy probe, or as suggested in connection with Fig. 12 and in connection with low input impedance devices, the use of two active pickoffs is recommended;

e. Several observations were made by closing one of the sink tubes. It was found that for a given ω, the output of the active pickoff does not double when the entire flow is directed into one sink tube. On the contrary, the output drops sharply. This is, obviously, due to drastic alteration of the radial flow near the center of the sensor. It is, therefore, recommended that a symmetrically built sensor be used. If a single ended sensor is desired, its closed side has to be modified considerably to provide a streamlined conical transition toward the sink tube;

f. Finally, extensive measurements were made to determine the effect of mass flow through the pickoff on the sensor output by connecting the device to a specially designed proportional amplifier. It was found that rates of rotation as low as one degree per second could be detected with significant pressure and flow gains. Experiments are being continued on the operation of the sensor with a staging amplifier.

ACKNOWLEDGEMENTS

The present study is part of a program of theoretical and experimental research on the characteristics of vortex-sink fluid motion being conducted at the Hydrodynamics Laboratory of the Department of Engineering Mechanics of the University of Nebraska. The research is sponsored by the Harry Diamond Laboratories of the United States Army Materiel Command under Contract No: DA-49-186-AMC-128(x).

The writer wishes to express his appreciation to Messrs. Joseph Kirshner, Kenneth R. Scudder, and John M. Goto for their encouragement and helpful suggestions.

NOMENCLATURE

a	distance to the center of the pickoff hole (see Fig. 7)
b	half width between the two coaxial disks
c	radius of the pickoff tube
E	viscous efficiency of the sensor, Γ_r/Γ_0
$f(n)$	a function in the boundary layer stream function
K_1, K_2	4 constants
n	an index
p	pressure
p_0	ambient pressure
Q	total flow rate, $Q = 4\pi R_0 b U_0$
r	radial distance, $r = R_0 - x$
r_{po}	radial distance to the center of pickoff hole
r_s	radius of sink tube
R_0	radial distance to porous coupling
Re	Reynolds number, $Qb/\nu R_0^2$
u	radial velocity in the boundary layer
$U(x)$	radial velocity in the potential flow region
U_0	radial velocity at the coupling
U_s	average axial velocity in the sink tube
v	absolute tangential velocity
v_{rt}	relative tangential velocity
w	axial velocity
x, y, z	coordinate axes, $R_0 - x = r$ (see Fig. 5)
Γ_0	vortex strength at the coupling
Γ_r	vortex strength at radial distance r
δ	boundary layer thickness
δ^*	displacement thickness
ϵ	a parameter
ζ	r/R_0
η	similarity parameter
θ	angle measured from the front stagnation point
μ	dynamic viscosity of fluid
ν	kinematic viscosity of fluid
ρ	density of fluid
τ	shear stress
τ_{0t}	tangential component of the shear stress on the disk
Ψ	boundary layer stream function
ω	angular velocity, rad/sec unless specified otherwise

FLOW PATTERNS IN A VORTEX AIR CHAMBER

By E. E. Bellinger*

NASA Langley Research Center
Langley Station, Hampton, Va.

INTRODUCTION

With the promising future of fluid-state technology, a large number of highly sensitive pure fluid transducers will be employed with fluid amplifiers to provide complete pure fluid control systems. One unit of importance in control systems is the annular vortex chamber.

A research program was initiated at the Langley Research Center to determine vortex chamber flow patterns. One objective was the determination of the effects of various geometrical design parameters on the flow patterns so that improvements could be made in the design of vortex chambers as well as output pickups.

In conducting these studies, smoke-trace pictures were taken of the airflow in a large vortex chamber. The changes in flow pattern were studied by independently varying each parameter and observing the resulting effect on the flow. The parameters for a thin, right-circular, cylindrical chamber considered in this paper were flow rate, coupling element diameter, exhaust orifice diameter, and cylinder height.

SYMBOLS

Q	flow rate in m^3/sec
h	height or spacing between flat surfaces in m
ν	kinematic viscosity in m^2/sec
R	radius of the coupling element in m
ω	angular rate of the chamber relative to laboratory in radians/sec
K	relative radius (ratio of any radius to R)
α_K	angle in radians at radius (KR) between the streamline relative to chamber and its radius (where $K \leq 1.0$) (fig. 4)

*Aerospace Engineer.

[illegible]

[illegible]

[illegible]

[illegible]

[illegible]

[illegible]

APPARATUS

The test chamber was [illegible] (24-in.) [illegible] having a clear plastic top (Fig. 1).* In order to obtain a variable width chamber, the lower surface, inside the coupling, was adjusted axially by attaching it to a threaded support (Fig. [illegible]).

Coupling elements were made of [illegible] elements with inside diameters of 0.0[illegible] m ([illegible] in.), 0.[illegible] m ([illegible] in.), and 0.[illegible] m ([illegible] in.) were used. The 0.[illegible]-m ([illegible]-in.) element was cylindrical in shape, whereas the other elements consisted of a number of flat felt washers (Fig. [illegible]) which could be stacked to obtain the desired thickness. The air input was through four holes into an annular ring at the periphery of the chamber. The air exhausted through the center of the lower adjustable plate which was constructed to take interchangeable plugs so that exhaust ports of various radii were available. Smoke entered the chamber perpendicular to the stream through an inlet in the upper surface near the outer periphery. Smoke injected perpendicular to the stream was used in an effort to reduce the possibility of supplying the smoke with a false radial velocity. However, this inlet caused turbulence. Observation indicated that this turbulence was attenuated within 0.0[illegible] m (1 in.) or less from the inlet location depending on the configuration. Efforts were made to avoid making measurements within the indicated turbulent zone.

The test chamber was mounted on a small rotate table modified to permit air to be delivered to the table. High speed movies were taken from the axis of the chamber with 16 mm film at 400 frames per second. The data were then read on a special purpose film reader which operated a card punch machine. The data cards were then processed in a computer for calibration and calculations.

---

*Figures start on page 337.

Tangential velocity = Δt

Radial velocity - (q_r mph)

For this case the initial flow conditions of the airstream entering the vortex chamber are:

decreased, but the initial tangential component of velocity is not affected. Thus, an increase in the measured angle would be expected as shown. This increase, however, is attenuated by the viscous interaction with the plates. Less vane is more available for the viscous forces to act. Insufficient data were taken to show, with timestrip graphs, the effect of a variation in plate spacing alone. This effect is illustrated in figure , which is a graph of tan the ratio at which is measured for various plate spacings for a 0.40 m (1.-in.) diameter coupling element.

A single radius-to-height ratio could be represented by one curve for any given configuration in the range where wall effects are negligible. However, in figures and 10 several curves are shown for a single value of R/h. This is possibly due to the physical size of h. The slope does tend to increase with decreasing h for constant Q/hv. Figures 11, 12, and 1 are graphs having other values for R/h and Q/hv.

Constant temperature is assumed in all measurements. An increase in viscosity due to transient heating from the camera lights would mean that the actual points lie to the left of the points plotted here. Some of the data scattering, for example, figure , may be caused by this effect.

CONCLUSIONS

An increase in tan( ) (ratio of tangential component to radial component of velocity) is observed when there is a decrease in flow rate. The results indicate that optimum radius-to-height ratios may exist for various flow rates. This maximum point is due to the fact that, as the R/h ratio initially increases, the inertial effects (the tendency to preserve direction) dominate. At the maximum, the inertial effects and viscous effects (plate drag) are of the same order. Finally, further increasing R/h leads to domination by the viscous effects since each fluid particle must travel a longer path nearer the walls and hence is acted upon by viscous forces over this longer path length. Further experiments will better determine the relation between R/h ratio and tan needed to accurately design a rate sensor for a particular application.

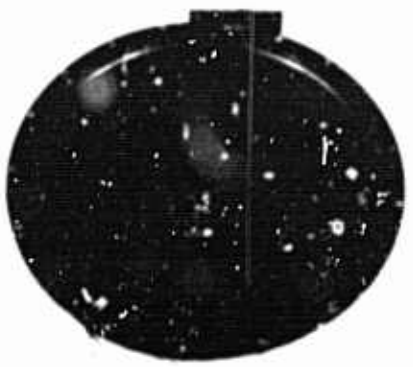

Figure 1.- Experimental vortex chamber.

Figure 2.- Lower housing showing threaded support.

Figure 3.- Interchangeable felt washers and exhaust ports.

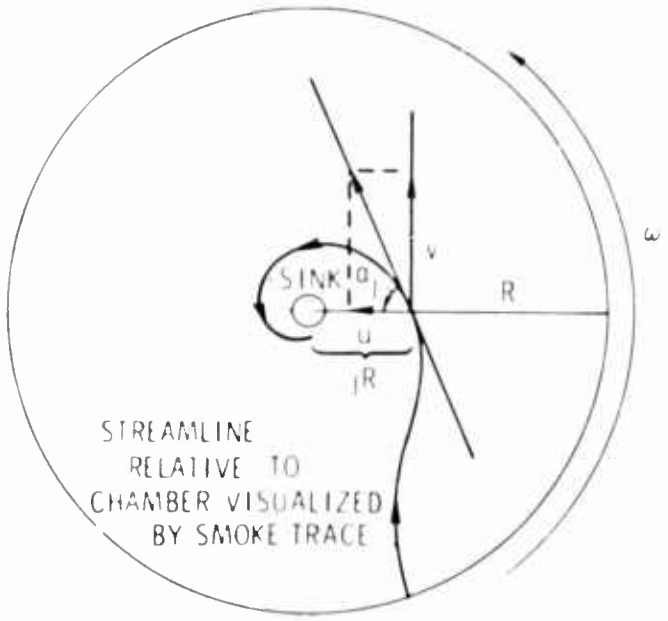

Figure 4.- Flow angle α of the streamline relative to the chamber.

Figure 5.- Effect of variation of plate spacing on $\tan(\alpha_{0.2})$ as a function of relative radius k. R = 0.15 m (6 in.); $Q = 6.6 \times 10^{-4}$ m^3/s; ω = 60 deg/s.

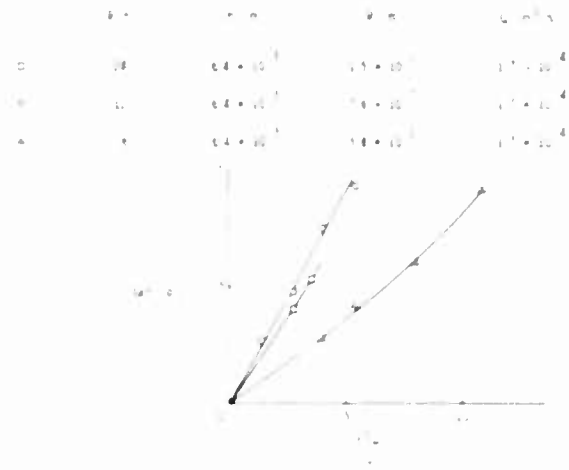

(a) $\frac{Q}{h\nu} = 1662.$

Figure 6.- Effect of variation of coupling element radius on $\tan(\alpha_{0.2})$ as a function of Reynolds number.

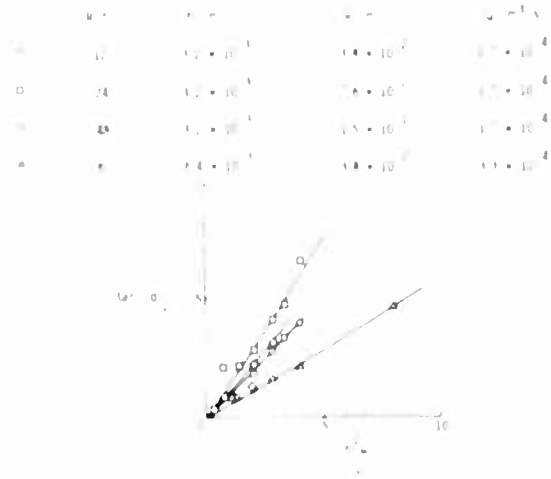

(b) $\frac{Q}{h\nu} = 3324.$

Figure 6.- Concluded.

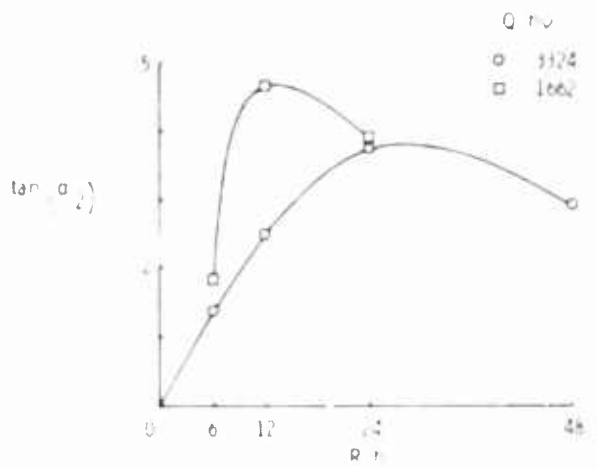

Figure 7.- Effect of $\frac{Q}{h\nu}$ on $\tan(\alpha_{0.2})$ versus $\frac{R}{h}$ indicating that an optimum value for $\frac{R}{h}$ exists for a particular $\frac{Q}{h\nu}$. $\frac{h^2\omega}{\nu} = 2.5$.

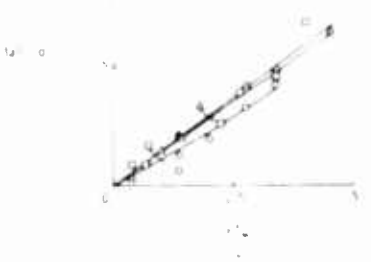

Figure 8.- Effect of flow rate on $\tan(\alpha_{0.2})$ versus Reynolds number.

(a) $\frac{Q}{h\nu} = 3324.$

Figure 9.- $\tan(\alpha_{C_{.2}})$ versus Reynolds number for constant $\frac{R}{h}$.

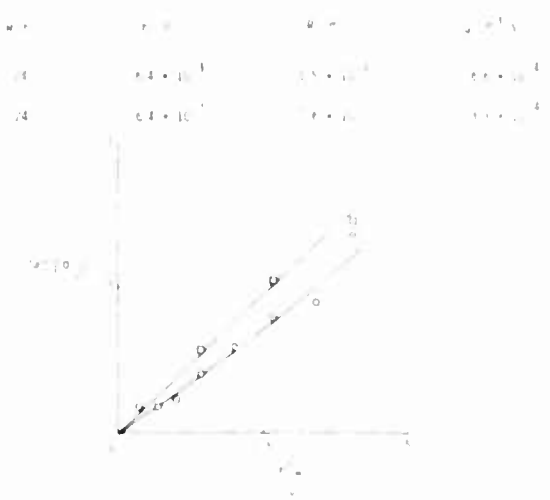

(b) $\frac{Q}{h\nu} = 6648.$

Figure 9.- Concluded.

(a) $\frac{Q}{h\nu} = 3324.$

Figure 10.- $\tan(\alpha_{0.2})$ versus Reynolds number for constant $\frac{R}{h}$.

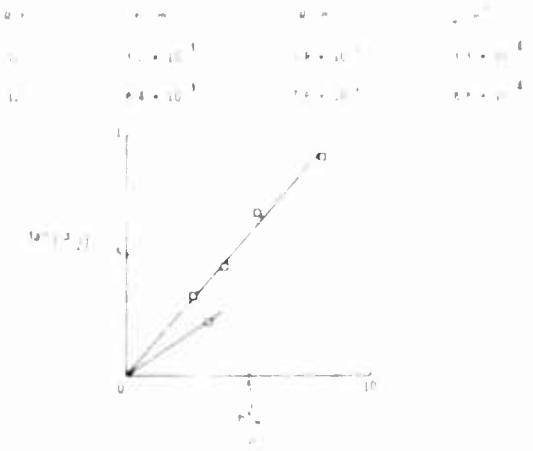

(b) $\frac{Q}{h\nu} = 6648.$

Figure 10.- Concluded.

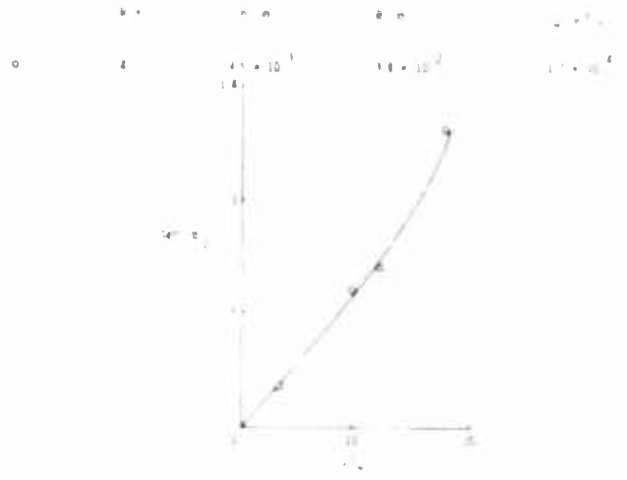

Figure 11.- Variation of $\tan(\alpha_{0.2})$ with $\frac{h^2\omega}{\nu}$ for other values of the parameters.

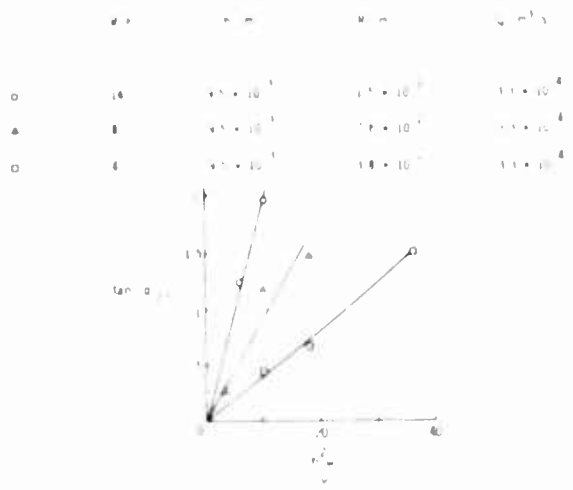

Figure 12.- Variation of $\tan(\alpha_{0.2})$ with $\frac{h^2\omega}{\nu}$ for other values of the parameters.

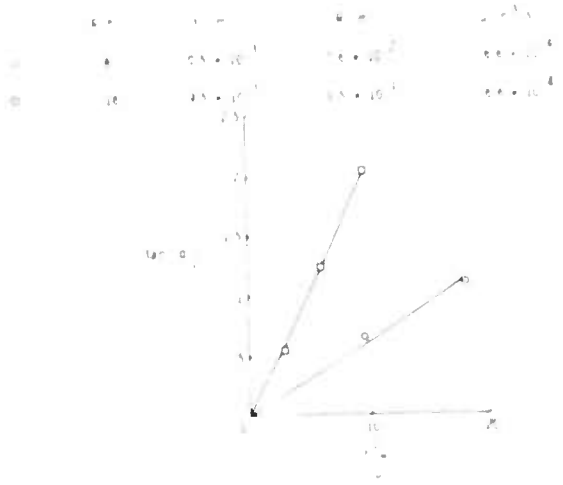

Figure 13.- Variation of $\tan(\alpha_{0.2})$ with $\frac{h^2\omega}{\nu}$ for other values of the parameters.

PHOTOVISCOUS FLOW VISUALIZATION IN FLUID STATE DEVICES

By

Endre A. Mayer

Submitted to the Fluid Amplification
Symposium to Be Held in
October 1965
at the
Harry Diamond Laboratories
Washington, D. C.

PHOTOVISCOUS FLOW VISUALIZATION IN FLUID STATE DEVICES

Endre A. Mayer*

Abstract

Photoviscosity is an excellent flow visualization technique applicable to a variety of fluid state components. A number of liquids exhibit double refracting properties which are a function of the viscous shear stress exerted on the liquid. The viscous shear is proportional to the velocity gradient in liquids, and the interference pattern is thus a function of the flow field. The photoviscous art was advanced significantly by F. A. Peebles, et al., in 1953 by reporting in detail on the photoviscous properties of a Milling Yellow Dye (MYD) solution. The MYD solution is highly sensitive, easy to prepare and handle, and the viscosity is similar to that of hydraulic oils. These properties made the MYD a desirable solution for photoviscous studies. Additional significant milestones in the use of photoviscosity with appropriate references are listed in the paper.

Typical results of photoviscous studies in noise investigation of proportional jet deflection amplifier design are shown. The switching transients of wall attachment jet devices are demonstrated for straight and cupped splitter designs. The demarcation between laminar and turbulent flow regimes may be seen in the various still pictures. The flow interaction between the tangential control jets and the radial supply flow in vortex chambers of different designs is also demonstrated at various levels of vorticity in the vortex chamber.

INTRODUCTION

Photoviscosity offers an excellent flow visualization technique applicable to a variety of fluid state components. Photoviscosity is very similar to the photoelastic technique used in the study of stress distributions of complex structures. The common principle is the stress or shear related double refraction, or birefringence, found in certain materials. Double refraction in liquids was discovered by J. C. Maxwell in 1866[1] using Canada balsam. Maxwell described a method of quantitative investigation of the relation of viscous shear and double refraction in liquid.

Maxwell's method was later used by many succeeding investigators of photoviscosity. The apparatus is shown in Figure 1. The fluid under study is between two concentric cylinders. One of the cylinders may be rotated at a desired speed, thus imparting to the fluid laminar shear stresses of controlled magnitude. Monochromatic or white light is passed through the polarizer before entering the fluid under investigation. The light leaving the fluid is observed through the analyzer, a second polarizing device. The axis of polarization of the polarizer and analyzer are crossed at 90 degrees; at zero velocity no light passes through the polariscope. If a photoviscous fluid is used, as the rotational velocity of the cylinder is increased a band of light becomes

*Staff Engineer, Energy Conversion and Dynamic Controls Laboratory
Bendix Research Laboratories, Southfield, Michigan

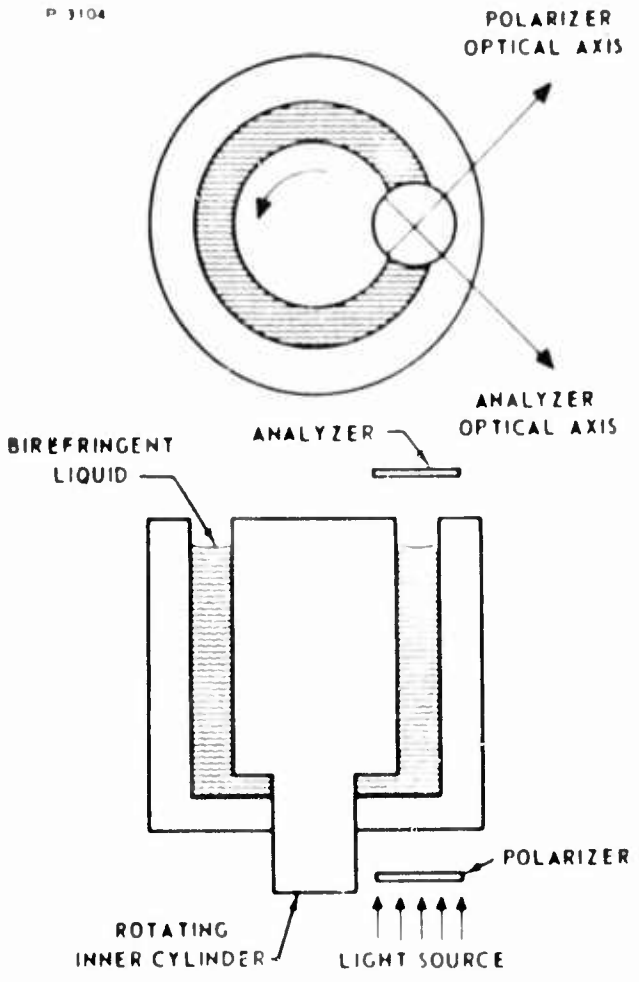

Figure 1 - Schematic of Maxwell's Photoviscous Test Setup

visible. Further increasing of the rotation of the cylinder produces additional bands of light, or fringes. Rotating both the polarizer and analyzer together will result in the disappearance of the fringes when the axis of either the polarizer or analyzer is lined up with the direction of the shear force in the liquid.

THEORY OF PHOTOVISCOSITY

The optical behavior of the photoviscous fluid is very similar to photoelasticity.[2,3,4,5] The intensity of light transmitted through the polarizer is defined by Malus' Law

$$I = I_m \cos^2 \theta \qquad (1)$$

where θ is the angle between the optical axis of the polarizer and analyzer.

Four basic phenomena are known to produce polarized light: Double refraction or birefringence, Reflection, Light Scattering and Dichroism. Light entering a birefringent material refracts into two distinct beams. One of the two beams follows the law of refraction established for materials, and is called the ordinary beam. The other beam, the extraordinary beam, deviates from the law of refraction. Both beams are polarized with the axis of polarization 90 degrees between the two beams. In certain crystals, one of the two beams is almost completely absorbed in the material. These crystals are the dichroic polarizers.

The two most widely used polarizers for photoviscous and photoelastic investigations are the Nicol prism and Polaroid sheets. The polarization of the Nicol prism is based on birefringence and that of the Polaroid sheet is based on dichroism. The Nicol is a very efficient polarizer, however, large area polarizers are difficult and expensive to make. The collimation of the light path with additional optical elements is required if a Nicol is to be used as a large area polarizer. For photoviscous flow visualization, large area Polaroid sheets provide inexpensive means of polarization.

In birefringent materials, the propagation of light is not uniform, and occurs in two directions designated as the principal vibration directions. When birefringent material is placed in a polariscope, as shown in Figure 2, the beam from the polarizer is separated into two components along the principal axis (A,B) of the birefringent material. The two components transmitted in the plane of the analyzer (a_1 and a_2) may not be equal. The intensity of the light transmitted through the analyzer will depend on the optical properties of the birefringent material, the thickness of the material, the wavelength of the light and the orientation of the birefringent material. By rotating the birefringent material in Figure 2 until the optical axis A is aligned with either the axis of the analyzer or the polarizer, the transmitted light intensity

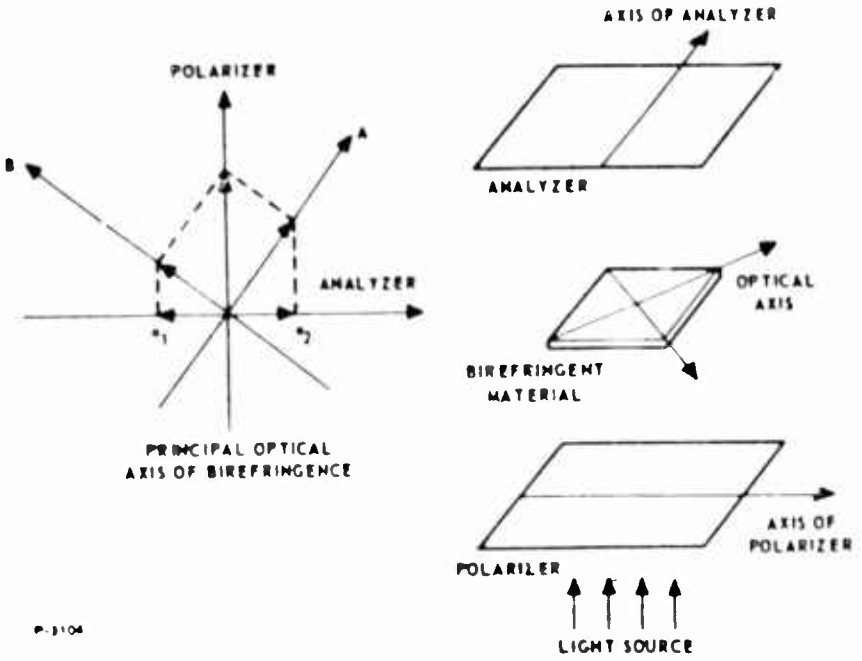

Figure 2 - Polarized Light Transmission in Birefringent Materials

is reduced to zero. The lines of zero intensity thus obtained are called isoclinics. The amount of birefringence in a photoviscous liquid is defined by Maxwell's Law

$$\Delta n = n_e - n_o = M\mu \frac{dV}{dS} t \qquad (2)$$

where n_e, n_o are the two indexes of refraction, M is the Maxwell constant, μ is the viscosity, dV/dS is the velocity gradient and t is the optical path in the liquid.

The Maxwell constant for most photoviscous liquids is of the order of 10^{-11}. A more convenient unit, the fringe value (N) may be used to designate the photoviscous property of the material.

$$N = \frac{\mu}{n} t \frac{dV}{dS} \qquad (3)$$

where n is the number of fringes observed.

The orientation of stress and the principal optical axis are closely aligned in the materials used in photoelastic investigations. The sensitive photoviscous liquids exhibit nonlinearity in this respect, the angle between the optical axis and the viscous shear is a function of the value of shear.

PHOTOVISCOUS FLOW VISUALIZATION

A large number of liquids exhibit some degree of photoviscosity. In most of the liquids the amount of birefringence is too small to develop the first order of fringe at velocity gradients of interest in hydraulic research.

Liquids with low photoviscous sensitivity require point by point evaluation of the amount of birefringence by optical compensation techniques. The pure liquids with low sensitivity have more linear physical characteristics, the optical axes have a fixed relation with the direction of shear, Maxwell's constant is independent of the value of shear, and the behavior of the fluid is more Newtonian -- the viscosity is independent of the shear force.

Liquids with much greater optical sensitivity, a factor of about 10^8, are colloidal solutions. The early photoviscous work, both qualitative and quantitative, is well summarized by Prados and Peebles.[6]

A review of the various theories proposed to explain the double refraction phenomena in fluids is given by Jerrard.[7] Vanadium Pentoxide solutions were used by Humphrey in 1923[8], indicating the demarcation between laminar and turbulent flow. Bentonite solutions were extensively used by Hauser and Dewey[9] around 1940 to visualize dynamic flow around complex model shapes such as various automobile body designs both with monochromatic and white lights. Further experiments planned to use bentonite solution are presented by Rosenberg[10] in 1952. Rosenberg includes a detailed bibliography and summarizes the non-linearities involved in the use of colloidal solutions for flow visualization. A comprehensive evaluation of the birefringent properties of 59 liquids is given by Weller.[11,12] On the basis of measurements using an apparatus of Maxwell's general design, Weller selected a solution of Ethyl Cellulose for flow visualization studies.

The discovery of the photoviscous properties of Milling Yellow Dye Solution (MYD) by Peebles, et. al.[13] gave a sensitive, stable, inexpensive and non-toxic, non-corrosive liquid for flow visualization studies. The properties of the solution, birefringence and viscosity are published.[14] Quantitative two-dimensional flow analysis may be conducted using MYD and photoviscous techniques. Quantitative techniques are demonstrated by Prados[6] for flow between parallel channels, converging and diverging sections and flow about a cylindrical obstacle in a rectangular flow channel. The quantitative measurements require point by point numerical integration and correction for the misalignment between the shear direction and the optical axis of the MYD solution. The procedure is moderately complex and laborious particularly for the more complex flow patterns found around obstacles. The quantitative photoviscous technique applies to two-dimensional, laminar flow only.

PHOTOVISCOUS INVESTIGATION OF FLUID STATE DEVICES

The photoviscous flow visualization techniques are very well suited to the general two-dimensional flow fields encountered in fluid state devices. Quantitative results, such as velocity profiles, are obtainable from photoviscous studies using a moderately complex procedure and close control on solution concentration and temperature. In the study of fluid state devices, the major advantages offered by photoviscous flow visualization are realized in the simple semi-quantitative study of dynamic flow changes. Photoviscous flow

visualization allows the operation of closed units at or near design condition, thus dynamic performance details may be directly observed or photographed. The following selected examples of flow patterns are shown as typical of results obtainable with a minimal optical system.

TEST SETUP

The schematic of the test setup is shown in Figure 3. White light was used for all visualization tests, because the color fringes provided a stronger visual contrast. Polaroid sheets were used both for the polarizer and analyzer. During the experiments the use of polaroid eye glasses was found to be a convenient expediency to examine three-dimensional flow patterns, such as the vortex chamber outlet flow. The lack of optical alignment was not seriously affecting the examination of the flow quality in this case.

The fluid system included a pressurized supply tank, an open drain container, two liquid pressure regulators and the required valving.

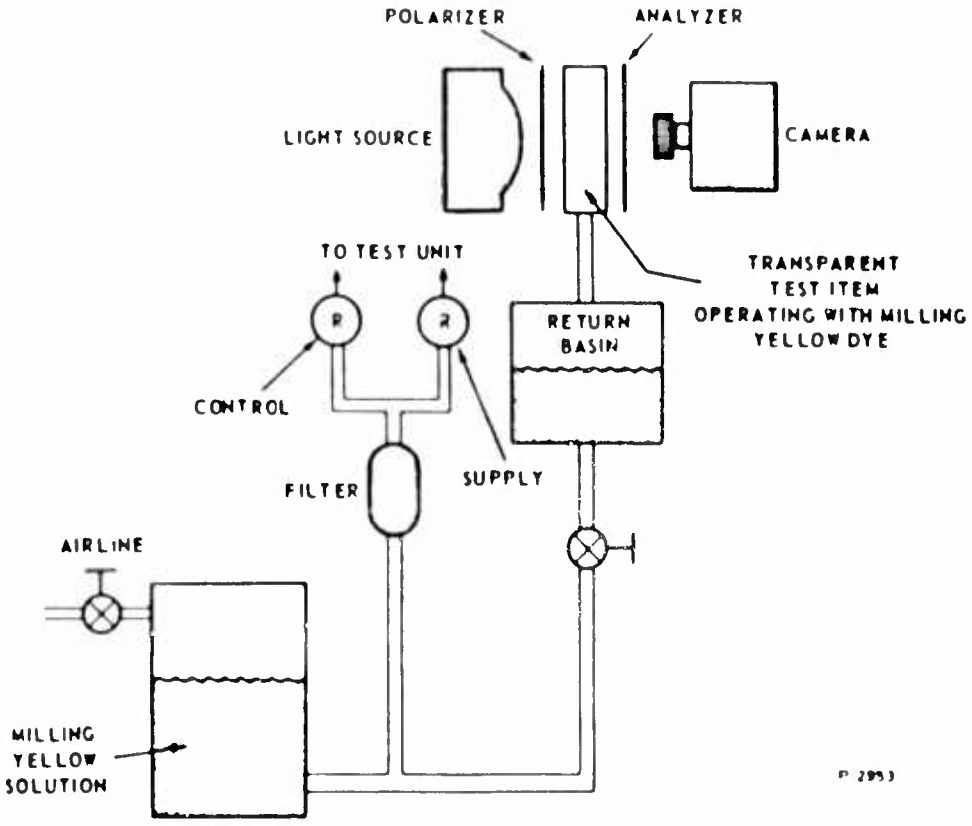

Figure 3 - Photoviscous Experiment Setup - Schematic

Both Kodachrome II Photoflood, and Ektachrome Photoflood color films were used with equal success to take 16mm movies. The exposure of the film was established for the various light intensity conditions using still color pictures taken with Polaroid color film and correcting the exposure for the differences in film speeds.

PREPARATION OF THE MILLING YELLOW DYE

The MYD solution was prepared as described by Peebles, et.al.[13] Powder form of the dye of commercial Milling Yellow Dye, MYNGS, purchased from Allied Chemical Corporation, was mixed with distilled water to give a one percent solution by dry weight. The solution then was boiled until a dye concentration of about 1.4 percent was reached. The birefringence of the slowly cooled solution was tested by inserting a sample between crossed polarizers and checking for interference by gently stirring the liquid.

The viscosity of the prepared MYD solution is similar to that of Mil 5606 hydraulic oil, thus pressure and flow conditions existing in hydraulic systems will be nearly duplicated in the photoviscous flow visualization tests.

TEST RESULTS

Flow visualizations were conducted on proportional jet amplifiers, jet-on-jet bistable elements with straight and cupped splitter designs and vortex chambers of several different configurations. The use of white light for illumination, and the lack of light transmission of the MYD solution in the blue spectral zone gives the same order of fringes as reported by Thurston[15]:

Fringe Order	Color
0	Black
1	Yellow
2	Red
3	Green
4	Yellow
5	Red
6	Green, etc.

Typical fringe patterns observed in a plastic proportional jet amplifier are shown in Figure 4. The control pressure applied to the left port is gradually increased from frame (a) through (d). The two large area vents were unrestricted but not submerged. In frame (a), the flow leaving the vents was nearly zero; however, there is strong evidence of circulation and vortex formation in the vent zones adjacent to the "free path" of the power jet. Interation of the recirculating flow with the power jet

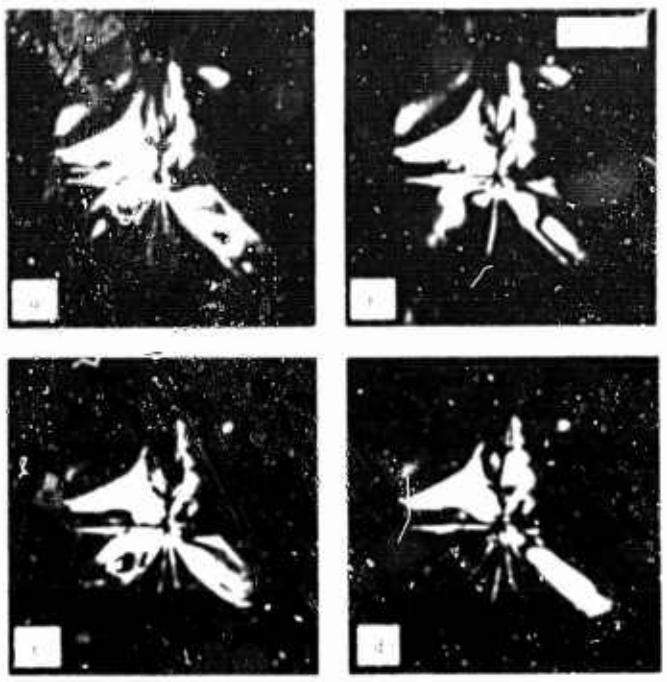

Figure 4 - Effect of Single Control Input on the Flow Pattern of a Proportional Jet Amplifier. Power Nozzle 0.020 inch

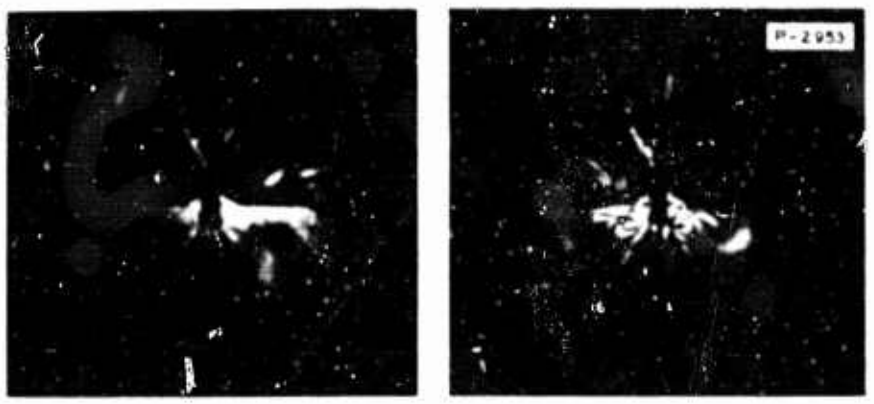

(a) BOTH CONTROL JETS FLOWING

(b) SINGLE CONTROL JET FLOWING

Figure 5 - Reduction of Vent Turbulence Through Flow Issuing from Both Control Jets

results in noise and instability of the power jet. Under certain conditions the turbulent flow may be eliminated, as shown in Figure 5. The flow provided by both of the control jets "washes away" the turbulence in the vent zone. The elimination of the turbulence reduced the random pressure fluctuation, or noise, in the two output legs.

The flow pattern during a switching transient of a jet-on-jet flip-flop is shown in Figure 6. The dark "brush" near the power jet is the high velocity core of the power jet, and indicates a zero order fringe. The device operated totally submerged. The low velocity, laminar entrainment flow is evident in both the vent region and the low pressure output leg. The turbulent flow in the high pressure output leg is bright yellow. The power flow switch is completed between the frames. The following frames indicate the slower establishment of the entrainment flow in the opposite leg.

The flow pattern of a flip-flop with a "cusp" type splitter is shown in Figure 7. The "memory" of this type of unit is normally much greater than the memory of units with a straight splitter design. This difference in the strength of attachment is very noticeable at lower supply pressures. The flow in Figure 7 is essentially in the laminar flow range. The transfer of the attachment is aided by the splitter "cusp".

Figure 8 shows the flow condition in the chamber of a vortex valve in radial and vortex flow pattern. The vortex valve had the tangential, or control flow, injected at a single location, and the asymmetry of the flow pattern is noticeable.

The effectiveness of control flow injection in vortex chambers is shown in Figure 9. This particular vortex valve has four control injectors and a large number of radial supply ports. The radial flow pattern is very uniform. At slight tangential bias, the low velocity control jets do not reach the complete circumference of the vortex chamber, and segments of straight radial flow are in evidence. At larger control pressures, the vortex flow covers the complete chamber. Flow turbulence is in evidence at the mixing of the radial and tangential flow regions.

A similar sequence is shown in Figure 10, but the mixing region between radial and tangential flow is modified to reduce the turbulence level. Significant improvement is evident in the reduction of the strong eddies visible in Figure 9. It may be seen, that if the efficient operation

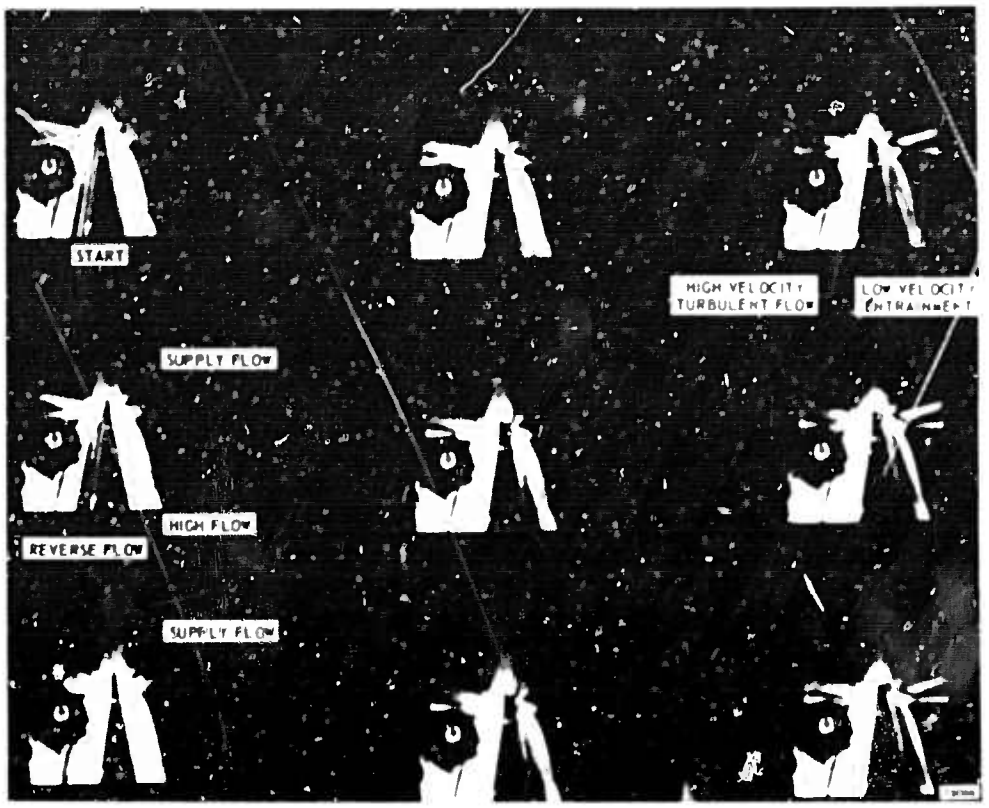

Figure 6 - Switching Transient of a Jet-on-Jet Flip-Flop

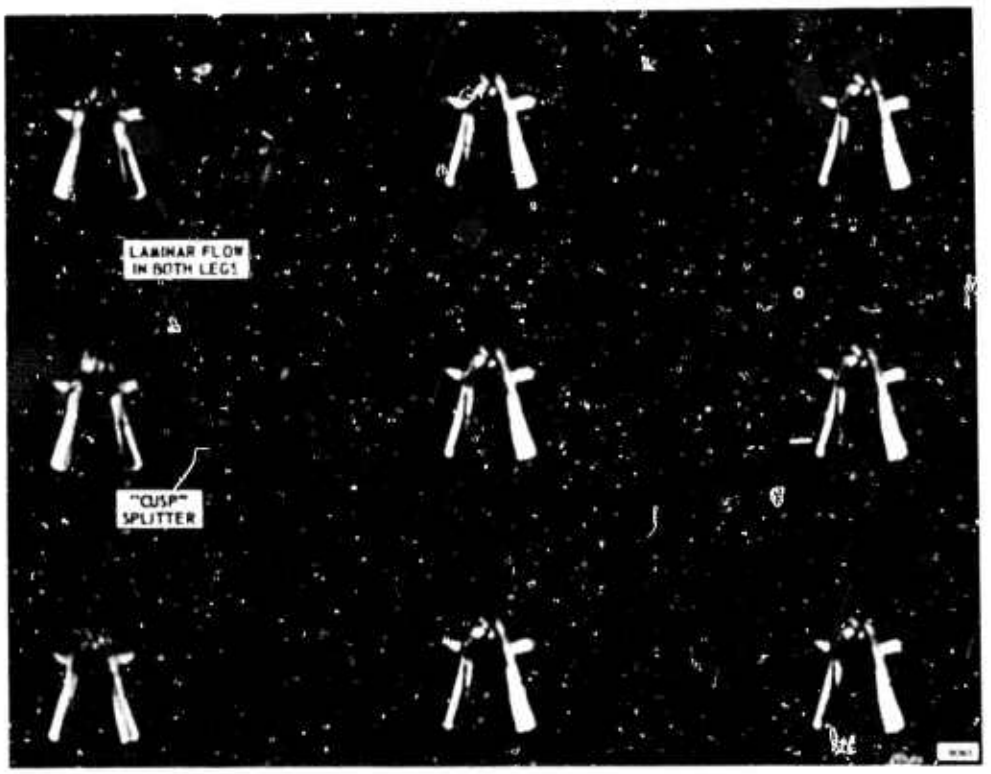

Figure 7 - Switching Transient of a Flip-Flop with "Cusp" Splitter

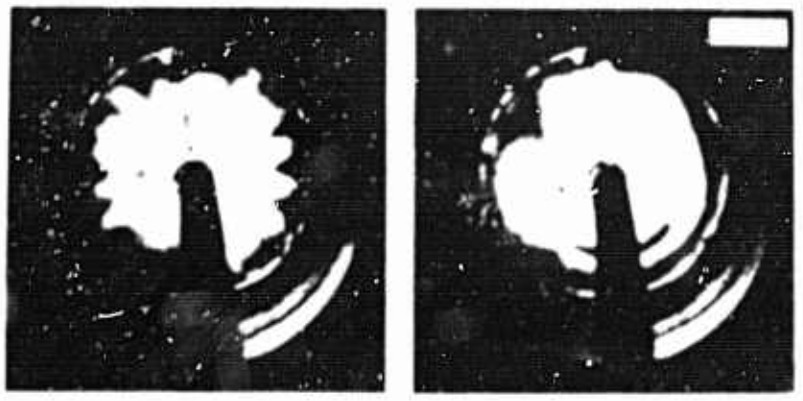

Figure 8 - Radial and Vortex Flow Pattern in a Vortex Valve

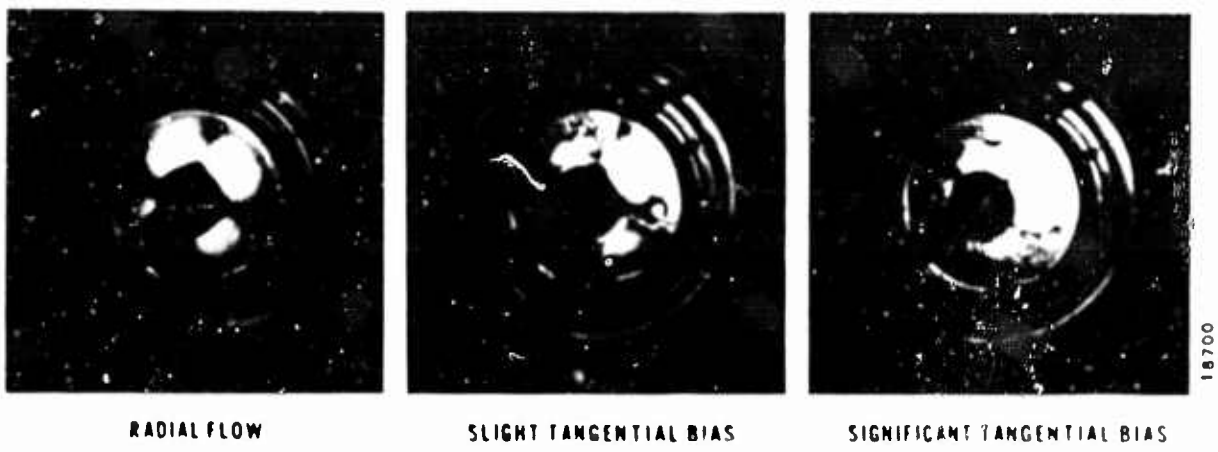

Figure 9 - Vortex Chamber Flow Pattern with Four Tangential Jets

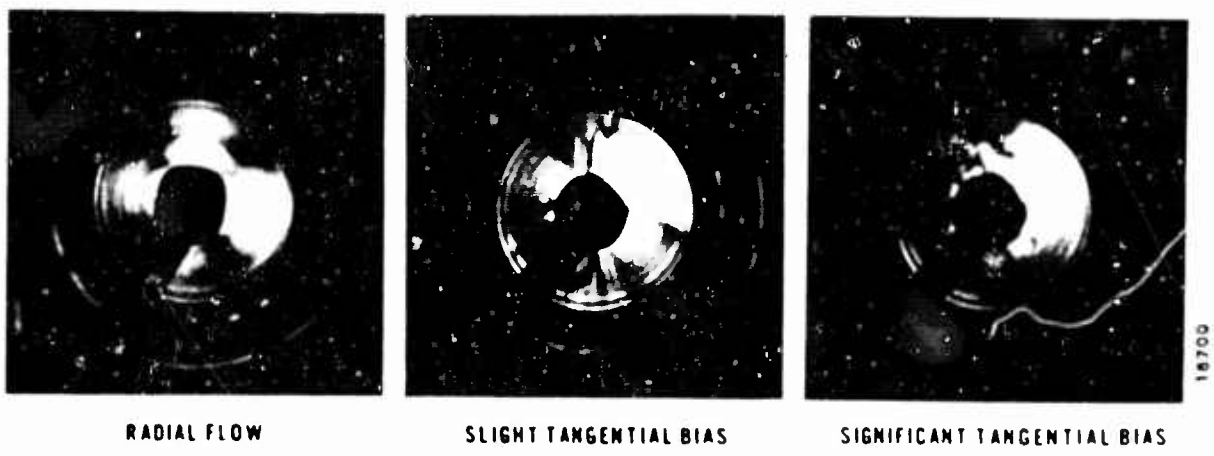

Figure 10 Turbulence Reduction in a Vortex Chamber with Redesigned Zone

of the vortex valve at low vorticity is important, additional tangential jets are required to cover the circumference of the vortex chamber shown.

The above examples were selected to illustrate the application of photoviscous flow visualization to a few of the typical two-dimensional flow situations observed in fluid state devices. The simple qualitative examples indicate how the technique may be used to analyze and further the understanding of noise and turbulence propagation within fluid state units. The photoviscous flow visualization may be extended in this field by the addition of high speed motion picture photography. In particular instances, it may be desirable to extend the technique to quantitative analysis of the velocity distributions as described in references cited. Particular dynamic flow condition may be investigated using photo-electric transducers to record light intensity fluctuations at a point of particular interest.[16] The examples of photoviscous flow visualization highlight a very simple and powerful method complementing other flow visualization techniques[17] used in the fluid amplifier field.

ACKNOWLEDGEMENT

The author wishes to thank the Bendix Research Laboratories for assistance in preparation and permission to publish this paper. The author also wishes to thank Mr. J. A. Peoples of NASA/George Marshall Space Flight Center, for the suggestion of the use of the milling yellow dye solution for flow visualization.

BIBLIOGRAPHY

1. Maxwell, J. Clerk, "Double Refraction of Viscous Fluids in Motion," Roy.Soc. Proc., XXII, (1873-4), p. 46.

2. Valasek, Joseph, Introduction to Theoretical and Experimental Optics, J. Wiley, 1949.

3. Frocht, M. M., Photoelasticity, J. Wiley, 1941.

4. Coker, E. Y. and E. N. G. Filon, A Treatise on Photoelasticity, Cambridge U. Press, 1931.

5. Polarized Light, Pamphlet F 3374, Polaroid Corporation, Polarizer Division, Cambridge, Massachusetts.

6. Prados, J. W. and F. N. Peebles, "Two-Dimensional Laminar Flow Analysis, Utilizing a Doubly Refracting Liquid," A.I.Ch.E. Journal, June 1959, Vol. 5, No. 2, p. 225.

7. Jerrard, H. G., "Theories of Streaming Double Refraction," Chem. Review Vol. 59, No. 3, June 1959.

8. Humphrey, R. H., "Demonstration of Refraction due to Motion," Proc. Phys. Soc., 35, 217, (1923).

9. Hauser, E. A. and D. R. Dewwy, "Visual Studies of Flow Patterns," Journal of Phys. Chem., Vol. 46, p. 212, (1942).

10. Rosenberg, B., "The Use of Doubly Refracting Solutions in the Investigation of Fluid Flow Phenomena," AD-609 632 (1952).

11. Weller, R., D. J. Middlehauss and R. Steiver, "The Photoviscous Properties of Fluids," NACA Tech. Note 841, (1941).

12. Weller, R., "The Optical Investigation of Fluid Flow," Journal of Appl. Mech., June 1947, p. A-103.

13. Peebles, F. N., H. J. Garbes, S. M. Jury, "Preliminary Studies of Flow Fluid Mech., U. Minnesota Press, (1953).

14. Peebles, F. N., J. W. Prados, E. H. Honeycutt. "Birefringent and Rheologic Properties of Milling Yellow Suspensions," Journal of Polymer Science, Part C, No. 5, p. 37.

15. Thurston, G. B., L. E. Hargrove, "Optical Birefringence Induced by Shear Wave Propagation in Aqueous Methyl Yellow Solutions," Reports 1 and 4, AD-134-151.

16. Thurston, G. B., "Shear Wave Propagation in a Birefringent Viscoelastic Medium," Journal of Appl. Physics, Vol. 35, No. 1, p. 144, January 1964.

17. Keto, J. R., "Flow Visualization, Compressible Fluids," AD-286-666, August, 1962.

TURBULENCE AMPLIFIER FOR INTEGRATED TWO-DIMENSIONAL FABRICATION

R-7-10-65

by

Eric E. Metzger
&
Charles G. Lomas
Bowles Engineering Corporation

TWO DIMENSIONAL TURBULENCE AMPLIFIER

I. Introduction

Large and complex logic circuits use considerable power. The power consumption can be minimized by reducing the power consumption per stage, and the number of stages. One way to achieve these goals is to use turbulence amplifiers, with their low flow rates and low power jet pressures, and their ability to accept a large number of inputs without interaction.

Heretofore, turbulence amplifiers have been manufactured in three-dimensional configurations, requiring elaborate interconnecting manifolds of tubing when assembled into logic packages. Reliability considerations dictate an integrated structure for use in military equipment. In order to demonstrate the feasibility of using turbulence amplifiers in military structures, with the attendant savings in power and circuit complexity, it is necessary to produce the same "solid state" manifolds as is used by jet deflection and boundary effect amplifier circuits.

This report describes the development and demonstration of a turbulence amplifier "and" gate in "optiform".

II. Principles of Turbulence Amplifiers

A. Basic Operation of Turbulence Amplifiers

The Turbulence Amplifier operates by using a control signal to switch a power jet from a laminar flow condition to a turbulent flow condition. The power jet issues from a power nozzle as a laminar jet, and impinges upon a receiving aperture while still laminar when it is undisturbed. In such a condition, considerable pressure can be recovered.

When an appropriate input signal appears, near the power nozzle exit, the jet will become turbulent before reaching the receiving aperture . Since the spread rate of a turbulent jet is much greater than that of a laminar jet, a considerable reduction in output pressure will be experienced. The relationship between input pressure and output pressure is shown in Figure 1, for the general class of Turbulence Amplifiers.

B. Amplification in the Boundary Layer

The boundary layer surrounding the immersed jets used in Turbulence Amplifiers can attenuate or amplify any instabilities existing in it, depending on the Reynolds Number of the jet. The amplification and attenuation regions are separated by a neutral stability curve. One example of such a curve is shown in Figure 2.

This curve indicates a critical Reynolds Number of five for amplification in a jet far from the source nozzle. Further discussion of this curve, and the significance of Reynolds Number is given below.

C. Transition to Turbulence

The amplification mechanism exists in the boundary layer. The signal which is amplified is a disturbance in a pseudostable boundary layer. The boundary layer grows at the expense of the regions immediately around it. When disturbances in the boundary layer are of the size of the layer, it is turbulent. Such turbulent boundary layers grow very rapidly, quickly consuming the laminar jets they are associated with, so that the entire laminar jet is carried into turbulence. Since the laminar boundary layer grows

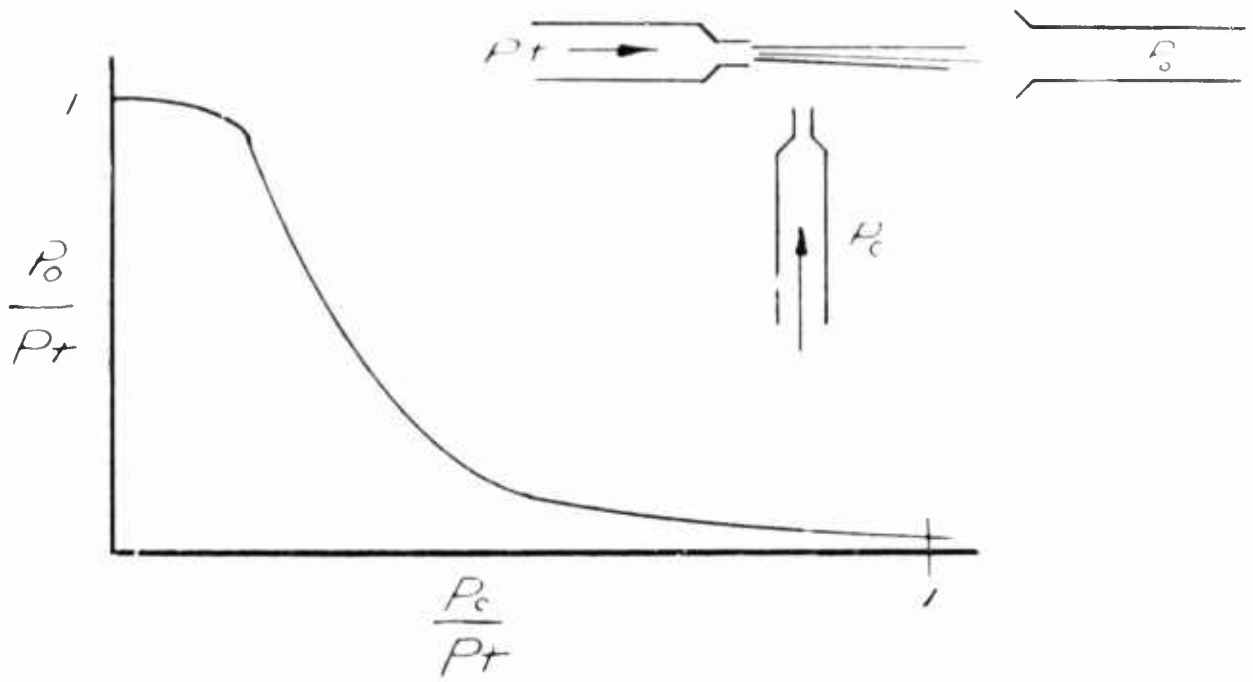

FIGURE 1

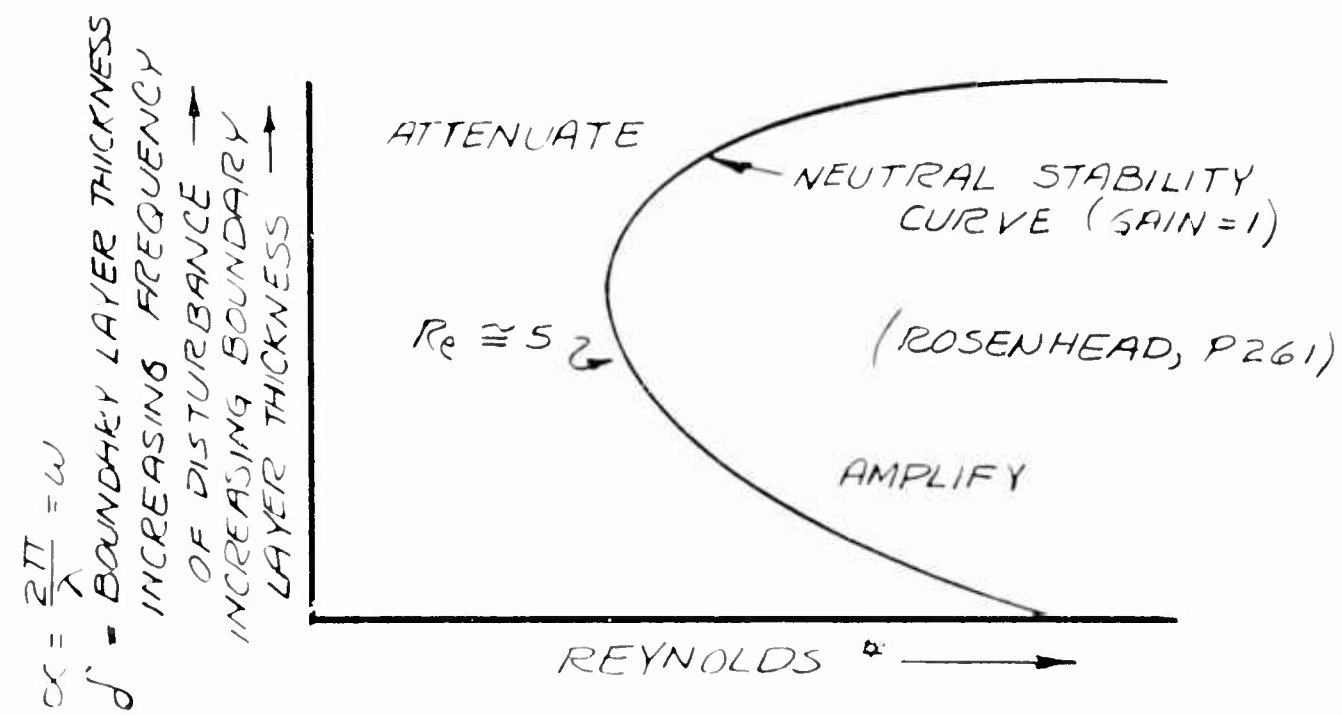

FIGURE 2

quickly, the jet transition is rapid. Once turbulent, the jet dissipates its energy in the immersing medium. Transition to turbulence of the jet is closely controlled by the character of the boundary layer. In turn, boundary layer transitions depend on initial disturbance size and boundary layer gain. Since the gain in the turbulence amplifier mechanism is very large, small variations in disturbance signals can significantly alter the jet transition point. Since any real fluid will have a small but finite variation in local properties, it must be anticipated that the transition point will move relative to the power nozzle in the x-direction. Only the most closely controlled jet flows and input signal levels can reduce this transition noise, which appears as an equivalent input noise.

D. The Significance of Reynolds Number for Turbulence Amplifiers

The existence of a Reynolds Number dependent neutral stability curve has already been mentioned earlier. The meaning of Reynolds Number in connection with turbulence amplifiers requires some clarification.

In pipe flows, Reynolds Number is given by $Re = \frac{V \times d}{\nu}$ where V is the free stream velocity, d is the pipe diameter, and ν is kinematic viscosity of the fluid. A critical Reynolds Number has been shown by experiment as high as 2300. This means that with great care a stable laminar flow can be made to exist at Reynolds Numbers up to this value, in pipes.

As soon as the jet leaves the pipe, however, this simplicity disappears. The jet is spreading and the velocity is decreasing. Assuming a constant momentum flow, M, then $M = \rho A V^2 = \rho \frac{\pi d^2}{4} V^2$ or $V = M / 4 \rho d^2$.

$$R_e = \frac{Vd}{\nu} = \frac{4M}{\rho \cdot d^2} \times \frac{d}{\nu} = \frac{4M}{\pi \rho \nu} \times \frac{1}{d}$$

The implication is that the Reynolds number drops as the jet expands.

Unfortunately, this simple picture is not sufficient. For slow expansion rates, such as for laminar jets, small changes in Reynolds Number should be anticipated. For large rates of change

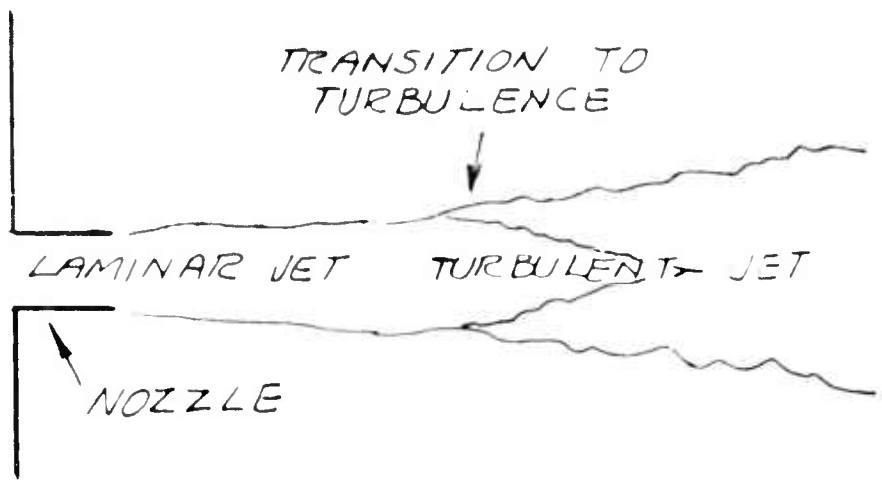

FIGURE 3

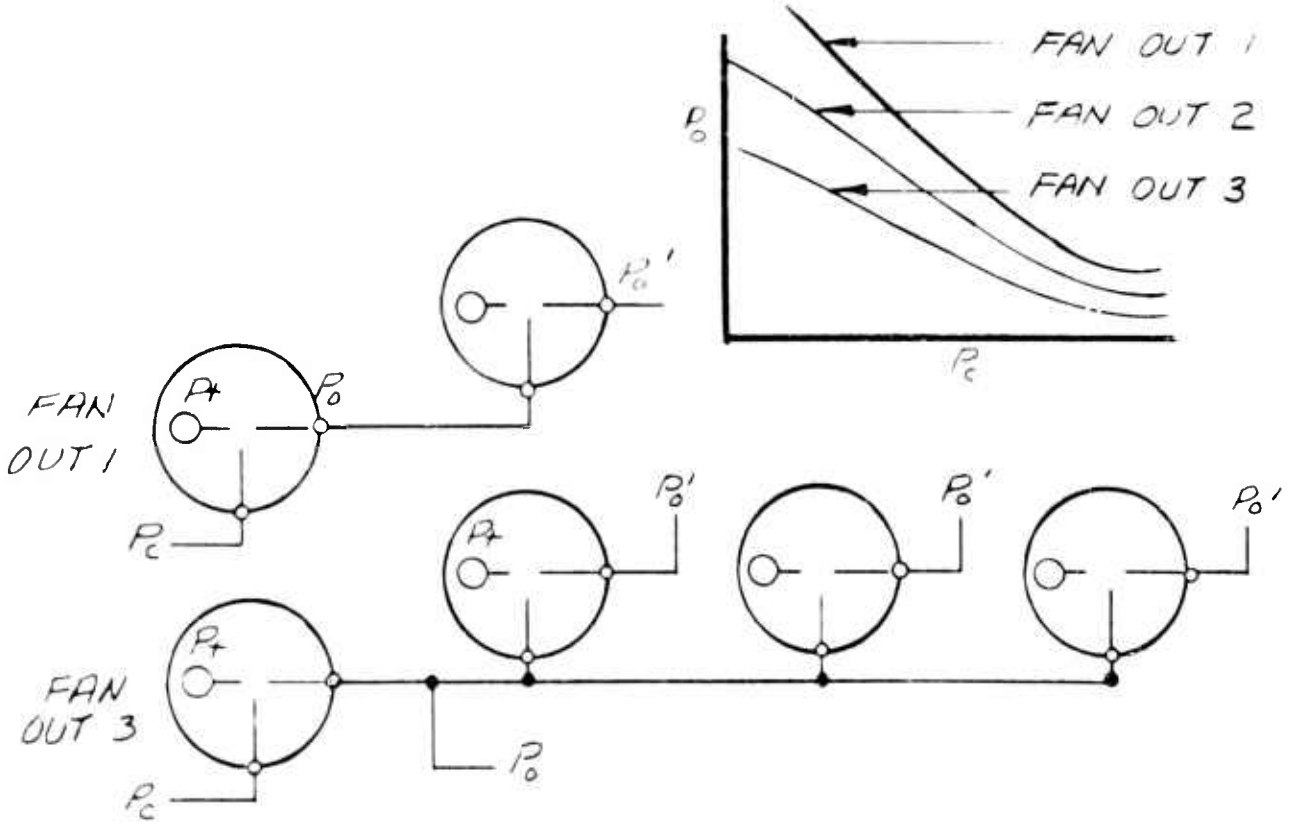

FIGURE 4

in jet width, the radial velocity component becomes significant, and quickly drives the jet into turbulence. It seems that the critical Reynolds Number must depend sharply on nozzle design, and in fact very low Reynolds Number flow from short nozzles can produce turbulent flow a short distance from the nozzle exit.

III. Design

The Turbulence Amplifier design must take into account a number of factors, related to the discussion above. This section discusses some of the design considerations.

A. Nozzle Design

A high gain amplifier must be operated close to the critical Reynolds Number for pipe, with the receiving aperture adjusted in distance from the power nozzle as required by the zero signal transition point. Unless sufficient pipe length is allowed leading to the power nozzle, laminar flow will not be achieved prior to the power nozzle exit, and an earlier transition to turbulence will be experienced, with a resulting lower amplifier gain. If rules for fully developed laminar flow in pipes is followed, then a good amplifier will result. A further difficulty may arise with a short nozzle design; a unit which has a small separation between nozzle and receiver. The rapid rate of spreading of a turbulent jet may not completely eliminate the power jet core. As a consequence, the minimum outlet pressure in the turbulent state will remain higher, producing a less satisfactory amplifier.

When high gain is not critical, then considerable power can be saved by reducing the power nozzle length. If operation at very low power levels is most important, low gain staged units may be more economical.

B. Receiver Configuration

The receiving aperture should have an area about the size of the power nozzle. Also, as much open space as feasible must be provided on all sides of the receiver to permit easy exit of flow which is not captured. Venting near the receiver is mandatory. Any resistance in this area reduces the effective flow rate, reducing gain, and increasing power consumption.

C. Control Nozzles

The purpose of the control nozzle is to deliver a turbulent flow to the power jet near the power nozzle exit, with a minimum of power consumption. The simplest way to assure this is to use a very short control nozzle, allow the control jet to spread rapidly to the power jet thickness, and use as small a nozzle as is consistent with available recovered pressure, and fan-out requirements.

Because power consumption in a nozzle for a given Reynolds number rises as the required driving pressure goes up, it seems reasonable to use large, low pressure nozzles at very low flow rates where possible. A pressure amplification of ten (10) is well within the state of the art today in Turbulence Amplifiers, so that larger, low pressure models can be used where space permits.

D. Steady State Matching

The turbulence amplifier as a digital circuit element can be matched to a load in the following manner.

Elaborating on the characteristic curve of Figure 1, a series of curves are plotted which give the pressure output of the element with the output connected to one, two, or more controls or subsequent units, as shown in Figure 4.

For purposes of an example a similar unit with a single output is to be used as the load (the second stage). The characteristic of this unit is plotted with its output as the abscissa and the input as the ordinate, the reverse of the above.

These two characteristics are superimposed in Figure 6 . The operating points are determined as follows: Assume a fan-out of 1. A control pressure P_a is applied to the control of the first unit. The output of the first unit is P_x. The signal P_x is the control pressure for the second stage. The second stage, with a fan-out of 1 will have an output of P_y . Continued iteration of this process reveals the crossover point is the eventual operating point of a cascade of elements.

A similar process can be repeated for a control signal of a pressure greater than for the pseudostable point shown. This will show the operating point to be the right hand crossover.

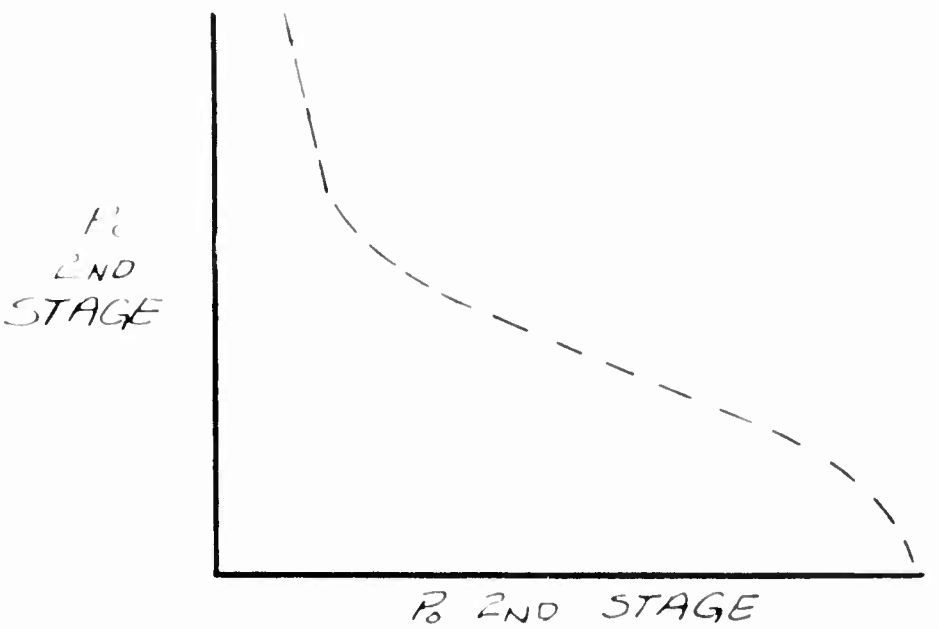

FIGURE 5

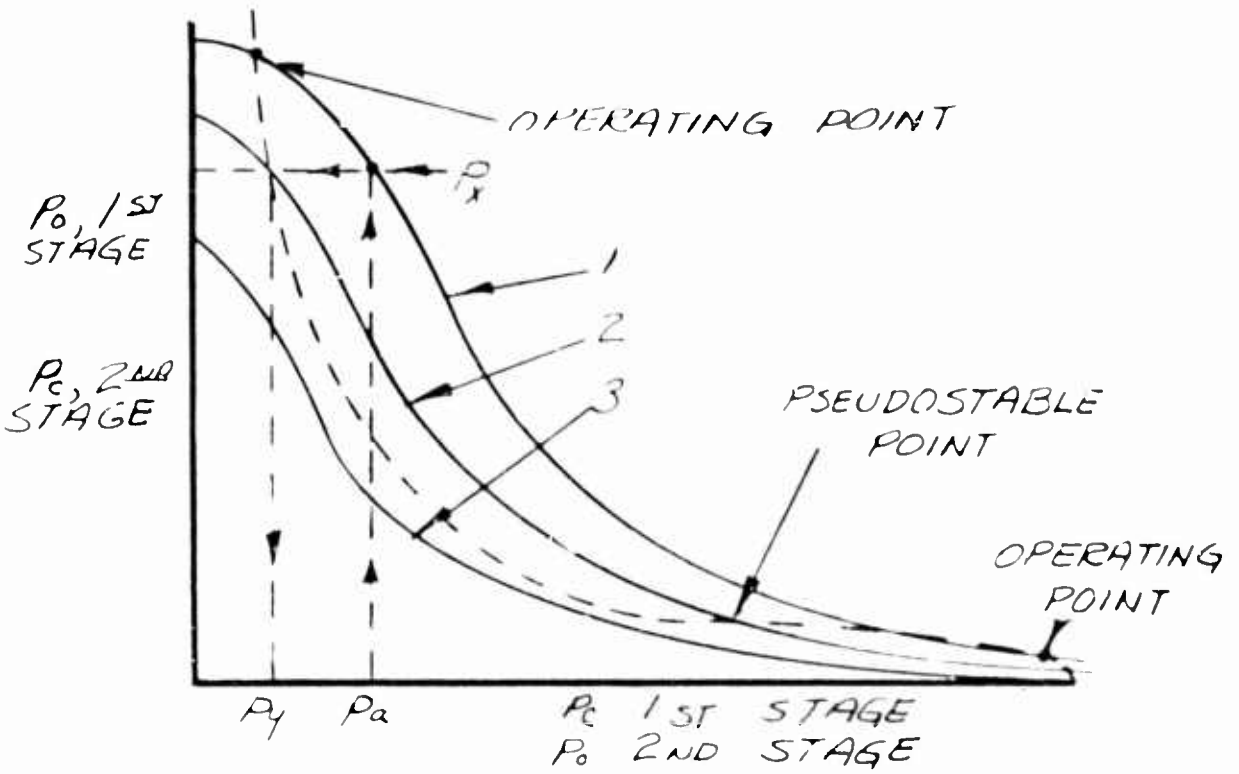

FIGURE 6

Continuing with the example shown in Figure 6, a fan-out of 3 has only one crossover and therefore only one operating point. It is not bistable in all cascade conditions. However, the lack of three crossovers does not preclude its use, if used with discretion.

In conclusion, superimposing the second stage and first stage relationships shows the sequence of steady-state operating conditions, and an input for pseudostability. The process can be expanded to superimpose curves for fan-outs in both planes to effect a universal design chart. It is also possible to plot the input output characteristics of the element for a variety of output load orifices so that the designer can draw in a specific load condition if it is relatable to an equivalent orifice.

IV. Experiments

A. As a demonstration of the turbulence amplifier in a flat configuration, an "And" gate was designed and constructed. The silhouette is shown in Figure 7, and a photograph in Figure 8.

The P+ manifold supplies power to the nozzles of the three amplifiers. The input signals are applied at P_{C1} and P_{C2}. The output signal is on only if both P_{C1} and P_{C2} are on. If either is removed, the output of that amplifier increases sufficiently to effect turbulence in amplifier 3, turning its output off.

Table I gives the results of tests of the amplifiers shown at supply pressures of 0.4 to .75 inches of water. The associated power flow and the output pressure for the on and off conditions are given for each test. The ratio shown is the ratio of these pressures which is given as a measure of performance. The power dissipated per stage is as low as 1.4 milliwatts. The data of Table I is plotted in Figure 9.

Table I

P+	.75	.70	.65	.60	.55	.40	in H_2O
Q+	1.35	1.30	1.25	1.20	1.10	.90	in^3/SEC
Off	.12	.10	.08	.08	.07	.04	in H_2O
On	.48	.50	2.55	.49	.44	.29	in H_2O
Ratio	4.0	5.0	6.8	6.1	6.3	7.2	
Pwr.	4.07	3.67	3.26	2.90	2.42	1.45	milliwatts

Power = P ("H_2O) Q (IN^3/SEC) x 4.03 x 10^{-3} Watts

"AND" gate Power Consumption Good stability, Open, In Quiet Room, Figures are supply Pressures in "H_2O .

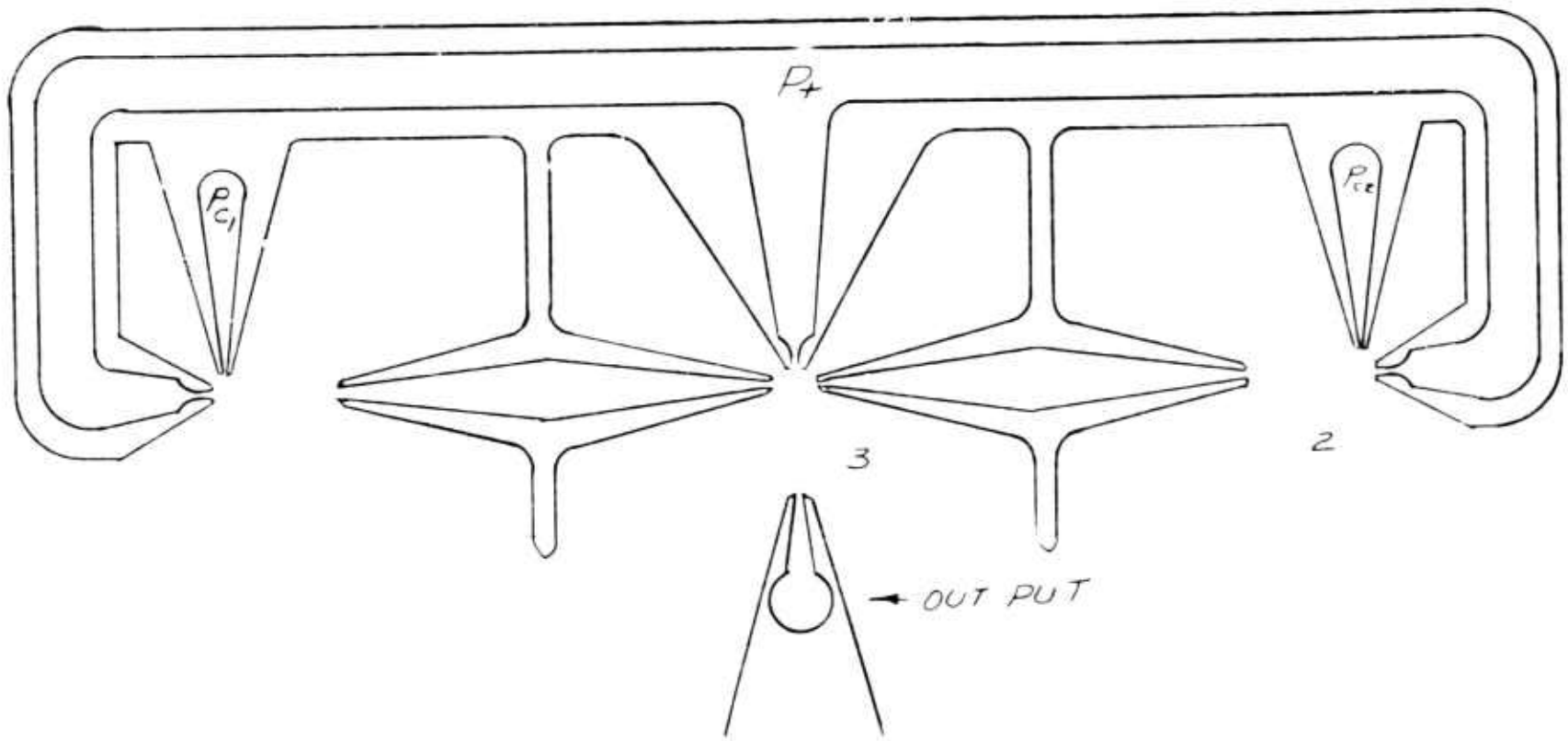

FIGURE 7

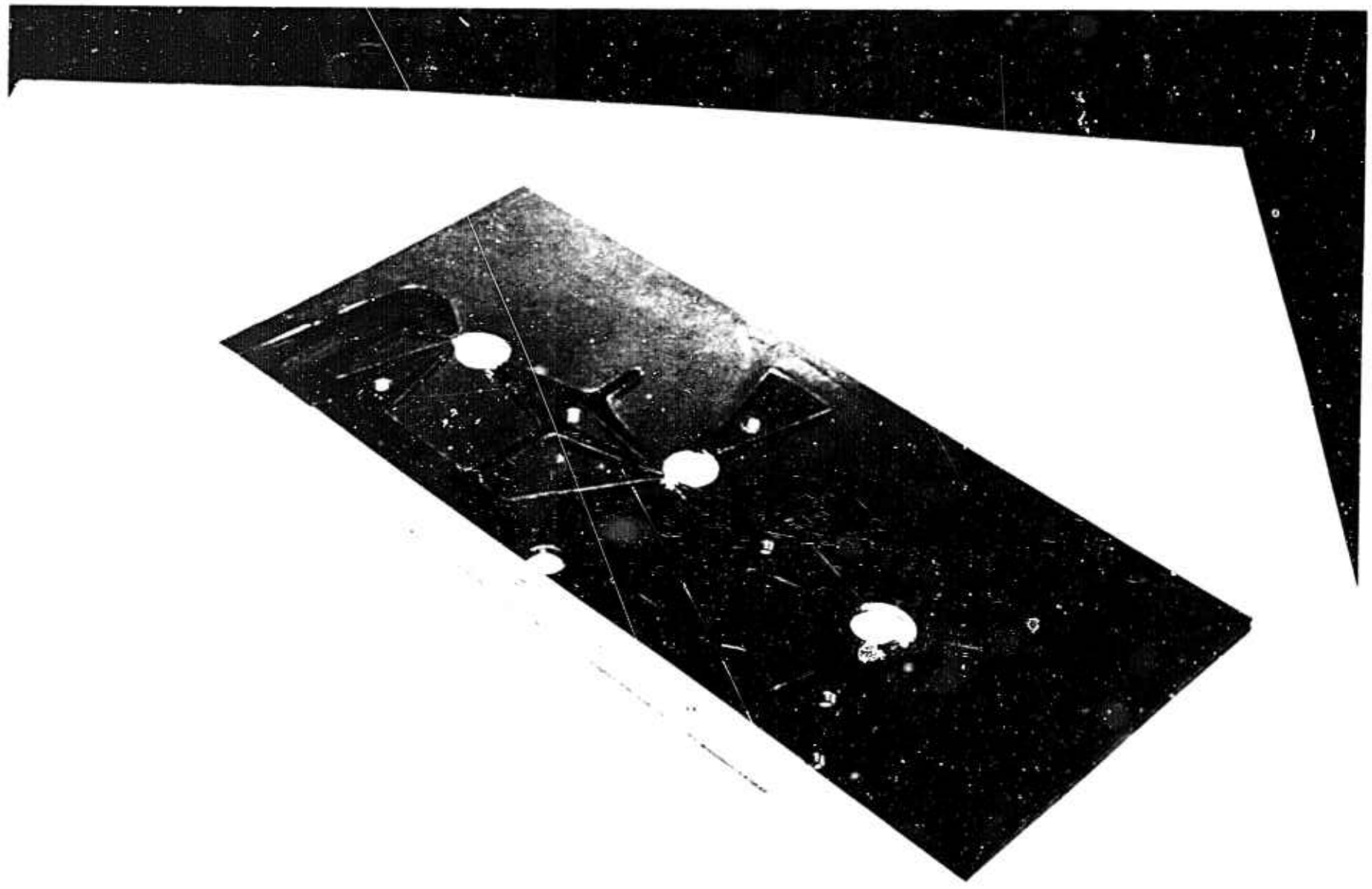

Figure 8. TURBULENCE AMPLIFIER IN OPTIFORM

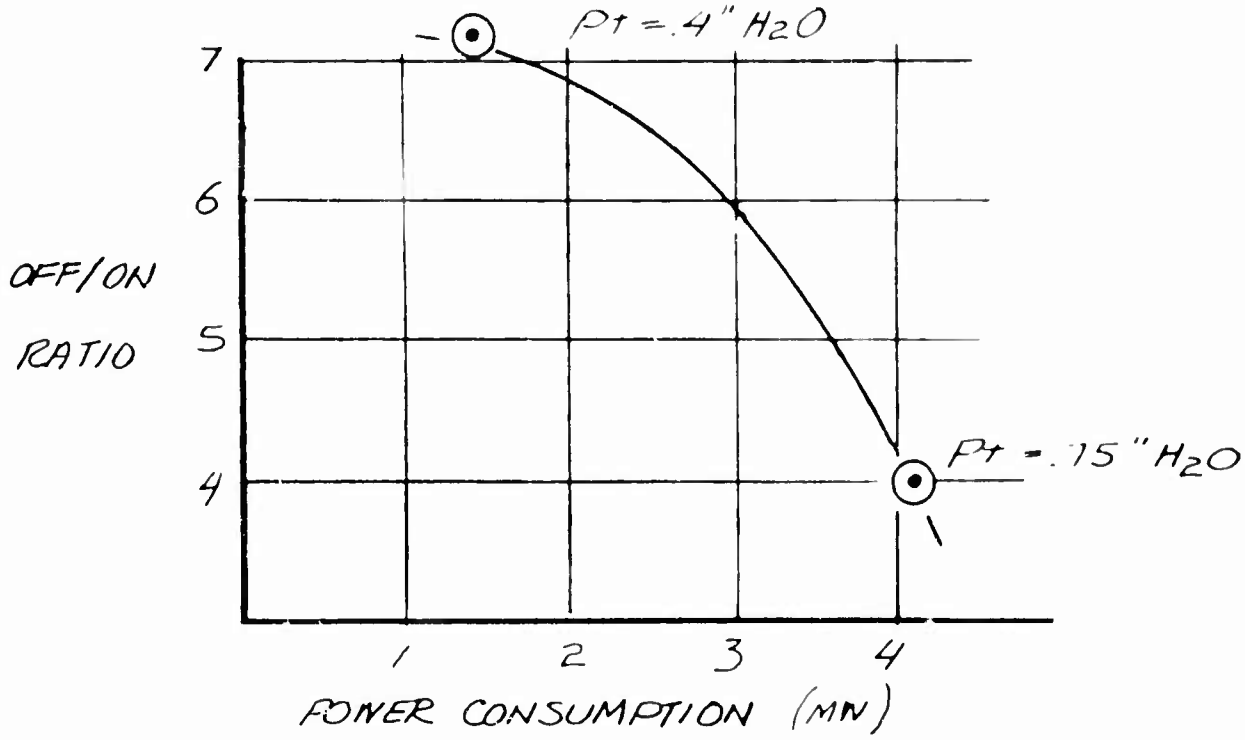

FIGURE 9

B. A test was performed to determine the maximum nozzle Reynold's number which would allow laminar flow between the power nozzle and the output nozzle of the BEC #1732-2 turbulence amplifier. Figure 11A is a diagram of the test apparatus. The supply pressure (P_+) was slowly increased and the output pressure (P_O) measured. The control jet was not used. The tabulated results are shown below and a graph is included in Figure 10.

P_+ (H_2O)	P_O (PSIG)
2.00	0.0038
1.75	0.0032
1.50	0.0028
1.25	0.0024
1.00	0.0024
0.75	0.0028
0.50	0.0020

Supply pressure for maximum laminar flow was found to be 0.75 inches of H_2O. The Reynold's number associated with such a pressure drop through the control nozzle was approximately 900.

C. An experiment was performed to determine the characteristic curves for a #1732-2 turbulence amplifier at a supply pressure of 0.75 inches of H_2O. The apparatus diagram is shown in Figure 11B. The control pressure (P_C) was varied and both P_C and P_O were recorded. This test was repeated with loads of 1, 2, and 3 control nozzles in parallel. The tabulated results are shown below and a graph is included in Figure 12 and 13.

Load (Orifices)	P_C (PSIG)	P_O (PSIG)	Load (Orifices)	P_C (PSIG)	P_O (PSIG)
1	0	0.0026	2	0	0.0016
1	0.005	0.0004	2	0.005	0.0002
1	0.004	0.0006	2	0.004	0.0004
1	0.003	0.0012	2	0.003	0.0007
1	0.002	0.0016	2	0.002	0.0010
1	0.001	0.0044	2	0.001	0.0022

OUT PUT PRESSURE VS SUPPLY PRESSURE
FOR #1732-2 TURBULENCE AMPLIFIER

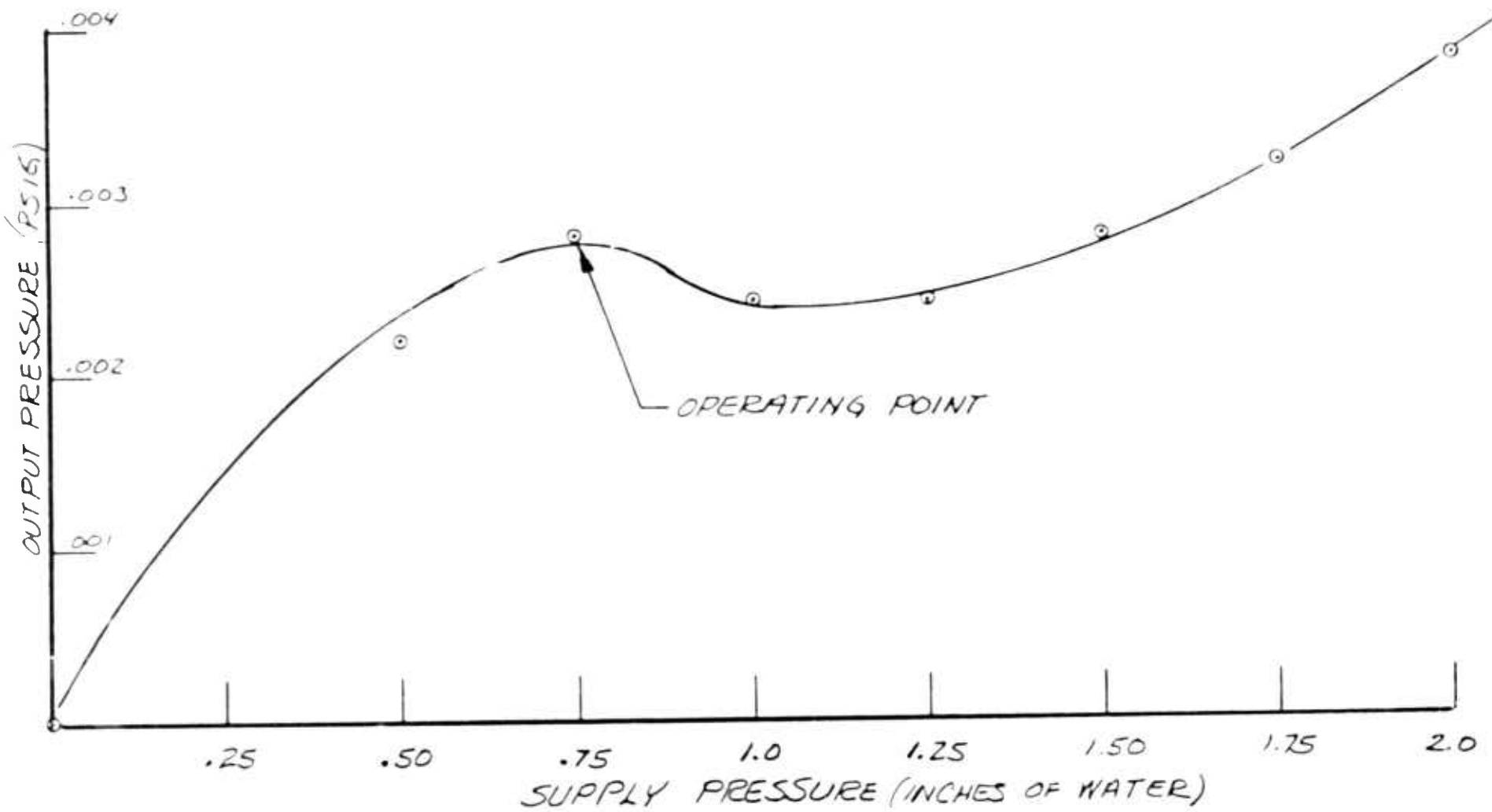

FIGURE 10

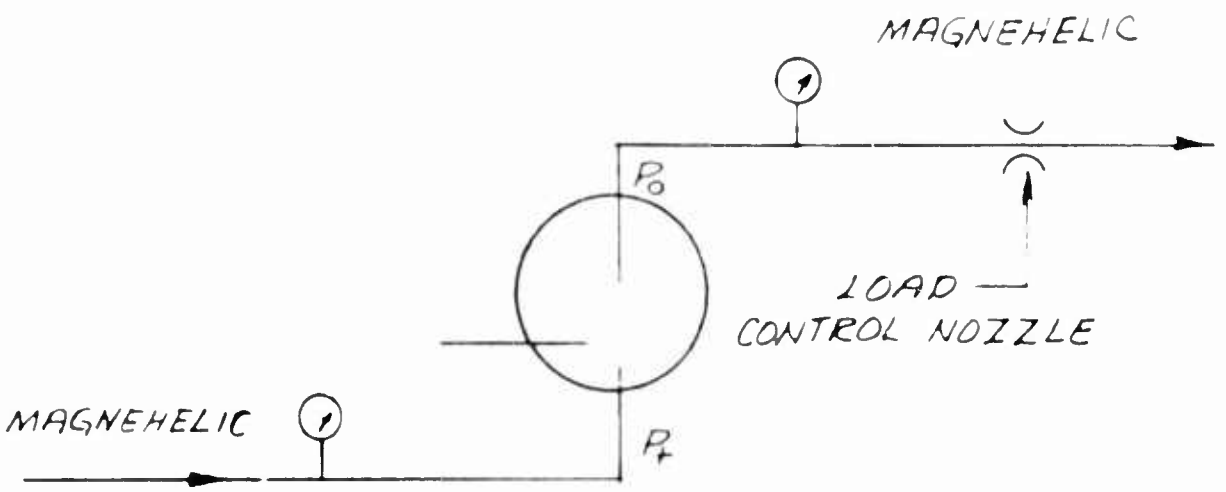

FIGURE 11A

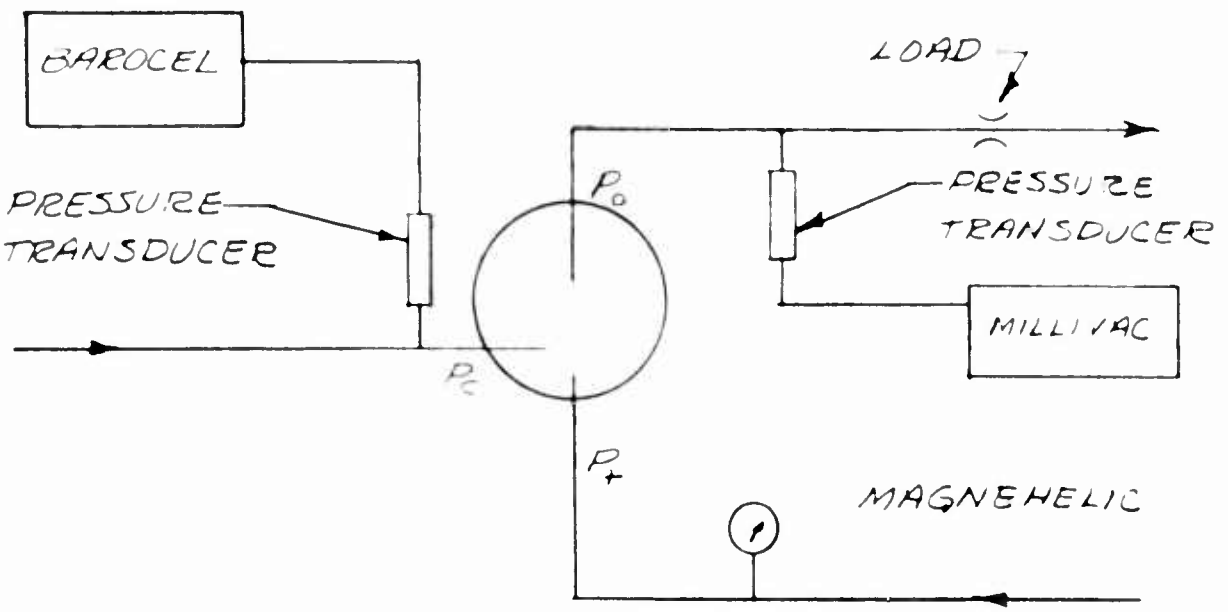

FIGURE 11B

TURBULENCE AMPLIFIER
CHARACTERISTICS CURVE
UNIT NO. [illegible]
P_s = .75 H_2O

LOAD - ONE CONTROL NOZZLE —⊙—

LOAD - TWO CONTROL NOZZLES —△—

LOAD - THREE CONTROL NOZZLES —□—

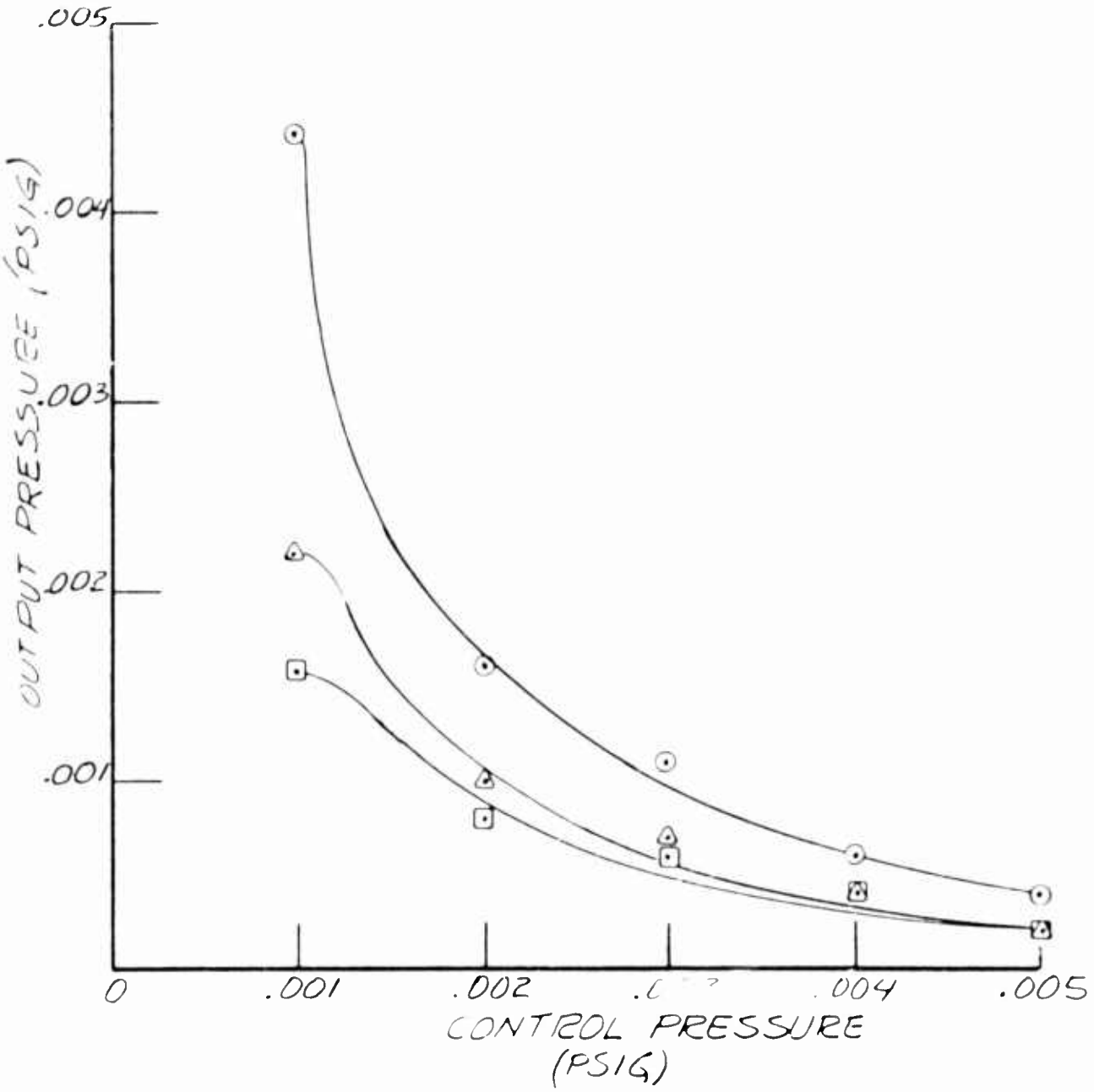

FIGURE 12

TURBULENCE AMPLIFIER IMPEDANCE MATCHING CURVE.
UNIT NO. 732-2

LOAD - ONE CONTROL NOZZLE —⊙—

LOAD - TWO CONTROL NOZZLES —△—

LOAD - THREE CONTROL NOZZLES —⊡—

P_T = .75 " H_2O

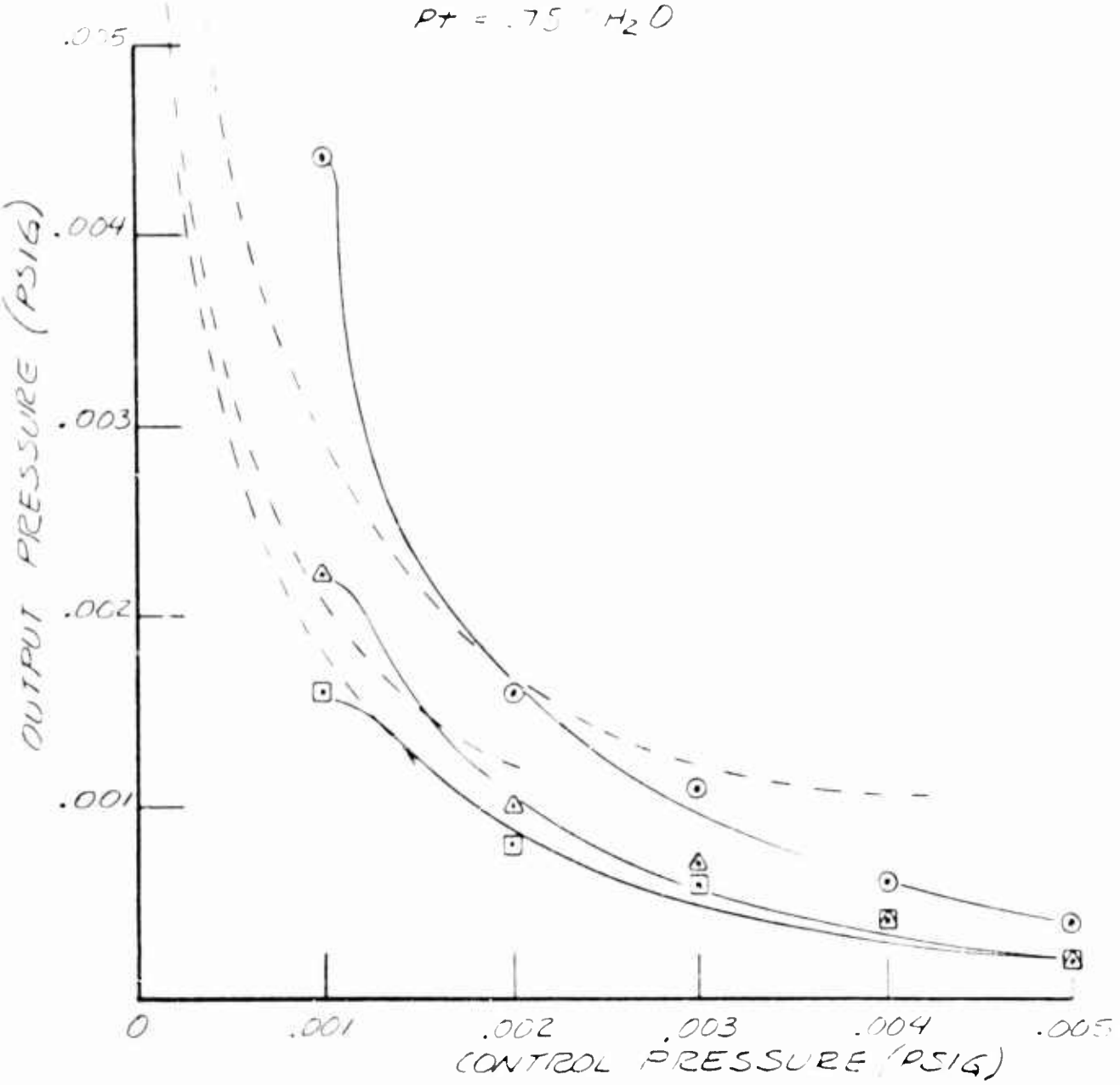

FIGURE 13

Load (Orifices)	P_C (PSIG)	P_O (PSIG)
3	0	0.0012
3	0.005	0.0002
3	0.004	0.0004
3	0.003	0.0006
3	0.002	0.0008
3	0.001	0.0016

E. An experiment was performed to determine the operating characteristics of the #1732-2 amplifier constructed without the center dump hole. This simplification would result in a reduction in fabrication time.

Proper supply pressure was investigated using the method outlined in experiment B. The tabulated results are shown below and a graph is included in Figure 14.

P+ ("H_2O)	P_O ("H_2O)
0.25	0.025
0.50	0.050
0.75	0.050
1.00	0.075
1.25	0.085
1.50	0.090
1.75	0.110
2.00	0.140

It was very difficult to determine the value of P+ which would cause the air flow to become turbulent at the output nozzle. Characteristic curves were determined using the method of experiment C. The tabulated results are shown below and a graph is included in Figure 15.

P+ = 0.5 "H_2O

P_C (PSIG)	P_O (PSIG)
0	0.00200
0.00280	0.00035
0.00210	0.00070
0.00125	0.00260
0.00085	0.00250

P+ = 0.0 "H_2O

P_C (PSIG)	P_O (PSIG)
0	0.00250
0.00685	0.00035
0.00500	0.00070
0.00340	0.00140
0.00240	0.00360

CUT PUT PRESSURE VS. SUPPLY PRESSURE FOR #1732-2 TURBULENCE AMPLIFIER (NO DUMP HOLES)

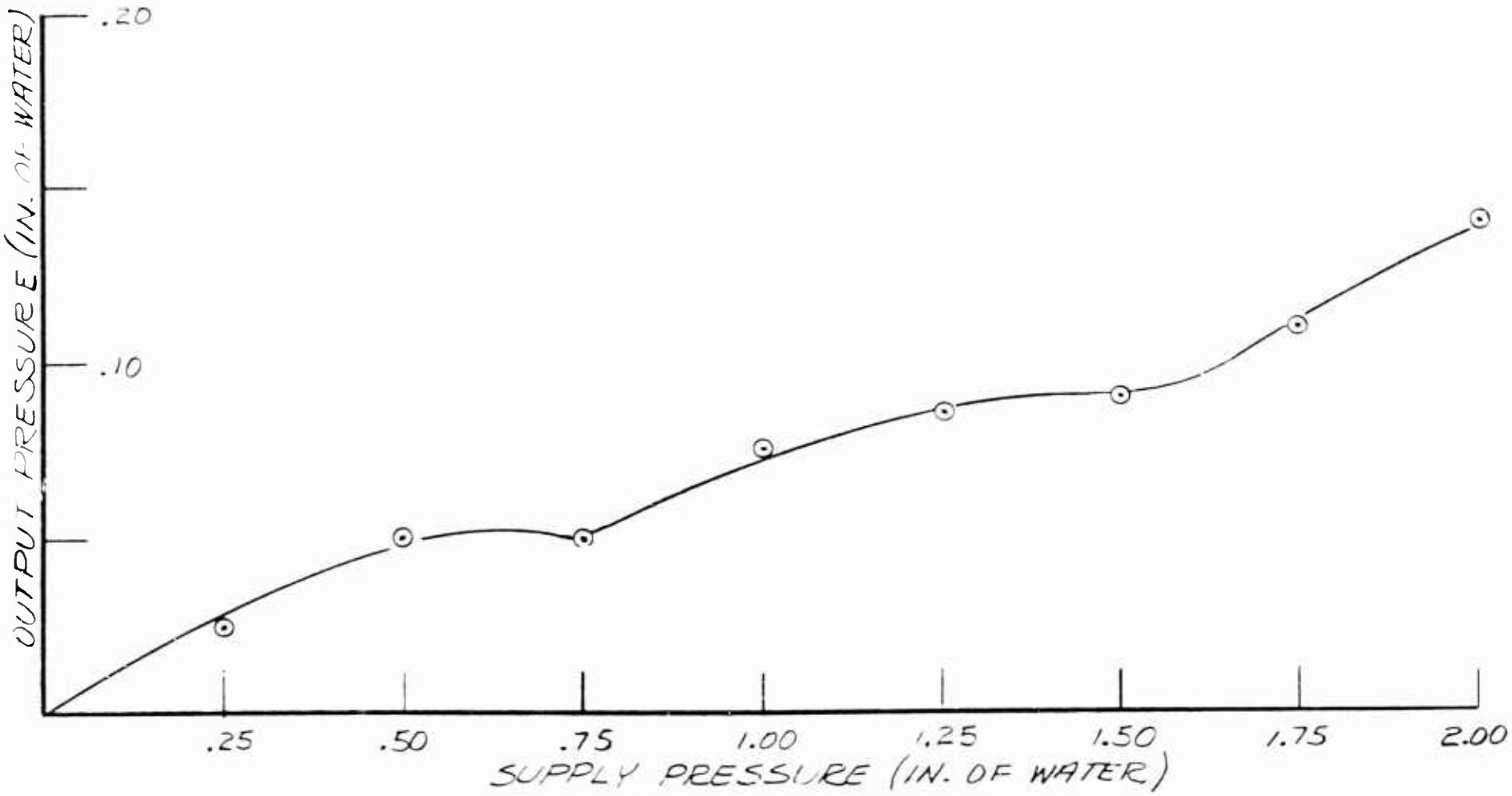

FIGURE 14

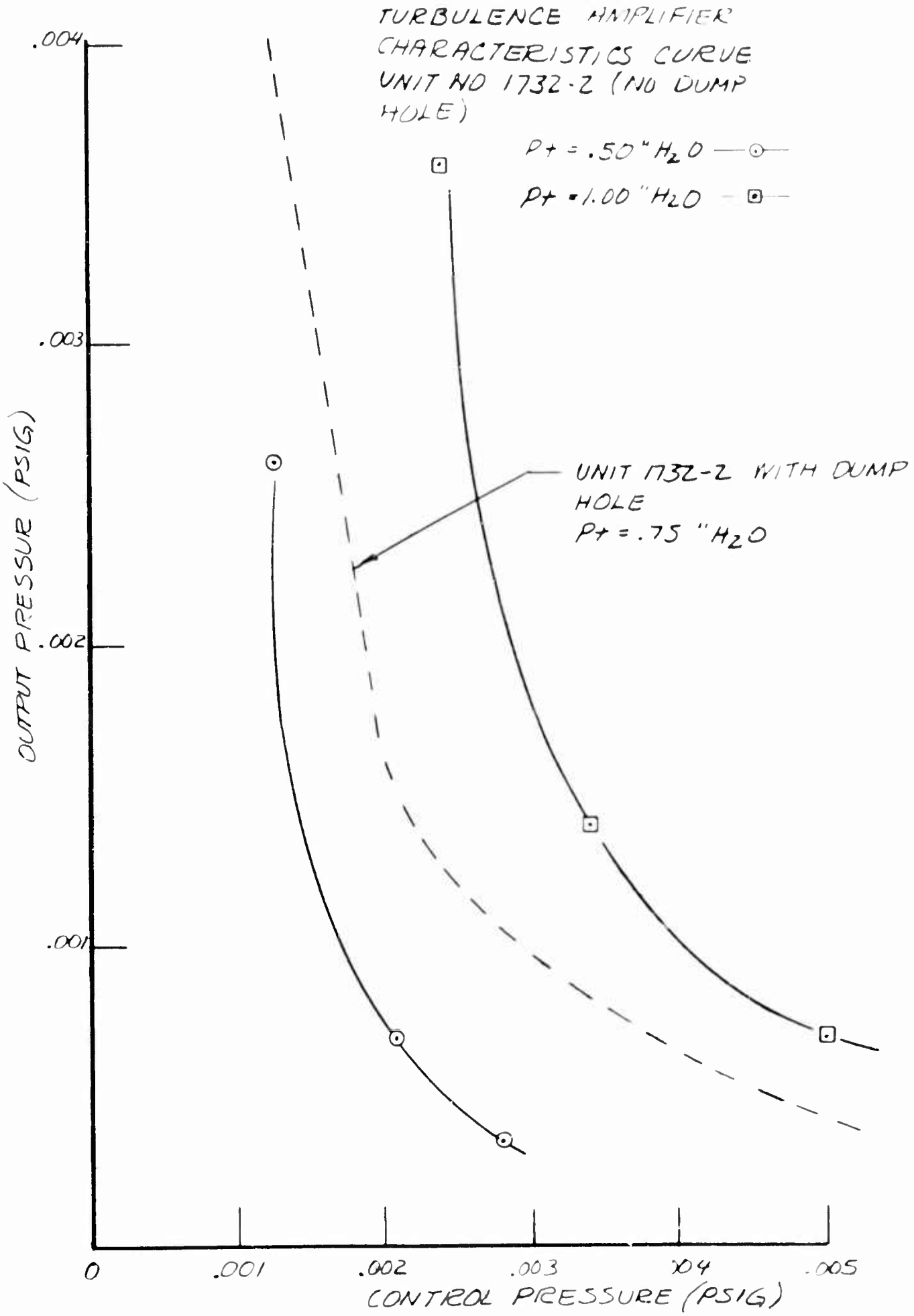
TURBULENCE AMPLIFIER CHARACTERISTICS CURVE UNIT NO 1732-2 (NO DUMP HOLE)
Pt = .50 "H2O
Pt = 1.00 "H2O
UNIT 1732-2 WITH DUMP HOLE
Pt = .75 "H2O
OUTPUT PRESSURE (PSIG)
.004
.003
.002
.001
0
.001
.002
.003
.004
.005
CONTROL PRESSURE (PSIG)

FIGURE 15

The characteristic curve of a #1732-2 amplifier with the dump hole cut and operating at $P_r = 0.7$ H_2O is superimposed on Figure 15. This graph shows that if some degradation in performance can be tolerated, the dump hole need not be cut and a great savings in fabrication time can be realized.

V. Conclusions:

This work has laid the foundations for circuit design in Flat Forms with turbulence amplifiers. It has shown a direction to follow for more rigorous evaluation of the basic amplification mechanism. There is no longer doubt that the flat configuration can provide low power circuitry using turbulence amplifiers. The present models were manufactured using the "Optiform" process. It is clear that size and power consumption is limited only by the space requirements for the [illegible]. There is strong evidence that satisfactory configurations can be made at lower Reynolds Number, with an attendant decrease in size. For "NOR" logic with two input limits, considerable leeway is available in circuit design to permit low gain digital amplifier operation, again with a consequent size reduction. Note that one particular "And" gate, for which data is presented, was operated at power jet Reynolds Numbers of approximately 100.

DIGITAL DATA HANDLING SPEEDS WITH PURE FLUID (PNEUMATIC) CIRCUITS

By

Peter Bauer
Eric E. Metzger
Bowles Engineering Corporation

ABSTRACT

Digital Data Handling is defined as the manipulation of numerical data in the form of discrete level signals, in this case, Pure Fluid signals. On the basis of this definition, present and future capabilities are construed, with the help of theoretical considerations supported by test results. Extreme boundaries are placed upon speed capabilities by considerations of logic requirements on one hand, and projected Pure Fluid element performance capabilities on the other hand.

Expectations and means of practically feasible future speed improvements are discussed, such as element and circuit design, miniaturization and power levels, pneumatic media, and logic circuit methods, with respect to the outlined boundaries. Numerical data handling applications suited to Pure Fluid circuit speed capabilities are mentioned.

The objective of the discussion, to guide present and future work into realistic channels, is recapitulated in the summary.

INTRODUCTION

The operation of Pure Fluid digital elements, i.e. discrete level switching elements and amplifiers, in circuits and systems, has been loosely called "digital." However, common usage of the word digital in this connection implies numerical data handling, popularly identified with digital computers. Conflict arises from this loose definition when so-called digital performance capabilities are quoted which are applicable to particular single elements under unspecified conditions. These

particular elements may not necessarily be able or even supposed to process numerical data. Such wrongly generalized data, often bordering on, however unintentional, misrepresentation, may cause unnecessary problems at a late stage of work.

Digital data handling speed capabilities of Pure Fluid circuits are one of the most misunderstood and at the same time most important performance criteria. This discussion aims to shed some light on these speed capabilities and intends to encourage meaningful performance specifications on one hand, and critical questioning of performance specifications on the other hand, with respect to numerical data processing with Pure Fluid circuits.

DEFINITIONS

For the purpose of this discussion, "Digital Data Handling" is defined as the manipulation of information in form of discrete numerically defined values (digits), where "manipulation" applies to fundamental arithmetic processes.

This definition precludes the manipulation of data in form of continuously variable frequencies, pulse widths, phase shifts, etc., and of course, amplitudes, even though some of such information handling has been called digital. So, for example, information contained as frequency in the continuously variable oscillation of a signal is not digital. However, the counting of such oscillations in a digital counter becomes a numerical operation, particularly when such counts are further processed as discrete numerical values. Nevertheless, the original information coded as a frequency or repetition rate is not recognizable in the counter until reference is made to, for example, units of time in compatible numerical form.

These definitions become very important in the consideration of the use of elements and circuits on the basis of their performance characteristics. For example, an element or a circuit may well be capable of handling, generating, or being excited by signals at frequencies orders of magnitude higher than the maximum digit rate at which the same device is able to process numerical information. Alternately, a device may be able to operate at very high signal frequencies, but handle only narrow bandwidths.

These considerations apply to any system, whether mechanical, electrical, electronic, or Pure Fluid. They are extremely important to Pure Fluid Digital Systems, since relatively broad bandwidths have to be utilized to handle error free digitized information to any required accuracy, and because of relatively low operating speed capabilities which place many applications on the borderline between feasible and not feasible depending on the state-of-the-art.

SPEED CAPABILITIES

This discussion is limited to digital data handling speeds with Pure Fluid (pneumatic) circuits, as defined in the preceding section.

Propagation Delay - Circuits:

The most important criterion with respect to data handling speed is the signal propagation time delay through any part of a circuit, whether it is the delay in the smallest length of a channel section, through a simple passive or active element, or the delay in a complex circuit or even a complete system.

If truly parallel handling of information in digital form were possible, which would preclude coding of any sort and would represent fixed processing of arithmetic in a baseless fashion, only signal delays through the longest path would need consideration. Furthermore, if this extreme case is assumed to operate in "open-loop" mode, even this propagation delay may be considered irrelevant to its speed capability. Unfortunately, this is an example of a virtually useless method of primitive data processing, analogous to, for example, addition of signals in lines, where each digital signal belongs to one line and there are as many lines as there are signals, i.e., a baseless number system. Whereas such systems might be able to perform some arithmetic processes in a fixed unchangeable fashion, they cannot seriously be considered to provide arithmetic capability, nor can they be considered practical or economical. However, the mention of this theoretically extreme case clears the way to the discussion of practical system logic requirements and their effects on data handling speeds.

In practice, numerical information is almost always contained in coded form, whether an artificial code with arbitrarily assigned digit values or an orderly code with naturally ensuing digit values, according to some strict rules, such as the commonly used decimal positional

notation or the well-known binary code. The resulting economy in signal paths permits the operation of practical arithmetic processing machines or digital computers, as we all know. For this reason, digital handling of numerical data inherently results in necessary cross-connections of, perhaps, otherwise parallel and independent signal paths, as well as signal feedback to the same signal originating line or to other lines (feedback in time only). Figures 1A, 1B, and 1C show diagrams of simple circuits with such feedback and cross-connections.

Also, feedback may already be required for other than arithmetic functions. Practical systems necessarily contain a large number of cross-connections and feedback paths providing "CARRY" for example (see Fig. 1A), to complete system feedback initiating repetitive or other operations through the whole system. Therefore, practical systems and circuits comprise many small loops and often operate as complete closed-loop systems. The signal propagation delay time in the various loops is a major criterion of the speed capability of a system, as obviously no loop may accept a new signal until the original signal has propagated completely around the loop.

Certain logical and arithmetical operations may be performed in parallel or in series in time, thus providing advantages of various kinds. However, truly parallel data handling in the strictest sense of the word does not provide arithmetic capability, as mentioned before.

Propagation Delay - Elements:

Considering a single Pure Fluid digital element, such as an amplifier, an OR/NOR gate, an AND gate, etc., as a fundamental building block of any circuitry, and assuming, for the sake of this argument, that no subdivision into smaller units with individual specifiable characteristics is necessary, basic performance criteria may be quoted for such a fundamental block or element. This applies to active and passive elements. However, this discussion will limit itself to active elements (powered devices providing a gain ≥ 1), since they represent a majority of circuit components and usually provide higher overall circuit speeds and less propagation delay.

Elements, as described, suitable for compatible operation in circuits provide a variety of speed characteristics between inputs and outputs. The signal propagation delay time through such an element is considered here as the speed criterion. Measurements and theoretical considerations have shown a range of propagation delay times of the

Fig. 1A

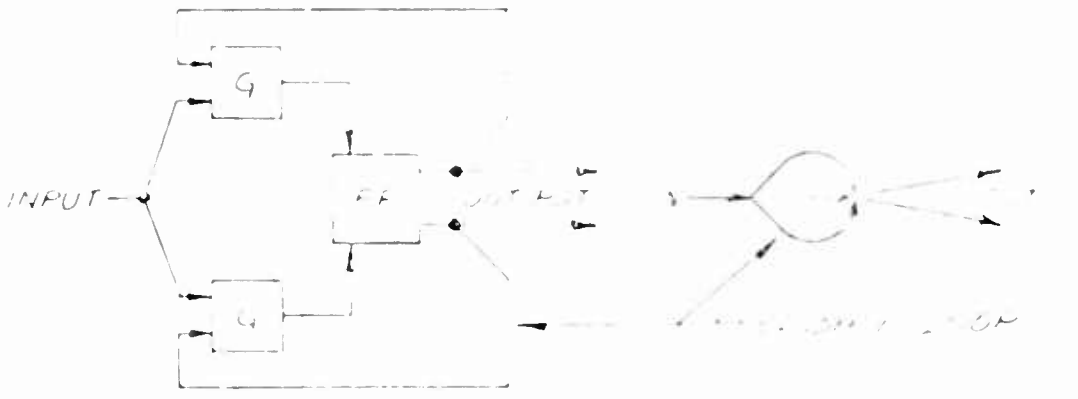

Fig. 1B Single Input Flip-Flop and Binary Scaler

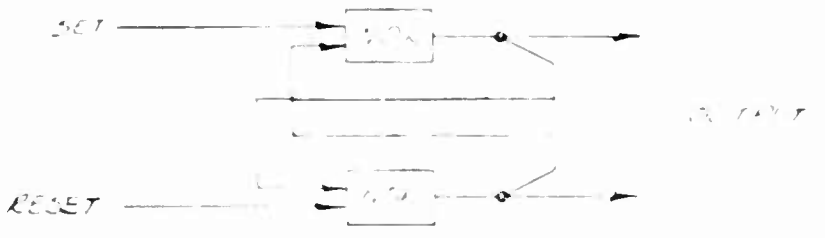

Fig. 1C Flip-Flop Circuit

order of tenths of milliseconds up to several milliseconds for elements utilizing low pressure air as the operating medium in sizes common in the present state-of-the-art. The smaller sizes comprise elements with nozzles of several thousandths of an inch in width and height, when power consumption is still reasonable, compatible interconnectability is feasible without excessive signal losses, and element switching speeds do not yet suffer.

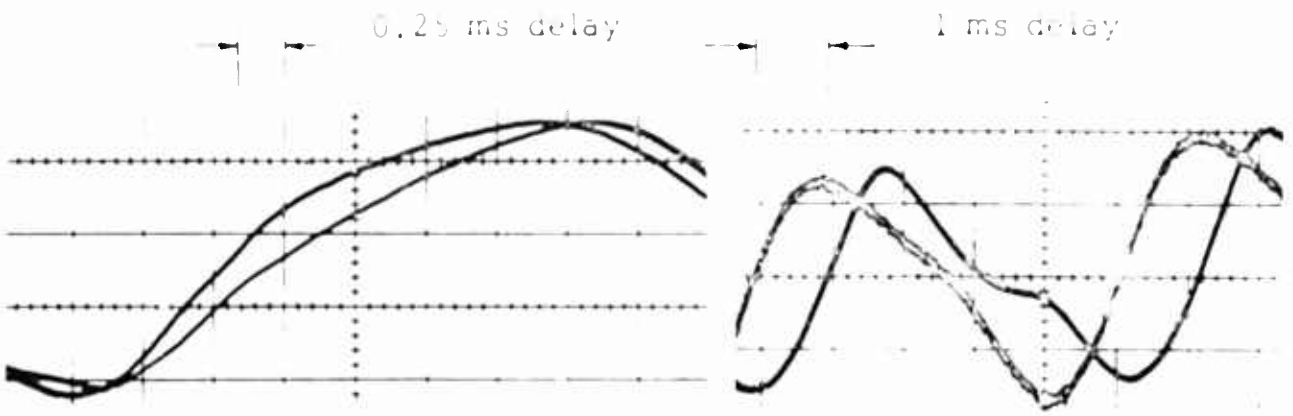

Fig. 2 Propagation Delay Time Measurements

Figure 2 shows two propagation delay time measurements through such typical amplifier (logic) elements. Delays of one quarter and one millisecond respectively are indicated in these oscilloscope traces for different conditions. However, rise times between 1.5 and 2.0 milliseconds are indicated, largely due to high capacitance terminal channels. Rise times of the order of the propagation delay time are obtainable with suitable connecting channel design. The measurements shown here were aimed at propagation delays only.

Size, Power Level, Fluid Medium:

If the length of the digital element from control nozzle to exit aperture is L, then the time elapsed in signal transmission is $\frac{L}{V}$,

where V is the signal velocity. No delaying effects aside from transit delay are considered here. Since the general digital circuit will involve feedback, the feedback will involve at least another $\frac{L}{V}$ delay, or a total

delay of $\frac{2L}{V}$. This situation is illustrated in Figure 3.

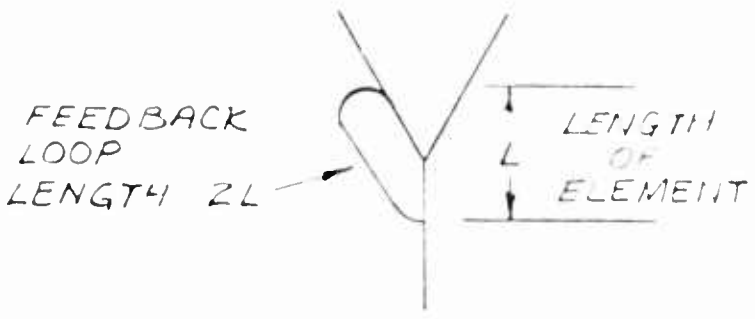

FIG. 3

This simple principle leads to the realization that increased frequency can be achieved by miniaturization and/or by increased signal transmission velocity.

By way of illustration, choose, first, a jet element which operates with a turbulent power flow. Such an element may be scaled in size by simple geometrical scaling rules.

Thus, if W is the nozzle width, the length may be 15W, the feedback loop may be 30W long, and total delay will be $\frac{60W}{V}$. On the face of it, then, a reduction to 1/10 the nozzle width produces a decrease in loop delay to 1/10 its former value.

The behavior of an element depends upon the nature of the flow within it. In order to maintain similarity of behavior, the smaller element should be operated at the Reynold's Number of its larger counterpart. This imposes a new condition, that $\frac{V \times W}{\nu}$ remain constant.

Recall that a minimum Reynold's Number for assured turbulent pipe flow is 2300. Applying this criterion to element operation, the delay now is $\frac{60W}{\frac{\nu R_e}{W}}$ or $\frac{60W^2}{R_e \nu}$ where only W, the nozzle width is a variable.

The power consumed by elements operating in a dynamically similar fashion can be calculated as follows:

The power is P x Q, where P is the dynamic pressure, or

$P = \frac{1}{2} \rho V^2$, and Q is the volume flow rate, or $Q = AV$. Further, the area A is related to the nozzle width by $A = KW^2$ where K is the aspect ratio.

Now,

$$P \times Q = \frac{1}{2} \rho V^2 \times AV$$

$$= \frac{1}{2} \rho KW^2 V^3$$

At constant Reynold's Number, $R_e = \frac{V \times W}{\nu}$

$$V = \frac{\nu R_e}{W} \quad \text{and} \quad V^3 = \frac{\nu^3 R_e^3}{W^3}$$

Now $P \times Q = \frac{1}{2} \rho KW^2 \frac{\nu^3 R_e^3}{W^3} = CR_e^3 \cdot \frac{1}{W}$, where

$$C = \frac{1}{2} \rho K \nu^3$$

Thus, the power consumed by a group of dynamically similar elements varies inversely as the nozzle width. The situation is illustrated in Figure 4. This figure illustrates an inescapable fact: the price of speed is power.

Suppose, now, that a particular element configuration is made to operate faster by increasing the fluid velocity only.
In this case

$$P \times Q = \frac{1}{2} \rho KW^2 V^3$$

Here the Reynold's Number is allowed to change. For such an element, the power/time delay relationship is illustrated in Figure 5. Here the price of increased response is again a considerable increase in power consumed.

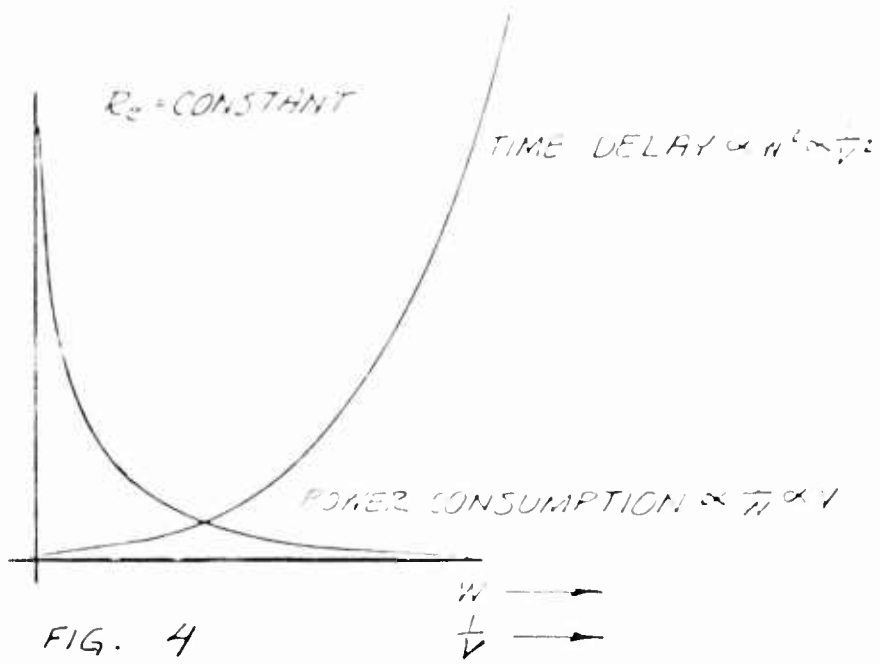

FIG. 4

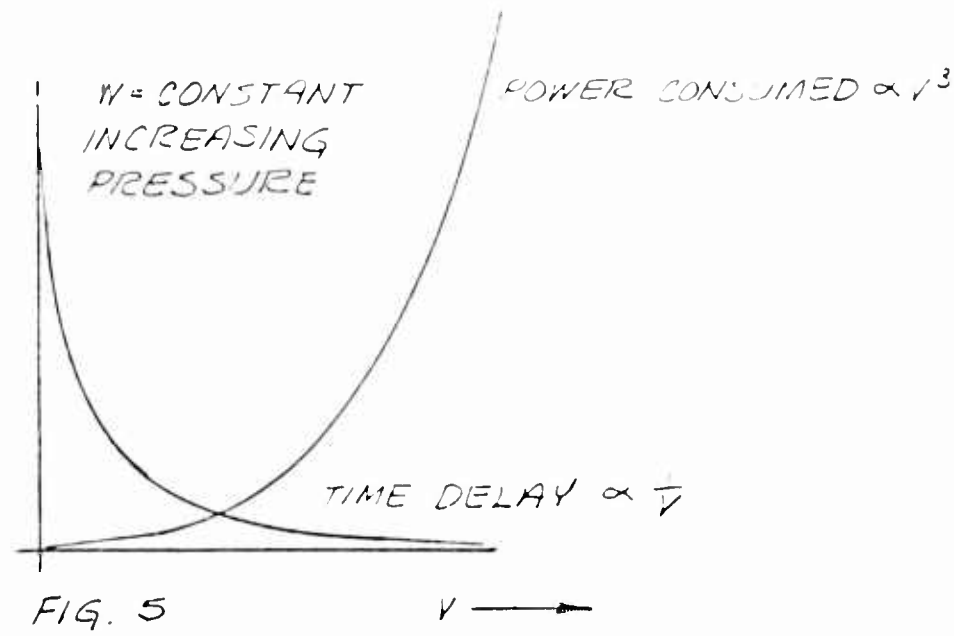

FIG. 5

The above illustration, Fig. 5, assumes flow propagation, and no acoustic signal propagation. If elements operating with acoustic signals are used, then the time delay will be $\frac{L}{C+V}$, where C is the acoustic velocity. For such elements, of course, the velocity V must be established by other considerations and cannot be freely chosen. Nonetheless, for subsonic flows, improved time delays are possible with no increase in pneumatic power consumption.

The use of other gases than air can be justified if decreased viscous losses, decreased inertia, or increased acoustic velocity are made available. Thus, the power consumption for a series of scaled models at constant Reynold's Number discussed earlier can be decreased considerably, since the power consumed depends on [illegible] where ρ is density, and ν is kinematic viscosity. The time delay with decreased [illegible] is increased, but only as the first power, so that a net advantage is achieved. The dynamic pressure P is proportional to density ρ so that a less dense gas will allow higher velocities at the same pressure, leading to higher operating speed with more modest increases in power levels. Thus, low viscosity and density are very helpful. Finally, by using gases which support a higher acoustic velocity, the power losses involved in supersonic flow are avoided until higher speeds are reached, again leading to improved efficiencies at higher speeds. One corollary of such thinking is that the same gas at lower static pressure leads to improved performance.

Speed Criteria:

From the preceding discussions, we can see the various data handling speed criteria.

1. Element switching and returning time or output signal rise and fall time, respectively (including signal qualities, such as noise, jitter, etc.).

2. Element signal propagation delay time.

3. Circuit signal propagation delay time.

4. Effects of feedback loops (including feedback in time).

For obvious reasons, elements will not pass data fed to them faster than switching and returning times will permit, since switching and returning will not occur or occur only incompletely (lowered gain).

Element signal propagation delay times determine the maximum rate at which signals may be fed back, since a loop may not accept a new signal until the original one has propagated completely around the loop.

Circuits and complete systems [illegible] and loops within loops, and circuit propagation [illegible] computed from the delay times through these. [illegible] operated in closed loop manner, the system's [illegible] time (information processing time) [illegible] handling rate of the system, for the same reasons [illegible] elements and feedback loops.

A simple example will clarify the [illegible]. In Figure 1B, a flip-flop may or may not accept an input [illegible] particular input, depending on the state of its outputs. [illegible] is fed back to inhibit a gate of the input. [illegible] signal must have passed through the gate, the flip-flop, the feedback loop and into the gate again before the next signal [illegible] at the gate input. Therefore, the complete loop delay [illegible] minimum time period between successive signal pairs. [illegible] example of a feedback which could be called "in time" [illegible] which has exactly the same effect. It is the "CARRY" [illegible] parallel adder circuit. A correct output signal (in the respective code) is not available until the lowest significance adder has [illegible] its output signals, has fed back any CARRY to the next higher significance adder, and so on, until all CARRY signals have been processed. Therefore, this feedback for each individual CARRY is equivalent to a feedback to the input of the adder, and the operation is performed serially. As a result, the total propagation delay time is the sum of all loop delays and no new signal should be accepted until correct output (sum) becomes available after this delay time.

Boundaries:

Extreme boundaries may be placed upon Pure Fluid digital data handling speeds based on the discussed criteria.

We are postulating an imaginary miniaturized circuit element, comprising a single feedback path of length 0.1 inches and a signal path length through this element of 0.033 inches. Further, let us assume that signals propagate at the speed of sound in air (13.3 inches per millisecond) throughout the complete loop of a total length of 0.133 inches (= circular loop of 0.043" dia.). This would result in a total delay time of 10 microseconds. For a clarification, let us assume that the feedback loop is the internal feedback (boundary layer effect) of a flip-flop which ensures bistable operations (see Fig. 6).

Fig. 6

The total delay time of 10 microseconds means that an input pulse must be at least 10 microseconds wide to assure distortion. Furthermore, finite rise and fall times have to be considered. As mentioned earlier, these times could be of the magnitude of the switching delay time, and we will assume them to increase the overall pulse width (50% amplitude) to a minimum of 25 microseconds.

This means that discrete information bits cannot be processed faster than one per 20 microseconds or at a maximum rate of 50,000 bits per second via such an imaginary element.

Let us now take a look at the next significant circuit component. Typical subcircuits, as shown for example in Figures 1B or 1C, containing a simple external feedback loop over one or two elements, drastically decrease the acceptable bit rate. For example, the single input flip-flop circuit with three elements (Fig. 1B) accepts an input pulse of 20 microseconds width at one of its gates. After an assumed 10 microseconds (element propagation delay), this signal appears at the gate output. From there it has to be propagated through a channel to the flip-flop input. The flip-flop again causes a 10-microsecond delay before the signal appears at its output. From there, it is fed back to the gate input through a channel. If we again assume a sub-miniature construction with both connecting channels (feedback loop) of 0.133 inches long each, or a total of 0.266 inches, we obtain a delay time of 20 microseconds plus another 20 microseconds through the two elements. Obviously, this subcircuit may not accept the next signal until the first 20-microsecond pulse has been processed (passed wholly around the loop), which takes a total of 40 microseconds. Therefore, such a circuit must be fed with pulses of a minimum of 20 microsecond width, and it will not accept such signals faster than at 40 microsecond intervals, or at rates of 25,000 bits per second.

Figure 1A shows a typical data processing circuit, a parallel adder, where each block can represent for the simplest case a binary

"THREE INPUT ADDER," containing [illegible] series to perform its function. Using [illegible] as before, and speed of sound (in air), [illegible] seconds delay through such a circuit. Thus, a [illegible] available after this time at its output. After [illegible] (0.8 inches), this CARRY signal reaches the input [illegible] for the next higher significance digit. A total of 1.0 [illegible] elapses for the passage of a CARRY for a single stage. This [illegible] multiplied by the number of binary digits required in the arithmetical operation of this circuit. If we assume an average of 15 binary digits, we can say that the total time for the number of additions within the [illegible] circuit to be completed will be 1540 microseconds (14 CARRY [illegible]). This means that only after this time will the sum be correct at the [illegible] outputs, and a new parallel input of a number must not be [illegible] until the last CARRY has been processed at least for a time of [illegible] microseconds, giving a minimum time between successive parallel inputs of [illegible] milliseconds. This is equivalent to a maximum processing rate of [illegible] numbers or parallel bits per second (or that many additions per second).

A complete digital data handling system for even simple tasks entails a considerable number of circuits of the order of the one given above, where all interconnections cannot be as short as the one given, and where feedback signals between circuits and subsystems result in still larger delay loops. Furthermore, successive system input data often depend on the results of the preceding processed output data, such that the complete system forms a feedback loop together with external components. Thus, one might consider a small hypothetical system of, for example, ten subcircuits in series (could also mean repetitive circuit processes) with data handling rates as given above, and consider it a closed loop containing an external component delay of the order of the system delay. Such a system could handle data at maximum rates of approximately 33 input signals per second (data processing time of 30 milliseconds).

Considering that a ratio of one to a million exists between the signal propagation velocities in air and electrical signal propagation velocities in conductors, it could be pointed out that a 15 bit addition time in a fluid circuit of 1.5 milliseconds might be analogous to a 15 bit addition time of 1.5 nanoseconds in an electronic circuit, which is not exactly current practice yet. Current electronic computation times for addition are at least three to four orders of magnitude longer than this.

Recapitulating the digital data handling speed [illegible], it is imperative that circuit and system [illegible] when speed is required. Individual [illegible] such as multi-megacycle rates, do not tell the [illegible] misleading.

It will be [illegible] propagate in all channels and particularly [illegible] speed of sound, lengths of channels or [illegible] able, etc. However, the used [illegible] and illuminate the problems to be considered.

Referring back to [illegible] switching times, element [illegible] etc. are at best of the [illegible] second for practical [illegible] This is one to two orders of magnitude [illegible] boundary case. A comparable 16 bit parallel addition time that presently take up to 150 milliseconds and the complete system [illegible] quoted earlier may only accept input numbers at intervals of [illegible] seconds.

As pointed out earlier, many parameters affect element and circuit speed; the fluid medium, absolute pressure levels, power levels, physical sizes, etc. The example for the extreme boundary case already utilized very small sizes. Additionally, one might consider Helium or Hydrogen as operating fluids and supersonic flow conditions to increase signal propagation speeds. Resulting boundary values for speed capabilities might thus be improved further by an order of magnitude at the expense of exorbitant power consumption, special element designs, and exotic packaging and peripheral construction.

IMPROVEMENTS

It seems appropriate to return to realistic and practical concepts at this stage, having dwelled on hypothetical considerations for a while. Ordinary, general purpose devices, suitable for multitudes of applications of Pure Fluid Systems may be improved to provide increased digital data handling speeds.

Two major areas are available for [illegible]:

1. Element speed improvement.
2. Circuit and system logic design.

Element speed improvement [illegible] which every element performance [illegible] within a system. It is beyond the [illegible] such methods. However, one [illegible] pointed out.

Conventional circuit [illegible] different computer [illegible] versal elements, such as NOR [illegible] when suitably interconnected. [illegible] built where system speeds are not [illegible] is not recommended for [illegible] functions can be performed in [illegible] compatible logic elements are available to form a circuit, [illegible] can overall functions be performed.

For example, it [illegible] flop, rather than a flip-flop circuit [illegible] in Fig. 1C). Also, [illegible] AND logic element than [illegible] inverters (NOR logic [illegible] apply to any logic [illegible] system functions with [illegible] are unable to [illegible] some of the functions are [illegible] complex circuits [illegible] functions, such as NOR, OR, NAND, AND, EXCLUSIVE OR, FLIP-FLOP, COUNTER, AND NOT, HALF ADDER, etc. Furthermore, [illegible] that fan-in and fan-out [illegible] as possible to avoid circuit delays due to additional OR, AND, and amplifier elements respectively.

Circuit and system logic design, if motivated by [illegible], can produce impressive speed improvement and conservation [illegible]. It is imperative that logic functions are performed in parallel, wherever possible and whenever this method results in speed improvement. Every possible trick should be considered to achieve faster processing, including approximation methods for arithmetic operations, and [illegible] hybrid

(analog) system functions. There is little merit to a speed that does not appear obvious. Unconventional circuit and logic design that provides unsuspected speed advantages, and a design philosophy oriented in such a direction can prove profitable.

APPLICATIONS

Pure fluid digital system applications may be divided into two categories, depending on the relationship between required speed requirements and the difficulty of fulfilling these requirements:

1. Applications where speed presents no problems.

2. Applications where only unconventional approaches and exceptional emphasis on high speed operation can suit the requirements.

The first category requires no special explanation. A very large application field is still open, and only rarely has equipment been developed for such purposes. An example of such an application is given in Figures 7 and 8, which show the front view and the rear view (housing removed), respectively, of a digital process sequence control system breadboard model. A number of operations are controllable in any sequence and in any combination, while each operation generates a feedback signal on completion, to initiate further sequence steps. The system is manually programmed and operates completely automatically thereafter. Sequencing times are very long and no speed problems arise.

The second category of applications covers a multitude of current projects. Considerable effort is being spent on solving the various speed problems. A simple example of such a system is a Pure Fluid Timer. Accurate and variable timing of operations is required. A timer may fundamentally consist of a time base (oscillator of constant frequency), and a frequency divider or counter, and a decoder. Variable elapsed times may be obtained by initially setting the counter to particular counts and decoding a fixed combination. Alternately, a variable decoder may be used or a number of decoders (one for every time interval). A combination of such methods may also be utilized.

A Pure Fluid Timer of such a variable [illegible] is shown in breadboard model form. A variable delay [illegible] facility which can be programmed by either hand [illegible] punched card (foreground).

The operating speed criteria [illegible] accuracy and resolution requirements. A signal propagation delay [illegible] substantially less than the resolution. Furthermore, the [illegible] the decoder must be constant for all settings and sufficiently [illegible] the resolution. In many cases, timers are [illegible] loop system. In such cases, the initiation of successive [illegible] operations is delayed by the processing time and by the [illegible] loop. It can be seen that accuracy and resolution for a variable [illegible] depends also on the total delay time, whereas a fixed timer could be calibrated, and thus take delays into account.

If a variable timer is intended, for example, to provide a resolution and accuracy of 0.01 second for any selected elapsed time, and the counter consists of a number of serially connected electronic circuits with a delay time of 1 millisecond per stage, a total counter ripple delay of 10 milliseconds will result from 10 stages of count. This means that a decoded very short time interval will be within the specification and a longer time interval, utilizing 9 counter output stages, will be only just within the specification. However, if there are more than 9 stages and a time interval is to be decoded utilizing more outputs, the decoder may not be able to function anymore. The least significant counter output (resolving 0.01 second intervals) has changed before the most significant output provides the correct signal (i.e., more than 0.009 seconds later).

Therefore, the logic of such a system has to be designed carefully to cater for such effects, as have been considered in the shown timer system. One way to avoid these effects is to delay the less significant output signals by relevant amounts, such that all output signals are received by the decoder simultaneously. A subtraction of the resulting maximum delay from the timer settings has to be performed to provide the required accuracies, and total elapsed times shorter than the maximum system delay cannot be utilized.

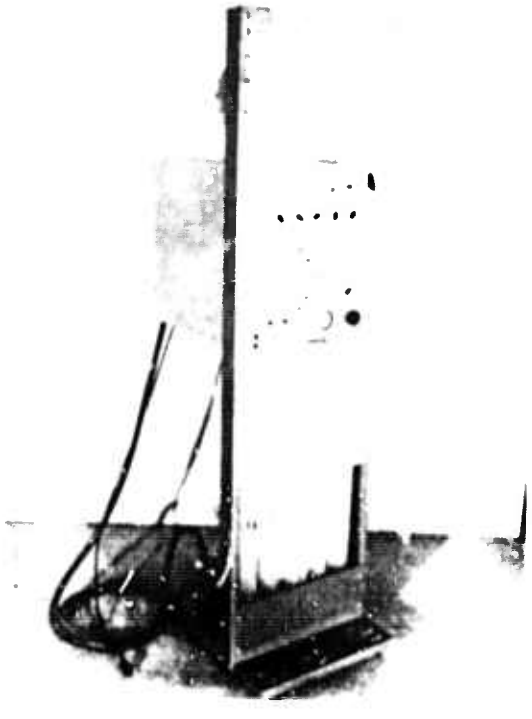

Fig. 7 Front View

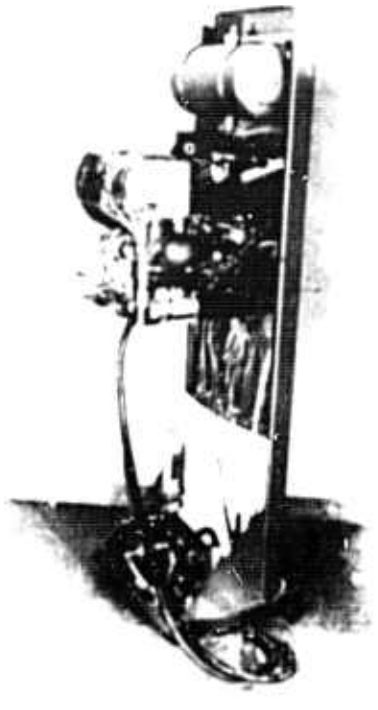

Fig. 8 Internal Rear View

Fig. 9 Pure Fluid Digital Timer System

CONCLUSIONS

This [illegible] Pure Fluid [illegible] operation [illegible] capabilities [illegible] boundaries are placed [illegible] for 15 bit binary [illegible] son with present state-of-the-art capabilities, which are one to two orders of magnitude slower for a similar operation.

Parameters affecting speed capabilities have been discussed, such as sizing, power levels, fluid media, and logic circuit design. Two examples of practical applications of Pure Fluid Digital Systems are given.

It is hoped that this paper will encourage meaningful performance specifications and critical questioning of such specifications with respect to data handling speeds with Pure Fluid Systems.

UNCLASSIFIED
Security Classification

DOCUMENT CONTROL DATA - R&D

(Security classification of title, body of abstract and indexing annotation must be entered when the overall report is classified)

1 ORIGINATING ACTIVITY (Corporate author) Harry Diamond Laboratories, Washington,D.C. 20438	2a REPORT SECURITY CLASSIFICATION UNCLASSIFIED 2b GROUP

3 REPORT TITLE
PROCEEDINGS OF THE FLUID AMPLIFICATION SYMPOSIUM--Volume II, October 1965

4 DESCRIPTIVE NOTES (Type of report and inclusive dates)
Compilation of 17 papers on fluidic theory and devices

5 AUTHOR(S) (Last name, first name, initial)

6 REPORT DATE October 1965	7a TOTAL NO OF PAGES 414	7b NO OF REFS
8a CONTRACT OR GRANT NO b PROJECT NO DA-1P010501A001 c AMCMS Code 5011.11.71200 d HDL Proj. 31100	9a ORIGINATOR'S REPORT NUMBER(S) 9b OTHER REPORT NO(S) (Any other numbers that may be assigned this report)	

10 AVAILABILITY/LIMITATION NOTICES
Qualified requesters may obtain copies of this report from DDC. DDC release to Clearinghouse for Federal Scientific and Technical Information is authorized.

11 SUPPLEMENTARY NOTES	12 SPONSORING MILITARY ACTIVITY Hq. AMC

13 ABSTRACT

This document is the second of five volumes, covering the October 1965 symposium on fluid amplification at the Harry Diamond Laboratories. These volumes include 55 papers, prepared by personnel from various Government agencies, universities, and industrial firms.

DD FORM 1473 (JAN 65)

UNCLASSIFIED
Security Classification

UNCLASSIFIED

Security Classification

14 KEY WORDS	LINK A		LINK B		LINK C	
	ROLE	WT	ROLE	WT	ROLE	WT
Pneumatic control systems Fluid circuit theory Flow isolation of fluid amplifiers Fluid amplifiers--theoretical analysis						

INSTRUCTIONS

1. ORIGINATING ACTIVITY: Enter the name and address of the contractor, subcontractor, grantee, Department of Defense activity or other organization *(corporate author)* issuing the report.

2a. REPORT SECURITY CLASSIFICATION: Enter the overall security classification of the report. Indicate whether "Restricted Data" is included. Marking is to be in accordance with appropriate security regulations.

2b. GROUP: Automatic downgrading is specified in DoD Directive 5200.10 and Armed Forces Industrial Manual. Enter the group number. Also, when applicable, show that optional markings have been used for Group 3 and Group 4 as authorized.

3. REPORT TITLE: Enter the complete report title in all capital letters. Titles in all cases should be unclassified. If a meaningful title cannot be selected without classification, show title classification in all capitals in parenthesis immediately following the title.

4. DESCRIPTIVE NOTES: If appropriate, enter the type of report, e.g., interim, progress, summary, annual, or final. Give the inclusive dates when a specific reporting period is covered.

5. AUTHOR(S): Enter the name(s) of author(s) as shown on or in the report. Enter last name, first name, middle initial. If military, show rank and branch of service. The name of the principal author is an absolute minimum requirement.

6. REPORT DATE: Enter the date of the report as day, month, year, or month, year. If more than one date appears on the report, use date of publication.

7a. TOTAL NUMBER OF PAGES: The total page count should follow normal pagination procedures, i.e., enter the number of pages containing information.

7b. NUMBER OF REFERENCES: Enter the total number of references cited in the report.

8a. CONTRACT OR GRANT NUMBER: If appropriate, enter the applicable number of the contract or grant under which the report was written.

8b, 8c, & 8d. PROJECT NUMBER: Enter the appropriate military department identification, such as project number, subproject number, system numbers, task number, etc.

9a. ORIGINATOR'S REPORT NUMBER(S): Enter the official report number by which the document will be identified and controlled by the originating activity. This number must be unique to this report.

9b. OTHER REPORT NUMBER(S): If the report has been assigned any other report numbers *(either by the originator or by the sponsor)*, also enter this number(s).

10. AVAILABILITY/LIMITATION NOTICES: Enter any limitations on further dissemination of the report, other than those imposed by security classification, using standard statements such as:

(1) "Qualified requesters may obtain copies of this report from DDC."

(2) "Foreign announcement and dissemination of this report by DDC is not authorized."

(3) "U. S. Government agencies may obtain copies of this report directly from DDC. Other qualified DDC users shall request through

_____ _____."

(4) "U. S. military agencies may obtain copies of this report directly from DDC. Other qualified users shall request through

_____."

(5) "All distribution of this report is controlled. Qualified DDC users shall request through

_____ _____."

If the report has been furnished to the Office of Technical Services, Department of Commerce, for sale to the public, indicate this fact and enter the price, if known.

11. SUPPLEMENTARY NOTES: Use for additional explanatory notes.

12. SPONSORING MILITARY ACTIVITY: Enter the name of the departmental project office or laboratory sponsoring *(paying for)* the research and development. Include address.

13. ABSTRACT: Enter an abstract giving a brief and factual summary of the document indicative of the report, even though it may also appear elsewhere in the body of the technical report. If additional space is required, a continuation sheet shall be attached.

It is highly desirable that the abstract of classified reports be unclassified. Each paragraph of the abstract shall end with an indication of the military security classification of the information in the paragraph, represented as *(TS)*, *(S)*, *(C)*, or *(U)*.

There is no limitation on the length of the abstract. However, the suggested length is from 150 to 225 words.

14. KEY WORDS: Key words are technically meaningful terms or short phrases that characterize a report and may be used as index entries for cataloging the report. Key words must be selected so that no security classification is required. Identifiers, such as equipment model designation, trade name, military project code name, geographic location, may be used as key words but will be followed by an indication of technical context. The assignment of links, rules, and weights is optional.